

Markus Bursch

Evaluation and Application of Efficient Quantum Chemical Methods for Sophisticated Simulation of Inorganic Molecular Chemistry



Dissertation

Evaluation and Application of Efficient Quantum Chemical Methods for Sophisticated Simulation of Inorganic Molecular Chemistry

Dissertation

zur

Erlangung des Doktorgrades (Dr. rer. nat.)

der

Mathematisch-Naturwissenschaftlichen Fakultät

der

Rheinischen Friedrich-Wilhelms-Universität Bonn

vorgelegt von

Markus Bursch

aus Bonn

–2021–

Dekan: Prof. Dr. Walter Witke

Erster Gutachter: Prof. Dr. Stefan Grimme

Zweiter Gutachter: Prof. Dr. Thomas Bredow

Tag der Disputation: 05.10.2021

Erscheinungsjahr: 2021

Angefertigt mit Genehmigung der Mathematisch-Naturwissenschaftlichen Fakultät der Rheinischen Friedrich-Wilhelms-Universität Bonn

In Liebe und Dankbarkeit meiner Familie gewidmet

*"Gib mir die Gelassenheit, Dinge hinzunehmen, die ich nicht ändern kann,
den Mut, Dinge zu ändern, die ich ändern kann,
und die Weisheit, das eine vom anderen zu unterscheiden."*

– Reinhold Niebuhr –

Publications

Parts of this thesis have been published in peer-reviewed journals:

1. Köring, L.; Sitte, N. A.; Bursch, M.; Grimme, S.; Paradies, J. "Hydrogenation of Secondary Amides Using Phosphane Oxide and Frustrated Lewis Pair Catalysis", *Chem. Eur. J.* **2021**, *27*, 14179–14183.
2. Bursch, M.; Kunze, L.; Vibhute, A. M.; Hansen, A.; Sureshan, K. M.; Jones, P. G.; Grimme, S.; Werz, D. B. "Quantification of Non-covalent Interactions in Azide-Pnictogen, -Chalcogen, and -Halogen Contacts", *Chem. Eur. J.* **2021**, *27*, 4627–4639.
3. Bursch, M.; Hansen, A.; Pracht, P.; Kohn, J. T.; Grimme, S. "Theoretical Study on Conformational Energies of Transition Metal Complexes", *Phys. Chem. Chem. Phys.* **2021**, *23*, 287–299.
4. Bursch, M.; Gasevic, T.; Stückrath, J. B.; Grimme, S. "Comprehensive Benchmark Study on the Calculation of ^{29}Si NMR Chemical Shifts", *Inorg. Chem.* **2021**, *60*, 272–285.
5. Bursch, M.; Neugebauer, H.; Grimme, S. "Structure Optimisation of Large Transition-Metal Complexes with Extended Tight-Binding Methods", *Angew. Chem. Int. Ed.* **2019**, *131*, 11195–11204.
6. Sitte, N. A.; Bursch, M.; Grimme, S.; Paradies, J. "Frustrated Lewis Pair Catalyzed Hydrogenation of Amides: Halides as Active Lewis Base in the Metal-Free Hydrogen Activation", *J. Am. Chem. Soc.* **2019**, *141*, 159–162.
7. Queen, J. D.; Bursch, M.; Seibert, J.; Maurer, L. R.; Ellis, B. D.; Fettinger, J. C.; Grimme, S.; Power, P. P. "Isolation and Computational Studies of a Series of Terphenyl Substituted Diplumbynes with Ligand Dependent Lead–Lead Multiple-Bonding Character", *J. Am. Chem. Soc.* **2019**, *141*, 14370–14383.
8. Stepen, A. J.; Bursch, M.; Grimme, S.; Stephan, D. W.; Paradies, J. "Electrophilic Phosphonium Cation-Mediated Phosphane Oxide Reduction Using Oxalyl Chloride and Hydrogen", *Angew. Chem. Int. Ed.* **2018**, *57*, 15253–15256.
9. McCrea-Hendrick, M. L.; Bursch, M.; Gullett, K. L.; Maurer, L. R.; Fettinger, J. C.; Grimme, S.; Power, P. P. "Counterintuitive Interligand Angles in the Diaryls $\text{E}\{\text{C}_6\text{H}_3\text{-2,6-(C}_6\text{H}_2\text{-2,4,6-}i\text{Pr}_3)_2\}_2$ (E = Ge, Sn, or Pb) and Related Species: The Role of London Dispersion Forces", *Organometallics* **2018**, *37*, 2075–2085.

10. Bursch, M.; Hansen, A.; Grimme, S. "Fast and Reasonable Geometry Optimization of Lanthanoid Complexes with an Extended Tight Binding Quantum Chemical Method", *Inorg. Chem.* **2017**, *56*, 12485–12491.
11. Teichmann, J.; Bursch, M.; Köstler, B.; Bolte, M.; Lerner, H.-W.; Grimme, S.; Wagner, M. "Trapping Experiments on a Trichlorosilanide Anion: a Key Intermediate of Halogenosilane Chemistry", *Inorg. Chem.* **2017**, *56*, 8683–8688. (ACS AuthorChoice)

Further publications:

12. Spicher, S.; Bursch, M.; Grimme, S. "Efficient Calculation of Small Molecule Binding in Metal–Organic Frameworks and Porous Organic Cages", *J. Phys. Chem. C* **2020**, *124*, 27529–27541.
13. Vibbert, H. B.; Neugebauer, H.; Norton, J. R.; Hansen, A.; Bursch, M.; Grimme, S. "Hydrogen Atom Transfer Rates from Tp-Containing Metal Hydrides to Trityl Radicals", *Can. J. Chem.* **2020**, *99*, 216–220.
14. Neugebauer, H.; Bohle, F.; Bursch, M.; Hansen, A.; Grimme, S. "Benchmark Study of Electrochemical Redox Potentials Calculated with Semiempirical and DFT Methods", *J. Phys. Chem. A* **2020**, *124*, 7166–7176.
15. Georg, I.; Bursch, M.; Stückrath, J. B.; Alig, E.; Bolte, M.; Lerner, H.-W.; Grimme, S.; Wagner, M. "Building up Strain in One Step: Synthesis of an Edge-Fused Double Silacyclobutene from an Extensively Trichlorosilylated Butadiene Dianion", *Angew. Chem. Int. Ed.* **2020**, *59*, 16181–16187.
16. Scholz, A. S.; Massoth, J. G.; Bursch, M.; Mewes, J.-M.; Hetzke, T.; Wolf, B.; Bolte, M.; Lerner, H.-W.; Grimme, S.; Wagner, M. "BNB-Doped Phenalenyls: Modular Synthesis, Optoelectronic Properties, and One-Electron Reduction", *J. Am. Chem. Soc.* **2020**, *142*, 11072–11083.
17. Schaub, T. A.; Prantl, E. A.; Kohn, J. T.; Bursch, M.; Marshall, C. R.; Leonhardt, E. J.; Lovell, T. C.; Zakharov, L. N.; Brozek, C. K.; Waldvogel, S. R.; Grimme, S.; Jasti, R. "Exploration of the Solid-State Sorption Properties of Shape-Persistent Macrocyclic Nanocarbons as Bulk Materials and Small Aggregates", *J. Am. Chem. Soc.* **2020**, *142*, 8763–8775.
18. Dohm, S.; Bursch, M.; Hansen, A.; Grimme, S. "Semiautomated Transition State Localization for Organometallic Complexes with Semiempirical Quantum Chemical Methods", *J. Chem. Theory Comput.* **2020**, *16*, 2002–2012. (Highlighted in [Computational Chemistry Highlights](#))
19. Gunasekara, T.; Abramo, G. P.; Hansen, A.; Neugebauer, H.; Bursch, M.; Grimme, S.; Norton, J. R. "TEMPO-Mediated Catalysis of the Sterically Hindered Hydrogen Atom Transfer Reaction between (C₅Ph₅)Cr(CO)₃H and a Trityl Radical", *J. Am. Chem. Soc.* **2019**, *141*, 1882–1886.
20. Bursch, M.; Caldeweyher, E.; Hansen, A.; Neugebauer, H.; Ehlert, S.; Grimme, S. "Understanding and Quantifying London Dispersion Effects in Organometallic Complexes", *Acc. Chem. Res.* **2019**, *52*, 258–266.

21. Malissa, H.; Miller, R.; Baird, D. L.; Jamali, S.; Joshi, G.; Bursch, M.; Grimme, S.; van Tol, J.; Lupton, J. M.; Boehme, C. "Revealing Weak Spin-Orbit Coupling Effects on Charge Carriers in a π -Conjugated Polymer", *Phys. Rev. B* **2018**, *97*, 161201(R).
22. Georg, I.; Teichmann, J.; Bursch, M.; Tillmann, J.; Endeward, B.; Bolte, M.; Lerner, H.-W.; Grimme, S.; Wagner, M. "Exhaustively Trichlorosilylated C₁ and C₂ Building Blocks: Beyond the Müller-Rochow Direct Process", *J. Am. Chem. Soc.* **2018**, *140*, 9696–9708.
23. Chen, G.-Q.; Kehr, G.; Daniliuc, C. G.; Bursch, M.; Grimme, S.; Erker, G. "Intermolecular Redox-Neutral Amine C-H Functionalization Induced by the Strong Boron Lewis Acid B(C₆F₅)₃ in the Frustrated Lewis Pair Regime", *Chem. Eur. J* **2017**, *23*, 4723–4729.
24. Ye, K.-Y.; Bursch, M.; Qu, Z.-W.; Daniliuc, C. G.; Grimme, S.; Kehr, G.; Erker, G. "Reversible Formylborane/SO₂ Coupling at a Frustrated Lewis Pair Framework", *Chem. Commun.* **2017**, *53*, 633–635.
25. Zell, D.; Müller, V.; Dhawa, U.; Bursch, M.; Rubio Presa, R.; Grimme, S.; Ackermann, L. "Mild Cobalt(III)-Catalyzed Allylative C–F/C–H Functionalizations at Room Temperature", *Chem. Eur. J.* **2017**, *23*, 12145–12148.
26. Zell, D.; Bursch, M.; Müller, V.; Grimme, S.; Ackermann, L. "Full Selectivity Control in Cobalt(III)-Catalyzed C-H Alkylations by Switching of the C-H Activation Mechanism", *Angew. Chem. Int. Ed.* **2017**, *56*, 10378–10382.
27. Zell, D.; Dhawa, U.; Müller, V.; Bursch, M.; Grimme, S.; Ackermann, L. "C–F/C–H Functionalization by Manganese(I) Catalysis: Expedient (Per)Fluoro-Allylations and Alkenylations", *ACS Catal.* **2017**, *7*, 4209–4213.
28. Jian, Z.; Kehr, G.; Daniliuc, C. G.; Wibbeling, B.; Wiegand, T.; Siedow, M.; Eckert, H.; Bursch, M.; Grimme, S.; Erker, G. "CO-Reduction Chemistry: Reaction of a CO-Derived Formylhydridoborate with Carbon Monoxide, with Carbon Dioxide, and with Dihydrogen", *J. Am. Chem. Soc.* **2017**, *139*, 6474–6483.

Presentations:

1. Poster: "Structure Optimisation of Large Transition Metal Complexes with Extended Tight-Binding Methods", *10th Triennial Congress of the International Society for Theoretical Chemical Physics (ISTCP)*, **2019**, Tromsø, Norway.
2. Talk: "Structure Optimisation of Large Transition Metal Complexes with Extended Tight-Binding Methods", *Vrije Universiteit Amsterdam*, **2019**, Amsterdam, Netherlands.
3. Poster: "Counterintuitive Interligand Angles in the Diaryls E{C₆H₃-2,6-(C₆H₂-2,4,6-iPr₃)₂}₂ (E = Ge, Sn, or Pb) and Related Species: The Role of London Dispersion Forces", *52nd Symposium on Theoretical Chemistry (STC)*, **2018**, Halle (Saale), Germany.

4. Poster: "Counterintuitive Interligand Angles in the Diaryls $E\{C_6H_3-2,6-(C_6H_2-2,4,6-iPr_3)_2\}_2$ (E = Ge, Sn, or Pb) and Related Species: The Role of London Dispersion Forces", *BIGS Chemistry Summer School*, **2018**, Bonn, Germany.
5. Talk: "Versatile Applications of an Extended Tight-Binding Quantum Chemical Method", *Max-Planck-Institut for Chemical Energy Conversion*, **2018**, Mülheim an der Ruhr, Germany.
6. Talk: "Fast and Reasonable Geometry Optimization of Lanthanoid Complexes with an Extended Tight-Binding Quantum Chemical Method", *BIGS Chemistry Summer School*, **2018**, Bonn, Germany.
7. Poster: "Fast and Reasonable Geometry Optimization of Lanthanoid Complexes with an Extended Tight-Binding Quantum Chemical Method", *International Symposium – Perspectives in Hypovalent Chemistry, Collaborative Research Center 813 (SFB813)*, **2017**, Bonn, Germany.
8. Poster: "Fast and Reasonable Geometry Optimization of Lanthanoid Complexes with an Extended Tight-Binding Quantum Chemical Method", *11th Triennial Congress of the World Association of Theoretical and Computational Chemists (WATOC)*, **2017**, Munich, Germany.
9. Poster: "GFN-xTB: A Versatile Utility Tool in Computational Chemistry", *JCF Frühjahrssymposium*, **2017**, Mainz, Germany.
10. Poster: "DFT-D3 Mechanistic Studies on Co(III)-catalyzed Hydroarylations", *52nd Symposium on Theoretical Chemistry (STC)*, **2016**, Bochum, Germany.

Abstract

This thesis is devoted to the evaluation and application of efficient quantum chemical methods for the simulation of inorganic molecular chemistry. These methods include dispersion corrected density functional theory (DFT-D) and semi-empirical electronic structure methods, which represent a beneficial compromise of computational speed and accuracy and can be applied to large systems with hundreds to thousands of atoms. Nevertheless, with increasing size and complexity of the investigated system, the number of reasonably applicable methods decreases rapidly. Especially semi-empirical quantum mechanical (SQM) methods are often not universally applicable due to incomplete parametrizations or conceptual shortcomings. Despite the desirable properties of efficient SQM methods, the so-called parametric methods (PM x) were for a long time the only more widely applicable representatives. This changed with the more recently developed extended tight binding methods of the GFN n -xTB family which are parametrized for a major part of the periodic table up to radon ($Z = 86$). Although the conception of the GFN n -xTB methods is generally promising, the performance for more exotic chemical systems or in combination with other methods to enable new efficient workflows for the computation of complex chemical properties, has yet to be examined. Therefore, the first part of this thesis deals with the application of the GFN n -xTB methods for the calculation of structures of large transition metal and lanthanoid complexes which are of high interest for various fields of modern chemistry. In the course of this, new comprehensive test scenarios are developed for testing the GFN n -xTB methods and supporting future method development. Such benchmark sets were not available in this form in the literature and are absolutely fundamental for an assessment of new methods. This evaluation is further extended to thermochemical properties, such as conformational energies of transition metal complexes for which the GFN n -xTB methods are compared to a large number of high-level double-hybrid DFT and local coupled cluster reference energies. It is shown that the GFN n -xTB methods yield good molecular geometries for a variety of challenging lanthanoid and transition metal complexes at a fraction of computation time compared to conventional DFT methods. In general, the GFN n -xTB methods outperform the only comparable competitor, the PM x methods by far in all aspects. This is specifically reflected by high success rates of the geometry optimizations for GFN1- and GFN2-xTB. The robust geometry optimization of such complexes, is further used in the context of automated sampling of the low energy conformation space. For the calculations of conformational energies, the GFN n -xTB methods outperform the PM x methods and yield reasonable energetic rankings, even though the accuracy of also evaluated composite DFT methods like B97-3c is not reached. Nevertheless, the unrivaled strength of combining GFN n -xTB and efficient composite DFT methods in the context of conformer sampling and energetic ranking is demonstrated. Based on the insights regarding the robust geometry optimization and reasonable energy calculations, the GFN n -xTB and DFT-3c methods are applied to chemical

problems in the field of frustrated Lewis pair (FLP) chemistry. A combination of fast GFNn-xTB based reaction path simulation and final geometry optimization with PBEh-3c is used to elucidate complex reaction mechanisms of interrelated FLP catalyzed hydrogenation reactions, for which final free energies are calculated at high (double-)hybrid DFT level of theory. This demonstration of the capabilities of reliable SQM/DFT-3c based workflows for mechanistic studies leads the way for future investigations involving even larger systems composed of various elements throughout the periodic table.

The last part of this thesis is accordingly devoted to inorganic main group chemistry, focusing on the group 14 elements. Here, in particular the role of London dispersion on bonding and structural features is investigated. This is demonstrated for various examples from inorganic main group chemistry, including the inorganic Lewis pair $[I_3Si-BI_3]^-$ as well as heavy analogues of carbenes and alkynes. For the latter, the GFNn-xTB methods are further used to investigate the structural flexibility of the Pb-Pb moiety and the consequences on structural and spectroscopic properties. It is shown, that the usually assumed picture of a rigid multiply bonded region as it is found in alkynes does not hold true for the situation in diplumbynes for which the unusual bonding situation is studied in detail.

Especially in the context of inorganic main group, and more specific group 14, chemistry, hetero nucleus nuclear magnetic resonance (NMR) spectroscopy is a highly indicative and frequently applied analytic method. While the computational prediction of NMR properties with respect to 1H or ^{13}C isotopes is well studied, the comprehensive evaluation of popular DFT methods for the prediction of ^{29}Si NMR chemical shifts is lacking. Therefore this thesis also deals with a comprehensive benchmark study on the prediction of ^{29}Si NMR covering the entire structural diversity of silicon compounds. This study allows computational chemists to make a profound method choice to reliably predict ^{29}Si NMR in the future and supports further method development in the field of chemical shift prediction for silicon compounds.

The final chapter of this thesis deals with an in depth study on non-covalent interactions in azide-pnictogen, -chalcogen, and -halogen adducts. Here, DFT-D and local coupled cluster methods are applied to calculate highly accurate association energies and local energy decomposition methods are used to understand the nature of the corresponding interactions in detail. As already done for the group 14 elements, London dispersion interactions are studied in detail, highlighting their crucial importance for the investigated adducts shedding new light on the non classical coordination of these formal Lewis acid and base pairs.

Overall, this thesis establishes the foundation for future studies in the fields of inorganic main group, transition metal, and lanthanoid chemistry based on efficient combination of London dispersion corrected SQM and DFT methods. The GFNn-xTB and DFT-3c methods are shown to be a reliable and invaluable tools for computational chemists, that reduce the computational demand for various quantum chemical applications. Specifically, the GFNn-xTB methods open up the fully quantum mechanical description of inorganic molecules and reaction mechanisms at previously inaccessible scales. Further, the benchmark sets created throughout this thesis will be of inestimable value for future method development. The detailed insights into the decisive role of London dispersion interactions and the bonding situation in complex inorganic molecules will also enhance the perception on London dispersion as an indispensable aspect in the design and planning of new chemical applications.

Kurzzusammenfassung

Die vorliegende Arbeit beschäftigt sich mit der Evaluation und Anwendung effizienter quantenchemischer Methoden zur Simulation anorganischer Molekülchemie. Zu diesen Methoden zählen dispersionskorrigierte Dichtefunktionaltheorie (DFT-D) und semiempirische Elektronenstrukturmethoden. Solche Methoden stellen einen günstigen Kompromiss zwischen Geschwindigkeit und Genauigkeit dar und können auf große Systeme mit hunderten bis tausenden von Atomen angewendet werden. Nichtsdestotrotz nimmt die Anzahl brauchbarer Methoden mit zunehmender Größe und Komplexität des untersuchten Systems stark ab. Insbesondere semiempirische quantenmechanische (SQM) Methoden, sind oft durch unvollständige Parametrisierungen oder konzeptionelle Schwachpunkte nicht universell anwendbar. Trotz der erstrebenswerten Eigenschaften effizienter SQM Methoden, stellten die sogenannten parametric methods (PM x) für lange Zeit die nahezu einzigen, breit anwendbaren Vertreter dar. Dies änderte sich mit der kürzlichen Entwicklung der erweiterten Tight Binding Methoden der GFN n -xTB Methodenfamilie, welche für einen Großteil des Periodensystems bis zu Radon ($Z = 86$) parametrisiert sind. Auch wenn das Konzept der GFN n -xTB Methoden allgemein vielversprechend ist, steht eine ausführliche Evaluation ihrer Leistungsfähigkeit für exotischere Systeme oder in Kombination mit anderen Methoden im Rahmen neuer effizienter Arbeitsabläufe zur Berechnung komplexer chemischer Eigenschaften aus. Entsprechend widmet sich der erste Part dieser Dissertation der Anwendung der GFN n -xTB Methoden zur Berechnung von Strukturen großer Übergangsmetall- und Lanthanoidkomplexe, welche von hohem Interesse für vielfältige Bereiche der modernen Chemie sind. Im Zuge dessen, wurden neue umfassende Testszenarien erstellt, um eine ausgiebige Erprobung der GFN n -xTB Methoden zu ermöglichen und zukünftige Methodenentwicklungen zu unterstützen. Derartige Testsätze waren vorher nicht in der Literatur verfügbar und sind absolut fundamental für die Einschätzung neuer Methoden. Die hier durchgeführte Evaluation wird weiterhin auf thermochemische Eigenschaften ausgeweitet. So werden die GFN n -xTB Methoden in diesem Kontext mit einer großen Anzahl an hochqualitativen Doppelhybrid DFT und lokalen Coupled Cluster Referenz Konformationsenergien für Übergangsmetallkomplexe verglichen. Es wird gezeigt, dass die GFN n -xTB Methoden gute Molekülgeometrien für eine Vielzahl anspruchsvoller Lanthanoid- und Übergangsmetallkomplexe, zu einem Bruchteil der Rechenzeit konventioneller DFT Methoden liefern. Insgesamt zeigen die GFN n -xTB Methoden in jeglicher Hinsicht eine eindeutige Überlegenheit gegenüber den einzig vergleichbaren Konkurrenzmethoden der PM x Familie. Dies wird insbesondere durch die sehr hohe Erfolgsrate bei Geometrieoptimierungen mit GFN1- und GFN2-xTB deutlich. Die robuste Geometrieoptimierung solcher Komplexe wird weiterhin im Kontext automatisierter Konformerensuche genutzt. Auch für die Berechnung von Konformationsenergien übertreffen die GFN n -xTB die PM x Methoden und liefern vernünftige energetische Reihenfolgen, auch wenn die Genauigkeit der ebenfalls getesteten Komposit-

methoden wie B97-3c nicht erreicht wird. Nichtsdestotrotz, wird die unangetastete Stärke der GFNn-xTB Methoden bei Kombination mit effizienten DFT basierten Kompositmethoden bei der schnellen Berechnung von Konformationsenergien demonstriert.

Basierend auf diesen Erkenntnissen bezüglich der robusten Geometrieoptimierung und vernünftigen Berechnung von relativen Energien, werden die GFNn-xTB und DFT-3c Methoden im zweiten Teil dieser Dissertation auf chemische Probleme im Bereich der Chemie frustrierter Lewispaare (FLPs) angewendet. Eine Kombination schneller GFNn-xTB basierter Reaktionspfadsimulation und finaler Geometrieoptimierung mit PBEh-3c wird genutzt, um komplexe Reaktionsmechanismen zu untersuchen. Hierbei wird ein detaillierter Einblick in miteinander zusammenhängende, FLP katalysierte Hydrogenierungsreaktionen gewonnen. Weiterhin werden diesbezüglich Gibbs Energien auf hohem (Doppel-) hybrid DFT Niveau berechnet. Diese Demonstration der Möglichkeiten zuverlässiger SQM/DFT-3c basierter Arbeitsabläufe, ebnet den Weg für zukünftige Untersuchungen noch größerer Systeme, bestehend aus einer Vielzahl verschiedenster Elemente des Periodensystems.

Der letzte Teil dieser Dissertation behandelt entsprechend die anorganische Hauptgruppenchemie, mit Fokus auf die Elemente der Gruppe 14. Hier wird insbesondere auch die Rolle von London Dispersionswechselwirkungen bezüglich der Bindungs- und Struktureigenschaften beleuchtet. Dies wird für verschiedene Beispiele aus der anorganischen Hauptgruppenchemie gezeigt. So zum Beispiel für das anorganische Lewispaar $[I_3Si-BI_3]^-$ und schwere Homologe der Carbene und Alkine. Für letztere wird die strukturelle Flexibilität der vorhandenen Pb-Pb Einheit und dessen Konsequenzen für strukturelle und spektroskopische Eigenschaften mit Hilfe der GFNn-xTB Methoden untersucht. Es wird gezeigt, dass das typischerweise angenommene Bild einer rigiden Mehrfachbindung, wie es auch in Alkinen der Fall ist, nicht auf die ungewöhnliche Bindungssituation in Diplumbinen anwendbar ist.

Insbesondere im Bereich der anorganischen Hauptgruppenchemie, und besonders für Gruppe 14, stellt die magnetische Kernresonanzspektroskopie (NMR) an Heterokernen eine hochindikative und häufig genutzte analytische Methode dar. Während die computergestützte Berechnung von NMR Eigenschaften für 1H oder ^{13}C Isotope gut untersucht ist, fehlen systematische und umfassende Studien im Bereich der Anwendbarkeit populärer DFT Methoden zur Berechnung von ^{29}Si chemischen Verschiebungen. Entsprechend widmet sich ein Teil dieser Dissertation einer umfassenden Evaluation bezüglich der Berechnung ^{29}Si chemischer Verschiebungen unter Abdeckung der gesamten strukturellen Diversität von Siliciumverbindungen. Diese Studie ermöglicht Computerchemikern eine fundierte Methodenwahl zur zuverlässigen Vorhersage von ^{29}Si chemischen Verschiebungen und unterstützt zukünftige Methodenentwicklung im Bereich der NMR Spektroskopie anorganischer Hauptgruppenverbindungen.

Das finale Kapitel dieser Arbeit beschäftigt sich mit einer detaillierten Studie der nichtkovalenten Wechselwirkungen in Azid-Pnictogen, -Chalcogen und -Halogen Addukten. Hierbei werden moderne DFT-D und lokale Coupled Cluster Methoden genutzt um hoch genaue Assoziationsenergien zu berechnen. Die Interaktionsenergie wird darüber hinaus mittels lokaler Energiedekompositionsmethoden zerlegt um die grundlegende Natur der untersuchten Wechselwirkung zu verstehen. Wie schon für die Elemente der Gruppe 14, werden London Dispersionswechselwirkungen detailliert untersucht und ihre Wichtigkeit bezüglich der untersuchten Addukte herausgestellt. Hierbei wird neues Licht auf die

nichtklassische Koordination dieser formalen Lewis Säure-Base-Paare geworfen.

Zusammenfassend etabliert diese Dissertation die Grundlage für zukünftige Studien im Bereich der anorganischen Hauptgruppen-, Übergangsmetall- und Lanthanoidchemie basierend auf effizienten Kombinationen London dispersionskorrigierter SQM und DFT Methoden. Es wird gezeigt, dass die GFNn-xTB und DFT-3c Methoden Werkzeuge von unschätzbarem Wert sind, um den Zeitaufwand bei vielfältigen computerchemischen Anwendungen zu verringern. Insbesondere die GFNn-xTB Methoden eröffnen die voll quantenmechanische Beschreibung anorganischer Moleküle und Reaktionsmechanismen in bislang unerreichbarer Größenordnung. Darüber hinaus sind die im Rahmen dieser Arbeit konstruierten Benchmark Sätze von unschätzbarem Wert für zukünftige Methodenentwicklungen. Die detaillierten Einblicke in die entscheidende Rolle von London Dispersionswechselwirkungen und die Bindungssituation komplexer anorganischer Moleküle, werden außerdem den Blick auf London Dispersion als unvernachlässigbaren Aspekt bei der Planung und dem Design neuer chemischer Anwendungen stärken.

Contents

I. Introduction and Theoretical Background	1
1. Introduction	3
2. Theoretical Background	9
2.1. Method Overview	9
2.2. Electronic Structure Methods	9
2.2.1. Definition of the Electronic Hamiltonian	9
2.2.2. Hartree-Fock Theory and Electron Correlation	11
2.2.3. Kohn-Sham Density Functional Theory	14
2.2.4. Dispersion Corrected DFT	18
2.2.5. Semi-Empirical Quantum Mechanical Methods	22
2.3. Multi-Level Approach and General Remarks	29
II. Studies on Extended Tight Binding Methods	31
3. Geometry Optimization of Lanthanoid Complexes with an Extended Tight Binding Method	35
3.1. Introduction	36
3.2. Computational Details	37
3.3. Results and Discussion	37
3.4. Conclusion and Outlook	44
4. Structure Optimization of Large Transition-Metal Complexes with Extended Tight Binding Methods	47
4.1. Introduction	48
4.2. Results and Discussion	49
4.3. Conclusion and Outlook	57
5. Theoretical Study on Conformational Energies of Transition Metal Complexes	61
5.1. Introduction	62
5.2. The TMCONF40 Benchmark Set	64
5.3. Results and Discussion	67
5.4. Conclusion and Outlook	77

III. Quantum Chemical Studies on Frustrated Lewis Pair Catalysis	79
6. FLP Catalyzed Hydrogenation of Amides: Halides as Active Lewis Base in the Hydrogen Activation	83
6.1. Introduction	84
6.2. Results and Discussion	85
6.3. Conclusion	89
7. EPC-Mediated Phosphane Oxide Reduction Using Oxalyl Chloride and H₂	91
7.1. Introduction	92
7.2. Results and Discussion	93
7.3. Conclusion and Outlook	96
8. Hydrogenation of Secondary Amides Using Phosphane Oxide and Frustrated Lewis Pair Catalysis	97
8.1. Introduction	98
8.2. Results and Discussion	98
8.3. Conclusion	104
IV. Quantum Chemical Studies on Inorganic Main Group Chemistry	107
9. Trapping Experiments on a Trichlorosilanide Anion: a Key Intermediate of Halogenosilane Chemistry	111
9.1. Introduction	112
9.2. Results and Discussion	114
9.3. Quantum Chemical Calculations	117
9.4. Conclusion	119
10. Counterintuitive Interligand Angles in Diaryltetraylenes and Related Species: The Role of Dispersion	121
10.1. Introduction	122
10.2. Experimental Section	123
10.3. Results and Discussion	126
10.4. Computational Studies	136
10.5. Conclusion	140
11. Terphenyl Substituted Diplumbynes with Ligand Dependent Lead–Lead Multiple-Bonding Character	141
11.1. Introduction	142
11.2. Experimental Section	144
11.3. Results and Discussion	147

11.4. Computational Studies	152
11.5. Conclusion and Outlook	157
12. Benchmark Study on the Calculation of ²⁹Si NMR Chemical Shifts	161
12.1. Introduction	162
12.2. Computational Details	163
12.3. Results and Discussion	164
12.4. Conclusion and Outlook	176
13. Quantification of Non-covalent Interactions in Azide-Pnictogen, -Chalcogen, and -Halogen Contacts	179
13.1. Introduction	180
13.2. Results and Discussion	182
13.3. Conclusion and Outlook	197
V. Final Summary and Conclusion	199
VI. Appendix	I
A1. Abbreviations	II
A2. Supporting Information to Chapter 3	V
A3. Supporting Information to Chapter 4	VII
A4. Supporting Information to Chapter 5	IX
A5. Supporting Information to Chapter 6	XII
A6. Supporting Information to Chapter 7	XV
A7. Supporting Information to Chapter 8	XVIII
A8. Supporting Information to Chapter 9	XXI
A9. Supporting Information to Chapter 10	XXVII
A10. Supporting Information to Chapter 11	XXXI
A11. Supporting Information to Chapter 12	XXXVIII
A12. Supporting Information to Chapter 13	LI
Bibliography	LV

Part I.

**Introduction and Theoretical
Background**

1. Introduction

In the last decades, computational simulations have become an integral part of modern science. Especially in chemistry, where a detailed understanding of complex chemical systems is essential for targeted development, computational chemistry has emerged as a powerful and efficient tool¹⁻¹². Quantum chemical methods are particularly valuable where the limits of experimental possibilities are reached, whether due to technical limitations, physical obstacles, or even limited resources. Thus, one of the highest goals of modern computational chemistry is the reliable prediction of chemical and physical properties of a wide variety of compounds. Such predictive power can optimally be used to save resources, guide the experiment, and understand previously unexplained findings^{3,13}. Research fields that can particularly benefit in this respect include catalysis research regarding catalyst design^{3,14-21}, pharmacological drug research^{10,11,22,23} and materials research^{20,21,24,25}. In this context, the relationship between molecular structure and physical and chemical properties plays a decisive role. Most experimental methods for structure determination, such as nuclear magnetic resonance (NMR), rotational and vibrational spectroscopy, or mass spectrometry, often only provide an indirect or incomplete picture of the molecular structure. The most established methods to comprehensively elucidate the three-dimensional structure of a molecule are diffraction experiments, where classical single crystal X-ray diffraction or increasingly gas phase X-ray diffraction experiments are the most common structure characterization methods²⁶. In the analysis of crystalline structures, however, solid-state effects can have a crucial influence on the structure present, and an agreement with the molecular structure in solution or in the gas phase is not necessarily given. At this point, computational chemistry provides an efficient alternative for the theoretical study of molecular structures, further allowing structural variation of the compounds studied in a much more resource-efficient manner and with significantly less effort than by synthetic means. Since the calculation and optimization of the molecular structure is correspondingly fundamental, numerous quantum chemical methods and computational algorithms have been developed for this purpose²⁷. The most prominent of physics-based molecular simulation methods are wave function theory (WFT), Kohn-Sham density functional theory (DFT), semi-empirical quantum mechanical (SQM) and force field (FF) methods (Figure 1.1)^{4,28,29}. Each of these method classes has different strengths and weaknesses depending on its construction and the degree of approximation used. Nevertheless, due to limited computational resources, choosing an appropriate method always requires a compromise between accuracy, speed and generality (Figure 1.2). Here, particular aspects to be taken into account are the size of the system, its electronic complexity, and the desired property to be examined. Therefore, two fundamental questions must always be asked: can the necessary computational resources be afforded and can the method guarantee a sufficient quality of the result? The latter is particularly critical when the simulation of the target system is increasingly challenging due

1. Introduction

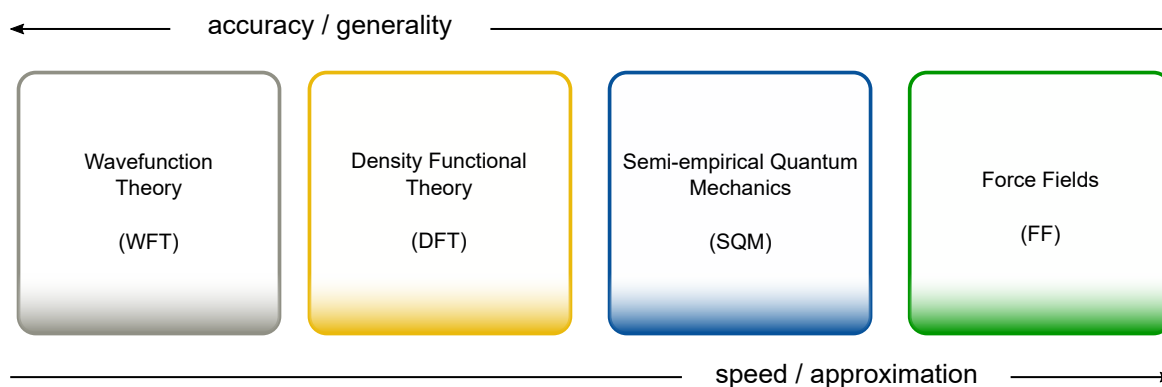


Figure 1.1.: Illustrative classification of prominent method families in terms of degree of approximation, specialization, speed, and accuracy.

to its chemical composition, size, flexibility, and complexity of its electronic structure. In such cases, the correct description of a variety of physical effects and interactions is fundamental, which makes the simulation of the complete system even more difficult. This is very often the case when transition metals, lanthanoids or heavier inorganic main group elements are involved. Molecules containing such elements often exhibit a great structural diversity that does not follow clear patterns, as it is the case in much of organic chemistry. This is mainly a consequence of the increasing relevance of orbitals of higher magnetic quantum numbers for electronic and structural properties of these compounds³⁰. Further, the chemistry of modern inorganic compounds often requires the introduction of large, sterically demanding substituents and ligands to control the reactivity and properties of the molecule. The electronic complexity can moreover result in so-called multi-reference situations, limiting the applicability of otherwise highly accurate methods that apply approximations regarding the nature of the electronic ground state. This problem correspondingly complicates the development of more efficient approximate methods for describing larger systems. Another aspect to consider is the role of relativistic effects in heavier elements. These can have a decisive influence on structural and spectroscopic properties

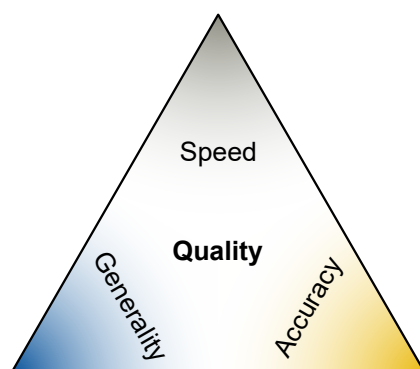


Figure 1.2.: Trade-off triangle of computational chemistry.

of the affected elements and molecules. In addition to these special problems that arise in inorganic compounds, generally important properties and interactions still have to be described correctly by computational methods. These include non-covalent interactions such as London dispersion, which plays a crucial role for structural properties of most chemical systems³¹⁻³³. Furthermore, another critical point preventing the development of reasonably accurate SQM and FF methods for inorganic chemistry is the lack of comprehensive benchmark scenarios. While numerous benchmark sets are available for a variety of properties of organic molecules³⁴⁻³⁶, the number of sets dealing with inorganic systems is significantly smaller. This lack of suitable reference data is even more crucial for molecular structures of inorganic molecules of relevant size. All of these challenges have resulted in little to no sufficiently accurate methods being developed to date that are suitable for simulating inorganic compounds of relevant size. Accordingly, the development of efficient, approximate but yet widely applicable methods in this field is particularly desirable and a close cooperation between experiment and theory to constantly improve such methods is indispensable. Nevertheless, the focus of development in the field of fast computational methods has long been on the description of very large organic molecules, such as proteins or other biomolecules. This is reflected in the large number of force fields designed exclusively for applications in bioorganic chemistry like the commonly used AMBER³⁷, CHARMM³⁸, and OPLS³⁹ force fields. The universal force field UFF by Rappe from 1992⁴⁰, the extensible and systematic force field ESFF⁴¹ and the SHAPES FF⁴² were almost the only representatives being generally applicable for transition metal complexes. Nevertheless, specialized variants like the UFF4MOF⁴³ or the MOMECC⁴⁴ FF, focusing on the optimization of metal organic frameworks, are available. The same holds for the less approximate but still very fast SQM methods^{45,46}, where MSINDO^{47,48} and the PMx⁴⁹⁻⁵² methods represented the only notable available SQM methods able to treat a significant number of transition metals. The sparsity of widely applicable and efficient methods is accordingly in strong contradiction to the immense importance of transition metal and lanthanoid complexes in diverse areas of chemistry like catalysis and life sciences. To fill this fatal gap, the family of GFNN-xTB and -FF methods⁵³⁻⁵⁷ has been developed over the last five years. These include the generic force field GFN-FF⁵⁶, as well as the density functional based tight binding methods GFN1-xTB⁵³ and GFN2-xTB⁵⁴. All these methods have been developed primarily with a focus on the name-giving core competencies, geometry optimization, frequency calculation, and non-covalent interactions, and are applicable to almost the entire periodic table of elements. Therefore, these methods conceptually allow a computational treatment of large inorganic compounds with several hundred to thousands of atoms. General and sufficiently accurate SQM and FF methods can further be used in tandem with efficient London dispersion corrected DFT methods^{31,58-60} to enable new computational chemistry work-flows, also in inorganic chemistry. The development and optimization of such processes through an interweaving of methods is particularly important. This becomes apparent from the fact, that the actual path from the conception of a project to finally answering the initial question usually requires large numbers of quantum chemical calculations, while the final calculations of the target properties often represent only the tip of the iceberg (Figure 1.3). In this context, each step leading to the full description of the chemical problem holds varying degrees of potential for efficiency optimization. Specifically, complex tasks such as conformational sampling or reaction path simulations for large molecules are common bottlenecks of modern com-

1. Introduction

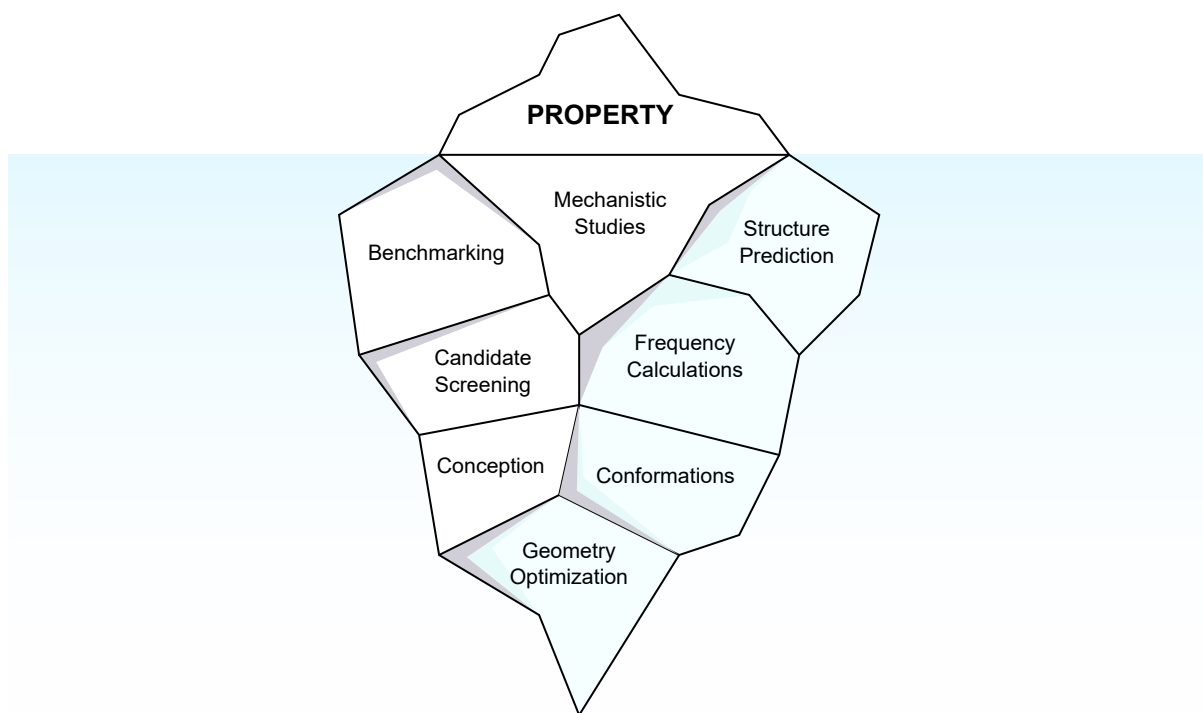


Figure 1.3.: Illustration of work time distribution of common computational chemistry applications.

putational chemistry approaches. These tasks typically demand large numbers of molecular dynamics simulations, geometry optimizations and vibrational frequency calculations which are computationally expensive, even at DFT level of theory. Even though many studies try to avoid such fundamental preliminary investigations by using single structure approaches or even starting the investigation based on experimentally determined structures, they proved indispensable for the correct prediction of a variety of molecular properties⁶¹⁻⁶⁴. Many of these processes can only be realized by the application of efficient SQM or FF methods and thus the appropriate treatment of inorganic compounds in this context was for a long time impossible or, if at all, very unreliable. At this point, the GFNn-xTB/-FF methods may represent the key to novel quantum chemical applications and studies in inorganic chemistry. Therefore, this thesis deals with the following objectives:

1. Creation of comprehensive benchmark scenarios for diverse inorganic systems of relevant molecular size.
2. Thorough testing of the new GFNn-xTB/FF methods for the geometry optimization and calculation of thermochemical properties of large inorganic molecules.
3. Pioneering the efficient combination of GFNn-xTB/FF and dispersion corrected DFT for multi-level applications in inorganic chemistry.
4. Expanding the understanding of London dispersion as an important interaction in inorganic complexes.

Overall, this thesis aims for the evaluation and application of efficient quantum chemical methods for the sophisticated simulation of inorganic molecular chemistry and the creation of a robust and comprehensive basis of test scenarios for future method developments. In this context, various subdomains and properties of inorganic compounds are studied in detail using cutting edge computational methods. These methods are being tested on an unprecedented scale, both for their independent performance and in combination with other methods to enable and optimize efficient quantum chemical investigations in various areas of inorganic chemistry.

In chapter 2 of part I, an overview of the theoretical background of selected key methods used throughout this thesis is given. The next major part deals with various necessities that pave the way for future quantum chemical work in inorganic chemistry using GFNn-xTB methods. This includes detailed assessment of the performance of GFNn-xTB and FF methods for geometry optimization of transition metal and lanthanoid complexes, as well as their applicability for the calculation of thermochemical quantities, such as reaction and conformational energies (Part II). Further, in part III, the GFNn-xTB methods are applied to investigate chemical problems in the field frustrated Lewis-pair (FLP)⁶⁵⁻⁶⁸ chemistry. Here, the GFN-xTB methods are combined with the efficient PBEh-3c⁶⁹ composite method to conduct sophisticated reaction path simulation for the elucidation of complex reaction mechanisms of metal-free dihydrogen activation reactions. In part IV, dispersion corrected density functional theory and SQM methods are used to study structural, thermochemical and spectroscopic properties of diverse inorganic compounds. These studies include the investigation of bonding situations and nuclear magnetic resonance spectroscopic chemical shifts of group 14 elements. Moreover, the role of London dispersion interactions in inorganic compounds is examined in detail. Part V finally summarizes the achievements of this thesis and provides perspectives regarding their use in future studies.

2. Theoretical Background

2.1. Method Overview

Parts of this thesis deal quantum chemical investigations supported by experimental studies involving complex experimental setups. Since the focus of this thesis is on quantum chemical studies, experimental details beyond those published directly in the respective publications, will not be discussed further. Any supplementary experimental details on the publications discussed in the following chapters can be found online in the corresponding Supporting Information materials of the original publications. In this chapter, an overview of the used computational methods is given, while the very details of the specific methods can be found in the respective original publications. This presented overview discusses the origins and basics of modern Kohn-Sham density functional theory (KS-DFT) (Sections 2.2.1–2.2.3), as well as London dispersion corrections to the same within the established DFT-D scheme. Further, composite methods based on the latter are discussed in the framework of the so-called DFT-3c concept. Subsequently, the fundamentals for semi-empirical quantum mechanical (SQM) methods intensively used in this work are described (Section 2.2.5).

2.2. Electronic Structure Methods

2.2.1. Definition of the Electronic Hamiltonian

A cornerstone of modern wave function based quantum chemical methods is the time-independent, non-relativistic Schrödinger equation (SE) (Equation 2.1)⁷⁰. The SE connects the molecular wavefunction Ψ , the energy E , and the molecular Hamiltonian \hat{H} . The latter is composed of kinetic and potential energy operators \hat{T} and \hat{V} for electrons and atomic nuclei, which are indicated by e and n , respectively (Equation 2.2). In the following, atomic units are used for clarity^{28,29,71}.

$$\hat{H}\Psi = E\Psi \quad (2.1)$$

$$\hat{H} \equiv \hat{H}_e = \hat{T}_e + \hat{T}_n + \hat{V}_{ne} + \hat{V}_{ee} + \hat{V}_{nn} \quad (2.2)$$

A commonly employed approximation is the Born-Oppenheimer approximation⁷². Here, it is assumed that the comparably light electrons move much faster compared to the heavier nuclei. Hence, the latter are generally treated as fixed particles when solving the electronic Schrödinger equation. Hereby the kinetic energy operator \hat{T}_n of the nuclei can be neglected and the potential energy operator \hat{V}_{nn} of the nucleus-nucleus interaction can be assumed as a constant that will not affect the electronic Hamiltonian. These approximations result in the molecular electronic Schrödinger equation (Eq. 2.3) and the

2. Theoretical Background

corresponding electronic Hamiltonian (Eq. 2.4).

$$\hat{H}_e \Psi_e = E_e \Psi_e \quad (2.3)$$

$$\hat{H} \equiv \hat{H}_e = \hat{T}_e + \hat{V}_{ne} + \hat{V}_{ee} = \hat{h}_e + \hat{V}_{ee} \quad (2.4)$$

The terms in the electronic Hamiltonian are the kinetic energy operator of the electrons \hat{T}_e (Eq. 2.5), the operator \hat{V}_{en} (Eq. 2.6), which describes the (Coulomb-) interaction between electrons and nuclei, and \hat{V}_{ee} (Eq. 2.7), the operator for the electron-electron interaction. All one-electron terms are often expressed as a one-electron operator \hat{h}_e . Here, subscripts i and j denote the electrons involved, A and B the corresponding nuclei. Z is the nuclear charge of the nucleus, while \mathbf{r} and \mathbf{R} represent the position vectors of the electrons and the nuclei, respectively.

$$\hat{T}_e = -\frac{1}{2} \sum_i^N \hat{\nabla}_i^2 \quad (2.5)$$

$$\hat{V}_{ne} = - \sum_i^N \sum_A^M \frac{Z_A}{|\mathbf{r}_i - \mathbf{R}_A|} \quad (2.6)$$

$$\hat{V}_{ee} = \sum_{i>j}^N \frac{1}{|\mathbf{r}_i - \mathbf{r}_j|} \quad (2.7)$$

Combined with the electronic SE, the electronic energy E_e is given by the expectation value of \hat{H}_e with respect to the normalized electron wave function Ψ_e (Eq. 2.8).

$$E_e = \langle \Psi_e | \hat{H}_e | \Psi_e \rangle \quad (2.8)$$

As only electronic energies are considered further on, the index e is dropped in the following. To describe the ground state wave function Ψ_0 of a system with N electrons, it can be reasonably approximated as a normalized Slater determinant (Eq. 2.9)^{73–75} with N independent one-electron wavefunctions ϕ_i , or molecular orbitals (MOs), occupied by N electrons. The Slater determinant is equivalent to an antisymmetrized product of one particle function and thus ensures the Pauli principle^{73,76} with respect to interchange of two electrons.

$$\Psi_0 \approx \Phi_0(1, 2, \dots, N) = \frac{1}{\sqrt{N!}} \begin{vmatrix} \phi_1(1) & \phi_2(1) & \cdots & \phi_N(1) \\ \phi_1(2) & \phi_2(2) & \cdots & \phi_N(2) \\ \vdots & \vdots & \ddots & \vdots \\ \phi_1(N) & \phi_2(N) & \cdots & \phi_N(N) \end{vmatrix} \quad (2.9)$$

2.2.2. Hartree-Fock Theory and Electron Correlation

The variational principle states that the energy expectation value of any test wave function $\tilde{\Phi}$ cannot be lower than that of the true wave function Ψ (Eq. 2.10).

$$\tilde{E} = \langle \tilde{\Phi} | \hat{H} | \tilde{\Phi} \rangle \geq \langle \Psi | \hat{H} | \Psi \rangle = E \quad (2.10)$$

Accordingly, in Hartree-Fock (HF) theory, a set of orbitals ϕ_i (cf. Eq. 2.9) is sought for which the energy expectation value is minimized. Orthonormality (Eq. 2.11) is enforced during the optimization by means of Lagrange multipliers (Eq. 2.12 and 2.13).

$$\langle \phi_i | \phi_j \rangle = \begin{cases} 0 & \text{for } i \neq j \\ 1 & \text{for } i = j \end{cases} \quad (2.11)$$

$$L = E - \sum_{ij} \lambda_{ij} (\langle \phi_i | \phi_j \rangle - \delta_{ij}) \quad (2.12)$$

$$\delta L = \delta E - \sum_{ij} \lambda_{ij} (\langle \delta \phi_i | \phi_j \rangle + \langle \phi_i | \delta \phi_j \rangle) = 0 \quad (2.13)$$

These conditions yield equation 2.14.

$$\hat{f}_i \phi_i = \sum_j \lambda_{ij} \phi_j \quad (2.14)$$

The resulting Hartree-Fock equations may be further simplified by unitary transformation, yielding the HF eigenvalue problem, where the canonical molecular orbitals ϕ_i are eigenfunctions of the effective one-electron Fock operator \hat{f}_i (Eq. 2.15). The one-electron operator \hat{h}_i contains the nuclear Coulomb interaction operator and the kinetic energy operator, each acting on one orbital i , while the electron-electron Coulomb interactions are approximated by the electron interaction with a mean field generated by all other electrons v_i (Eq. 2.15a), which is described by the Coulomb operator \hat{J}_{ij} (Eq. 2.16) and the exchange operator \hat{K}_{ij} (Eq. 2.17). The exchange operator \hat{K}_{ij} originates from the wave function anti-symmetry and occurs only for two electrons of the same spin.

$$\hat{f}_i \phi_i = \epsilon_i \phi_i \quad (2.15)$$

$$= \left(\hat{h}_i + v_i^{HF} \right) \phi_i \quad (2.15a)$$

$$= \left[\hat{h}_i + \sum_j \left(\hat{J}_{ij} - \hat{K}_{ij} \right) \right] \phi_i \quad (2.15b)$$

$$\hat{J}_{ij} |\phi_i\rangle = \langle \phi_j | \frac{1}{r_{ij}} | \phi_j \rangle | \phi_i \rangle \quad (2.16)$$

$$\hat{K}_{ij} |\phi_i\rangle = \langle \phi_j | \frac{1}{r_{ij}} | \phi_i \rangle | \phi_j \rangle \quad (2.17)$$

2. Theoretical Background

Following that $\langle \phi_i | \hat{K}_{ii} | \phi_i \rangle$ equals $\langle \phi_i | \hat{J}_{ii} | \phi_i \rangle$, no artificial interaction of an electron with itself is obtained, and thus the HF method is free of the so-called self-interaction error (SIE). As HF is a difficult system of integrodifferential equations, yet unknown MOs ϕ_i can be approximated as linear combination of a set of known atomic orbitals or basis functions ψ_μ following the linear-combination of atomic orbitals (LCAO) approach (Eq. 2.18) with $C_{\mu i}$ being molecular orbital coefficients. The LCAO approach is exact for a complete set of basis functions (complete basis set, CBS).

$$\phi_i = \sum_{\mu} C_{\mu i} \psi_{\mu} \quad (2.18)$$

Based on equation 2.15, the HF eigenvalue problem can be reformulated as a linear matrix equation. This results in the so-called Roothaan-Hall equation (Eq. 2.19) with the Fock matrix \mathbf{F} , the LCAO coefficient matrix \mathbf{C} and the overlap matrix \mathbf{S} ^{77,78}. Due to the non-orthogonality of the AOs, \mathbf{S} contains only elements of the form $S_{ij} = \langle \phi_i | \phi_j \rangle$.

$$\mathbf{FC} = \mathbf{SC}\epsilon \quad (2.19)$$

Since the Fock operator \mathbf{F} depends directly on the orbital coefficients \mathbf{C} , the equation must be solved iteratively, e.g., by linear variation of \mathbf{C} in a self-consistent field (SCF) approach. The obtained set of self-consistent molecular orbitals can then be used to calculate the HF energy according to equation 2.20a. The computational effort of Hartree-Fock calculations formally scales to $\mathcal{O}(N^4)$ with respect to N atomic orbitals.

$$E_{HF} = \sum_i^N \langle \phi_i | \hat{h}_i | \phi_i \rangle + \frac{1}{2} \sum_{ij}^N \left(\langle \phi_i | \hat{J}_{ij} | \phi_i \rangle - \langle \phi_i | \hat{K}_{ij} | \phi_i \rangle \right) \quad (2.20)$$

The orbitals are occupied according to the "Aufbau" principle where this electron configuration is divided into occupied and unoccupied or virtual orbitals (Figure 2.1). As a consequence of the mean-field approximation, explicit electron interaction \hat{V}_{ee} is not described. While the interaction between two electrons with the same spin (Fermi correlation) is considered following the Pauli principle, the mean-field approximation results in an uncorrelated motion of two electrons with opposite spins. Therefore, the correlation of the spatial positions of these electrons that results from their Coulomb repulsion (Coulomb correlation) is neglected. Accordingly, even when using a complete set of basis functions, the HF energy for any system with more than one electron is always larger than that of the exact solution of the non-relativistic Schrödinger equation within the Born-Oppenheimer approximation. The missing energy contribution, whose largest component is Coulomb correlation, is usually referred to as correlation energy E_{corr} (Eq. 2.21).

$$E_{corr.} = E - E^{HF} \quad (2.21)$$

The magnitude of the correlation energy with respect to total energies is usually small for many electronic ground states and in typical mean-field methods about 99% of the total energy can be reproduced. However, with respect to relative energies, molecular properties, or even the correct description of covalent bonds, e.g. in the context of bond dissociation, the correlation energy takes on an important role. Further, London dispersion interactions, an attractive part of van-der-Waals interactions, are also

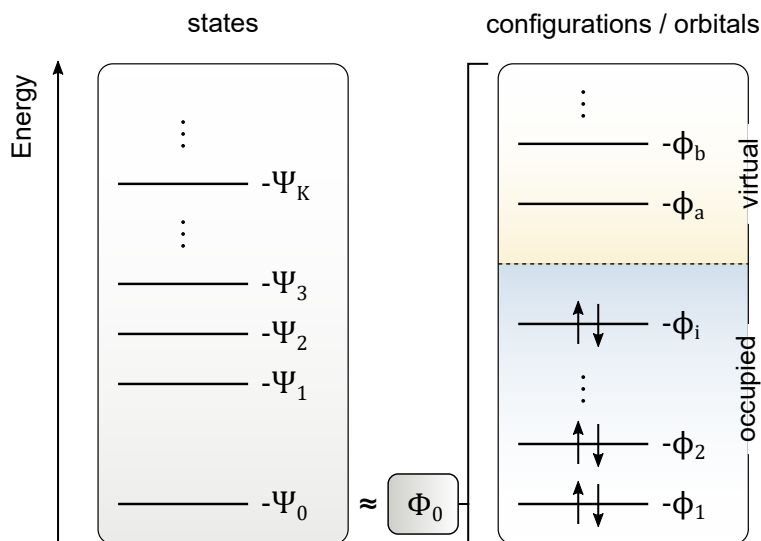


Figure 2.1.: Schematic depiction of the approximation of the ground state wave function Ψ_0 by a single Slater determinant Φ_0 following the "Aufbau" principle by variational ground state methods. Figure adapted from ref. 63.

a result of the long-range part of the electron correlation and, accordingly, are not described within the Hartree-Fock method. To overcome these shortcomings, several approaches have been developed to calculate the correlation energy. The most notable non-perturbative approaches are configuration interaction (CI)^{28,29,71} and coupled cluster (CC)^{28,71,79,80}. Both are based on a single HF determinant from which new electron configurations are generated by exciting the electrons into virtual orbitals. The wave function is then represented as combination of Slater determinants with expansion coefficients or amplitudes being optimized. The variant of CI considering all possible configurations is termed FullCI. Although these methods provide more accurate results as higher excitations are taken into account, their applicability is limited by the sharp increase in computer effort. Accordingly, a truncation of the expansion is often necessary and the CC variant considering singles, doubles, and perturbative triples, also called CCSD(T), has established itself as the so-called "gold standard" in computational chemistry^{28,71,80,81}. Even this truncated variant already scales with $O(N^7)$. Therefore, such calculations are usually performed only for very small systems, and the results obtained often serve as a reference for the development of faster, more approximate methods. The DLPNO-CCSD(T) method represents a comparatively new approach to reducing computational costs. Here the DLPNO stands for domain-based local pair natural orbitals, which are used to reduce the number of operations by defining the most relevant electron domains that contribute most to the correlation energy. As the reduced computational demand allows for computations of larger systems at still high accuracy, DLPNO-CCSD(T)⁸²⁻⁸⁴ is often applied as reference method, where CCSD(T) is not feasible anymore.

The most prominent and lowest-scaling wavefunction based electron correlation approach is 2nd order Møller-Plesset perturbation (MP2) theory⁸⁵ where the correlation energy correction is obtained from

2. Theoretical Background

equation 2.22 with i and j indicating occupied and a and b unoccupied orbitals²⁸.

$$E^{MP2} = \sum_{i < j}^{occ.} \sum_{a < b}^{virt.} \frac{[\langle \phi_i \phi_j | \phi_a \phi_b \rangle - \langle \phi_i \phi_j | \phi_b \phi_a \rangle]^2}{\epsilon_i + \epsilon_j - \epsilon_a - \epsilon_b} \quad (2.22)$$

Equation 2.22 immediately reveals the major weakness of the MP2 approach. The difference of the orbital energies in the denominator can lead to a strong overestimation of the MP2 energy in systems where this becomes very small or even close to zero, e.g. for dissociation or 3d transition metal complexes. Nevertheless, due to its formally relatively small computational scaling of $O(N^5)$ (resulting from the transformation of AO to MO integrals), and its non iterative nature, MP2 correlation energy corrections are frequently applied.

2.2.3. Kohn-Sham Density Functional Theory

The idea that the properties of a system correlate with the electron density ($\rho(\mathbf{r})$), a three-dimensional observable, goes back to the assumptions of Thomas and Fermi in 1927^{86,87}. It is supposed that the electronic ground state of a system can be described by a density functional, which was proven by Hohenberg and Kohn in 1964⁸⁸. Accordingly, the first Hohenberg-Kohn theorem states that a density functional $E[\tilde{\rho}]$ exists which relates the electron density of the ground state to the energy of the system. Following the second Hohenberg-Kohn theorem, this density functional yields an energy for any test density $\tilde{\rho}$ that is always higher than or equal to the true one (Eq. 2.23)⁸⁹.

$$E[\tilde{\rho}] \geq E_0 \quad (2.23)$$

While the Hohenberg-Kohn theorems form the basis for density functional theory, they do not provide guidance for constructing the exact density functional whose composition is unknown. Therefore, the best possible approximation of the exact density functional is the decisive goal of modern research in the field of density functional theory. In analogy to the electronic Hamiltonian operator (*vide supra*), the density functional can be decomposed into interaction specific components (Eq. 2.24). These are the kinetic energy of the electron $T_e[\rho]$, the interelectronic Coulomb interactions $V_{ee}[\rho]$, and the interaction of the electrons with the nuclei $V_{ne}[\rho]$. $V_{ee}[\rho]$ is further split into an exchange part $K[\rho]$ and a Coulomb part $J[\rho]$ (Eq. 2.24a)^{28,90}.

$$E_{DFT}[\rho] = T_e[\rho] + V_{ne}[\rho] + V_{ee}[\rho] \quad (2.24)$$

$$= T_e[\rho] + V_{ne}[\rho] + (J[\rho] + K[\rho]) \quad (2.24a)$$

This basic DFT approach is inherently orbital free, but the exact description of the kinetic energy in particular remains problematic, which is why early attempts by Thomas and Fermi failed. A breakthrough regarding the calculation of the kinetic energy was made by Kohn and Sham, who developed the idea of a fictitious reference system of non-interacting particles, which has the same electron density as the real system⁹¹. The resulting Kohn-Sham density functional theory (KS-DFT) is one of the workhorses of modern quantum chemistry⁹². To calculate the kinetic energy, a Slater determinant

approach ($T_{SD}[\rho]$) with orbitals is used in analogy to Hartree-Fock theory. The missing difference in kinetic energy, as well as the correlation and exchange energy, are formally described by the introduced exchange-correlation functional $E_{XC}[\rho]$ (Eq. 2.25). The latter is commonly divided into an exchange part $E_X[\rho]$ and a correlation part $E_C[\rho]$ (Eq. 2.25b). Based on this approach, a plethora of density functional approximations (DFAs) has been developed, following different strategies including (semi-)empirical and physically motivated approaches⁹³⁻⁹⁶.

$$E_{KS}[\rho] = T_{SD}[\rho] + V_{ne}[\rho] + J[\rho] + E_{XC}[\rho] \quad (2.25)$$

$$= \left[\sum_{i=1}^N \langle \phi_i | -\frac{1}{2} \nabla^2 | \phi_i \rangle \right] + V_{ne}[\rho] + J[\rho] + E_{XC}[\rho] \quad (2.25a)$$

$$= \left[\sum_{i=1}^N \langle \phi_i | -\frac{1}{2} \nabla^2 | \phi_i \rangle \right] + V_{ne}[\rho] + J[\rho] + (E_X[\rho] + E_C[\rho]) \quad (2.25b)$$

In analogy to the HF equation (Eq. 2.15), the energy is calculated iteratively with the Kohn-Sham equation (Eq. 2.26) where the exchange-correlation potential $v_{XC}[\rho]$ and the one-electron Kohn-Sham operator $\hat{f}_i^{KS}[\rho]$ are introduced (Eq. 2.26a). The exchange-correlation functional $E_{XC}[\rho]$ is linked to $v_{XC}[\rho]$ by its derivative with respect to the electron density ρ following equation 2.27.

$$\hat{f}_i^{KS}[\rho] \phi_i = \epsilon_i \phi_i \quad (2.26)$$

$$= \left[\hat{h}_i[\rho] + \sum_j^N \left(\hat{J}_{ij}[\rho] + v_{XC}[\rho] \right) \right] \phi_i \quad (2.26a)$$

$$v_{XC} = \frac{\delta E_{XC}[\rho]}{\delta \rho} \quad (2.27)$$

The (semi-)local density dependent exchange-correlation functional $E_{XC}[\rho]$ can be formulated in a more general form following equation 2.28 with ϵ_{XC} being the energy density or energy per particle and ∇^γ indicating the dependence on the density or its derivatives^{28,93}.

$$E_{XC}[\rho] \equiv E_X[\rho] + E_C[\rho] = \int \rho(\mathbf{r}) \epsilon_{XC}[\nabla^\gamma \rho(\mathbf{r})] d\mathbf{r} \quad (2.28)$$

This dependence and further modifications of density functional approximations allow a categorization of DFAs in terms of accuracy and computational demand according to the so-called "Jacob's ladder", a metaphoric DFA hierarchy coined by Schmidt and Perdew in 2001 (Figure 2.2)⁹³. The "Hartree world" at the bottom is connected with the "Heaven" of chemical accuracy rungs of established DFA categories that will be discussed briefly in the following.

Local (Spin) Density Approximation

The local density approximation (LDA) is based on the idea of the uniform electron gas (UEG) which assumes only small variations in the electron density of the system and its more general form regarding individual α and β densities is termed local spin density approximation. It directly depends on the local

2. Theoretical Background

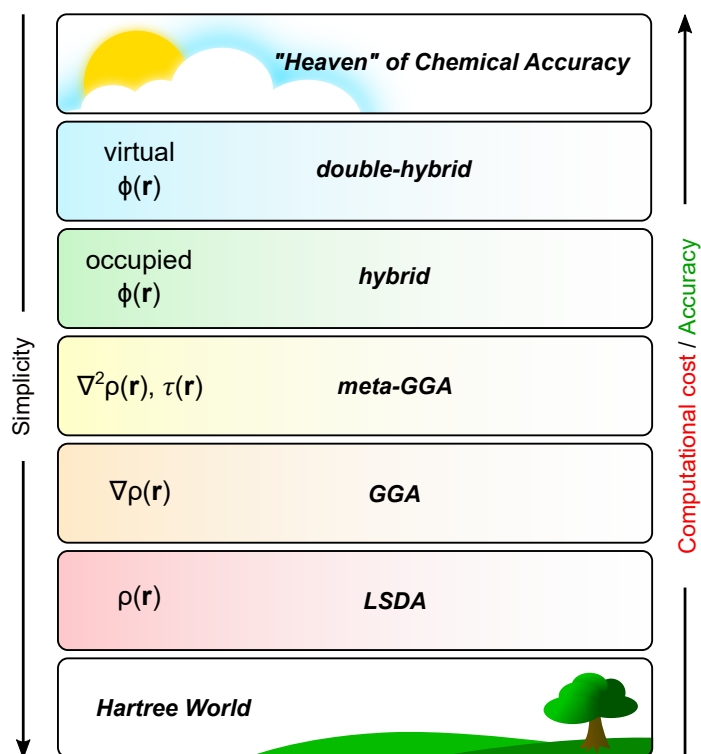


Figure 2.2.: Schematic presentation of DFA categorization according to the "Jacob's ladder" coined by Schmidt and Perdew. ρ is the electron density, τ the kinetic orbital energy, ∇ the Nabla operator, and ϕ a molecular orbital.

density $\rho(\mathbf{r})$ and the exchange functional is based on the early formulation by Dirac (Eq. 2.29)^{97,98} the correlation part is omitted for brevity. Further, in the following the only the case of equal α and β densities is discussed, for which LSDA equals LDA.

$$E_X^{LSDA}[\rho] \equiv K_D[\rho] = -\frac{3}{4} \left(\frac{3}{\pi}\right)^{\frac{1}{3}} \int \rho(\mathbf{r})^{\frac{4}{3}} d\mathbf{r} \quad (2.29)$$

Due to the UEG foundation, systems with a homogeneous electron density like metals are described well by LSDA approaches, while its performance for systems with inhomogeneous electron densities as found in most molecules is poor.

Generalized Gradient Approximation

To overcome the shortcomings of the LSDA approach for systems with inhomogeneous electron densities, the general gradient approximation (GGA) modifies LSDA by an enhancement factor $F_{XC}^{GGA}[\rho, \nabla\rho]$. This enhancement factor depends on the local electron density and its gradient (Eq. 2.30). As the latter introduces information about the electron density in the immediate vicinity of the local density, these

DFAs are typically referred to as semi-local DFAs.

$$E_{XC}^{GGA} = \sum_{\sigma=a,b} \int \rho \epsilon_{XC}^{LSDA}[\rho] F_{XC}^{GGA}[\rho, \nabla \rho] d\mathbf{r} \quad (2.30)$$

Even though the description of molecules is greatly improved for semi-local DFAs, (semi-)local DFAs suffer from the self-interaction error (SIE). The SIE is not canceled properly for $i = j$ as it is the case in HF by the corresponding exchange term. A direct consequence of the SIE, is a pronounced or over-delocalization of the electron density.

Meta-Generalized Gradient Approximation

The next rung of Jacob's ladder is taken by meta-generalized gradient approximation (meta-GGA) functionals. These typically involve the second order derivatives of the electron density described by the Laplacian $\nabla^2 \rho$ in addition to the known GGA approach. As the Laplacian is known to show numerical instability, it is often replaced by the kinetic orbital energy $\tau(\mathbf{r})$ (Eq. 2.31)⁹⁹.

$$\tau(\mathbf{r}) = \frac{1}{2} \sum_{\sigma=a,b} \sum_i^{N_\sigma} |\nabla \phi_i(\mathbf{r})|^2 \quad (2.31)$$

Unlike the significant improvement moving from LSDA to GGA functionals, the meta-GGA approach typically only yields comparably small improvement over GGA functionals.

Hybrid DFT

To further improve (semi-)local DFAs, they can be modified by non-local information involving the occupied Kohn-Sham orbitals⁹⁵. Typically the exchange functional is modified by a fraction a_X of exact exchange from HF, called Fock exchange. This is based on the idea of interpolating the non-correlated Hartree-Fock and the correlated DFT method in the so-called adiabatic connection. The introduction of Fock exchange typically reduces the SIE in global hybrid functionals which mostly outperform (semi-)local DFAs for the calculation of many ground- and excited state properties^{34,94,100-102}.

$$E_{XC}^{hybrid} = E_C^{(meta-)GGA} + (1 - a_X) E_X^{(meta-)GGA} + a_X E_X^{HF} \quad (2.32)$$

Nevertheless, global hybrid functionals still suffer from the fact that the (meta-)GGA type potentials v_{XC} decay with $\frac{1}{r_{12}}$ and thus the exchange potential is not described correctly in the asymptotic limit. To correct for this, a range-separation scheme is established separating the exchange part into a short-ranged and a long-ranged regime (Eq. 2.33)¹⁰³⁻¹⁰⁷.

$$\frac{1}{r_{12}} = \underbrace{\frac{1 - a'_X - a''_X \text{erf}(\mu r_{12})}{r_{12}}}_{\text{short-range}} + \underbrace{\frac{a'_X + a''_X \text{erf}(\mu r_{12})}{r_{12}}}_{\text{long-range}} \quad (2.33)$$

2. Theoretical Background

The short-ranged regime is typically described by a modified (semi-)local DFA while the long-ranged regime is described by regular and modified Fock exchange terms scaled by a'_X and a''_X , respectively. An error function is applied to interpolate between both regimes with an interpolation steepness parameter μ .

Double-hybrid DFT

As already indicated in section 2.2.2, mean field methods typically lack a sufficient description of the correlation energy. Thus, the fifth rung of Jacob's ladder, the so-called double-hybrid functionals, introduce information of the virtual Kohn-Sham orbitals to the correlation part by modified perturbation theory treatments like second order Møller-Plesset perturbation theory⁸⁵ or random phase approximation (RPA)¹⁰⁸ (Eq. 2.34). Double-hybrid functionals were pioneered by Truhlar in 2004¹⁰⁹ and Grimme in 2006^{110,111} and since then a plethora of variants has been developed. Generally, double-hybrid functionals applying an MP2 treatment are still the most prominent and typically perform well for thermochemistry and basic molecular properties^{34,112}. Due to the MP2 correlation energy calculation based on the KS orbitals from the hybrid calculation, the computational scaling of typical double-hybrid functionals rises to $O(N^5)$, thus limiting their applicability to large systems. Nevertheless, double-hybrid functionals typically achieve much better accuracy than MP2 and in some cases even reach the accuracy of CC methods^{34,112}.

$$E_{XC}^{double-hybrid} = (1 - a_X)E_X^{(meta-)GGA} + a_X E_X^{HF} + (1 - a_C)E_C^{(meta-)GGA} + a_C E_C^{PT2} \quad (2.34)$$

2.2.4. Dispersion Corrected DFT

DFT-D3

Electronic structure methods based on mean field approximations like HF and (semi-)local Kohn-Sham DFT can not describe long-range correlation effects. One of these effects is the London dispersion, an attractive type of van-der-Waals interactions. It is a crucial part of non-covalent interactions. London and Eisenschitz derived the well-known asymptotic formula of the dispersion energy in 1930 (Eq. 2.35) from perturbation theory with the distance R and the pair-specific dispersion coefficient C_6 ^{113,114}.

$$E_{disp}^{AB} \approx -\frac{C_{6,approx}^{AB}}{R^{-6}} \quad (2.35)$$

In a more general form, perturbation theory yields the isotropic pair-wise dispersion energy $E_{disp}(R_{AB})$ following equation 2.36. The dispersion coefficients of n^{th} order C_n^{AB} , are chosen to be generally positive in this thesis. A damping function $f_{damp}^{(n)}$ is introduced to avoid erroneous behavior at small distances.

$$E_{disp}^{AB} = \sum_{n=6,8,10,\dots} E_{disp}^{(n)} = - \sum_{AB} \sum_{n=6,8,10,\dots} \frac{C_n^{AB}}{R_{AB}^{(n)}} f_{damp}^{(n)} \quad (2.36)$$

Such dispersion energy corrections can be used to correct DFT or other mean field methods (Eq. 2.37) and the most prominent and efficient of such correction schemes is the DFT-D approach of Grimme and co-workers³¹.

$$E^{MF-D} = E^{MF} + E_{disp}^D \quad (2.37)$$

For the sake of brevity, only the newer commonly applied variants DFT-D3⁵⁹ and DFT-D4^{115,116} will be discussed in the following, with the prior ones DFT-D1¹¹⁷ and DFT-D2⁵⁸ being mentioned for completeness. The DFT-D3 approach was reported by Grimme and co-workers in 2010 and extends the D2 approach by explicitly considering the structural environment. To achieve this, empirically determined fractional coordination numbers (CNs) are defined. For the atom A and B the CN is obtained following equation 2.38 with the element specific covalent radii R_{cov} ¹¹⁸.

$$CN^A = \sum_{B \neq A}^{N_{atoms}} \frac{1}{1 + e^{-16(4(R_{A,cov} + R_{B,cov}) / (3R_{AB}) - 1)}} \quad (2.38)$$

Additionally, reference dispersion coefficients $C_{6,ref}^{AB}(CN^A, CN^B)$ are calculated using electric dipole polarizabilities $\alpha^A(i\omega)$ in a modified Casimir-Polder approach (Eq. 2.39)¹¹⁹. These are calculated for the isolated atom as well as for model systems A_mH_n and B_kH_l i.e. hydrides with different coordination patterns.

$$C_{6,ref}^{AB}(CN^A, CN^B) = \frac{3}{\pi} \int_0^\infty \frac{1}{m} \left[\alpha^{A_mH_n}(i\omega) - \frac{n}{2} \alpha^{H_2}(i\omega) \right] \frac{1}{k} \left[\alpha^{B_kH_l}(i\omega) - \frac{1}{2} \alpha^{H_2}(i\omega) \right] d\omega \quad (2.39)$$

Atom pair specific dispersion coefficients are then obtained from equation 2.40.

$$C_6^{AB} \equiv C_6^{AB}(CN^A, CN^B) = \frac{\sum_i^{N_A} \sum_j^{N_B} C_{6,ref}^{AB}(CN_i^A, CN_j^B) e^{-4[(CN^A - CN_i^A)^2 + (CN^B - CN_j^B)^2]}}{\sum_i^{N_A} \sum_j^{N_B} e^{-4[(CN^A - CN_i^A)^2 + (CN^B - CN_j^B)^2]}} \quad (2.40)$$

Dispersion coefficients for dipole-quadrupole contributions C_8^{AB} are obtained following equation 2.41 with the atomic number Z and the multipole expectation values $\langle r^4 \rangle$ and $\langle r^2 \rangle$ which are derived from atomic densities¹²⁰.

$$C_8^{AB} = 3C_6^{AB} \sqrt{Q_A Q_B} = 3C_6^{AB} \sqrt{\sqrt{Z_A} \frac{\langle r_A^4 \rangle}{\langle r_A^2 \rangle} \sqrt{Z_B} \frac{\langle r_B^4 \rangle}{\langle r_B^2 \rangle}} \quad (2.41)$$

All dispersion coefficients considered in the DFT-D3 model are based on either the geometry of the system or pre-computed reference data. Thus, DFT-D3 is highly efficient and the computational cost even for huge systems is almost negligible. The final DFT-D3 pair-wise dispersion correction energy is obtained from equation 2.42.

$$E_{disp}^{D3,AB} = \sum_{n=6,8} E_{disp}^{(n)} = - \sum_{AB} \sum_{n=6,8} s_n \frac{C_n^{AB}}{R_{AB}^{(n)}} f_{damp}^{(n)}(R) \quad (2.42)$$

2. Theoretical Background

s_n are DFA specific scaling parameters for the respective multipolar contributions. As damping function $f_{damp}^{(n)}(R)$ two variants can be applied, the originally applied zero-damping (Eq. 2.43) or the more frequently used Becke-Johnson damping^{121–123} (Eq. 2.44), indicated as D3(0) and D3(BJ), respectively.

$$f_{damp,zero}^{(n)}(R) = \frac{1}{1 + 6(R/(s_{r,n}R_0))^{a_n}} \quad (2.43)$$

$$f_{damp,BJ}^{(n)}(R) = \frac{R^n}{R^n + (a_1R_0 + a_2)^n} \quad (2.44)$$

For these damping functions $R_0 = \sqrt{C_8^{AB}/C_6^{AB}}$, and $s_{r,n}$, a_1 , a_2 are functional specific parameters. For $f_{damp,zero}^{(n)}(R)$ $a_6 = 14$ and $a_8 = 16$. Beside pair wise dipole-dipole and dipole-quadrupole interactions, three-body dipole-dipole-dipole contributions can be incorporated by means of an Axilrod-Teller-Muto (ATM)^{124,125} term as described in equation 2.45.

$$E_{disp}^{D3-ATM} = - \sum_{AB} \sum_{n=6,8} s_n \frac{C_n^{AB}}{R^n} f_{damp}^{(n)}(R) - \sum_{ABC} s_9 \frac{C_9^{ABC} (3\cos\theta_a \cos\theta_b \cos\theta_c + 1)}{(R_{AB}R_{AC}R_{BC})^3} f_{damp}^{(9)}(\bar{R}_{ABC}) \quad (2.45)$$

DFT-D4

DFT-D4^{33,115,116} represents a further development of DFT-D3 and introduces an atomic partial charge dependence of the atomic reference polarizabilities $\alpha(i\omega)$ that are used to calculate reference dispersion coefficients according to equation 2.39. Thus, a scaling function $\zeta(z^A, z^{A,ref})$ is introduced (Eq. 2.46) with z^A being the effective nuclear charge directly depending of the atomic partial charge q^A (Eq. 2.47).

$$\zeta(z^A, z^{A,ref}) = \exp \left[\beta_1 \left\{ 1 - \exp \left[\gamma^A \left(1 - \frac{z^{A,ref}}{z^A} \right) \right] \right\} \right] \quad (2.46)$$

$$z^A = Z^A + q^A \quad (2.47)$$

Applying this scaling function subsequently yields the scaled atomic reference polarizabilities following equation 2.48.

$$\alpha^{A,ref}(i\omega, z^A) = \alpha^{A,ref}(i\omega) \zeta(z^A, z^{A,ref}) \quad (2.48)$$

The element specific polarizabilities $\alpha^{A,ref}(i\omega)$ are only defined for infinitely separated systems, and are thus approximated by equation 2.49 for all X atoms with the stoichiometric factor l .

$$\alpha^{A,ref}(i\omega) = \frac{1}{m} \left[\alpha^{A_m X_n}(i\omega) - \frac{n}{l} \alpha^{X_l}(i\omega) \zeta(z^A, z^{A,ref}) \right] \quad (2.49)$$

In similarity to DFT-D3 fractional coordination numbers are calculated by equation 2.50 utilizing the electronegativity (EN) dependent term δ_{AB}^{EN} (Eq. 2.51) where k_n ($n=0,1,2,3$) are empirical parameters.

$$CN^A = \sum_A \sum_{B \neq A} \frac{\delta_{AB}^{EN}}{2} \left(1 + \operatorname{erf} \left(-k_0 \left(\frac{R_{AB} - R_{AB}^{cov}}{R_{AB}^{cov}} \right) \right) \right) \quad (2.50)$$

$$\delta_{AB}^{EN} = \frac{(k_1 \exp(|EN_A + EN_B| + k_2)^2)}{k_3} \quad (2.51)$$

Final CN and charge dependent polarizabilities are subsequently obtained from equation 2.52 with the manually adjusted parameter $\beta_2 = 2$ and the reference system specific number of Gaussian functions N^s utilized in the weighting procedure.

$$\alpha^A(i\omega) \equiv \alpha^{A,ref}(i\omega, z^A, CN^A) = \sum_{A,ref=1}^{N^{A,ref}} \alpha^{A,ref}(i\omega, z^A) \frac{\sum_{j=1}^{N^s} \exp(-\beta_2 j (CN^A - CN^{A,ref})^2)}{\sum_{A,ref=1}^{N^{A,ref}} \sum_{j=1}^{N^s} \exp(-\beta_2 j (CN^A - CN^{A,ref})^2)} \quad (2.52)$$

With $\alpha^A(i\omega)$, atom pair wise dispersion coefficients can be calculated according to equation 2.53 that are further used to calculate a pair wise dispersion energy correction in analogy to the DFT-D3 approach (cf. Eq. 2.42).

$$C_6^{AB} \equiv C_6^{AB}(CN^A, z^A, CN^B, z^B) = \frac{3}{2\pi} \sum_{j=1}^{22} (\omega_{j+1} - \omega_j) \left(\alpha^A(i\omega_{j+1}) \alpha^B(i\omega_{j+1}) + \alpha^A(i\omega_j) \alpha^B(i\omega_j) \right) \quad (2.53)$$

The usually recommended DFT-D4 approach applies a Becke-Johnson type damping function as well as the three-body ATM treatment discussed in the context of DFT-D3 by default. The atomic partial charges can generally be obtained from various sources, with the default atomic partial charges being calculated by an electronegativity equilibrium (EEQ) model as described by Goedecker and co-workers¹²⁶.

Composite Methods

Due to their efficiency, the discussed dispersion corrections can be used to construct new DFT based methods with significantly improved performance at negligible additional computational cost. Even though the problematic description of long range dispersion effects is solved by the DFT-D approach, typically DFAs have to be applied in conjunction with almost converged numbers of basis functions, i.e. large basis sets, to yield sufficiently accurate results. This goes hand in hand with drastically increasing computational effort, hence limiting the applicability to large systems. A successful approach to address this problem are composite methods like the HF-3c and DFT-3c, where the "3c" indicates corrections to the basic electronic structure method^{60,69,127-130}. In the 3c composite methods, relatively small modified basis sets are applied and corrected for the resulting basis set superposition error (BSSE) by geometrical counterpoise (gCP) correction^{131,132}. Further, short-ranged basis set (SRB) errors, mainly influencing covalent bond lengths in most (meta-)GGA DFAs, can be addressed by a specific correction. For some of the 3c methods, even direct modifications in the exchange correlation part are made. All 3c composite methods moreover apply either the accurate D3 or D4 London dispersion correction. The combination of various corrections allows good results at comparably small computational effort for a variety of chemical systems and thus the 3c composite methods provide a collection of efficient electronic structure methods, which are intensively used in the course of this thesis. An overview of the

2. Theoretical Background

most important 3c composite methods and the respectively applied corrections is shown in Table 2.1.

Table 2.1.: Overview of 3c composite methods and their specific components and modifications.

	HF-3c ¹²⁷	PBEh-3c ^{a 69}	B97-3c ¹²⁹	r ² SCAN-3c ¹³⁰
AO basis set	MINIX	def2-mSV(P)	mTZVP ^b	mTZVPP ^b
# parameters in F _X ^c	0	2	4	0
# parameters in F _C ^c	0	1	6	0
Fock exchange / %	100	42	0	0
Dispersion correction	D3	D3	D3	D4
SRB correction	yes	no	yes	no
gCP correction	yes	yes	no	yes

^aThe screened non-local exchange variant of PBEh-3c dubbed HSE-3c uses Fock exchange range-separation.

^bModified def2-TZVP basis sets.

^cEnhancement factors to the exchange and correlation treatments.

2.2.5. Semi-Empirical Quantum Mechanical Methods

Modified Neglect of Differential Overlap (MNDO) Methods

Some of the most prominent SQM methods are based on the neglect of diatomic differential overlap (NDDO) approach and its modified variant called modified neglect of differential overlap (MNDO)⁴⁹. These methods typically apply minimal Slater-type orbital (STO) basis sets, that are restricted to the valence shells. Moreover, the common idea of MNDO based methods is the approximation of the Fock matrix by further reducing the number of calculated two-electron repulsion integrals. The respective expression for a Fock matrix element $F_{\mu\nu}$ is given by equation 2.54 with the density matrix $D_{\lambda\sigma}$.

$$F_{\mu\nu} = \langle \mu | \hat{h} | \nu \rangle + \sum_{\lambda\sigma}^{AO} D_{\lambda\sigma} [\langle \mu\nu | \lambda\sigma \rangle - \langle \mu\lambda | \nu\sigma \rangle] \quad (2.54)$$

Here, all basis function products are neglected that depend on same electron coordinates but at different atoms. Consequently, the overlap matrix $S_{\mu\nu}$ is reduced to a unity matrix according to equation 2.55 for basis functions of s- or p-type being indicated by μ , ν , λ , and σ at centers A and B .

$$S_{\mu\nu} = \langle \mu | \nu \rangle = \delta_{\mu\nu} \delta_{AB} \quad (2.55)$$

Further, all three-center one-electron integrals are assumed to equal zero. The remaining one-electron integrals are given by equations 2.56 and 2.57 with Z' being the effective nuclear charge, removing the core electrons.

$$\langle \mu_A | \hat{h} | \nu_A \rangle = \langle \mu_A | -\frac{1}{2} \nabla^2 - \frac{Z'_A}{|\mathbf{R}_A - \mathbf{r}|} | \nu_A \rangle - \sum_{a \neq A}^M \langle \mu_A | \frac{Z'_a}{|\mathbf{R}_a - \mathbf{r}|} | \nu_A \rangle \quad (2.56)$$

$$\langle \mu_A | \hat{h} | \nu_B \rangle = \langle \mu_A | -\frac{1}{2} \nabla^2 - \frac{Z'_A}{|\mathbf{R}_A - \mathbf{r}|} - \frac{Z'_B}{|\mathbf{R}_B - \mathbf{r}|} | \nu_B \rangle \quad (2.57)$$

Additionally, all four- and three-center two-electron integrals are neglected (Eq. 2.58).

$$\langle \mu_A \nu_B | \lambda_C \sigma_D \rangle = \delta_{AC} \delta_{BD} \langle \mu_A \nu_B | \lambda_A \sigma_B \rangle \quad (2.58)$$

For the chosen basis set of s and p basis functions, only six unique one-center two-electron integrals remain, with five being approximated by orbital- and element-specific parameters (Eq. 2.59–2.63).

$$\gamma_{ss} = \langle ss | ss \rangle \quad (2.59)$$

$$\gamma_{pp} = \langle pp | pp \rangle \quad (2.60)$$

$$\gamma_{sp} = \langle ss | pp \rangle \quad (2.61)$$

$$\gamma_{pp'} = \langle pp | p'p' \rangle \quad (2.62)$$

$$\tilde{\gamma}_{sp} = \langle sp | sp \rangle \quad (2.63)$$

The sixth is calculated from γ_{pp} and $\gamma_{pp'}$ according to equation 2.64.

$$\tilde{\gamma}_{pp'} = \langle pp' | pp' \rangle = \frac{1}{2} (\gamma_{pp} - \gamma_{pp'}) \quad (2.64)$$

The most general MNDO methods in terms of applicability are the parametric methods x with the most popular representatives PM6⁵¹ and PM7⁵². They apply an spd basis set and are parametrized for most elements, including transition metals. Both methods were further extended by inclusion of several corrections, like the D3 dispersion or hydrogen bonding corrections to overcome the intrinsic shortcomings of MNDO type SQM methods.

Extended Tight Binding Methods

A different popular approach to construct SQM methods is density functional tight binding (DFTB). In contrast to MNDO type methods it is not based on HF but on DFT and does not apply any zero-differential overlap (ZDO) approximation. Nevertheless, both share the concepts of valence shell restriction and small basis sets. The most prominent representatives of this class of SQM methods are the DFTB methods developed by Elstner and co-workers^{45,133–139} and the more recently developed extended tight binding methods of the GFNn-xTB method family^{53–55,57}. As a major part of this thesis focuses on the evaluation and application of the latter, only the GFN1-⁵³ and GFN2-xTB⁵⁴ methods are discussed in the following. The basic idea of DFTB is to employ an Taylor expansion of the energy around $\Delta\rho = 0$ (for a reference system of neutral atoms) according to equation 2.65 which is typically truncated after the third-order term⁵⁷.

$$E[\rho] = E^{(0)}[\rho_0] + E^{(1)}[\rho_0, \delta\rho] + E^{(2)}[\rho_0, (\delta\rho)^2] + E^{(3)}[\rho_0, (\delta\rho)^3] + \dots \quad (2.65)$$

2. Theoretical Background

GFN1-xTB

The first generation of the GFNn-xTB methods, GFN1-xTB is composed of energy terms up to third order according to equation 2.66.

$$E_{GFN1-xTB} = E_{rep} + E_{disp}^{D3} + E_{XB}^{GFN1} + E_{EHT} + E_{\gamma} + E_{\Gamma}^{GFN1} + G_{Fermi} \quad (2.66)$$

E_{rep} is the classical pair wise repulsion energy and is given by equation 2.67 with Z^{eff} being effective nuclear charges screened by the reference core density. α are element specific fit parameters, k_f is a global parameter ($k_f = \frac{3}{2}$ for GFN1-xTB), and R_{AB} is the interatomic distance between the atoms A and B .

$$E_{rep} = \frac{1}{2} \sum_{A,B} \frac{Z_A^{eff} Z_B^{eff}}{R_{AB}} e^{-\sqrt{\alpha_A \alpha_B} (R_{AB})^{k_f}} \quad (2.67)$$

E_{disp}^{D3} is the D3 London dispersion correction and E_{XB}^{GFN1} is a GFN1-xTB specific, geometry dependent halogen bond correction (Eq. 2.68) with the damping function $f_{damp,AXB}$ for the halogen X (Eq. 2.69).

$$E_{XB}^{GFN1} = \sum_{AXB}^{N_{XB}} f_{damp,AXB} k_X \left[\left(\frac{k_{XR} R_{cov,AX}}{R_{AX}} \right)^{12} - k_{X2} \left(\frac{k_{XR} R_{cov,AX}}{R_{AX}} \right)^6 \right] \left[\left(\frac{k_{XR} R_{cov,AX}}{R_{AX}} \right)^{12} + 1 \right]^{-1} \quad (2.68)$$

$$f_{damp,AXB} = \frac{1}{2} \left(1 - \frac{1}{2} \frac{R_{XA}^2 + R_{XB}^2 + R_{AB}^2}{|R_{XA}| |R_{XB}|} \right)^6 \quad (2.69)$$

Covalent bond formation is described by the first-order energy term E_{EHT} derived from extended Hückel theory (EHT) and is described by equations 2.70 and 2.71, where $P_{\mu\nu}$ is the density matrix of the valence electrons in a nonorthogonal atomic orbital basis.

$$E_{EHT} = \sum_{\mu\nu} P_{\mu\nu} H_{\mu\nu}^{EHT} \quad (2.70)$$

$$H_{\mu\nu}^{EHT} = \frac{1}{2} K_{AB}^{ll'} S_{\mu\nu} (H_{\mu\mu} + H_{\nu\nu}) X(EN_A, EN_B) \Pi(R_{AB}, l, l') Y[\zeta_l^A, \zeta_{l'}^B], \forall \mu \in l(A), \nu \in l'(B) \quad (2.71)$$

Here, $H_{\mu\mu}$ corresponds to the extended Hückel matrix elements (Eq. 2.72), for which an atomic environment dependence is introduced by atomic fractional coordination numbers CN derived from the D3 model (*vide supra*). They further depend on global angular momentum-specific parameters k and shell- and element-specific parameters h .

$$H_{\mu\mu} = h_A^l (1 + k_{CN,l} CN_A), \forall \mu \in l \in A \quad (2.72)$$

The distance-dependent scaling function $\Pi(R_{AB}, l, l')$ is given by equation 2.73 and contains the summed atomic covalent radii $R_{cov,AB}$ for an atom pair AB and the shell- and element-specific parameters k^{poly} .

For GFN1-xTB, the shell-exponent dependent term $Y[\zeta_l^A, \zeta_{l'}^B]$ equals one.

$$\Pi(R_{AB,l,l'}) = \left(1 + k_{A,l}^{poly} \left(\frac{R_{AB}}{R_{cov,AB}}\right)^{\frac{1}{2}}\right) \left(1 + k_{B,l'}^{poly} \left(\frac{R_{AB}}{R_{cov,AB}}\right)^{\frac{1}{2}}\right) \quad (2.73)$$

X directly depends on the difference in Pauling electronegativities ΔEN_{AB} and a global parameter k_{EN} (Eq. 2.74).

$$X(EN_A, EN_B) = (1 + k_{EN} \Delta EN_{AB}^2) \quad (2.74)$$

The second-order exchange-correlation and isotropic electrostatic energy contributions incorporated in E_Y are described by equation 2.75 where q_l represents Mulliken¹⁴⁰ partial shell charges and $\gamma_{AB,ll'}$ the Coulomb interaction energy (Eq. 2.76) damped by the term $\eta_{AB,ll'}$ (Eq. 2.77). In this short-range damping function, η is an element-specific atomic hardness parameter and κ a shell-dependent scaling parameter.

$$E_Y = \frac{1}{2} \sum_{A,B}^{N_{atoms}} \sum_{l \in A} \sum_{l' \in B} q_l q_{l'} \gamma_{AB,ll'} \quad (2.75)$$

$$\gamma_{AB,ll'} = \frac{1}{\sqrt{R_{AB}^2 + \eta_{AB,ll'}^{-2}}} \quad (2.76)$$

$$\eta_{AB,ll'} = 2 \left(\frac{1}{\eta_A(1 + \kappa_A^l)} + \frac{1}{\eta_B(1 + \kappa_B^{l'})} \right)^{-1} \quad (2.77)$$

The third-order exchange-correlation and isotropic electrostatic energy correction E_T^{GFN1} includes the Mulliken partial charge q_A which is defined as the sum over all partial shell charges for $l \in A$ and the so-called element-specific atomwise Hubbard parameter¹⁴¹ Γ (Eq. 2.78).

$$E_T^{GFN1} = \frac{1}{3} \sum_A^{N_{atoms}} (q_A)^3 \Gamma_A \quad (2.78)$$

To incorporate static electron correlation effects, which arise when a single Slater determinant is not sufficient to describe the electronic ground state, the GFNn-xTB energy expressions are augmented by an electronic entropy, or Fermi-smearing term G_{Fermi} that is described by equation 2.79¹⁴². This finite electronic temperature treatment enables the dissociation of covalent bonds and increases the stability of the GFNn-xTB methods for the description of, e.g. transition-states and transition metal complexes, significantly. Usually moderate electronic temperatures are used, with the default value for T_{el} being 300 K. For equation 2.79, k_B is the Boltzmann constant and $n_{i\sigma}$ the fractional occupation number with respect to a spin molecular orbital $\psi_{i\sigma}$. $n_{i\sigma}$ is defined by the Fermi distribution according to equation 2.80 with the respective Fermi levels ϵ_F^σ and the energies ϵ_i of the spatial MOs whose occupation numbers refer to $n_i = n_{i\alpha} + n_{i\beta}$. α and β indicate the respective spin orbital space.

$$G_{Fermi} = k_B T_{el} \sum_{\sigma=\alpha,\beta} \sum_i [n_{i\sigma} \ln(n_{i\sigma}) + (1 - n_{i\sigma}) \ln(1 - n_{i\sigma})] \quad (2.79)$$

2. Theoretical Background

$$n_{i\sigma} = \frac{1}{\exp[(\epsilon_i - \epsilon_F^\sigma)/(k_B T_{el})] + 1} \quad (2.80)$$

As a consequence of the generally spin-restricted nature of the GFNn-xTB methods, spin state splitting energies are generally described badly and a low-spin configuration is always favored within the GFNn-xTB framework. Nevertheless, this behaviour also improves the robustness of the methods with respect to complicated electronic structures. With the GFNn-xTB methods being generally parametrized for all elements up to radon ($Z = 86$), they are also able to treat the lanthanoids. The lanthanoids have special properties with respect to binding and coordination due to the fact that the 4f shell is typically located below the 5d shell and thus does not have a strongly reduced influence on chemical binding. Therefore, the GFNn-xTB methods apply an "f-in-core" approximation¹⁴³, treating the lanthanoids as 4d transition metals with three valence electrons. The f-electrons are thus only treated implicitly by means of parametrization or pseudopotentials.

GFN2-xTB

The second generation GFNn-xTB method, GFN2-xTB, shares many of the concepts and energy contributions already applied in GFN1-xTB (*vide supra*). Accordingly, only the GFN2-xTB specific differences and extensions are discussed in the following, including multipole electrostatics, exchange-correlation anisotropy, and a charge-dependent London dispersion correction. The GFN2-xTB energy is calculated according to equation 2.81.

$$E_{GFN2-xTB} = E_{rep} + E_{disp}^{D4} + E_{EHT} + E_V + E_{AES} + E_{AXC} + E_{\Gamma}^{GFN2} + G_{Fermi} \quad (2.81)$$

For GFN2-xTB the shell-exponent dependent term $Y(\zeta_l^A, \zeta_{l'}^B)$ is described by equation 2.82 with the orbital exponents ζ_l^A .

$$Y(\zeta_l^A, \zeta_{l'}^B) = \left(\frac{2\sqrt{\zeta_l^A \zeta_{l'}^B}}{\zeta_l^A + \zeta_{l'}^B} \right)^{\frac{1}{2}} \quad (2.82)$$

The extended Hückel matrix diagonal elements $H_{\kappa\kappa}$ are described by equation 2.83 introducing an element- and shell-specific parameter $\delta h_{CN'_A}^l$ and a modified fractional coordination number CN'_A .

$$H_{\kappa\kappa} = h_A^l - \delta h_{CN'_A}^l CN'_A \quad (2.83)$$

The modified short-range damping parameter $\eta_{AB, ll'}$ for GFN2-xTB is given by equation 2.84.

$$\eta_{AB, ll'} = \frac{1}{2} \left[\eta_A(1 + \kappa_A^l) + \eta_B(1 + \kappa_B^{l'}) \right] \quad (2.84)$$

While GFN1-xTB applies the D3 dispersion correction, GFN2-xTB uses the more recent charge dependent D4 correction in a modified form (Eq. 2.85) here using self-consistently solved atomic partial

charges from a Mulliken population analysis.

$$\begin{aligned}
E_{disp}^{D4'} = & - \sum_{A \geq B} \sum_{n=6,8} s_n \frac{C_n^{AB}(q_A, CN_{cov}^A, q_B, CN_{cov}^B)}{R_{AB}^n} f_{damp,BJ}^{(n)}(R_{AB}) \\
& - s_9 \sum_{A \geq B \geq C} \frac{(3\cos(\theta_{ABC})\cos(\theta_{BCA})\cos(\theta_{CAB}) + 1)C_9^{ABC}(CN_{cov}^A, CN_{cov}^B, CN_{cov}^C)}{(R_{AB}R_{AC}R_{BC})^3} \\
& \times f_{damp,zero}^{(9)}(R_{AB}, R_{AC}, R_{BC})
\end{aligned} \tag{2.85}$$

For E_{Γ}^{GFN2} a shell-specific global parameter K_l^{Γ} is introduced according to equation 2.86.

$$E_{\Gamma}^{GFN2} = \frac{1}{3} \sum_A^{N_{atoms}} \sum_{l \in A} (q_l)^3 K_l^{\Gamma} \Gamma_A \tag{2.86}$$

The most crucial improvement of GFN2-xTB over its predecessor is the explicit treatment of anisotropic electrostatic interactions in a multipole expansion (Eq. 2.87) and thus being free from of any hydrogen- or halogen bond corrections. For an atom A , the cumulative atomic multipole moments (CAMM)¹⁴⁴ are given by the cumulative atomic dipole moment μ_A and its traceless quadrupole moment Θ_A . The distance dependence damping function $f_n(R_{AB})$ is defined by equation 2.88 with the global parameters a_n .

$$E_{AES} = E_{q\mu} + E_{q\Theta} + E_{\mu\mu} \tag{2.87}$$

$$\begin{aligned}
= & \frac{1}{2} \sum_{A,B} \{ f_3(R_{AB}) [q_A(\mu_B^T \mathbf{R}_{BA}) + q_B(\mu_A^T \mathbf{R}_{AB})] \\
& + f_5(R_{AB}) [q_A \mathbf{R}_{AB}^T \Theta_B \mathbf{R}_{AB} + q_B \mathbf{R}_{AB}^T \Theta_A \mathbf{R}_{AB} - 3(\mu_A^T \mathbf{R}_{AB})(\mu_B^T \mathbf{R}_{AB}) + (\mu_A^T \mu_B) R_{AB}^2] \}
\end{aligned} \tag{2.87a}$$

$$f_n(R_{AB}) = \frac{f_{damp}(a_n, R_{AB})}{R_{AB}^n} = \frac{1}{R_{AB}^n} \frac{1}{1 + 6 \left(\frac{R_0^{AB}}{R_{AB}} \right)^{a_n}} \tag{2.88}$$

Based on the CAMM introduced in equation 2.87, the anisotropic second-order exchange-correlation energy E_{AXC} is calculated following equation 2.89 with the element-specific parameters $f_{XC}^{\mu A}$ and $f_{XC}^{\Theta A}$.

$$E_{AXC} = \sum_A \left(f_{XC}^{\mu A} |\mu_A|^2 + f_{XC}^{\Theta A} \|\Theta_A\|^2 \right) \tag{2.89}$$

As GFN1- and GFN2-xTB apply slightly different STO basis sets, an overview of the respective basis set compositions is given in table 2.2.

2. Theoretical Background

Table 2.2.: Composition of the Slater-type atomic orbital basis sets applied in GFN1- and GFN2-xTB.^{a,b}

group or element	basis functions	
	GFN1-xTB	GFN2-xTB
H	$ns, (n+1)s$	ns
He	ns	$ns, (n+1)p$
Ne	$nsp, (n+1)d$	$nsp, (n+1)d$
Be-F	nsp	nsp
1	nsp	nsp
2	$nsp, (n-1)d$	$nsp, (n-1)d$
3-11	$nsp, (n-1)d$	$nsp, (n-1)d$
12	nsp	nsp
13	$nspd$	$nspd$
14	$nspd$	$nspd$
15	$nspd$	$nspd$
16	$nspd$	$nspd$
17	$nspd$	$nspd$
lanthanoids	$nsp, (n-1)d$	$nsp, (n-1)d$
Tl-Bi	nsp	nsp
Po	$nsp, (n-1)d$	nsp

^a n denotes the principal quantum number of the element specific valence shell (for d ($l = 2$) up to $n = 5$).

^bThe compositions shown differ in parts from those mentioned in the original literature, but reflect those used in the final versions of the respective methods.

2.3. Multi-Level Approach and General Remarks

Throughout this thesis various computational methods are applied and discussed in the context of efficiency and computational speed. Therefore, a classification of the applied methods regarding computational demand, accuracy and applicability with respect to the size of the system is necessary. A simplified classification of prominent method families is shown in figure 2.3. At this point it is to note, that technical settings, the choice of the basis set, as well as method specific thresholds and specifications can influence the final computational demand significantly. Nevertheless, the presented classification reflects a simplified picture of the expected performance considering the method intrinsic computational demand. This estimate is based on typically applied methodological and technical setups and serves only for orientation. As different computational tasks require varying degree of computational

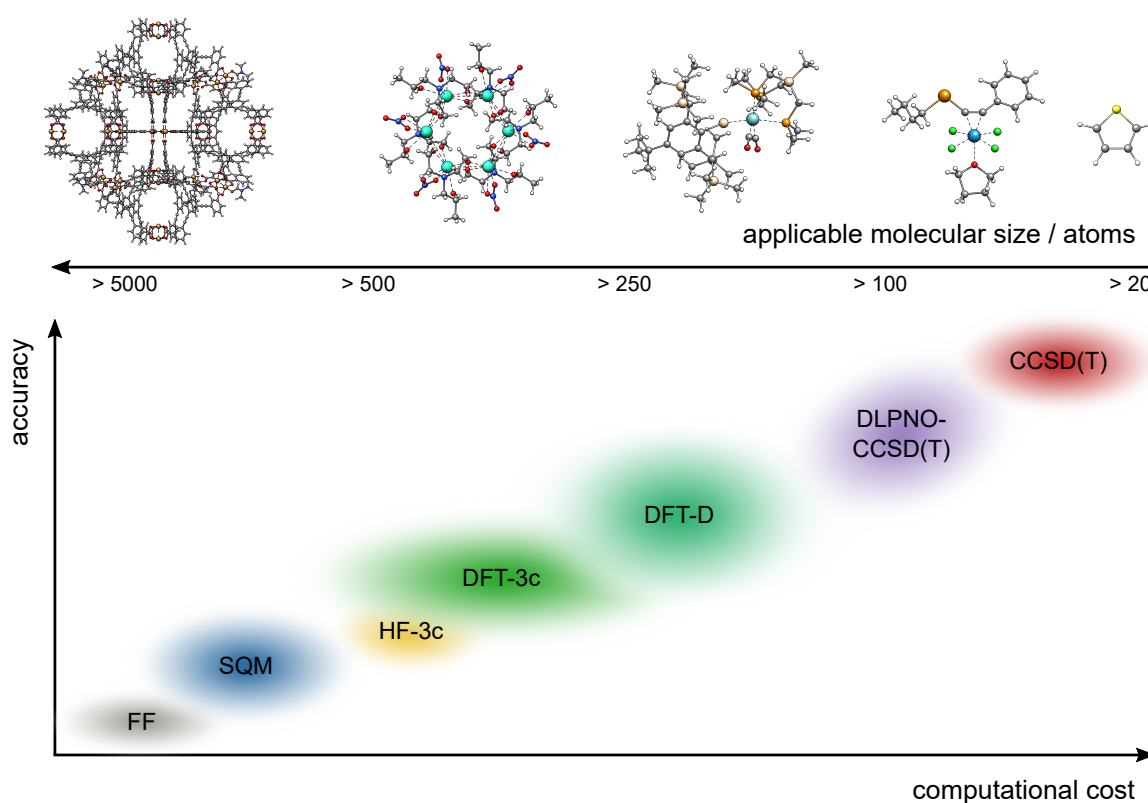


Figure 2.3.: Schematic depiction of the accuracy of prominent computational methods as function of their computational cost. See chapter 2.2 for explanations regarding the depicted methods.

effort, it is impossible to choose the most accurate available method for each of these tasks. Therefore, so-called multi-level approaches are common practice in computational chemistry. In such approaches, very time consuming calculations are typically conducted with fast but also more approximate methods. For example, even a single point calculation with CCSD(T) applying a sufficiently large basis set, can take weeks to months for small to average sized molecules. Therefore, geometry optimizations that require many optimization cycles are not feasible with such accurate but computationally demanding methods. Accordingly, more efficient methods are applied for such tasks, with DFT being the most frequently used choice. Typically, the errors resulting from such substitutions are relatively small if the

2. Theoretical Background

used methods are appropriate for the computational tasks they are chosen for³⁴. Generally, the cost-benefit ratio of such multi-level approaches is sufficiently good and for larger systems they are usually inevitable (cf. table 2.3). With increasing size of the system, even more approximate methods such as SQM methods and FFs have to be applied to allow any treatment of such systems. Further, multi-level approaches can be used to increase the efficiency of tasks in computational chemistry.

Table 2.3.: Exemplary classification of methods employed in multi-level approaches regarding the task and the system size. Note that no comment is made on the applied basis set or technical specifications.

Task	System size (N_{atoms})			
	small (< 100)	medium ($100-500$)	large ($500-5000$)	huge (> 5000)
Conformational sampling	SQM	SQM	FF	-
Reaction path simulation	DFT	DFT/SQM	SQM	-
Geometry optimization	DFT	DFT/SQM	SQM	FF
Vibrational frequencies	DFT	DFT/SQM	SQM/FF	FF
Single point energies	WFT/DFT	WFT/DFT	DFT/SQM	SQM/FF

Part II.

**Studies on Extended Tight Binding
Methods**

Many quantum chemical investigations require hundreds or thousands of quantum chemical calculations or deal with large systems with more than 500 atoms. Such chemical problems are typically untreatable by usual DFT or WFT methods anymore due to the drastically increasing computational demand. Thus, semi-empirical quantum chemical methods are needed that combine sufficient accuracy and small computational cost relative to higher levels of theory. As the speed usually comes at the cost of accuracy resulting from progressive approximation, the development of SQM methods mainly focused on the treatment of elements and systems that are electronically simple like it is often the case for organic chemistry, involving light elements of the first and second row of the periodic table⁴⁵. Focusing on such systems, a plethora of SQM methods was developed based on HF theory and (semi-)local DFT, applying variants of the NDDO and DFTB approximations, respectively. NDDO-based SQM methods include AM1¹⁴⁶, the OMx^{46,147–149} and RM1¹⁵⁰ methods, and the PMx^{50–52,151–153} methods with the prominent representatives PM6⁵¹ and PM7⁵², to name just a few⁴⁹. The most prominent DFTB based methods are those developed by Porezag, Frauenheim, Elstner and co-workers. These include DFTB1¹³⁴, SCC-DFTB^{136,137} (DFTB2), and DFTB3¹³⁸, which are frequently used for molecular and solid-state simulations^{133,154}. Nevertheless, most of these methods are not generally applicable, mostly due to the lack of a comprehensive parametrization including large parts of the periodic table. The most general of these methods, and almost the only ones also applicable to most transition metals, are PM6 and PM7. This lack of SQM methods applicable to transition metals, lanthanoids, and heavy inorganic main group elements, may origin from their often complex electronic structures and unprecedented chemical behavior compared to organic, carbon based chemistry. The small number of

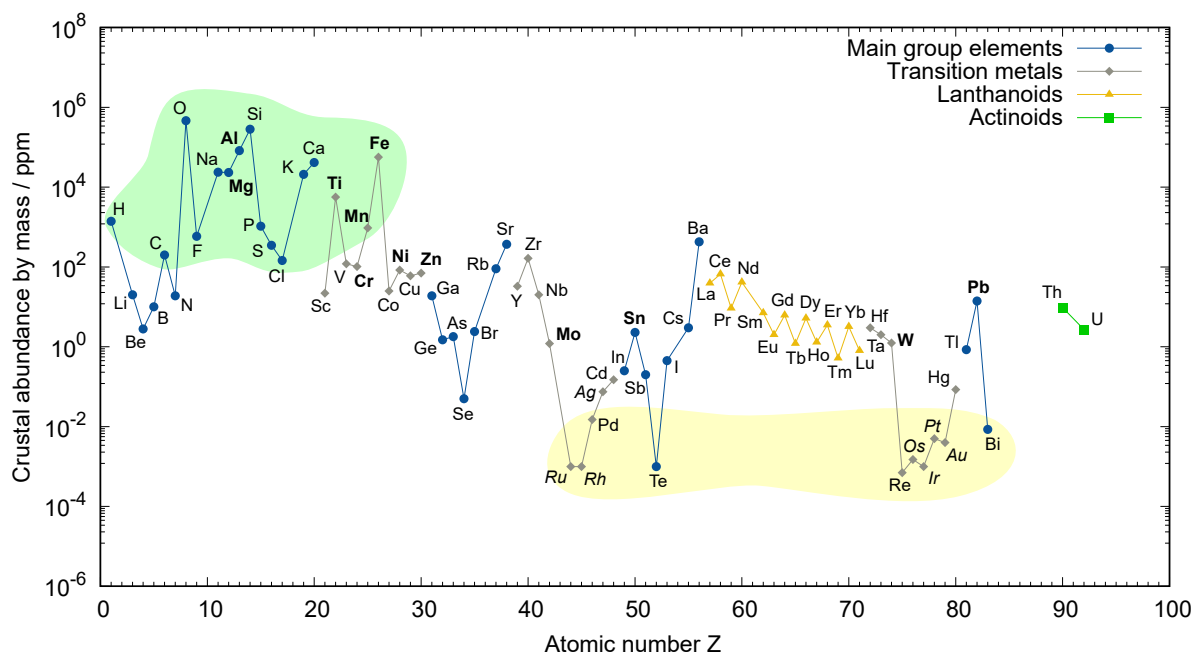


Figure 2.4.: Estimated element abundance in the upper continental crust of the Earth in ppm by mass. Noble gases and elements with very low abundances are excluded. The green area covers the rock-forming elements and the yellow the rarest metals¹⁴⁵.

II. Studies on Extended Tight Binding Methods

suitable SQM methods stands in strong contrast to the importance of these elements in diverse areas of modern chemistry, such as organometallic catalysis, bioinorganic chemistry, or metalorganic material research^{155–157,157–165}. Further, the chemistry of the lanthanoids has developed rapidly in the last decades and their importance for biological systems has received new attention¹⁶⁶. Their perception was also coined by their consideration as so-called "rare earth" elements even though their estimated abundance in the earth crust is comparable to that of many metals that are heavily used in industry (cf. 2.4). Nevertheless, these elements have seen a renaissance being used in bioinorganic, medicinal and photochemistry, as well as in catalysis and synthesis^{166–172}. Inspired by this development and the high demand for more sophisticated and generally applicable SQM methods, the family of GFNn-xTB extended tight binding methods has been developed by Grimme and co-workers more recently^{53–55,57}. Further, a generic FF termed GFN-FF⁵⁶ has been developed in the spirit of the GFNn-xTB methods as well to cover even larger systems. The target properties of these methods are the efficient calculation of geometries, frequencies, and non-covalent interactions as reflected by the acronym GFN. All GFN methods share a comprehensive parametrization for a major part of the periodic table up to radon ($Z = 86$). With these new tools at hand the quantum mechanical investigation of a variety of chemical systems involving transition metals and lanthanoids as well as efficient workflows to enable large scale screening of organometallic compounds become possible. Therefore, part II is devoted to the evaluation and application of the new GFN methods for the description of transition metal and lanthanoid complexes for which suitable testing scenarios, yet unavailable in the literature, were created. In this context chapter 3 deals with the fast and reasonable geometry optimization of lanthanoid complexes with the GFN1-xTB method. Further, chapter 4 extends the evaluation of the GFNn-xTB methods to GFN2-xTB for large to huge transition metal complexes using a newly created benchmark set termed TMG145. Based on the insights from chapter 4, the GFNn-xTB methods were used for automated conformer generation applying the CREST approach, and were evaluated for their application in multi-level based calculation of conformational energies of transition metal complexes.

3. Fast and Reasonable Geometry Optimization of Lanthanoid Complexes with an Extended Tight Binding Quantum Chemical Method

Markus Bursch,^a Andreas Hansen,^a and Stefan Grimme^a

Received 3 August 2017, Published online 5 October 2017

Reprinted (adapted) with permission[†] from

Bursch, M.; Hansen, A.; Grimme, S. *Inorg. Chem.* **2017**, *56*, 12485–12491.

— Copyright © 2017 American Chemical Society.

DOI [10.1021/acs.inorgchem.7b01950](https://doi.org/10.1021/acs.inorgchem.7b01950)

Own manuscript contribution

- Performing all calculations except for DFT optimizations
- Interpretation of the results
- Writing the manuscript

^aMulliken Center for Theoretical Chemistry, Institut für Physikalische und Theoretische Chemie, Rheinische Friedrich-Wilhelms-Universität Bonn, Beringstraße 4, 53115 Bonn, Germany

[†]Permission requests to reuse material from this chapter should be directed to the American Chemical Society.

3. Geometry Optimization of Lanthanoid Complexes with an Extended Tight Binding Method

Abstract The recently developed tight binding electronic structure approach GFN1-xTB is tested in a comprehensive and diverse lanthanoid geometry optimization benchmark containing 80 lanthanoid complexes. The results are evaluated with reference to high-quality X-ray molecular structures obtained from the Cambridge Structural Database (CSD) and theoretical DFT-D3(BJ) optimized structures for a few Pm ($Z = 61$) containing systems. The average structural heavy atom root-mean-square deviation (RMSD) of GFN1-xTB (0.65 Å) is smaller compared to its competitors, the Sparkle/PM6 (0.86 Å) and HF-3c (0.68 Å) quantum chemical methods. It is shown that GFN1-xTB yields chemically reasonable structures, less outliers, and performs well in terms of overall computational speed compared to other low-cost methods. The good reproduction of large lanthanoid complex structures corroborates the wide applicability of the GFN1-xTB approach and its value as efficient low-cost quantum chemical method. Its main purpose is the search for energetically low-lying complex conformations in the elucidation of reaction mechanisms.

3.1. Introduction

Lanthanoid complexes of various size are of interest in a broad field of applications like photo-emitting materials¹⁷³, bio imaging¹⁷⁴, luminescent lanthanoid-based metal organic frameworks^{175–177}, and homogeneous catalysis¹⁷⁸ to name only a few known applications. Thus, the correct computation of such lanthanoid complex structures is fundamental for theoretical and mechanistic studies in these fields of research. In the last decades the Sparkle^{179–181} model extensions of several semi-empirical methods like AM1^{146,182–191}, PM3^{50,192–198}, PM6^{51,199}, PM7^{52,200}, and RM1^{150,201} were developed to optimize the geometries of coordination complexes containing +3 charged lanthanoid ions. Specifically Sparkle/PM6 still represents the state-of-the-art for semi-empirical methods in this field, in which theoretical alternatives are lacking. In this work, we investigate the applicability of the recently developed GFN1-xTB⁵³ tight binding electronic structure approach for geometry optimization of a large and diverse set of common lanthanoid complexes. High-quality X-ray molecular structures obtained from the Cambridge Structural Database (CSD)²⁰² and theoretical DFT-D3(BJ) reference structures for Pm ($Z = 61$) containing systems are taken as reference. The competitive quantum chemical methods Sparkle/PM6 as well as HF-3c¹²⁷ are applied to the same set of structures in order to put the quality of the new method into some perspective. While GFN1-xTB and PM6 should formally have the same computational cost (for practical computation times see Section Computation time3.3), HF-3c usually is 1-2 orders of magnitude slower (but an order of magnitude faster than DFT-D3 with a reasonable AO basis set). Energetic (thermochemical) properties are not considered here but we note, that GFN1-xTB has recently been applied successfully to study high energy processes like the dissociation of transition metal complexes in electron ionization mass spectrometry²⁰³ (QCEIMS method²⁰⁴). Furthermore, reasonable atomic charges are in general obtained from GFN1-xTB which were recently used to improve the widely used D3 dispersion model¹¹⁵. In a few examples we further demonstrate the ability of GFN1-xTB for the search of energetically low-lying conformations for complexes with flexible ligands.

3.2. Computational Details

The semi-empirical tight binding method GFN1-xTB is parametrized for all elements up to $Z = 86$. The number of parameters is kept small and element-pair-specific parameters are largely avoided. As the GFN1-xTB method does not focus on the description of electronic (spectroscopic) or magnetic properties, the lanthanoids are treated like 4d transition metals in a 'f-in-core' approximation¹⁴³. Accordingly, the f-electrons are not explicitly considered and all lanthanoids contribute three valence electrons to the electronic structure. Note, that in the Sparkle/PM6 approach no electrons (basis functions) are provided by the lanthanoid atom meaning that all bonding is basically of electrostatic origin. Furthermore the parametrization of the lanthanoids was simplified by linear interpolation with the nuclear charge Z , where only Ce ($Z = 58$) and Lu ($Z = 71$) were fitted as the start and end points. As reference data mainly structures including hard bases as ligands (halides, amines, carboxylates etc.) were employed, as these are predominantly observed in most common lanthanoid complexes. Nevertheless, several inorganic ligands (alanates, boranes, metal organic ligands) were also included in the parametrization set. The coordination numbers of the utilized structures ranges from 3 to 15. For further methodological details on GFN1-xTB and its parameters see reference⁵³. All Sparkle/PM6 calculations were carried out with the MOPAC2016²⁰⁵ program package. HF-3c¹²⁷ calculations were conducted with the TURBOMOLE 7.0.2^{206,207} program and the DFT-D3(BJ)-ATM reference structures were calculated with the ORCA 4.0.0^{208,209} program package at the ZORA-PBE0-D3(BJ)-ATM^{31,59,121,122,124,125,210-213}/ZORA-def2-TZVP²¹⁴ all electron level of theory applying the SARC2-ZORA-QZV²¹⁵ basis set for the lanthanoid atoms and a fine numerical integration grid (*GRID7* as implemented in ORCA). The GFN1-xTB structure optimizations were carried out with the xtb 4.8²¹⁶ stand alone program which can be obtained free of charge for academic use. GFN1-xTB default convergence criteria were used (SCF: $1.0 \cdot 10^{-6} E_h$; Gradient: $1.0 \cdot 10^{-3} E_h$). Sparkle/PM6 calculations were conducted with identical convergence criteria. For HF-3c calculations slightly changed TURBOMOLE convergence criteria were used (SCF: $1.0 \cdot 10^{-7} E_h$; Gradient: $1.0 \cdot 10^{-4} E_h$). For further details see appendix A2.

3.3. Results and Discussion

General Remarks

Our benchmark set consists of 77 disorder-free high-quality crystallographic structures with R-factors below 0.05 extracted from the Cambridge Structural Database. Three additional promethium containing complex structures were calculated as molecular reference (due to its radioactivity, no crystal structures are available). The structure numbering and the corresponding CSD identification numbers can be found in tables 3.1 and 3.2. Missing entries indicate not achieved convergence or failed SCF convergence occurred during geometry optimization. We observed this in four GFN1-xTB, three Sparkle/PM6 and six HF-3c calculations. For GFN1-xTB this was rarely observed for larger multi nuclear lanthanoid clusters with small bridging anionic ligands. In these special cases an artificial contraction of the lanthanoid framework was observed. The benchmark set contains mono-, multi nuclear, and lanthanoid-transition metal mixed complexes with versatile organic and inorganic ligands. Neutral and ionic mono- and

3. Geometry Optimization of Lanthanoid Complexes with an Extended Tight Binding Method

multi dentate ligands of variable flexibility and size are included. Four structural quality criteria for comparison of experimental and theoretical molecular structures are applied: (i) heavy-atom (all except H) root-mean-square deviation (RMSD), (ii) absolute mean coordination number (CN) change of the lanthanoid atoms (ΔCN_{mean}), (iii) the mean absolute deviation (MAD) of the Ln-Ligand bond distances ($d_{\text{A-B}}$) and (iv) structural correctness (SC). The latter criteria indicates chemical or coordinative changes that might not be reflected by the previous criteria.

Geometry Optimization

Overall GFN1-xTB performs well in all quality criteria compared to the well established method Sparkle/PM6 (for the raw data see the online Supporting Information of the original publication). It yields a smaller mean heavy atom RMSD (Figure 3.2a, table 3.4) of 0.65 Å compared to Sparkle/PM6 (0.86 Å) and HF-3c (0.68 Å) indicating, that ligand-ligand and electrostatic interactions are well described within GFN1-xTB on a competitive level. The investigation of the lanthanoid-ligand bond distances indicates that GFN1-xTB reproduces the direct coordination sphere with a MAD of 0.23 Å slightly worse than Sparkle/PM6 with a MAD of 0.19 Å. HF-3c clearly outperforms both, GFN1-xTB and Sparkle/PM6, with a MAD of only 0.10 Å. The performance of GFN1-xTB for this property can be partly explained by several outliers of sterically overloaded structures containing cyclopentadienyl

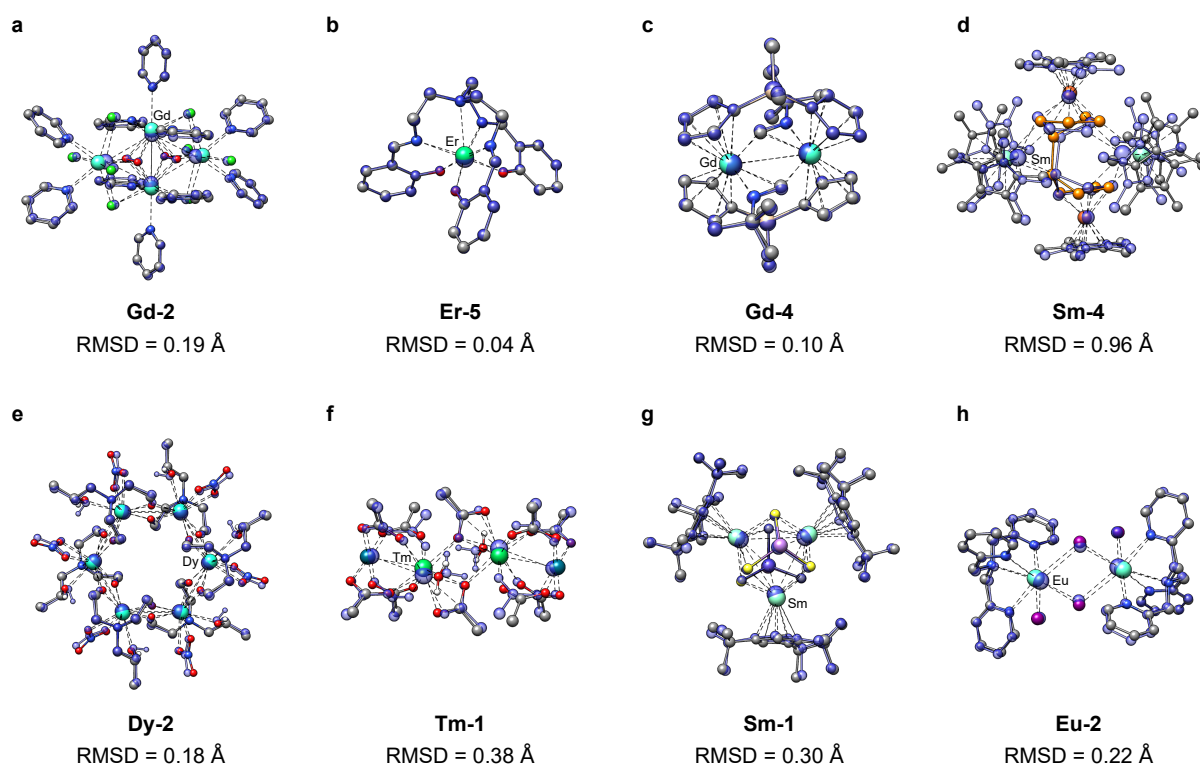


Figure 3.1.: Overlays of structures for eight selected lanthanoid complexes. The GFN1-xTB optimized structures are depicted in transparent blue, the X-ray structures with color coded atoms. Most hydrogen atoms are omitted for clarity. The heavy atom RMSD is given in Å.

Table 3.1.: Data comparison for complexes containing elements La–Eu. The RMSD is given in Å, wall time (WT) in seconds. Structural Correctness (SC): Yes = Y; No = N.

entry	CSD	CHRG	GFN1-xTB					Sparkle/PM6				
			RMSD	WT	cycles	ΔCN_m	SC	RMSD	WT	cyc.	ΔCN_m	SC
La-1	1406265	0	0.63	39	87	0.43	Y	0.58	144	597	1.15	Y
La-2	1409125	0	1.08	22	146	0.84	Y	0.92	197	997	0.65	Y
La-3	1410388	0	0.49	10	48	0.02	Y	0.90	29	270	4.43	N
La-4	1418152	-1	1.68	19	98	5.22	N	2.82	177	1699	2.4	N
La-5	215859	0	0.70	46	62	1.48	Y	0.44	117	350	1.07	Y
La-6	913893	0	0.50	19	51	2.42	Y	0.45	80	301	1.82	Y
Ce-1	1044879	0	-	-	-	-	-	-	-	-	-	-
Ce-2	1409131	0	0.58	12	84	0.30	Y	0.55	58	278	0.95	Y
Ce-3	636475	0	0.32	21	53	0.57	Y	0.43	35	195	1.94	Y
Ce-4	774594	0	0.89	229	179	0.39	N	1.21	208	219	1.6	N
Ce-5	797225	+4	0.41	12	40	1.91	Y	1.33	45	333	0.5	Y
Ce-6	804892	0	1.33	7	155	1.64	N	1.99	6	103	0.55	N
Ce-7	836189	-1	0.77	101	100	0.24	N	0.69	306	397	2.35	Y
Ce-8	904596	0	-	-	-	-	-	1.18	752	549	1.38	N
Ce-9	220013	0	0.47	7	33	0.15	Y	1.67	39	127	1.83	N
Ce-10	862911	0	0.34	6	39	0.37	N	1.31	24	426	0.97	Y
Pr-1	211410	0	0.18	9	26	0.42	Y	0.76	52	327	0.19	Y
Pr-2	222805	+3	0.17	5	32	1.00	Y	0.34	17	323	0.2	Y
Pr-3	229509	0	0.65	18	107	0.67	Y	0.45	15	202	0.56	Y
Pr-4	789537	0	-	-	-	-	-	1.11	230	386	0.81	N
Pr-5	812633	0	0.28	13	36	0.44	Y	0.43	11	78	0.89	Y
Pr-6	815090	0	0.47	23	75	0.02	Y	0.57	87	757	0.86	Y
Nd-1	1058297	0	1.67	57	219	0.27	N	1.14	124	102	0.09	N
Nd-2	1409126	0	0.55	23	91	1.57	Y	0.50	65	291	0.19	Y
Nd-3	186711	0	0.47	58	71	0.80	Y	1.22	364	536	0.01	Y
Nd-4	789536	0	0.95	139	153	0.47	N	0.67	265	524	1.08	Y
Nd-5	906651	0	1.02	142	151	3.52	Y	0.97	276	424	0.35	Y
Pm-1		0	0.28	2	27	0.60	Y	0.18	2	37	2.89	N
Pm-2		0	0.13	1	19	1.22	Y	0.70	7	174	0.14	Y
Pm-3		0	0.06	0	9	0.15	Y	0.31	01	66	1.54	N
Sm-1	1016561	0	0.30	63	77	0.29	Y	0.68	56	98	1.54	N
Sm-2	209486	0	0.17	3	19	1.01	Y	0.82	7	187	0.71	Y
Sm-3	228522	0	1.23	58	177	0.48	Y	0.27	253	209	0.21	Y
Sm-4	914587	0	0.96	260	196	0.64	Y	1.11	528	364	0.8	Y
Sm-5	963104	-2	0.15	0	17	1.95	Y	0.13	0	25	0.62	Y
Eu-1	1151903	0	1.43	144	343	1.11	Y	1.45	28	71	1.54	N
Eu-2	1402204	0	0.22	22	55	0.66	Y	0.76	2934	213	0.66	N
Eu-3	815914	+2	0.82	20	75	0.42	Y	2.59	141	597	1.01	N
Eu-4	1158110	+2	0.17	4	25	0.82	Y	0.20	13	198	0.06	Y
Eu-5	1158110	-2	0.56	3	98	0.41	N	1.29	10	637	2.49	Y

3. Geometry Optimization of Lanthanoid Complexes with an Extended Tight Binding Method

Table 3.2.: Data comparison for complexes containing elements Gd–Lu. The RMSD is given in Å, wall time (WT) in seconds. Structural Correctness (SC): Yes = Y; No = N.

entry	CSD	CHRG	GFN1-xTB					Sparkle/PM6				
			RMSD	WT	cycles	ΔCN_m	SC	RMSD	WT	cyc.	ΔCN_m	SC
Gd-1	1145951	0	0.16	2	27	1.23	Y	0.80	7	126	0.41	Y
Gd-2	191242	0	0.19	21	31	0.37	Y	0.75	80	126	1.28	Y
Gd-3	809026	0	0.78	194	133	0.36	Y	0.69	506	536	1.59	N
Gd-4	854536	0	0.10	6	25	0.28	Y	0.43	18	119	1.32	Y
Gd-5	908963	0	0.75	44	70	0.63	N	1.84	40	65	3.25	N
Tb-1	1008454	0	0.65	18	60	1.69	N	0.31	20	135	1.01	Y
Tb-2	741843	0	1.51	96	179	2.58	N	0.89	249	476	1.05	Y
Tb-3	914007	0	0.81	119	184	0.39	Y	–	–	–	–	–
Tb-4	132373	0	0.81	98	151	0.31	Y	1.06	261	419	0.17	N
Tb-5	1227115	0	0.60	24	81	0.40	Y	0.86	45	160	1.7	Y
Dy-1	789527	0	1.41	139	196	1.73	N	0.96	65	137	0.83	Y
Dy-2	920636	0	0.18	58	53	5.59	Y	0.52	252	476	0.76	Y
Dy-3	642445	0	1.91	10	105	0.43	N	0.75	19	111	2.13	N
Dy-4	938031	0	0.35	27	42	1.95	N	0.65	134	382	2.5	N
Dy-5	1209340	0	0.39	4	34	1.08	Y	0.81	38	397	1.38	Y
Ho-1	1160702	0	0.28	2	28	0.28	Y	0.24	1	18	3.59	N
Ho-2	949430	0	0.17	3	38	2.31	Y	0.41	3	60	0.26	N
Ho-3	1008527	0	0.58	113	166	1.37	Y	0.82	186	386	0.19	Y
Ho-4	1107060	0	1.80	108	260	0.46	N	1.60	30	33	0.61	Y
Ho-5	287100	0	0.15	2	19	0.17	Y	0.50	5	141	0.53	Y
Er-1	1063556	–2	1.36	232	307	0.47	N	–	–	–	–	–
Er-2	1140170	0	1.14	30	130	2.87	Y	2.13	91	351	1.02	Y
Er-3	186712	0	0.75	78	121	0.34	Y	1.28	790	1204	0.02	N
Er-4	1276830	0	0.49	17	56	0.42	Y	0.21	36	90	0.09	Y
Er-5	1282289	0	0.04	1	11	0.27	Y	0.40	16	268	0.47	Y
Tm-1	695868	0	0.38	20	100	0.36	Y	0.52	30	216	0.85	Y
Tm-2	752927	0	–	–	–	–	–	1.11	59	226	1.63	Y
Tm-3	241797	0	2.06	129	233	0.70	N	1.82	450	1359	0.66	Y
Tm-4	984462	0	0.17	62	52	0.51	Y	0.61	264	531	0.72	Y
Tm-5	1130736	0	0.99	36	161	0.17	Y	1.13	69	419	0.6	Y
Yb-1	1016562	0	0.21	19	59	0.56	Y	1.28	62	213	1.26	N
Yb-2	136019	0	0.52	33	53	0.74	Y	0.49	1283	496	0.37	Y
Yb-3	1404893	0	0.27	25	46	0.15	Y	0.68	914	123	0.97	Y
Yb-4	153628	0	0.61	29	75	1.07	Y	0.72	51	173	0.7	Y
Yb-5	174206	0	0.63	28	91	1.22	Y	0.76	140	540	0.43	Y
Lu-1	1164391	0	0.21	10	25	0.16	Y	0.48	243	369	0.93	Y
Lu-2	213481	0	0.53	60	105	1.76	Y	0.97	138	326	0.66	Y
Lu-3	233097	0	1.40	290	241	1.85	Y	0.36	256	337	0.62	Y
Lu-4	138662	0	0.39	26	61	0.09	Y	0.40	117	287	0.1	Y
Lu-5	1236083	0	0.39	14	47	0.13	Y	0.61	11	31	0.57	Y

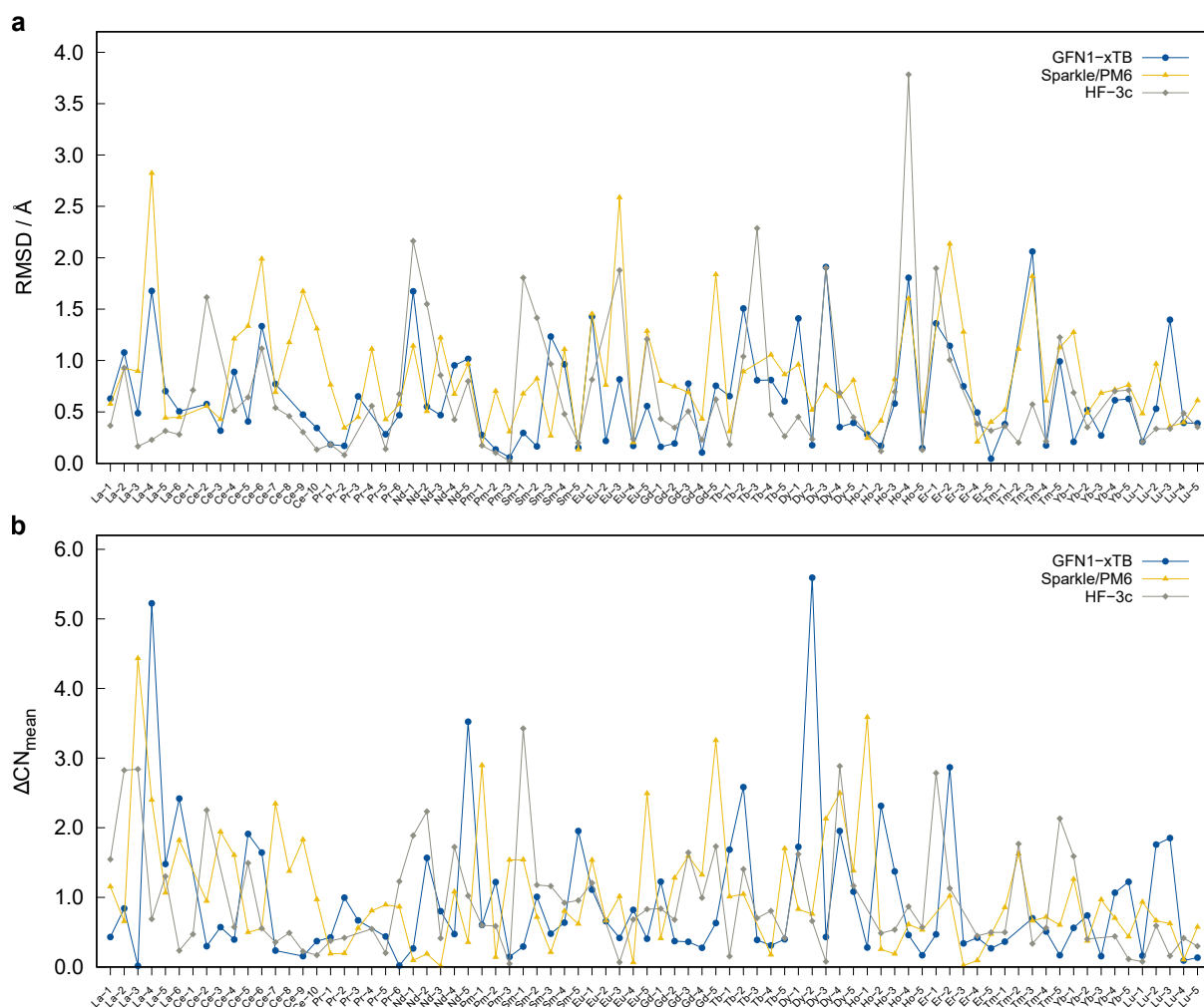


Figure 3.2.: Mean absolute coordination number change of the lanthanoid atoms relative to the reference structures and overall mean absolute deviations for GFN1-xTB (blue), Sparkle/PM6 (yellow) and HF-3c (gray).

ligands, where a partial decoordination of these ligands causes large deviations. The mean absolute deviation of the mean coordination number of the lanthanoid atoms (Figure 3.2b) shows comparably good performance with a MAD of 0.95 compared to 1.04 for Sparkle/PM6 and 0.93 for HF-3c. The few outliers (**La-4**, **Nd-4** and **Dy-1**) for GFN1-xTB refer to hydride bridged lanthanoid cluster structures that show strong reorganization of the inner ligand sphere during the optimization. The individual data as well as the structural correctness criterion are shown in table 3.1 and 3.2. Overall the structures obtained with GFN1-xTB are of good quality and some examples are depicted in figure 3.1. Remarkably good structures are obtained for structures including conformationally well defined multi dentate ligands like **Er-5** (RMSD = 0.04 Å) or **Gd-4** (RMSD = 0.10 Å). Even for the chemically rather 'exotic' cases as **Sm-1**, a thioarsenite bridged trinuclear samarium complex, or **Tm-1**, including short Tm-Pd contacts, reasonable RMSD values of 0.32 Å and 0.38 Å, respectively, are obtained with GFN1-xTB. The obtained overall structural quality data are summed up in table 3.3. At this point we emphasize that GFN1-

3. Geometry Optimization of Lanthanoid Complexes with an Extended Tight Binding Method

Table 3.3.: Obtained overall structural quality data for GFN1-xTB, Sparkle/PM6 and HF-3c.

Method	MRMSD / Å	MD _(d_{A-B}) / Å	MAD _(d_{A-B}) / Å	MAD _(CN_m)
GFN1-xTB	0.65	0.10	0.23	0.95
Sparkle/PM6	0.86	-0.09	0.19	1.04
HF-3c	0.68	-0.01	0.10	0.93

xTB is less heavily parametrized compared to many other semi-empirical methods in common use (e.g. DFTB^{133–138}) and mainly employs a small number of global and element-specific parameters. A direct comparison of six GFN1-xTB optimized structures with high quality DFT-D3(BJ)-ATM reference structures (Table 3.4) further reveals a good and even better accordance of the GFN1-xTB structures and the high level DFT results for isolated molecules. This indicates that a small part of the residual deviations between theory and experiment are due to crystal “packing” effects, which, however, presently due to technical reasons can not be resolved by periodic calculations. Particularly, the deviations for spatially expanded structures or such with highly flexible ligand spheres are expected to be significantly smaller in comparison to gas phase reference data which should be kept in mind when judging the results.

Table 3.4.: RMSD and ΔCN_m of the GFN1-xTB optimized structures to the X-ray structures (RMSD_{X-ray}) and exemplary DFT-D3(BJ)-ATM optimized structures (RMSD_{calc.}).

entry	CSD	RMSD _{X-ray} / Å	$\Delta\text{CN}_{m, \text{X-ray}}$	RMSD _{calc.} / Å	$\Delta\text{CN}_{m, \text{calc.}}$
Pm-1	–	–	–	0.28	1.22
Pm-2	–	–	–	0.13	0.15
Pm-3	–	–	–	0.06	0.29
Ho-5	287100	0.15	0.47	0.09	0.00
Pr-5	812633	0.28	0.02	0.28	0.51
Sm-5	963104	0.15	1.11	0.08	0.77

Computation Time

In terms of computation (wall) time, GFN1-xTB clearly outperforms Sparkle/PM6 in most cases (Figure 3.3). The generally low computation times (small number of electronic self-consistent field (SCF) cycles) and the small number of required optimization steps emphasizes the high efficiency and robustness of GFN1-xTB and the corresponding code. Specifically the highly efficient optimizer in the xtb code in combination with fast SCF calculations lead to the short computation times observed. Note, that all

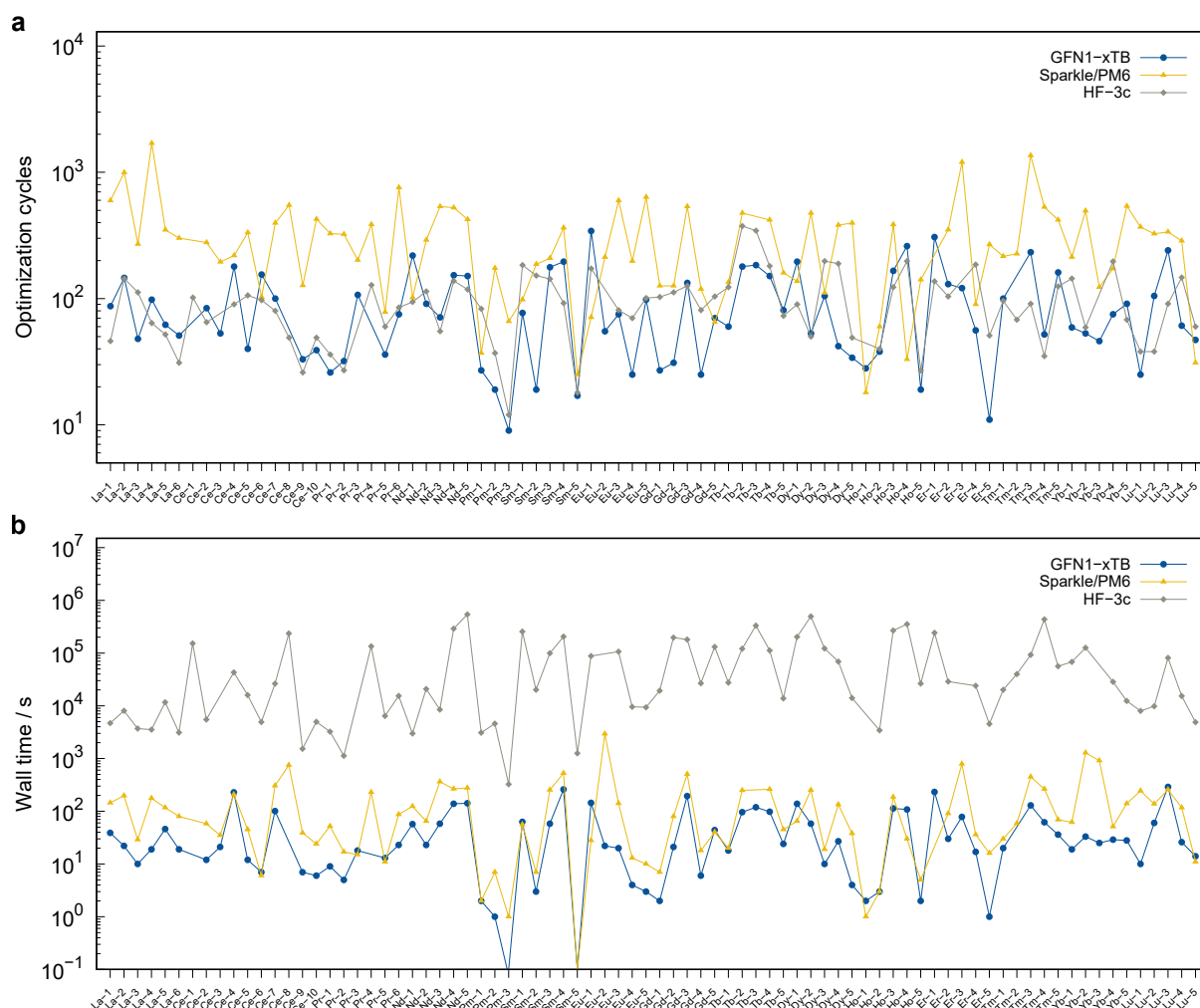


Figure 3.3.: Serial computation (wall) time in seconds for GFN1-xTB (blue) and Sparkle/PM6 (yellow).

timings refer to a single CPU and hence, parallel runs which are possible further extend the broad applicability of the method to even larger systems at reasonably turnaround times.

Conformational Search Application

For the complexes **Er-2** and **Ce-9**, which have more flexible ligands, we conducted automated conformational searches using a newly developed normal-mode-following algorithm that is implemented in the xtb code and which will be published separately. The search was started with the optimized X-ray structure and the resulting ensemble of energetically low-lying structures was re-evaluated by single point energy calculations at the ZORA-PBE0-D3(BJ)/ZORA-def2-TZVP(SARC2-ZORA-QZV@Ln)//GFN1-xTB level of theory. The input structures and the energetically lowest conformers at the DFT level are depicted in figure 3.4. Specifically for **Er-2** the maximization of attractive ligand-ligand interactions (π stacking) in the absence of crystal packing becomes apparent in the energetically lowest conformer found. Even though the GFN1-xTB conformer energy ranking may vary from that of higher

3. Geometry Optimization of Lanthanoid Complexes with an Extended Tight Binding Method

level computations, the generation of an almost complete conformer ensemble of good structural quality is far from being trivial and the structure generation represents in many applications the most time consuming step. Therefore the use of GFN1-xTB in efficient composite approaches is of high value. An application and details on the automated conformational search algorithm based on GFN1-xTB were recently shown in the context of fully automated quantum chemistry based computations of spin-spin coupled nuclear magnetic resonance spectra⁶¹.

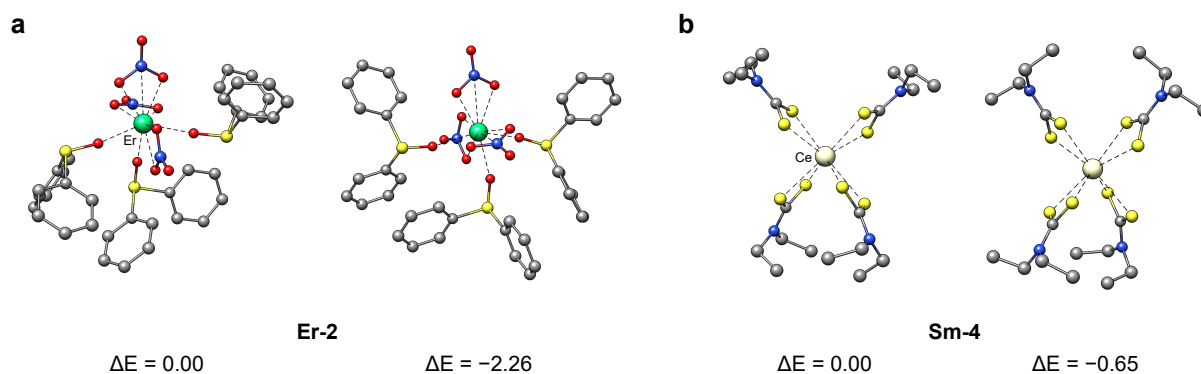


Figure 3.4.: Exemplary conformational search for a) **Er-2** and b) **Ce-9**. GFN1-xTB optimized X-ray cutout (left) and the corresponding energetically lowest conformer after re-evaluation obtained by the automated conformational search (right) with their relative ZORA-PBE0-D3(BJ)-ATM/ZORA-def2-TZVP(SARC2-ZORA-QZV@Ln)//GFN1-xTB energies in kcal mol⁻¹.

3.4. Conclusion and Outlook

The new GFN1-xTB method proved to be a versatile and fast semi-empirical tool for the computation of molecular structures containing elements up to $Z = 86$ including all lanthanoids ($Z = 57-71$), the latter specifically considered in this work. Its flexible and robust design qualifies this method to deal with a broad field of chemical applications without requiring large computational resources. The ability to optimize lanthanoid complex structures at state-of-the-art semi-empirical or better quality and with very low computational cost was demonstrated in this work for a very versatile and diverse set of 80 reference structures (77 X-ray structures). For 44 out of the 80 cases, the RMSD to the X-ray structure was less than 0.6 Å meaning that the theoretical structure more or less coincides with the experimental one. Part of the residual deviations are attributed to crystal packing/crystal field effects which are neglected in our study. The robustness of GFN1-xTB combined with its excellent cost/accuracy ratio enables the consistent computation of molecular structures up to a few thousand atoms which also allows the investigation of large lanthanoid frameworks. A periodic implementation to enable three dimensional crystal structure optimization for material design is in progress in our lab. Large scale screening investigations are now possible also for lanthanoid complexes allowing computational chemists and experimentalists to gain more insight into the structural characteristics of such systems. Furthermore, conformational analysis for systems with flexible ligands can be conducted quite routinely, which is

important for the elucidation of reaction mechanisms or then the computation of spectra.

Acknowledgements

This work was supported by the DFG in the framework of the Gottfried Wilhelm Leibniz prize to S.G. The authors thank Dr. C. Bannwarth, P. Pracht, J. Pisarek and Dr. C. Bauer for many fruitful discussions and all experimentalists for providing high quality X-ray data to the CSD.

4. Structure Optimization of Large Transition-Metal Complexes with Extended Tight Binding Methods

Markus Bursch,^a Hagen Neugebauer,^a and Stefan Grimme^a

Received 2 April 2019, Published online 8 July 2019

Reprinted (adapted) with permission[†] from

Bursch, M.; Neugebauer, H.; Grimme, S. *Angew. Chem. Int. Ed.* **2019**, *131*, 11195–11204.

— Copyright © 2019, WILEY-VCH Verlag GmbH & Co. KGaA, Weinheim.

DOI [10.1002/anie.201904021](https://doi.org/10.1002/anie.201904021)

Own manuscript contribution

- Performing the calculations
- Interpretation of the results
- Writing the manuscript

^aMulliken Center for Theoretical Chemistry, Institut für Physikalische und Theoretische Chemie, Rheinische Friedrich-Wilhelms-Universität Bonn, Beringstraße 4, 53115 Bonn, Germany

[†]Permission requests to reuse material from this chapter should be directed to WILEY-VCH.

Abstract Large transition metal complexes are used in numerous areas of chemistry. Computer-aided theoretical investigations of such complexes are limited by the sheer size of real systems often consisting of hundreds to thousands of atoms. Accordingly, the development and thorough evaluation of fast semi-empirical quantum mechanical methods, which are universally applicable for a large part of the periodic table, is indispensable. Here we report on the capability of the recently developed GFNn-xTB method family for full quantum mechanical geometry optimization of medium to very large transition metal complexes and organometallic supramolecular structures. Furthermore, the results for a specially compiled benchmark set of 145 diverse closed-shell transition metal complex structures for all metals up to Hg are presented.

4.1. Introduction

Although the power of generally available computer hardware has increased tremendously in recent years, the demand for fast, efficient and yet accurate quantum chemical methods still exists. Where wave function and density functional theory based methods reach their limits regarding the feasible system size, semi-empirical quantum mechanical (SQM) methods like GFNn-xTB^{53,54}, DFTB^{133,134,136-138}, PMx⁵⁰⁻⁵² or OMx¹⁴⁷⁻¹⁴⁹ to name only a few, have established themselves as valuable computational tools. However, most SQM methods are limited in their applicability to a few elements of the periodic table by incomplete or very specialized parametrization. In particular, the treatment of transition metals is limited or even impossible in many SQM methods. This is contradicting the importance of transition metals being used in numerous and diverse areas of chemistry partly involving very large or extended molecular or periodic systems. Examples are supramolecular organometallic aggregates such as metal organic polyhedra (MOP) or macrocycles (MOM), metal organic frameworks (MOF), and metal containing biomolecules such as metalloproteins or a combination to metal-biomolecule frameworks (MBioF)²¹⁷. Such compounds are not only highly interesting from a fundamental chemical point of view, but their unique properties also make them valuable for industrial technologies. They are used, for example, in catalysis¹⁶⁰, for fuel storage^{218,219}, as semi-conductor materials²²⁰, in ferro-electrics²²¹, as filtration or selection materials, in biomedical applications like bioimaging and sensing²²², biomimetic mineralization¹⁶¹, or as drug delivery^{223,224} systems²²⁵⁻²²⁷. The potential field of application for efficient SQM methods is correspondingly large. However, universally applicable methods that are fully parametrized for transition metals is mostly limited to two method families, namely the already frequently used neglect of diatomic differential overlap (NDDO) based PMx (Parametric Method x) methods⁵⁰⁻⁵² and the recently introduced extended tight binding methods GFNn-xTB^{53,54} (Geometries, vibrational frequencies and non-covalent interactions extended tight binding) from our lab. The robustness and quality of the GFNn-xTB methods has already been demonstrated in numerous applications with a predominantly organic chemistry focus. These applications include simulation of electron ionization mass spectrometry^{203,204}, fully automated computation of spin-spin-coupled nuclear resonance spectra⁶¹ including conformer-rotamer ensemble generation, atomic charge generation for the new D4 dispersion correction^{115,116}, geometry optimization of lanthanoid complexes²²⁸, automated determination of protonation sites²²⁹, pKa calculation in the SAMPL6 blind challenge²³⁰,

meta-dynamics based exploration of chemical compound conformation and reaction space²³¹, and few studies on organometallic systems^{232–236}. The focus here is on demonstrating the quality of GFN2-xTB and its precursor GFN1-xTB for structure optimization of transition metal complexes and in particular of very large organometallic systems which are to date not possible otherwise. The recently published GFN2-xTB approach features less empiricism, improved electrostatic interactions (multipole terms up to atomic dipole-quadrupole interactions), as well as a density(atomic charge)-dependent London dispersion energy correction^{31,33} at even slightly reduced computational cost. Theoretically it seems interesting to investigate how this improved physical description effects the performance for large 'real-life' applications. Note that the GFNn-xTB methods usually describe also vibrational frequencies well if the basic structure is obtained reasonably well and hence our conclusions furthermore have important consequences for the efficient treatment of IR spectra or the computation of thermostistical data (enthalpy and free energy).

Computational Methods

All quantum mechanical calculations were performed with the TURBOMOLE 7.0.2^{206,207} (DFT, UFF⁴⁰), xtb 6.0²³⁷ (GFN1-xTB⁵³, GFN2-xTB⁵⁴), and MOPAC 2016²⁰⁵ (PM6-D3⁵¹, PM6-D3H4¹⁵², PM7⁵²) program packages. The ANCOpt optimizer was applied for GFNn-xTB and PMx optimizations as implemented in the xtb 6.0 program package for comparability with default convergence criteria for energies and gradients ($E_{\text{conv}} = 5 \cdot 10^{-6} E_{\text{h}}$; $G_{\text{conv}} = 1 \cdot 10^{-3} E_{\text{h}} \cdot \text{bohr}^{-1}$). All reference structures were optimized starting from X-ray structure cutouts applying the TPSSH^{238,239} meta hybrid functional with the def2-TZVPP²⁴⁰ basis set with default convergence criteria for energies and gradients as implemented in TURBOMOLE. The D3⁵⁹ dispersion correction scheme with Becke-Johnson damping¹²¹ and Axilrod-Teller-Muto^{124,125} three-body contributions was applied. The default effective core potentials (ECP) *ECP-28* and *ECP-60*^{241,242} were used for all elements with atomic number larger than 36 (Kr) in order to take account of scalar relativistic effects in the DFT calculations. The resolution-of-identity approximation for Coulomb integrals (RIJ)^{243–245} was generally used to speed up the DFT calculations. All calculations were performed on a Intel® Xeon® E5-2660 v4 @ 2.00 GHz machine. For further details see appendix A3.

4.2. Results and Discussion

Benchmark Study

Structural benchmarking is challenging, mainly because of the lack of reasonable, and easily comparable reference data. As quantum mechanical approaches generally yield zero-temperature equilibrium and not thermally and zero-point vibrational motion expanded structures, a direct comparison to structures obtained by e.g. X-ray diffraction methods has to be made with caution. High quality gas-phase electron diffraction data are only available for comparably small molecules, and in general are rare for transition-metal complexes^{246–248}. In addition, solid state structures include interactions with the crystal environment (packing effects) that are difficult to estimate. Therefore we decided

4. Structure Optimization of Large Transition-Metal Complexes with Extended Tight Binding Methods

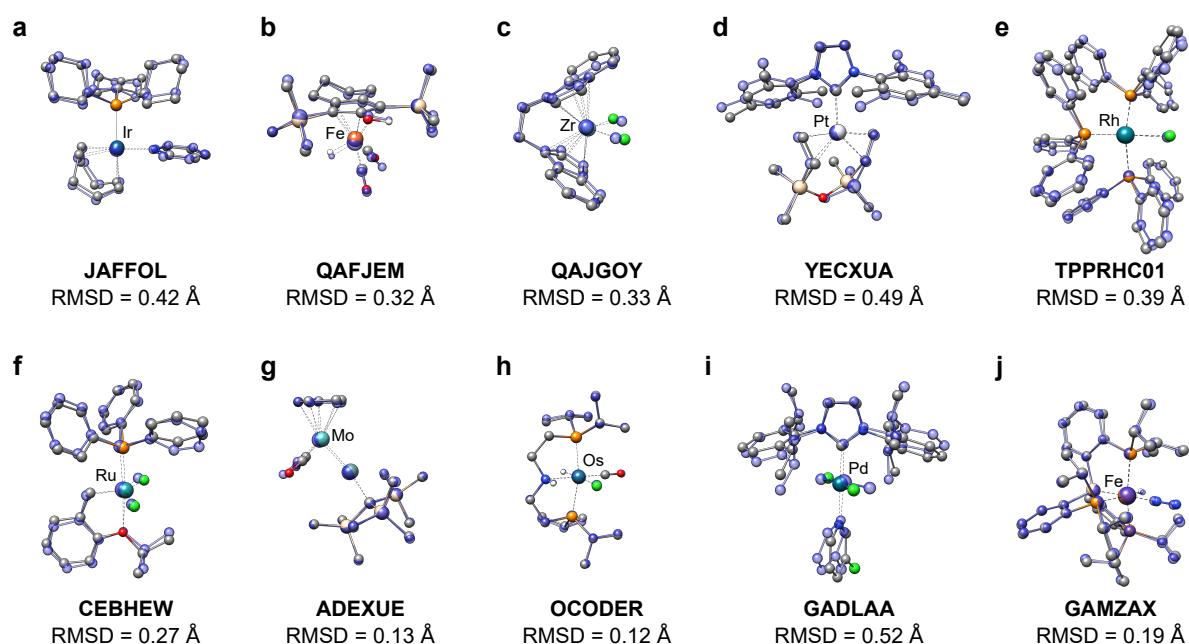


Figure 4.1.: Exemplary structure overlays of unusual transition metal complexes and catalysts. Shown is the DFT reference structure in color code and the GFN2-xTB optimized structure (transparent blue). Hydrogen atoms bound to carbon are omitted for clarity. a) Crabtree catalyst; b) Knölker catalyst; c) Brintzinger-Kaminsky catalyst; d) Karstedt's catalyst variant; e) Wilkinson's catalyst; f) Grubbs-Hoveyda I catalyst; g) Molybdenumgermylydine complex; h) Alcohol dehydrogenation catalyst; i) PEPPSI catalyst; j) terminal dinitrogen complex.

to test the discussed SQM approaches first with reference to high quality DFT optimized structures (TPSSH-D3(BJ)-ATM/def2-TZVPP level) which agree usually very well with appropriate experimental data^{35,246–248}. The new benchmark set, in the future referred to as TMG145 (Transition Metal Geometries), consists of 145 (five for each 1st, 2nd and 3rd row transition metal up to Hg) medium sized (25-200 atoms), diverse transition metal complexes derived from high quality molecular X-ray data. It was selected independently from the fit set underlying the parametrization of the GFNn-xTB methods. All structures have been taken from the Cambridge Structural Database (CSD; all CSD reference codes are given in bold font, e.g. **JAFFOL**) and meet the following selection criteria: 1. high quality structure ($R^2 < 0.5$, no disorders, no polymers), 2. singlet, closed-shell electronic structure, 3. mononuclear complexes, and 4. diversity with respect to bonding patterns, ligand types, coordination polyhedra and oxidation states. The quality of the SQM optimized structures is assessed on the basis of 941 bond distances ($d(A-B)$) including mainly transition metal ligand bond distances and few crucial intraligand bonds, in pm). Further the overall heavy-atom (all elements except H) root-mean-square deviation (RMSD in Å) and the reproduction of 2846 bond angles around the transition metal center ($\angle(A-M-B)$ in °) are used for evaluation. A chemical intuition based structural correctness (SC) criterion by visual inspection of each structure is used to identify structures, that are chemically transformed, dissociated or critically deformed during optimization (cf. ref. 228). Statistical standard deviations correlate well with mean absolute deviations (MAD) and hence only the later are discussed in addition to

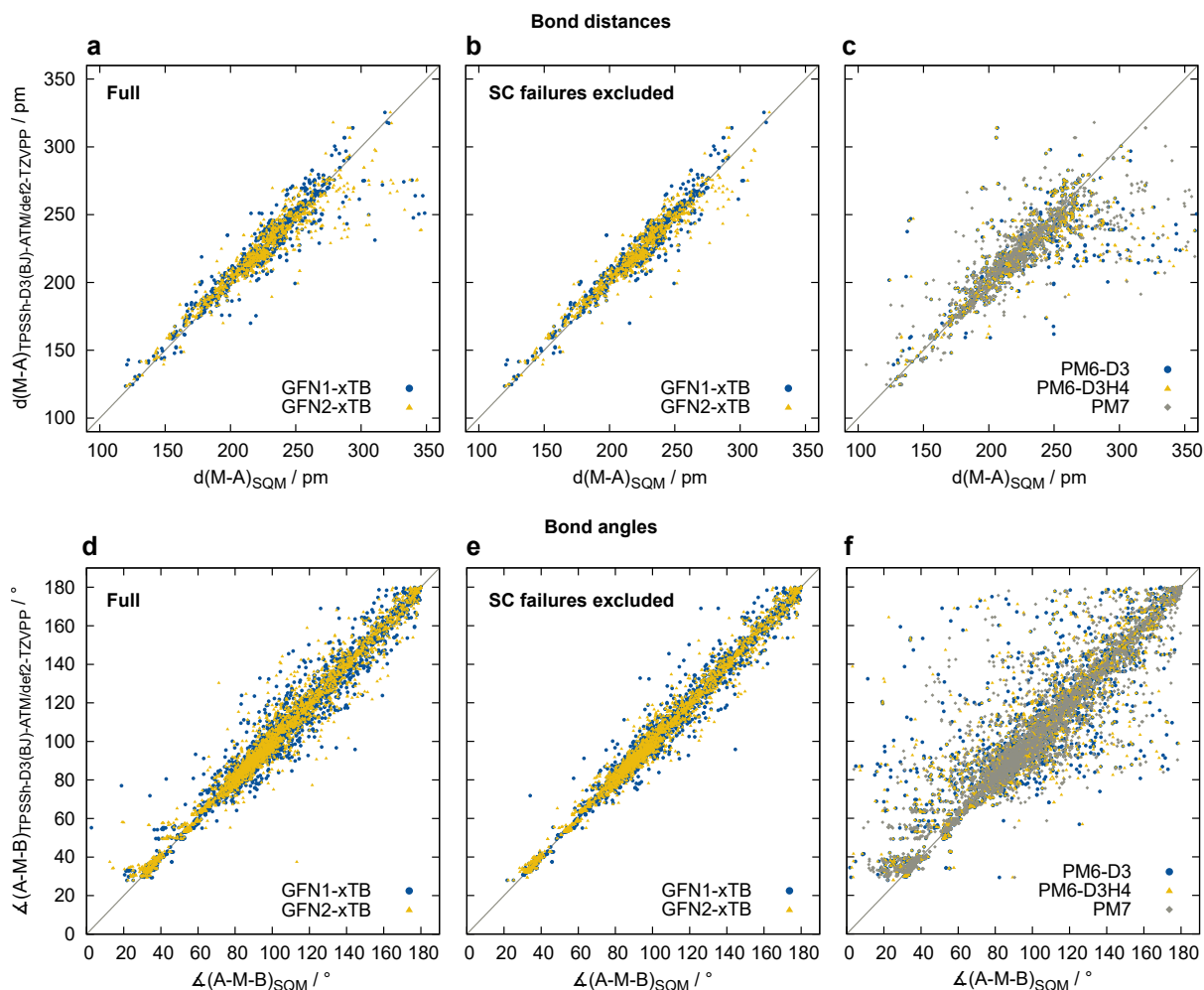


Figure 4.2.: Performance for bond distances and angles in the TMG145 benchmark set. Correlation plots for bond distances and angles obtained with GFN1-xTB, GFN2-xTB and the PM x methods with reference to the DFT structures. Bond distances in pm (a–c) and angles in $^{\circ}$ (d–f). b) and e) show the results upon exclusion of structurally incorrectly optimized structures.

the mean deviation (MD) which usually indicates systematic errors. The GFN n -xTB methods perform very well over the whole set of transition metal complexes. A selection of representative catalysts and some unusual complexes is shown in figure 4.1. Overall, reasonably small statistical deviations of bond distances ($MD_{GFN1} = 0.3$ pm; $MAD_{GFN1} = 7.5$ pm; $MD_{GFN2} = 2.1$ pm; $MAD_{GFN2} = 8.3$ pm) and angles ($MD_{GFN1} = -0.2^{\circ}$; $MAD_{GFN1} = 4.0^{\circ}$; $MD_{GFN2} = -0.5^{\circ}$; $MAD_{GFN2} = 3.9^{\circ}$, cf. figure 4.2a) are obtained. The mean Cartesian RMSD (MRMSD) over the entire set of 0.34 Å for GFN1-xTB and 0.33 Å for GFN2-xTB match these observations. 93% of the GFN2-xTB and 89% of the GFN1-xTB optimized structures remain structurally correct upon optimization while the tested PM x methods perform worse with values of only 61% for PM6-D3 and PM6-D3H4 and 56% for PM7, respectively. The comparably bad performance of the PM x methods is further reflected by large statistical deviations for all three tested methods, PM6-D3 (MRMSD = 0.74 Å; bond distances: MD = 21.7 pm; MAD = 30.2 pm; angles: MD = -3.0° ; MAD = 9.5°), PM6-D3H4 (MRMSD = 0.71 Å; bond distances: MD = 20.9 pm; MAD = 28.9 pm; angles:

4. Structure Optimization of Large Transition-Metal Complexes with Extended Tight Binding Methods

MD = -2.9° ; MAD = 9.3°) and PM7 (MRMSD = 0.70 \AA ; MD = 21.3 ; MAD = 29.7 ; angles: MD = -0.1 ; MAD = 9.3). The collected statistical data are shown in table 4.1. The larger amount of high deviations for longer bonds can mainly be assigned to the few structures that are not structurally correctly optimized. Upon their exclusion, the statistical data for both GFNN-xTB methods greatly improve (see figure 4.2b). For both GFNN-xTB methods, both MAD and SD are reduced on average by 25% and 43% respectively. The improvement in the PMx methods is even greater due to the very large number of structurally incorrectly optimized structures. Nevertheless, even after the exclusion of all those outliers, the PMx methods still perform worse in almost all statistical descriptors. To put this into perspective, the Universal Force Field (UFF)⁴⁰ which is also available for almost all elements, has also been tested. It performs worse than the GFNN-xTB methods (MRMSD = 0.70 \AA ; bond distances: MD = 2.3 pm ; MAD = 14.4 pm ; angles: MD = -0.2° ; MAD = 8.4°) but better than the PMx methods tested here (the number of incorrectly optimized structures is also relatively high at 52%). The very bad description of cyclopentadienyl-like ligands is particularly striking for UFF. This underlines the difficulty in generating a robust description of the widely varying and often difficult electronic structure in metallic compounds which has been achieved in GFNN-xTB but not in the PMx methods. We can only speculate at this point if this is more related to the better underlying reference theory (DFT for GFNN-xTB versus Hartree-Fock for PMx) or to the way how important many-body and basis set effects are ac-

Table 4.1.: Statistical data for all tested semi-empirical methods with reference to TPSSh-D3(BJ)-ATM/def2-TZVPP optimized geometries.

		GFN1-xTB	GFN2-xTB	PM6-D3	PM6-D3H4	PM7	UFF
d(A-B)	MD / pm	0.3	2.1	21.7	20.9	21.3	2.3
	MAD / pm	7.5	8.3	30.2	28.9	29.7	14.4
	SD / pm	15.2	15.1	75.1	71.1	65.0	20.8
	AMAX / pm	224.9	155.3	697.6	669.6	483.2	188.4
	MRMSD / \AA	0.34	0.33	0.74	0.71	0.70	0.70
	MD _{SC} / pm	-0.8	0.6	2.9	3.0	1.7	3.6
	MAD _{SC} / pm	5.5	6.4	8.6	8.7	8.7	12.2
	SD _{SC} / pm	7.9	9.4	13.4	13.8	13.9	16.0
	AMAX _{SC} / pm	50.1	75.8	99.9	93.1	76.0	76.7
	MRMSD _{SC} / \AA	0.31	0.30	0.37	0.40	0.42	0.59
$\angle(A-M-B)$	MD / $^\circ$	-0.2	-0.5	-3.0	-2.9	-2.9	-0.2
	MAD / $^\circ$	4.0	3.9	9.5	9.3	9.3	8.4
	SD / $^\circ$	6.7	6.6	17.6	16.9	15.8	12.0
	AMAX / $^\circ$	58.2	75.7	130.5	141.7	98.2	73.8
	MD _{SC} / $^\circ$	-0.1	-0.1	-0.4	-0.3	-0.1	0.2
	MAD _{SC} / $^\circ$	3.1	3.0	3.7	3.8	4.0	6.5
	SD _{SC} / $^\circ$	5.2	4.6	5.9	5.9	6.0	9.5
	AMAX _{SC} / $^\circ$	48.8	27.4	51.3	42.3	39.6	53.9

counted for indirectly in the GFNn-xTB methods by coordination number dependent Fock matrix elements^{53,54}. In addition to the quality of structural optimizations, which among others represents the core property of the GFNn-xTB family, the qualitatively correct calculation of reaction energies plays an important role in typical applications. Especially the fast screening of reaction mechanisms and transition states can be facilitated and massively accelerated by effective SQM methods. The performance of the GFNn-xTB methods was tested on the MOR41, WCCR10 (reaction energies of metal organic reactions) and MOBH35^{112,249,250} (back and forth barriers of metal organic reactions) benchmark sets (Table 4.2). Although our methods were not explicitly adapted and parametrized to the reproduction of reaction energies, both GFN2-xTB and GFN1-xTB perform well. While they are inferior to the best DFT methods, they are almost in the range of poorer GGA functionals for the MOBH35 set ($MAD_{GFN1} = 12.3$ kcal mol⁻¹, $MAD_{GFN2} = 10.5$ kcal mol⁻¹). For the MOR41 and WCCR10 sets the GFNn-xTB methods also achieve good results (MOR41: $MAD_{GFN1} = 13.2$ kcal mol⁻¹, $MAD_{GFN2} = 11.8$ kcal mol⁻¹; WCCR10: $MAD_{GFN1} = 10.9$ kcal mol⁻¹, $MAD_{GFN2} = 10.7$ kcal mol⁻¹), whereby the tested DFT methods generally performed better. Both GFNn-xTB methods clearly outperform the PMx methods which yield totally unreasonable energetics and are practically of little use. Overall, the reaction energies provided by the GFNn-xTB methods are reasonable and allow e.g. their application for initial reaction mechanisms exploration²⁵¹.

Table 4.2.: Performance of all tested semi-empirical methods on the MOBH35, MOR41 and WCCR10 reaction energy benchmark sets. All values given in kcal mol⁻¹.

		GFN1-xTB	GFN2-xTB	PM6-D3	PM6-D3H4	PM7
MOBH35	MAD	12.3	10.5	16.6	15.4	51.6
	SD	16.7	14.6	22.2	20.9	89.8
	AMAX	50.4	69.5	67.4	61.1	372.4
MOR41	MAD	13.2	11.8	62.5	61.3	51.6
	SD	17.4	14.6	86.8	86.7	89.8
	AMAX	55.3	37.0	295.6	294.9	372.4
WCCR10	MAD	10.9	10.7	67.1	67.1	26.0
	SD	15.0	15.1	121.7	121.8	35.3
	AMAX	34.4	31.7	372.8	373.8	67.2

Optimization of Large Organometallic Structures

The good and very robust performance of the GFNn-xTB methods for various medium sized transition metal complexes was shown in the previous section. A strength of the GFNn-xTB methods compared to standard DFT is their efficiency, thus allowing a full QM treatment of much larger systems with up to thousands of atoms. The GFNn-xTB methods are several orders of magnitude faster than even lower

4. Structure Optimization of Large Transition-Metal Complexes with Extended Tight Binding Methods

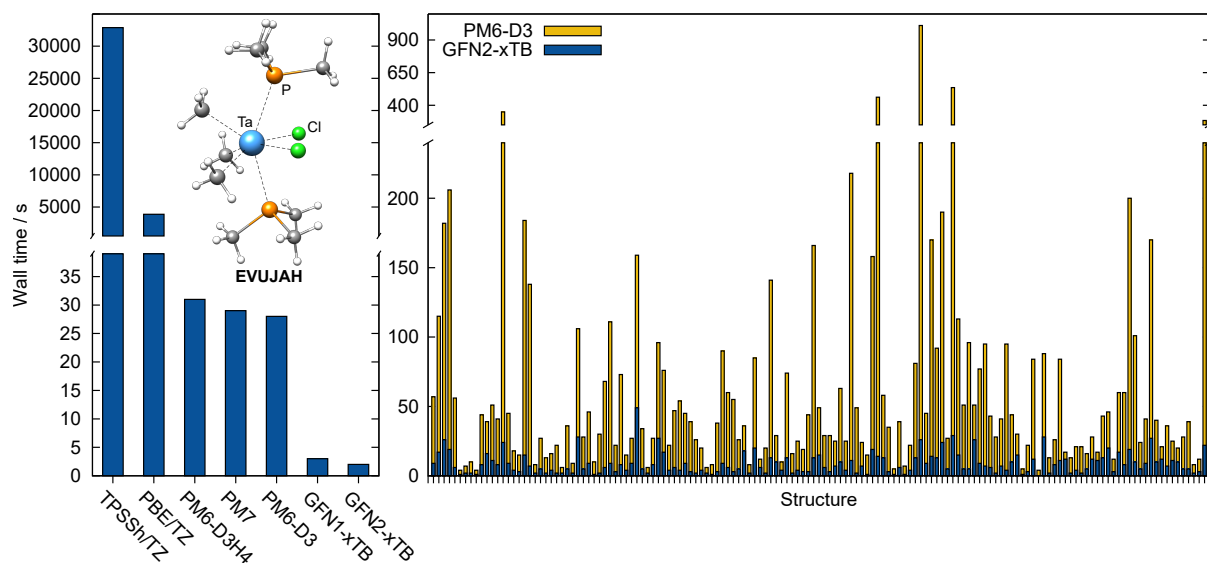


Figure 4.3.: Computational wall times for the Ta complex optimization **EVUJAH** in seconds with various SQM (on a single CPU core) and DFT methods (on eight CPU cores).

level DFT methods (see figure 4.3). Compared to e.g. PM6 variants, the GFNn-xTB methods prove to be computationally faster on average by a factor of approx. six (GFN1-xTB) to eight (GFN2-xTB) even for medium-sized systems. The higher speed results mainly from the better converging self-consistent charge iterations in the GFNn-xTB methods compared to the self-consistent field in the PMx methods. The much larger number of optimization steps required for optimization into structurally incorrect minima also plays a role in the particularly conspicuous outliers. Note that the same efficient geometry optimizer in the xtb code has been used for all SQM methods in order to allow a decent comparison. With all elements up to $Z = 86$, including the lanthanoids, being parametrized in the GFNn-xTB methods, there are almost no limitations in the applicability to a manifold of chemically different systems. Further, the GBSA (Generalized Born Solvent-Accessible surface area)²⁵² implicit solvation model allows a realistic (charge-screened) treatment of highly charged or extensive, flexible systems with e.g. large cavities or voids inherent to various structures. Here we present the capability of the GFNn-xTB methods to optimize large to huge transition metal complexes. Metal organic polyhedra and metal organic framework cutouts (Figures 4.4 and 4.5) are taken as examples. We are not aware of any realistic full QM treatment of such structures in the literature. Figure 4.5e shows a cutout of the crystal structure of the highly porous MOF DUT-60, which has a void fraction of 90.3% with a pore size of up to $37 \times 42 \text{ \AA}$ is shown²⁵³. Such high porosities are of particular interest for the design of high performance materials and their applications for e.g. fuel storage or catalysis²²⁶. The molecular structure of the larger mesopore of DUT-60 can be reproduced with GFNn-xTB methods in excellent quality ($\text{RMSD}_{\text{GFN2}} = 0.82 \text{ \AA}$) with the octahedral Zn_4O^{6+} nodes staying intact during optimization. This is indicated by the small mean deviation of 4.8 pm ($\text{MAD} = 5.0 \text{ pm}$) of the Zn-O bond distances. The pore structure, here determined by the mean distances between opposite central oxygen atoms of the Zn_4O^{6+} nodes ($d(\text{O}_{\text{cent}} - \text{O}_{\text{cent}'})$), is only slightly compressed by 100.8 pm ($d(\text{O}_{\text{cent}} - \text{O}_{\text{cent}'})_{\text{X-ray}} = 4768 \text{ pm}$;

$d(\text{O}_{\text{cent}}-\text{O}_{\text{cent}})_{\text{GFN2}} = 4668 \text{ pm}$). This compression can be mainly attributed to the missing periodic network structure and the use of an implicit solvation model as replacement. Nevertheless, the high structural stability of the DUT-60 mesopore is in good agreement with the experimentally observed physical and mechanical properties of the DUT-60 MOF. One example of a complex MOP is the very large coordination cage SK-1A (Figure 4.4)²⁵⁴. It can be described as a supramolecular Keplerate due to its two-shell structure consisting of a cuboctahedral (Archimedean body) outer layer and an octahedral (Platonic body) inner layer. Here Cu_2 paddle-wheel units serve as nodes, which are connected by rotation-flexible ligands. These node units are experimentally characterized by relatively labile terminal coordination to solvent molecules (H_2O removed for simplicity), which could be used post-synthetically e.g. to bind guest molecules. Note that the GFNn-xTB methods by construction (and also in practice) describe non-covalent interactions well and hence could be used e.g. in studies of adsorption in such systems. SK-1A is optimized with GFN2-xTB in high quality with a small RMSD of 0.40 \AA compared to the X-ray data. The Cu_2 nodes remain intact and the Cu-Cu distances are reproduced with a small mean deviation of 6.5 pm (MAD = 6.5 pm). This also applies to the Cu-O bonds to the benzoate groups of the bridging ligands. These are well reproduced with a mean deviation of 5.0 pm (MAD = 5.4 pm). The particularly large cross-sectional diameter (here defined as the mean distance between the opposing oxygen atoms of coordinated dimethylformamide molecules) of 4868 pm is retained after optimization with GFN2-xTB with 4918 pm . An even larger example is the tetravalent Goldberg polyhedron $[\text{Pd}_{30}\text{L}_{60}]^{60+}$ self assembled from 30 Pd^{2+} ions and 60 ligands synthesized by Fujita and co-workers (Figure 4.5b)²⁵⁵. The structure, consisting of 2430 atoms including the BF_4^- counter ions, can be fully

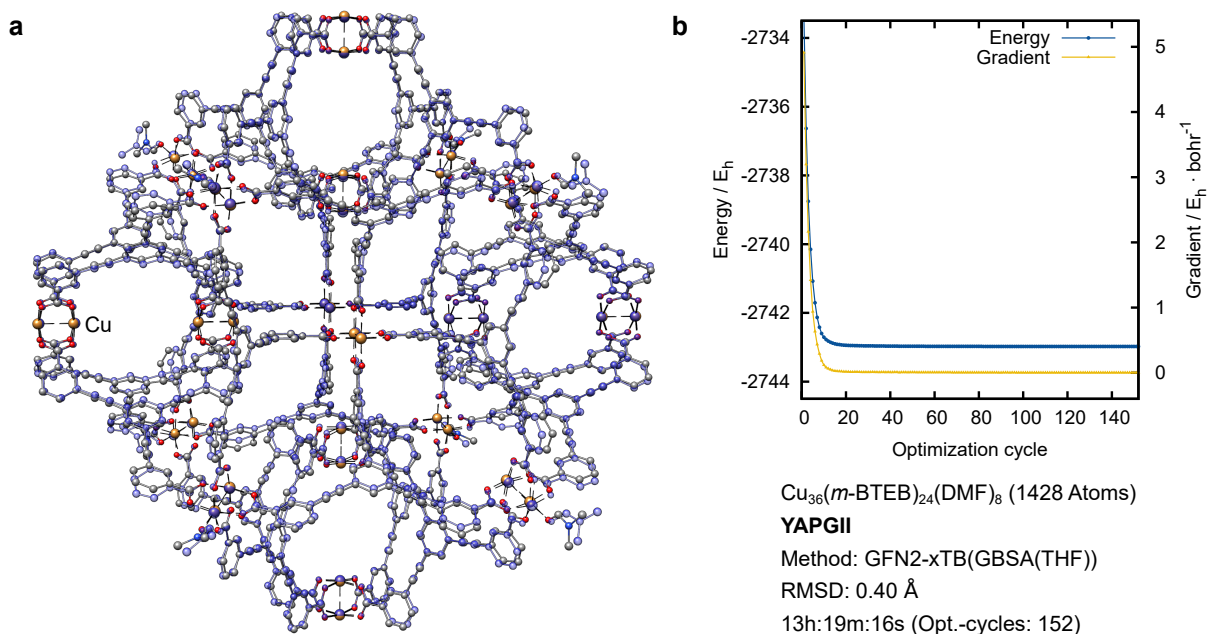


Figure 4.4.: a) Molecular structure overlay of the X-ray reference (color code) and the GFN2-xTB optimized structure (transparent blue) for the Keplerate cage SK-1A. Hydrogen atoms bound to carbon are omitted for clarity. b) Energy and gradient curve during optimization. Computational wall time obtained at 4 CPUs.

4. Structure Optimization of Large Transition-Metal Complexes with Extended Tight Binding Methods

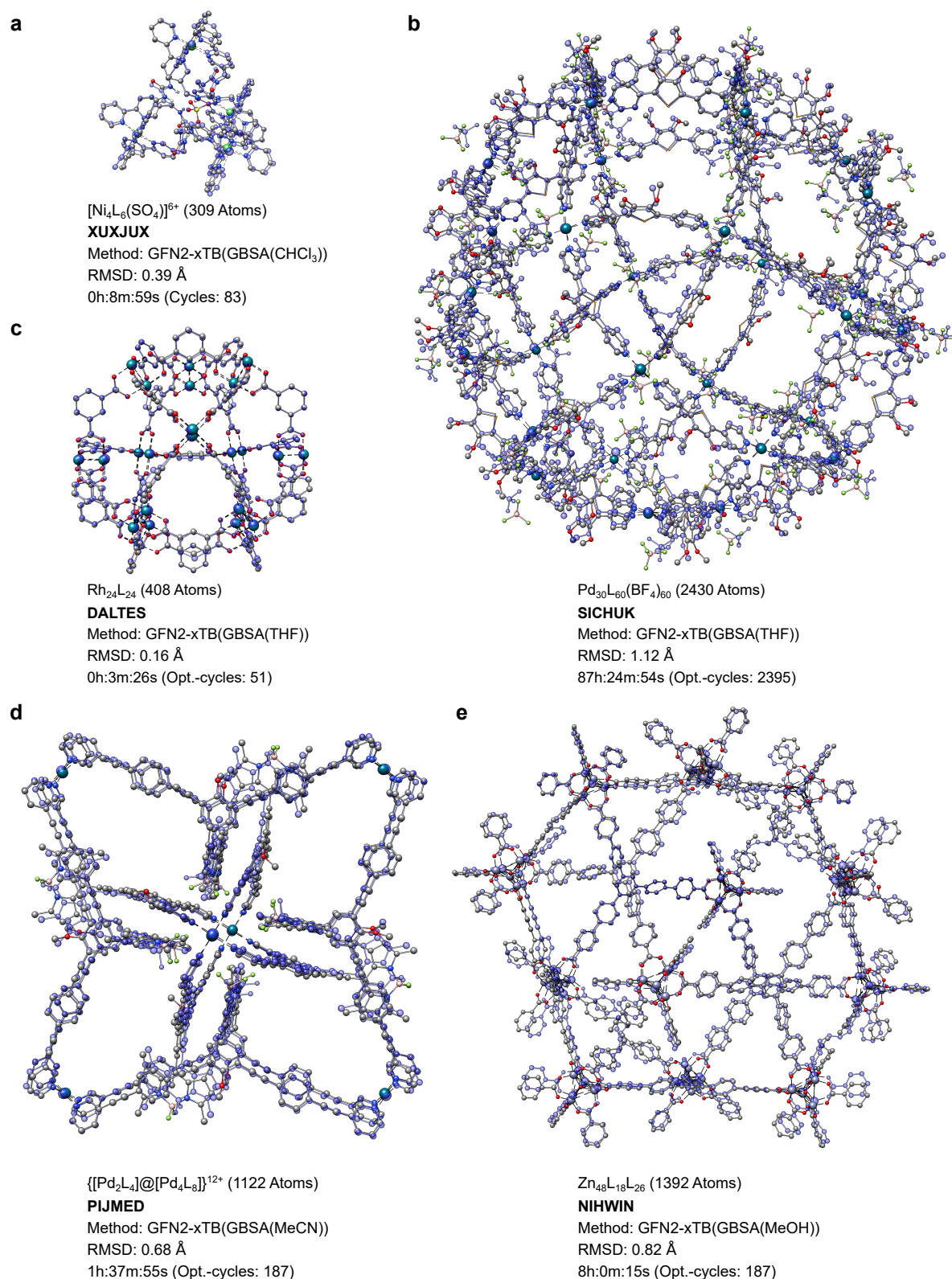


Figure 4.5.: Molecular structure overlays of the X-ray reference structure (color code) and the GFN2-xTB optimized structure for large MOP (transparent blue). Hydrogen atoms bound to carbon are omitted for clarity. Timings obtained using 4 CPUs for a), c), d), e) and 14 CPUs for b).

optimized with the GFNn-xTB(GBSA) methods. GFN2-xTB yields a good quality structure with a reasonable RMSD of 1.12 Å (with the largest deviations resulting from the flexible counter ions). The units of planar coordinated Pd ions with bonds to four N terminal ligands each are well reproduced. The Pd-N bond lengths deviate on average only by 3.9 pm (MAD = 4.2 pm) from those in the crystal structure. With a relatively small mean deviation of -15.2 pm (MAD = 32.9 pm) of the distances of all not directly connected Pd atoms from the optimized structure features only a low compression in comparison to the crystal structure. Again, slightly smaller theoretical structures are expected due to the application of an implicit solvation model instead of the real potential of the solid and the neglect of thermal as well as zero-point vibrational effects usually leading to structural expansion. Non-covalently bound aggregates of several MOPs can also be described. An example of this is the rotaxane-like cage-in-ring aggregate $\{[\text{Pd}_2\text{L}_4]@[\text{Pd}_4\text{L}_8]\}(\text{BF}_4)_{12}$ synthesized by Lützen and co-workers (Figure 4.5d)²⁵⁶. The BOD-IPY (4,4-Difluoro-4-bora-3a,4a-diaza-s-indazene) ligands with three pyridyl binding sites belong to a widely used ligand family often used in Pd^{II} MOP host-guest complexes, e.g. as drug carrier. GFN2-xTB optimization of this 1122 atom large organometallic aggregate yields a structure with a small RMSD of 0.68 Å compared to the experimental structure. The Pd-L bonds of the quadratic planar node units are reproduced with a small mean deviation of 1.6 pm (MAD = 2.6 pm) and the cage-in-ring superstructure is preserved. The broad applicability of the GFNn-xTB methods for a multitude of more complex binding situations and electronic states is finally demonstrated by some examples shown in figure 4.6. Among others, open shell systems with high-spin states can also be described (Figures 4.6a-c). Here the Fermi-smearing technique, allowing fractional orbital occupations, inherent to the GFNn-xTB methods can often be advantageous. Also complexes with participation of the metal atom in aromatic or Moebius aromatic systems (Figures 4.6d-f) and (delocalized) metal-metal multiple bonds (Figure 4.6k, h, and i) are well described, whereby the latter with GFN2-xTB tend to be slightly too long. Non-covalent metal-metal contacts are well described by the inherently used D3 (GFN1-xTB) or D4 (GFN2-xTB) dispersion energy schemes (Figure 4.6j). A good description of hydrogen bonds also enables the optimization of very large hydrogen bonded organometallic complex aggregates (Figure 4.6g).

4.3. Conclusion and Outlook

We have tested the recently developed extended tight binding approaches GFN1- and in particular the new GFN2-xTB for their ability to optimize transition metal complexes and evaluated the results with respect to high quality hybrid DFT (TPSSH-D3(BJ)-ATM/def2-TZVPP) gas phase or X-ray structures. It is shown that the tested GFNn-xTB methods consistently provide robust and good results for all transition metals up to Hg ($Z = 80$). Both methods reproduce metal ligand bond distances as well as characteristic bond angles around the metal atom with good accuracy (bond distances: $\text{MAD}_{\text{GFN1}} = 7.5$ pm; $\text{SD}_{\text{GFN1}} = 15.2$ pm; $\text{MAD}_{\text{GFN2}} = 8.3$ pm; $\text{SD}_{\text{GFN2}} = 15.1$ pm; angles: $\text{MAD}_{\text{GFN1}} = 4.0^\circ$; $\text{SD}_{\text{GFN1}} = 6.7^\circ$; $\text{MAD}_{\text{GFN2}} = 3.9^\circ$; $\text{SD}_{\text{GFN2}} = 6.6^\circ$). Only a few molecules (approx. 7% with GFN2-xTB) could not be optimized satisfactorily, i.e., are obtained with qualitatively incorrect chemical structure. The excellent cost/benefit ratio enables a standard full-QM optimization of small to medium-sized transition metal complexes as well as a reliable treatment of very large complexes with up to several thousand atoms,

4. Structure Optimization of Large Transition-Metal Complexes with Extended Tight Binding Methods

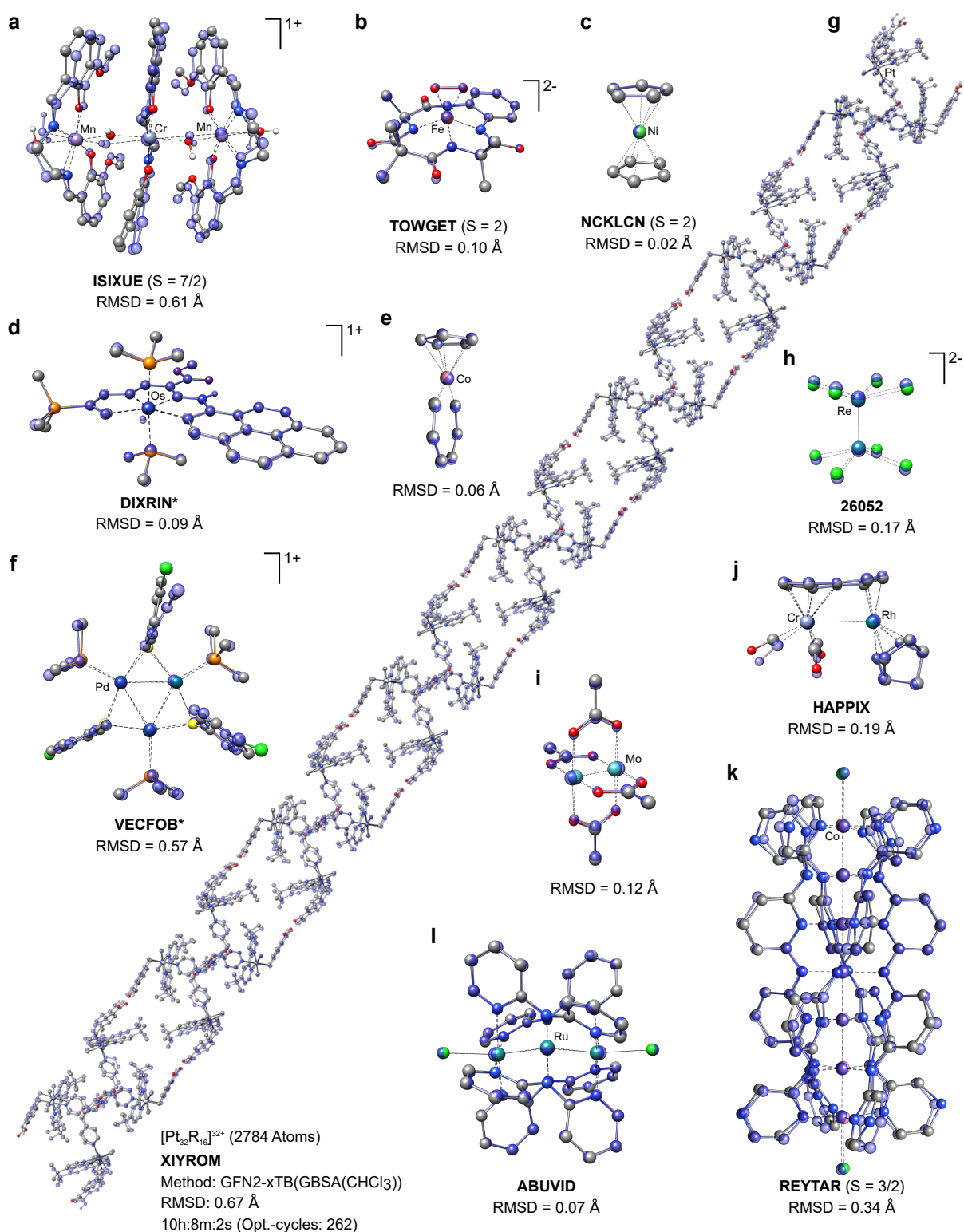


Figure 4.6.: Molecular structure overlay of the X-ray (a, g, k) or TPSSh (b–f, h–j, l) reference (color code) and the GFN2-xTB optimized structure (transparent blue) for various systems with complicated electronic states. Hydrogen atoms bound to carbon are omitted for clarity. Computational wall time obtained at 14 CPUs. An * indicates simplification of the ligand sphere compared to the original crystal structure. S is the total spin angular momentum.

e.g. extended metal organic polyhedra or metal organic frameworks. Furthermore, this opens a route for standardized conformational search procedures for large metallic systems which are to date not possible due to the lack of reasonably accurate underlying potential energy surfaces. Overall the new GFN2-xTB method featuring an improved theoretical description of the basic electronic structure seems to provide slightly better results than its predecessor. Particularly due to their easy, universal applicability and speed coupled with reasonable accuracy and high numerical precision, the GFNn-xTB methods represent an yet unrivaled quantum-mechanical tool for large organometallic structures. The availability of almost all elements of the periodic table, the generally robust treatment also of complicated electronic structures, a reasonable treatment of large parts of the potential energy surface including non-covalent interactions, and the coupled implicit solvent model allows even the targeted design of new large organometallic constructs. Future implementations under periodic boundary conditions for solids will further increase the range of applications to fields like polymorph screening or solid state material science. Furthermore, we propose the here investigated benchmark set TMG145 as standard test for future theoretical method developments.

Acknowledgements

The authors thank S. Ehlert for steady support of the xtb code and fruitful discussions. The German science foundation (DFG) is gratefully acknowledged for financial support in the framework of the Gottfried Wilhelm Leibniz prize to S.G.

5. Theoretical Study on Conformational Energies of Transition Metal Complexes

Markus Bursch,^a Andreas Hansen,^a Philipp Pracht,^a Julia Therese Kohn,^a and Stefan Grimme^a

This article is part of the themed collection: [Quantum Theory: The Challenge of Transition Metal Complexes](#)

Received: 6 September 2020, Published online: 26 November 2020

Reprinted (adapted) with permission[†] from

Bursch, M.; Hansen, A.; Pracht, P.; Kohn, J. T.; Grimme, S. *Phys. Chem. Chem. Phys.* **2020**, *23*, 287–299.

– Copyright © 2020, the Royal Society of Chemistry.

DOI [10.1039/D0CP04696E](https://doi.org/10.1039/D0CP04696E)

Own manuscript contribution

- Conception of the study and choice of methods
- Performing all DFT, SQM and FF calculations
- Interpretation of the results
- Writing the manuscript

^aMulliken Center for Theoretical Chemistry, Institut für Physikalische und Theoretische Chemie, Rheinische Friedrich-Wilhelms-Universität Bonn, Beringstraße 4, 53115 Bonn, Germany

[†]Permission requests to reuse material from this chapter should be directed to the Royal Society of Chemistry.

Abstract Conformational energies are an important chemical property for which a performance assessment of theoretical methods is mandatory. Existing benchmark sets are often limited to biochemical or main group element containing molecules, while organometallic systems are generally less studied. A key problem herein is to routinely generate conformers for these molecules due to their complexity and manifold of possible coordination patterns. In this study we used our recently published CREST protocol [Pracht *et al.*, *Phys. Chem. Chem. Phys.*, 2020, 22, 7169-7192] to generate conformer ensembles for a variety of 40 challenging transition metal containing molecules, which were then used to form a comprehensive conformational energy benchmark set termed TMCONF40. Several low-cost semi-empirical, density functional theory (DFT) and force field (FF) methods were compared to high level DLPNO-CCSD(T1) and double-hybrid DFT reference values. Close attention was paid to the energetic ordering of the conformers in the statistical evaluation. With respect to the double-hybrid references, both tested low-cost composite DFT methods produce high Pearson correlation coefficients of $r_{p, \text{mean, B97-3c/B97-3c}} = 0.922$ and $r_{p, \text{mean, PBEh-3c/B97-3c}} = 0.890$, with mean absolute deviations close to or below 1 kcal mol^{-1} . This good performance also holds for a comparison to DLPNO-CCSD(T1) reference energies for a smaller subset termed TMCONF5. Based on DFT geometries, the GFNN-xTB methods yield reasonable Pearson correlation coefficients of $r_{p, \text{mean, GFN1-xTB/B97-3c}} = 0.617$ ($\text{MAD}_{\text{mean}} = 2.15 \text{ kcal mol}^{-1}$) and $r_{p, \text{mean, GFN2-xTB/B97-3c}} = 0.567$ ($\text{MAD}_{\text{mean}} = 2.68 \text{ kcal mol}^{-1}$), outperforming the widely used PMx methods on the TMCONF40 test set. Employing the low-cost composite DFT method B97-3c on GFN2-xTB geometries yields an slightly improved correlation of $r_{p, \text{mean, B97-3c/GFN2-xTB}} = 0.632$. Furthermore, for 68% of the investigated complexes at least one low-energy conformer was found that is more stable than the respective crystal structure conformation, which signals the importance of conformational studies. General recommendations for the application of the CREST protocol and DFT methods for transition metal conformational energies are given.

5.1. Introduction

Transition metal (TM) complexes are an indispensable class of molecules, both in basic chemical research and in industrial and pharmaceutical chemistry¹⁵⁵⁻¹⁵⁷. In addition, transition metal complexes are crucial for numerous biological processes^{158,159}. Accordingly, efforts to study this class of substances by means of quantum chemical methods are also great and more recent Kohn-Sham density functional theory (DFT)^{33,107,129,257-262} and modern wave function theory (WFT) based methods such as DLPNO-CCSD(T)⁸³ have established themselves as reliable tools in computational organometallic chemistry^{3,263-266}. Unfortunately, such methods quickly reach their limits regarding the size of the systems to be investigated and even with more efficient low-cost composite methods like B97-3c¹²⁹ or PBEh-3c⁶⁹, only systems with up to 500 atoms can routinely be studied. For larger systems significantly faster semi-empirical quantum mechanical (SQM) (< 5000 atoms) or force field (FF) methods (> 5000 atoms) are necessary. This is especially the case if complex reaction mechanisms are to be elucidated or a large number of conformers play a role. Contrary to the importance of TM complexes, many of these methods like DFTB^{45,133,138}, OMx^{46,149} or the prominent Amber²⁶⁷, CHARMM²⁶⁸, and

OPLS^{269,270} FFs are mostly limited to application to (bio-)organic systems, either conceptually or due to the lack of a comprehensive parametrization for the whole periodic table. For a long time the only notable exceptions were the well-known PMx^{51,52,152,153} methods and the general force field UFF⁴⁰. More recently, the range of SQM and FF methods with comprehensive parametrization for the 3-5d transition metals (and lanthanoids) has been extended by the GFNn-xTB^{53-55,57} and GFN-FF⁵⁶ family of methods. Besides the sheer size of many real transition metal complexes, the amount of required calculations is often a limiting factor and decisive for sampling the relevant low-energy chemical space. A particularly important aspect here is the investigation of the conformational space, since a profound knowledge of the molecular conformation is mandatory for an accurate calculation of various molecular properties. Due to the manifold coordination patterns and electronic structures of transition metal complexes, automated conformer sampling is difficult and only a few approaches are available that can be applied almost generally^{64,271,272}. The most universal approach for the generation of conformers is the sampling based on molecular dynamics (MD) simulations employing FFs²⁷³. However, most standard FFs are not parametrized for transition metals and therefore not applicable. Conformational sampling in an *ab initio* molecular dynamics (AIMD)^{274,275} approach (mostly at DFT/GGA level) solves the parametrization problem but becomes prohibitively expensive with increasing system size and simulation length. The question if very recent on-the-fly machine learning techniques can help to solve the problem in the future remains open^{276,277}. The here proposed usage of robust and fast semi-empirical methods in combination with metadynamics simulations provides a practical alternative (and significant acceleration) to the MD/AIMD approach²³¹. In this study the meta-dynamics based iMTD-GC algorithm, as implemented in the recently published CREST⁶⁴, was used to routinely generate high quality conformer ensembles. CREST utilizes the GFNn-xTB family of methods to sample potential energy surface on-the-fly and is designed to generate physically plausible conformers employing an (almost) black-box procedure. The second step after the conformer generation and optimization, the energetic (re)ranking of the conformers, is comparably crucial and time consuming with conventional quantum mechanical (QM) methods like DFT or DLPNO-CCSD(T). This is due to the typically large amount of considered structures and the individual size of the investigated molecules, and thus a sufficiently accurate energy pre-ranking using SQM methods is desirable in a multi-level approach. A few conformational benchmark sets, such as the SCONF²⁷⁸ and UPU23²⁷⁹ subsets of the GMTKN55 database³⁴, or the recently published MPCONF196²⁸⁰ and PEPCONF²⁸¹ sets are readily available for the evaluation of conformational energies. Even though the GFNn-xTB methods proved to yield reasonable conformational energies for (bio)organic molecules^{64,282,283}, the complexity of organometallic systems is much more challenging and far less data is available for the latter. Minenkov and co-workers showed that the prominent PMx methods are not reliably applicable to calculate conformational energies of transition metal complexes²⁸⁴. Therefore, this work focuses on testing, if the GFNn-xTB methods can do better for conformational gas-phase energies of transition metal complexes. The goal is to compose a corresponding diverse benchmark data set that serves as basis for future studies. In this context, the black-box conformer ensemble generation for this compound class using the CREST program was thoroughly tested and some recommendations for its reliable application to transition metal complexes are given. Moreover, the relation of crystal structure conformers to their gas-phase counterparts was

5. Theoretical Study on Conformational Energies of Transition Metal Complexes

investigated. Taking the crystal structure as basis for computational work is still common practice but may be questionable if different conformations are energetically clearly favored in different states (solid/liquid/gas).

Computational Details

All quantum chemical and FF calculations were conducted with the TUBOMOLE 7.3.1^{206,285}, ORCA 4.2.1^{208,286,287}, xtb 6.3.1²⁸⁸, and MOPAC2016²⁰⁵ program packages. DFT geometry optimizations were performed with the B97-3c composite method as implemented in TURBOMOLE. All semi-empirical geometry optimizations and energy calculations were carried out with the xtb program directly or as driver for MOPAC. Final DFT single point energy (SPE) calculations and fractional occupation density (FOD) analyses^{289,290} were conducted with ORCA applying *TightSCF* and *Grid5/NoFinalGrid* options. Except for the low-cost composite methods, the quadruple- ζ def2-QZVP²⁴⁰ basis set was used for all DFT calculations. The D4 London dispersion correction scheme^{33,115,116} (v2.5.0) was generally applied for the non-composite density functional approximations (DFAs) calculations, except for MN15²⁹¹. The RI approximation²⁴³ for coulomb (RIJ) and exchange (RIJK) integrals was used in combination with matching auxiliary basis sets^{244,245} as implemented in TURBOMOLE and ORCA (*def2/j*, *def2/jk* options, *def2-QZVPP/C*²⁹² for the MP2 correlation part) to speed up the DFT calculations. For elements with $Z > 36$, Stuttgart-Dresden ECPs^{241,242} were generally applied. DLPNO-CCSD(T1) calculations^{82-84,293} employed the def2-TZVPP and def2-QZVPP basis sets with *VeryTightPNO* settings. If applicable the CBS extrapolation as suggested by Neese and Valeev²⁹³ was applied for the SCF and correlation energies. For fully automated conformer searches, GFN2-xTB was applied in conjunction with a development version (2.11) of the CREST program using the iMTD-GC algorithm. For further details see appendix A4.

5.2. The TMCNF40 Benchmark Set

The benchmark set to study the performance of low-cost DFT and semi-empirical GFNn-xTB methods for the calculation of conformational energies of transition metal complexes consists of 40 realistic closed-shell complexes obtained from the CSD²⁰². The entries are denoted by their respective CSD identifier. Diverse coordination patterns, ligands and transition metals are included. Part of the set was adapted from the work of Minenkov *et al.*²⁸⁴, even though five of the 27 complexes were excluded as qualitative FOD analysis indicated possible multi-reference character (See appendix A4) and thus no reliable reference data can be obtained in the framework of single-reference DFT and coupled cluster (CC) calculations used in this work. To ensure comprehensiveness of the benchmark, the remaining structure collection (22 molecules) was extended by 18 new complexes. The full collection of transition metal complexes is depicted in figure 5.1 and an overview of the involved elements in figure 5.2. For all 40 complexes a fully automated conformer search was conducted, applying GFN2-xTB and the default iMTD-GC algorithm as implemented in the CREST program. The resulting conformer ensembles (CEs) were simplified in a clustering approach, utilizing a combined principle component analysis (PCA) dimensionality reduction^{294,295} and k-means clustering algorithm^{296,297}. The clustering approach based

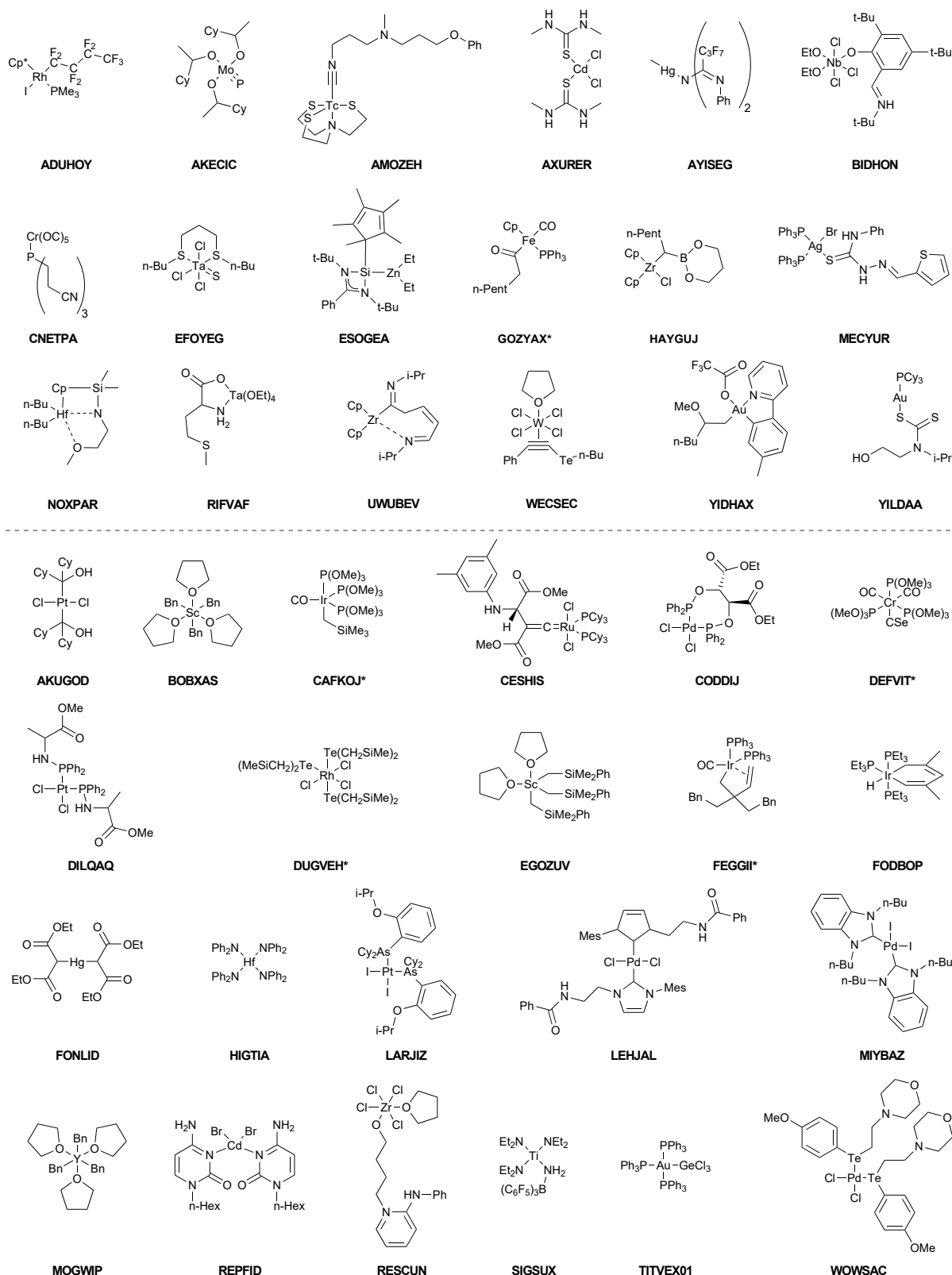


Figure 5.1.: Structure collection forming the TMCONF40 benchmark set and the CSD identifiers of the original X-ray structure. Systems marked with an asterisk transformed chemically in the automated conformer search and thus, the transformed structure ensemble was used for evaluation.

Spearman correlation coefficient (r_s):

$$r_s = \frac{\sum_{i=1}^n (R_{x_i} - \bar{R}_x)(R_{r_i} - \bar{R}_r)}{\sqrt{\sum_{i=1}^n (R_{x_i} - \bar{R}_x)^2 \sum_{i=1}^n (R_{r_i} - \bar{R}_r)^2}} \quad (5.2)$$

with E_i being the relative energy of the i^{th} of n conformers, and \bar{E} the average relative conformer energy over all n conformers for the tested method x and the reference r . For the Spearman correlation coefficient ρ_s the same notation is applied for conformer rankings R instead of their relative conformer energies.

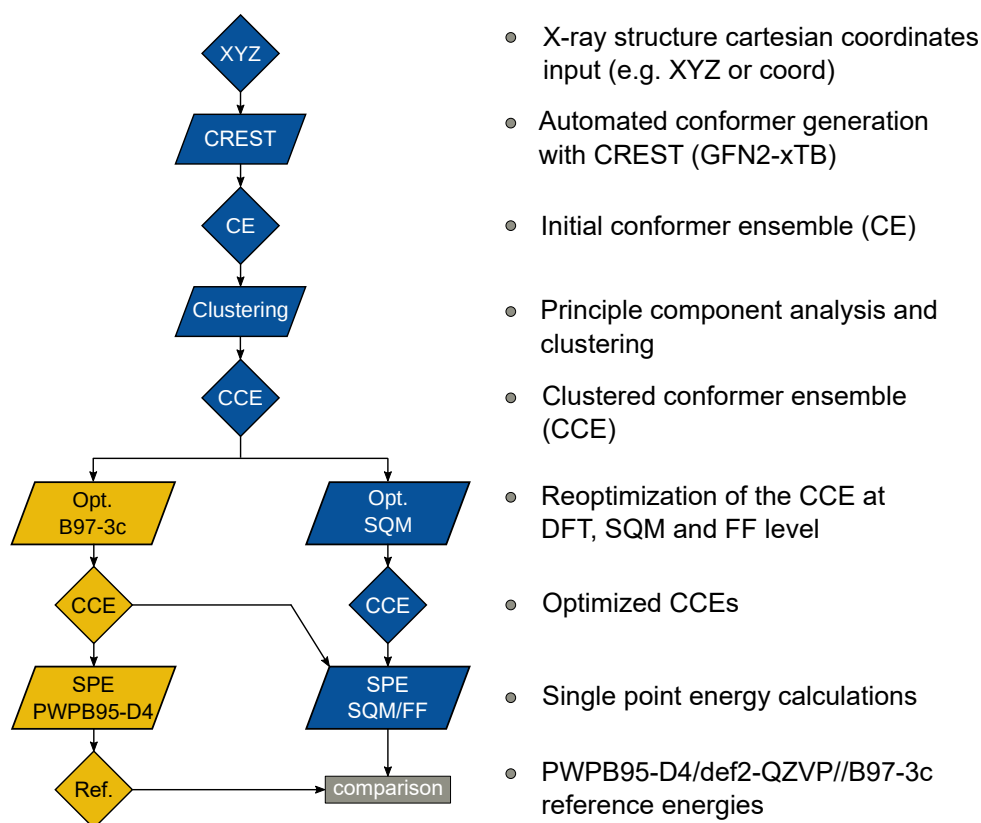


Figure 5.3.: TMCONF40 testset generation procedure. All conformers were generated fully automatic at the SQM level using CREST prior to DFT based post-processing.

5.3. Results and Discussion

Choice of the DFT Reference Level

To justify the use of a DFT method to compute reference conformational energies for the TMCONF40 set and to choose the best candidate for this purpose, we conducted accurate energy calculations at DLPNO-CCSD(T1)/def2-TZVPP/*VeryTightPNO* level for the complex **AYISEG** and at DLPNO-CCSD(T1)/

5. Theoretical Study on Conformational Energies of Transition Metal Complexes

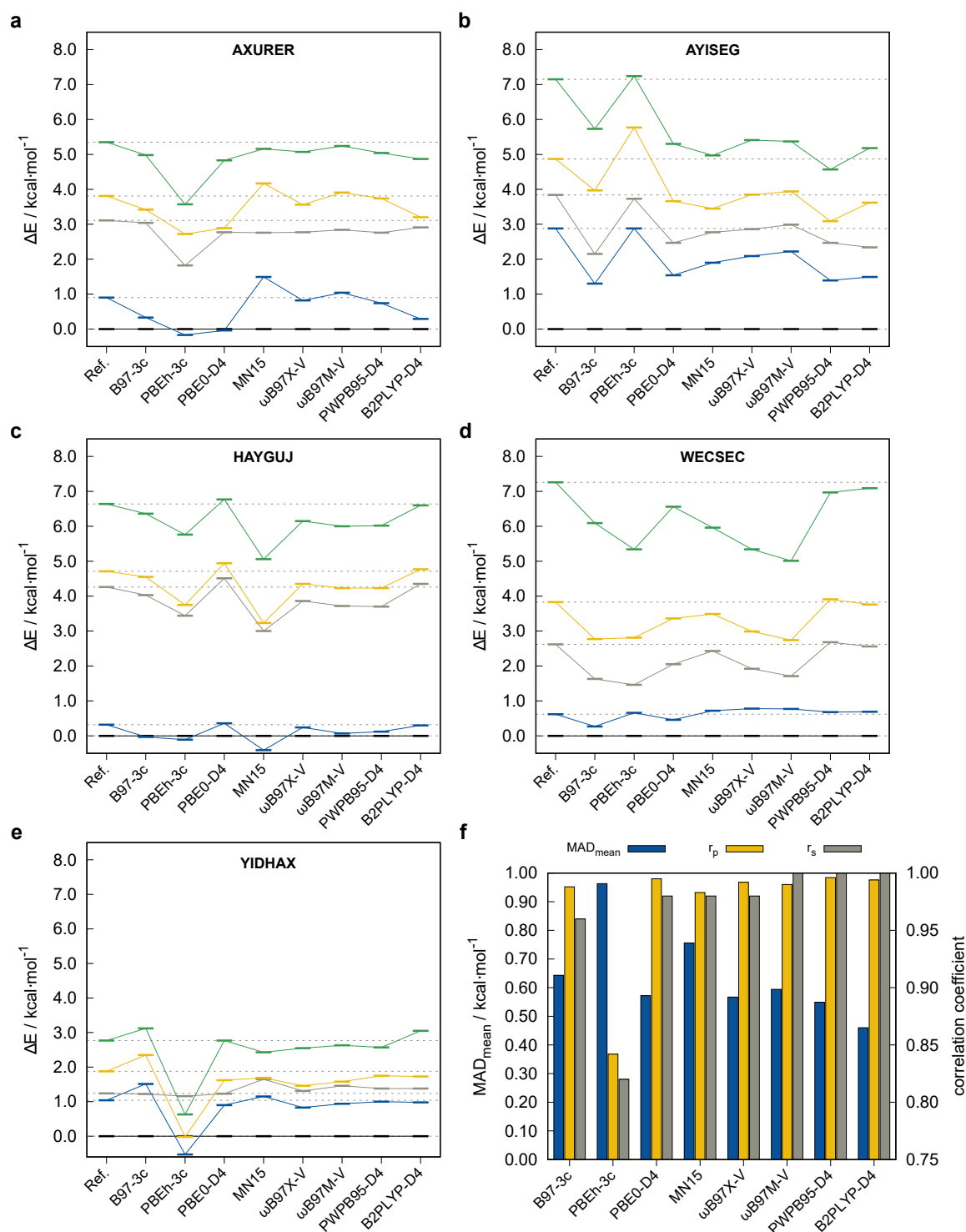


Figure 5.4.: Conformer energy correlation diagrams for the TMCONF5 subset relative to DLPNO-CCSD(T1)/CBS(def2-TZVPP/def2-QZVPP) (**AXURER**, **YIDHAX**, **WECSEC**, **HAYGUJ**) and DLPNO-CCSD(T1)/def2-TZVPP (**AYISEG**) conformational energies. **f**) Mean MAD, Pearson (r_p), and Spearman (r_s) correlation coefficients. Dashed lines indicate the reference conformational energies. The mean conformational energy is $3.45 \text{ kcal mol}^{-1}$. The color code represents individual conformers **CC-1** = black; **CC-2** = blue; **CC-3** = grey; **CC-4** = yellow; **CC-5** = green.

CBS(def2-TZVPP/def2-QZVPP)/*Very-TightPNO* level for **AXURER**, **HAYGUJ**, **YIDHAX**, and **WECSEC** with five conformers each and a mean conformational energy of 3.45 kcal mol⁻¹. Due to the overall high number of investigated conformers in the TMCONF40 set and the size of the systems, a general calculation of conformational energies at a comparable level has been refrained from. Five London dispersion corrected DFAs and MN15 that are known to perform well for thermochemistry of closed-shell transition metal complexes based on the results for the MOR41¹¹², WCCR10²⁴⁹ and TMC151²⁹⁸ benchmark sets were tested. The two smaller basis set composite-methods PBEh-3c and B97-3c were tested as well. The other investigated DFAs are the (range-separated) hybrid functionals PBE0-D4^{116,213}, ω B97X-V²⁵⁸, ω B97M-V²⁵⁹, as well as the PWPB95-D4²⁶⁰ and B2PLYP-D4¹¹⁰ double hybrid functionals²⁹⁹ in conjunction with the large quadruple- ζ basis set def2-QZVP²⁴⁰. A general application of London dispersion corrections, e.g., the D3^{59,121} or D4¹¹⁶ scheme should be regarded as indispensable, as prior studies demonstrated their important role for transition metal chemistry^{33,112,300} and conformational energies in general³⁴. The performance of the tested methods for the subset termed TMCONF5 with respect to the DLPNO-CCSD(T1) reference data is depicted in figure 5.4 and table 5.1. Overall, the tested hybrid and double-hybrid DFAs with a large AO basis set perform comparably well with small mean MADs between 0.4 and 0.6 kcal mol⁻¹ and high mean Pearson ($r_{p, \text{mean}}$) and Spearman ($r_{s, \text{mean}}$) correlation coefficients above 0.990 and 0.960 (except for MN15 with $\text{MAD}_{\text{mean}} = 0.76$ kcal mol⁻¹ and $r_{p, \text{mean}} = 0.983$), respectively. B2PLYP-D4 yields the smallest mean MAD of 0.46 kcal mol⁻¹ but comparably small Pearson correlation coefficient of $r_{p, \text{mean}} = 0.994$ compared to PWPB95-D4. The best compromise of best possible mean correlation coefficients and mean MAD is provided by PWPB95-D4 with almost perfect correlation coefficients of $r_{p, \text{mean}} = 0.996$ and $r_{s, \text{mean}} = 1.000$, as well as a small mean

Table 5.1.: Collected statistics for the TMCONF5 subset with respect to DLPNO-CCSD(T1)/CBS(def2-TZVPP/def2-QZVPP) (**AXURER**, **YIDHAX**, **WECSEC**, **HAYGUJ**) and DLPNO-CCSD(T1)/def2-TZVPP (**AYISEG**) reference conformational energies. MD = mean deviation in kcal mol⁻¹, MAD = mean absolute deviation in kcal mol⁻¹.

Method	MD _{mean}	MAD _{mean}	$r_{p, \text{mean}}$	$r_{s, \text{mean}}$
PBEh-3c/B97-3c	-0.86	0.96	0.842	0.820
B97-3c//B97-3c	-0.51	0.64	0.988	0.960
PBE0-D4//B97-3c	-0.51	0.57	0.995	0.980
MN15//B97-3c	-0.60	0.76	0.983	0.980
ω B97X-V//B97-3c	-0.54	0.57	0.992	0.980
ω B97M-V//B97-3c	-0.53	0.59	0.990	1.000
PWPB95-D4//B97-3c	-0.51	0.55	0.996	1.000
B2PLYP-D4/B97-3c	-0.40	0.46	0.994	1.000
PM6//B97-3c	-7.49	8.73	0.033	0.080
PM6-D3H4X//B97-3c	-7.57	8.87	0.046	0.120
PM7//B97-3c	-2.66	3.40	0.356	0.380
GFN2-xTB//B97-3c	-2.83	2.96	0.542	0.700
GFN1-xTB//B97-3c	-1.25	2.46	0.758	0.780
GFN-FF//B97-3c	-1.31	1.78	0.648	0.680
UFF//B97-3c	1.57	8.14	0.131	0.280

5. Theoretical Study on Conformational Energies of Transition Metal Complexes

MAD of 0.55 kcal mol⁻¹. The low-cost composite method B97-3c performs comparably well with only slightly worse correlation coefficients of $r_{p, \text{mean}} = 0.988$, $r_{s, \text{mean}} = 0.960$. PBEh-3c, which by construction employs the small def2-mSVP basis set and a high amount of Fock exchange (42%), not unexpectedly performs worst with a comparably high mean MAD of 0.96 kcal mol⁻¹ and lower $r_{p, \text{mean}} = 0.842$, $r_{s, \text{mean}} = 0.820$. At this point it should be noted, that due to the small number of conformers per system included in the subset, deviations in the Spearman correlation coefficient should not be overinterpreted. Based on these results and the experience from other benchmark studies mentioned *vide supra*, where good double-hybrid functionals typically outperform range-separated hybrid functionals upon comparison to CBS extrapolated DLPNO-CCSD(T1) reference data, PWPB95-D4 was selected as DFT based reference for testing low-cost methods on the full benchmark set. Thus, the PWPB95-D4/def2-QZVP reference values are expected to be sufficiently accurate to evaluate the performance of several magnitudes faster semi-empirical and force field methods.

Benchmark Study of Low-Cost Methods

The performance of several low-cost DFT, SQM and FF methods and their combinations for calculation of conformational energies was evaluated on the full TMCONF40 benchmark set (for the raw data see the online Supporting Information of the original publication). These method combinations include, SPEs calculated on the B97-3c geometries for all tested methods, as well as combinations of SPEs calculated on SQM or FF geometries with focus on the GFNn-xTB/FF method family (See figure 5.5 and table 5.2). In general, a successful application of a multi-level Ansatz, combining two different PESs for energy calculation and geometry optimization, requires sufficient parallelism of both. Therefore,

Table 5.2.: Collected statistics for all tested methods on the full TMCONF40 set with respect to PWPB95-D4/def2-QZVP//B97-3c reference conformational energies. MD = mean deviation in kcal mol⁻¹, MAD = mean absolute deviation in kcal mol⁻¹.

Method	MD _{mean}	MAD _{mean}	$r_{p, \text{mean}}$	$r_{s, \text{mean}}$
PBEh-3c//B97-3c	-0.11	1.12	0.890	0.867
B97-3c//B97-3c	-0.33	0.85	0.922	0.902
PM6//B97-3c	-0.57	4.32	0.369	0.329
PM6-D3H4X//B97-3c	-0.12	4.10	0.455	0.419
PM7//B97-3c	-1.17	3.37	0.382	0.329
GFN2-xTB//B97-3c	-2.30	2.68	0.567	0.563
GFN1-xTB//B97-3c	-1.73	2.15	0.617	0.593
UFF//B97-3c	0.90	12.07	0.234	0.220
GFN-FF//B97-3c	-0.46	5.01	0.304	0.328
B97-3c//GFN2-xTB	-0.36	3.01	0.632	0.628
B97-3c//GFN1-xTB	-1.47	3.51	0.599	0.577
B97-3c//GFN-FF	0.80	6.62	0.331	0.338
GFN2-xTB//GFN2-xTB	-2.79	3.17	0.356	0.347
GFN1-xTB//GFN1-xTB	-2.44	2.84	0.366	0.365
GFN2-xTB//GFN-FF	-0.74	5.65	0.234	0.233
GFN-FF//GFN-FF	-0.89	9.69	0.145	0.180

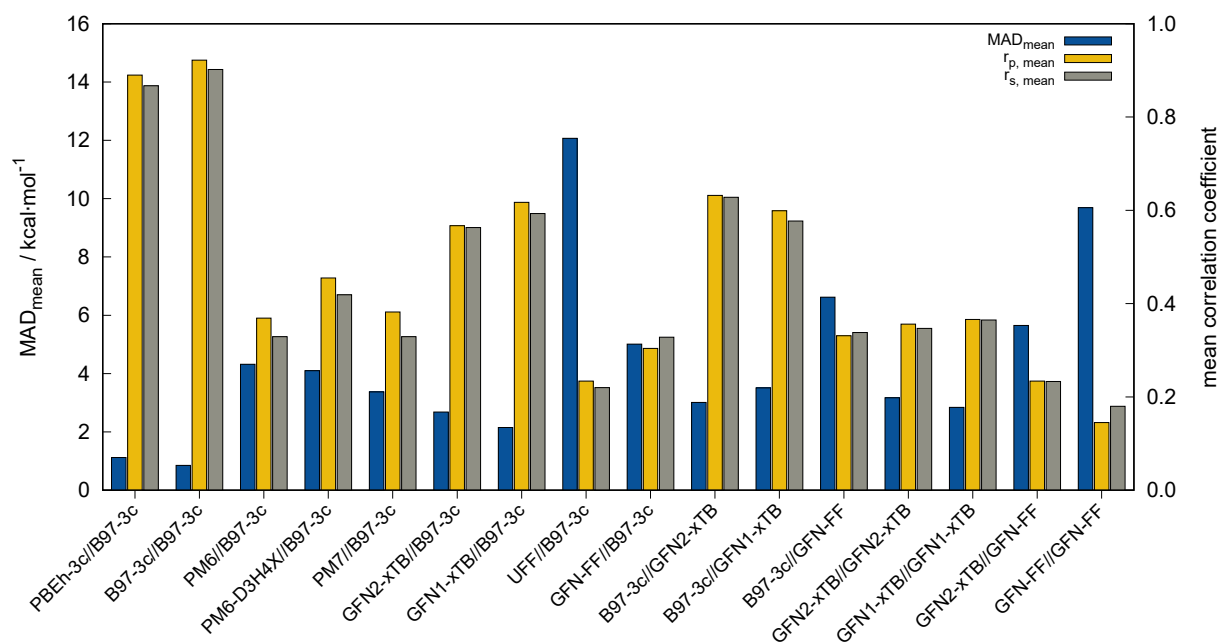


Figure 5.5.: Mean absolute deviation (MAD_{mean}), mean Pearson ($r_{p, \text{mean}}$), and Spearman ($r_{s, \text{mean}}$) correlation coefficients for all tested method combinations with reference to PWPB95-D4/def2-QZVP//B97-3c results. The methods are sorted by descending computational cost.

a thorough evaluation of such method combinations is of interest. The calculation of high-level SPEs on lower level structures (e.g., WFT energies for DFT structures) is standard practice in computational chemistry because computation times can be reduced strongly. In the following, these method combinations are labeled as “*SPE//geometry*” with “*SPE*” being the energy calculation method and “*geometry*” being the method applied for geometry optimization. Only mean correlation coefficients and MAD over all systems are discussed in the following. First of all, both tested low-cost composite DFT methods, B97-3c//B97-3c and PBEh-3c//B97-3c yield satisfactory (> 0.85) mean correlation coefficients of $r_{p, \text{B97-3c//B97-3c}} = 0.922$, $r_{s, \text{B97-3c//B97-3c}} = 0.902$ and $r_{p, \text{PBEh-3c//B97-3c}} = 0.890$, $r_{s, \text{PBEh-3c//B97-3c}} = 0.867$. Further, both yield relatively small mean MAD of $MAD_{\text{B97-3c//B97-3c}} = 0.85$ and $MAD_{\text{PBEh-3c//B97-3c}} = 1.12$ kcal mol⁻¹, respectively. With average errors in the sub-kcal mol⁻¹ range with reference to the much more costly double-hybrid PWPB95-D4, B97-3c provides an excellent cost-to-accuracy ratio. Considering the comparably high correlation coefficients, B97-3c and PBEh-3c are suitable for (at least preliminary) energetic sorting of most closed-shell transition metal complex conformers (See below). For SPEs calculated with SQM methods, as well as GFN-FF, on B97-3c geometries much smaller correlation coefficients are obtained. Here, GFN1-xTB//B97-3c performs best with $r_p = 0.617$, closely followed by GFN2-xTB//B97-3c ($r_p = 0.567$). The slightly poorer performance of the physically more sophisticated GFN2-xTB method compared to its predecessor GFN1-xTB is unusual but is probably statistically insignificant. The PMx methods perform worse yielding mean correlation coefficients between $r_p = 0.369$ to 0.455 which is slightly better than the results for (the orders of magnitude faster) GFN-FF ($r_{p, \text{GFN-FF//B97-3c}} = 0.304$; $MAD = 5.01$ kcal mol⁻¹). The only generally applicable competing force

5. Theoretical Study on Conformational Energies of Transition Metal Complexes

field UFF yields a very low correlation coefficient of $r_{p, \text{UFF//B97-3c}} = 0.234$ and a very high mean MAD of $12.07 \text{ kcal mol}^{-1}$. The results for the PMx methods are in line with those reported by Minenkov *et al.*²⁸⁴, although it must be noted that the latter were obtained for a much smaller number of conformers and less accurate reference values. Calculation of DFT, e.g., B97-3c, SPEs on SQM or FF geometries represents a possible step for further increasing the efficiency of conformer search procedures because the costly DFT geometry optimization may be replaced by a much faster SQM or FF one (Figure 5.6). If the low-level method structure is reasonable, even the very costly Hessian calculations for thermo-statistical free energy corrections can be conducted efficiently as recently shown for large supramolecular complexes³⁰¹. For these method combinations, at least semi-qualitatively correct conformational energies are required since they may be used as the basis for pre-selections. Therefore, in figure 5.6 method combinations with high average correlation coefficients and very few outliers (correlation < 0.0 , anti-correlation) are to be preferred. B97-3c SPEs calculated on GFN2-, GFN1-xTB and GFN-FF geometries yield mean correlation coefficients of $r_{p, \text{B97-3c//GFN2-xTB}} = 0.632$, $r_{p, \text{B97-3c//GFN1-xTB}} = 0.599$, and $r_{p, \text{B97-3c//GFN-FF}} = 0.331$, respectively. These results are in between those for GFNn-xTB//B97-3c and B97-3c//B97-3c. Calculating the geometry and the SPE purely at SQM and/or FF level further significantly decreases the correlation with the double-hybrid reference method (cf. table 5.2). For a given geometry, i.e., SPEs for the SQM methods on B97-3c geometries, GFNn-xTB methods clearly outperform their PMx competitors, even though they still perform worse than the two low-cost composite DFAs. Errors for GFNn-xTB increase slightly if the geometries are also optimized at the respective level, but trends of the performances are maintained. The comparably low average correlation coefficients (< 0.4) and the error increase due to geometry optimizations at SQM level indicate non-parallel PESs. This results in partially large deviations between the B97-3c and the GFN2-xTB structures and thus hardly comparable energy calculations. In such cases both errors, the decreased accuracy of the SQM energy calculation, and the difference in geometry, accumulate, resulting in worse performance compared to e.g. B97-3c//GFN2-xTB. Nevertheless, previous studies³⁰² showed that the GFN methods provide mostly good geometries of transition metal complexes and high robustness of the respective calculations compared to other SQM methods. Considering the results discussed in this section, there seems to be an obvious discrepancy between the quality of the structure and its energy at the SQM level. Regarding the mean reference conformational energy of only $3.53 \text{ kcal mol}^{-1}$, a relatively poor performance of the SQM and FF methods may be expected. Possibly increasing errors upon descending the periodic table due to shortcomings of the use of effective core potentials³⁰³⁻³⁰⁵ to implicitly cover relativistic effects, were not observed. For all method combinations discussed in figure 5.6, the overall mean Pearson coefficients amount to 0.320 for the 3d, 0.360 for the 4d, and 0.339 for the 5d transition metals. The comparably lower mean Pearson coefficient for the 5d row mainly results from the generally bad performance of most combinations for **BIDHON**. As discussed in section 5.3 (Figure 5.4), even sophisticated DFAs with very large basis sets yield residual mean MAD of around $0.5 \text{ kcal mol}^{-1}$ for the small subset. This is a further indication that the electronically complicated structures require a high theoretical level for the correct description of conformational energies. All tested SQM and FF methods should only be used with great care (i.e., with a large energy selection window in filtering steps, see below) for energetic ranking of conformational energies of transition metal complexes. They may

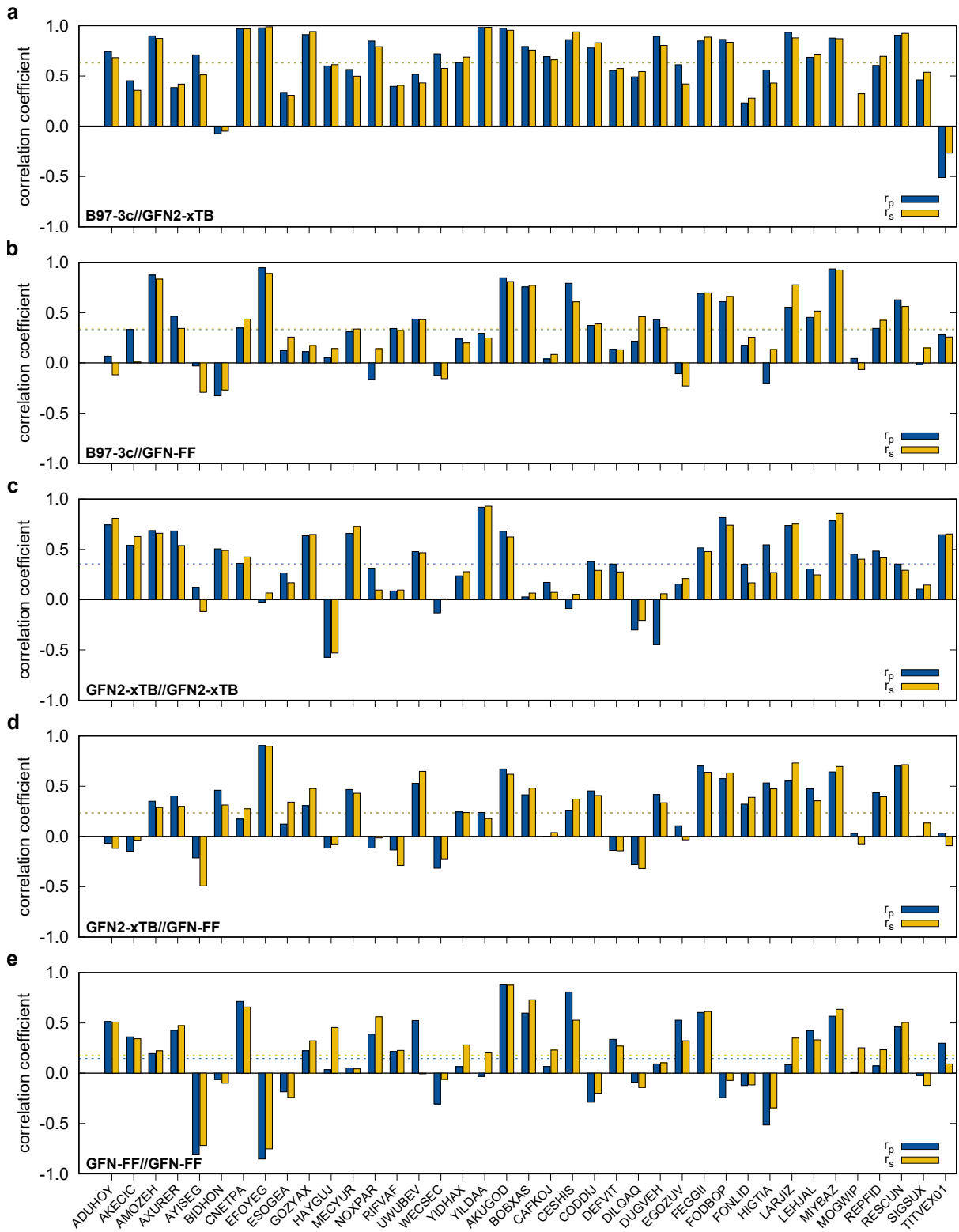


Figure 5.6.: Individual Pearson (r_p) and Spearman (r_s) correlation coefficients for a) B97-3c//GFN2-xTB, b) B97-3c//GFN-FF, c) GFN2-xTB//GFN2-xTB, d) GFN2-xTB//GFN-FF, and e) GFN-FF//GFN-FF with reference to PWPB95-D4/def2-QZVP//B97-3c results. Dashed lines show the average values.

5. Theoretical Study on Conformational Energies of Transition Metal Complexes

be used for initial pre-sorting to exclude very high energy conformers and to reduce the investigated conformational space, but for further refinement a combination with more sophisticated methods, e.g., B97-3c, is strongly advisable. In fact this holds to a weaker extend already for conformational energies of larger organic molecules regarding this very difficult chemical property. Furthermore, energy thresholds for successive conformer post-processing at higher theoretical levels should be chosen more conservatively (i.e., larger), compared to those applied for purely organic systems to account for non-parallel PESs. Depending on the system a factor of two to three proved reliable. The calculation of SPEs with B97-3c on GFN2-xTB geometries is particularly promising. B97-3c//GFN2-xTB yields reasonable results and only a very small number of outliers w.r.t. energetic ordering (cf. figure 5.6a; **BIDHON**, **MOGWIP**, **TITVEX**). Such an approach is still much cheaper than the full B97-3c geometry optimization (few minutes vs. several hours). In general, the quality of a method for the conformer generation and the final refinement should also be judged with respect to its applicability.

Difference Between Gas-Phase and Crystal Structure

It has previously been noted that conformations can significantly differ between the gas-phase and the crystal structure^{64,306,307}. The practical problem in this context is the very limited availability of the gas-phase conformers from experimental data. Experimental techniques for the determination of gas-phase conformers for example include rotational and vibrational spectroscopy^{308,309}, or more specialized methods such as gas-phase electron diffraction^{307,310}, but all of them are usually limited to small molecules. Crystal structures from X-ray diffraction experiments, on the other hand, are readily available even for large and complicated systems and have become the *de facto* standard for structure determination. However, for computational work it is essential to investigate the molecular conformation in the actual state, i.e., typically solution or the gas-phase. Because energy differences between low-energy conformers can reach several kcal mol⁻¹, finding the optimum conformer is necessary, e.g., for *in silico* design of catalytic cycles, thermochemical properties^{230,311}, or the prediction of spectra^{61,62}. Here we compare the optimized crystal structure conformer directly to the calculated minimum energy conformation found in a CREST run. Both, the total energy difference and the heavy

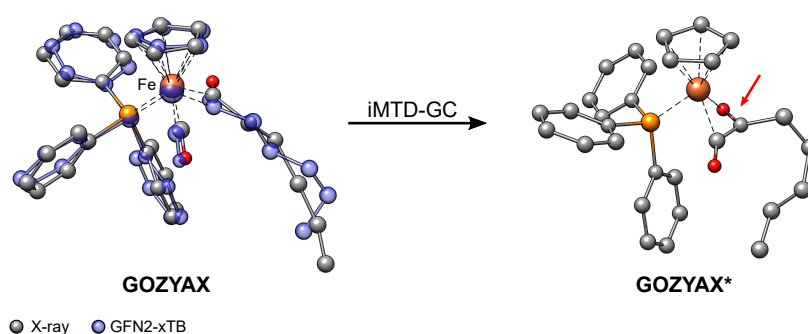


Figure 5.7.: Artificial chemical transformation of **GOZYAX** to **GOZYAX*** during the iMTD-GC procedure. The GFN2-xTB correctly optimized X-ray structure cutout is depicted in transparent blue for comparison.

atom root-mean-square-deviation (RMSD)³¹² of the atomic Cartesian coordinates are used to analyze differences between the conformers. Importantly, for 68% of the investigated complexes at least one conformer lower in energy than the respective crystal structure conformation was found. In five cases (**FEGGII**, **DUGVEH**, **DEFVIT**, **CAFKOJ**, **GOZYAX**) the automated conformer search based on GFN2-xTB yields mainly chemically transformed structures, i.e., no energetically lower conformers but a new conformer ensemble of the transformed structure (Figure 5.7). This problem is mainly observed for carbonyl ligands and may be avoided by application of GFN-FF for the automated structure generation, because by construction new covalent bonds can not be formed at the force field level. Despite their mediocre performance for the energetic ranking of conformers, the GFNn-xTB/FF methods generally proved to be well suited for the generation of transition metal complex conformer ensembles. The reason for this is an at least qualitatively correct description of the *intramolecular* forces within the molecules and the moderate performance for structural parameters³⁰². Differences between conformations in different phases are most likely the result of preferred *intermolecular* non-covalent interactions in the solid phase (packing effects) opposed to the gas-phase (or solution). Figure 5.8 shows an example in which non-covalent interactions in the crystal strongly influence the preferred conformation. The here depicted bis(diethyl malonate)-mercury(II) complex (**FONLID**) is characterized by a *S*-shaped non-covalent bonding pattern in the solid phase, which can be seen in a $2\times 2\times 2$ supercell (Figure 5.8a). Formation of this non-covalent network is enabled by the pairwise coordination of a malonate group to the neighboring monomers metal center via the dicarboxylic oxygen atoms. This can easily be observed already for the two monomers contained in the crystal structure unit cell, where the pairwise coordination is indicated by the black arrows in figure 5.8b. Each of the **FONLID** monomers is coordinated by two other monomers in this way, which strongly influences the molecular geometry. In the gas-phase, however, both diethyl malonate groups can freely move in the isolated monomer. During the conformational search this mainly leads to changes in the relative orientation of the two malonate groups relative to each other. At the PWPB95-D4/def2-QZVP//B97-3c level the most stable gas-phase con-

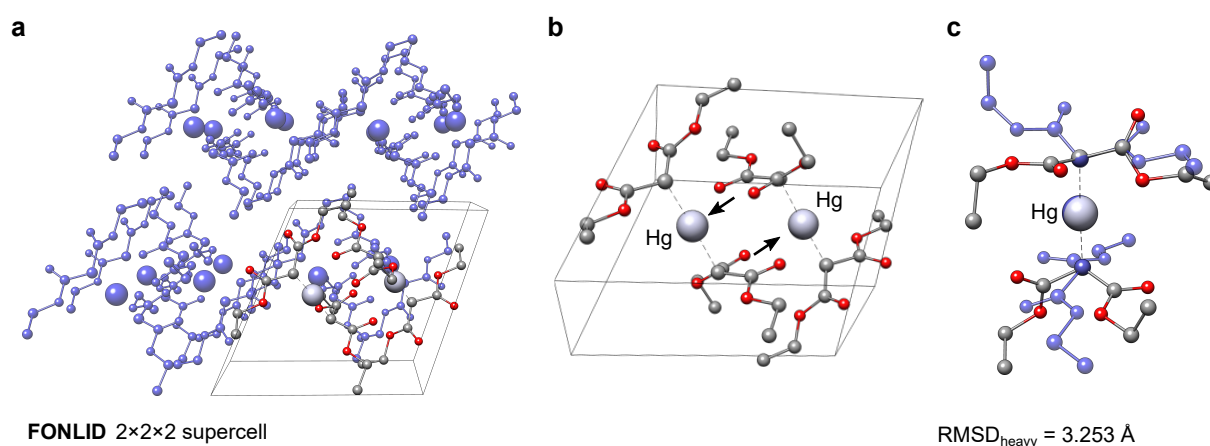


Figure 5.8.: The **FONLID** structure. a) $2\times 2\times 2$ supercell b) unit cell c) overlay between the crystal structure (transparent blue) and gas-phase (solid color) conformer of the **FONLID** monomer. Hydrogen atoms are omitted for clarity.

5. Theoretical Study on Conformational Energies of Transition Metal Complexes

former is favored by $-1.03 \text{ kcal mol}^{-1}$ over the reoptimized crystal structure monomer. With a heavy atom RMSD ($\text{RMSD}_{\text{heavy}}$) of 3.25 \AA the two conformers show large structural differences. An overlay of the two structures can be seen in figure 5.8c. As a second example the **YIDHAX** molecule is shown in figure 5.9. In this structure the monomers align along the crystallographic a-axis and form π -bonded columns, as can be seen in figure 5.9a. This leads to a parallel alignment of the 2-methoxyhexyl ligands between neighboring **YIDHAX** monomers. From the overlay of the crystal structure monomer and the most stable gas-phase conformer in figure 5.9b large structural changes (mainly for the 2-methoxyhexyl ligand) become apparent, which result in a sizable $\text{RMSD}_{\text{heavy}}$ of 2.65 \AA . The gas-phase conformer of **YIDHAX** is more stable than the reoptimized crystal structure monomer by $-0.94 \text{ kcal mol}^{-1}$. The two examples **FONLID** and **YIDHAX** demonstrate that structural changes between the gas-phase and the crystal structure may be attributed to well-defined non-covalent interactions. However, the entirety of packing effects is typically very complicated in the crystal structure and molecular conformations should generally be investigated at the beginning of a computational project referring to the gas-phase or solution.

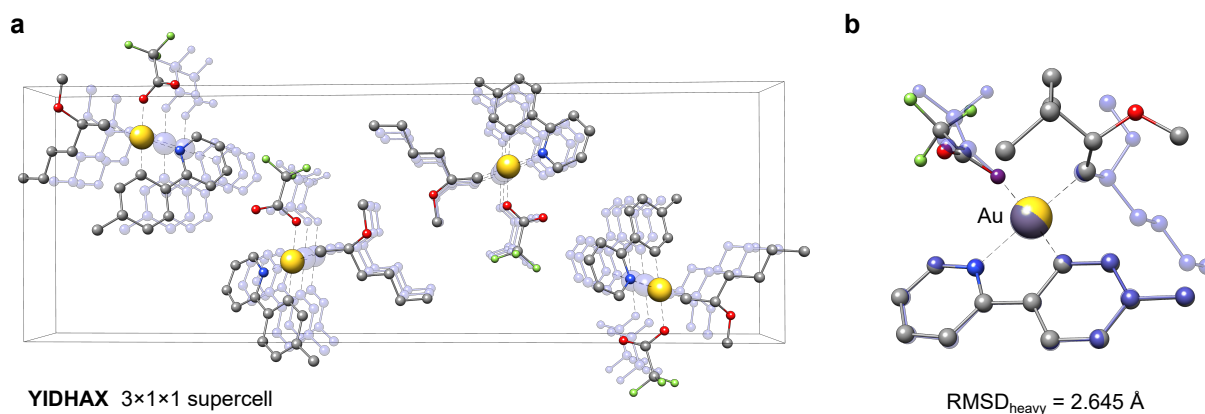


Figure 5.9.: The **YIDHAX** structure. a) $3 \times 1 \times 1$ supercell b) overlay between the crystal structure (transparent blue) and gas-phase (solid color) conformer of the **YIDHAX** monomer. Hydrogen atoms are omitted for clarity.

Recommendations for CREST

Based on this study showing that the GFNn-xTB/FF methods can routinely be applied for conformer generation of transition metal complexes, some recommendations for applying the iMTD-GC algorithm in CREST for fully automated conformer search and subsequent conformer ensemble reranking with e.g. ENSO³¹³ for organometallic complexes can be made:

- During long meta-dynamics simulations in CREST, the RMSD bias potential might add up too strongly and lead to bond dissociation or chemical transformations as shown in figure 5.7. To remedy this problem additional bond constraints can be applied in the conformational search with the `-cbonds` or `-cmetal` keywords. A default force constant of $0.02 E_h$ is used for the bond constraints, but can manually be increased for critical cases.

- With an increasing level of electronic complexity it becomes more difficult to pre-select the correct structures at a cheap SQM/DFT level. To ensure a correct pre-processing very conservative sorting criteria should be chosen for the energetic ranking thresholds in post-processing programs like ENSO. An increase of typical default values between 2.0 and 4.0 kcal mol⁻¹ by a factor of 2-3 should be considered.
- For very fast conformer ensemble sampling, the general force field GFN-FF may be applied. Here, the additional bond constraint options are applied by default to avoid dissociation in the metadynamics simulations. A further increase in the iMTD-GC energy windows may be necessary, typically from the default of 6.0 to 10.0 kcal mol⁻¹.
- B97-3c//GFNn-xTB may be applied as an intermediate energy screening level, drastically reducing the number of considered conformers in further optimizations.

Note, that even though the convenient, fully automatic conformer ensemble generation can be applied almost black-box in this way, for complex molecules with challenging electronic structures the obtained results should be analyzed carefully by an experienced computational chemist.

5.4. Conclusion and Outlook

Accurate conformational energies are very important for the correct description of molecular systems in various areas of chemistry. Many conformer benchmarks are available for mostly organic systems, but only very few studies of organometallic conformational energies exist. One reason for this is the lack of conformer generation methods that are able to routinely handle transition metal containing systems. In this study we composed a benchmark set of 40 organometallic molecules to investigate the performance of low-cost composite DFT and SQM methods for this problem. Conformers for the 40 molecules were automatically generated using the recently published iMTD-GC workflow with crystal structure geometries as input, i.e., all studied systems are chemically existing and relevant. Up to 30 conformers were selected for each of the complexes, leading to overall 969 conformational energies for the benchmark termed TMCONF40. Besides errors for relative energies, two correlation coefficients (Pearson, Spearman) were used in the evaluation as a measure for parallelism between different potential energy surfaces. In a first step, several composite, hybrid and double-hybrid DFAs were investigated on a small subset of TMCONF40 in comparison to high level DLPNO-CCSD(T1) values. Based on these results the PWPB95-D4/def2-QZVP level was chosen as the theoretical reference for the full set. Here, several combinations of low-cost composite DFAs, SQM methods and generic FFs were tested. Overall, SQM methods perform worse than low-cost DFAs for the conformational energies, which is consistent with findings from other benchmark studies for organic systems. Within the SQM class, GFNn-xTB methods in general outperform the PMx methods. The combination of SQM derived geometries with efficient composite DFAs like B97-3c (B97-3c//GFN2-xTB) yields reasonable conformational energies and is recommended for first steps in multi-level procedures. The automated conformer generation within the CREST program, which is done at the GFNn-xTB/FF level, proved to reliably yield low-energy conformers in a black-box approach despite the only mediocre performance for conformational energies.

5. Theoretical Study on Conformational Energies of Transition Metal Complexes

However, some transition metal complexes require an adjusted technical setup in CREST due to their complicated coordination patterns. A chemically important result of our study is, that experimental solid state conformers provided by X-ray diffraction in probably many cases do not correspond to the lowest energy structure in gas-phase (and likely also not to the solution structure). Thus, application of automated procedures like the one proposed here in addition to automated post-processing tools like ENSO (for which an updated version will be made available soon) are strongly recommended. The electronic complexity of transition metal complexes remains challenging, especially for semi-empirical and force field methods, even though recent developments like the GFNn-xTB/FF methods are promising. This complexity of transition metal complexes generally renders the careful analysis by experienced scientists indispensable. This not only holds for SQM or FF methods, but also for DFT and WFT based methods. Further development, e.g., in the direction of ligand field molecular mechanics (LFMM)³¹⁴ based on available composite DFT and SQM/FF methods, may further increase the reliability of automated workflows also for TM complexes. The TMCONF40 benchmark set represents a valuable tool for the evaluation of such further developments in the future.

Acknowledgements

This work was supported by the Deutsche Forschungsgemeinschaft (DFG) in the framework of the Gottfried Wilhelm Leibniz prize awarded to S.G.

Availability

The xtb and CREST programs can be obtained from our GitHub page (<https://github.com/grimme-lab/xtb> and <https://github.com/grimme-lab/crest>).

Part III.

Quantum Chemical Studies on Frustrated Lewis Pair Catalysis

Frustrated Lewis pairs (FLPs) are pairs of a Lewis acid and a Lewis base, for which the formation of a strongly bound adduct is hindered by steric, structural or electronic aspects (Figure 5.10). Since the first steps of FLP chemistry in the middle of the 20th century^{315,316}, it has seen a strong scientific interest and the development of new concepts and representatives is still a highly topical field of research^{65–68,317–322}. Specifically, the metal-free activation of small molecules like dihydrogen represents a key application

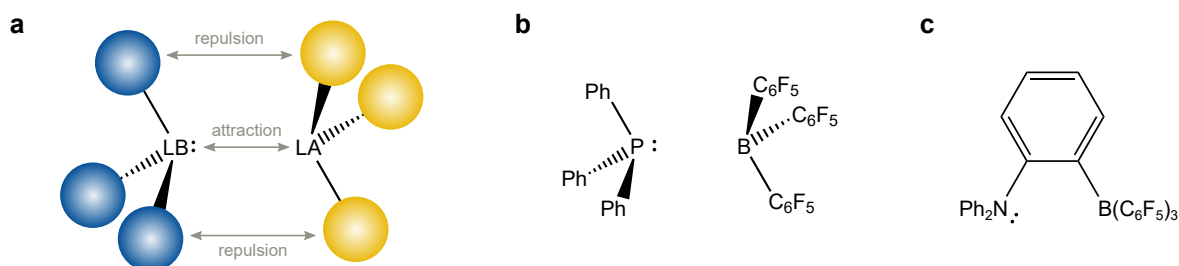


Figure 5.10.: a) Schematic depiction of a frustrated Lewis pair, b) example of an P/B intermolecular FLP, and c) intramolecular N/B FLP.

of FLPs and a plethora of chemical variants has been developed since. Further, the variety of possible elements and substituents used in FLPs has grown rapidly, including other main group elements such as phosphorus and aluminum or even transition metals. This chemical flexibility further enabled new applications, such as the capture or reduction of green house gases like nitrogen oxides, SO₂ or CO₂^{251,323–325}. As the variety of stoichiometric and catalytic FLP applications is still growing, their quantum chemical description has been intensively studied as well^{326–334}. Specifically, the involved mechanisms and chemical concepts are of high interest to understand the nature of FLP based chemistry and allow for a prediction and even design of new FLP systems and reactions. In this context, due to the increasing complexity and often also the size of the investigated FLP systems, reliable and efficient computational methods are required. Therefore, DFT based methods are commonly applied to study FLP chemistry. Nevertheless, mechanistic studies at the DFT level are still time consuming due to the large amount of simulations and calculations needed to find the most probable reaction mechanism. In particular, the often complex modeling of the transition states involved, usually requires high computational effort. Thus, multi-level approaches may be used to reduce the computational effort in time-consuming parts of the computational investigation, such as reaction path simulations. This can be done by using more efficient quantum chemical methods based on either DFT composite schemes, or even faster SQM methods such as GFNn-xTB³³⁵. Therefore, part III is devoted to the application of the DFT-3c and GFNn-xTB methods for the elucidation of complex reaction mechanisms in the field of frustrated Lewis pair chemistry. Here, chapter 6 deals with the special role of halides in the FLP catalyzed hydrogenation of amides, while chapter 7 describes the electrophilic phosphonium cation (EPC) mediated reduction of phosphane oxides by oxalyl chloride and molecular hydrogen. Chapter 8 utilizes the insights gained from chapters 6 and 7, combining both concepts in the FLP catalyzed hydrogenation of secondary amides using phosphane oxides.

6. Frustrated Lewis Pair Catalyzed Hydrogenation of Amides: Halides as Active Lewis Base in the Metal-Free Hydrogen Activation

Nikolai A. Sitte,^a Markus Bursch,^b Stefan Grimme,^b and Jan Paradies^a

Received: 4 December 2018, Published online: 13 December 2018

Reprinted (adapted) with permission[†] from

Sitte, N. A.; Bursch, M.; Grimme, S.; Paradies, J. *J. Am. Chem. Soc.* **2019**, *141*, 159–162.

— Copyright © 2018, American Chemical Society.

DOI [10.1021/jacs.8b12997](https://doi.org/10.1021/jacs.8b12997)

Own manuscript contribution

- Performing all quantum chemical calculations
- Interpretation of the computational results
- Co-writing the manuscript

^aDepartment of Chemistry, University of Paderborn, Warburger Straße 100, 33098 Paderborn, Germany

^bMulliken Center for Theoretical Chemistry, Institut für Physikalische und Theoretische Chemie, Rheinische Friedrich-Wilhelms-Universität Bonn, Beringstraße 4, 53115 Bonn, Germany

[†]Permission requests to reuse material from this chapter should be directed to the American Chemical Society.

6. FLP Catalyzed Hydrogenation of Amides: Halides as Active Lewis Base in the Hydrogen Activation

Abstract A method for the metal-free reduction of carboxylic amides using oxalyl chloride as an activating agent and hydrogen as the final reductant is introduced. The reaction proceeds via the hydrogen splitting by $B(2,6-F_2-C_6H_3)_3$ in combination with chloride as the Lewis base. Density functional theory calculations support the unprecedented role of halides as active Lewis base components in the frustrated Lewis pair mediated hydrogen activation. The reaction displays broad substrate scope for tertiary benzoic acid amides and α -branched carboxamides.

6.1. Introduction

The reduction of carboxylic amides is one of the most important key transformations in preparative chemistry on both the laboratory and industrial scale. The development of mild, chemoselective, and robust general methods relying on catalytic reactions is of great importance for the pharmaceutical industry, since this serves as a platform for the implementation of the structural diversity of amines. Most abundant reductions of carboxamides require strong nucleophilic “ate” hydride donors, such as aluminum or boron reagents. Catalytic processes are highly demanded because of the reduced functional group tolerance, safety issues of these pyrophoric reagents, and byproduct separation. The most desirable reduction of carboxylic amides with molecular hydrogen³³⁶ (H_2) was reported in 1934 by the use of a heterogeneous Cu/Cr catalyst and required over 990 bar at 250°C^{337,338}. These drastic conditions were improved (10–30 bar, 160°C) by the application of a bimetallic Pd/Re@graphite³³⁹ and a homogeneous ruthenium catalyst^{340,341}. Milder amide reductions were realized using stoichiometric hydrosilane based reduction equivalents in combination with metals, e.g. iron³⁴², platinum^{343,344}, or zinc^{345,346}, and main group Lewis acids, such as boronic acids³⁴⁷, $B(C_6F_5)_3$ (**1**)^{348,349}, and electrophilic phosphonium cations³⁵⁰. Triflic anhydride proved to be a useful, but difficult to handle, carbonyl activation agent for the direct reduction with Hantzsch’s esters³⁵¹ or silanes³⁵², with the significant drawback

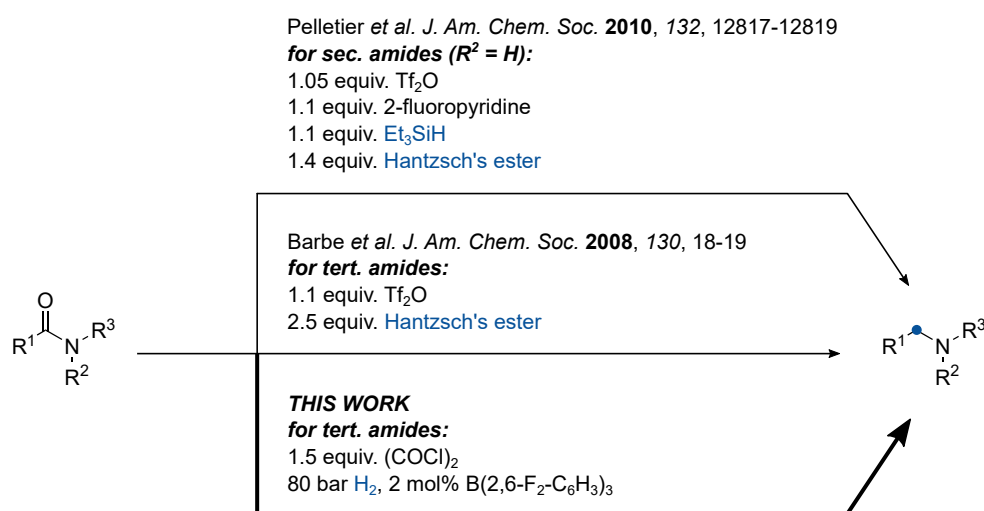


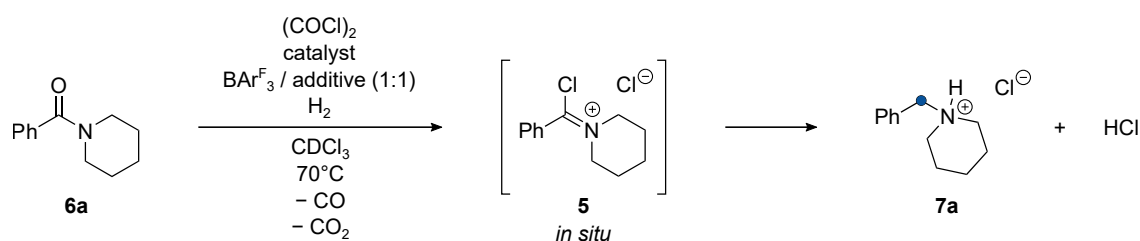
Figure 6.1.: Metal-free reductions of secondary and tertiary amides.

of producing stoichiometric amounts of byproducts. In light of this, frustrated Lewis pairs (FLPs) offer a unique catalytic access to borohydrides from H_2 ^{67,68,317,319,321,353,354} and may serve as a reduction equivalent in the metal-free reduction of activated carboxamides (Figure 6.1).

6.2. Results and Discussion

Here we present the metal-free hydrogenation of carboxamides to amines in excellent yields under mild conditions (50–70°C, 80 bar), taking advantage of oxalyl chloride as an activating reagent. The produced amines are furnished as hydrochloride salts, enabling the most convenient isolation by filtration. Mechanistic details support the unparalleled role of chloride as the Lewis base in the frustrated Lewis pair catalyzed hydrogenation^{67,317,319,353,355}. We initiated our investigation using the FLP system consisting of $B(C_6F_5)_3$ (**1**), $B(2,4,6-F_3-C_6H_2)_3$ (**2**)^{356,357}, or $B(2,6-F_2-C_6H_3)_3$ (**3**)^{356–359} in combination with 2,6-lutidine (**4**) and the *in situ* generated chloroiminium chloride **5** from the reaction of the amide **6a** with oxalyl chloride^a (Table 6.1)^{360–362}. The hydrogenation of **6a** with the FLP **1/4** was not observed because **1** was inhibited by the chloride (Entry 1) as evidenced by the ¹¹B NMR resonance at 6.53 ppm (see the online Supporting Information of the original publication for details). However, in the presence of 20 mol% **2/4** or **3/4** the hydrochloride salt of N-benzyl piperidine (**7a**) was obtained within 18 h in 40% and 90% yield respectively (entries 2 and 3). These results are surprising, since the base is proto-

Table 6.1.: One-pot activation and FLP-catalyzed hydrogenation of amide **6a**.^a



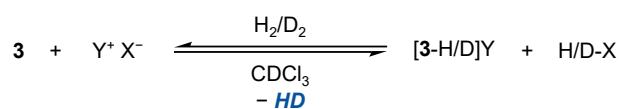
entry	cat. / mol%	add. 4 / mol%	equiv. $(COCl)_2$	H_2 / bar	time / h	yield / %
1	20 (1)	20	1.0	4	18	0
2	20 (2)	20	1.0	4	18	40
3	20 (3)	20	1.0	4	18	90
4	0	20	1.0	4	18	0
5	20 (3)	–	1.0	4	18	85
6	10 (3)	–	1.2	4	48	90
7	5 (3)	–	1.5	12	28	90
8	2 (3)	–	1.5	80	22	90

^aConditions: 2–20 mol% **3**, 0–20 mol% **4**, 0.1 mmol of **6a** in $CDCl_3$ (0.16 M), 1.0–1.5 equiv. of oxalyl chloride in 0.2 mL $CDCl_3$, 4–80 bar of H_2 .

^aThe reaction can also be performed with oxalyl bromide.

6. FLP Catalyzed Hydrogenation of Amides: Halides as Active Lewis Base in the Hydrogen Activation

nated under the reaction conditions and should no longer engage in the H₂-activation event. Control experiments clearly revealed that the borane is necessary for the hydrogenation (Entry 4) whereas the Lewis base 2,6-lutidine (**4**) had essentially no impact on the reaction (Entry 5). The catalyst loading could be reduced to 2 mol% using 1.5 equiv. of oxalyl chloride and 80 bar of H₂ at 70°C in the absence of a supporting base (Entries 6–8). Further studies support chloride operating as a weak Lewis base in the transient³⁶³ FLP-mediated H₂-activation. In contrast to **1**, the boranes **2** and **3** show dynamic ¹¹B NMR spectra in the temperature range 20 to 60°C in the presence of a chloride source which assures the availability of free Lewis acid in solution.^b Halides have not yet been considered as a Lewis base in borane-mediated H₂ activation probably due to two obvious reasons. First, the halide, particularly, chloride and fluoride, forms an irreversible adduct with strong Lewis acids. Second, the basicity of the halide decreases dramatically going from fluoride to iodide. However, very weak Lewis bases, e.g. fluorinated phosphanes or ethers, have been reported as an active component in the FLP-catalyzed hydrogenation of olefins^{363,364} and in the reduction of carbonyls^{365,366}. Systematic studies focusing on the dependence of FLP-reactivity on the pK_a of the conjugate Brønsted acid^{356,358,363} support that chloride should be able to activate H₂ (pK_a (MeCN): 10.30)³⁶⁷ provided that it does not deactivate the Lewis acid (*vide supra*). We were able to exclude the amide and the chloroimine, which may arise from nucleophilic ring opening^{368,369} as active Lewis bases in the H₂ splitting (see the online Supporting Information of the original publication). Instead we observed the fast isotope scrambling of a H₂/D₂ mixture by **3** in the presence of the chloride sources **8**, **9**, and **10** at 50–70°C (Figure 6.2). HD was



X = Cl, Y = PPh ₄	(8)
X = Cl, Y = NBu ₄	(9)
X = Cl, Y = BMIM	(10)
X = Br, Y = BMIM	(11)
X = I, Y = BMIM	(12)

Figure 6.2.: H₂/D₂-scrambling using B(2,6-F₂-C₆H₃)₃ (**3**) and halides. BMIM = 1-Butyl-3-methylimidazolium.

unmistakably identified by its ¹H NMR resonance at 4.43 ppm with the characteristic coupling constant of ¹J_{H-D} = 43 Hz. The three chloride sources **8**, **9**, and **10** featured identical performance in the H/D exchange supporting the role of the chloride as an active Lewis base. Importantly, the 1-butyl-3-methylimidazolium (BMIM) bromide and iodide salts **11** and **12** also displayed activity in the H/D scrambling; however, elevated temperatures were required (**11**, 70°C; **12**, 90°C). Quantum chemical investigations at the PW6B95-D3(BJ)-ATM+COSMO-RS(CHCl₃)/def2-QZVP//PBEh-3c(COSMO(CHCl₃)) level of theory^{31,59,69,121,122,124,125,206,240,370–375} (See appendix A5 for further details) strongly support the activity of halides as an active Lewis base in the heterolytic splitting of H₂ in combination with **3**. The reaction of **3** with dihydrogen and a halide cation pair [Me₄N]X was investigated in chloroform at 50°C for X = Cl⁻, Br⁻, and I⁻. For all three halides, transition states (**TS**_X) for a H₂ splitting with **3** were

^bThe boranes remained intact throughout the reaction as evidenced by ¹H and ¹¹B NMR spectroscopy despite the strong acidic conditions.

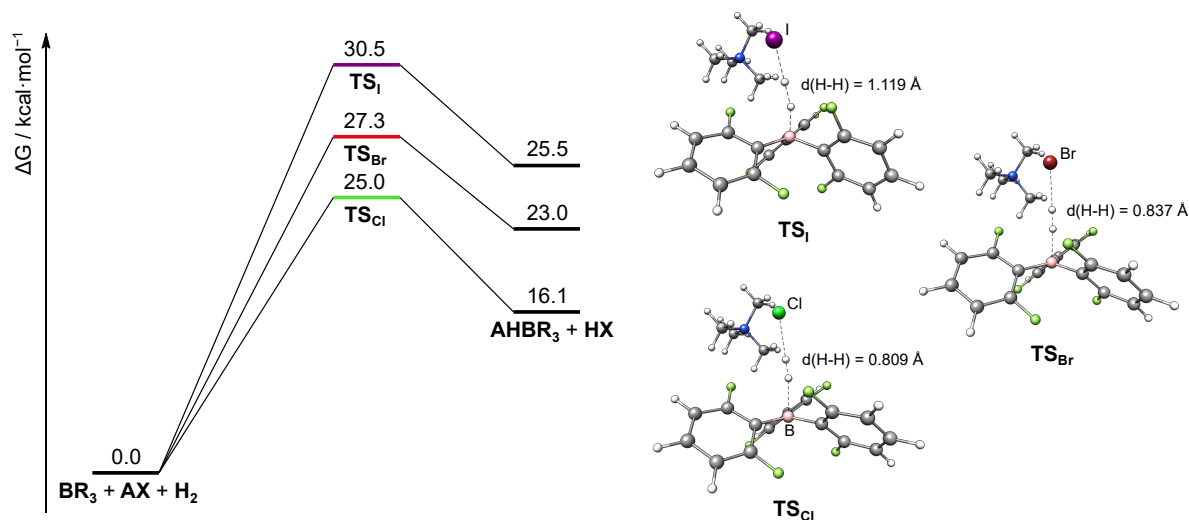


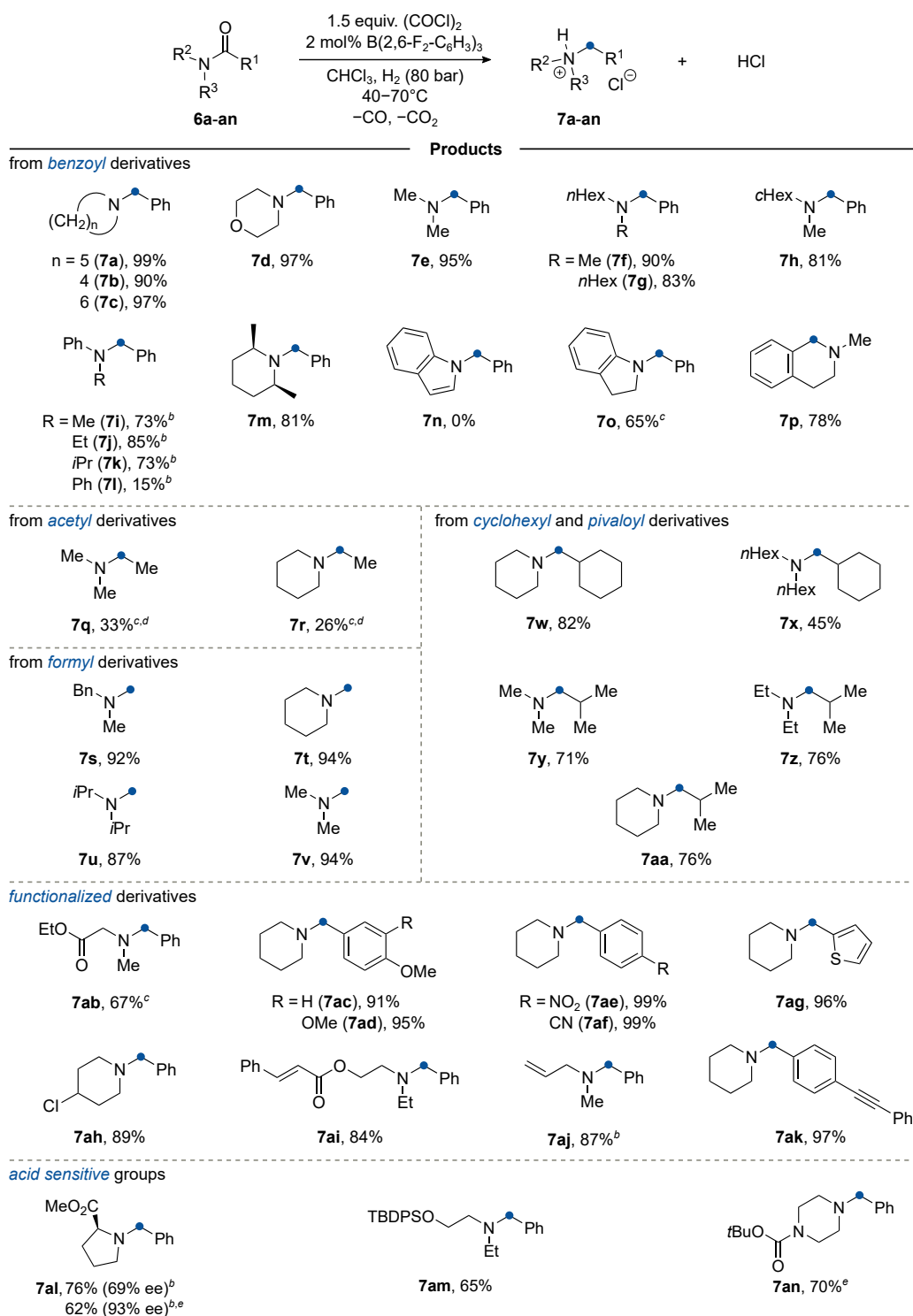
Figure 6.3.: Relative Gibbs free energy diagram and transition state structures of the H_2 splitting reactions. All energies given are in kcal mol^{-1} relative to the corresponding separated reactants. $\text{A} = \text{Me}_4\text{N}^+$; $\text{R} = 2,6\text{-F}_2\text{-C}_6\text{H}_3$; $\text{X} = \text{Cl}^-$ (green), Br^- (red), I^- (purple).

identified in a thermally accessible energy range (Figure 6.3). All investigated reactions are endergonic giving rise to the observed transient formation of a borohydride upon H_2 splitting at the given reaction conditions as evidenced by the NMR experiments. The observed trend of energetically higher lying transition states in the order $\text{Cl} < \text{Br} < \text{I}$ is reflected by the increased demand of heating upon using Br and I salts. The bond length of the split hydrogen molecule in the TS increases from Cl over Br to I as bases. The value computed for the most active system of about 0.8 \AA is similar to that observed in typical $\text{P} \cdots \text{B}$ FLP systems and points to an early TS³²⁶. The substrate scope of the metal-free hydrogenation of amides was explored (Figure 6.4). Benzoic amides bearing cyclic and acyclic alkyl chains, heterocycles, or aromatic substituents were hydrogenated in excellent yields (**7a–k**). Notably, small N-Me substituted amides as well as amides bearing steric encumbrance in the α -position (**6m**) were reduced in excellent yields. Highly reactive aromatic compounds, e.g. the diphenylamine **6l** and the indole **6n**, decomposed under the reaction conditions. However, electron-rich compounds such as indoline **6o** or the lactam **6p** cleanly underwent reduction in high yields. Benzoic amides derived from primary amides were cleanly activated, but the corresponding chloro imines were not susceptible to FLP-catalyzed hydrogenation.^c Nonetheless, the protocol enables the reduction of amides derived from aliphatic carbonic acids (**6q–6aa**). The acetyl derivatives **7q** and **7r** were obtained in low yields.^d However, the formyl and branched amides **6s–6aa** were converted to the corresponding N-methyl amines **7s–v** and α -branched amines **7w–7aa** in high to excellent yields. Furthermore, we investigated the functional group tolerance of the reaction. Esters, ethers, nitro, cyano, or thiophenyl groups were well tolerated (**7ab–ag**, 67–99%). Amides bearing reactive multiple bonds as in the acrylate **6ai**, the allyl amine **6aj**, or in the alkyne **6ak**

^cThe corresponding chloroimine is not protonated under the reaction conditions so that it remains unreactive to hydride addition. The calculated pK_a of a chloroimine is ca. 5, whereas the pK_a of HCl is 9.92 (exptl. 10.3, see SI for details). The chloroimine is not active as a Lewis base in the H_2 -splitting with **3**.

^dThis is the result of the high propensity of enamine formation of the corresponding chloroiminium chlorides and subsequent polymerization. Accordingly, aliphatic carboxamides and lactones were not compatible with the reaction conditions.

6. FLP Catalyzed Hydrogenation of Amides: Halides as Active Lewis Base in the Hydrogen Activation



^aReactions were typically performed with 1 equiv. of amide in CHCl₃ (0.16 M), 2 mol% **3**, 1.5 equiv. of (COCl)₂, 80 bar at 40–70°C for 22–48 h. ^b5 mol% **3**. ^c20 mol% **3**. ^dPerformed on NMR-scale. ^eIn the presence of 1.0 equiv. of 2,6-di-*t*-bu-pyridine (**7al**) or 2,6-lutidine (**7am**, **7an**); • denotes former position of the carbonyl group.

Figure 6.4.: Substrate scope for the FLP-catalyzed reduction of amides.

remained unchanged, and the amines **7aj–ak** were isolated in high to excellent yields. Even substrates bearing acid-sensitive groups were reduced in good yields. The proline derivative **7al** was obtained in 65% yield in the presence of 1.0 equiv. of 2,6-di-*t*bu-pyridine with marginally diminished enantiomeric purity of 93% ee (without base 76%, 69% ee). The TBDPS- (*tert*-Butyldiphenylsilyl) and even the Boc (*tert*-Butyloxycarbonyl) group were stable under the reaction conditions and enabled the reduction of silyl ether **6am** and of the carbamate **6an** in 65% and 70% yield, respectively.

6.3. Conclusion

In summary, we developed the FLP-catalyzed hydrogenation of carboxylic amides with the aid of oxalyl chloride as a deoxygenating agent. Mechanistic and quantum-mechanical investigations strongly support the role of halides in the FLP-mediated H₂-activation. The reaction displays broad generality and high functional group tolerance, providing access to tertiary amines in the presence of hydride sensitive functional groups.

Acknowledgements

The German Science Foundation (DFG) and the Fonds der Chemischen Industrie (FCI) are gratefully acknowledged for financial support (PA 1562/6-1 and Gottfried Wilhelm Leibniz prize to S.G.) and for a stipend to N.A.S.

7. Electrophilic Phosphonium Cation-Mediated Phosphane Oxide Reduction Using Oxalyl Chloride and Hydrogen

Arne J. Stepen,^a Markus Bursch,^b Stefan Grimme,^b Douglas W. Stephan,^c and Jan Paradies^a

Received: 11 August 2018, Published online: 17 October 2018

Reprinted (adapted) with permission[†] from

Stepen, A. J.; Bursch, M.; Grimme, S.; Stephan, D. W.; Paradies, J. *Angew. Chem. Int. Ed.* **2018**, *57*, 15253–15256.

– Copyright © 2018, Wiley-VCH Verlag GmbH & Co. KGaA, Weinheim.

DOI [10.1002/anie.201809275](https://doi.org/10.1002/anie.201809275)

Own manuscript contribution

- Performing all quantum chemical calculations
- Interpretation of the computational results
- Co-writing the manuscript

^aDepartment of Chemistry, University of Paderborn, Warburger Straße 100, 33098 Paderborn, Germany

^bMulliken Center for Theoretical Chemistry, Institut für Physikalische und Theoretische Chemie, Rheinische Friedrich-Wilhelms-Universität Bonn, Beringstraße 4, 53115 Bonn, Germany

^cDepartment of Chemistry, University of Toronto, 80 St. George St, Toronto Ontario M5S3H6, Canada

[†]Permission requests to reuse material from this chapter should be directed to Wiley-VCH Verlag GmbH & Co. KGaA, Weinheim.

Abstract The metal-free reduction of phosphane oxides with molecular hydrogen (H₂) using oxalyl chloride as activating agent was achieved. Quantum-mechanical investigations support the heterolytic splitting of H₂ by the *in situ* formed electrophilic phosphonium cation (EPC) and phosphane oxide and subsequent barrierless conversion to the phosphane and HCl. The reaction can also be catalyzed by the frustrated Lewis pair (FLP) consisting of B(2,6-F₂-C₆H₃)₃ and 2,6-lutidine or phosphane oxide as Lewis base. This novel reduction was demonstrated for triaryl and diaryl phosphane oxides providing access to phosphanes in good to excellent yields (51–93%)

7.1. Introduction

The reduction of phosphane oxides, in particular triphenyl-phosphane oxide (Ph₃PO, **1a**), is of great interest since Ph₃PO is produced on ton-scale in the industrial Wittig reaction for the synthesis of vitamins³⁷⁶. Typical processes to recycle the phosphane oxides rely on the reductive deoxygenation with hydrosilanes at elevated temperatures in the presence of amines^{377–386}. Only recently, a metal-free reduction of phosphane oxides using phosphites as reduction equivalent was reported³⁸⁷. Alternative oxygen trapping reagents are phosgene derivatives and oxalyl chloride^{388,389} that convert the phosphane oxides to the corresponding dichlorophosphoranes³⁹⁰, which are in equilibrium with the corresponding ionic chlorophosphonium chlorides (Figure 7.1). Treatment of these phosphorus(V) elec-

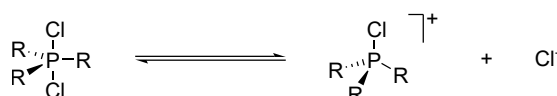


Figure 7.1.: Equilibrium of dichlorophosphorane and chlorophosphonium chloride.

trophiles with elemental main-group metals (Si or Al) or sodium borohydride produces the corresponding phosphanes accompanied with stoichiometric amounts of aluminum/silicon chlorides or boron species^{362,388,391–393}. The use of molecular hydrogen (H₂) as stoichiometric reductant would be highly desirable since only hydrochloric acid is produced. To date, no catalyst has been reported for such application. Only one patent details the reduction of phosgene-generated chlorotriphenylphosphane chloride with 150 bar H₂ at 160°C. Neither further examples were presented nor the mechanism has been explored³⁹⁴. Boron-derived Lewis acids show outstanding reactivity in small-molecule activation providing unique catalytic access to hydride species directly from H₂^{65–68,317,319,320}. Similarly, EPCs act as active Lewis acids and demonstrate high reactivity in bond activation^{395–400} and in hydrogenations⁴⁰¹. Both classes of main-group-derived Lewis acids found wide application in hydro-silane reductions, reductive defluorinations³⁹⁵, and deoxygenations^{350,400,402–412}. The reduction of phosphane oxides or derived chlorophosphoranes using H₂ as final reductant and main-group Lewis acid catalysts have so far not been preceded.

7.2. Results and Discussion

We initiated our investigations by pressurizing a mixture of **1a** and 1.5 equiv. oxalyl chloride in CDCl₃ with H₂ (4 bar). The typical ³¹P NMR resonances of the phosphane oxide (δ = 38.3 ppm) vanished over a period of 30 min with concomitant appearance of two new resonances, which were assigned to the dichlorotriphenylphosphorane (δ = -46.2 ppm) and to the chlorophosphonium chloride (δ = 65.5 ppm)^a (lit. ref. δ = -47.0 ppm; 65.5 ppm)⁴¹³⁻⁴¹⁶. However, the reduction of these phosphorus species was not observed, potentially due to the absence of a suitable Lewis acid and/or Lewis base for H₂-activation (Figure 7.2). This prompted us to use a FLP catalyst consisting of the weak Lewis acid

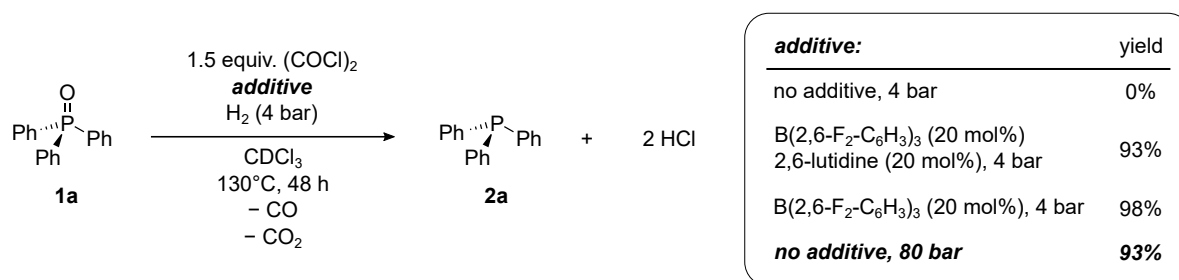


Figure 7.2.: FLP-catalyzed reduction of triphenylphosphane oxide (**1a**) by (COCl)₂/H₂. Yields were determined after column chromatography.

B(2,6-F₂-C₆H₃)₃^{356-359,417} (**3**) and 2,6-lutidine (**4**) to generate hydroborate species *in situ*. Indeed, the presence of 20 mol% of **3/4** and 4 bar H₂ resulted in 93% yield triphenylphosphane (**2a**). This result is remarkable, since 2 equiv. HCl are produced in the reaction, which protonates 2,6-lutidine and should shut-down the hydrogenation. The control experiment with **3** (20 mol%) alone provided the product in almost quantitative yield of 98%. We identified triphenylphosphane oxide **1a** as the active Lewis base in the activation of H₂ (Figure 7.3). The reaction of a 1:1 mixture of **3** and **1a** with H₂/D₂ (4 bar) at 80°C resulted within 5 d in the isotope scrambling to HD/H₂/D₂. These observations clearly indicate the ability of **3/1a** to act as hydrogenation catalyst. Finally, we investigated the reaction at 80 bar H₂ in the absence

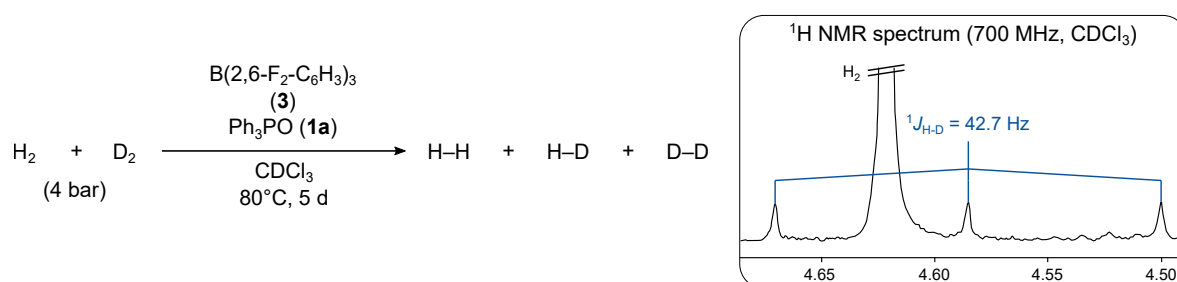


Figure 7.3.: Isotope exchange experiment with the FLP consisting of B(2,6-F₂-C₆H₃)₃ (**3**) and Ph₃PO (**1a**) as Lewis base.

^aIn chloroform the equilibrium was shifted to the chlorophosphonium species, whereas in toluene the dichlorophosphorane was the dominant species.

7. EPC-Mediated Phosphane Oxide Reduction Using Oxalyl Chloride and H₂

of borane or amine. Surprisingly, under these conditions the product **2a** was obtained in 93% yield. The reduction proceeds presumably through the activation of H₂ by a Lewis pair consisting of Ph₃PO (**1a**) and of the electrophilic phosphonium cation [Ph₃PCl]⁺. Careful consultation of the ³¹P NMR spectra of the reaction revealed small quantities of phosphane oxide, most probably arising from water traces in the H₂ atmosphere. As control experiment, a sample of Ph₃PCl₂ was allowed to react with purified H₂ (4 bar) for 24 h at 130°C in CDCl₃, but the formation of PPh₃ was not observed. After addition of phosphane oxide **1a** (20 mol%) to the sample, re-pressurization with purified H₂ (4 bar), and heating to 130°C for 24 h, **2a** was produced in 25% yield. The reduced reaction rate must be attributed to the drastic pressure decrease. Nevertheless, these experiments strongly support the role of phosphane oxide as active Lewis base. Quantum mechanical investigations at the double-hybrid PWPB95-D3(BJ)-ATM+COSMO-RS(CHCl₃)/def2-QZVPP//PBEh-3c(COSMO(CHCl₃))^{31,59,69,121,122,124,125,206–209,240,260,286,371–373,375} level of theory with structure pre-optimizations applying GFN1-xTB^{53,418} revealed the ability of [Ph₃PCl]⁺ to act as Lewis acid in combination with Ph₃PO as Lewis base (Figure 7.4). The triphenylchlorophosphonium cation **5a** is obtained in a strongly exergonic reaction from the triphenylphosphane oxide (**1a**) and (COCl)₂. Cation **5a** is in an almost barrierless equilibrium with the energetically slightly favored triphenyldichlorophosphorane (**5a-Cl**) (ΔΔG = 1.2 kcal mol⁻¹). An O-P coordinated, π-stacked adduct **1a/5a** (see appendix A6) of **1a** and **5a** is disfavored by 4.2 kcal mol⁻¹ with respect to its isolated fragments in solution, while the gas-phase association free energy amounts to -3.0 kcal mol⁻¹. The heterolytic activation of H₂ by **5a** and the phosphane oxide **1a** requires 35.8 kcal mol⁻¹ with an overall reaction barrier of 37.0 kcal mol⁻¹ with respect to **5a-Cl**, which is in agreement with the required drastic reaction conditions. The transition state **TS_a** has an asymmetric, non-linear O-H-H-P unit (angles / °: O-H-H 176.1, P-H-H 142.7; distances / Å: O-H 1.337, P-H 1.864) with a significantly elongated H-H bond length of 0.904 Å. Some short intermolecular C-C interligand distances of approximately 3.5 Å in the structure of the transition state indicate the significance of attractive intermolecular interligand interactions, including π-π stacking for the stabilization of the transition state³²⁶. The subsequent conversion of

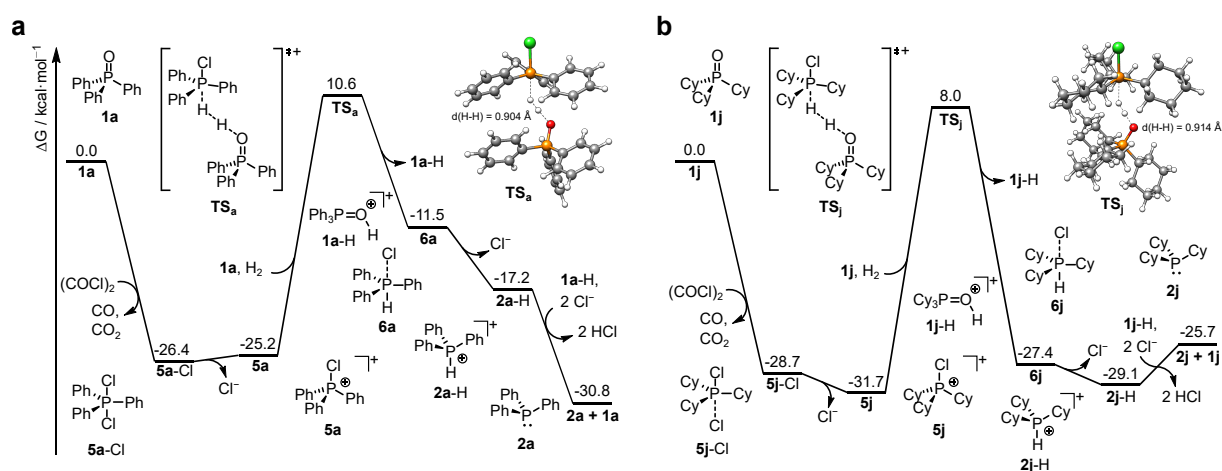
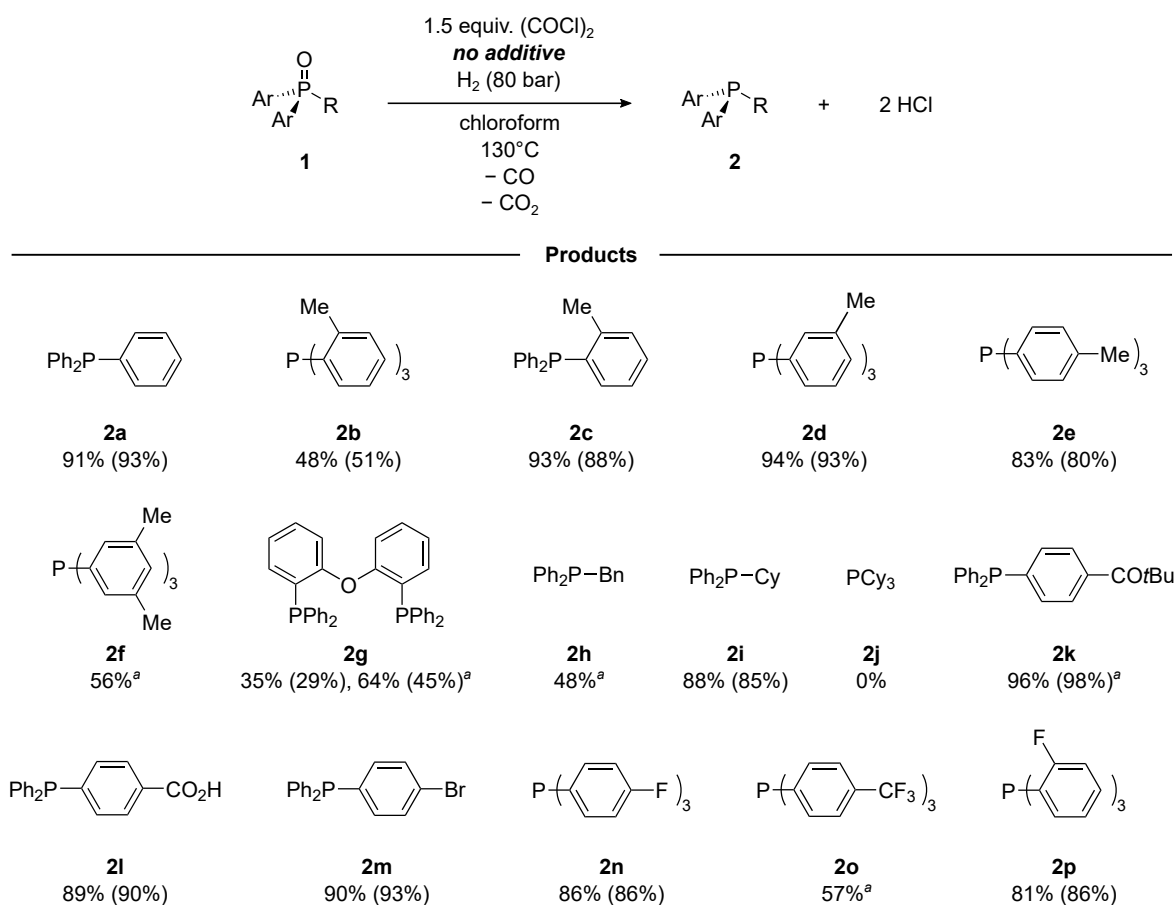


Figure 7.4.: Relative Gibbs free energy diagram of the phosphane oxide reduction in CHCl₃. All energy values in kcal mol⁻¹ relative to **1a** and **1j**, respectively. T = 130°C.

the triphenylhydrochlorophosphorane (**6a**) into the protonated phosphane (**2a-H**) by chloride loss is exergonic by $-5.7 \text{ kcal mol}^{-1}$ leading to an overall exergonic process of $-30.8 \text{ kcal mol}^{-1}$ after deprotonation of the protonated phosphane oxide intermediate (**1a-H**) and **2a-H** re-yielding **1a** and **2a**, respectively. According to this mechanistic model, the competence of the phosphane oxide/phosphonium Lewis pair to activate H_2 is strongly influenced by their electronic and steric properties. We investigated the reduction of a series of phosphane oxides (Figure 7.5) at 80 bar H_2 (the results of the FLP-catalyzed low-pressure variant are summarized in the online Supporting Information of the original publication). Generally, triaryl and diaryl phosphane oxides were efficiently reduced. The diminished Lewis acidity of more electron-rich chlorophosphonium ions is apparently counterbalanced by the increased Lewis basicity of the corresponding phosphane oxides in the H_2 -activation step. In detail, triphenylphosphane oxide **1a** was reduced in excellent yield. Increase of steric bulk resulted in decrease of yields,



^a Reactions were performed in the presence of 20 mol% $\text{B}(\text{2,6-F}_2\text{-C}_6\text{H}_3)_3$ (**3**) and 20 mol% 2,6-dimethylpyridine (**4**) at 4 bar H_2 -pressure.

Figure 7.5.: Reduction of phosphane oxides with oxalyl chloride/hydrogen and its phosphane products. Yields were determined by NMR spectroscopy, values in parentheses correspond to isolated yields after column chromatography.

7. EPC-Mediated Phosphane Oxide Reduction Using Oxalyl Chloride and H₂

as observed for P(*o*Tol)₃ (**1b**, 51%) and Ph₂P(*o*Tol) (**1c**, 88%). Methyl groups in *meta* or *para* position in **1d–f** were well tolerated and yields of 56% to 93% were obtained. The steric impact on the reactivity is also observed for bisphosphane derivatives. Although the dioxide derivatives of BINAP, xantphos, and DPEphos (**1g**) were cleanly converted into the corresponding bis(chlorophosphonium) chlorides, only the DPEphos derivative (**2g**) could be reduced in moderate yield of 45%. Next, we investigated the reactivity of alkyl-substituted phosphane oxides. Both, the benzyl and cyclohexyl derivatives **2h** and **2i** were reduced in 48% and 85% yield, respectively, although differing methods were required. The low yield of **2h** may arise from a nucleophilic substitution on the chlorophosphonium intermediate by chloride. Steric hindrance in **1i** provides some kinetic stabilization and leads to significantly enhanced yield. Higher steric congestion in the tricyclohexyl derivative **1j** did not result in the formation of **2j** although quantitative formation of the corresponding chlorophosphonium chloride was observed. This is in agreement with a higher computed reaction barrier of 39.7 kcal mol⁻¹ and an endergonic reaction free energy of 6 kcal mol⁻¹ from **5j** to **2j** (for details see appendix A6). Finally, we investigated the impact of electron-withdrawing groups on the arene ring. Substituents in the 4-position of the arene ring in **1k–m** were well tolerated and the functionalized phosphanes were obtained in 90–98% yield. Also, fluorinated triphenylphosphane derivatives **1n–p** were reactive. Whereas the 4-fluoro derivative **1n** was reduced in 86% yield, the corresponding CF₃-substituted derivative **1o** was only reactive in the presence of 20 mol% of the FLP. However, the 2-fluorophenyl derivative **2p** was obtained in high yield of 86%.

7.3. Conclusion and Outlook

In summary, we have developed the metal-free reduction of phosphane oxides using oxalyl chloride and H₂. Quantum-mechanical calculations support the EPC-mediated heterolytic splitting of H₂ by the *in situ* generated chlorophosphonium ion followed by barrierless conversion to the phosphane and HCl. The applicability of the reduction was demonstrated for electron-donating and electron-withdrawing group substituted triaryl phosphane oxides providing the products in 51–98% yield.

Acknowledgements

The German Science Foundation (DFG) and the Fonds der Chemischen Industrie (FCI) are gratefully acknowledged for financial support (PA 1562/6-1, PA 1562/16-1 and Gottfried-Wilhelm Leibniz prize to S.G.). D.W.S. acknowledges the support of NSERC of Canada and is grateful for the award of a Canada Research Chair and a Einstein Visiting Professorship in Berlin.

8. Hydrogenation of Secondary Amides Using Phosphane Oxide and Frustrated Lewis Pair Catalysis

Laura Köring,^a Nikolai A. Sitte,^a Markus Bursch,^b Stefan Grimme,^b and Jan Paradies^a

Received: 5 January 2021, Published online: 18 January 2021

Reprinted (adapted) with permission[†] from

Köring, L.; Sitte, N. A.; Bursch, M.; Grimme, S.; Paradies, J. *Chem. Eur. J.* **2021**, *27*, 14179–14183.

— Copyright © 2018, Wiley-VCH Verlag GmbH & Co. KGaA, Weinheim.

DOI [10.1002/chem.202100041](https://doi.org/10.1002/chem.202100041)

Own manuscript contribution

- Performing all quantum chemical calculations
- Interpretation of the computational results
- Co-writing the manuscript

^aDepartment of Chemistry, University of Paderborn, Warburger Straße 100, 33098 Paderborn, Germany

^bMulliken Center for Theoretical Chemistry, Institut für Physikalische und Theoretische Chemie, Rheinische Friedrich-Wilhelms-Universität Bonn, Beringstraße 4, 53115 Bonn, Germany

[†]Permission requests to reuse material from this chapter should be directed to Wiley-VCH Verlag GmbH & Co. KGaA, Weinheim.

Abstract The metal-free catalytic hydrogenation of secondary carboxylic acid amides is developed. The reduction is realized by two new catalytic reactions. First, the amide is converted into the imidoyl chloride by triphosgene ($\text{CO}(\text{OCCl}_3)_2$) using novel phosphorus(V) catalysts. Second, the *in situ* generated imidoyl chlorides are hydrogenated in high yields by an FLP-catalyst. Mechanistic and quantum mechanical calculations support an autoinduced catalytic cycle for the hydrogenation with chloride acting as unusual Lewis base for FLP-mediated H_2 -activation.

8.1. Introduction

The acylation of primary and secondary amines serves as a highly efficient method for the construction of simple secondary and tertiary amides, complex molecules⁴¹⁹, natural products⁴²⁰ and in late stage macrocyclizations⁴²¹. Such readily available key intermediates are valuable starting points for the selective synthesis of secondary and tertiary amines. Therefore, the reduction of carboxamides is a key transformation for the selective synthesis of symmetrical and unsymmetrical amines⁴²². The reduction can be realized using stoichiometric amounts of strongly reducing metal hydrides but these reagents suffer from major drawbacks such as limited functional group tolerance and require a rigorous protection group strategy. Metal catalyzed hydrogenations of amides are by far the most atom economic reductions⁴²³ but require drastic conditions³³⁷. Recently, milder reaction conditions were realized^{339,340,424–426}, however selectivity issues due to C–N bond cleavage of hemiacetals^{424,427} or exhaustive reduction of functional groups such as alkenes and alkynes are still prevailing problems. The hydrosilylation of amides facilitates the reduction by the removal of the oxygen atom as siloxane, but comes at the cost of atom efficiency (Figures 8.1a and 8.1b). Nonetheless, high tolerance towards hydrogenation susceptible functionalities was achieved with inorganic^{428–433} and organic^{352,434–437} catalysts. Recently, we reported the highly effective hydrogenation of tertiary amides using an FLP-catalyst^{319,322,353} and oxalyl chloride as low molecular weight deoxygenation reagent⁴³⁸. However, the hydrogenation of secondary amides remained a major challenge. Thus, a new strategy for the hydrogenation of secondary amides is required.

8.2. Results and Discussion

We envisioned a new phosphane oxide catalyzed conversion of the sec. amide to the imidoyl chloride, which is subsequently reduced with H_2 in the presence of an FLP catalyst (Figures 8.1c and d). This approach required the development of two new catalytic reactions with particular consideration of compatible conditions. First, we set out to investigate the efficient formation of the imidoyl chloride which will later serve as *in situ* formed substrate for the FLP-catalyzed hydrogenation. We observed that SOCl_2 cleanly converts the amide **1a** into the imidoyl chloride **2a** in excellent yields under mild conditions (Table 8.1, entry 1)^{439,440}. However, SOCl_2 was incompatible with the conditions of the FLP-catalyzed hydrogenation. The addition of $(\text{COCl})_2$ to the amide **1a** furnished mostly acylation products (Entry 2). Alternatively, *in situ* generated dichlorotriphenyl phosphorane^{389,441,442} is a

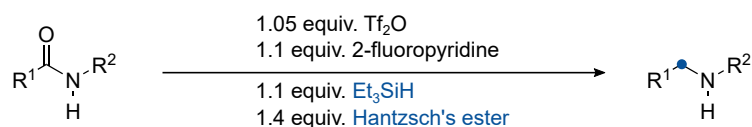
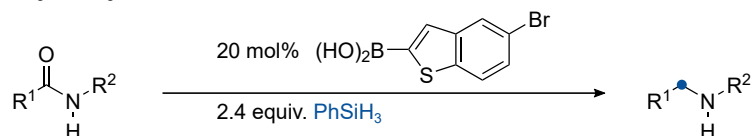
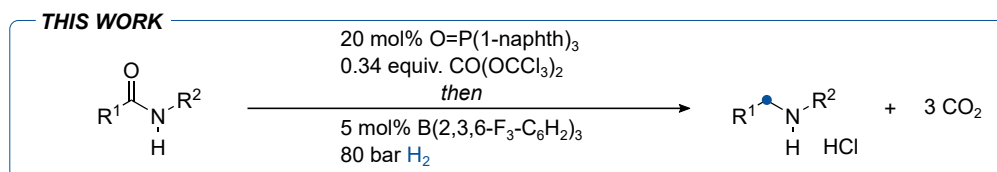
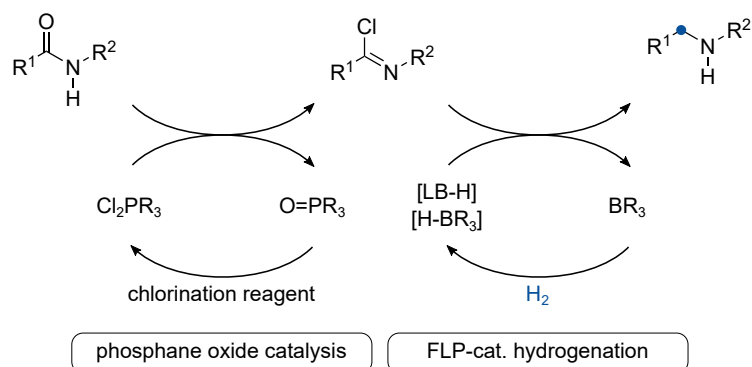
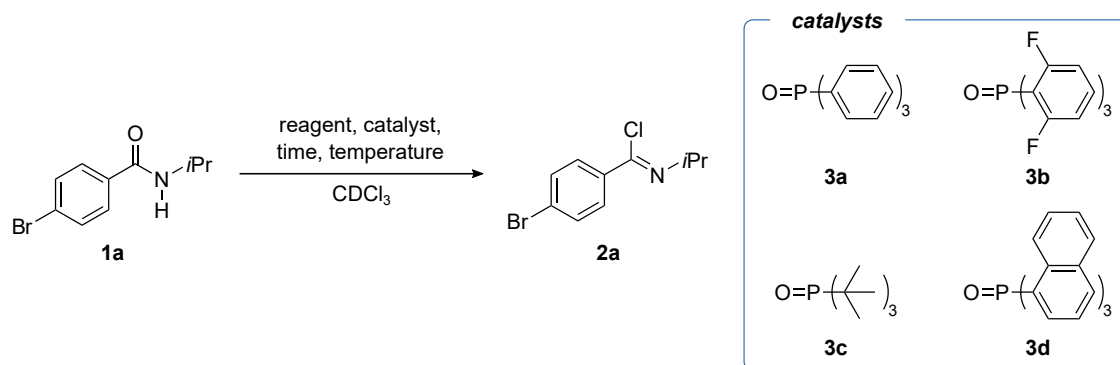
a Metal-free reduction of sec. amides:**b Catalytic hydrosilylation of sec. amides:****c Phosphane oxide and FLP-catalyzed reduction of sec. amides:****d Proposed strategy:**

Figure 8.1.: Metal-free reductions of secondary carboxamides. LB = active Lewis base.

known dehydrating reagent^{443,444}. We investigated the conversion of **1a** into **2a** in the presence of 1.0 equiv. O=PPh₃ and indeed, **2a** was obtained in 93% yield (Entry 3). The catalytic version with (COCl)₂ could not be elaborated because the acylation could not be outcompeted by the phosphane oxide reaction (Entry 4). We found with triphosgene (CO(CCl₃)₂) a selective alternative for the conversion of O=PPh₃ to PPh₃Cl₂ in shorter reaction times without noticeable background reaction (Table 8.1, entry 6). The catalytic conversion of **1a** by CO(CCl₃)₂ is achieved in the presence of all four investigated phosphane oxides (O=PPh₃ (**3a**), O=P(2,6-F₂-C₆H₃)₃ (**3b**), O=P*t*Bu₃ (**3c**) and O=P(1-naphth)₃ (**3d**), entries 6-9). Up to >98% yield within 18 h was obtained at 90 °C. Among the investigated phosphine oxides, **3d** performed best (Entry 10) and displayed in contrast to **3a** and **3b** no interference with the borane **4e** in the FLP-catalyzed hydrogenation (*vide infra*).^a Whereas the mechanism of the phosphane

^a**3a** and **3b** strongly interacted with the borane **4e**, whereas **3c** and **3c** did not. The reactivity of **3c** was inferior compared to **3d** due to steric bulk.

Table 8.1.: Phosphine oxide catalyzed imidoyl chloride formation.



entry	reagent (equiv.)	cat. / mol%	temp. / °C	time / h	yield / % ^a
1	SOCl ₂ (10)	–	70	3	>98
2	(COCl) ₂ (1.1)	–	70	18	0 ^b
3	(COCl) ₂ (1.1)	3a (100)	70	110	93
4	(COCl) ₂ (1.1)	3a (20)	70	18	20 ^c
5	CO(OCCl ₃) ₂ (0.4)	–	70	18	<20
6	CO(OCCl ₃) ₂ (0.4)	3a (20)	70	34	>98 (>98) ^{a, d}
7	CO(OCCl ₃) ₂ (0.4)	3b (20)	70	18	80 (90) ^e
8	CO(OCCl ₃) ₂ (0.4)	3c (20)	70	18	<30 (55) ^e
9	CO(OCCl ₃) ₂ (0.4)	3d (20)	70	42	85
10	CO(OCCl ₃) ₂ (0.4)	3d (20)	90	18	>98

^aDetermined by ¹H NMR spectroscopy.

^bContaminated with >98% of acylation product.

^cContaminated with 5% **1a** and 75% of acylation product.

^d18 h.

^ePerformed at 90°C.

oxide dichlorophosphorane interconversion is known⁴⁴², the subsequent reaction with sec. amides to the imidoyl chloride is so far unreported. Quantum-mechanical calculations at the PW6B95-D4/def2-QZVP+COSMO-RS(CHCl₃)/PBEh-3c(COSMO(CHCl₃))^{69,116,206,240,285,370–373,375} level of theory level (for details see appendix A7) identify the S_N2-type addition of the amide oxygen (**TS1b**) to the chloro phosphonium ion as rate determining step (Figure 8.2) with a reactions barrier of 27.0 kcal mol⁻¹ under chloride loss and formation of **INT1b**. Deprotonation of **INT1b** by a chloride anion yields **INT4b** via **TS2b** (22.4 kcal mol⁻¹). Phosphane oxide **3a** is reformed via **TS3b** (26.7 kcal mol⁻¹), yielding **2b** after chloride addition. The overall free reaction energy amounts to 6.5 kcal mol⁻¹, indicating that the subsequent deoxygenation of the formed phosphane oxide (not shown in figure 8.2), which is known to be strongly exergonic, is needed as driving force⁴⁴². The generally high reaction barriers qualitatively agree with the necessity of heating the reaction mixture and relatively slow reactions. This observation is supported by the increased reactivity of the fluorinated aryl phosphane **3b** compared to **3a** or **3c**. The steric restrictions also play a significant role due to the back-side attack of the amide to the

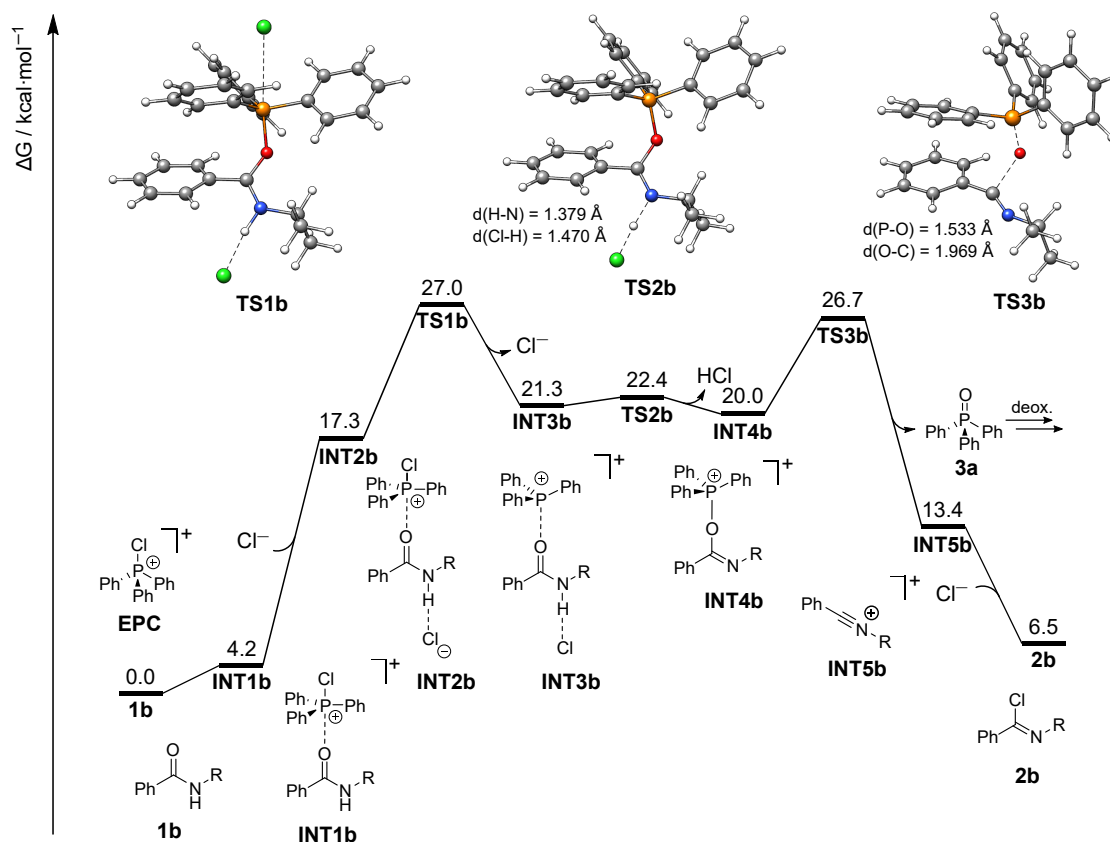


Figure 8.2.: Free energy diagram of the conversion of carboxamides to imidoyl chlorides at the PW6B95-D4/def2-QZVP+COSMO-RS(CHCl₃)/PBEh-3c(COSMO(CHCl₃)) level of theory. All free energies in kcal mol⁻¹.

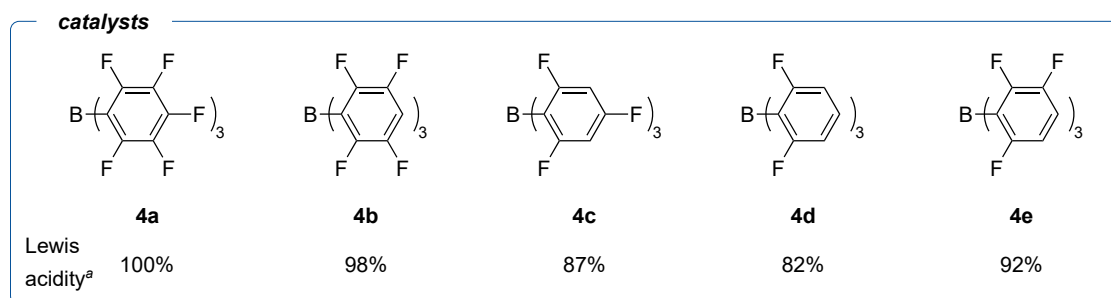
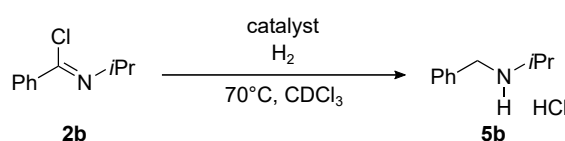
phosphorane in order to form the P-O bond. The second challenge of the amide reduction is the FLP-catalyzed hydrogenation of the imidoyl chloride intermediate. We investigated the catalytic hydrogenation of **2b** with a series of the five boranes **4a-e**, comprising Lewis acidities between 100% and 82%. Treatment of **2b** (0.16M) in chloroform with H₂ (4 bar) at 70°C in the presence of 20 mol% of the two strongest Lewis acids **4a** and **4b** in our study resulted in essentially no conversion as a consequence of catalyst inhibition. However, the application of the weaker Lewis acid **4c** provided the product **5b** as hydrochloride salt in 53% yield (Table 8.2, entries 1-3). Further decrease of the Lewis acidity to 82% (**4d**, entry 4) resulted in inefficient H₂-activation by the imidoyl chloride/borane Lewis pair and caused the drastic decrease of the catalytic productivity⁴³⁸. The Lewis acid **4e** with an acidity between 87% and 98% provided an even more efficient catalyst, which produced the product in quantitative yield (Entry 5). Moreover, the catalyst loading was reduced to 5 mol% employing 80 bar H₂ without yield depletion in 20 h (Entry 6). Finally, we successfully merged both catalytic processes in a one-pot hydrogenation of sec. amides. The carboxylic amide was reacted with 0.34 equiv. CO(COCl₂)₂ in the presence of 20 mol% **3d** at 90°C for 0.5-15 h. Then, 5 mol% **4e** dissolved in chloroform was added and the reaction was pressurized with H₂ (80 bar) for 18 h at 70°C.^b A series of benzamides bearing aliphatic, benzylic

^bSequential addition of the hydrogenation catalyst **4e** and H₂ at 70°C was necessary because the amide formed an irreversible adduct with the borane.

8. Hydrogenation of Secondary Amides Using Phosphane Oxide and Frustrated Lewis Pair Catalysis

and aromatic N-substituents were hydrogenated in good to excellent yields (Table 8.3, 58-95%). The reaction displayed excellent functional group tolerance, resulting in the high yielding hydrogenation of bromide **5a**, ester **5j**, ether **5k** and even the nitro compound **5l**. Notably, α,β -unsaturated esters and alkynes remained fully intact. The chiral amide **1h** was reduced in 73% yield with full conservation of the stereochemical purity. N-phenyl substitution of the benzoic amide (**1f**) required the application of 2,6-lutidine as auxiliary Lewis base and the product **5f** was obtained in 61% yield. Furthermore, amines with small N-substituent (**5c**, **5d**) were accessible in high yields, which is so far unprecedented in FLP-catalyzed imine hydrogenation^{317,450-452}. Finally, we investigated the hydrogenation mechanism by kinetic and quantum mechanical experiments. The reaction profile of the catalytic hydrogenation of **2b** with 10 mol% **4e** in CDCl₃ (0.16M) and 4 bar H₂ displayed an induction period (cf. the online Supporting Information of the original publication). This increase of the reaction rate over the first three hours suggests the slow activation of H₂ by the FLP consisting of **4e** and **2b** (Compare figure 8.4, simple catalytic cycle). The imidoyl chloride salt [**2b-H**][**H-4e**] collapses to the corresponding iminium salt [**6b-H**][**Cl-4e**], which is hydrogenated by the Cl⁻/**4e** FLP to yield **5b**·HCl salt as uncompetitive Lewis base for H₂-activation. These last two steps can be considered as fast, since neither **6b** nor the intermediates [**2b-H**][**H-4e**] and [**6b-H**][**Cl-4e**] were detected by NMR spectroscopy. The preferred splitting of H₂ by Cl⁻/**4e** in contrast to **2b**/**4e** is supported by the difference of the pK_a of the conjugate

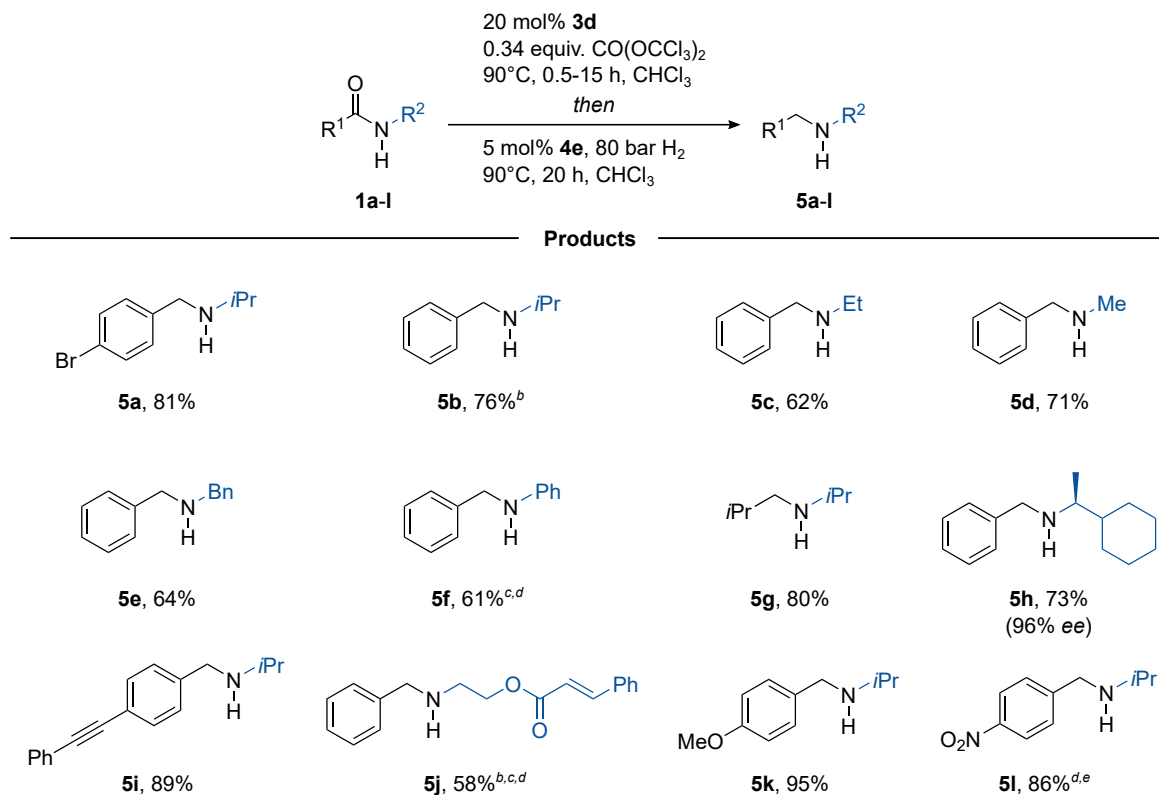
Table 8.2.: FLP-catalyzed hydrogenation of imidoyl chloride **2b**.



entry	cat. (mol%)	H ₂ / bar	time / h	yield / % ^b
1	4a (20)	4	90	traces
2	4b (20)	4	90	0
3	4c (20)	4	90	53
4	4d (20)	4	90	12
5	4e (20)	4	90	99
6	4e (5)	80	20	99

^aAccording to Gutmann-Beckett with B(C₆F₅)₃ referenced to 100% Lewis acidity⁴⁴⁵⁻⁴⁴⁹.

^bDetermined by ¹H NMR spectroscopy.



^aReactions were typically performed with 1 equiv. of **1** in CDCl_3 (0.83 M), 0.34 equiv. $\text{CO}(\text{OCCl}_3)_2$, 20 mol% **3d** at 90°C for 0.5-15 h, followed by the addition of 5 mol% **4e** in CHCl_3 giving a 0.17 M solution, H_2 (80 bar), 90°C for 20 h. ^b10 mol% **4e**. ^c1.0 equiv. 2,6-Lutidine added. ^dPerformed at 70°C . ^e40 h.

Figure 8.3.: Catalytic hydrogenation of secondary amides.

acids ($\text{pK}_a([\text{H}-\mathbf{2b}]^+) = 5$, $\text{pK}_a(\text{HCl}) = 10.3$)⁴³⁸ as a measure for the activation potency^{356,358,363}. A second, autoinduced, catalytic cycle is opened up with a lower barrier for the H_2 activation (*vide infra*) as a result of the slow increase of Cl^- . The autocatalysis is supported by the drastic rate increase when 20 mol% of the product **2b**-HCl is added at the beginning of the reaction (cf. the online Supporting Information of the original publication). In contrast to the FLP-catalyzed imine hydrogenation³⁵⁶, the imidoyl chloride hydrogenation displays saturation kinetic and follows zeroth-rate order after equal amounts of the product compared to the borane are generated (cf. the online Supporting Information of the original publication). This indicates that the chloride anion is reversibly bound to the borane, which is in concert with the observed broadening in the ^{11}B and ^{19}F NMR spectra (see the online Supporting Information of the original publication). Free energy calculations reveal that the heterolytic splitting of H_2 by the FLP **2b/4e** to the chloro iminium hydroborate $[\mathbf{2b}-\text{H}][\text{H}-\mathbf{4e}]$ is endergonic by 9.7 kcal mol^{-1} over a barrier of 25.5 kcal mol^{-1} (**TS4b**, simple catalytic cycle, figures 8.4 and 8.5). In contrast, the splitting of H_2 by $\text{Cl}^-/\mathbf{4e}$ (**TS6**) requires 0.7 kcal mol^{-1} less energy than **TS4b** rendering this step kinetically more favorable. The comparison of the H-H bond lengths in **TS4b** and **TS6** indicates an early transition state for the H_2 -activation for the $\text{Cl}^-/\mathbf{4e}$ FLP. In case of the simple catalytic cycle the formed chloride ions also increasingly form $\text{Cl}^-/\mathbf{4e}$ ($-2.5 \text{ kcal mol}^{-1}$) thus further disadvantaging

the H₂-splitting via TS4.

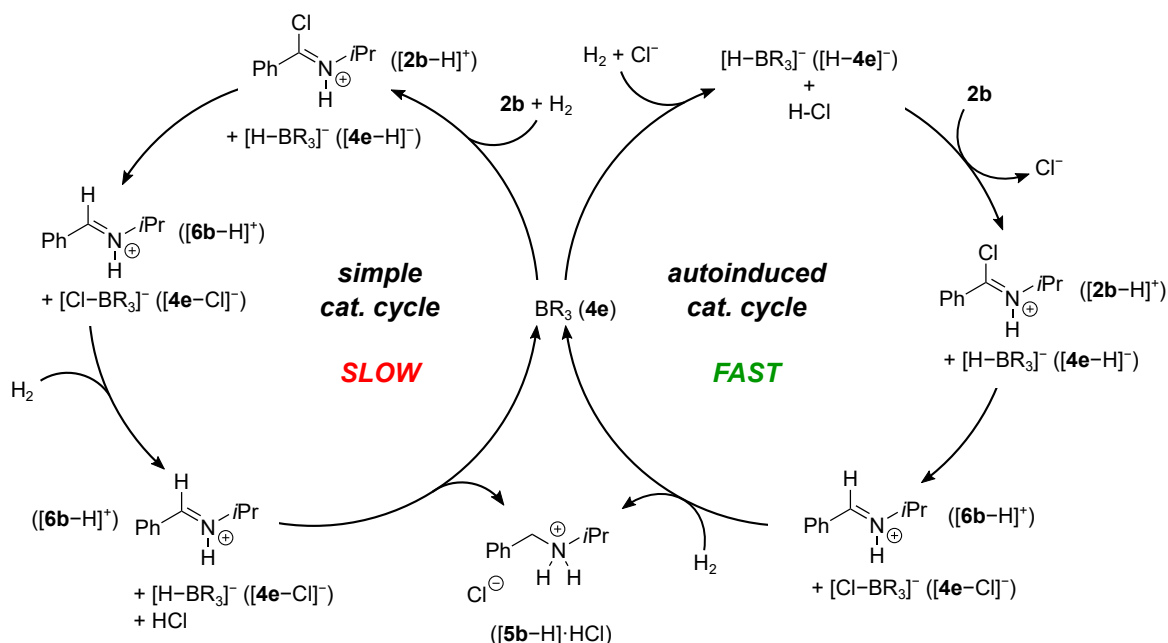


Figure 8.4.: Proposed simplified catalytic cycle of the FLP-catalyzed hydrogenation of imidoyl chlorides.

8.3. Conclusion

In summary, we developed the FLP-catalyzed hydrogenation of amides to yield secondary amines. The in situ formed imidoyl chloride intermediate was generated by the new developed phosphane oxide catalysis and triphosgene as oxygen scavenger. The final hydrogenation of the intermediate proceeds through two catalytic cycles as revealed by DFT-calculations, incorporating H₂-activation by the imidoyl chloride and by chloride as active Lewis base. The reaction displays high functional group tolerance towards Lewis basic sites and hydrogenation susceptible groups and provides the secondary amines in high yields under mild conditions.

Acknowledgements

The German Science Foundation (DFG) and the Fonds der Chemischen Industrie (FCI) is gratefully acknowledged for financial support to J.P. (PA 1562/18-1) and Kekulé-Stipendium to L.K. and N.A.S., and Gottfried Wilhelm Leibniz prize to S.G.

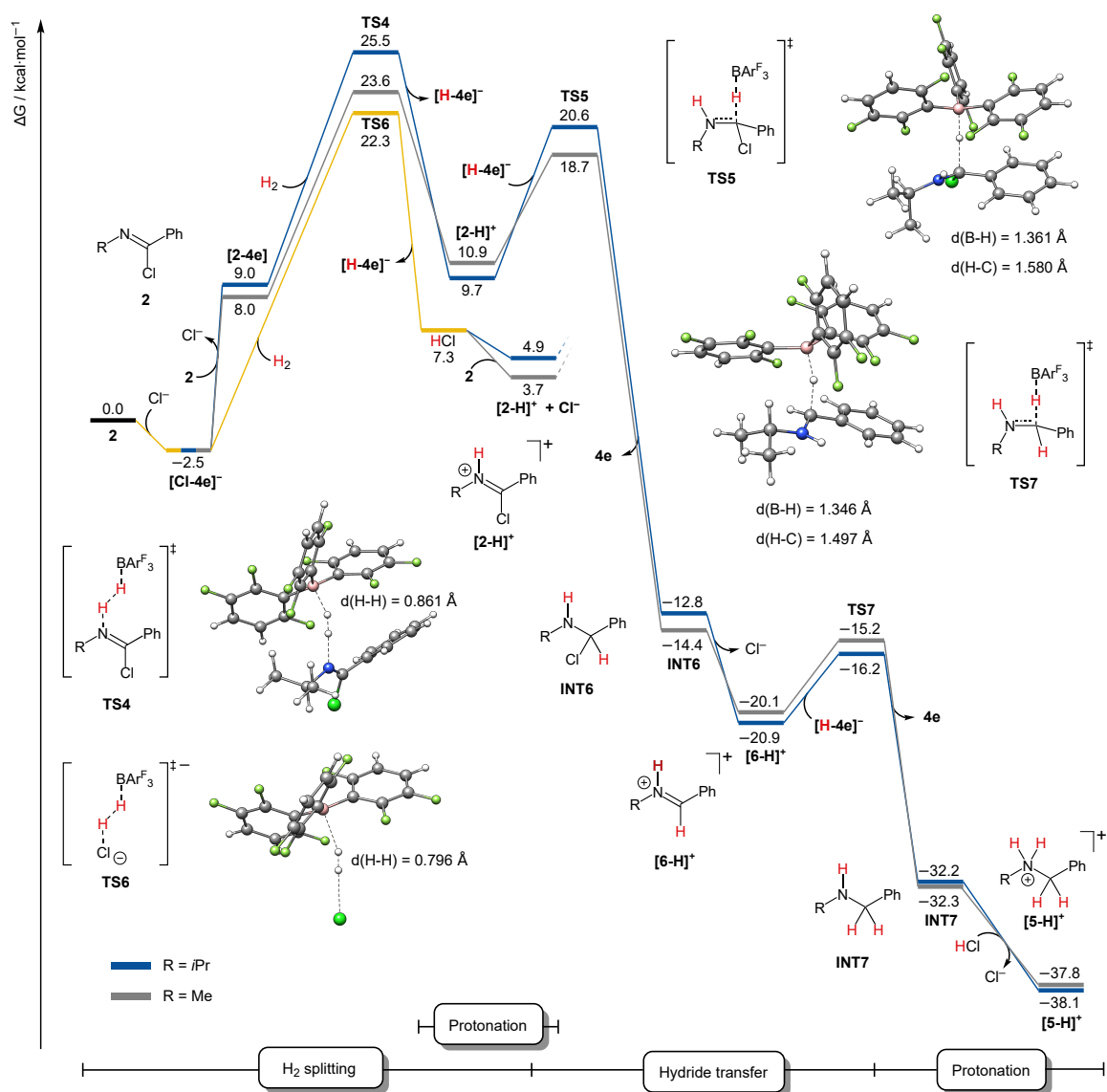


Figure 8.5.: Free energy diagrams of the H₂-activation by the FLPs **2b/4e** and Cl⁻/**4e** at the PW6B95-D4/def2-QZVP+COSMO-RS(CHCl₃)/PBEh-3c(COSMO(CHCl₃)) level of theory. All free energies in kcal mol⁻¹.

Part IV.

Quantum Chemical Studies on Inorganic Main Group Chemistry

IV. Quantum Chemical Studies on Inorganic Main Group Chemistry

Inorganic main group elements tend to have less predictable and thus much more diverse chemical and structural properties than their organic counterparts^{30,453–462}. This is partly due to an increasing electronic flexibility descending the periodic table by successively involving orbitals of higher angular momentum quantum numbers, such as d-type orbitals. Further, relativistic effects can have an increasing influence on the structure and the properties of heavy elements⁴⁶³. A prominent case of such an influence is the switch in the energetic ordering of the s- and p-type valence molecular orbitals descending group 14 from tin to lead. Here the 6s orbital is energetically lowered below the corresponding 6p orbitals by relativistic effects resulting in a 6s localized lone-pair that has significant influence on the chemical bonding in lead compounds. As many compounds involving inorganic main group elements tend to be highly reactive and are thus prone to unintended chemical conversion, kinetic hindering by introducing sterically demanding ligands is common practice. Besides increasing the controllability of the reactivity of the compounds, the introduction of large ligands can have other beneficial effects. For example, large ligands can cause an unprecedented stabilization of usually unstable compounds contradicting the expectation of increasing intramolecular repulsion with increasing size of the ligand. This is for example the case in formally multiply bonded heavy main group compounds, like in heavy alkyne and alkene homologues, where intramolecular non-covalent interactions between the ligands strongly influence the bonding energy. The most crucial attractive component of such non-covalent interaction may be London dispersion, which is increasingly being used as conceptual part of synthetic strategies in inorganic and organometallic chemistry³². As such interactions can play an decisive role regarding the structural features of such compounds, part IV is devoted to quantum chemical investigations of non-covalent interactions in inorganic main group compounds and their influence on structural features, thermochemistry, and spectroscopic properties. Thus chapter 9 deals with a key intermediate of halogenosilane chemistry, the trichlorosilanide anion, which is transformed into the corresponding triiodo compound in an attempt to trap the anion with the Lewis base BI₃. Chapter 10 discusses the role of London dispersion on the counterintuitive interligand angles of diaryltetraylenes, with chapter 11 extending the investigation to the bonding situation in diplumbynes, the heavy homologues of alkynes. In this context the influence of structural flexibility on spectroscopic properties is investigated. A key analytical method of inorganic molecular chemistry of group 14 compounds is nuclear magnetic resonance (NMR) spectroscopy. In particular ²⁹Si NMR spectroscopy yields invaluable insights into the chemical environment of specific Si atoms, which are typically representing the reactive region of the molecule⁴⁶⁴. Thus, the reliable computational prediction of ²⁹Si NMR chemical shifts is desirable and the performance of popular DFAs for the calculation of such is evaluated in chapter 12. The last chapter of part IV is devoted to a in depth energy decomposition study of non-covalent interactions in azide-pnictogen, chalcogen and halogen contacts applying cutting edge DFT and WFT methods.

9. Trapping Experiments on a Trichlorosilanide Anion: a Key Intermediate of Halogenosilane Chemistry

Julian Teichmann,^a Markus Bursch,^b Benedikt Köstler,^a Michael Bolte,^a Hans-Wolfram Lerner,^a Stefan Grimme,^b and Matthias Wagner^a

Received 24th of January 2017, Published online: 20 March 2017

Selected as ACS AuthorChoice article.

Reprinted (adapted) with permission[†] from

Teichmann, J.; Bursch, M.; Köstler, B.; Bolte, M.; Lerner, H.-W.; Grimme, S.; Wagner, M. *Inorg. Chem.* **2017**, *56*, 8683–8688.

– Copyright © 2017 American Chemical Society.

DOI [10.1021/acs.inorgchem.7b00216](https://doi.org/10.1021/acs.inorgchem.7b00216)

Own manuscript contribution

- Performing the calculations
- Interpretation of the results
- Writing the manuscript

^aInstitut für Anorganische Chemie, Goethe-Universität Frankfurt am Main, Max-von-Laue-Straße 7, 60438 Frankfurt am Main, Germany

^bMulliken Center for Theoretical Chemistry, Institut für Physikalische und Theoretische Chemie, Rheinische Friedrich-Wilhelms-Universität Bonn, Beringstraße 4, 53115 Bonn, Germany

[†]Permission requests to reuse material from this chapter should be directed to ACS Publications.

Abstract Treatment of Si_2Cl_6 with $[\text{Et}_4\text{N}][\text{BCl}_4]$ in CH_2Cl_2 furnished the known products of a chloride-induced disproportionation reaction of the disilane, such as SiCl_4 , $[\text{Si}(\text{SiCl}_3)_3]^-$, and $[\text{Si}_6\text{Cl}_{12}\cdot 2\text{Cl}]^{2-}$. No Si–B-bonded products were detectable. In contrast, the addition of Si_2Cl_6 to $[\text{Et}_4\text{N}][\text{BI}_3\text{Cl}]$ afforded the Si–B adduct $[\text{Et}_4\text{N}][\text{I}_3\text{SiBI}_3]$. Thus, a quantitative Cl/I exchange at the silicon atom accompanies the trihalogenosilanide formation. $[\text{Et}_4\text{N}][\text{I}_3\text{SiBI}_3]$ was also accessible from a mixture of Si_2I_6 , $[\text{Et}_4\text{N}]\text{I}$, and BI_3 . According to X-ray crystallography, the anion $[\text{I}_3\text{SiBI}_3]^-$ adopts a staggered conformation with an Si–B bond length of 1.977(6) Å. Quantum chemical calculations revealed a polar covalent Si–B bond with significant contributions from intramolecular $\text{I}\cdots\text{I}$ London dispersion interactions.

9.1. Introduction

Perchlorinated oligosilanes (PCSs) are valuable precursors for the deposition of silicon thin films. The PCS sample is either thermolyzed directly to give elemental silicon in a disproportionation reaction⁴⁶⁵ or converted to the corresponding perhydrogenated oligosilanes prior to thermolysis^{466,467}. Apart from these industrial applications, PCSs are also attractive in their own right because they exhibit rich molecular chemistry, which often proceeds via intriguing intermediates to finally furnish products with sophisticated structural frameworks. The underlying mechanistic pathways are characterized by the tendency of covalent Si–Si bonds to undergo rearrangement reactions, a dynamic behavior that can be triggered deliberately by the addition of Lewis bases. As one of the first examples, Urry and co-workers reported that hexachlorodisilane (Si_2Cl_6) undergoes quantitative transformation to perchlorinated neopentasilane $\text{Si}(\text{SiCl}_3)_4$ and SiCl_4 upon the catalytic action of various trialkylamines (R_3N)^{468–473}. Recent experimental and quantum chemical studies have shown that dichlorosilylene adducts $\text{R}_3\text{N–SiCl}_2$ play a decisive role in the course of this reaction^{474–477}. Certain diarylmethanones can also liberate dichlorosilylenes from Si_2Cl_6 , albeit only at elevated temperatures. Under these conditions, the resulting ketone– SiCl_2 adducts ultimately lead to the reductive coupling of carbonyl compounds to afford tetraarylethylenes (sila-McMurry reaction)⁴⁷⁸. Reduction reactions have also successfully been performed on organic nitro compounds, phosphane oxides, and sulfoxides by means of Si_2Cl_6 or $\text{HSiCl}_3/\text{R}_3\text{N}$ ^{380,479–484}. In most cases, donor-stabilized SiCl_2 has been proposed as the key intermediate. One of the simplest Lewis bases that can be employed for the disproportionation of Si_2Cl_6 is the chloride ion. Depending on the reaction temperatures and the molar ratios of the starting materials, treatment of the disilane with soluble chloride salts $[\text{R}_4\text{N}]\text{Cl}$ in CH_2Cl_2 leads either to open-chain oligosilane-chloride adducts, such as $[\text{Si}_3\text{Cl}_9]^-$ and the branched $[\text{Si}_6\text{Cl}_{15}]^-$, or to chloride-complexed cyclohexasilanes, such as $[\text{Si}_6\text{Cl}_{12}\cdot 2\text{Cl}]^{2-}$ (Figure 9.1)⁴⁸⁵.^a The propensity of the underlying PCSs to coordinate additional chloride ions not only testifies to the high Lewis acidity of these species but also facilitates their isolation and crystallographic characterization. In the case of the cyclohexasilane diadduct, the two chloride ions can be conveniently abstracted using AlCl_3 , which opens up a facile route for preparing $\text{Si}_6\text{Cl}_{12}$ on a larger scale⁴⁸⁹. In addition to chainlike and cyclic PCSs, monodisperse silicon cluster compounds are also readily accessible: Our group has recently prepared the first Si_{20} dodecahe-

^aThe $[\text{Si}_6\text{Cl}_{12}\cdot 2\text{Cl}]^{2-}$ ion has previously been prepared by amine-promoted disproportionation of HSiCl_3 , and the electronic structure of this diadduct has been investigated by quantum chemical calculations, see refs. 486–488.

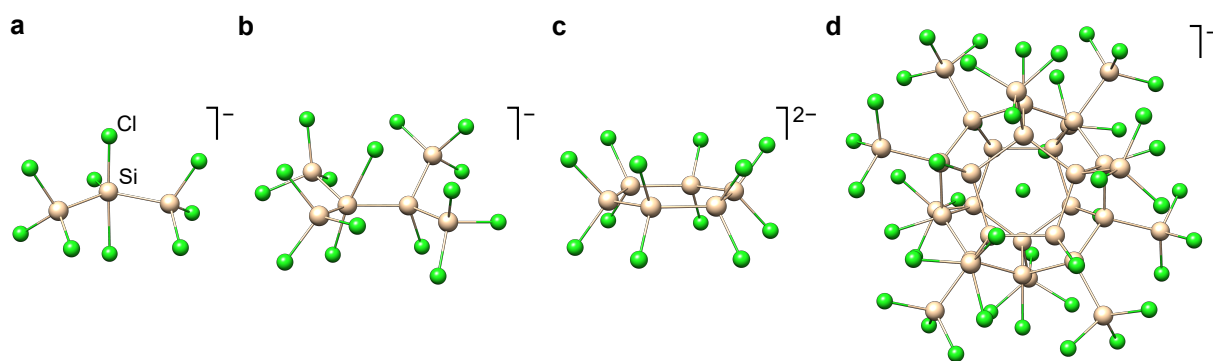


Figure 9.1.: X-ray crystallographically determined molecular structures of the anions a) $[\text{Si}_3\text{Cl}_9]^-$, b) $[\text{Si}_6\text{Cl}_{15}]^-$, c) $[\text{Si}_6\text{Cl}_{12} \cdot 2 \text{Cl}]^{2-}$, and d) $[\text{Si}_{32}\text{Cl}_{45}]^-$.

drane (“silafullerane“) from Si_2Cl_6 , $[\text{nBu}_4\text{N}]\text{Cl}$, and nBu_3N through a one-step self-assembly protocol in 27% yield (Figure 9.1)⁴⁹⁰. Each silafullerane cage hosts an endohedral chloride ion and thereby acquires a negative charge. Moreover, the clusters are decorated regioselectively with 12 SiCl_3 substituents, which may serve as anchor groups to link individual silafulleranes together. A quantum chemical assessment of the chloride-induced disproportionation of Si_2Cl_6 indicates an initial nucleophilic attack of the chloride ion on one of the silicon atoms with subsequent heterolytic cleavage of the Si–Si bond and formation of SiCl_4 and an $[\text{SiCl}_3]^-$ anion^{485–488}. $[\text{SiCl}_3]^-$ ions have previously been proposed as key intermediates of the so-called “Benkeser reactions“, which employ a $\text{HSiCl}_3/\text{R}_3\text{N}$ combination to introduce SiCl_3 groups into various different substrates via a nucleophilic pathway^{491–499}. In view of these mechanistic models, $[\text{SiCl}_3]^-$ represents an important link between the chemistries of Si_2Cl_6 , on the one hand, and HSiCl_3 , on the other hand. A second link relates $[\text{SiCl}_3]^-$ to SiCl_2 chemistry because the ion can be viewed as a chloride-stabilized dichlorosilylene. However, only a small amount of experimental data have been gathered on $[\text{SiCl}_3]^-$ to date, despite its importance for preparative (organo)silicon chemistry and its formal analogy to the well-known $[\text{CX}_3]^-$ ions ($\text{X} = \text{Cl}, \text{Br}, \text{I}$; compare the Appel⁵⁰⁰, Corey-Fuchs⁵⁰¹, and haloform⁵⁰² reactions). Collision-induced dissociation experiments carried out in a mass spectrometer on mixtures of $\text{Si}(\text{SiCl}_3)_4$ and $[\text{Et}_4\text{N}]\text{Cl}$ in CH_2Cl_2 produced a peak at m/z 134.9, which is assignable to $[\text{SiCl}_3]^-$ and thus indicates that this ion can indeed be generated in the gas phase⁵⁰³. Moreover, the above-mentioned species $[\text{Si}_3\text{Cl}_9]^-$ can be viewed not only as a chloride adduct of the trisilane Si_3Cl_8 but also as the trapping product of $[\text{SiCl}_3]^-$ by 1 equiv. of the starting material Si_2Cl_6 . This latter result encouraged us to try to trap $[\text{SiCl}_3]^-$ also with other Lewis acids and thereby to prove its intermediate appearance. In order to be able to unequivocally distinguish between the trapping reagent and a coordinating $[\text{SiCl}_3]^-$ ion, the Lewis acid needs to be silicon-free, which led to our choice of boron trihalides. Herein, we report on the reactions of Si_2X_6 with $[\text{R}_4\text{N}]\text{X}$ in the presence of BX_3 ($\text{X} = \text{Cl}, \text{I}$) and on the characterization of the unique Si–B adduct $[\text{I}_3\text{SiBI}_3]^-$ by means of X-ray crystallography. The electronic structure of the anion was elucidated by quantum chemical calculations.

lography and energy-dispersive X-ray (EDX) spectroscopy. As a downside of this approach, two types of halogen atoms are now present in the sample such that various mixed-halogen species are likely to be formed. Indeed, an ^{11}B NMR spectroscopic investigation of the sample revealed the presence of all five possible tetrahalogenoborate anions $[\text{BCl}_n\text{I}_{4-n}]^-$ ($n = 0-4$), and the corresponding ^{29}Si NMR spectrum contained the signals of SiCl_4 and SiCl_3I (see the online Supporting Information of the original publication for more details). The NMR tube was stored at room temperature in the dark in order to avoid photolysis of iodoborane species. After 24 h, single crystals had grown on top of an amorphous precipitate, which were identified as $[\text{Et}_4\text{N}][\text{I}_3\text{SiBI}_3]$ by means of X-ray crystallography (Figure 9.3). Compound $[\text{Et}_4\text{N}][\text{I}_3\text{SiBI}_3]$ represents the desired borane adduct of an $[\text{SiX}_3]^-$ ion; however, all originally silicon-bonded chloro substituents have been replaced by iodine atoms. Improved yields of the adduct should thus be achievable by employing Si_2Cl_6 and BI_3 in a 1:2 ratio rather than a 1:1 ratio. A corresponding synthesis was subsequently carried out on a preparative scale and furnished crystals of $[\text{Et}_4\text{N}][\text{I}_3\text{SiBI}_3]$ in 44 % yield (Figure 9.2b). With the aim of minimizing the number of byproducts from

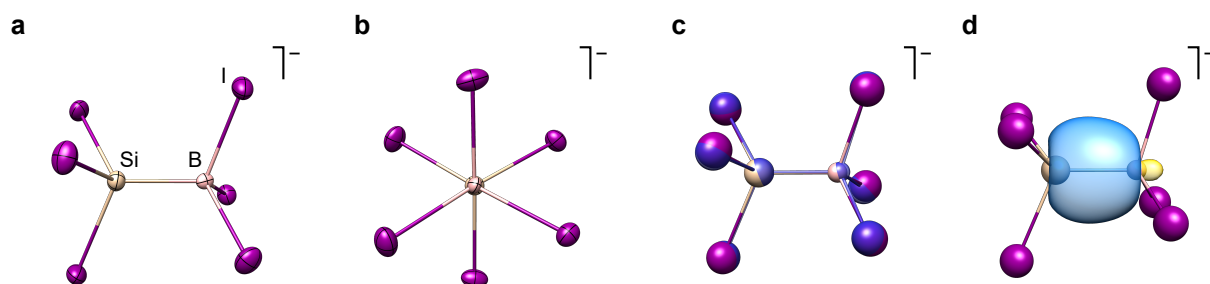


Figure 9.3.: Solid-state structure of $[\text{Et}_4\text{N}][\text{I}_3\text{SiBI}_3]$ (cation omitted for clarity; thermal ellipsoids at 50 % probability; Si, gold; B, pink; I, purple): a) side view of the anion and b) projection along the Si–B axis. Selected bond lengths in Å and bond angles in $^\circ$: Si–B = 1.977(6), Si–I = 2.457(2) / 2.454(2) / 2.451(2), B–I = 2.261(6) / 2.249(6) / 2.246(6); Si–B–I = 108.5(3) / 110.8(3) / 109.4(3), B–Si–I = 112.9(2) / 112.2(2) / 112.3(2), I–B–I = 108.9(2) / 108.9(3) / 110.2(3), I–Si–I = 106.8(1) / 106.3(1) / 105.9(1). c) Overlay of the X-ray (color code) and the PBE0-D3(BJ)/def2-QZVP optimized (blue) structure of $[\text{I}_3\text{SiBI}_3]^-$. d) Foster-Boys localized molecular orbital representing the Si–B σ -bond. Isosurface value = $e^{-1/2} \cdot \text{bohr}^{-3/2}$.

which $[\text{Et}_4\text{N}][\text{I}_3\text{SiBI}_3]$ has to be separated, we finally conducted the synthesis starting from Si_2I_6 ⁵⁰⁶, $[\text{Et}_4\text{N}]\text{I}$, and BI_3 in a stoichiometric ratio of 1:1:1 (Figure 9.2c). Single crystals of $[\text{Et}_4\text{N}][\text{I}_3\text{SiBI}_3]$ grew upon storage of the mixture in the dark at room temperature for 10 days. The comparatively long reaction time is likely due to the poor solubilities of Si_2I_6 and $[\text{Et}_4\text{N}]\text{I}$ in CH_2Cl_2 . An ^{11}B NMR spectrum recorded on the mother liquor revealed almost exclusively the resonance of the $[\text{BI}_4]^-$ ion (cf. the online Supporting Information of the original publication for a plot of the spectrum).^b Consequently, this sample of the Si–B adduct was used for elemental analysis and EDX spectroscopy. In contrast to $[\text{Et}_4\text{N}][\text{BI}_4]$, the target compound $[\text{Et}_4\text{N}][\text{I}_3\text{SiBI}_3]$ is only sparingly soluble in CH_2Cl_2 as well as all other common inert solvents. We, nevertheless, noticed a loss of crystalline material during extensive washing. In parallel, a resonance at $\delta = -32.4$ ppm, which we assign to an unknown decomposition

^bThe resonance of the minor component $[\text{BI}_3\text{Cl}]^-$ was also present in the ^{11}B NMR spectrum, arising from a side reaction of BI_3 and the solvent CH_2Cl_2 .

product, became increasingly apparent in the ^{11}B NMR spectrum of the washing solution. The yield of the single-crystalline $[\text{Et}_4\text{N}][\text{I}_3\text{SiBI}_3]$ left over after repeated rinsing with CH_2Cl_2 amounted to 31 %.

Characterization of $[\text{Et}_4\text{N}][\text{I}_3\text{SiBI}_3]$

The generally poor solubility of the adduct $[\text{Et}_4\text{N}][\text{I}_3\text{SiBI}_3]$ precluded its characterization by solution-phase NMR spectroscopy. Solid-state magic-angle-spinning NMR spectroscopy also did not provide interpretable data, likely because the ^{29}Si NMR resonance is severely broadened due to coupling with the ^{10}B and ^{11}B nuclei ($S = 3$ and $3/2$, respectively). The quadrupolar nature of the boron nuclei leads to a further broadening of the ^{29}Si NMR signal and also affects the resolution of the ^{11}B NMR resonance. The experimental characterization of $[\text{Et}_4\text{N}][\text{I}_3\text{SiBI}_3]$ will therefore be based on elemental analysis, EDX spectroscopy, and X-ray crystallography. Elemental analysis of $[\text{Et}_4\text{N}][\text{I}_3\text{SiBI}_3]$ gave satisfactory values for hydrogen [2.32 % (requires: 2.17 %)], carbon [11.05 % (10.33 %)], nitrogen [1.60 % (1.51 %)], iodine [79.7 % (81.8 %)], and silicon [3.51 % (3.02 %)]. According to EDX analysis, the crystals contained silicon and iodine in a ratio of Si:I = 1:5.7 (± 0.04). We note that the experimentally determined carbon/hydrogen/nitrogen content is slightly too high, while the iodine content is somewhat too low. A contamination of the sample with a small amount of $[\text{Et}_4\text{N}][\text{BI}_4]$ could well account for these deviations, however, the corresponding ^{11}B resonance should be detectable by NMR spectroscopy, which is not the case. Moreover, our EDX measurements do not support the presence of excess iodine (with respect to silicon). As an alternative explanation, we propose that the sample contains a few chloro substituents in place of the iodo substituents: In addition to the signals assignable to silicon and iodine atoms, the EDX measurements indeed showed a small signal indicating the presence of chlorine atoms (cf. the online Supporting Information of the original publication for a plot of the spectrum). As a conceivable chlorine source, we identified the solvent CH_2Cl_2 , which undergoes some halogen exchange with BI_3 to furnish small amounts of CH_2ICl and BCl_2 (cf. the online Supporting Information of the original publication). The ultimate proof of the composition of $[\text{Et}_4\text{N}][\text{I}_3\text{SiBI}_3]$ was provided by X-ray crystallography (Figure 9.3 and table 9.1). The crystal lattice of the compound contains $[\text{Et}_4\text{N}]^+$ cations

Table 9.1.: Comparison of experimentally determined bond lengths and bond angles of $[\text{Et}_4\text{N}][\text{I}_3\text{SiBI}_3]$ with the corresponding calculated values.^a

	$[\text{Et}_4\text{N}][\text{I}_3\text{SiBI}_3]$	calcd. $[\text{I}_3\text{SiBI}_3]^-$ ^b	$[\text{Et}_3\text{Si}(\text{H})\text{BFlu}]^-$ ^c	Cy_3PBI_3 ^d	I_3SiSiI_3
$d(\text{Si}-\text{B}) / \text{\AA}$	1.977(6)	2.011	2.018(2)		
$d(\text{Si}-\text{I})_{\text{mean}} / \text{\AA}$	2.454	2.474			2.425(1)
$d(\text{B}-\text{I})_{\text{mean}} / \text{\AA}$	2.252	2.228		2.241	
$\Sigma \angle(\text{I}-\text{Si}-\text{I}) / ^\circ$	319.0	316.8			333.3
$\Sigma \angle(\text{I}-\text{B}-\text{I}) / ^\circ$	328.0	335.2		326.7	

^aKey geometric parameters of three selected literature-known compounds are included for comparison.

^bCalculated bond lengths obtained at the PBE0-D3(BJ)/def2-QZVP level of theory.

^c $[\text{Et}_3\text{Si}(\text{H})\text{BFlu}]^-$ = adduct between $[\text{SiEt}_3]^-$ and 9H-9-borafluorene.

^d Cy_3P = tricyclohexylphosphane⁵⁰⁷⁻⁵⁰⁹.

and $[\text{I}_3\text{SiBI}_3]^-$ anions in a 1:1 ratio. The anion can be interpreted as the adduct between $[\text{SiI}_3]^-$ and BI_3 with an Si–B bond length of 1.977(6) Å (cf. Si–B = 2.018(2) Å in the adduct between $[\text{SiEt}_3]^-$ and 9H-9-borafluorene⁵⁰⁷). As a prominent structural feature, $[\text{I}_3\text{SiBI}_3]^-$ adopts an almost perfectly staggered conformation with the absolute values of the smaller I–Si–B–I torsion angles ranging from 56.8(3)° to 63.0(3)°. The average Si–I bond length amounts to 2.454 Å and thus lies close to that of Si_2I_6 (2.425(1) Å; Table 9.1). The average B–I bond length also possesses almost the same value as that in the comparable P–B adduct Cy_3PBI_3 (2.252 vs. 2.241 Å; Cy = cyclohexyl). Both the silicon and boron centers are fully pyramidalized, which points toward a strong covalent Si–B bond.

9.3. Quantum Chemical Calculations

In order to obtain more information about the electronic structure of the $[\text{I}_3\text{SiBI}_3]^-$ anion, quantum-chemical calculations were performed to answer the following questions: (i) Is the molecule mainly bound by a covalent Si–B bond or do intramolecular dispersion interactions between the six iodo substituents also play an important role? (ii) What is the driving force behind the observed Cl/I exchange reaction on the silicon center? The computational studies were carried out using density functional theory. Geometry optimizations were conducted using the D3(BJ) dispersion corrected^{31,59,121} PBE0²¹³ hybrid functional in conjunction with the def2-QZVP²⁴⁰ basis set. Final gas-phase single-point energies were obtained at the B2PLYP-D3(BJ)¹¹⁰/def2-QZVP//PBE0-D3(BJ)/def2-QZVP level of theory. Gibbs

Table 9.2.: Dissociation free energies and its components for $[\text{I}_3\text{SiBI}_3]^-$ in kcal mol⁻¹ at the B2PLYP- and B3LYP-D3(BJ)/def2-QZVP+COSMO-RS(CH_2Cl_2)/PBE0-D3(BJ)/def2-QZVP levels of theory.

	B2PLYP				
	ΔG_{diss}^a	ΔE^b	ΔG_{RRHO}^c	$\Delta\delta G_{\text{solv}}^d$	ΔE_{D3}^e
$[\text{I}_3\text{SiBI}_3]^-$	24.3	35.9	-16.5	-4.2	9.1
$[\text{Cl}_3\text{SiBI}_3]^-$	34.3	52.0	-16.0	-8.3	6.7
$[\text{I}_3\text{SiBCl}_3]^-$	13.3	23.0	-14.9	-0.6	5.7
$[\text{Cl}_3\text{SiBCl}_3]^-$	23.2	37.8	-14.8	-4.3	4.4
	B3LYP				
	ΔG_{diss}	ΔE	ΔG_{RRHO}	$\Delta\delta G_{\text{solv}}$	ΔE_{D3}
$[\text{I}_3\text{SiBI}_3]^-$	26.2	30.8	-16.5	-4.2	16.0
$[\text{Cl}_3\text{SiBI}_3]^-$	34.3	46.5	-16.0	-8.3	12.2
$[\text{I}_3\text{SiBCl}_3]^-$	15.1	20.2	-14.9	-0.6	10.6
$[\text{Cl}_3\text{SiBCl}_3]^-$	23.7	34.4	-14.8	-4.3	8.3

^a ΔG_{diss} = dissociation free energy.

^b ΔE_{E} = electronic gas-phase energy difference.

^c ΔG_{RRHO} = ro-vibrational energy correction difference.

^d $\Delta\delta G_{\text{solv}}$ = solvation free energy correction difference.

^e ΔE_{D3} = D3 dispersion correction.

9. Trapping Experiments on a Trichlorosilanide Anion: a Key Intermediate of Halogenosilane Chemistry

free energies were obtained by summing the dispersion corrected electronic energies, ro-vibrational corrections from a modified harmonic oscillator statistical treatment based on harmonic frequencies⁵¹⁰, and solvation corrections computed by means of the COSMO-RS^{371,372} model (2014 parametrization for dichloromethane). All calculations were conducted with the TURBOMOLE 7.0.2 program package^{206,207} and COSMOTHERM, version C3.0, release 16.01³⁷⁵. For further computational details, see appendix A8. The solid-state structure of the $[I_3SiBI_3]^-$ anion in a staggered conformation was reproduced in good accordance in the gas phase at the PBE0-D3(BJ)/def2-QZVP level of theory (Figure 9.3, table 9.1). The strongly pyramidalized boron atom indicates a covalent B–Si bond. This assumption is supported by analysis of the Foster-Boys⁵¹¹ localized molecular orbitals (LMOs) obtained at the PBE0/def2-QZVP(-g) level of theory. The LMO representing the Si–B bond is predominantly of the σ type with a major local-

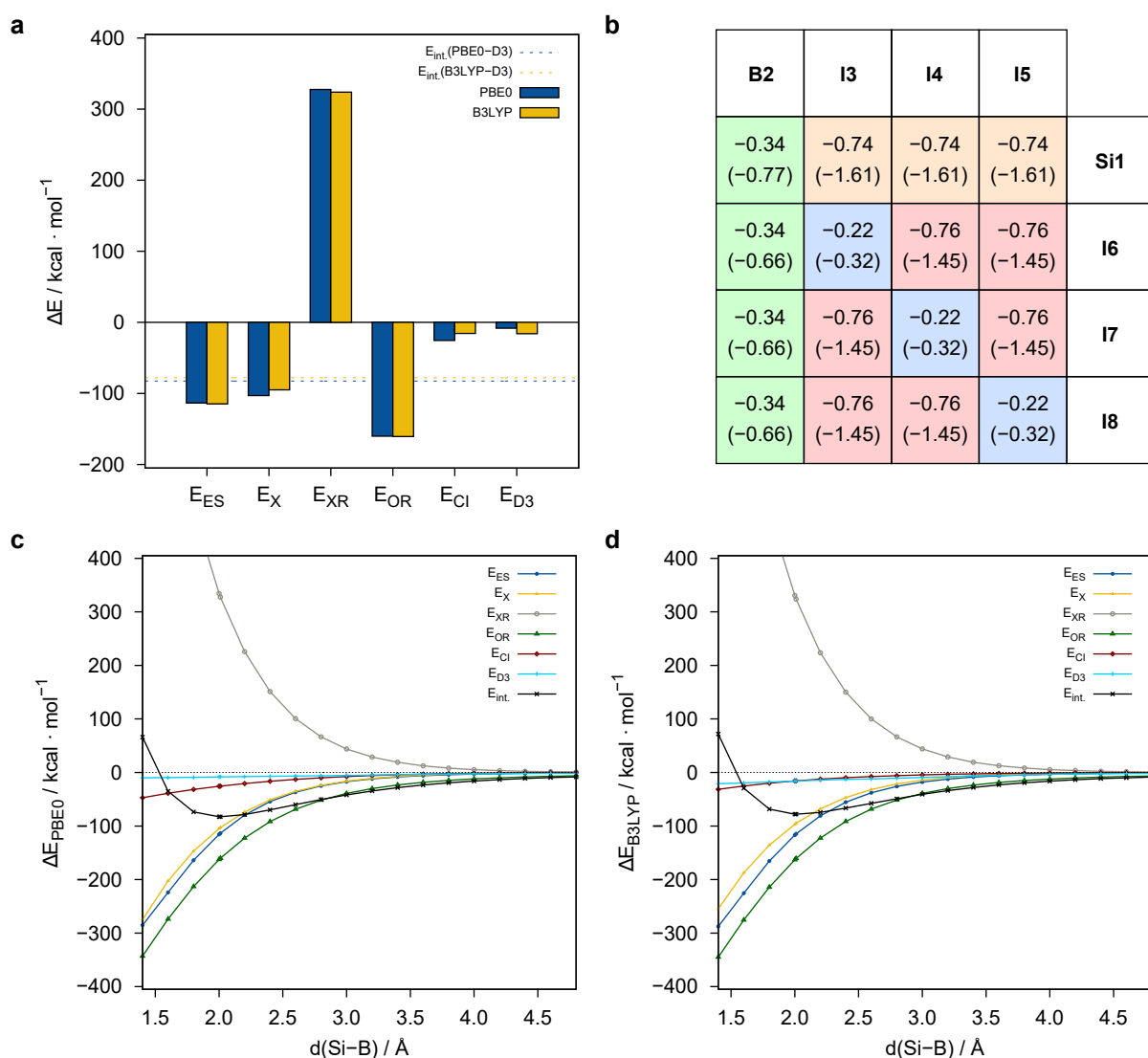


Figure 9.4.: a) EDA of $[I_3Si-BI_3]^-$; b) Interfragment pair-wise D3(BJ) dispersion correction matrix for PBE0 (B3LYP results in parentheses); Unrelaxed potential energy surface scan and EDA along the Si–B bond for c) PBE0 and d) B3LYP. All calculations apply the def2-QZVPD basis set.

ization at the silicon center (populations: Si, 0.748; B, 0.335). The atomic orbitals involved in the Si–B bond are mainly of s character at the silicon center (s, 75.0 %; p, 23.8 %) and mainly of p character for the boron atom (s, 40.2 %; p, 61.3 %), which matches the expectation of an s-type lone pair at the $[\text{SiI}_3]^-$ fragment, forming a strong bond with the vacant p_z orbital of the Lewis acid BI_3 . The calculated dissociation free energy of $\Delta G_{\text{diss}} = 24.3 \text{ kcal mol}^{-1}$ for $[\text{I}_3\text{SiBI}_3]^-$ at the B2PLYP-D3(BJ)/def2-QZVP+COSMORS(CH_2Cl_2)/PBE0-D3(BJ)/def2-QZVP level of theory further indicates a relatively strong Si–B bond. Analysis of the relative energy contributions to the dissociation free energy (Table 9.2) indicates that dispersion interactions ($\Delta E_{\text{D3, B2PLYP}} = 9.1 \text{ kcal mol}^{-1}$, $\Delta E_{\text{D3, B3PLYP}} = 16.0 \text{ kcal mol}^{-1}$) contribute significantly to stabilization of the $[\text{SiI}_3]^-$ and BI_3 fragments upon bond formation. Especially for the B3LYP functional, which is known to almost not account for any dispersion effects indirectly by its parametrization, the dispersion contribution represents 61% of the dissociation free energy. Due to the repulsive nature of B3LYP, the D3 dispersion contribution can be used as reasonable dispersion energy estimate. In $[\text{I}_3\text{SiBI}_3]^-$ the major contributions to the total intramolecular dispersion interaction between the BI_3 and the SiI_3^- originates from the interaction between the respective iodine atoms (Figure 9.4b). A Morokuma type energy decomposition analysis (EDA)⁵¹² as function of the Si–B distance in an unrelaxed scan supports the picture of a polar bond dominated by orbital relaxation effects with significant dispersion contribution (Figure 9.4c, d). Because the full mechanism of the formation of $[\text{I}_3\text{SiBI}_3]^-$ has yet to be elucidated, we investigated the reaction free energies for a stepwise halide exchange between the $[\text{SiX}_3]^-$ and BX_3 fragments (Figure 9.5). This consideration indicates that the Cl^-/I^- exchange starting from $[\text{SiCl}_3]^-$ with BI_3 is overall strongly exergonic ($\Delta G = -18.2 \text{ kcal mol}^{-1}$). Each exchange step is exergonic itself until a complete halide exchange between the silicon and boron fragments has taken place. We conclude that the strongly exergonic exchange reactions represent the driving force of the $[\text{I}_3\text{SiBI}_3]^-$ formation. The reaction free energy is dominated by the enthalpic component.

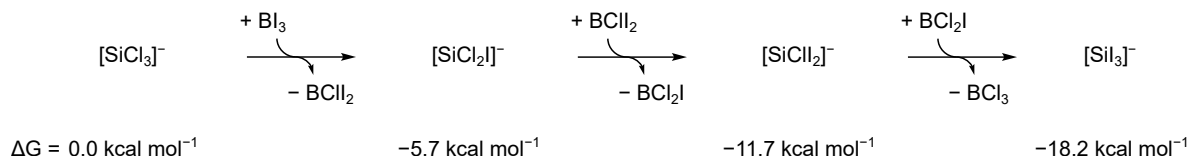


Figure 9.5.: Calculated relative Gibbs free energies of the species involved in progressive halide exchange between $[\text{SiCl}_3]^-$ and BI_3 at the B2PLYP-D3(BJ)/def2-QZVP+COSMORS(CH_3C_3)/PBE0-D3(BJ)/def2-QZVP level of theory. All free energies in kcal mol^{-1} are given relative to the corresponding starting compound $[\text{SiCl}_3]^-$ in the context of the given model reaction.

9.4. Conclusion

It has been postulated that the deprotonation of HSiCl_3 with amine bases as well as the chloride-induced disproportionation of Si_2Cl_6 result in the formation of $[\text{SiCl}_3]^-$ ions as the primary intermediates. However, to date, only a small amount of experimental evidence exists to support this suggestion. We have now shown that the treatment of Si_2Cl_6 with $[\text{Et}_4\text{N}]\text{Cl}$ in the presence of BI_3 leads to the single-crystalline adduct $[\text{Et}_4\text{N}][\text{I}_3\text{SiBI}_3]$. The isolation of $[\text{Et}_4\text{N}][\text{I}_3\text{SiBI}_3]$ not only represents the first suc-

9. Trapping Experiments on a Trichlorosilanide Anion: a Key Intermediate of Halogenosilane Chemistry

successful trapping of a trihalogenosilanide with a boron Lewis acid but also reveals a quantitative Cl/I exchange reaction at the silicon center under the conditions applied. The same product was obtained from a mixture of Si_2I_6 , $[\text{Et}_4\text{N}]\text{I}$, and BI_3 . The Si–B bond length amounts to 1.977(6) Å (calculated value: 2.011 Å); the SiI_3 and BI_3 fragments are pronouncedly pyramidalized. These experimental observations, together with quantum chemical calculations, point toward a strong, yet highly polarized covalent bond. The atomic orbitals involved in bonding possess mainly s character at the silicon center and p character at the boron center. In addition to the direct Si–B dative bond, intramolecular dispersion interactions between the six iodo substituents contribute significantly to the stability of the $[\text{I}_3\text{SiBI}_3]^-$ anion ($\Delta G_{\text{diss, B2PLYP}} = 24.3 \text{ kcal mol}^{-1}$, $\Delta G_{\text{diss, B3LYP}} = 26.2 \text{ kcal mol}^{-1}$; $\Delta E_{\text{D3, B2PLYP}} = 9.1 \text{ kcal mol}^{-1}$, $\Delta E_{\text{D3, B3LYP}} = 16.0 \text{ kcal mol}^{-1}$).

Acknowledgements

The authors are grateful to Prof. Dr. A. Terfort and Thalia Vavaleskou for recording the EDX spectra. They also thank Prof. Dr. J. Schmedt auf der Günne and Wenyu Li for solid-state NMR measurements. This work was supported by the DFG through the priority program “Control of London dispersion interactions in molecular chemistry” (SPP 1807).

10. Counterintuitive Interligand Angles in the Diaryls $E\{C_6H_3-2,6-(C_6H_2-2,4,6-iPr_3)_2\}_2$ (E = Ge, Sn, or Pb) and Related Species: The Role of London Dispersion Forces

Madison L. McCrea-Hendrick,^a Markus Bursch,^b Kelly L. Gullett,^a Leonard R. Maurer,^b James C. Fettinger,^a Stefan Grimme,^b and Philip P. Power^a

Received: 16 April 2018, Published online: 22 June 2018

Reprinted (adapted) with permission[†] from

McCrea-Hendrick, M. L.; Bursch, M.; Gullett, K. L.; Maurer, L. R.; Fettinger, J. C.; Grimme, S.; Power, P. P. *Organometallics* **2018**, *37*, 2075–2085.

– Copyright © 2018 American Chemical Society.

DOI [10.1021/acs.organomet.8b00225](https://doi.org/10.1021/acs.organomet.8b00225)

Own manuscript contribution

- Performing all molecular DFT calculations
- Interpretation of the computational results
- Co-writing the manuscript

^aDepartment of Chemistry, University of California-Davis, 1 Shields Avenue, Davis, California 95616, USA

^bMulliken Center for Theoretical Chemistry, Institut für Physikalische und Theoretische Chemie, Rheinische Friedrich-Wilhelms-Universität Bonn, Beringstraße 4, 53115 Bonn, Germany

[†]Permission requests to reuse material from this chapter should be directed to the American Chemical Society.

Abstract The straightforward reaction of two equivalents of the lithium salt of the bulky terphenyl ligand $\text{Li}(\text{OEt}_2)\text{C}_6\text{H}_3\text{-2,6-(C}_6\text{H}_2\text{-2,4,6-}i\text{Pr}_3)_2$ with suspensions of $\text{GeCl}_2\cdot\text{dioxane}$, SnCl_2 , or PbBr_2 in diethyl ether resulted in the isolation of the very crowded σ -bonded diaryl tetrylenes of formula $\text{E}\{\text{C}_6\text{H}_3\text{-2,6-(C}_6\text{H}_2\text{-2,4,6-}i\text{Pr}_3)_2\}_2$ ($\text{E} = \text{Ge}$ (**1**), Sn (**2**), Pb (**3**)) as blue crystalline solids. Despite their high level of steric congestion, X-ray crystallography showed that compounds **1–3** possess $\text{C}_{\text{ipso}}\text{-E-C}_{\text{ipso}}$ interligand bond angles in the range $107.61\text{--}112.55^\circ$, which are narrower than those observed in analogous species with less bulky terphenyl substituents. Compounds **1–3** were characterized by ^1H , $^{13}\text{C}\{^1\text{H}\}$ (**1–3**), and $^{119}\text{Sn}\{^1\text{H}\}$ (**2**) NMR spectroscopy, whereas solution $^{207}\text{Pb}\{^1\text{H}\}$ NMR spectroscopy of **3** has not yet afforded a signal under ambient conditions. FT-IR and UV/VIS spectra of **1–3** were also recorded. The relatively narrow interligand angles displayed by **1–3** are attributed in part to the increase in attractive London dispersion interactions between the two Ar^{iPr_6} ($\text{Ar}^{i\text{Pr}_6} = \text{-C}_6\text{H}_3\text{-2,6-(C}_6\text{H}_2\text{-2,4,6-}i\text{Pr}_3)_2$) groups from carbon atoms in some of the isopropyl substituents and several carbon atoms from the flanking aryl rings. Density functional theory (DFT) calculations carried out on the full series of diaryl tetrylenes, $\text{E}(\text{Ar}^{i\text{Pr}_6})_2$, $\text{E}(\text{Ar}^{i\text{Pr}_4})_2$ ($\text{Ar}^{i\text{Pr}_4} = \text{-C}_6\text{H}_3\text{-2,6-(C}_6\text{H}_3\text{-2,6-}i\text{Pr}_2)_2$), and $\text{E}(\text{Ar}^{\text{Me}_6})_2$ ($\text{Ar}^{\text{Me}_6} = \text{-C}_6\text{H}_3\text{-2,6-(C}_6\text{H}_2\text{-2,4,6-Me}_3)_2$), afford London dispersion contributions to the interaction energies of up to 27 kcal mol^{-1} at the PBE0-D3(BJ)-ATM/def2-QZVP level (36 kcal mol^{-1} for B3LYP).

10.1. Introduction

Since the discovery of the first stable diorgano tetrylenes, $\text{E}\{\text{CH}(\text{SiMe}_3)_2\}_2$ ($\text{E} = \text{Ge}$, Sn , or Pb)^{513–518}, the study of their physical, spectroscopic, and structural properties as well as their reactivity has been a major research theme in main group chemistry^{519–521}. Studies of these and related dialkyl species have been complemented by work on tetrylenes with aryl^{522–524}, silyl⁵²⁵, boryl⁵²⁶, thiolato^{527,528}, amido^{529–537}, aryloxo^{538–543}, or heteroleptic^{544,545} substituents (Figure 10.1). Recent work has also shown that the reactivity of the related aryl tin(II) hydrides $\{\text{Ar}^{i\text{Pr}_6}\text{Sn}(\mu\text{-H})\}_2$ ($\text{Ar}^{i\text{Pr}_6} = \text{C}_6\text{H}_3\text{-2,6-(C}_6\text{H}_2\text{-2,4,6-}i\text{Pr}_3)_2$), and $\text{Ar}^{i\text{Pr}_4}\text{Sn}(\mu\text{-H})_2$ ($\text{Ar}^{i\text{Pr}_4} = \text{-C}_6\text{H}_3\text{-2,6-(C}_6\text{H}_3\text{-}i\text{Pr}_2)_2$) with olefins and alkynes was strongly affected by the presence or absence of an additional isopropyl group at the remote para position on the flanking ring^{546,547}. The most prominent terphenyl-substituted tetrylenes involve either Ar^{Me_6} ($\text{Ar}^{\text{Me}_6} = \text{C}_6\text{H}_3\text{-2,6-(C}_6\text{H}_2\text{-2,4,6-Me}_3)_2$) or the bulkier Ar^{iPr_4} ligand as substituents but their structures displayed a pattern in which there is little correlation between the ligand size and the interligand angle at the tetrel atom⁵²³. Thus, we became interested in the effects of the size of terphenyl substituents on the structures to see if the unusual steric effects observed for Ar^{Me_6} and Ar^{iPr_4} substituents also extended to the bulkier Ar^{iPr_6} derivatives. We note that in earlier work⁵²⁸ on the chalcogenato ($\text{Ch} = \text{O}$, S , or Se) derivatives $\text{E}(\text{ChR})_2$ ($\text{E} = \text{Si}$, Ge , Sn , or Pb ; $\text{R} = \text{Ar}^{\text{Me}_6}$, Ar^{iPr_4} , Ar^{iPr_6} , and $\text{Ar}^{i\text{Pr}_8} = \text{-C}_6\text{H}_3\text{-3,5-}i\text{Pr}_2\text{-2,6-(C}_6\text{H}_2\text{-2,4,6-}i\text{Pr}_3)_2$) (See figure 10.2 for images of the terphenyl ligands) DFT disclosed similar irregularities in the Ch-E-Ch angles, and dispersion-corrected calculations on the $\text{ChAr}^{i\text{Pr}_8}$ derivatives supported the presence of significant dispersion force effects⁵²⁸. Herein we report the synthesis and characterization of the heavier tetrylenes $\text{E}\{\text{C}_6\text{H}_3\text{-2,6-(C}_6\text{H}_2\text{-2,4,6-}i\text{Pr}_3)_2\}_2$ ($\text{E} = \text{Ge}$ (**1**), Sn (**2**), or Pb (**3**)) and in addition computational studies on **1–3** and their Ar^{Me_6} - and Ar^{iPr_4} -substituted counterparts and show that the

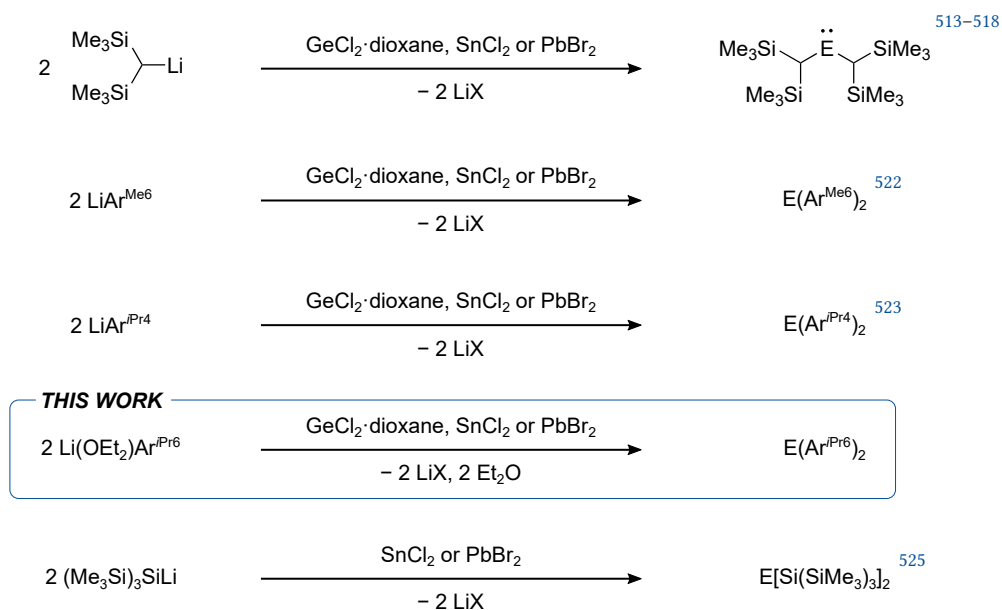


Figure 10.1.: Synthesis of selected examples of tetrylenes by metathesis reactions. E = Ge, Sn, or Pb; X = Cl or Br.

narrower $C_{ipso}-E-C_{ipso}$ angles observed for the bulkier substituents is probably a result of the interligand London dispersion force attractions between the two terphenyl groups, which were calculated to range between ca. 15–25 kcal mol⁻¹ at the chosen level of theory in the nine compounds studied in this paper.

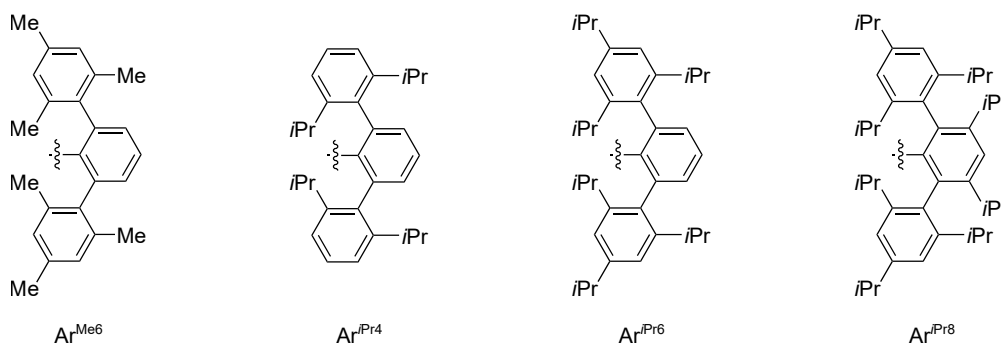


Figure 10.2.: Schematic depiction of the discussed terphenyl ligands.

10.2. Experimental Section

General Considerations

All manipulations were performed under anaerobic and anhydrous conditions using Schlenk techniques or a Vacuum Atmospheres drybox. $\text{Li}(\text{OEt}_2)\text{Ar}^{\text{Pr6}}$ was prepared by a literature procedure⁵⁴⁸. $\text{GeCl}_2 \cdot \text{dioxane}$ (Gelest), SnCl_2 (Acros), and PbBr_2 (Acros) were purchased from the named commercial

10. Counterintuitive Interligand Angles in Diaryltetraylenes and Related Species: The Role of Dispersion

suppliers and used as received. Solvents were dried over alumina columns, stored over potassium, and degassed via three freeze–pump–thaw cycles. ^1H , $^{13}\text{C}\{^1\text{H}\}$, $^{119}\text{Sn}\{^1\text{H}\}$, and $^{207}\text{Pb}\{^1\text{H}\}$ NMR spectra were collected on a Varian 600 MHz spectrometer and referenced internally to known solvent signals or externally to SnMe_4 (0.0 ppm) in C_6D_6 or PbMe_4 (0.0 ppm) in C_6D_6 . IR spectra were recorded as Nujol mulls between CsI plates on a PerkinElmer 1430 spectrometer. UV/VIS spectra were recorded as dilute hexanes (as a mixture of *n*-hexane and methyl cyclopentane) solutions in 3.5 mL quartz cuvettes using an Olis 17 Modernized Cary 14 UV/VIS/NIR spectrophotometer. Melting points were determined with a Meltemp II apparatus using glass capillaries sealed with vacuum grease and are uncorrected.

X-ray Crystallography

Crystals of **1–3** suitable for single-crystal X-ray diffraction studies were covered in Paratone oil and attached to a glass fiber on the mounting pin of the goniometer. Crystallographic measurements were collected at 90 K with a Bruker APEX II DUO diffractometer using $\text{Mo K}\alpha$ ($\lambda = 0.71073 \text{ \AA}$) radiation or Cu ($\lambda = 1.54178 \text{ \AA}$) radiation. The crystal structures were corrected for Lorentz and polarization effects with SAINT⁵⁴⁹ and absorption using Blessing's method as incorporated into the program SADABS^{550,551}. The SHELXTL program was used to determine the space groups and set up the initial files⁵⁵². The structures were determined by direct methods using the program SHELXS and refined with the program SHELXL⁵⁵³. All non-hydrogen atoms were refined with anisotropic displacement parameters. Hydrogen atoms were placed in idealized positions throughout the refinement process and refined as riding atoms with individual isotropic refinement parameters. A summary of data collection and refinement parameters is given in the online Supporting Information of the original publication.

$\text{Ge}(\text{Ar}^{i\text{Pr}6})_2$ (**1**)

A diethyl ether (20 mL) solution of $\text{Li}(\text{OEt}_2)\text{Ar}^{i\text{Pr}6}$ (2.81 g, 5.0 mmol) was added dropwise to a rapidly stirred diethyl ether (ca. 10 mL) suspension of $\text{GeCl}_2 \cdot \text{dioxane}$ (0.556 g, 2.4 mmol) cooled in an ice bath. The reaction mixture gradually changed color from yellow to green to blue. It was stirred for a further 12 h and subsequently warmed to room temperature. The solvent was removed under reduced pressure and hexanes (ca. 30 mL) were added. The solids were allowed to settle, and the supernatant liquid was filtered via a filter-tipped cannula. The filtrate was concentrated to ca. 5 mL and stored in ca. -18°C freezer to afford air sensitive blue crystals of $\text{Ge}(\text{Ar}^{i\text{Pr}6})_2$ (**1**) that were suitable for X-ray diffraction studies. Yield (1.51 g, 60.5%). mp 90°C (dec). ^1H NMR (600 MHz, C_6D_6 , 298 K, ppm) δ : 0.62 (br, 6H, CHMe_2); 1.05 (br, 9H, CHMe_2); 1.20 (dd, $^3J = 6 \text{ Hz}$, 6H, CHMe_2); 1.30 (d, $^3J = 6 \text{ Hz}$, 15H, CHMe_2); 2.54 (br, 2H, CHMe_2); 2.84 (sept, $^3J = 6 \text{ Hz}$, 3H, CHMe_2); 2.97 (sept, $^3J = 6 \text{ Hz}$, 1H, CHMe_2); 6.85 (t, $^3J = 6 \text{ Hz}$, 1H, ArH); 7.03 (s, 2H, ArH); 7.09 (s, 2H, ArH); 7.14 (br, 1H, ArH); 7.20 (s, 1H, ArH). $^{13}\text{C}\{^1\text{H}\}$ NMR (150 MHz, C_6D_6 , 298 K, ppm) δ : 24.57, 24.70, 24.88, 24.91, 25.03, 26.35, 31.30, 32.40, 34.97, 35.32, 35.40, 121.18, 122.58, 127.63, 128.76, 132.41, 133.56, 138.02, 141.68, 145.41, 146.75, 148.83, 150.06, 174.97. λ_{max} (nm, ϵ in $\text{L mol}^{-1} \text{ cm}^{-1}$): 617 (770).

Sn(Ar^{iPr6})₂ (2)

A rapidly stirred diethyl ether (ca. 10 mL) suspension of SnCl₂ (0.427 g, 2.25 mmol) cooled in an ice bath was treated dropwise with a diethyl ether solution (ca. 40 mL) of Li(OEt)₂Ar^{iPr6} (2.589 g, 4.60 mmol). The reaction solution, initially colorless, gradually changed to yellow then to green and finally to blue. After 30 min of stirring at 0°C, the reaction solution was warmed to room temperature and stirring was continued for 12 h. The solvent was removed under reduced pressure, and hexanes (ca. 40 mL) were added. The solids were allowed to settle, and the supernatant liquid was filtered via a filter-tipped cannula. The filtrate was concentrated to ca. 5 mL and stored in ca. -18°C freezer to afford crystals of the product that were suitable for X-ray diffraction studies. Sn(Ar^{iPr6})₂ (2) was isolated as an air-, moisture-, and light-sensitive blue crystalline solid. Yield (1.977 g, 81%). mp 132°C (dec). ¹H NMR (600 MHz, C₆D₆, 298 K, ppm) δ: 0.93 (br, 9H, CHMe₂); 1.07 (d, 9H, CHMe₂); 1.20 (dd, ³J = 6 Hz, 6H, CHMe₂); 1.31 (d, ³J = 6 Hz, 12H, CHMe₂); 2.85 (sept, ³J = 6 Hz, 2H, CHMe₂); 2.97 (sept, ³J = 6 Hz, 1H, CHMe₂); 3.16 (br, 3H, CHMe₂); 6.89 (s, 2H, ArH); 7.06 (s, 2H, ArH); 7.14–7.18 (m, 2H, ArH); 7.20 (s, 1H, ArH). ¹³C{¹H} NMR (150 MHz, C₆D₆, 298 K, ppm) δ: 23.16, 24.67, 24.76, 24.88, 24.91, 25.03, 26.32, 31.30, 31.94, 35.01, 35.32, 121.17, 122.46, 126.47, 128.75, 132.40, 134.53, 137.36, 138.01, 141.68, 147.03, 147.27, 148.46, 148.83, 148.94, 169.01, 197.85. ¹¹⁹Sn{¹H} NMR (223.6 MHz, C₆D₆, 298 K, ppm) δ: 2129. λ_{max} (nm, ε in L mol⁻¹ cm⁻¹): 612 (720).

Pb(Ar^{iPr6})₂ (3)

A rapidly stirred diethyl ether (ca. 10 mL) suspension of PbBr₂ (0.880 g, 2.4 mmol) at 0°C was treated dropwise with a diethyl ether solution (ca. 20 mL) of Li(OEt)₂Ar^{iPr6} (2.81 g, 5.0 mmol). The reaction mixture changed color from yellow to green and finally to dark blue with further stirring for 12 h. The solvent was removed under reduced pressure, and hexanes (ca. 30 mL) were added. The solids were allowed to settle, and the supernatant liquid was filtered via a filter-tipped cannula. The solvent was concentrated to ca. 5 mL and stored in ca. -18°C freezer to afford crystals that were suitable for X-ray diffraction studies. Pb(Ar^{iPr6})₂ was isolated as an air-, moisture-, and light-sensitive dark blue crystalline solid. Yield (1.67 g, 59.2%). mp 127°C (dec). ¹H NMR (600 MHz, C₆D₆, 298 K, ppm) δ: 0.97 (d, ³J = 6 Hz, 9H, CHMe₂); 1.04 (d, ³J = 6 Hz, 9H, CHMe₂); 1.20 (dd, ³J = 6 Hz, 6H, CHMe₂); 1.29 (d, ³J = 6 Hz, 3H, CHMe₂); 1.32 (d, ³J = 6 Hz, 9H, CHMe₂); 2.87 (sept, ³J = 6 Hz, 2H, CHMe₂); 2.97 (sept, ³J = 6 Hz, 2H, CHMe₂); 3.15 (sept, ³J = 6 Hz, 2H, CHMe₂); 7.08 (s, 2H, ArH); 7.14 (s, 1H, ArH); 7.20 (s, 2H, ArH); 7.22 (t, ³J = 6 Hz, 1H, ArH); 7.59 (d, ³J = 6 Hz, 1H, ArH). ¹³C{¹H} NMR (150 MHz, C₆D₆, 298 K) δ: 23.91, 24.07, 24.11, 24.19, 25.40, 30.45, 30.91, 34.16, 34.49, 120.31, 121.64, 123.20, 131.63, 136.63, 137.27, 140, 84, 142.54, 146.41, 147.35, 147.80, 147.96, 148.36. Ipso carbon not found. ²⁰⁷Pb{¹H} NMR (125 MHz, C₆D₆, 298 K, ppm) δ: not observed. λ_{max} (nm, ε in L mol⁻¹ cm⁻¹): 588 (1070).

10.3. Results and Discussion

Synthesis

Compounds **1–3** were synthesized by the dropwise addition of a 2:1 ratio of an ethereal solution of $\text{Li}(\text{OEt}_2)\text{Ar}^{\text{iPr}_6}$ to the appropriate tetrel dihalide suspended in diethyl ether chilled in an ice bath. After being stirred for ca. 30 min, the solutions were warmed to room temperature, and stirring was continued for a further 12 h, whereupon the solvent was removed under reduced pressure. The blue residues were extracted with hexanes (as a mixture of *n*-hexane and methylcyclopentane) (ca. 40 mL), and any remaining solids were removed by filtration. Compounds **1**, **2**, and **3** were isolated as air- and moisture-sensitive blue solids in yields of ca. 60–80% by reduction of filtrate volume to ca. 5 mL and cooling in a ca. -18°C freezer. In addition to being air- and moisture-sensitive, **2** and **3** are also light-sensitive as evident by a color change from blue to green for **2** and the deposition of elemental lead for **3** upon standing as a solution under ambient light. Blue crystals of **1–3** suitable for X-ray diffraction were grown from saturated hexanes solutions.

X-ray Data and Crystal Structures

The X-ray data for **1** showed that one molecule of *n*-hexane and one molecule of methylcyclopentane (present in hexanes solvent) co-crystallized with $\text{Ge}(\text{Ar}^{\text{iPr}_6})_2$. Because of severe disorder of methylcyclopentane, SQUEEZE⁵⁵⁴ was used to truncate the X-ray data. Figure 10.3 depicts the single crystal X-ray structure of $\text{Ge}(\text{Ar}^{\text{iPr}_6})_2$ (**1**). There are short C–H–H–C contacts between the isopropyl groups

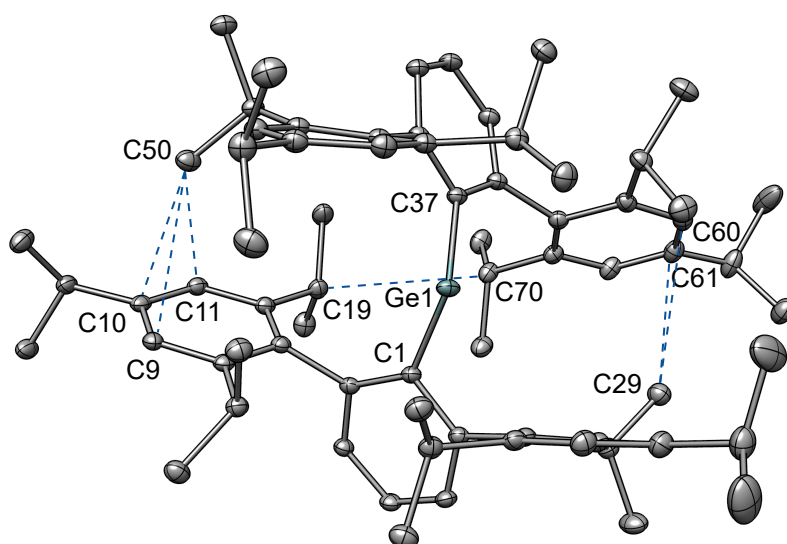


Figure 10.3.: Plot of the crystallographically determined structure of $\text{Ge}(\text{Ar}^{\text{iPr}_6})_2$ (**1**) with several short C–C contacts. Thermal ellipsoids are shown at 30% of electronic probability. Hydrogen atoms and co-crystallized solvent molecules are omitted for clarity. Selected bond lengths in Å and angles in $^\circ$: C(1)–Ge(1), 2.0389(15) Å; C(37)–Ge(1), 2.0430(15) Å; C(1)–Ge(1)–C(37), 112.55(6) $^\circ$.

in the range ca. 2.08–2.49 Å³². There are also several short C–C contacts between carbon atoms from the isopropyl moieties and those from the flanking aryl rings that span the range of ca. 3.37–3.55 Å. The proximity may be a result of attractive intramolecular London dispersion interaction between each terphenyl ligand based on the sum of the van der Waals radii between CH–HC (2.40 Å) and C–C (3.54 Å)^{555,556}. The Ge–C_{ipso} bond lengths in **1** are very similar to each other having the values 2.0389(15) and 2.0430(15) Å, which slightly exceed the sum of the single bond radii of carbon (0.77 Å) and germanium (1.22 Å)¹¹⁸ and are similar to the Ge–C_{ipso} distances observed in other terphenyl-stabilized germanium tetrylenes that span the range 2.019(2)–2.051(3) Å.^(11,45–47) The C_{ipso}–Ge–C_{ipso} angle is 112.55(6)°, which is marginally narrower than the corresponding angles in the less crowded Ge(Ar^{iPr4})₂, 112.77(4)°, and Ge(*p*-Cl-Ar^{Me6})₂, 112.64(7)°³². The C_{ipso}–Ge–C_{ipso} angles in other reported germanium tetrylenes vary from 102.71(9)° in Ge{2,6-(1-naphthyl)phenyl}₂ (Ge–C = 2.030(2), 2.036(2) Å)⁵⁵⁷ to 124.45(9)° in the more crowded species Ge{C₆H-2,6-(2,4,6-Me₃-C₆H₂)₂-3,5-*i*Pr₂}₂, which has additional isopropyl substituents on the central aryl ring⁵⁵⁸. The C_{ipso}–E–C_{ipso} angles in the less crowded Ge(Ar^{Me6})₂⁵²⁴, 114.4(2)°, and Ge(*p*-SiMe₃-Ar^{Me6})₂⁵⁵⁸, 115.85(14)° are wider than that in **1** by ca. 2–3° despite the increased size of the terphenyl substituent Ar^{iPr6} in **1**. The X-ray structure of **2** is shown in figure 10.4 and displays short C–H–H–C contacts that range from 2.235 to 2.500 Å. In this structure, several short C–C contacts are also present that range ca. 3.32–3.53 Å^{555,556}. The C_{ipso}–Sn bond lengths are 2.281(2) and 2.263(3) Å, which are slightly longer than those reported for other terphenyl-stabilized tetrylenes that range between 2.226(5) and 2.261(4) Å^{523,524,558}. The C_{ipso}–Sn–C_{ipso} angle is

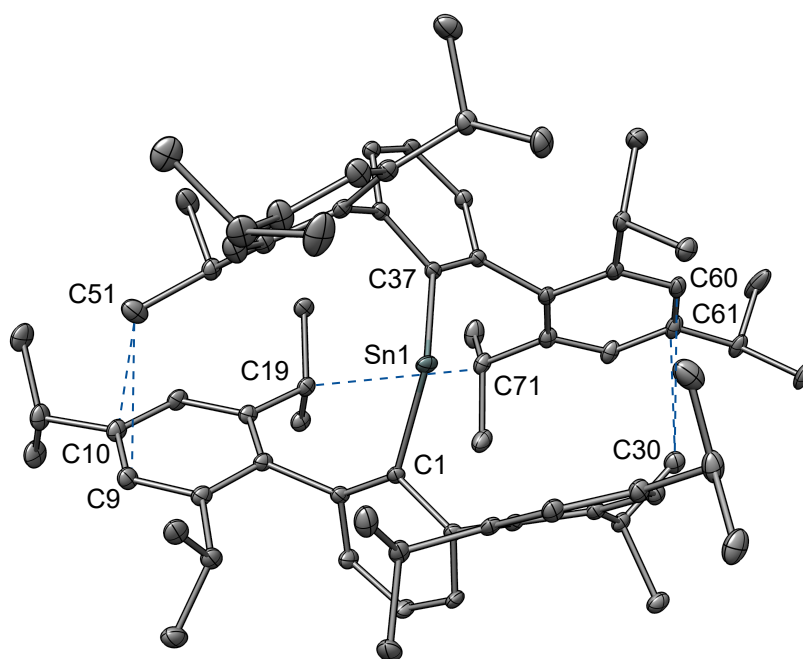


Figure 10.4.: Plot of the crystallographically determined structure of Sn(Ar^{iPr6})₂ (**2**) with several short C–C contacts. Thermal ellipsoids are shown at 30% of electronic probability. Hydrogen atoms are omitted for clarity. Selected bond lengths in Å and angles in °: C(1)–Sn(1), 2.281(2) Å; C(37)–Sn(1), 2.263(3) Å; C(1)–Sn(1)–C(37), 107.61(9)°.

107.61(9)° and is the narrowest angle of any of the reported terphenyl-substituted stannylenes. For example, it is ca. 10° narrower than the 117.56(8)° in the slightly less crowded stannylene, Sn(Ar^{iPr4})₂, and it is also narrower than the C_{ipso}-Sn-C_{ipso} angles in the *para*-substituted terphenyl tetraylenes of formula Sn(*p*-R-Ar^{Me6})₂ (R = H, Cl, SiMe₃) that range between 114.7(3)° and 115.39(12)°. In contrast, the highly crowded Sn(C₆H-2,6-(2,4,6-Me₃-C₆H₂)₂-3,5-*i*Pr₂)₂, which carries *meta* isopropyl substituents on the central aryl ring, has a much wider C_{ipso}-Sn-C_{ipso} angle of 123.44(14)°^{523,524,558}. The structure of Pb(Ar^{iPr6})₂ (**3**) is shown in figure 10.5 and contains short C-H-H-C contacts between the isopropyl groups that span 2.10–2.46 Å. The short C-C contacts between the carbon atoms of some of the isopropyl groups and flanking aryl rings of the second terphenyl ligand bound to the tetrel atom span the range of ca. 3.38–3.56 Å^{555,556}. The C_{ipso}-Pb bond lengths are 2.372(3) and 2.391(3) Å, which are similar to those of other reported terphenyl-stabilized lead tetraylenes that range between 2.322(4) and 2.391(8) Å^{32,523,524}. The C_{ipso}-Pb-C_{ipso} angle is 108.12(9)°, which is narrower by ca. 6° than those observed in the less bulky Ar^{Me6}-substituted Pb(Ar^{Me6})₂ whose C_{ipso}-Pb-C_{ipso} angle is between 114.5(6) and 115.30(8)°, and it is almost 14° narrower than the 121.5(3)° C_{ipso}-Pb-C_{ipso} angle observed in Pb(Ar^{iPr4})₂⁵²³, which bears the smaller Ar^{iPr4} substituent. The presence of isopropyl groups at the 3,5-position of the central aryl ring in Pb(C₆H-2,6-(2,4,6-Me₃-C₆H₂)₂-3,5-*i*Pr₂)₂ causes the C_{ipso}-Pb-C_{ipso} angle to increase to 123.89(12)° whereas the C_{ipso}-Pb-C_{ipso} angle observed in Pb(Ar^{iPr4})₂ is 121.5(3)°. The C_{ipso}-Pb-C_{ipso} angle in **3** is wider than that observed in Pb(2,6-(1-naphthyl)phenyl)₂ (100.39(17)°), which carries no alkyl substituents on the flanking aryl ring⁵⁵⁷. Thus, the change of ligand from Ar^{iPr4} to the nominally

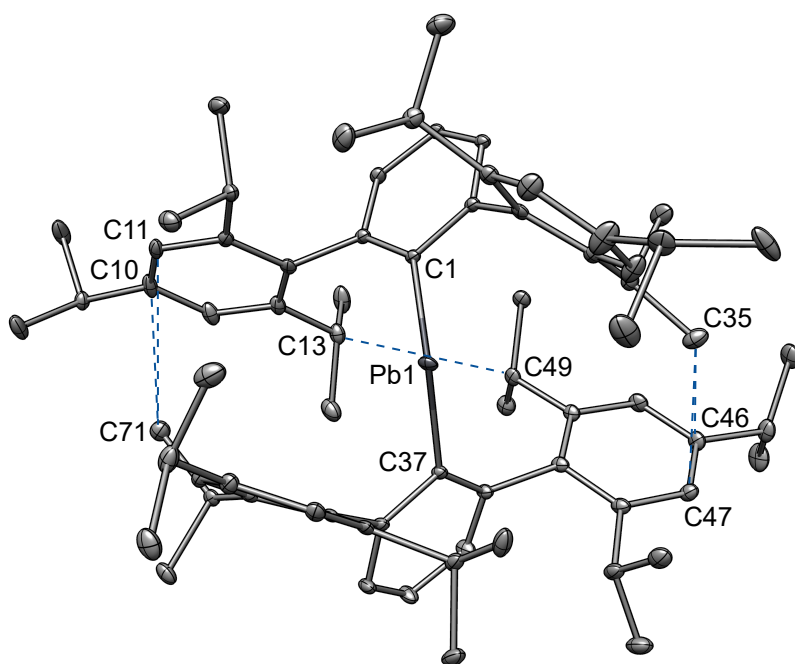


Figure 10.5.: Plot of the crystallographically determined structure of Pb(Ar^{iPr6})₂ (**3**) with several short C-C contacts. Thermal ellipsoids are shown at 30% of electronic probability. Hydrogen atoms are omitted for clarity. Selected bond lengths in Å and angles in °: C(1)-Pb(1), 2.372(3) Å; C(37)-Pb(1), 2.391(3) Å; C(1)-Pb(1)-C(37), 108.12(9)°.

bulkier Ar^{iPr6} group causes a narrowing of the C_{ipso}-E-C_{ipso} angle from 117.56(8) to 107.61(9)° in the tin derivatives and from 121.5(3) to 108.12(9)° in the lead species. Curiously, this effect is not seen in the germanium analogue, perhaps as a result of limited flexibility in these species as a result of extreme steric congestion caused by the smaller radius of germanium (1.22 Å) in comparison to tin (1.40 Å) or lead (1.45 Å)¹¹⁸. Table 10.1 summarizes the C_{ipso}-E-C_{ipso} angles of selected heavier group 14 tetrylenes. The data show that for the Ge, Sn, and Pb derivatives of the smaller terphenyl ligand Ar^{Me6}, the C_{ipso}-E-C_{ipso} angles are essentially invariant. For the Ar^{iPr4} derivatives, however, the angles become wider in increments of ca. 4–5° as the group is descended Ge to Sn to Pb. In contrast for the Ar^{iPr6} derivatives, the C_{ipso}-E-C_{ipso} angle decreases by ca. 5° from Ge to Sn with the C_{ipso}-Pb-C_{ipso} angle being slightly wider than that of the tin species. Thus, the C_{ipso}-E-C_{ipso} angles display no consistent pattern but in several instances the changes are contrary to steric expectations. The E-C_{ipso} bonds lengthen modestly with the E-C_{ipso} distances in the ligand order Ar^{iPr6} > Ar^{iPr4} > Ar^{Me6} (cf. table 10.1). For example, for the tin diaryls, the Sn(Ar^{iPr6})₂ has Sn-C_{ipso} distances that are ca. 0.02 Å longer than those in Sn(Ar^{iPr4})₂ which, in turn, has Sn-C_{ipso} distances that are ca. 0.02 Å longer than those in Sn(Ar^{Me6})₂.

Table 10.1.: E-C_{ipso} bond lengths in Å and C_{ipso}-E-C_{ipso} angles in ° of selected *m*-terphenyl-stabilized tetrylenes^{523,524}.

	GeAr ₂	Ge-C _i	SnAr ₂	Sn-C _i	PbAr ₂	Pb-C _i
Ar ^{Me6}	114.4(2)	2.034(4)	114.7(3)	2.226(5)	114.5(6)	2.332(12)
Ar ^{iPr4}	112.77(9)	2.033(2), 2.048(3)	117.56(8)	2.2532(16)	121.5(3)	2.378(8), 2.391(8)
Ar ^{iPr6}	112.55(6)	2.0389(15), 2.0430(15)	107.61(9)	2.263(3), 2.281(2)	108.12(9)	2.372(3), 2.391(3)

Angular Distortions Compounds 1–3

In addition to the trends in the bond lengths and angles at the central E atom discussed above, the structures 1–3 display several other noteworthy features. Inspection of the C_{ortho}-C_{ipso}-E angles involving the central aryl ring of the ligand show that they have large variations from values that are expected to be near the trigonal planar angle of 120°. For example, in the least crowded germylene, Ge(Ar^{Me6})₂ the C_{ortho}-C_{ipso}-Ge angles, 112.7(3)° and 128.2(3)°, differ by 15.5°. In the more crowded germylene, Ge(Ar^{iPr4})₂, the C_{ortho}-C_{ipso}-E angles are 102.68(16)°/113.83(16)° and 125.51(15)°/131.42(17)°, affording larger differences of 22.83° and 17.59° (the pairs of values are from two crystallographically independent molecules). The most sterically encumbered germylene, Ge(Ar^{iPr6})₂ (**1**), has C_{ortho}-C_{ipso}-Ge angles of 108.68(11)°/108.97(10)° and 133.57(11)°/133.9(11)°, giving an average difference near 24.9° (two crystallographically independent molecules). Thus, the data show that as the ligands become larger, the C_{ortho}-C_{ipso}-Ge angles display more deviation from the trigonal value and become more unequal. In addition to the C_{ortho}-C_{ipso}-Ge angular distortions, there are also distortions in which the Ge-C_{ipso}

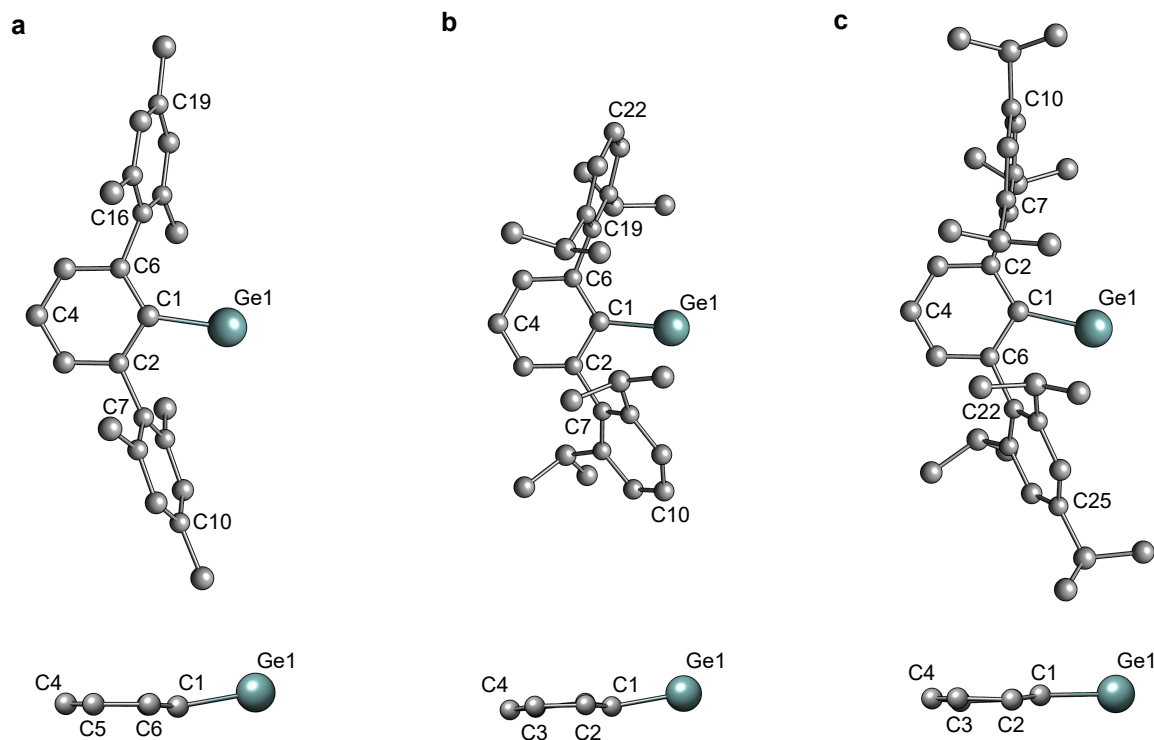


Figure 10.6.: Plots of the crystallographically determined GeAr units in a) $\text{Ge}(\text{Ar}^{\text{Me}6})_2$, b) $\text{Ge}(\text{Ar}^{\text{iPr}4})_2$ and c) $\text{Ge}(\text{Ar}^{\text{iPr}6})_2$ showing the $\text{Ge}(1)\text{-C}_{\text{ipso}}\text{-C}_{\text{ortho}}$ angles and the deviation of the $\text{Ge}(1)\text{-C}_{\text{ipso}}$ bond from the averaged plane of the central ring⁵²⁴. Hydrogen atoms are omitted for clarity.

bond deviates from the plane of the C_{ipso} ring. In the least crowded germylene, $\text{Ge}(\text{Ar}^{\text{Me}6})_2$ (Figure 10.6a), the angle between the $\text{Ge}(1)\text{-C}_{\text{ipso}}$ bond and the averaged plane of the $\text{C}(1)$ ring is $14.2(2)^\circ$. However, an increase in the size of the ligand from $\text{Ar}^{\text{Me}6}$ to $\text{Ar}^{\text{iPr}4}$ (Figure 10.6b) affords the angles $10.50(14)^\circ$ and $27.6(1)^\circ$ between the $\text{Ge}(1)\text{-C}_{\text{ipso}}$ bonds and the plane of the rings to which they are attached. The corresponding angles in $\text{Ge}(\text{Ar}^{\text{iPr}6})_2$, (Figure 10.6c) are $12.7(8)^\circ$ and $13.1(8)^\circ$ for the two crystallographically independent ligands. Of these three *m*-terphenyl-substituted germylenes, the $\text{Ar}^{\text{iPr}4}$ substituent displays the most angular distortion between each substituent. The flanking aryl rings also display deviations from expected geometries. For example, the crowding causes the $\text{C}_{\text{ortho}}\text{-C}_{\text{ipso}}$ bond to de-

Table 10.2.: Key angles and angular distortions in $^\circ$ in selected germanium tetrylenes^{523,524}.

	Ge-C1-C2	Ge-C1-C6	Ge-C1-C4	$\text{C}_o\text{-C}_i\text{-flank.-C}_p\text{-flank.}$	$\text{C}_o\text{-C}_i\text{-flank.-C}_p\text{-flank.}$
$\text{Ge}(\text{Ar}^{\text{Me}6})_2$	112.7(3)	128.2(3)	14.2(2)	5.8(3)	14.6(3)
$\text{Ge}(\text{Ar}^{\text{iPr}4})_2$	113.83(16), 131.42(17)	125.51(15), 102.68(16)	10.50(14), 27.6(1)	5.47(19), 8.52(18)	15.9(2), 1.47(18)
$\text{Ge}(\text{Ar}^{\text{iPr}6})_2$	133.57(11), 108.68(11)	108.98(10), 133.91(11)	12.7(8), 13.1(8)	0.71(11), 16.87(12)	16.15(12), 1.70(3)

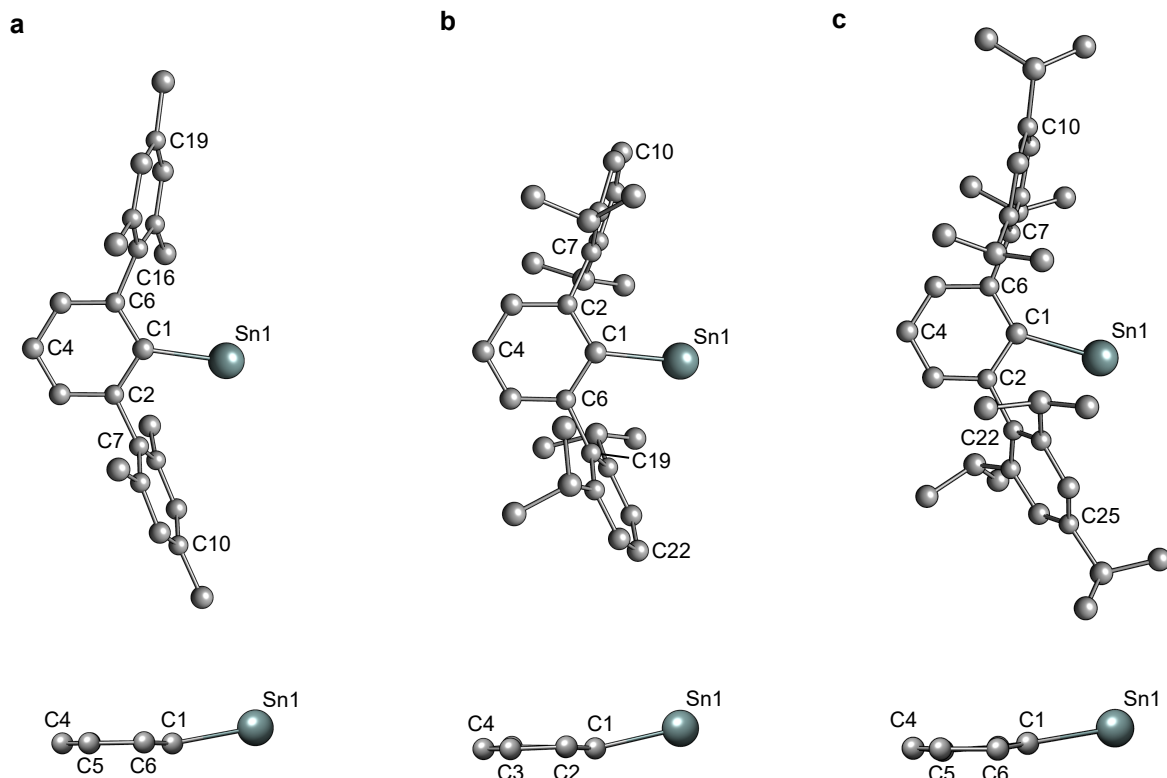


Figure 10.7.: Plots of the crystallographically determined SnAr units in a) $\text{Sn}(\text{Ar}^{\text{Me}6})_2$, b) $\text{Sn}(\text{Ar}^{\text{iPr}4})_2$ and c) $\text{Sn}(\text{Ar}^{\text{iPr}6})_2$ showing the Sn(1)–C_{ipso}–C_{ortho} angles and the deviation of the Sn(1)–C_{ipso} bond from the averaged plane of the central ring⁵²³. Hydrogen atoms and co-crystallized solvent molecules are omitted for clarity.

viate from the plane of the flanking C_{ipso} ring. In $\text{Ge}(\text{Ar}^{\text{Me}6})_2$, the deviations have values of 5.8(3)° and 14.6(3)°. The more crowded germylene $\text{Ge}(\text{Ar}^{\text{iPr}4})_2$ displays four angles with values of 5.47(19)°, 8.52(18)°, 15.9(2)°, and 1.47(18)° (two crystallographically independent molecules). The most crowded germylene, $\text{Ge}(\text{Ar}^{\text{iPr}6})_2$ (**1**), also displays two distinct pairs of distorted angles involving the flanking rings of the terphenyl to the central aryl ring which have the values of 0.71(11)°, 16.87(12)°, 16.15(12)°, and 1.70(3)°. A summary of these data is given in table 10.2. The Sn–C_{ipso}–C_{ortho} angles for the central aryl ring of the least crowded stannylene, $\text{Sn}(\text{Ar}^{\text{Me}6})_2$, are 111.7(3)° and 129.6(3)° (Figure 10.7a). The slightly more crowded stannylene, $\text{Sn}(\text{Ar}^{\text{iPr}4})_2$ displays angles of 114.71(11)° and 125.45(11)° (Figure 10.7b). The

Table 10.3.: Key angles and angular distortions in ° in selected tin tetraarylenes^{523,524}.

	Sn–C1–C2	Sn–C1–C6	Sn–C1–C4	C _o –C _{i, flank} –C _{p, flank}	C _o –C _{i, flank} –C _{p, flank}
$\text{Sn}(\text{Ar}^{\text{Me}6})_2$	111.7(3)	129.6(3)	14.2(3)	4.1(3)	4.0(3)
$\text{Sn}(\text{Ar}^{\text{iPr}4})_2$	125.45(11)	114.71(11)	14.0(8)	1.31(13)	8.37(12)
$\text{Sn}(\text{Ar}^{\text{iPr}6})_2$	107.37(17), 135.47(17)	136.13(18), 107.31(17)	16.3(1), 14.8(1)	3.72(18), 12.28(17)	16.6(2), 8.17(19)

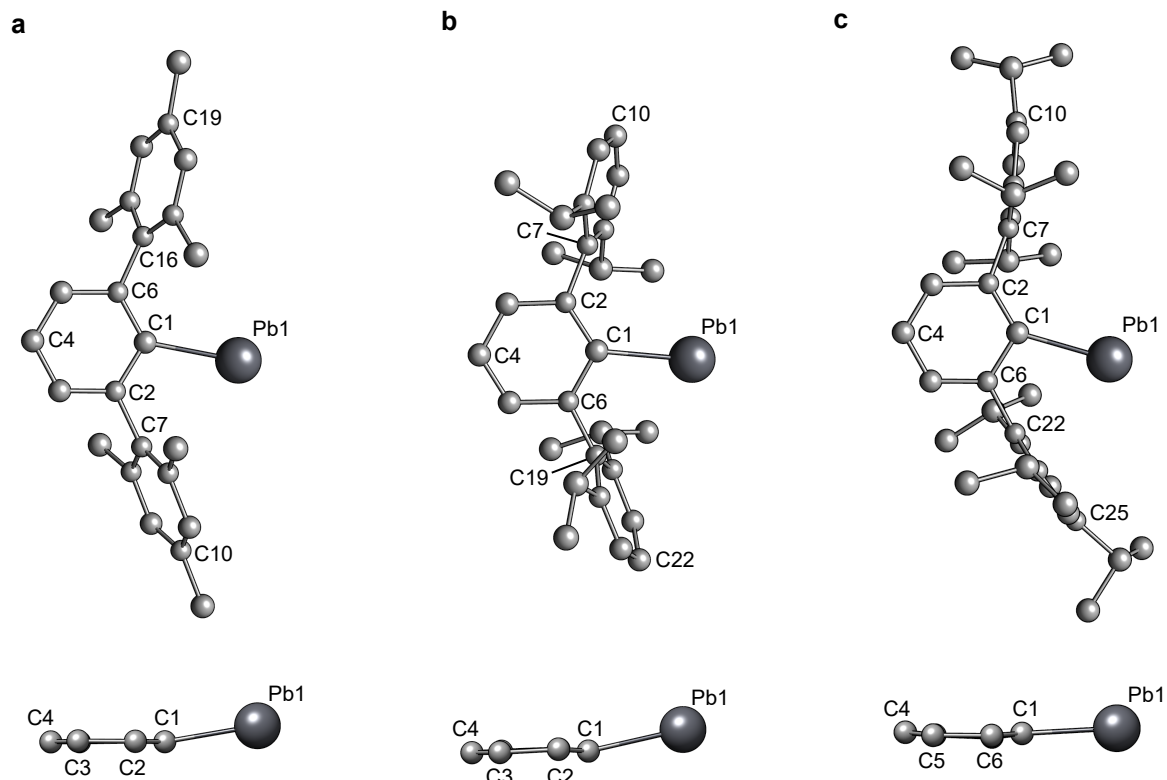


Figure 10.8.: Plots of the crystallographically determined PbAr units in a) $\text{Pb}(\text{Ar}^{\text{Me}6})_2$, b) $\text{Pb}(\text{Ar}^{\text{iPr}4})_2$ and c) $\text{Pb}(\text{Ar}^{\text{iPr}6})_2$ showing the $\text{Pb}(1)\text{-C}_{\text{ipso}}\text{-C}_{\text{ortho}}$ angles and the deviation of the $\text{Pb}(1)\text{-C}_{\text{ipso}}$ bond from the averaged plane of the central ring⁵²⁴. Hydrogen atoms are omitted for clarity.

largest stannylene, $\text{Sn}(\text{Ar}^{\text{iPr}6})_2$, has slightly less distortion with angles of $107.37(17)^\circ/107.31(17)^\circ$ and $135.47(17)^\circ/136.13(18)^\circ$ due to two crystallographically independent substituents (Figure 10.7c). The other angular distortions for the tin species are listed in table 10.3. The key angular distortions in the lead diaryls (Figures 10.8a-c) are given in table 10.4. Despite the larger size of lead¹¹⁸ the distortions are generally greater than those in the germanium and tin series, perhaps because of the greater ionic character of the $\text{Pb}\text{-C}_{\text{ipso}}$ bond. The partial charges at the respective atoms (Mulliken partial charges for **3**: Pb, 0.305 e; C_{ipso} , -0.528 e) indicate a strongly polarized bond, that may facilitate increasing dis-

Table 10.4.: Key angles and angular distortions in $^\circ$ in selected lead tetraylenes^{523,524}.

	Pb-C1-C2	Pb-C1-C6	Pb-C1-C4	$\text{C}_o\text{-C}_{i, \text{flank.}}\text{-C}_{p, \text{flank.}}$	$\text{C}_o\text{-C}_{i, \text{flank.}}\text{-C}_{p, \text{flank.}}$
$\text{Pb}(\text{Ar}^{\text{Me}6})_2$	110.6(9)	129.8(8)	14.0(6)	4.7(1)	3.4(8)
$\text{Pb}(\text{Ar}^{\text{iPr}4})_2$	126.8(7), 132.8(8)	112.5(6), 110.8(5)	14.1(4), 14.5(4)	7.7(6), 4.9(7)	9.7(6), 9.1(6)
$\text{Pb}(\text{Ar}^{\text{iPr}6})_2$	136.68(17), 106.33(18)	105.79(17), 136.83(18)	16.3(1), 17.0(3)	7.5(2), 15.2(2)	11.62(17), 4.10(18)

tortions in favor of conformational rearrangement and interlocking of the high steric demand of the ligands.

^1H NMR Spectroscopy

The ^1H NMR spectra of **1–3** were recorded in C_6D_6 at 25°C . They revealed a complex pattern of alkyl hydrogen signals for **1** and **2** indicating the existence of several hydrogen atom environments caused by restricted rotations of the isopropyl groups. The ^1H NMR spectrum of **1** reveals four resonances assignable to the methyl hydrogens. Of these resonances, two are broad (0.62 ppm, 6H, and 1.05 ppm, 9H) and two are well resolved as a doublet of doublets centered at 1.20 ppm (6H) with a $^3J_{\text{H-H}}$ coupling of 6 Hz and a doublet centered at 1.30 ppm (15H) also with coupling of 6 Hz. The broadening of the signals at 0.62 and 1.05 ppm is due to the restricted rotation of the terphenyl substituents which is also observed in the ^1H NMR spectrum of $\text{Ge}(\text{Ar}^{i\text{Pr}4})_2$ ⁵²³. When rotation of the flanking aryl rings of the terphenyl ligand is unrestricted, the ^1H NMR spectrum displays three well resolved resonances for the isopropyl groups, each integrating to 12 hydrogen atoms. Figure 10.9 shows cutouts of the ^1H NMR spectra of the isopropyl methyl groups for **1–3**. As group 14 is descended, the broad resonances become sharper and are more fully resolved. In the ^1H NMR spectrum of **2**, two broad resonances are shifted downfield to 0.93 ppm (9H) and 1.07 ppm (9H). The remaining two isopropyl – CH_3 resonances are observed as a doublet of doublets, centered at 1.20 (6H) ppm and a doublet centered at 1.31 ppm (12H), each with couplings of 6 Hz. In the ^1H NMR spectrum of **3**, all of the isopropyl methyl hydrogens are well resolved, and the spectrum features four separate well-resolved doublets centered at 0.97 ppm (9H), 1.04 ppm (9H), 1.28 ppm (3H), and 1.32 ppm (9H) with $^3J_{\text{H-H}}$ couplings of 6 Hz. There is also a doublet of doublets centered at 1.20 ppm integrating to 6 hydrogen atoms with $^3J_{\text{H-H}}$ couplings of 6 Hz. In the ^1H NMR spectra of **1–3**, there are also three methine hydrogen resonances from the isopropyl substituents that appear further downfield between 2.5 and 3.3 ppm. For the methine signals of **1**, one of these is very broad (full width at half-height = 42 Hz), centered at 2.54 ppm, and corresponds to two hydrogen atoms. A second resonance centered at 2.85 ppm has a septet pattern and integrates to three hydrogen atoms with $^3J_{\text{H-H}}$ couplings of 6 Hz. The third methine resonance is centered at 2.97 ppm and corresponds to a single hydrogen atom also with $^3J_{\text{H-H}}$ coupling of 6 Hz. The three methine resonances indicate that the sterically encumbered environment of the ligands is due to the restricted

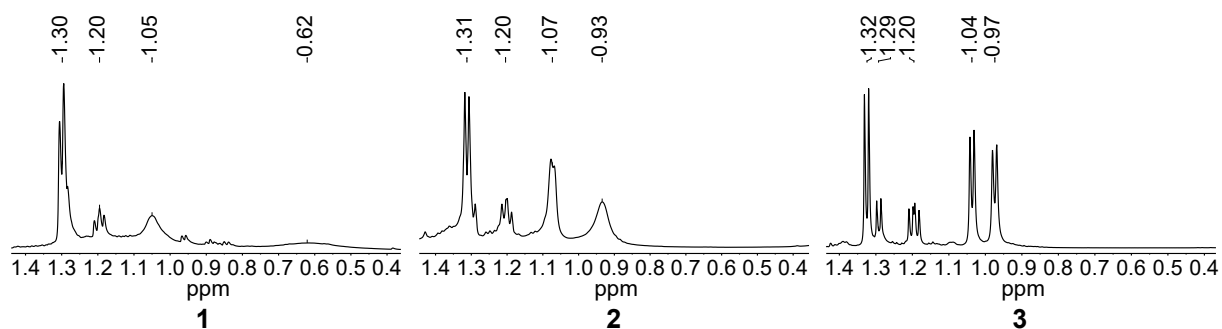


Figure 10.9.: ^1H NMR spectra cutouts of **1–3** between 0.4 and 1.4 ppm recorded in C_6D_6 at 25°C .

rotation of the Ar^{iPr6} group. When rotation is unrestricted, two septets corresponding to the ortho and para positions are observed for the methine hydrogens of the isopropyl groups for Ar^{iPr6}, integrating to 4H and 2H, respectively. Two of the three resonances for the isopropyl methine hydrogen atoms in **2** are displayed as poorly resolved septet patterns and are centered at 2.85 ppm (2H) and 2.97 ppm (1H) with coupling of 6 Hz. The third methine resonance is centered at 3.16 ppm (3H) and is broad due to the steric congestion that restricts rotation of the terphenyl substituents. The ¹H NMR spectrum of **3** displays three well-resolved methine septets centered at 2.87, 2.96, and 3.15 ppm each integrating to two hydrogen atoms with ³J_{H-H} = 6 Hz. Figure 10.10 shows cutouts of the ¹H NMR spectra of the isopropyl methine groups for **1–3**. Because of the steric congestion in tetraylenes **1–3**, the flanking aryl

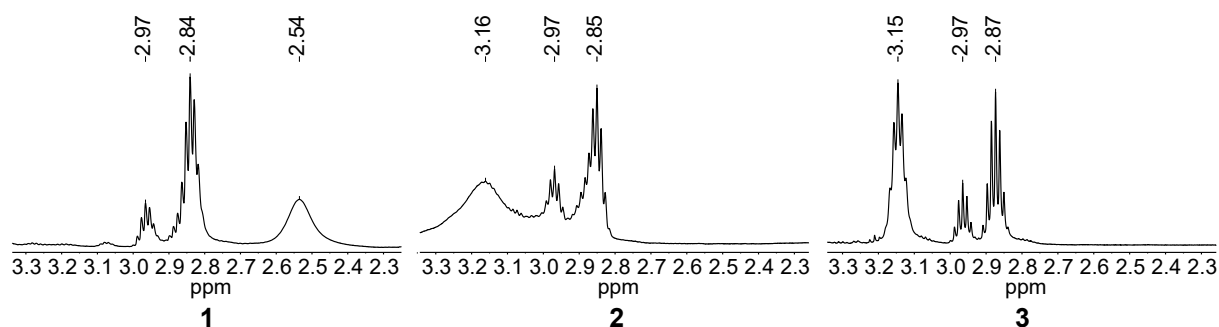


Figure 10.10.: ¹H NMR spectra cutouts of **1–3** between 2.25 and 3.30 ppm recorded in C₆D₆ at 25°C illustrating the resonances of the isopropyl methine groups.

rings of each terphenyl ligand are magnetically inequivalent. The aryl hydrogens of the flanking rings are observed as two singlets centered at 7.03 and 7.09 ppm for **1**, 6.89 and 7.07 ppm for **2**, and 7.08 and 7.20 ppm for **3**, each integrating to two hydrogen atoms. The *meta*-hydrogen atoms of the central aryl ring are also magnetically inequivalent. A singlet is observed at 7.20 ppm for both **1** and **2** which corresponds to one of the hydrogen atoms. The second *meta*-hydrogen resonance is broad and poorly resolved due to the overlap of the C₆D₅H resonance of the deuterated solvent. In **3**, one hydrogen atom resonance is moderately well-resolved at 7.14 ppm while the second resonance is clearly resolved at 7.59 ppm as a doublet with ³J_{H-H} coupling of 6 Hz. The *para*-hydrogen atom is observed as a triplet signal centered at 6.85 ppm for **1** and 7.22 ppm for **3**. In **2**, this hydrogen atom is not resolved due to overlapping resonances. In essence, as group 14 is descended the ¹H NMR spectra show that the isopropyl signals become more resolved due to the relief of steric crowding caused by the increasing size of the tetraylene atom, which allows faster rotation of the Ar^{iPr6} ligands.

¹¹⁹Sn NMR Spectroscopy

The ¹¹⁹Sn{¹H} NMR spectrum of **2** was recorded at 25°C in a C₆D₆ solution and displays a single downfield resonance at 2129 ppm and is within the range of other two coordinate diorgano tin(II) species that range between 1200 and 2600 ppm.^(8,11,43–45,47) The X-ray structure of Sn(Ar^{Me6})₂ shows that the C_{ipso}–Sn–C_{ipso} angle is 114.7(3)°, and a solution ¹¹⁹Sn{¹H} NMR spectrum affords a signal centered at 1971 ppm⁵²³. The X-ray structure of Sn(Ar^{iPr4})₂ displays a wider C_{ipso}–Sn–C_{ipso} angle of 117.56(8)° and a solution ¹¹⁹Sn{¹H} NMR signal further downfield at 2235 ppm⁵²⁴. If the X-ray structure is correlated

with the $^{119}\text{Sn}\{^1\text{H}\}$ NMR spectrum, the $^{119}\text{Sn}\{^1\text{H}\}$ NMR chemical shift of **2** should appear upfield to those of $\text{Sn}(\text{Ar}^{\text{Me6}})_2$ and $\text{Sn}(\text{Ar}^{i\text{Pr4}})_2$. However, the $^{119}\text{Sn}\{^1\text{H}\}$ NMR chemical shift of **2** lies between those of $\text{Sn}(\text{Ar}^{\text{Me6}})_2$ and $\text{Sn}(\text{Ar}^{i\text{Pr4}})_2$. Tetrylenes substituted at the *para* position of the central aryl ring with the *p*-R-Ar^{Me6} moiety (R = -Cl or -SiMe₃) exhibit $^{119}\text{Sn}\{^1\text{H}\}$ resonances that are shifted upfield with respect to **2** at 1891 ppm (-Cl) and 1975 ppm (-SiMe₃) with X-ray structures having C_{ipso}-Sn-C_{ipso} angles of 115.30(8)° and 114.93(14)°, respectively⁵⁵⁸. The $^{119}\text{Sn}\{^1\text{H}\}$ NMR spectrum for $\text{Sn}(\text{C}_6\text{H}_2-2,6-(2,4,6-\text{Me}_3-\text{C}_6\text{H}_2)_2-3,5-i\text{Pr}_2)_2$ is also shifted upfield with respect to **2** and displays a resonance at 2081 ppm with a C_{ipso}-E-C_{ipso} angle of 123.89(12)° in the solid state.

²⁰⁷Pb NMR Spectroscopy

Despite numerous efforts to observe the $^{207}\text{Pb}\{^1\text{H}\}$ NMR of **3**, including changes of acquisition times, relaxation delays, and pulse angles, the $^{207}\text{Pb}\{^1\text{H}\}$ NMR of **3** was not observed, possibly as a result of the large anisotropies in the chemical shift tensor. Nonetheless, the $^{207}\text{Pb}\{^1\text{H}\}$ NMR gas phase chemical shift of **3** was calculated to resonate at 7374.46 ppm at the SO-ZORA-PBE0/ZORA/TZ2P//PBE0-D3(BJ)-ATM/def2-TZVP^{210,211,559-562} level of theory applying gauge-including atomic orbitals (GIAO)^{561,563,564} as implemented in the ADF2016 program package⁵⁶⁵, which is upfield to the values observed experimentally for $\text{Pb}(\text{Ar}^{\text{Me6}})_2$ (δ : 8884 ppm)⁵²⁴ and $\text{Pb}(\text{Ar}^{i\text{Pr4}})_2$ (δ : 9430 ppm)⁵²³ in solution (for details see the online Supporting Information of the original publication).

UV/VIS Spectroscopy

Compounds **1-3** have an intense blue color due to an n→p transition⁵²⁰. The λ_{max} for **1** (617 nm), **2** (612 nm), and **3** (588 nm) are red-shifted in comparison to the terphenyl-substituted tetrylenes, $\text{E}(\text{Ar}^{\text{Me6}})_2$ and $\text{E}(\text{Ar}^{i\text{Pr4}})_2$ (E = Ge, Sn, or Pb), consistent with a decrease in the HOMO-LUMO gap of the tetrylenes reported here, which also suggests an increase in reactivity. The tetrylene $\text{Ge}\{\text{C}_6\text{H}_2-2,6-(2,4,6-\text{Me}_3-\text{C}_6\text{H}_2)_2-3,5-i\text{Pr}_2\}_2$ displays a λ_{max} value of 622 nm, which is similar to the λ_{max} of **1**⁵⁵⁸. The λ_{max} values of $\text{E}\{\text{C}_6\text{H}_2-2,6-(2,4,6-\text{Me}_3-\text{C}_6\text{H}_2)_2-3,5-i\text{Pr}_2\}_2$ (E = Sn (591 nm) or Pb (566 nm)) are red-shifted compared to those of **2** and **3** respectively, indicating that **2** and **3** may be more reactive than the $\text{E}\{\text{C}_6\text{H}_2-2,6-(2,4,6-\text{Me}_3-\text{C}_6\text{H}_2)_2-3,5-i\text{Pr}_2\}_2$ series⁵⁶⁶. The λ_{max} data from selected tetrylenes are summarized in table 10.5.

Table 10.5.: UV/VIS absorption maxima λ_{max} in nm of selected tetrylenes^{523,524}.

	GeAr ₂	SnAr ₂	PbAr ₂
Ar ^{Me6}	578	553	526
Ar ^{iPr4}	608	600	586
Ar ^{iPr6}	617	612	588

10.4. Computational Studies

Computational studies were carried out applying Kohn-Sham Density Functional Theory (DFT) at the PBE0-D3(BJ)-ATM/def2-QZVP//PBE0-D3(BJ)-ATM/def2-TZVP^{213,240} level of theory for all nine tetrel ligand combinations. All molecular structures were optimized in the gas phase, and London dispersion corrections were included by the D3 dispersion correction model^{31,59,121} generally applying Becke–Johnson damping (BJ)^{122,123} if not otherwise stated. The Axilrod–Teller–Muto (ATM)^{124,125} type three-body dispersion energy was included to the total dispersion correction $E_{D3(BJ)-ATM}$. All molecular PBE0 calculations except $^{207}\text{Pb}\{^1\text{H}\}$ NMR chemical shift predictions were conducted with the TURBOMOLE 7.2 program package³⁷⁴. Crystal structures were fully optimized applying a scaled minimal basis set Hartree–Fock method with semi-classical correction potentials (sHF-3c)^{60,127,128} as implemented in the CRYSTAL17^{567,568} program package. The calculated gas-phase molecular structures of the tetraylenes show significant structural differences upon inclusion of dispersion corrections. The statistical deviations are shown by the mean absolute deviation (MAD) and the mean deviation (MD) relative to the crystallographically determined molecular structure cutout. The non-dispersion-corrected molecular geometries deviate significantly more from the crystallographic structures with systematically larger $C_{ipso}\text{--E--}C_{ipso}$ angles (MAD = 3.1°; MD = 3.1°) and elongated E– C_{ipso} bond distances (MAD = 0.021 Å; MD = 0.020 Å). Upon including the D3 dispersion correction the agreement of the calculated structures compared to the experiment increases significantly. The $C_{ipso}\text{--E--}C_{ipso}$ angles are reproduced well with a small MAD of 1.2° and a MD of 0.3° indicating that the computed values are scattering slightly around the experimental value. Also, the E– C_{ipso} bond distances (MAD = 0.011 Å; MD = 0.003 Å) are improved significantly. Furthermore, the experimentally observed structural distortion of the E– $C_{ipso}\text{--}C_{ortho}$ angles is shown to be clearly influenced by attractive dispersion interactions between both terphenyl ligands indicated by MADs of 1.2° for the dispersion corrected structure and 2.5° for the uncorrected structure. The other key structural distortions indicated by the angles E– $C_{ipso}\text{--}C_{para}$ and $C_{ortho}\text{--}C_{ipso,flanking}\text{--}C_{para,flanking}$ are deviating more strongly from the experimental structures with only slightly worse results for the uncorrected structures. An overview of the statistical data for the key structural characteristics is shown in table 10.6. The overall improvement is further indicated

Table 10.6.: Overall mean absolute deviation (MAD), mean deviation (MD), and maximal absolute deviation (AMAX) for the key structural characteristics of the calculated molecular structures with respect to the experimental structures: bond lengths in Å and angles in °.

		E– C_i	$C_i\text{--E--}C_i$	E– $C_i\text{--}C_o$	E– $C_i\text{--}C_p$	$C_o\text{--}C_{i,flank.}\text{--}C_{p,flank.}$
PBE0-D3	MAD	0.010	1.2	1.2	2.6	2.6
	MD	0.003	0.3	–0.12	0.3	1.0
	AMAX	0.021	2.4	4.8	9.6	5.5
PBE0	MAD	0.021	3.1	2.5	2.5	2.8
	MD	0.020	3.1	–0.04	0.16	1.2
	AMAX	0.035	9.3	6.2	15.0	7.0

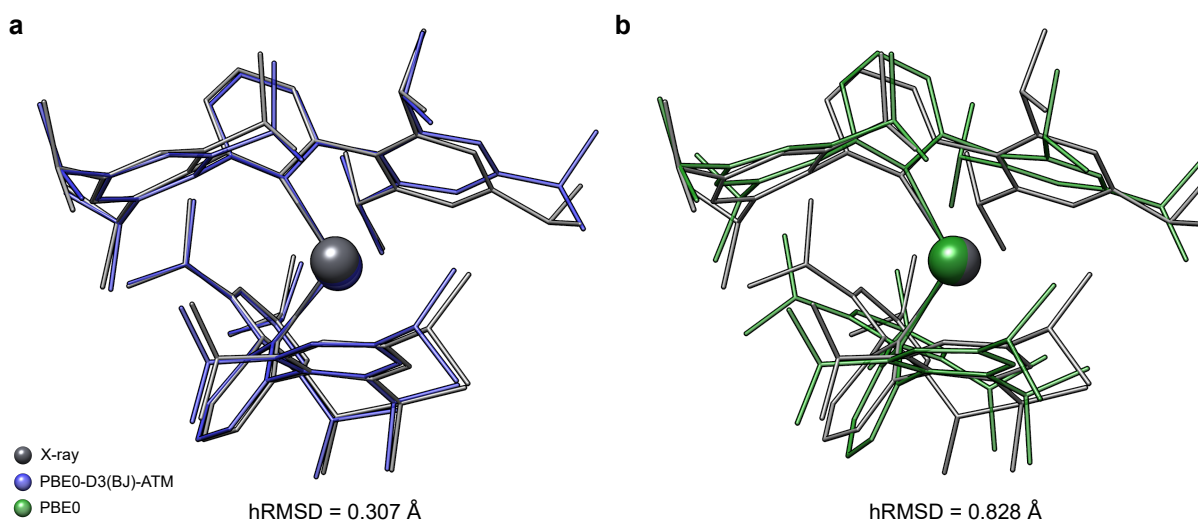


Figure 10.11.: Molecular overlays of the experimental and the optimized structures of **3** at the a) PBE0-D3(BJ)-ATM/def2-TZVP and the b) PBE0/def2-TZVP levels of theory.

by the mean heavy atom (all except H) root-mean-square deviations (MRMSD) of 0.55 Å without and 0.41 Å with dispersion corrections. As an example, the overlay of the calculated structure of $\text{Pb}(\text{Ar}^{i\text{Pr}_6})_2$ and the experimental structure is depicted in figure 10.11. Even though the calculated structural parameters and trends fit the crystal structure cutout-based data very well, a direct comparison of computed molecular gas-phase and experimental solid-state structures is far from being trivial as thermal expansion and so-called packing effects (intermolecular interactions) are not considered theoretically in a molecular approach. The literature on reliable theoretical treatments of packing effects is scarce. A few years ago, we studied the intramolecular sulfur–sulfur distance in a representative organic molecule with two intramolecularly π -stacked aromatic rings⁵⁶⁹ by periodic DFT-D3 calculations and derived a crystal-induced expansion of the S–S non-covalent contact of 0.1 Å. This is similar to the difference of $\Delta(d(\text{C}-\text{C})_{2,\text{X-ray}} - d(\text{C}-\text{C})_{2,\text{gas}}) = 0.094$ Å for the shortest C–C contact in **3** ($d(\text{C}-\text{C})_{2,\text{X-ray}} = 3.435$ Å to $d(\text{C}-\text{C})_{2,\text{gas}} = 3.341$ Å), indicating a physically sound behavior of the methods applied here. Furthermore, we can deduce that in cases for which we observe almost near coincidence between molecular and solid-state interatomic distances, packing effects play a minor role may be because the interacting fragments are not sufficiently exposed to the neighboring molecules in the unit cell to cause significant intramolecular structural deviations. To further validate a molecular approach and the importance of dispersion interactions for the presented systems, we conducted exemplary periodic crystal structure optimizations applying the fast sHF-3c method for **3** with and without D3 dispersion corrections. The calculated crystal structure including the D3 dispersion correction shows good agreement with the experiment (Figure 10.12, $\text{RMSD}_{15} = 0.553$ Å)^a while exclusion of dispersion corrections causes a complete breakdown of the crystal structure causing no further RMSD_{15} match and reducing the unit cell density significantly ($\Delta\rho = -0.659$ g·cm⁻³). A comparison of the calculated solid-state and gas-phase

^aFor the crystal structure comparison the RMSD_1 represents the root-mean-square derivation of a mononuclear cutout while RMSD_{15} represents the deviation of a cutout consisting of a cluster of 15 molecules.

10. Counterintuitive Interligand Angles in Diaryltetrelenes and Related Species: The Role of Dispersion

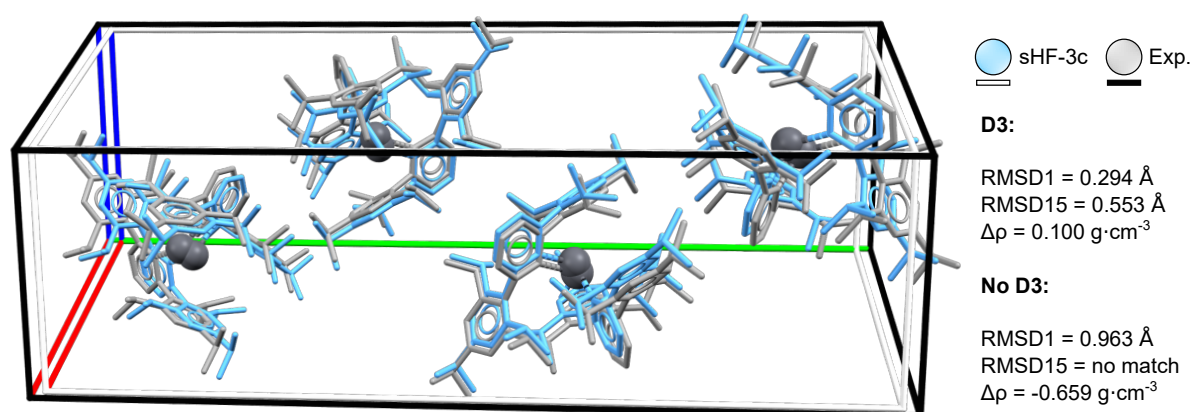


Figure 10.12.: Overlay plot of the calculated unit cell (light blue molecules, white cell border) at sHF-3c level of theory including the D3 dispersion correction and the crystallographically obtained unit cell of **3** (gray molecules, black cell border).

molecular structures of **3** at sHF-3c level of theory indicates only very small influence of intermolecular interactions to the $C_{ipso}-E-C_{ipso}$ angles in the presented systems with a deviation of only 0.4° . The analysis of the intramolecular interligand dispersion interaction energies between the terphenyl ligands (Table 10.7) shows two expected trends of a decrease with the increased size of the tetrel atom ($E_{D3,interligand}(\text{Ge}) > E_{D3,interligand}(\text{Sn}) > E_{D3,interligand}(\text{Pb})$) and an increase in the number of introduced isopropyl groups and therefore the size of the ligand ($E_{D3,interligand}(\text{Pb}, \text{Ar}^{\text{Me}6}) < E_{D3,interligand}(\text{Pb}, \text{Ar}^{\text{iPr}4}) < E_{D3,interligand}(\text{Pb}, \text{Ar}^{\text{iPr}6})$). A more detailed analysis involving the distance distribution of the pairwise dispersion energies in $\text{Pb}(\text{Ar}^{\text{iPr}6})_2$ (Figure 10.13a) shows that the distance region between 2.7 and 4.5 Å is the most important in terms of stabilizing interligand dispersion interactions between the two

Table 10.7.: D3 London dispersion energy corrections for PBE0 and B3LYP calculated on PBE0-D3(BJ)-ATM/def2-TZVP geometries. All energies in kcal mol^{-1} .^a

	PBE0		B3LYP	
	$E_{D3(\text{BJ})-\text{ATM}}$	$E_{D3, interligand}$	$E_{D3(\text{BJ})-\text{ATM}}$	$E_{D3, interligand}$
$\text{Ge}(\text{Ar}^{\text{Me}6})_2$	-100.882	-17.167	-182.762	-23.372
$\text{Sn}(\text{Ar}^{\text{Me}6})_2$	-100.481	-15.533	-182.464	-21.016
$\text{Pb}(\text{Ar}^{\text{Me}6})_2$	-100.602	-14.952	-183.070	-20.154
$\text{Ge}(\text{Ar}^{\text{iPr}4})_2$	-141.996	-22.965	-252.616	-30.230
$\text{Sn}(\text{Ar}^{\text{iPr}4})_2$	-144.223	-21.634	-257.453	-28.864
$\text{Pb}(\text{Ar}^{\text{iPr}4})_2$	-143.033	-20.213	-256.116	-26.754
$\text{Ge}(\text{Ar}^{\text{iPr}6})_2$	-171.659	-27.504	-304.430	-36.061
$\text{Sn}(\text{Ar}^{\text{iPr}6})_2$	-172.981	-26.543	-307.371	-35.095
$\text{Pb}(\text{Ar}^{\text{iPr}6})_2$	-171.610	-24.614	-305.678	-32.501

^a $E_{D3,interligand}$ represents the interligand dispersion correction contribution compared to the total $E_{D3(\text{BJ})-\text{ATM}}$.

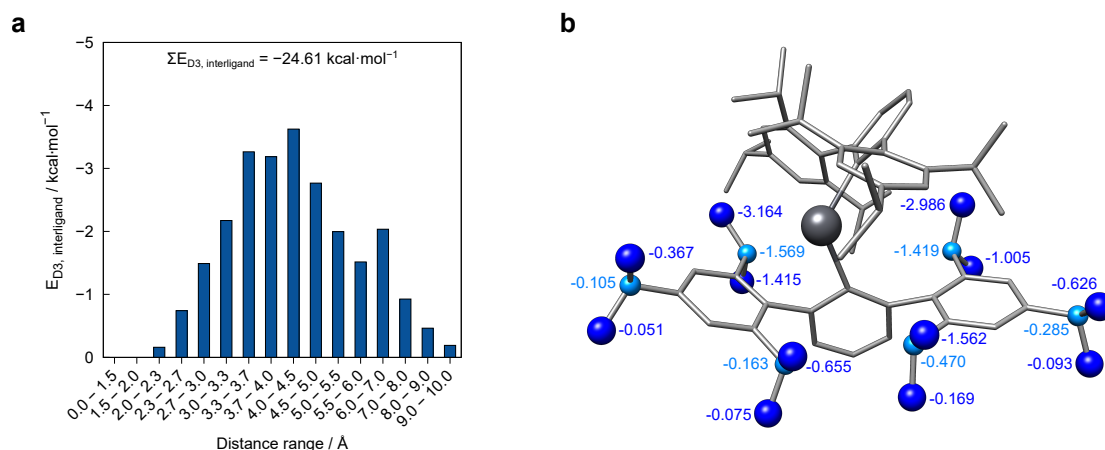


Figure 10.13.: a) Distance distribution of the interligand dispersion correction contributions in $\text{Pb}(\text{Ar}^{i\text{Pr}6})_2$. b) Simplified plot of the isopropyl groups in $\text{Pb}(\text{Ar}^{i\text{Pr}6})_2$ with methyl groups in blue and the methine moieties in cyan. The sums of all pairwise contributions of the respective moieties are given in kcal mol^{-1} .

terphenyl ligands in the discussed compound class. The role of the isopropyl groups in $\text{Ar}^{i\text{Pr}6}$ can be understood by investigating their specific contribution to the interligand dispersion (Figure 10.13b). The pairwise interactions of the isopropyl groups with the other ligand yield $-16.18 \text{ kcal mol}^{-1}$, which represents 66% of the whole interligand dispersion correction. A detailed look at selected pairwise contributions including the largest overall pairwise contribution $-0.123 \text{ kcal mol}^{-1}$ between the carbon atom of a methyl moiety of an isopropyl group and an aryl carbon of the other terphenyl ligand is depicted in figure 10.14, in which the interactions are indicated as dashed blue lines.

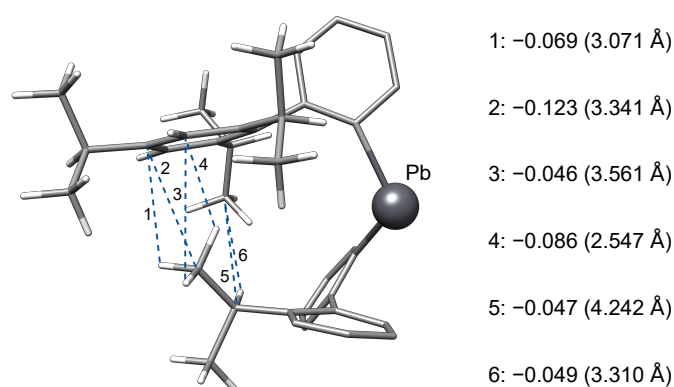


Figure 10.14.: Plot of the cutout of the highest contributing isopropyl moiety to the interligand interaction in $\text{Pb}(\text{Ar}^{i\text{Pr}6})_2$ and selected pairwise dispersion contributions. All energy values in kcal mol^{-1} .

10.5. Conclusion

In conclusion, the combined computational and experimental studies indicate that the experimentally observed $C_{ipso}-E-C_{ipso}$ angles appear to be contracted partially due to attractive dispersion force interactions in contrast to an increase in the $C_{ipso}-E-C_{ipso}$ angle that is expected from steric considerations. The large influence of the isopropyl groups on the interligand attraction can be used to strongly influence the structural characteristics of bis(terphenyl) tetraylenes. A good description of dispersion interactions, e.g. with the D3 dispersion model applied to DFT, has once more proven indispensable for the correct calculations and understanding of molecular structures of organometallic compounds involving large ligand systems.

Acknowledgements

We wish to thank the National Science Foundation (CHE-1565501) for support of this work and for the funding (Grant Nos. 0840444 and 1531193) for the purchase of a dual-source and dual-microsource X-ray diffractometer. This work was further supported by the Deutsche Forschungsgemeinschaft (DFG) in the framework of the Gottfried Wilhelm Leibniz prize to S.G. We further thank Dr. J. G. Brandenburg for support with the periodic calculations.

11. Isolation and Computational Studies of a Series of Terphenyl Substituted Diplumbynes with Ligand Dependent Lead–Lead Multiple-Bonding Character

Joshua D. Queen,^a Markus Bursch,^b Jakob Seibert,^b Leonard R. Maurer,^b Bobby D. Ellis,^a James C. Fettinger,^a Stefan Grimme,^b and Philip P. Power^a

Received: 8 July 2019, Published online: 7 August 2019

Reprinted (adapted) with permission[†] from

Queen, J. D.; Bursch, M.; Seibert, J.; Maurer, L. R.; Ellis, B. D.; Fettinger, J. C.; Grimme, S.; Power, P. P. *J. Am. Chem. Soc.* **2019**, *141*, 14370–14383.

– Copyright © 2019 American Chemical Society.

DOI [10.1021/jacs.9b07072](https://doi.org/10.1021/jacs.9b07072)

Own manuscript contribution

- Performing all DFT and SQM calculations (except for the MD simulations)
- Interpretation of the computational results
- Co-writing the manuscript

^aDepartment of Chemistry, University of California-Davis, 1 Shields Avenue, Davis, California 95616, USA

^bMulliken Center for Theoretical Chemistry, Institut für Physikalische und Theoretische Chemie, Rheinische Friedrich-Wilhelms-Universität Bonn, Beringstraße 4, 53115 Bonn, Germany

[†]Permission requests to reuse material from this chapter should be directed to the American Chemical Society.

11. Terphenyl Substituted Diplumbynes with Ligand Dependent Lead–Lead Multiple-Bonding Character

Abstract A series of formally triply bonded diplumbyne analogues of alkynes of the general formula ArPbPbAr (Ar = terphenyl ligand with different steric properties) was synthesized by two routes. All diplumbyne products were synthesized by a simple reduction of the corresponding Pb(II) halide precursor ArPb(Br) by DIBAL-H with yields in the range 8–48%. For one of the diplumbynes $\text{Ar}^{i\text{Pr}_4}\text{PbPbAr}^{i\text{Pr}_4}$ ($\text{Ar}^{i\text{Pr}_4} = \text{C}_6\text{H}_3\text{-2,6-(C}_6\text{H}_3\text{-2,6-}i\text{Pr}_2)_2$) it was shown that reduction of $\text{Ar}^{i\text{Pr}_4}\text{Pb(Br)}$ using a magnesium(I) β -diketiminate afforded a much improved yield in comparison (29 vs. 8%) to that obtained by reduction with DIBAL-H. The more sterically crowded diplumbyne $\text{Ar}^{i\text{Pr}_8}\text{PbPbAr}^{i\text{Pr}_8}$ ($\text{Ar}^{i\text{Pr}_8} = \text{C}_6\text{H-3,5-}i\text{Pr}_2\text{-2,6-(C}_6\text{H}_2\text{-2,4,6-}i\text{Pr}_3)_2$) displayed a shortened Pb–Pb bond with a length of 3.0382(5) Å and wide Pb–Pb–C angles of 114.73(7)° and 116.02(6)° consistent with multiple-bond character with a bond order of up to 1.5. The others displayed longer metal-metal distances and narrower Pb–Pb–C angles that were consistent with a lower bond order that approached one. Computational studies of the diplumbynes yielded detailed insight of the unusual bonding and explained their similar electronic spectra arising from the flexibility of the C–Pb–Pb–C core in solution. Furthermore, the importance of London dispersion interactions for the stabilization of the diplumbynes was demonstrated.

11.1. Introduction

The first stable, heavy group 14 element analogue of an alkyne was the diplumbyne $\text{Ar}^{i\text{Pr}_6}\text{PbPbAr}^{i\text{Pr}_6}$ ($\text{Ar}^{i\text{Pr}_6} = \text{C}_6\text{H}_3\text{-2,6-(C}_6\text{H}_2\text{-2,4,6-}i\text{Pr}_3)_2$) (**1**), the syntheses and characterization of which was reported in 2000⁵⁷⁰. The following four years saw the synthesis of the remaining heavy element compounds of the series REER ($\text{E} = \text{Si, Ge, Sn}$; $\text{R} = \text{aryl, silyl}$)^{571–575} and a growing number of group 14 dimetallynes of the elements Si–Sn continue to appear in the literature^{576–584}. No further examples of diplumbynes have been characterized, however. As a class the heavier group 14 element analogues have garnered interest because of their peculiar structures and bonding that differ markedly from their carbon congeners. Unlike the carbon-based alkynes, they all possess trans-bent REER cores (**B**, figure 11.1), whose bending increases as the group is descended, until it reaches nearly 90° in the case of lead (**C**, figure 11.1) (cf. 94.26(4)°, experimental value for the diplumbyne **1** below)⁵⁷⁰. In effect, the increasing atomic

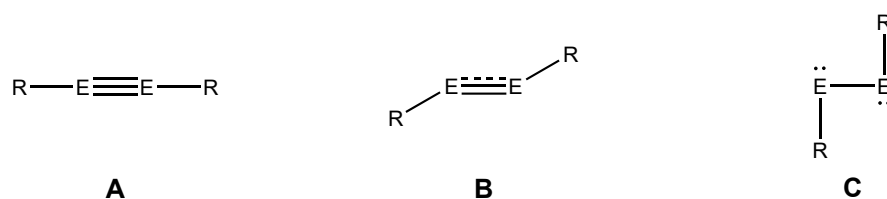


Figure 11.1.: Bonding motifs of REER ($\text{E} = \text{C-Pb}$, $\text{R} = \text{alkyl, aryl, amide, silyl}$).

number upon descending the group results in increasing nonbonding, lone pair character at the group 14 element. The original triple bond in the carbon-based alkynes is transformed into a single bond and two nonbonded pairs in the case of lead. These pairs are now mostly 6s in character and the remaining single bond is a result of head-to-head overlap of a 6p orbital from each lead atom which affords an unusually long Pb–Pb bond (3.1881(1) Å in **1**), (cf. 2.9 Å expected from the sum of the single bond

radii)⁵⁸⁵. This result is consistent with decreasing hybridization of the elements that occurs upon descending the group⁵⁸⁶. Early calculations by Frenking and co-workers suggested that the single bonded structure of the original diplumbyne $\text{Ar}^{i\text{Pr}_6}\text{PbPbAr}^{i\text{Pr}_6}$ in the crystalline phase is partially stabilized by packing forces and indicated via calculations on less crowded model terphenyl ligands that structures having wider bending angles and some multiple Pb–Pb bond character were more stable⁵⁸⁷. Later calculations by Takagi and Nagase proposed that the diplumbyne assumes a less trans-bent multiple bonded isomeric form in solution and that the multiple and single bonded forms might be distinguishable by UV/VIS spectroscopy⁵⁸⁸. Previous work by our group on terphenyl substituted distannynes, which generally take multiply bonded trans-bent structures in the crystalline phase, showed that use of a *para*-substituent on the central ring of the terphenyl ligand can afford a single bonded distannyne in the crystalline form⁵⁷⁶. Presumably, this occurs as a result of changed packing forces, but this possibility has not been examined in detail, however. Nonetheless, UV/VIS spectroscopy has shown that the spectra of all distannynes are similar in solution and consistent with a multiple bonded structure⁵⁸⁹. Calculations have shown that the energy difference between the single and multiple bonded structures is relatively small, only ca. 5 kcal mol⁻¹ in the case of 4-Me₃Si-Ar^{*i*Pr₄}SnSnAr^{*i*Pr₄}-4-SiMe₃, an amount that is in the range of interactions generalized under the collective term “packing effects” in the solid phase (i.e., intermolecular London dispersion interactions)^{558,589–591}. Ziegler and co-workers showed that isopropyl groups on the terphenyl substituents play an important role in stabilizing the group 14 alkyne analogue structures via intramolecular dispersion interactions (cf. –44.0 kcal mol⁻¹ stabilization energy in the case of Ar^{*i*Pr₆}PbPbAr^{*i*Pr₆})⁵⁹². Given these observations, and the calculations of Takagi and Nagase which assume that in a gas phase structure without packing effects the multiple bonded structure is preferred, we sought to isolate an array of the multiple bonded diplumbyne isomers by altering the substituents on the terphenyl ligand. These investigations have afforded a series of new diplumbynes, ArPbPbAr, (Ar = terphenyl) (Figure 11.2) that show a considerable variation of the trans-bending and torsion angles as well as the Pb–Pb distance in the C_{*ipso*}–Pb–Pb–C_{*ipso*} core, including the highly substituted Ar^{*i*Pr₈}PbPbAr^{*i*Pr₈} (Ar^{*i*Pr₈} = C₆H-2,6-(C₆H₂-2,4,6-*i*Pr₃)₂-3,5-*i*Pr₂) which contains a shortened Pb–Pb bond with bond orders between 1.2 and 1.5.

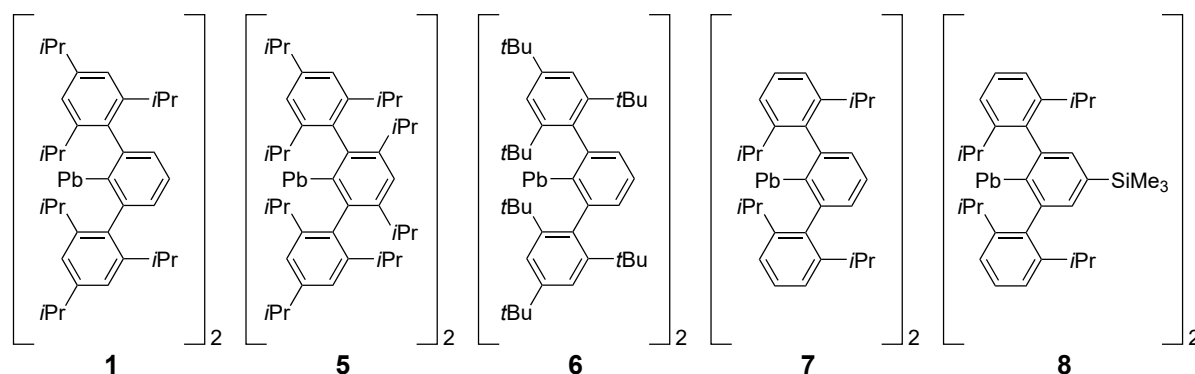


Figure 11.2.: Lewis representations of compounds 1, 5-8.

11.2. Experimental Section

General Procedures

All manipulations were carried out using modified Schlenk techniques or in a Vacuum Atmospheres OMNI-Lab drybox under a N₂ or argon atmosphere. Manipulations of the lead compounds were carried out with careful exclusion of light when possible due to the tendency of low-valent lead compounds to decompose or disproportionate. Solvents were dried over columns of activated alumina using a Grubbs type purification system⁵⁹³ (Glass Contour), stored over Na (Et₂O) or K (hexanes, pentane, toluene) mirrors, and degassed via three freeze-pump-thaw cycles prior to use. ¹H and ¹³C{¹H} spectra were recorded on a Varian Inova 600 MHz spectrometer and were referenced to the residual solvent signals in C₆D₆⁵⁹⁴. UV/VIS spectra were recorded in dilute hexane solutions in 3.5 mL quartz cuvettes using an Olis 17 Modernized Cary 14 UV/VIS/NIR spectrophotometer. Melting points were measured in glass capillary tubes sealed under argon using a Mel-Temp II apparatus and are uncorrected. [Li(Et₂O)Ar^{iPr8}] was synthesized from Ar^{iPr8}I⁵³⁸ (see the online Supporting Information of the original publication). [Li(Et₂O)₂Ar^{tBu6}]⁵⁹⁵ (Ar^{tBu6} = C₆H₃-2,6-(C₆H₂-2,4,6-*t*Bu₃)₂), LiAr^{iPr4}-4-SiMe₃⁵⁹⁶ (Ar^{iPr4}-4-SiMe₃ = C₆H₂-4-SiMe₃-2,6-(C₆H₃-2,6-*i*Pr₂)₂), {Pb(μ-Br)Ar^{iPr4}}₂⁵⁹⁷ (Ar^{iPr4} = C₆H₃-2,6-(C₆H₃-2,6-*i*Pr₂)₂), and [Mg^{Mes}Nacnac]₂ (MesNacnac = [HC{MeCN(C₆H₂-2,4,6-Me₃)₂}]₂)⁵⁹⁸ were synthesized according to the literature methods. PbBr₂ and DIBAL-H (neat or 1.0 M in hexanes) were purchased commercially and used without further purification.

{Pb(μ-Br)Ar^{iPr8}}₂ (2)

A solution of [Li(Et₂O)Ar^{iPr8}] (3.12 g, 4.82 mmol) in Et₂O (ca. 40 mL) was added dropwise over ca. 30 min to a stirred suspension of PbBr₂ (1.77 g, 4.82 mmol) in Et₂O (ca. 10 mL) cooled to ca. 0°C in an ice bath. The mixture was allowed to warm to ambient temperature and stirred for a further 16 h. The ether solvent was removed under reduced pressure and the orange residue was extracted with ca. 60 mL hexanes. The filtrate was concentrated to ca. 15 mL under reduced pressure and allowed to stand at ambient temperature overnight to give orange crystals of **2**. Yield: 2.15 g (52%). mp 159-162°C (dec). ¹H NMR (600 MHz, C₆D₆, 298 K) δ 7.59 (s, 2H, ArH), 7.24 (s, 8H, ArH), 3.01 (sept, ³J = 6.9 Hz, 8H, -CH(CH₃)₂), 2.80 (sept, ³J = 6.9 Hz, 4H, -CH(CH₃)₂), 2.71 (sept, ³J = 6.8 Hz, 4H, -CH(CH₃)₂), 1.44 (d, ³J = 6.8 Hz, 24H, -CH(CH₃)₂), 1.27 (d, ³J = 6.7 Hz, 24H, -CH(CH₃)₂), 1.24 (d, ³J = 6.9 Hz, 24H, -CH(CH₃)₂), 1.15 (d, ³J = 6.8 Hz, 24H, -CH(CH₃)₂). ¹³C{¹H} NMR (151 MHz, C₆D₆, 298 K) δ 156.0, 149.3, 147.6, 141.8, 134.2, 122.7, 121.4, 34.8, 30.7, 30.6, 26.1, 25.5, 25.4, 24.3. UV/VIS (hexanes) λ_{max} (nm, ε in L mol⁻¹ cm⁻¹): 456 (750).

{Pb(μ-Br)Ar^{tBu6}}₂ (3)

A solution of [Li(Et₂O)₂Ar^{tBu6}]⁵⁹⁵ (1.19 g, 1.65 mmol) in Et₂O (ca. 30 mL) was added dropwise over ca. 5 min to a stirred suspension of PbBr₂ (0.606 g, 1.65 mmol) in Et₂O (ca. 10 mL) cooled to ca. 0°C in an ice bath. The mixture was warmed to ambient temperature after ca. 30 min and stirred for 18 h. The ether solvent was removed under reduced pressure and the yellow-orange solid was extracted twice

with ca. 60 mL hexanes. The combined filtrates were concentrated to ca. 20 mL under reduced pressure and stored at ca. 8°C overnight to give yellow crystals of **3**. Yield: 0.625 g (44%). mp 215-220°C (dec). ^1H NMR (600 MHz, C_6D_6 , 298 K) δ 8.41 (d, $^3J = 7.6$ Hz, 4H, ArH), 7.61 (s, 8H, ArH), 7.11 (t, $^3J = 7.6$ Hz, 2H, ArH), 1.35 (s, 72H, $-\text{C}(\text{CH}_3)_3$), 1.34 (s, 36H, $-\text{C}(\text{CH}_3)_3$). $^{13}\text{C}\{^1\text{H}\}$ NMR (151 MHz, C_6D_6 , 298 K) δ 149.8, 148.1, 141.6, 123.5, 39.1, 35.0, 31.5. UV/VIS (hexanes) λ_{max} (nm, ϵ in $\text{L mol}^{-1} \text{cm}^{-1}$): 415 nm (960).

$\{\text{Pb}(\mu\text{-Br})\text{Ar}^{i\text{Pr}4}\text{-4-SiMe}_3\}_2$ (4**)**

A solution of $\text{LiAr}^{i\text{Pr}4}\text{-4-SiMe}_3$ (**29**) (1.73 g, 3.36 mmol) in Et_2O (ca. 20 mL) was added dropwise over ca. 10 min to an Et_2O (ca. 10 mL) suspension of PbBr_2 (1.33 g, 3.62 mmol) cooled to ca. 0°C in an ice bath. The green mixture was warmed to room temperature and stirred for three days to afford an orange solution. The ether solvent was removed under reduced pressure and the orange residue was extracted twice with hexanes (ca. 80 mL). The combined extracts were concentrated to ca. 15 mL under reduced pressure and stored at ca. -18°C to give yellow crystals of **4**. Yield: 1.35 g (51%). mp 206-210 °C (dec). ^1H NMR (600 MHz, C_6D_6 , 298 K) δ 8.25 (s, 4H, ArH), 7.23 (t, $^3J = 7.4$ Hz, 4H, ArH) 7.16 (d, $^3J = 7.4$ Hz, 8H, ArH), 3.13 (sept, $^3J = 6.8$ Hz, 8H, $-\text{CH}(\text{CH}_3)_2$), 1.34 (d, $^3J = 6.8$ Hz, 24H, $-\text{CH}(\text{CH}_3)_2$) 1.03 (d, $^3J = 6.8$ Hz 24 H, $-\text{CH}(\text{CH}_3)_2$), 0.25 (s, 18H, $-\text{Si}(\text{CH}_3)_3$). $^{13}\text{C}\{^1\text{H}\}$ NMR (151 MHz, C_6D_6 298 K) δ 147.9, 146.8, 142.6, 138.9, 137.4, 129.3, 123.7, 30.8, 26.2, 23.7, -1.3. UV/VIS (hexanes) λ_{max} (nm, ϵ in $\text{L mol}^{-1} \text{cm}^{-1}$): 423 (840).

$\text{Ar}^{i\text{Pr}8}\text{PbPbAr}^{i\text{Pr}8} \cdot 1.5 \text{C}_7\text{H}_8$ (5**·1.5 C_7H_8)**

A solution of **2** (0.429 g, 0.250 mmol) in Et_2O (ca. 30 mL) was cooled to ca. -78°C with an ethanol/dry ice bath. A freshly prepared solution of DIBAL-H (0.10 mL, 0.56 mmol) in Et_2O (ca. 15 mL) was added dropwise over ca. 10 min. The mixture was slowly warmed over 2 h to ambient temperature then stirred for an additional ca. 30 min. The volatile components were removed under reduced pressure and the dark red residue was extracted with hexanes (ca. 40 mL). The solvent was removed under reduced pressure and the residue was dissolved in ca. 3 mL of toluene. Storage at ca. -30°C overnight gave **5** as red crystals. Yield: 0.196 g (48%). mp 141-146°C (dec). ^1H NMR (600 MHz, C_6D_6 , 298 K) δ 6.96 (s, 8H, ArH), 5.77 (s, br, 2H, ArH), 3.10 (sept, br, $^3J = 8\text{H}$), 3.01 (sept, $^3J = 7.0$ Hz, 4H), 2.37 (sept, $^3J = 6.7$ Hz, 4H), 1.43 (d, $^3J = 6.9$ Hz, 24H), 1.36 (d, $^3J = 6.6$ Hz, 24 H), 1.30 (d, $^3J = 6.5$ Hz, 24H), 1.16 (d, $^3J = 6.7$ Hz, 24H). $^{13}\text{C}\{^1\text{H}\}$ NMR (151 MHz, C_6D_6 298 K) δ 149.7, 147.4, 137.9, 133.4 129.3, 128.6, 125.7, 125.1, 34.6, 31.9, 30.89, 26.4, 24.8, 24.2, 21.5. UV/VIS (hexanes) λ_{max} (nm, ϵ in $\text{L mol}^{-1} \text{cm}^{-1}$): 429 nm (9300), 757 (2700).

$\text{Ar}^{t\text{Bu}6}\text{PbPbAr}^{t\text{Bu}6}$ (6**)**

A solution of **3** (0.200 g, 0.117 mmol) in Et_2O (ca. 15 mL) was cooled to ca. -78°C with an ethanol/dry ice bath. A freshly prepared solution of DIBAL-H (0.45 mL, 0.25 mmol) in Et_2O (ca. 5 mL) was added dropwise over ca. 2 min. The mixture was warmed to ambient temperature over 1 h and stirred for an additional ca. 30 min. The solvent was removed under reduced pressure and the dark green residue was extracted with pentane (ca. 30 mL). The solution was concentrated to ca. 10 mL and stored at ca.

11. Terphenyl Substituted Diplumbynes with Ligand Dependent Lead–Lead Multiple-Bonding Character

–30°C overnight to give **6** as green blocks. Yield: 0.045 g (23%). mp 132–140°C (dec). ^1H NMR (600 MHz, C_6D_6 , 298 K) δ 7.91 (d, $^3J = 7.5$ Hz, 2H, ArH), 7.62 (s, 4H, ArH), 6.63 (t, $^3J = 7.6$ Hz, 1H, ArH), 1.43 (s, 18H, *p*- $\text{C}(\text{CH}_3)_3$), 1.26 (s, 36H, *o*- $\text{C}(\text{CH}_3)_3$). $^{13}\text{C}\{^1\text{H}\}$ NMR (151 MHz, C_6D_6 298 K) δ 157.2, 150.6, 148.3, 143.1, 136.4, 123.6, 39.3, 37.5, 34.9, 34.3, 32.5, 31.6, 31.5. UV/VIS (hexanes) λ_{max} (nm, ϵ in $\text{L mol}^{-1} \text{ cm}^{-1}$): 388 (7000), 668 (900).

$\text{Ar}^{i\text{Pr}4}\text{PbPbAr}^{i\text{Pr}4}$ (7)

Method A: A solution of $\{\text{Pb}(\mu\text{-Br})\text{Ar}^{i\text{Pr}4}\}_2$ ⁵⁹⁷ (0.525 g, 0.383 mmol) in Et_2O (50 mL) was cooled to ca. –78°C with an ethanol/dry ice bath and 1.0 DIBAL-H in hexanes (0.78 mL, 0.78 mmol) was added via syringe. The mixture was warmed to room temperature over 30 min and stirred an additional 2 h. The reaction mixture was filtered and the solution was stored at ca. –18°C for 2 weeks to give amber blocks of **7**. Yield: 0.035 g (8%). Method B: A solution of $\{\text{Pb}(\mu\text{-Br})\text{Ar}^{i\text{Pr}4}\}_2$ (0.400 g, 0.292 mmol) in ether (ca. 15 mL) was cooled to ca. 0°C in an ice/water bath. A solution of $[\text{Mg}^{\text{Mes}}\text{Nacnac}]_2$ ⁵⁹⁶ (0.210 g, 0.292 mmol) in ether (ca. 10 mL) was added dropwise over ca. 3 min, resulting in an immediate darkening of the solution. The reaction mixture was removed from the cooling bath and stirred a further 15 min. The ether was decanted and the dark powder washed with hexanes (ca. 15 mL). The olive-green powder was identified as **7** by its ^1H NMR spectrum and sharp melting point (dec). Yield: 0.104 g (29%). mp = 168–171°C (dec). ^1H NMR (600 MHz, C_6D_6 , 298 K) δ 7.66 (d, $^3J = 7.5$ Hz, 4H, ArH) 7.24 (t, $^3J = 7.7$ Hz, 4H, ArH), 6.99 (d $^3J = 7.8$ Hz, 8H, ArH) 6.69 (t, $^3J = 7.5$ Hz, 2H, ArH) 3.29 (sept, $^3J = 6.9$ Hz, 8H, $-\text{CH}(\text{CH}_3)_2$), 1.09 (d, $^3J = 6.8$ Hz, 24H, $-\text{CH}(\text{CH}_3)_2$), 0.93 (d, $^3J = 7.0$ Hz, 24H, $-\text{CH}(\text{CH}_3)_2$). $^{13}\text{C}\{^1\text{H}\}$ NMR (151 MHz, C_6D_6 298 K) δ 148.2, 136.5, 133.0, 128.7, 128.4, 124.7, 31.7, 28.8, 26.7. UV/VIS (hexanes) λ_{max} (nm, ϵ in $\text{L mol}^{-1} \text{ cm}^{-1}$): 682 (1200), 400 (11000).

4- $\text{Me}_3\text{Si-Ar}^{i\text{Pr}4}\text{PbPbAr}^{i\text{Pr}4}$ -4- $\text{SiMe}_3 \cdot \text{Et}_2\text{O}$ (8· Et_2O)

A solution of **4** (0.600 g, 0.396 mmol) in diethyl ether (ca. 30 mL) was cooled to ca. –78°C in an ethanol/dry ice bath and 1.0 M DIBAL-H in hexanes (0.79 mL, 0.79 mmol) was added via syringe. The mixture was warmed to ambient temperature over ca. 30 min and stirred an additional 2 h. The solvent was removed under reduced pressure and the residue extracted with pentane (ca. 20 mL). The filtrate was concentrated to ca. 10 mL and stored at ca. –30°C overnight to give amber-green dichroic blocks of **8·Et₂O**. Yield: 0.173 g (32%). mp = 151–156°C (dec). ^1H NMR (600 MHz, C_6D_6 , 298 K) δ 7.49 (s, 4H, ArH), 7.34 (t, $^3J = 7.7$ Hz, 4H, ArH), 7.22 (d, $^3J = 7.7$ Hz, 8H, ArH), 2.95 (sept, $^3J = 6.8$ Hz, 8H, $-\text{CH}(\text{CH}_3)_2$), 1.16 (mult, $^3J = 6.9$ Hz, 48H, $-\text{CH}(\text{CH}_3)_2$), 0.21 (s, 18H, $-\text{Si}(\text{CH}_3)_3$). $^{13}\text{C}\{^1\text{H}\}$ NMR (151 MHz, C_6D_6 298 K) δ 147.0, 140.4, 140.2, 140.1, 133.1, 133.0, 128.5, 31.0, 30.8, 24.50, 24.46, 24.39, 24.35, –1.2. UV/VIS (hexanes) λ_{max} (nm, ϵ in $\text{L mol}^{-1} \text{ cm}^{-1}$): 410 (18000), 655 (860).

X-ray Crystallography

Crystals of **2–8** were removed from a Schlenk flask under a stream of nitrogen and immediately covered with hydrocarbon oil. A suitable crystal was selected, attached to a glass fiber on a copper pin and placed in the cold N_2 stream on the diffractometer. Data were collected at 90 K on a Bruker APEX

II diffractometer with Mo K_{α} radiation ($\lambda = 0.71073 \text{ \AA}$). Absorption corrections were applied using SADABS⁵⁹⁹ (2, 3, 5, 6, 8) or TWINABS⁶⁰⁰ (4, 7) The crystal structures were solved by intrinsic phasing methods using SHELXT⁶⁰¹ and refined by full matrix least-squares procedures using SHELXL⁶⁰². All non-H atoms were refined anisotropically. Disordered solvent in **3** was treated using the SQUEEZE algorithm⁵⁵⁴.

Computational Methods

Quantum mechanical calculations were performed with the TURBOMOLE 7.0.2^{206,207}, ORCA 4.1.0^{208,603}, xtb 6.1.0^{57,604}, and NBO6.0⁶⁰⁵ program packages. Geometries were preoptimized in the gas-phase from the experimental structures applying the GFN2-xTB⁵⁴ extended tight binding method. All structures were further optimized at TPSS⁶⁰⁶-D3(BJ)^{31,59,121}-ATM^{124,125}/def2-TZVP²⁴⁰ level of theory. Gibbs free energies were calculated at PBE0²¹³ and B3LYP^{607,608}+COSMO-RS^{371,372,609}(toluene)/def2-TZVPP level in combination with the D3 and D4^{115,116} dispersion correction schemes. All bond order and orbital analyses were conducted at TPSS-D3(BJ)-ATM/def2-TZVP level of theory. UV/VIS spectra were calculated at sTDA-xTB⁶¹⁰(GBSA(toluene))/TPSS-D3(BJ)-ATM/def2-TZVP and sTD^{611,612}-BHLYP⁹⁵/def2-TZVP level. Molecular dynamics simulations were performed at GFN2-xTB(GBSA(toluene)) level. For further computational details see the appendix A10.

11.3. Results and Discussion

Synthesis and Spectroscopy

The terphenyl lead(II) bromide precursors **2-4** were synthesized following established procedures^{597,613,614} by addition of a diethyl ether solution of the terphenyl lithium salt to a diethyl ether suspension of PbBr_2 . During the preparation of **4**, the reaction mixture assumed a dark green color, likely due to some formation of the diarylplumbylene $\text{Pb}(\text{Ar}^{i\text{Pr}4}\text{-4-SiMe}_3)_2$. Continued stirring of the reaction mixture for an extended time (ca. 3 days) leads to redistribution with the remaining unreacted PbBr_2 to afford **4**. The aryl lead bromides form yellow to orange crystals which are thermally stable up to their melting points, but are prone to decomposition by light over extended periods of time, noted by a darkening of color or deposition of lead metal. The diplumbyne **1** was originally synthesized in ca. 10% yield

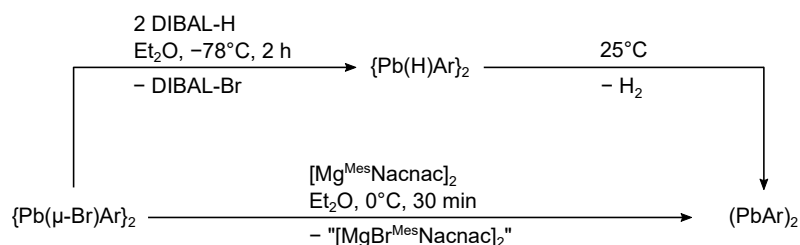


Figure 11.3.: Synthetic routes for diplumbynes. Reduction of the aryl lead(II)bromides with DIBAL-H forms the lead(II) hydride *in situ*, which releases H_2 upon warming to give compounds **1**, **5-8**. Alternatively, reduction with $[\text{Mg}^{\text{Mes}}\text{Nacnac}]_2$ was used to give **1** and **7**.

11. Terphenyl Substituted Diplumbynes with Ligand Dependent Lead–Lead Multiple-Bonding Character

by addition of LiAlH_4 to $\{\text{Pb}(\mu\text{-Br})\text{Ar}^{i\text{Pr}_6}\}_2$ in diethyl ether solution at ca. -78°C .⁽¹⁾ The diplumbynes **5-8** were synthesized by addition of a DIBAL-H solution in diethyl ether or hexanes to the respective aryl lead bromide cooled to ca. -78°C with an ethanol/dry ice bath as shown in figure 11.3. It was proposed originally⁵⁷⁰ that an aryl lead hydride “ $\text{Pb}(\text{H})\text{Ar}$ ” is formed as an intermediate, which upon warming releases dihydrogen to form the diplumbyne. More recent work by Wesemann and his group have shown that this hypothesis is essentially correct and the hydride can be isolated and structurally characterized as the hydrogen-bridged dimeric species $\{\text{Pb}(\mu\text{-H})\text{Ar}^{i\text{Pr}_6}\}_2$ which, however, decomposes to the diplumbyne and dihydrogen above ca. -40°C .⁶¹⁵ The resulting diplumbyne **1** and compounds **5-8** also have limited thermal stability and are sensitive to light, which lowers the yields of the reactions and necessitates quick workup and isolation of the products. They are stable for extended periods of time in the solid state but tend to decompose in solution at ambient temperature, resulting in a deposition of lead metal and protonated ligand, likely due to H atom abstraction from solvent molecules. The diplumbyne **5** is stable in solution for at least several weeks at ambient temperature in the absence of light, while **7** and **8** are stable in solution only at low temperature, ca. -20°C , and slowly decompose at ambient temperature. Diplumbyne **6** decomposes in solution at temperatures as low as -30°C and rapidly decomposes at ambient temperature. Compound **7** exhibited poor solubility in common hydrocarbon and ethereal solvents, and as a result only low yields ($<10\%$) could be isolated from the treatment of $\{\text{Pb}(\mu\text{-Br})\text{Ar}^{i\text{Pr}_4}\}_2$ with DIBAL-H. Additionally, the low stability of **7** in solution and the comparatively high solubility of the protonated terphenyl ligand formed by decomposition prevented an accurate determination of the purity of **7** by ^1H NMR spectroscopy (only ca. 1:1 ratios of **7** and $\text{Ar}^{i\text{Pr}_4}\text{H}$ were observed in C_6D_6 at 298 K). However, the crystals of **7** showed a sharp melting/decomposition point in the range $168\text{-}171^\circ\text{C}$, during which the amber colored crystals turned black. We found that higher yields (ca. 30%) of **7** (as well as **1**, see the online Supporting Information of the original publication) could be isolated by reduction of $\{\text{Pb}(\mu\text{-Br})\text{Ar}^{i\text{Pr}_4}\}_2$ with the magnesium(I) reagent $[\text{Mg}^{\text{Mes}}\text{Nacnac}]_2$.⁵⁹⁸

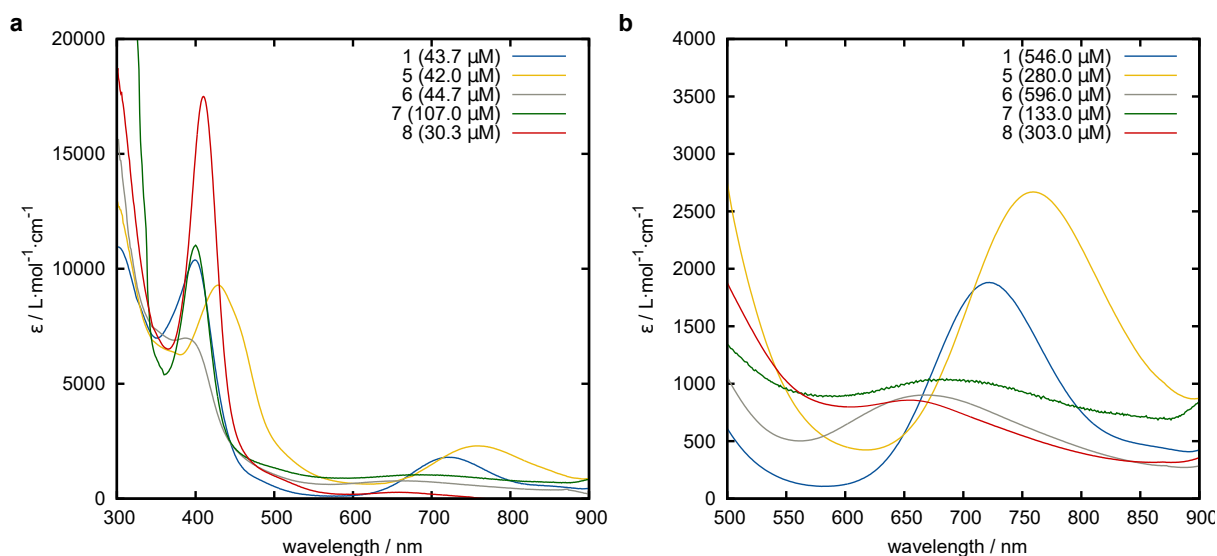


Figure 11.4.: UV/VIS spectra of **5-8** in the range a) 300-900 nm and b) 500-900 nm.

reported by Jones and co-workers. Addition of one equivalent of $[\text{Mg}^{\text{Mes}}\text{Nacnac}]_2$ to $\{\text{Pb}(\mu\text{-Br})\text{Ar}^{\text{iPr4}}\}_2$ in diethyl ether at 0°C resulted in an immediate color change from yellow-orange to dark brown. After removing the volatile components under reduced pressure and washing the solid with hexanes, **7** was obtained as an olive-green powder, which had a decomposition point matching that of crystalline **7** and identical ^1H and $^{13}\text{C}\{^1\text{H}\}$ NMR spectra. The UV/VIS spectra of **5-8** in hexanes show two absorptions: one between 388 and 429 nm and another in the range of 655-759 nm. (Figure 11.4 and table 11.1) The observation of two absorptions in the solution spectra are consistent with predicted spectra for structures containing multiple bond character in solution (a single absorption, $n_- \rightarrow \pi$, would be expected for a single-bonded, strongly trans-bent structure), and have previously been calculated to belong to the $n_- \rightarrow n_+$ and $\pi \rightarrow \pi^*$ transitions^{588,589}. The absorbances appear at lower energy in comparison to those of the analogous digermynes (320-380 nm, 430-510 nm) and distannynes (402-403 nm, 582-612 nm)⁵⁷⁶, consistent with the decreasing strength of the E-E bond as the group is descended.

Table 11.1.: Summary of key structural and spectroscopic data for **1, 5-8**.

	$(\text{PbAr}^{\text{iPr6}})_2^a$ (1)	$(\text{PbAr}^{\text{iPr8}})_2^b$ (5)	$(\text{PbAr}^{\text{iBu6}})_2^b$ (6)	$(\text{PbAr}^{\text{iPr4}})_2^b$ (7)	$(\text{PbAr}^{\text{iPr4-4-SiMe}_3})_2^b$ (8)
Pb-Pb / Å	3.1881(1)	3.0382(6)	3.0394(9)	3.1751(4)	3.2439(9), 2.945(5) (6%)
C-Pb / Å	2.303(2)	2.311(3), 2.314(2)	3.357(6), 3.366(6)	2.301(2)	2.3076(17), 2.282(3)
C-Pb-Pb / °	94.30(9)	114.73(7), 116.02(6)	101.77(14), 103.93(15)	98.60(5)	95.22(5), 100.82(15)
C-Pb-Pb-C / °	180	-133.64(9)	136.8(2)	180	180
λ_{max} / nm	397	429	388	400	410
$(\epsilon / \text{L mol}^{-1} \text{ cm}^{-1})$	$(10000)^b$	(9300)	(7000)	(11000)	(18000)
$n_- \rightarrow n_+$					
λ_{max} / nm	719	759	668	682	655
$(\epsilon / \text{L mol}^{-1} \text{ cm}^{-1})$	$(1800)^b$	(2700)	(900)	(1200)	(860)
$\pi \rightarrow \pi^*$					

^aRef. 570.^bThis work.

X-ray Structures

The structures of the diplumbynes are shown in figures 11.5 and 11.6. The most important structural parameters of the diplumbynes **5-8** are the Pb-Pb bond lengths and the $C_{\text{ipso}}\text{-Pb-Pb}$ bending and torsion angles. These and other selected structural data are summarized in table 11.1. Diplumbynes **5** and **6** have the shortest aggregate Pb-Pb distances of 3.0382(6) Å and 3.0394(9) Å respectively. Both structures are noncentrosymmetric, the $C_{\text{ipso}}\text{-Pb-Pb}$ angles in **5** being $114.73(7)^\circ$ and $116.02(6)^\circ$ (cf. $94.30(9)^\circ$ in the original diplumbyne **1**) with a $C_{\text{ipso}}\text{-Pb-Pb-C}_{\text{ipso}}$ torsion angle of $-133.64(9)^\circ$, while **6** has $C_{\text{ipso}}\text{-Pb-Pb}$ angles of $101.77(17)^\circ$ and $103.93(15)^\circ$, and a $C_{\text{ipso}}\text{-Pb-Pb-C}_{\text{ipso}}$ torsion angle of $136.8(2)^\circ$. In **7**

11. Terphenyl Substituted Diplumbynes with Ligand Dependent Lead–Lead Multiple-Bonding Character

the Pb–Pb distances is 3.1751(4) Å and the structure is centrosymmetric with C_{ipso} –Pb–Pb angles of 98.60(5)°. The two lead atoms in the core of **8** are disordered over two sites in 94% and 6% occupancies. Both components are centrosymmetric, with the major component having a Pb–Pb distance of 3.2439(9) Å and a C_{ipso} –Pb–Pb angle of 95.22(5)°, while the minor component has a Pb–Pb bond length of 2.945(5) Å and the C_{ipso} –Pb–Pb angle is 100.82(15)°. These parameters may be compared to the Pb–Pb distance (3.1881(1) Å), C_{ipso} –Pb–Pb angle (94.30(9)°) and 180° torsion angle in the original diplumbyne **1**. Unlike in the structure of **6**, the C_{ipso} –Pb–Pb bond angles in **5** are substantially widened compared to that in the original **1**. This is likely due to the steric demand of the highly substituted Ar^{iPr8} ligand and corresponds to a shortening of the Pb–Pb bond by about 0.15 Å in comparison to **1** (3.1881(1) Å). The wide angle, approaching 120°, suggests a multiple bonded isomer of the diplumbyne analogous to the structures seen for its Si, Ge, and Sn analogues. The bond parameters of **5** are very close to the Pb–Pb distance (3.071 Å), C_{ipso} –Pb–Pb trans-bending angle (117.7°), and the C_{ipso} –Pb–Pb– C_{ipso} torsion angle (119.8°, although fixing the torsion angle at 140° only raised the energy by 0.7 kcal mol⁻¹) predicted by

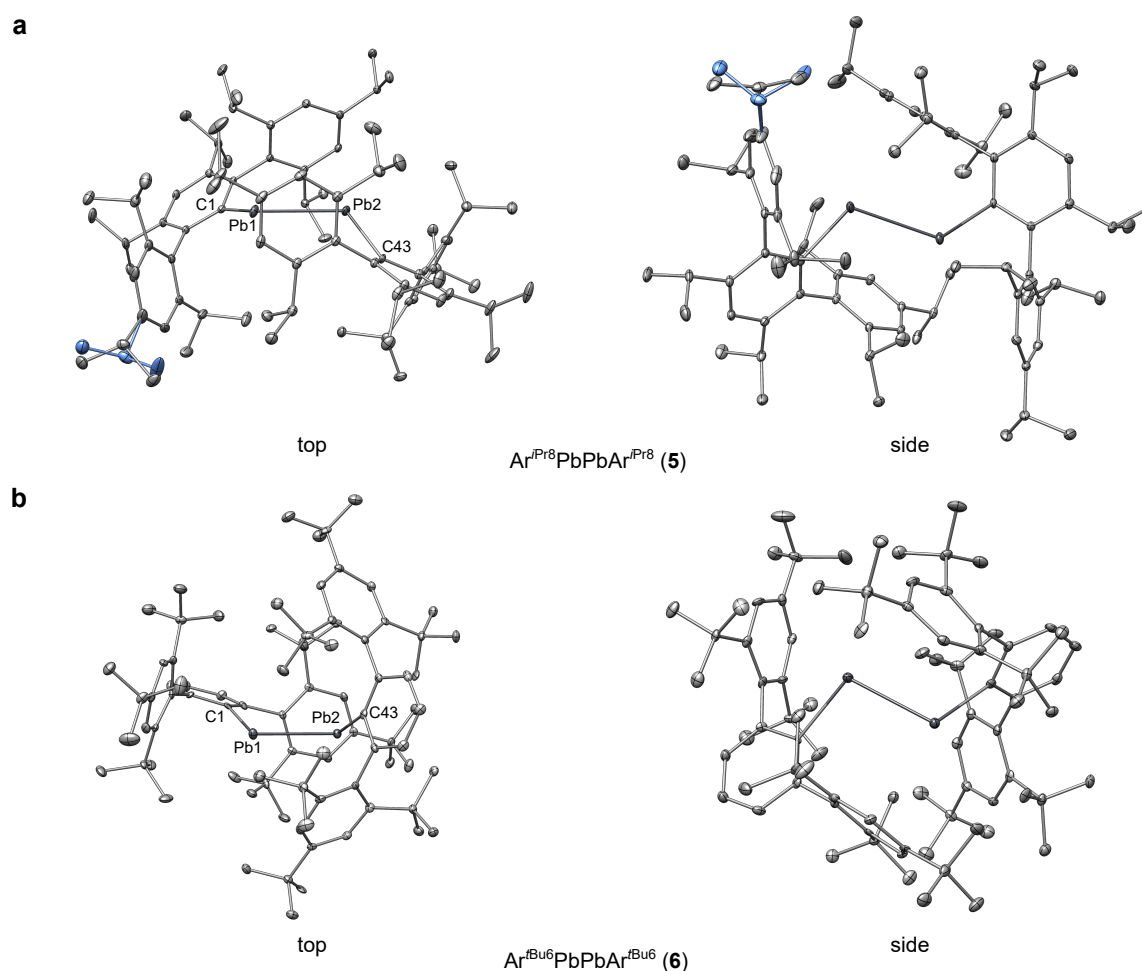


Figure 11.5.: Plot of the crystallographically determined structures of the new diplumbynes **5** and **6**. Thermal ellipsoids are shown at 30% of electronic probability. Hydrogen atoms are omitted for clarity. Light blue color indicates disordered groups.

Nagase and Takagi for the multiply bonded isomer of **1**⁵⁸⁸. The bond parameters of **7** and the major component of **8** are close to the Pb–Pb bond (3.1881(1) Å) and the C_{ipso} –Pb–Pb angles (94.30(9)°) originally reported in **1** and are consistent with a Pb–Pb single bonded structure. The structures of **6** and the minor component of **8** have short Pb–Pb bonds comparable to **5** but relatively narrow angles near 100° similar to **1** and **7**. This is in contrast with the singly bonded distannynes 4-Me₃Si–Ar^{*i*Pr⁴}SnSnAr^{*i*Pr⁴}–4-SiMe₃ and 4-Me₃Ge–Ar^{*i*Pr⁴}SnSnAr^{*i*Pr⁴}–4-GeMe₃ which show lengthened Sn–Sn bonds at angles of 97.79(17)–99.07(3)°⁵⁷⁶. The short bonds in **5**, **6**, and **8** (Pb2–Pb2A) are still longer than typical Pb–Pb singles bonds in diplumbanes (cf. 2.84 Å in Ph₃PbPbPh₃)⁶¹⁶, but are similar to the Pb–Pb distances in reported diplumbenes said to contain Pb–Pb double bonds: 3.0515(3) Å in Trip₂Pb=PbTrip₂(63) (Trip = 2,4,6-*i*Pr₃-C₆H₂), 2.9899(5) Å in Trip(Hyp)Pb=Pb(Hyp)Trip(64) (Hyp = Si(SiMe₃)₃) and 2.9033(9) Å in Mes(Hyp)Pb=Pb(Hyp)Mes⁶¹⁷.

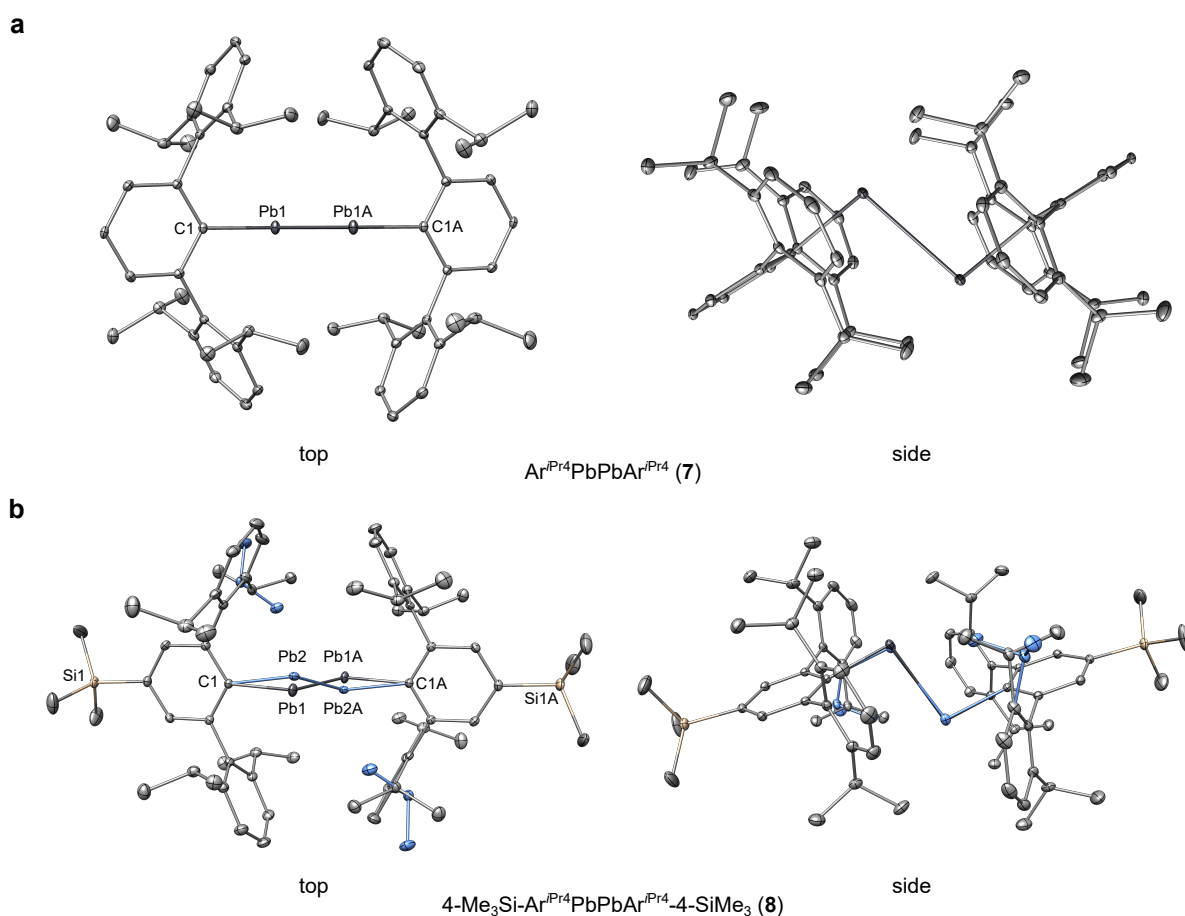


Figure 11.6.: Plot of the crystallographically determined structures of the new diplumbynes **7** and **8**. Thermal ellipsoids are shown at 30% of electronic probability. Hydrogen atoms are omitted for clarity. Light blue color indicates disordered groups.

11.4. Computational Studies

To investigate the structure-bonding relationship and the influence of intramolecular London dispersion interactions in compounds **1** and **5-8**, their molecular structures were cut out of the crystal structures and optimized in the gas-phase with and without the D3 dispersion correction. In addition, the opposing structural motif (strongly trans-bent with a longer Pb–Pb bond (Figure 11.1, structure motif **C**) vs. less trans-bent with short Pb–Pb bond (Figure 11.1, structure motif **B**) was generated from the basic structure of the corresponding crystal structure cutout. The generated structures are denoted by an asterisk (e.g., **1***). In all structures, the underlying structure motif **B** or **C** is retained after geometry optimization. This reflects the existence of two dominant structural minima. The structures with a shorter Pb–Pb bond and a less pronounced trans-bent angle (**5**, **6**, **1***, **7***, **8***) are unusual. For the experimental structures, the dispersion corrected optimized gas-phase structures show good agreement of the key structural parameters: the Pb–Pb bond length ($d(\text{Pb-Pb})$), the trans-bent angle ($\varphi(\text{C-Pb-Pb})$) and the torsion angle of the C–Pb–Pb–C unit ($\theta(\text{C-Pb-Pb-C})$) (Table 11.2). Upon neglecting the dispersion correction (Table 11.2, values in parentheses), both a stretching of the Pb–Pb bond and a pronounced increase of the trans-bent angle are observed. This indicates a large influence of intramolecular dispersion interactions on the molecular structure by partial compensation of steric repulsion between the large terphenyl ligands. The intramolecular dispersion interaction energy (ΔE_{disp}) varies unsystematically between the structures in a range of 20–33 kcal mol^{−1} (PBE0) or 30–51 kcal mol^{−1} (B3LYP), respectively (Table 11.3). Previous studies showed that the D3 and especially the D4 dispersion corrections for the repulsive B3LYP hybrid functional correlate well with the dispersion energy contribution to the interaction energy obtained from DLPNO-CCSD(T) local energy decomposition calculations³³. It is noteworthy that the calculated dispersion interaction energies far exceed the dissociation free energies (ΔG_{diss}) for all systems and are a dominant factor in the stabilization of diplumbynes against dissociation.

Table 11.2.: Selected calculated gas-phase bond parameters for **1**, **5-8** and **1***, **5*-8*** at the TPSS-D3(BJ)-ATM/def2-TZVP level of theory. Parameters calculated without London dispersion correction are given in parentheses.^a

	Pb–Pb / Å	C–Pb1 / Å	C–Pb2 / Å	C–Pb1–Pb2 / °	C–Pb2–Pb1 / °	C–Pb1–Pb2–C / °
1	3.216 (3.314)	2.329 (2.349)	2.329 (2.349)	93.5 (100.5)	93.5 (100.5)	180.0 (180.0)
5	2.972 (2.965)	2.319 (2.328)	2.318 (2.332)	118.2 (131.6)	118.5 (128.9)	−145.3 (144.2)
6	3.079 (3.192)	2.389 (2.387)	2.390 (2.384)	98.9 (114.2)	100.3 (105.5)	133.9 (131.9)
7	3.207 (3.268)	2.321 (2.341)	2.321 (2.341)	94.8 (102.4)	94.8 (102.4)	180.0 (180.0)
8	3.207 (3.270)	2.318 (2.338)	2.317 (2.338)	94.3 (102.4)	94.2 (102.0)	−178.9 (−179.8)
1*	3.022 (3.072)	2.337 (2.335)	2.336 (2.333)	110.4 (120.7)	109.6 (119.9)	−109.2 (−113.7)
5*	3.294 (3.468)	2.358 (2.368)	2.366 (2.367)	102.0 (109.8)	99.3 (109.7)	−174.4 (−177.0)
6*	3.281 (3.379)	2.355 (2.375)	2.354 (2.375)	99.7 (104.8)	99.7 (104.8)	180.0 (180.0)
7*	3.001 (3.073)	2.324 (2.333)	2.325 (2.334)	111.6 (118.8)	111.2 (119.3)	−119.8 (−120.0)
8*	3.003 (3.077)	2.323 (2.331)	2.323 (2.332)	110.9 (118.6)	110.9 (119.0)	−117.8 (−119.5)

^aThe asterisk * indicates the non-isolated calculated structure.

tion into two doublet fragments. For all compared structure pairs, the experimental structure motifs are favored over the generated model systems in terms of free energy, with the difference increasing with increasing congestion of the terphenyl ligands. This is supported by a qualitative conformer search at GFN2-xTB(GBSA(toluene)) level applying the iMTD-GC²³¹ algorithm within the CREST⁶⁴ program, which confirms the experimental structure motifs being favored in solution for all studied compounds.

Table 11.3.: Gibbs free energies and dispersion interaction energy contributions for **1**, **5-8** and **1***, **5*-8*** at the PBE0/def2-TZVPP//TPSS-D3(BJ)-ATM/def2-TZVP and B3LYP/def2-TZVPP/TPSS-D3(BJ)-ATM/def2-TZVP (in parentheses) levels of Theory. All values are given in kcal mol⁻¹.

	$\Delta G_{\text{diss.}}$	$\Delta G_{\text{diss.}}(\text{D3})$	$\Delta G_{\text{diss.}}(\text{D4})$	$\Delta E_{\text{disp.}}(\text{D3})$	$\Delta E_{\text{disp.}}(\text{D4})$	$\Delta G_{\text{G-G}^*}(\text{D3})$	$\Delta G_{\text{G-G}^*}(\text{D4})$
1	-11.9 (-23.7)	16.4 (19.7)	14.8 (15.2)	-30.9 (-48.2)	-29.9 (-44.4)	3.5 (5.1)	3.3 (5.0)
5	-19.1 (-31.3)	9.4 (12.1)	7.5 (7.2)	-28.8 (-44.1)	-27.5 (-40.1)	9.3 (10.4)	9.0 (10.3)
6	-16.0 (-28.1)	16.2 (20.8)	14.1 (15.4)	-33.1 (-51.0)	-31.7 (-46.4)	12.2 (12.8)	12.6 (13.1)
7	-4.6 (-14.5)	18.6 (22.0)	17.3 (18.0)	-24.9 (-40.0)	-24.2 (-36.7)	6.5 (8.6)	6.2 (8.6)
8	-6.3 (-16.8)	17.9 (21.1)	16.5 (17.1)	-25.0 (-40.0)	-24.3 (-36.9)	8.8 (10.9)	8.5 (10.8)
1*	-13.1 (-26.7)	13.0 (14.6)	11.5 (10.2)	-26.8 (-42.0)	-25.3 (-38.4)		
5*	-28.8 (-42.5)	0.1 (1.7)	-1.6 (-3.1)	-29.1 (-44.8)	-27.8 (-40.5)		
6*	-23.8 (-34.0)	3.9 (8.1)	1.5 (2.3)	-28.7 (-43.8)	-27.3 (-39.7)		
7*	-10.3 (-23.3)	12.2 (13.3)	11.0 (9.4)	-21.2 (-33.9)	-20.2 (-30.5)		
8*	-13.4 (-27.0)	9.1 (10.2)	8.0 (6.3)	-21.3 (-34.1)	-20.4 (-30.8)		

Bonding in Diplumbynes

Electronic structure calculations, analysis of the Kohn-Sham frontier orbitals (Figure 11.7) and NBO analyses (Figure 11.8) yield insight in the correlation of the Pb-Pb bonding in the structural motifs **B** and **C** and their key structural features. All structures with motif **C** show a HOMO which reflects a σ bond consisting of symmetrical overlap of two Pb centered 6p orbitals. With a widening of the trans-bent angle and stronger torsion of the C-Pb-Pb-C unit in motif **B**, the HOMO is twisted and now resembles an out-of-plane p-p single bond. For both structural motifs, the analysis of the Kohn-Sham molecular orbitals does not reveal any characteristics of a π -like multiple bond. However, the NBO analysis reveals a decisive difference between the two structural motifs. While the NBO analysis (in agreement with Foster-Boys localized MOs) for motif **C** yields only one Pb-Pb single bond corresponding to the shape of the HOMO, all structures with motif **B** show distinct donor-acceptor interactions between a Pb centered 6s-lone pair and a vacant 6p orbital at the opposite Pb atom (Figure 11.8). The severity of these interactions is strongly dependent on the trans-bent and torsion angles and is reflected by the second order perturbation estimate ($\Sigma E^{(2)}$) from the NBO analysis. The observation of a single bond with donor-acceptor contributions in motif **B** is also consistent with Wiberg, Mayer, Löwdin, and NLMO/NPA bond orders (BO) that do not exceed a maximum of 1.5 for the terphenyl substituted sys-

11. Terphenyl Substituted Diplumbynes with Ligand Dependent Lead–Lead Multiple-Bonding Character

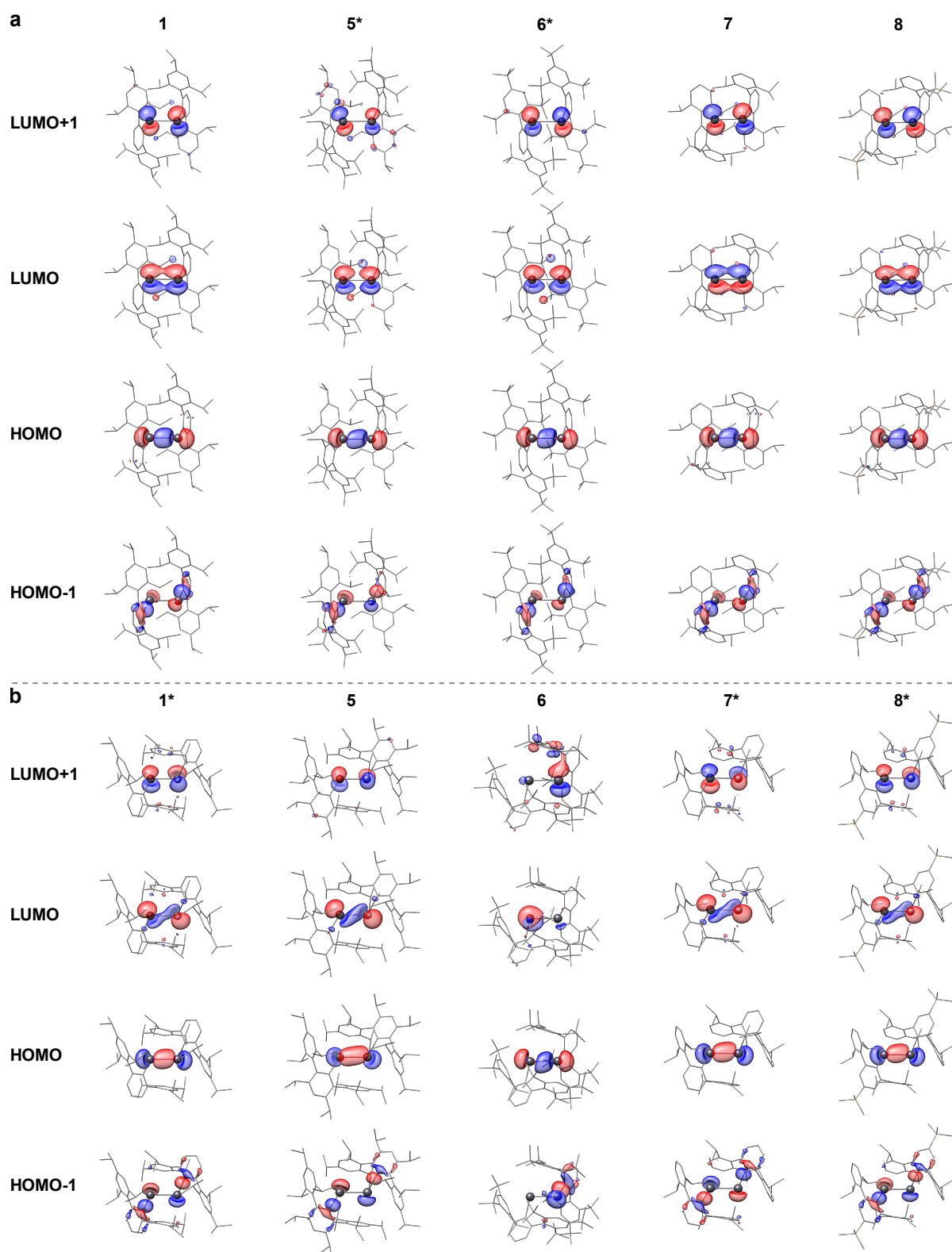


Figure 11.7.: Selected frontier Kohn-Sham orbitals for a) the single-bonded motif **C** and b) multiple-bonded motif **B** of **1**, **5-8** and **1***, **5*-8*** at the TPSS-D3(BJ)-ATM/def2-TZVP level of theory. Isosurface value = $0.05 \text{ e}^{-1/2} \text{ bohr}^{-3/2}$.

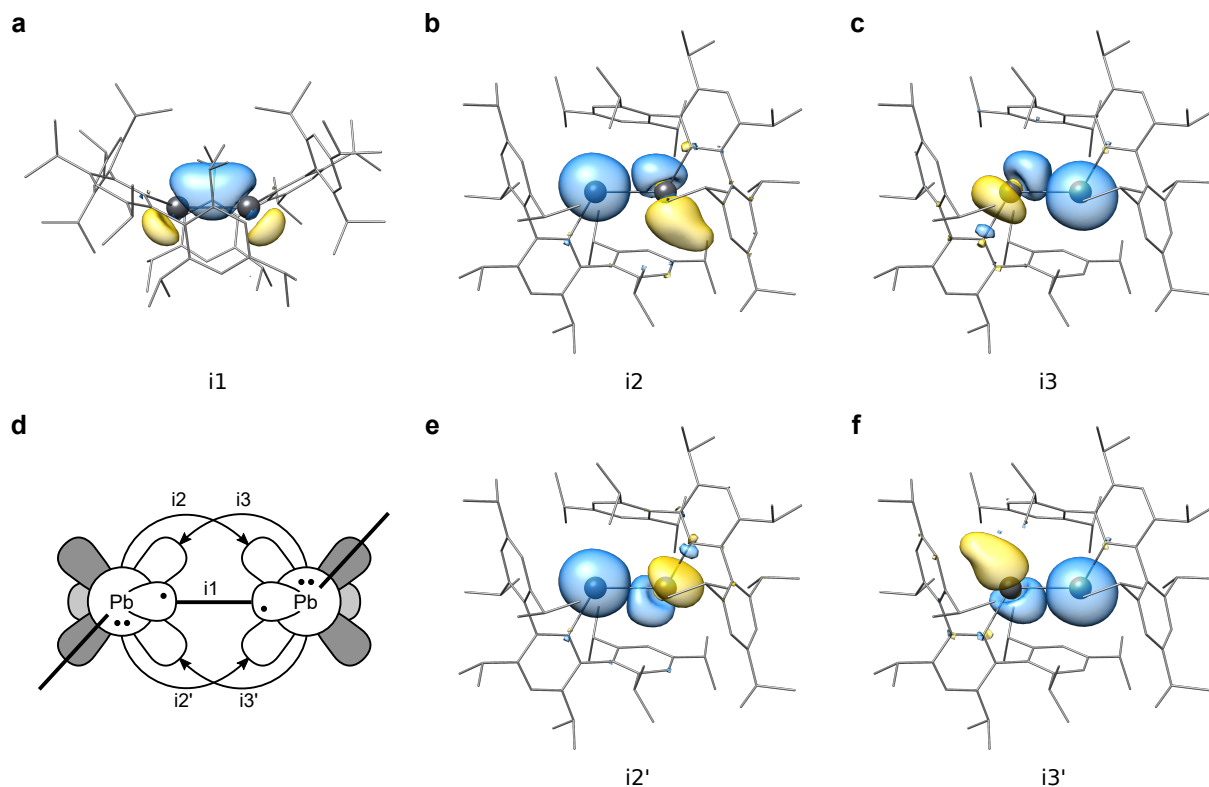


Figure 11.8.: Schematic illustration of the bonding in **5**. NBO of the Pb–Pb single bond in **5** (i1) and NBO combinations reflecting the Pb(s)→Pb(p) donor-acceptor interactions (i2, i3, i2', i3'). Isosurface value = $0.05 e^{-1/2} \text{ bohr}^{-3/2}$.

tems (Table 11.4, figure 11.9). For motif **C** no $E^{(2)}$ contributions between the Pb atoms are present and all bond orders are close to or are slightly below a value of one. A two-dimensional scan of $\varphi(\text{C-Pb-Pb})$ ($0-130^\circ$) and $\theta(\text{C-Pb-Pb-C})$ ($90-180^\circ$) for a model system Ph–Pb–Pb–Ph yields further detailed insight into the dependence of the discussed quantities on the trans-bent angle and torsion angle (Figure 11.10). sTD-DFT calculations of the UV/VIS excitation spectra confirm a relationship between structure and pronunciation of the excitation at longer wavelengths (Figure 11.11a,b). This only occurs in minimum structures of motif **B** and corresponds to a HOMO→LUMO+1 excitation (Figure 11.11b). Molecular dynamics simulations at GFN2-xTB(GBSA(toluene)) level reveal, that the manifestation of the absorption band at longer wavelengths (approximately 600-800 nm, table 11.5) only provides a limited indication of the structural motif of the observed minimum structure. The high flexibility of the C–Pb–Pb–C unit in regard to the trans-bent angle as well as the Pb–Pb bond length leads to approximately comparable UV/VIS spectra for the minimum structures of both structural motifs (Figure 11.11c,d).

11. Terphenyl Substituted Diplumbynes with Ligand Dependent Lead–Lead Multiple-Bonding Character

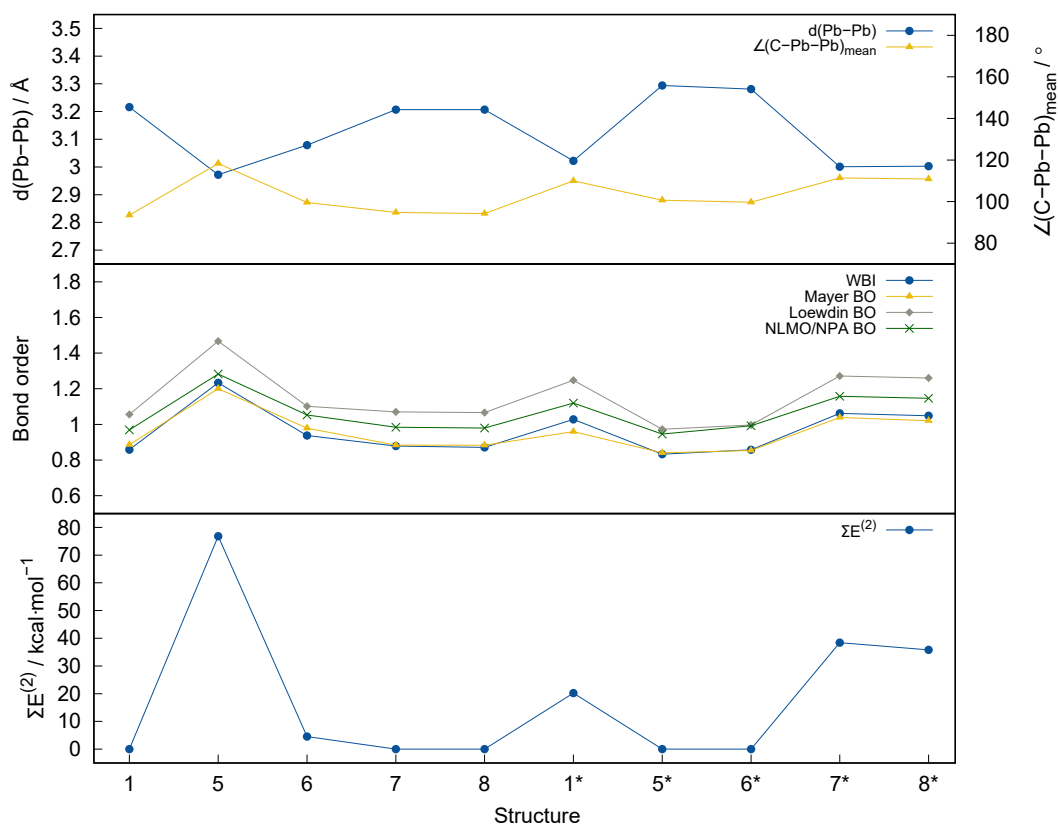


Figure 11.9.: Summary of key structural parameters of the Pb–Pb bonding, bond order analyses, and second order perturbation estimate ($\Sigma E^{(2)}$) of Pb(s)→Pb(p) donor-acceptor interactions in the NBO basis.

Table 11.4.: Bond order and NBO analyses of the Pb–Pb bonding in **1**, **5–8** and **1***, **5*–8*** at the TPSS-D3(BJ)-ATM/def2-TZVP level of theory.^a

	WBI	Mayer BO	Löwdin BO	NLMO/NPA BO	$\Sigma E^{(2)} / \text{kcal mol}^{-1}$
1	0.859	0.886	1.056	0.969	0.0
5	1.233	1.200	1.467	1.283	76.8
6	0.938	0.979	1.102	1.053	4.6
7	0.879	0.884	1.070	0.984	0.0
8	0.872	0.883	1.066	0.980	0.0
1*	1.028	0.959	1.247	1.119	20.2
5*	0.833	0.840	0.973	0.946	0.0
6*	0.858	0.854	0.997	0.993	0.0
7*	1.062	1.038	1.272	1.158	38.4
8*	1.049	1.021	1.260	1.147	35.8

^a $\Sigma E^{(2)}$ is the sum of the second order perturbation estimate of Pb(s)→Pb(p*) donor-acceptor interactions in the NBO basis.

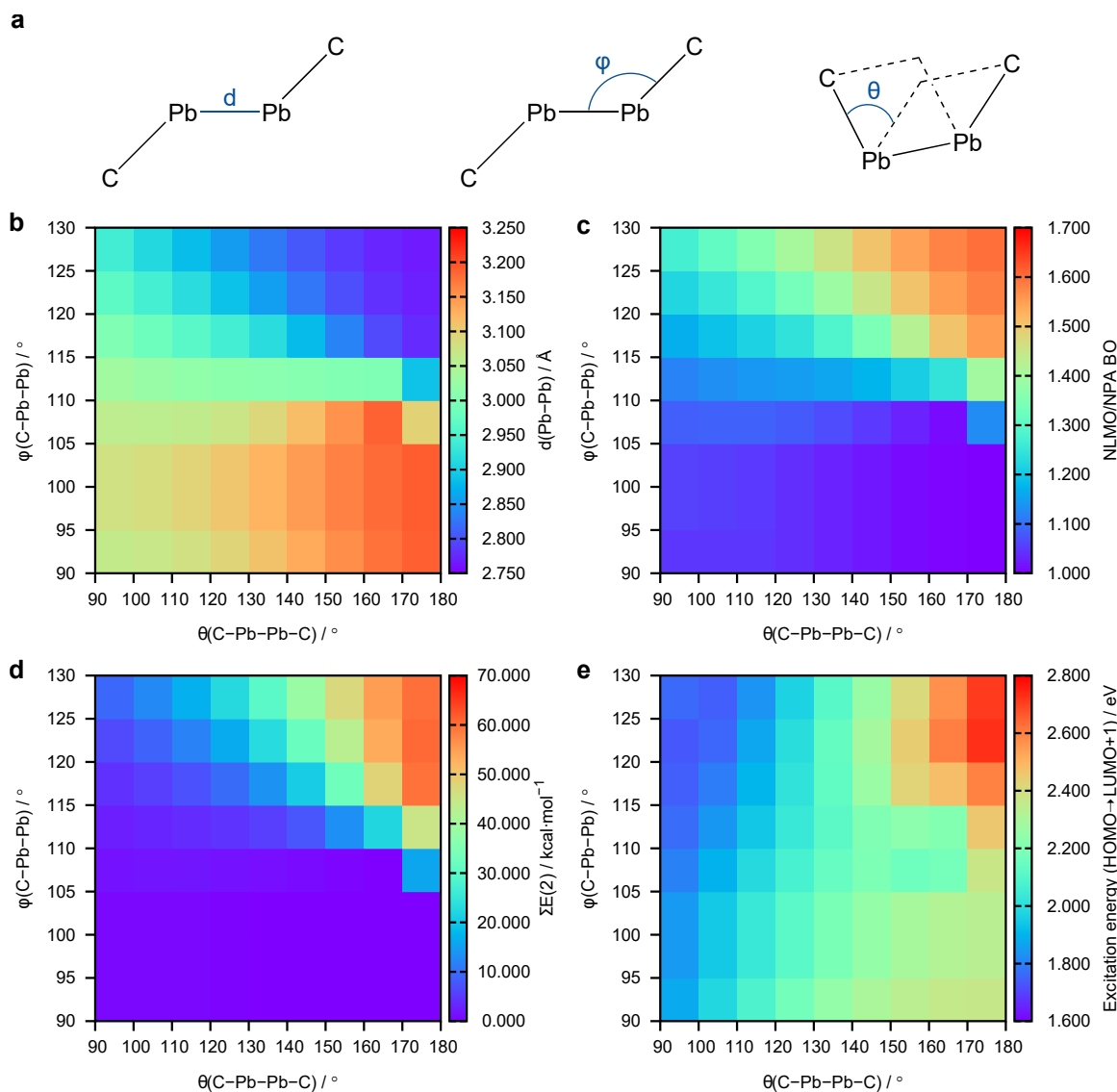


Figure 11.10.: 2D structure scan of the trans-bent angle $\varphi(\text{C-Pb-Pb})$ (0 to 130°) and dihedral angle $\theta(\text{C-Pb-Pb-C})$ (90 to 180°) for a model system Ph-Pb-Pb-Ph at TPSS-D3(BJ)-ATM/def2-TZVP level. a) Structure parameter definition; b) Pb-Pb bond length; c) NLMO/NPA BO; d) $\Sigma E^{(2)}$; e) Excitation energy (sTD-BHLYP/def2-TZVP) of the HOMO \rightarrow LUMO+1 transition.

11.5. Conclusion and Outlook

A series of new diplumbynes has been synthesized by two facile routes. Their structures show a large variation in their Pb-Pb bond lengths and $C_{\text{ipso}}\text{-Pb-Pb}$ angles in the solid state. The Pb-Pb distances range from 3.0382(6) \AA for $\text{Ar}^{i\text{Pr}8}\text{PbPbAr}^{i\text{Pr}8}$ (**5**) to 3.2439(9) \AA for 4- $\text{Me}_3\text{Si-Ar}^{i\text{Pr}4}\text{PbPbAr}^{i\text{Pr}4}$ -4- SiMe_3 (**8**) (cf. 2.945(5) \AA in its minor component) with respective bond angles of 114.73(7)-116.02(6)° in **5** and 95.22(5)° in **8**. Thus, the variation in Pb-Pb distance is ca. 0.3 \AA , ca. 10%. The apparent “softness” of the Pb-Pb distances and bending angles are in agreement with the calculations of Frenking and co-workers indicating that they are susceptible to alteration by changes in the packing effects (i.e., London disper-

11. Terphenyl Substituted Diplumbynes with Ligand Dependent Lead–Lead Multiple-Bonding Character

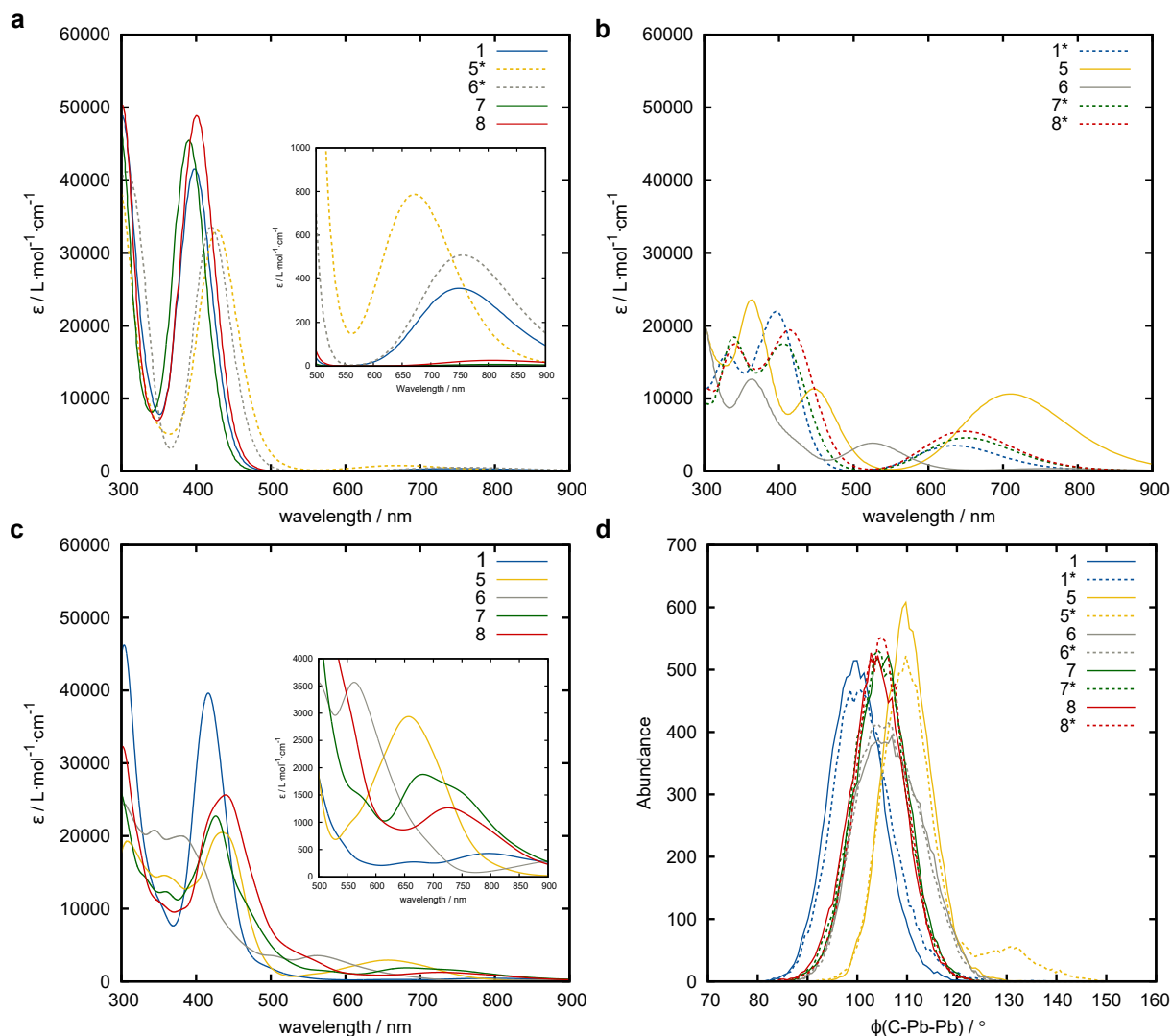


Figure 11.11.: Calculated UV/VIS spectra for the minimum structures of a) motif **C** and b) **B** at the sTD-BHLYP(CPCM(*n*-hexane))/def2-TZVP//TPSS-D3(BJ)-ATM/def2-TZVP level (applied shift = -0.2 eV). c) MD based averaged UV/VIS spectra for structures **1**, **5-8** at the sTD-BHLYP(CPCM(*n*-hexane))/GFN2-xTB(GBSA(toluene)) level of theory (applied shift = -0.2 eV). d) $\phi(\text{C-Pb-Pb})$ angle distributions for the MD simulation of all investigated structures. MD simulation time of 1 ns.

sion interactions)⁵⁸⁷. Additionally, the structure of **5** is in good agreement with structural parameters predicted by Nagase and co-workers for the isomer of $\text{Ar}^{i\text{Pr}_6}\text{PbPbAr}^{i\text{Pr}_6}$ (**1**) containing multiple bond character⁵⁸⁸. DFT computational studies verify the different bonding in the observed structural motifs, highlighting a donor-acceptor interaction augmentation of the Pb–Pb bond upon widening of the trans-bent angle, resulting in shortened Pb–Pb bonds with bond orders up to 1.5. London dispersion interactions prove crucial for stabilizing all sterically congested diplumbynes investigated in this study, strongly influencing the trans-bent angle. High steric congestion and the associated ligand fixation enable the stabilization of less trans-bent structural motifs. sTD-DFT calculations reveal a clear corre-

Table 11.5.: Tabulated absorption maxima of the calculated UV/VIS spectra of **1**, **5-8** and **1***, **5*-8*** between 350 and 900 nm (applied shift = -0.2 eV).

	single structure $\lambda / \text{nm} (\epsilon / \text{L mol}^{-1} \text{ cm}^{-1})$	MD averaged $\lambda / \text{nm} (\epsilon / \text{L mol}^{-1} \text{ cm}^{-1})$
1	397 (41530), 751 (357)	416 (39630), 667 (274), 797 (429)
5	364 (23541), 448 (11314), 708 (10616)	357 (14590), 435 (20480), 657 (2939)
6	364 (12638), 525 (3847), 770 (364)	344 (20780), 379 (20000), 562 (3565)
7	390 (45496)	359 (12340), 426 (22740), 682 (1878)
8	410 (48898)	440 (25630), 726 (1265)
1*	331 (15994), 396 (21931), 636 (3510)	411 (32120), 550 (1412), 847 (313)
5*	428 (33129), 670 (787)	366 (18510), 377 (18530), 425 (18190), 638 (3134)
6*	420 (33605), 756 (509)	385 (20600), 515 (3534), 562 (3667)
7*	340 (18433), 405 (17520), 653 (4585)	420 (22000), 658 (1245), 749 (1160)
8*	341 (17488), 413 (19419), 649 (5499)	356 (12220), 437 (25940), 706 (1772)

lation between changes in the Pb–Pb bonding due to the trans-bent angle and the appearance of the electronic spectra of the minimum structures. Further MD simulations show that the high flexibility of the C–Pb–Pb–C unit leads to similar UV/VIS spectra for both structure motifs with increased intensity of the HOMO→LUMO+1 excitation.

Acknowledgements

We wish to acknowledge the US National Science Foundation (CHE-1565501) for support of this work and for purchase of a dual-source X-ray diffractometer (CHE-0840444). The Deutsche Forschungsgemeinschaft (DFG) is gratefully acknowledged for financial support in the framework of the Gottfried Wilhelm Leibniz prize to S.G.

12. Comprehensive Benchmark Study on the Calculation of ^{29}Si NMR Chemical Shifts

Markus Bursch,^a Thomas Gasevic,^a Julius B. Stückrath,^a and Stefan Grimme^a

Received: 30 September 2020, Published online: 15 December 2020

Reprinted (adapted) with permission[†] from

Bursch, M.; Gasevic, T.; Stückrath, J. B.; Grimme, S. *Inorg. Chem.* **2021**, *60*, 272–285

– Copyright © 2020, American Chemical Society.

DOI [10.1021/acs.inorgchem.0c02907](https://doi.org/10.1021/acs.inorgchem.0c02907)

Own manuscript contribution

- Conception of the study and choice of methods
- Basis set and structure dependence study
- Interpretation of the results
- Writing the manuscript

^aMulliken Center for Theoretical Chemistry, Institut für Physikalische und Theoretische Chemie, Rheinische Friedrich-Wilhelms-Universität Bonn, Beringstraße 4, 53115 Bonn, Germany

[†]Permission requests to reuse material from this chapter should be directed to the American Chemical Society.

12. Benchmark Study on the Calculation of ^{29}Si NMR Chemical Shifts

Abstract A comprehensive and diverse benchmark set for the calculation of ^{29}Si NMR chemical shifts is presented. The *SiS146* set includes 100 silicon containing compounds with 146 experimentally determined reference ^{29}Si NMR chemical shifts measured in nine different solvents in a range from -400 to $+828$ ppm. Silicon atoms bound to main group elements as well as transition metals with coordination numbers of 2-6 in various bonding patterns including multiple bonds, coordinative, and aromatic bonding are represented. The performance of various common and specialized density functional approximations including (meta-)GGA, hybrid, and double-hybrid functionals in combination with different AO basis sets and for differently optimized geometries is evaluated. The role of scalar-relativistic effects is further investigated by inclusion of the zeroth order regular approximation (ZORA) method into the calculations. GGA density functional approximations (DFAs) are found to outperform hybrid DFAs with B97-D3 performing best with an MAD of 7.2 ppm for the subset including only light atoms ($Z < 18$) while TPSSh is the best tested hybrid functional with a MAD of 10.3 ppm. For ^{29}Si cores in vicinity of heavier atoms, the application of ZORA proved indispensable. Inclusion of spin-orbit effects into the ^{29}Si NMR chemical shift calculation decreases the mean absolute deviations by up to 74 % compared to calculations applying effective core potentials.

12.1. Introduction

Nuclear magnetic resonance (NMR) spectroscopy is one of the most powerful analytic methods used on a daily basis throughout various chemical research fields providing much information on the geometrical and electronic structure of molecules and solids. Besides the most common ^1H NMR spectroscopy, other atomic nuclei are of great interest for special research questions, one of which is the ^{29}Si NMR nucleus. The vast applicability of NMR spectroscopy has evoked a general interest in the theoretical calculation of chemical shifts^{61,618–622}. As for many computational applications, density functional theory (DFT) methods represent an efficient compromise between accuracy and computational demand also for NMR calculations using the gauge-including atomic orbital (GIAO) method^{563,564,623,624}. Still, it is not trivial to find the most efficient choice out of the large amount of existing density functionals, especially for nontheoretical chemists. Benchmark sets can help to gain an overview over the performance of the most common computational methods. Common organosilicon compounds such as alkyl silanes, silanols and silyl ethers have already been studied with respect to the calculation of ^{29}Si NMR chemical shifts^{625–630}. Nevertheless, more complex molecules containing, e.g., multiple bonded, transition metal bonded, and low-coordinate silicon are mainly studied in an experimental context or in very specialized studies^{631–634} and lack a thorough comprehensive assessment. Compounds like triply bonded silicon compounds have been studied regarding the prediction of ^{29}Si NMR chemical shifts. In 2005⁶³⁵ and 2011⁶³⁶, three different functionals were tested for tetra-, penta- and hexacoordinate organosilicon compounds highlighting the good performance of the HCTH407⁶³⁷ density functional approximation (DFA). Related studies by Zhang *et al.*⁶³⁸ and Fedorov *et al.*⁶³⁹ included relativistic and solvent effects in the computational treatment of tetracoordinate organosilicon compounds. Regarding the high demand for ^{29}Si NMR chemical shift calculations, a comprehensive benchmark study, covering the chemical versatility of silicon compounds is yet missing. Therefore, in this work a large benchmark set comprised

of 146 experimentally determined ^{29}Si NMR chemical shifts is presented including aromatic, hypervalent, multiple bonded and tetrahedral coordinated silicon compounds as well as cyclosilanes, silylenes and organosilicon transition metal complexes. Various common DFAs and basis sets are tested for the calculation of ^{29}Si NMR chemical shifts and the basis set size and structure dependence of the ^{29}Si NMR chemical shift calculations are investigated. The role of relativistic effects is further evaluated for a subset of silicon compounds with heavy elements in the vicinity of the silicon atom. An empirical linear scaling approach to improve the calculated chemical shifts is tested. These investigations may enable computational and experimental chemists to make a profound DFA choice for a reliable calculation of this property.

12.2. Computational Details

All quantum chemical calculations were conducted applying the ORCA 4.2.1^{208,286,287}, ADF2019.303^{640,641}, and xtb 6.3.3⁶⁴² program packages. For preoptimization of the structures the GFN2-xTB⁵⁴ extended tight binding method was applied with the GBSA implicit solvation model⁵⁷. Geometries were further optimized at the PBEh-3c⁶⁹ composite level (*GRID4*) in combination with the CPCM⁶⁴³ implicit solvation model for the respective solvents (for details see the appendix A11). For all other noncomposite DFT geometry optimizations, the D4 London dispersion correction scheme^{33,115,116} was applied. Structures were verified as minima on the potential energy surface by the absence of imaginary frequencies below $-i\omega = 30 \text{ cm}^{-1}$ in the numerical harmonic frequencies calculation. NMR chemical shielding tensors were calculated with ORCA applying the gauge-including atomic orbital (GIAO)⁵⁶³ method, CPCM implicit solvation, and either Ahlrichs' def2-TZVP²⁴⁰ or Jensen's pcSseg-2⁶⁴⁴ Gaussian-type orbital (GTO) basis set. Further basis sets used for the basis set convergence study are MINIX^{127,645}, def2-mXVP (X = S, TZ), def2-XVP(P) (X = S, TZ, QZ), pcSseg-n (n = 0–3), pc-n (n = 0–3)⁶⁴⁶, and cc-pVXZ(-PP)^{647–649} (X = D, T, Q). The RIJCOSX⁶⁵⁰ scheme with *GRID5* and *GRIDX6* options was applied for the chemical shielding tensor calculations and RIJ²⁴³ was used to accelerate geometry optimizations. Both were conducted with matching *def2/j*²⁴⁵ and *def2-TZVP/C*²⁹² auxiliary basis sets as implemented in ORCA. For double-hybrid calculations, the grid of the response operator on the right-hand side of the Z-vector equations was set to 2 and no frozen core approximation was applied. Stuttgart-Dresden def2 effective core potentials (ECPs)^{241,242} were used if not stated else. For cc-pVXZ(-PP) basis set calculations SK-MCDHF-RSC⁶⁴⁸ ECPs were used. The scalar-relativistic (SR) version of the zeroth order regular approximation (ZORA)^{210–212,651} to account for relativistic effects was used in combination with matching recontracted ZORA/SARC-def2-TZVP basis sets^{652,653}. For all SR-ZORA calculations conducted with ORCA, tightened radial grid options were applied (*Grid7*, *IntAcc 10*). For chemical shift calculations with ADF, the Slater-type orbital (STO) ZORA/TZP⁵⁶⁰ basis set and the COSMO implicit solvation model⁶⁵⁴ were applied. In ADF both SR-, and spin-orbit (SO-)ZORA⁵⁵⁹ relativistic approximations were used. All ^{29}Si NMR chemical shifts were calculated with reference to tetramethylsilane (TMS). The reference shielding tensors were recalculated for the respective solvents used for the experimental measurements. A list of all tested method combinations is shown in table 12.1. Chemical shifts were calculated according to Equation 12.1 with $\sigma(^{29}\text{Si}_{\text{TMS}})$ being the ^{29}Si NMR shielding constant for TMS calculated on the

12. Benchmark Study on the Calculation of ^{29}Si NMR Chemical Shifts

structure reoptimized in the respective solvent.

$$\delta(^{29}\text{Si}) = \sigma(^{29}\text{Si}_{\text{TMS}}) - \sigma(^{29}\text{Si}) \quad (12.1)$$

12.3. Results and Discussion

General Considerations

The calculation of chemical shifts involves some difficulties and a few general computational aspects have to be considered. These include the role of the geometry optimization method (equilibrium struc-

Table 12.1.: Tested methods, basis sets and relativistic approximations.

class	method	basis set	relativistic treatment	
HF	HF	def2-TZVP, pcSseg-2	ECP, SR-ZORA	
composite	HF-3c ¹²⁷	MINIX	ECP	
	PBEh-3c ⁶⁹	def2-mSVP	ECP	
(meta-)GGA	PBE ⁶⁵⁵	def2-TZVP, pcSseg-2, TZP	ECP, SR/SO-ZORA	
	revPBE ⁶⁵⁶	def2-TZVP, pcSseg-2, TZP	ECP, SR/SO-ZORA	
	OLYP ⁶⁵⁷	def2-TZVP, pcSseg-2, TZP	ECP, SR/SO-ZORA	
	BP86 ^{658,659}	def2-TZVP, pcSseg-2, TZP	ECP, SR/SO-ZORA	
	B97-D3 ⁵⁸	def2-TZVP, pcSseg-2	ECP, SR-ZORA	
	TPSS ⁶⁰⁶	def2-TZVP, pcSseg-2	ECP, SR-ZORA	
	revTPSS ^{660,661}	def2-TZVP, pcSseg-2	ECP, SR-ZORA	
	M06-L ⁶⁶²	def2-TZVP, pcSseg-2	ECP, SR-ZORA	
	KT2 ⁶⁶³	def2-TZVP, pcSseg-2, TZP	ECP, SR/SO-ZORA	
	SCAN ⁶⁶⁴	def2-TZVP, pcSseg-2	ECP, SR-ZORA	
	HCTH407 ⁶³⁷	def2-TZVP, pcSseg-2	ECP, SR-ZORA	
	(meta-)hybrid	PBE0 ²¹³	def2-TZVP, pcSseg-2, TZP	ECP, SR/SO-ZORA
B3LYP ^{607,608,665}		def2-TZVP, pcSseg-2, TZP	ECP, SR/SO-ZORA	
CAM-B3LYP ⁶⁶⁶		def2-TZVP, pcSseg-2	ECP, SR-ZORA	
BHLYP ⁹⁵		def2-TZVP, pcSseg-2	ECP, SR-ZORA	
BMK ⁶⁶⁷		def2-TZVP, pcSseg-2	ECP, SR-ZORA	
ω B97X-D3 ^{106,107,257}		def2-TZVP, pcSseg-2	ECP, SR-ZORA	
PW6B95 ³⁷⁰		def2-TZVP, pcSseg-2	ECP, SR-ZORA	
TPSSH ^{238,239}		def2-TZVP, pcSseg-2	ECP, SR-ZORA	
M06 ⁶⁶⁸		def2-TZVP, pcSseg-2	ECP, SR-ZORA	
M06-2X ⁶⁶⁸		def2-TZVP, pcSseg-2	ECP, SR-ZORA	
double-hybrid		revDSD-PBEP86 ^{262,669,670}	def2-TZVP, pcSseg-2	ECP
		revDSD-BLYP ^{670,671}	def2-TZVP, pcSseg-2	ECP
	B2GP-PLYP ⁶⁷²	def2-TZVP, pcSseg-2	ECP	
	mPW2PLYP ⁶⁷³	def2-TZVP, pcSseg-2	ECP	

ture), the application of implicit or explicit solvation models, the influence of molecular conformations and finally the choice of the best density functional approximation (DFA). The quality of geometries obtained with a certain DFA must not necessarily coincide with the quality of properties calculated with the same. Further, geometry optimizations are computationally demanding and thus more sophisticated DFAs are often not applicable. Multi-level approaches are a widely accepted compromise. Efficient DFT based composite methods like PBEh-3c⁶⁹ or B97-3c,¹²⁹ yield excellent molecular geometries at low to moderate cost and are generally recommended. Solvation effects should be considered when highly polar, charged or structurally affected molecules are investigated. Specifically, ¹H NMR is prone to the account of solvation. Nevertheless, electrostatic effects are often sufficiently described by implicit solvation models like COSMO³⁷³ or PCM^{643,674}. Explicit solvation should be considered, if strongly bound solute-solvent complexes are to be expected. Otherwise, explicit solvation may limit the applicability of some methods due to the increased computational demand in particular regarding sampling. Furthermore, the role of molecular conformations can become important if structural motifs, that have large impact on the chemical environment of the core under investigation, are thermodynamically accessible under the given reaction conditions. Nevertheless, in common, saturated compounds this influence is small and far less pronounced compared to more exposed cores like ¹H. Fully automated conformer and rotamer sampling tools like the recently developed CREST⁶⁴ program can be applied to find such conformations and thus critical cases could be investigated individually. Finally, these points highly depend on the system under investigation and have to be considered on a case by case basis. Nevertheless, the routine consideration of molecular conformations and application of implicit solvation models is recommended. Overall, the most crucial point that has to be assessed is the choice of the DFA for the computation of chemical shielding tensors and thus the resulting chemical shifts. At this point, for general use, not only accuracy and numerical precision but also the robustness and applicability of the method should be considered. To do so, a sufficiently large and representative benchmark set with a consistent level of high quality reference data has to be compiled to test a wide range of commonly applied DFAs.

Benchmark Set

The benchmark set consists of 146 experimentally determined ²⁹Si NMR chemical shifts of 100 diverse Si-containing compounds with chemical shifts in a range from -400 to +828 ppm (Figure 12.1) and molecule sizes between 5 and 234 atoms. Solvents include chloroform, dichloromethane, benzene, chlorobenzene, bromobenzene, toluene, acetonitrile, cyclohexane and THF. Coordination and bonding patterns of the Si-atom range from coordination numbers of 2 to 6 including single, double, triple, coordinative and aromatic bonding patterns. Si bonds to main group elements as well as transition metals are represented. Selected examples are depicted in Figure 12.1 and a detailed overview of all compounds can be found in appendix A11. Molecular geometries are optimized consistently at the PBEh-3c(CPCM) level of theory applying the CPCM implicit solvation model for the respective solvent of the experimental ²⁹Si NMR chemical shift measurement. The benchmark set is divided into two categories: (i) a set containing only elements up to argon ($Z = 18$), further denoted as “light” subset SiS-L (compounds **1** to **55**), and (ii) a set of structures containing elements with $Z > 18$ adjacent to the Si atom,

12. Benchmark Study on the Calculation of ^{29}Si NMR Chemical Shifts

further denoted as “heavy” subset *SiS-H* (compounds **56** to **100**, SiCl_4 is also included as it is known to be prone to spin-orbit coupling effects).

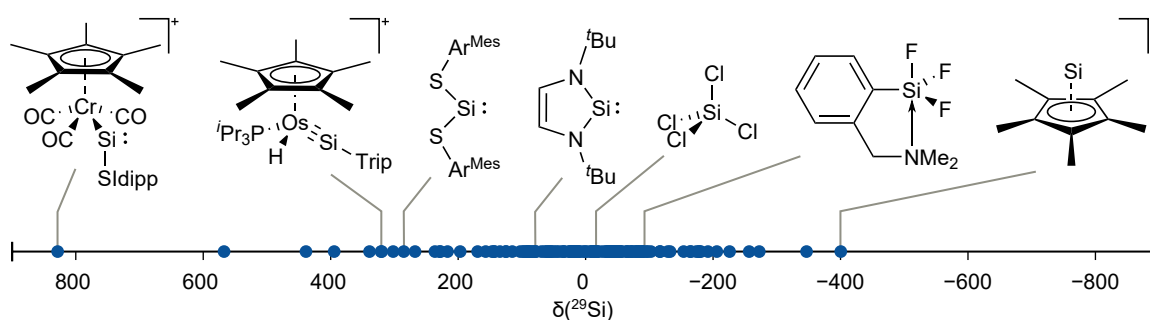


Figure 12.1.: Scale of investigated ^{29}Si NMR chemical shifts in ppm.

Benchmark of Density Functional Approximations for the Calculation of ^{29}Si NMR Chemical Shifts

Overall, the performance of 25 conventional DFAs, 11 (meta-)GGA, 10 (meta-)hybrid and four double-hybrid functionals was assessed. Further, the two composite methods HF-3c and PBEh-3c as well as the Hartree-Fock theory were tested. All DFAs were applied in conjunction with either the def2-TZVP or pcSseg-2 basis sets with ECPs and explicit relativistic ZORA treatment was evaluated.

The Light Atom Subset *SiS-L*

As for def2-TZVP and pcSseg-2 with ECPs, very similar trends and qualitative results are observed, and only the def2-TZVP values will be discussed in the following. For both basis sets no typical “Jacob’s ladder”^{93,675} behavior (better performance with increased theoretical level) is observed. In fact, the lower level (meta-)GGA class functionals yield better results (class mean absolute deviation, $\text{MAD}_{\text{GGA}} = 10.9$ ppm) than the tested (meta-)hybrid ($\text{MAD}_{\text{hybrid}} = 16.7$ ppm) functionals (Figure 12.2, table 12.2). Specifically, the GGA type B97-D3 ($\text{MAD} = 7.2$ ppm, $R^2 = 0.993$) and HCTH407 ($\text{MAD} = 8.1$ ppm, $R^2 = 0.991$) functionals show good results for the *SiS-L* subset. The KT2 functional that was specifically designed for NMR chemical shielding calculations also performs well with an MAD of 8.8 ppm and $R^2 = 0.989$. KT2 already yielded good results for ^{29}Si NMR chemical shifts in previous studies for a smaller set of molecules⁶⁷⁶. For B97-D3/def2-TZVP, bad results are obtained for $[(\text{Idipp})(\text{Me})\text{Si}=\text{Si}(\text{Idipp})]^+$ ⁶⁷⁷ (**45**, $\text{Idipp} = \text{C}[\text{N}(\text{C}_6\text{H}_3-2,6-\text{iPr}_2)\text{CH}]_2$) with a deviation of 28.9 ppm for the silicon atom (shift 89; exp. shift = 115.2 ppm) in the formal oxidation state of II. In this case the ^{29}Si NMR chemical shift may be quite sensitive to deviations in the double bond length from the effective one in solution. Further, partly dynamic hyperconjugative effects involving the methyl ligand may influence the chemical shift of the respective silicon atom. The largest deviation is observed for the silylene silicon atom in Kira’s cyclosilylene 2,2,5,5-tetrakis(trimethylsilyl)silacyclopentane-1,1-diyl⁶⁷⁸ (**49**) with a deviation of 66.6 ppm (shift 94; exp. shift = 567.4 ppm) which may also correspond to deviations of the silylene bond angle compared to an effective angle in the experiment. In both cases, the discussed

^{29}Si NMR chemical shifts seem to be problematic for a majority of the tested methods. The generally worst performing GGA is SCAN with an MAD of 18.8 ppm and $R^2 = 0.975$. From the (meta-)hybrid class of functionals, TPSSh performs best (MAD = 10.3 ppm, $R^2 = 0.990$) but still significantly worse than B97-D3. M06-2X yields by far the worst results in this class with a very poor MAD of 32.0 ppm ($R^2 = 0.966$). The popular B3LYP and PBE0 functionals yield reasonable MADs of 11.3 ($R^2 = 0.993$) and 12.1 ppm ($R^2 = 0.992$), respectively. For the *SiS-L* subset, the pcSseg-2 basis set generally yields slightly improved results compared to def2-TZVP. The most remarkable improvement is obtained for SCAN, decreasing the MAD from 18.8 to 11.5 ppm and increasing R^2 to 0.987. Double-hybrid density functional

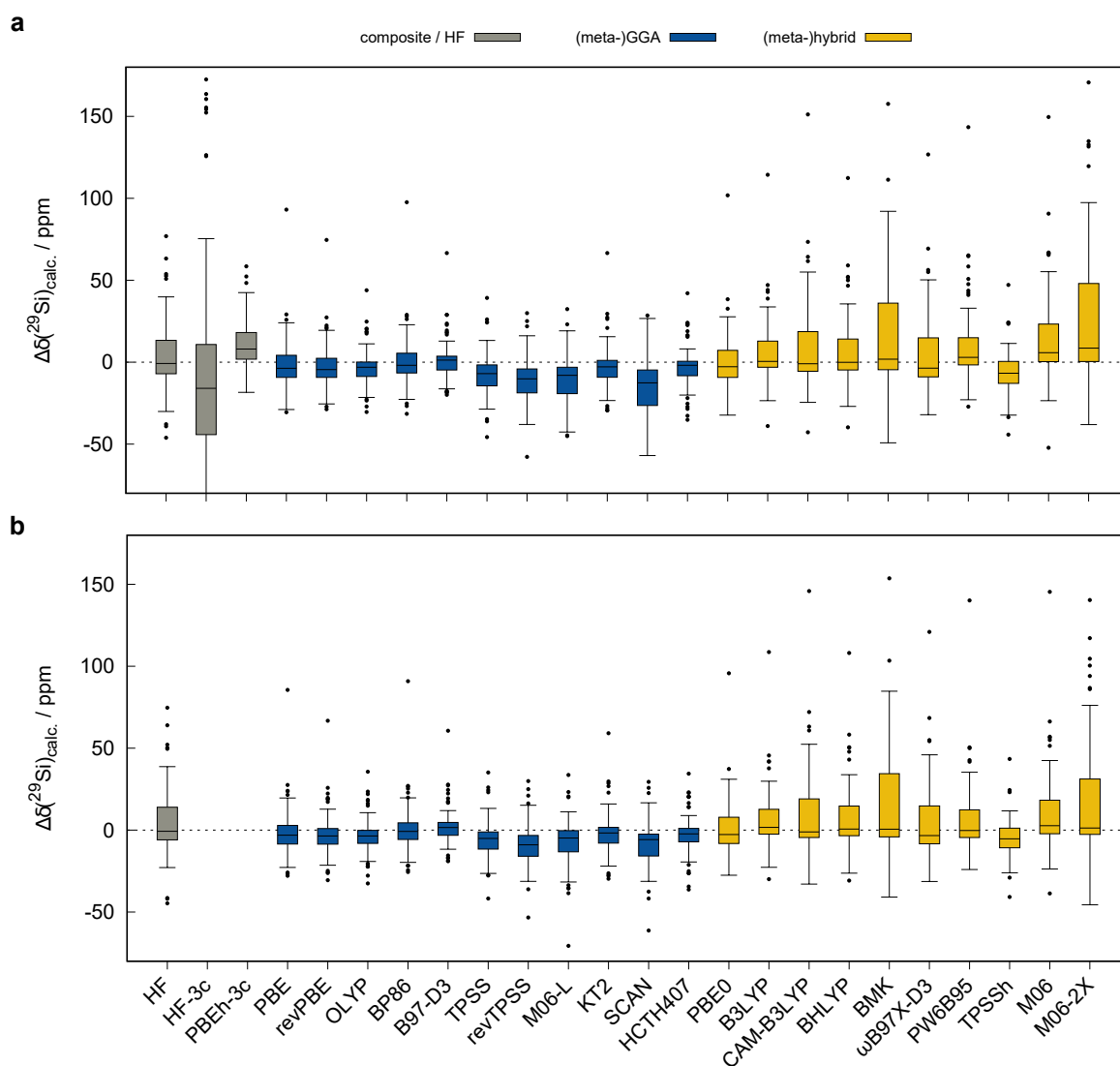


Figure 12.2.: Box plots for all assessed composite/HF, (meta-GGA) and hybrid DFAs applying the a) def2-TZVP or b) pcSseg-2 basis set (except for composite methods that use specialized basis sets) for the *SiS-L* subset. The central black line represents the median value and the whiskers represent the most distant points within 1.5 times the interquartile range. Black dots represent outliers outside this threshold.

12. Benchmark Study on the Calculation of ^{29}Si NMR Chemical Shifts

approximations (DH DFAs) that were shown to perform well for the calculation of ^1H , ^{13}C , and ^{31}P NMR properties were also tested. Unfortunately, the drastically increased memory demand of the calculations proved problematic, specifically for the larger structures included in the *SiS146*. Nevertheless, they only yield no to small improvement over the well performing (meta-)GGA DFAs, even though a direct comparison should be made with care considering the smaller number of data points. For the *SiS-L* subset the best DH DFA (DSD-BLYP) yields a MAD of 8.3 ppm ($R^2 = 0.992$), and mPW2PLYP as the worst a MAD of 11.5 ppm ($R^2 = 0.961$). All data for the DHDFAs can be found in the online Supporting Information of the original publication and is not further discussed.

Table 12.2.: Mean deviation (MD), Mean absolute deviation (MAD), linear scaled MAD ($\text{MAD}_{\text{scaled}}$) in ppm, and determination coefficient R^2 for all tested methods with the def2-TZVP and pcSseg-2 basis sets on the *SiS-L* subset.

<i>SiS-L</i>	def2-TZVP				pcSseg-2			
	MD	MAD	R^2	$\text{MAD}_{\text{scaled}}^a$	MD	MAD	R^2	$\text{MAD}_{\text{scaled}}$
HF	4.46	14.34	0.986	9.62	4.68	14.17	0.985	9.69
HF-3c ^b	-8.39	45.07	0.863	34.56	-	-	-	-
PBEh-3c ^c	10.49	12.95	0.986	10.25	-	-	-	-
PBE	-1.77	10.33	0.991	7.13	-1.54	9.26	0.991	7.06
revPBE	-2.86	9.70	0.991	7.06	-2.74	8.82	0.991	7.02
OLYP	-3.59	8.36	0.992	6.94	-3.68	7.98	0.992	7.01
BP86	0.25	9.49	0.992	6.57	0.66	8.45	0.992	6.60
B97-D3	1.31	7.19	0.993	6.24	1.88	6.89	0.993	6.43
TPSS	-7.17	10.77	0.989	8.34	-5.41	9.23	0.991	7.49
revTPSS	-10.71	13.78	0.986	9.86	-9.16	12.27	0.989	8.75
M06-L	-11.86	14.58	0.980	12.26	-7.18	10.91	0.986	9.90
KT2	-2.68	8.80	0.989	8.05	-1.92	8.14	0.989	7.96
SCAN	-16.01	18.81	0.975	14.07	-8.48	11.51	0.987	9.54
HCTH407	-2.94	8.09	0.991	7.32	-2.94	7.80	0.991	7.41
PBE0	0.35	12.05	0.992	7.21	0.61	11.14	0.992	7.14
B3LYP	4.94	11.33	0.993	6.41	5.17	10.84	0.993	6.51
CAM-B3LYP	7.93	16.49	0.990	8.62	8.18	15.63	0.990	8.48
BHLYP	6.24	13.34	0.992	7.65	6.52	12.78	0.992	7.59
BMK	13.78	22.45	0.982	11.58	12.77	21.35	0.984	10.96
ω B97X-D3	4.72	16.70	0.988	9.32	5.00	15.86	0.988	9.24
PW6B95	9.20	13.61	0.990	8.15	4.25	11.87	0.991	6.92
TPSSh	-5.90	10.30	0.990	7.98	-4.38	8.99	0.992	7.30
M06	13.43	18.80	0.989	8.88	9.07	15.43	0.992	7.51
M06-2X	26.25	32.03	0.966	16.65	17.26	25.67	0.979	12.51

^aThe linear scaling approach principally yields MD = 0 and does not influence the R^2 values.

^bMINIX basis.

^cdef2-mSVP basis.

Linear Scaling

Based on a sufficiently large data set, an empirical, linear scaling approach can be applied to derive method dependent scaling parameters α and β that represent the slope and the intercept of the linear best fit with respect to the experimental data. As shown in previous works^{679–683}, α and β can be applied according to equation 12.2 to correct for systematic errors.

$$\delta_{calc.,scaled} = \frac{(\delta_{calc.} - \beta)}{\alpha} \quad (12.2)$$

We applied this approach to all tested functionals on the *SiS-L* subset. Overall, the MAD can be reduced by 0.8 ppm (8%, KT2) to 15.4 ppm (53%, M06-2X) with 31% improvement on average for the def2-TZVP basis set (Table 12.2). The effect of linear scaling for B97-D3 and M06-2X is depicted in figure 12.3.

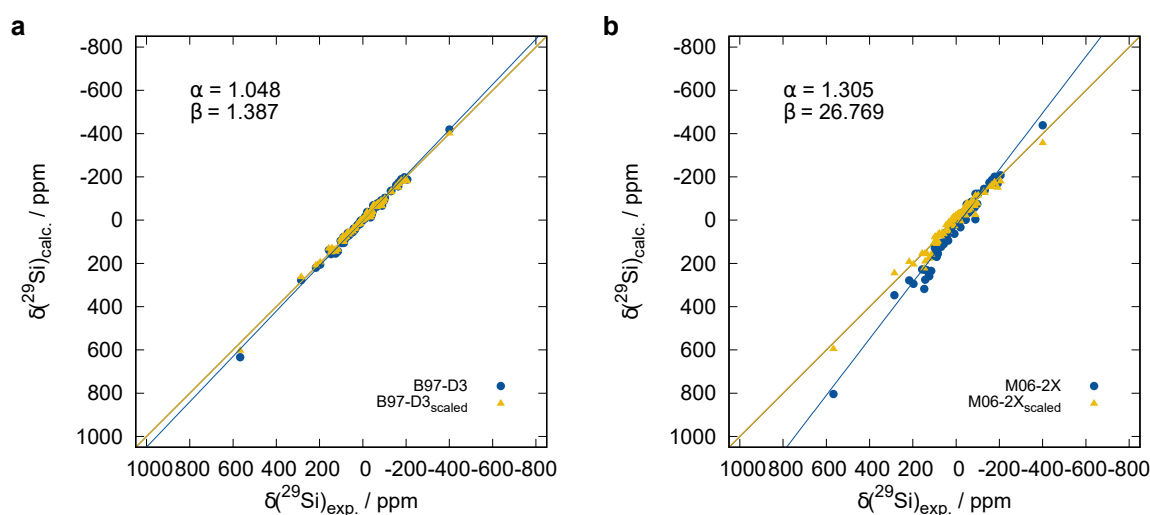


Figure 12.3.: Correlation plots with respect to the experimental chemical shifts for a) B97-D3 and b) M06-2X before and after linear scaling correction applying the def2-TZVP basis set on the *SiS-L* subset.

Basis Set Dependence

As the choice of the applied basis set always inherits the question of efficiency and applicability, we investigated the basis set dependence of the chemical shifts on the *SiS-L* subset with the Ahlrichs def2-*X* (*X* = SVP, mSVP, TZVP, mTZVP, TZVPP, QZVP, QZVPP), Jensen's polarization-consistent pcSseg-*n* and pc-*n* (*n* = 0–3), and Dunning's correlation-consistent cc-pVXZ (*X* = D, T, Q) basis set families for B97-D3. For all tested families, a rapid convergence is observed regarding the mean absolute deviations and determination coefficients R^2 on the *SiS-L* subset (Figure 12.4). Increasing the basis set beyond triple- ζ quality does not improve the results significantly and leads to drastically increased computation times. Thus, the def2-TZVP and pcSseg-2 basis sets can be recommended as both offer a good compromise between speed and performance. Nevertheless, for pc-*n* and pcSseg-*n* basis sets beyond *n* = 2, increasing SCF convergence problems were observed. A better performance of Dunning's correlation consistent

12. Benchmark Study on the Calculation of ^{29}Si NMR Chemical Shifts

cc-pVXZ(-PP) basis sets compared to def2-X and pcSseg-n basis sets, as reported for ^{13}C NMR and ^1H NMR⁶⁸⁴ was not observed. Further, it should be noted that specifically the pc-n and pcSseg-n basis sets are only available up to Kr ($Z = 36$), and hence for the heavier elements, the corresponding def2-X basis set was applied. The small MINIX basis set produces large errors and a low determination coefficient of 0.865.

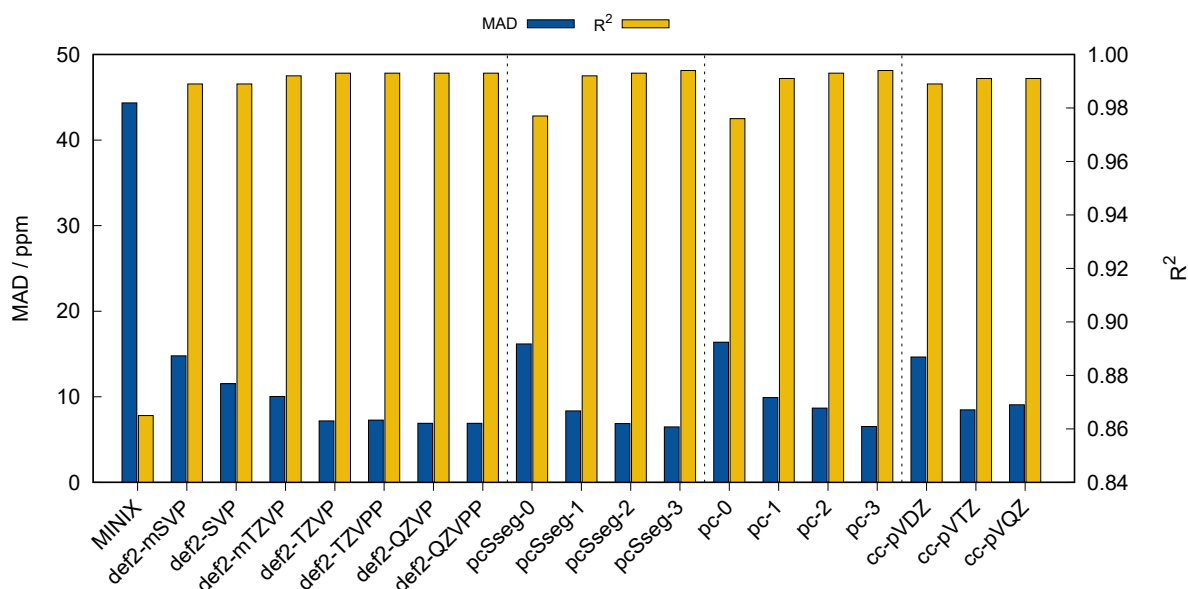


Figure 12.4.: MAD in ppm and determination coefficient R^2 for the SiS-L subset calculated with B97-D3 and various AO basis sets.

The Heavy Atom Subset SiS-H and Relativistic Effects

The vicinity of the silicon atom to a heavier atom requires consideration of relativistic effects on its chemical shift. Generally, such so-called heavy atom effects on the light atom (HALA) include scalar or spin-free relativistic (SFR) and the often dominant spin-orbit (SO)-HALA effects^{685–689} that can have a huge impact on the quality of the chemical shift calculation⁶⁹⁰. Popular treatments to account for HALA effects are (SO-)ECPs or the widely used (SO-)ZORA^{559,691} approximation. As ECPs and the scalar-relativistic (SR) version of ZORA are the most common and easily accessible methods for the calculation of NMR shielding constants, we herein focus on to what extent scalar-relativistic treatments can improve the results for ^{29}Si NMR chemical shift calculations. Nevertheless, it must be stressed that particularly pronounced SO-HALA effects require more sophisticated theory, and such cases should be assessed individually. Besides the ECP and SR-ZORA calculations for all tested DFAs we applied the two-component SO-ZORA for seven GGA and hybrid functionals for the SiS-H subset consisting of 44 molecules with heavy atoms ($Z > 18$) in direct neighborhood to the silicon atom as well as for SiCl_4 (Table 12.3). Selected structures and calculated ^{29}Si NMR chemical shifts are depicted in figure 12.5. For the SiS-H subset HALA effects are expected to play an important role for the ^{29}Si NMR chemical

shifts. To investigate the HALA effects in more detail, the commonly used SR-ZORA and SO-ZORA approaches were further evaluated in conjunction with the Slater-type orbital TZP basis set as implemented in the ADF2019.303 program package^{640,641} (Table 12.3). For the *SiS-H* subset no improvement upon application of scalar relativistic ZORA in conjunction with the def2-TZVP basis set is observed (Figures 12.6a, b). Instead mostly a slightly increased MAD is observed except for the hybrid DFAs M06, PW6B95, ω B97X-D3, BMK, and CAM-B3LYP (Table 12.3). SR-ZORA with the TZP basis set also yields no clear trend of improvement, increasing the MAD for KT2 by 5.1 ppm which may be attributed to disturbed error compensation due to the construction of the KT2 functional being explicitly fitted to NMR shielding constants⁶⁶³. For B3LYP on the other hand, an MAD improvement by 3.1 ppm is observed. While the effect of both SR-ZORA approaches is generally small, the introduction of SO-ZORA drastically decreases the MADs by 30.1 ppm (71%, KT2) to 36.0 ppm (68%, B3LYP) with respect to the ECP/def2-TZVP results. Thus, the SO-ZORA treatment is strongly recommended to obtain reasonable ²⁹Si NMR chemical shifts for compounds with expected HALA effects. An example with tremendous spin-orbit relativistic effects is tetraiodosilane (**83**, SiI₄) with an experimental shift of -346.6 ppm. Here ECP and SR-ZORA based PBE0 calculations yield drastically wrong chemical shifts of 91.9 to 105.0 ppm,

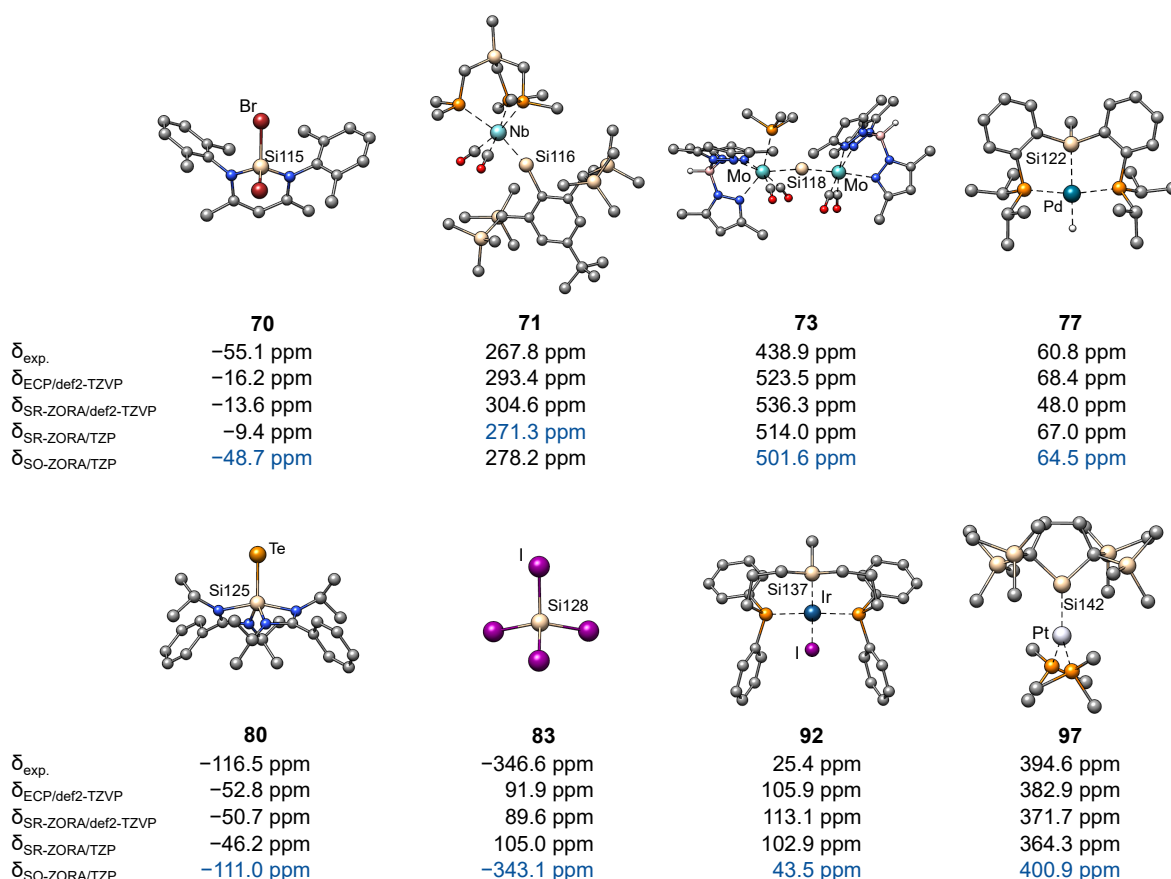


Figure 12.5.: Selected molecules with heavy atoms in the vicinity of the Si atom. Chemical shifts were calculated with the PBE0 functional. The shift that deviates least from the experimental reference is marked in blue. Hydrogen atoms attached to carbon are omitted for clarity.

12. Benchmark Study on the Calculation of ^{29}Si NMR Chemical Shifts

and only the SO-ZORA approach yields a good result of -343.1 ppm. Overall, robust GGA DFAs like BP86, revPBE or OLYP can be recommended for the use with SO-ZORA and a TZP basis set for the calculation of ^{29}Si NMR chemical shifts of HALA affected silicon atoms (SiS-H $\text{MAD}_{\text{SO-ZORA-BP86/TZP}} = 12.3$ ppm, $R^2 = 0.993$). The PBE0 hybrid functional may represent a valuable alternative if explicit Fock-exchange is needed (SiS-H $\text{MAD}_{\text{SO-ZORA-PBE0/TZP}} = 13.6$ ppm, $R^2 = 0.995$). For SO-ZORA-BP86/TZP the largest remaining deviation on the SiS-H subset is observed for Filippou's cationic chromio silylene complex $[(\eta^5\text{-C}_5\text{Me}_5)(\text{CO})_3\text{Cr-Si}(\text{SiDipp})]^+$ (**58**, $\text{SiDipp} = 1,3\text{-bis}(2,6\text{-diisopropylphenyl})\text{imidazolidin-2-}$

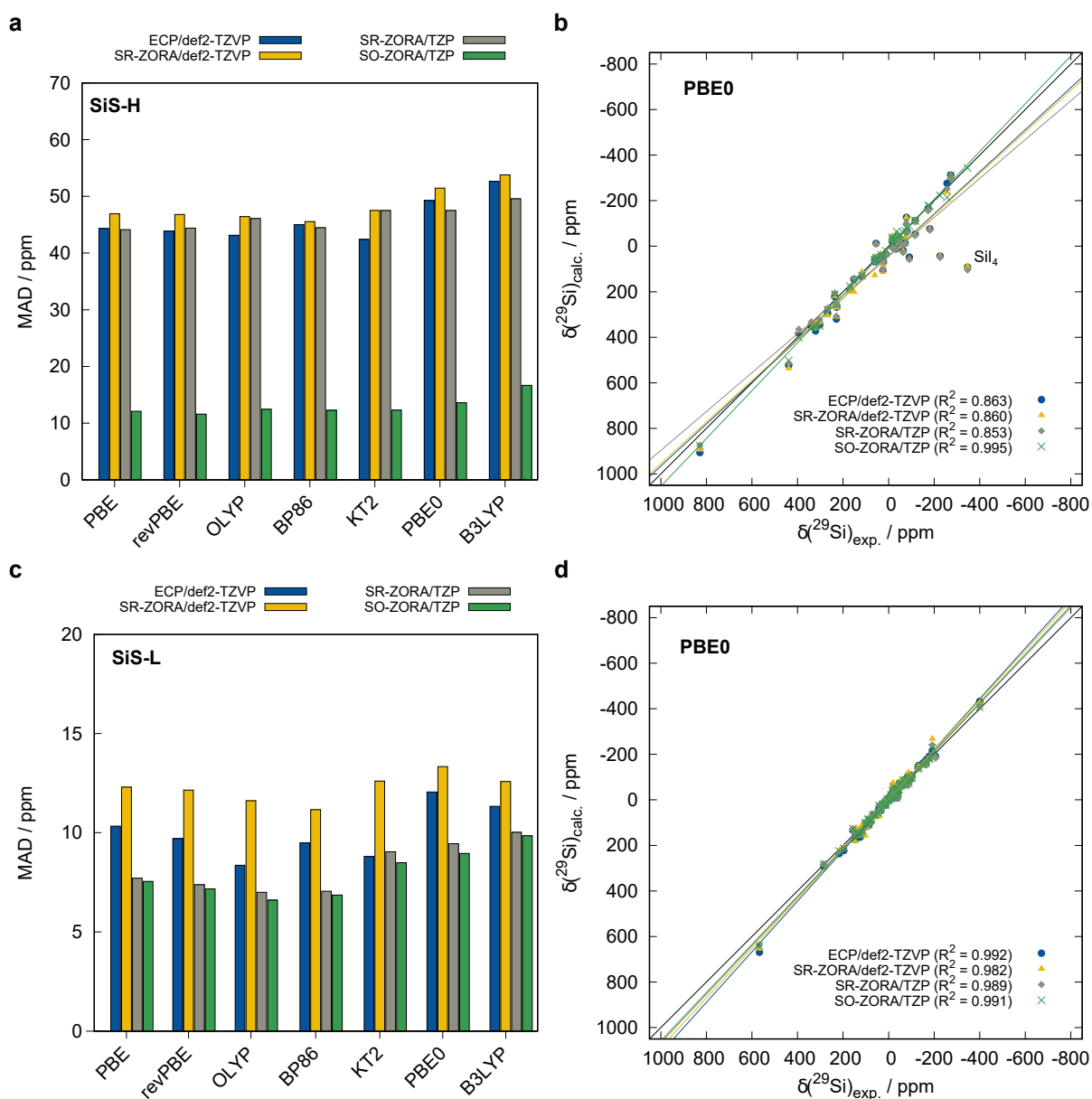


Figure 12.6.: Mean absolute deviations for various relativistic approaches for the a) SiS-H and the c) SiS-L subsets. Correlation plots of experimentally obtained ^{29}Si NMR chemical shifts and those calculated with the PBE0 functional combined with different relativistic approaches (a) SiS-H and d) SiS-L .

Table 12.3.: Mean absolute deviation (MAD) in ppm and determination coefficient (R^2) for several relativistic approaches for the *SiS-H* subset with expected strong HALA effects.

<i>SiS-H</i>	ECP/def2-TZVP		SR-ZORA/def2-TZVP ^a		SR-ZORA/TZP ^b		SO-ZORA/TZP ^b	
	MAD	R^2	MAD	R^2	MAD	R^2	MAD	R^2
HF	63.01	0.794	70.75	0.778	–	–	–	–
HF-3c ^c	80.17	0.827	–	–	–	–	–	–
PBEh-3c ^d	52.72	0.840	–	–	–	–	–	–
PBE	44.32	0.859	46.94	0.858	44.13	0.852	12.10	0.993
revPBE	43.86	0.860	46.80	0.858	44.40	0.851	11.58	0.994
OLYP	43.15	0.859	46.43	0.857	46.09	0.847	12.44	0.994
BP86	45.00	0.859	45.56	0.858	44.45	0.852	12.25	0.993
B97-D3	44.80	0.858	48.63	0.856	–	–	–	–
TPSS	43.87	0.856	48.86	0.863	–	–	–	–
revTPSS	45.87	0.853	47.43	0.862	–	–	–	–
M06-L	50.68	0.844	51.38	0.864	–	–	–	–
KT2	42.39	0.860	47.52	0.859	47.49	0.843	12.30	0.994
SCAN	49.83	0.847	58.13	0.872	–	–	–	–
HCTH407	44.03	0.856	47.68	0.852	–	–	–	–
PBE0	49.25	0.863	51.44	0.860	47.50	0.853	13.60	0.995
B3LYP	52.63	0.861	53.80	0.859	49.56	0.853	16.66	0.997
CAM-B3LYP	63.14	0.862	63.00	0.862	–	–	–	–
BHLYP	61.48	0.861	63.84	0.857	–	–	–	–
BMK	69.85	0.863	67.16	0.861	–	–	–	–
ω B97X-D3	58.73	0.863	57.69	0.863	–	–	–	–
PW6B95	57.80	0.866	56.78	0.838	–	–	–	–
TPSSh	43.97	0.858	48.62	0.864	–	–	–	–
M06	63.93	0.861	58.03	0.839	–	–	–	–
M06-2X	83.79	0.856	84.56	0.820	–	–	–	–

^aZORA-def2-TZVP and/or SARC-def2-TZVP recontracted basis sets within ORCA.

^bZORA/TZP basis set within ADF.

^cMINIX basis.

^ddef2-mSVP basis.

ylidene)⁶⁹² with a calculated shift of 775.9 ppm and a deviation of 52.7 ppm. Further, a relatively large deviation is observed for the iridium complex [IrIH(biPSi)] (**92**, biPSi = κ -*P,P*,*Si*-Si(Me){(CH₂)₃PPh₂}₂)⁶⁹³ with a calculated chemical shift of 70.3 ppm and a deviation of 44.9 ppm. For the *SiS-L* subset, the effect of SO-ZORA is much smaller with 1 % (KT2) to 25 % (BP86) improvement by SO-ZORA compared to the ECP results (Figures 12.6c, d). Thus, nonrelativistic chemical shift calculations on non-HALA affected silicon atoms should be sufficiently accurate for most purposes. For the *SiS-L* subset, a slight deterioration of the results was observed applying the SR-ZORA/def2-TZVP approach. Even though an empirical linear scaling correction cannot be applied reasonably to the ECP data due to strong scattering of the data points and very low determination coefficients (cf. figures 12.6b, d), it can further

12. Benchmark Study on the Calculation of ^{29}Si NMR Chemical Shifts

improve the results of the ZORA relativistic calculations.

Structure Dependence of ^{29}Si NMR Calculated Chemical Shifts

To estimate the influence of the geometry optimization level on the calculated ^{29}Si NMR chemical shift, ^{29}Si NMR chemical shifts are calculated for five structures from each, the *SiS-L* and *SiS-H* subsets, that were reoptimized on different theoretical levels (Figure 12.7). These are, B97-3c from the 3c-composite method family, the GFN2-xTB extended tight binding method, the GFN-FF⁵⁶ generic force-field, TPSS-D4/def2-TZVP, and B3LYP-D4/def2-SVP. Overall, the MAD varies only slightly depending on the geometry optimization method when changing the DFA. The largest deviation in the DFA class is observed on B3LYP-D4/def2-SVP structures with an MAD change of 1.9 ppm for PBE0 (2.1 ppm for PBE) compared to the results at the reference PBEh-3c structures. Application of the semi-empirical quantum mechanical (SQM) extended tight binding method GFN2-xTB for geometry optimization results in significantly increased MADs, i.e., by 15.8 ppm for PBE0 and 11.9 ppm for PBE, respectively, more than doubling the MAD for the evaluated subset. Even worse results are obtained for geometries optimized with the GFN-FF generic force-field (FF) which mainly results from deviations in bonding angles of low coordinated silicon atoms. Nevertheless, the errors introduced by geometry optimization with a low-cost SQM or FF method can be partly compensated by linear scaling (Figure 12.8) which is strongly recommended in this case. For the SO-ZORA/BP86 DFA applied on GFN-FF structures, the *SiS-H* subset MAD can be reduced by 19.8 ppm (47 %) resulting in an $\text{MAD}_{\text{scaled}}$ of 22.0 ppm (Figure 12.8d). Thus, even though an optimization at the low-cost DFT level is recommended to obtain the best results, substitution of the computational demanding geometry optimization by SQM or FF methods may be applied in com-

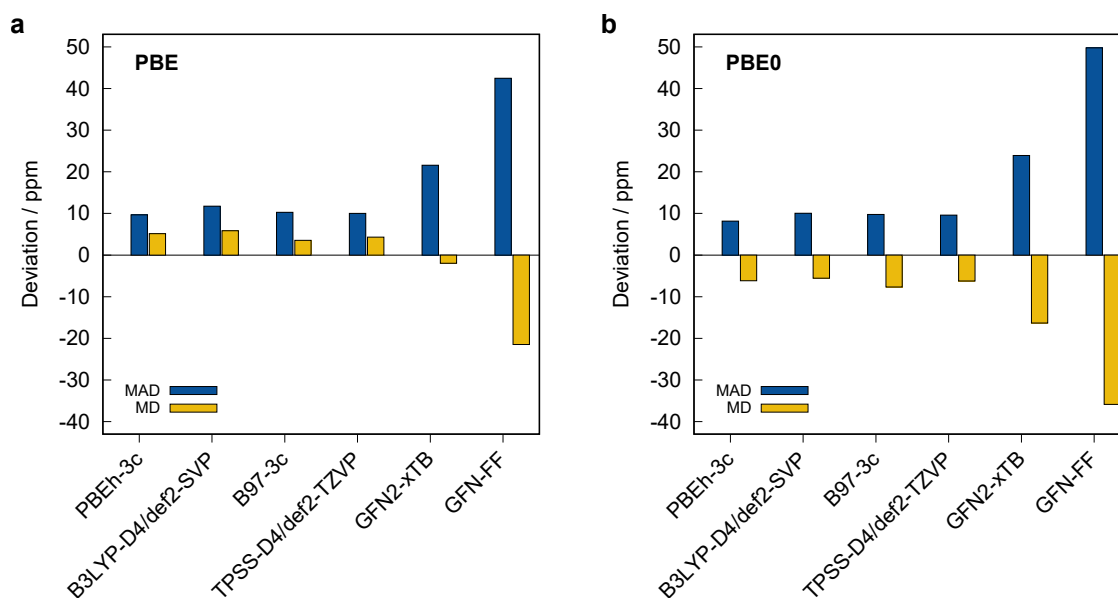


Figure 12.7.: Deviations for a) PBE, and b) PBE0 ^{29}Si NMR chemical shifts calculated on differently optimized geometries for a selection of ten representative structures applying the SO-ZORA treatment and the TZP basis set. All deviations are given in ppm.

bination with a linear scaling correction to obtain reasonable results. This approach may be applied to efficiently calculate ^{29}Si NMR chemical shifts of large structures. Respective scaling parameters for selected, well performing methods based on the *SiS146* set for use on SQM or FF method optimized geometries are provided in table 12.4. Structures that are chemically destroyed upon optimization with the respective SQM/FF method were excluded from the evaluation.

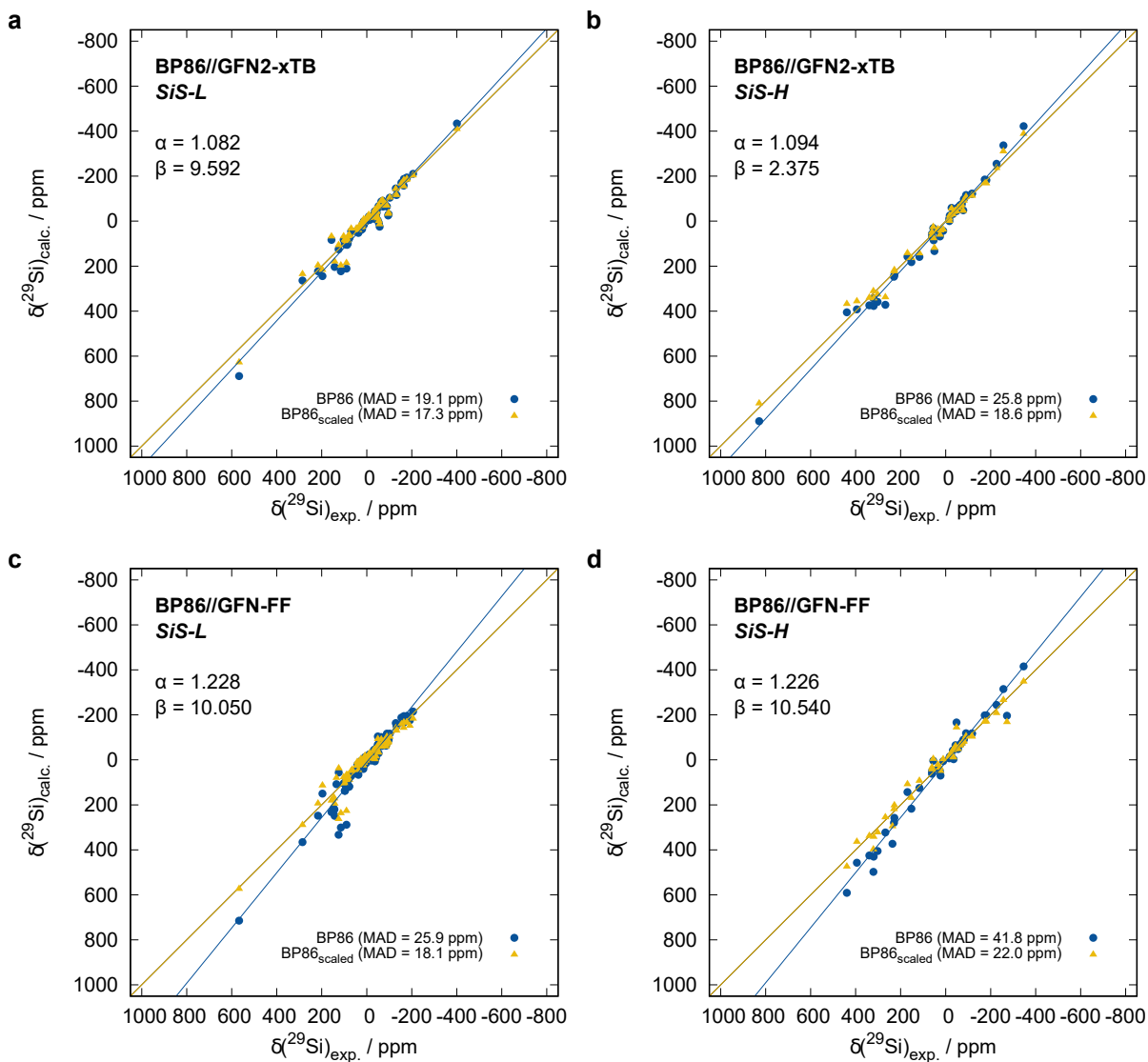


Figure 12.8.: Uncorrected and linear scaling corrected ^{29}Si NMR chemical shifts (SO-ZORA/BP86/TZP) at GFN2-xTB and GFN-FF structures for the *SiS-L* and *SiS-H* subsets. Respective MADs are given in parentheses.

12. Benchmark Study on the Calculation of ^{29}Si NMR Chemical Shifts

Table 12.4.: Scaling parameters derived from the *SiS146* set for ^{29}Si NMR chemical shift calculations on GFN2-xTB and GFN-FF geometries.

<i>SiS-L</i>	GFN2-xTB				GFN-FF			
	MAD	MAD _{scaled}	α	β	MAD	MAD _{scaled}	α	β
BP86/def2-TZVP	20.75	17.17	1.130	11.189	29.33	18.86	1.282	11.249
B97-D3/def2-TZVP	21.00	17.21	1.094	11.754	25.99	17.99	1.234	11.765
PBE0/def2-TZVP	22.18	17.49	1.159	13.667	32.42	20.41	1.323	12.034
B3LYP/def2-TZVP	26.34	18.71	1.183	17.130	32.82	19.95	1.342	16.740
BP86/pcSseg-2	20.57	17.23	1.116	11.244	28.27	18.78	1.267	11.491
B97-D3/pcSseg-2	20.88	17.53	1.080	11.958	25.19	17.90	1.220	12.207
PBE0/pcSseg-2	21.61	17.32	1.145	13.623	31.18	20.39	1.308	12.261
B3LYP/pcSseg-2	26.07	18.85	1.170	17.034	31.86	19.92	1.328	16.950
SO-ZORA-BP86/TZP	19.05	17.25	1.082	9.592	25.92	18.10	1.228	10.050
SO-ZORA-PBE0/TZP	20.33	18.01	1.108	13.261	31.67	22.11	1.227	9.037
<i>SiS-H</i>	GFN2-xTB				GFN-FF			
	MAD	MAD _{scaled}	α	β	MAD	MAD _{scaled}	α	β
SO-ZORA-BP86/TZP	25.79	18.59	1.094	2.375	41.78	21.96	1.226	10.540
SO-ZORA-PBE0/TZP	26.50	16.53	1.142	9.087	43.14	26.76	1.250	12.297

12.4. Conclusion and Outlook

The ^{29}Si NMR spectroscopy is a highly valuable analytical tool for academic and industrial researchers due to the well defined ^{29}Si core with a spin of $\frac{1}{2}$. It is sensitive to details of the chemical surroundings, and the high range of observed chemical shifts is suited as a reliable indicator for chemical coordination and bonding patterns. Thus, an efficient computational prediction of these chemical shifts is highly desirable. Nevertheless, several previous studies only covered a narrow range of already well studied structural motifs or only a small number of methods regarding the calculation of ^{29}Si NMR chemical shifts. Therefore, a comprehensive benchmark set termed *SiS146* containing 146 experimentally determined ^{29}Si NMR chemical shifts for 100 small to large sized compounds with diverse bonding situations at the silicon center was composed. For this benchmark set, the performance of 26 common DFT based methods with several AO basis sets was tested for the calculation of ^{29}Si NMR chemical shifts. It is sectioned into two subsets: the *SiS-L* containing only compounds composed of light elements ($Z < 18$), and the *SiS-H* subset including compounds with heavier elements. For the *SiS-H* subset, the role of explicit treatment of relativistic effects (SR/SO-ZORA) is evaluated. Further, the basis set convergence and geometry optimization method dependence are investigated exemplarily. Overall, the B97-D3 GGA functional performs best (with the def2-TZVP basis set) with an MAD of 7.2 ppm and a high determination coefficient of 0.993 for the *SiS-L* subset. Generally, the tested (meta-)GGA DFAs outperform hybrid functionals with TPSSh producing the smallest MAD of 10.3 ppm in the hybrid class. These results do not follow a trend of improved results for higher rungs of the Jacob's ladder that is known for, i.e., ther-

mochemical calculations but is in agreement with prior studies on other elements⁶⁹⁴. The worst results are obtained with the M06-2X DFA, yielding a high MAD of 32.0 ppm. Application of Jensen's pcSseg-2 basis set generally yields slightly smaller (mostly about 1 ppm) MADs compared to the def2-TZVP basis set but is not generally available for heavier elements. For the worse methods, a linear scaling approach may be applied to significantly improve the results. For both, the def2-X and the pcSseg-n basis sets, the results proved to be sufficiently converged with respect to the basis set size at the triple- ζ level (def2-TZVP, pcSseg-2), representing a good compromise between computational cost and accuracy. For the *SiS-H* subset, the application of ECPs proved insufficient due to in part pronounced HALA effects. While scalar-relativistic ZORA approaches do not yield significant improvements, spin-orbit ZORA improves the calculated ²⁹Si NMR chemical shifts drastically. The SO-ZORA treatment reduces the MADs by up to 74%, which corresponds to an MAD decrease of, e.g., 32.3 ppm for revPBE compared to the ECP result. Thus, an explicit spin-orbit relativistic treatment for HALA prone ²⁹Si cores is highly recommended. The DFT geometry optimization level has only minor influence on the quality of the results as long as no serious structural issues are observed. For a representative selection of structures from the *SiS146* set the variations in the MADs compared to those calculated on PBEh-3c geometries only amount up to about 2 ppm. Geometry optimization by semi-empirical or force-field methods may be applied in combination with a linear scaling correction of the shifts to obtain reasonable MADs in combination with a well performing ²⁹Si NMR chemical shift calculation DFA. In conclusion, robust GGA methods like B97-D3/def2-TZVP can be used reliably for the calculation of ²⁹Si NMR chemical shifts based on PBEh-3c geometries. The triple- ζ basis sets def2-TZVP and pcSseg-2 provide a good cost to accuracy ratio for efficient chemical shift calculations. For ²⁹Si cores in the vicinity of heavier atoms ($Z > 18$), explicit spin-orbit relativistic treatment, e.g., by the SO-ZORA approach, is indispensable to obtain reliable results. In this context, i.e. the SO-ZORA-BP86/TZP method proved to be a reliable choice with a relatively small MAD of 12.3 ppm and a high correlation coefficient of 0.993 for the *SiS-H* subset. Other GGAs like revPBE perform comparably well. If a hybrid DFA is needed, SO-ZORA-PBE0/TZP can be used alternatively with an MAD of 13.6 ppm and $R^2 = 0.995$. The presented *SiS146* benchmark set provides a comprehensive, diverse and robust test set for further method development and enables computational chemists to make a profound method choice for calculating ²⁹Si NMR chemical shifts.

Acknowledgements

The authors thank Fabian Bohle and Karola Schmitz for fruitful discussions, all experimental groups for synthesizing manifold silicon containing molecules accompanied by high quality ²⁹Si NMR measurements, and Prof. Yitzhak Apeloig for bringing the topic of this study to our attention. This work was supported by the Deutsche Forschungsgemeinschaft (DFG) in the framework of the Gottfried Wilhelm Leibniz prize awarded to S.G. Financial support by the Fonds der Chemischen Industrie (FCI) to J.B.S. is gratefully acknowledged.

13. Quantification of Non-covalent Interactions in Azide-Pnictogen, -Chalcogen, and -Halogen Contacts

Markus Bursch,^a Lukas Kunze,^a Amol M. Vibhute,^b Andreas Hansen,^a Kana M. Sureshan,^c Peter G. Jones,^d Stefan Grimme,^a and Daniel B. Werz^b

This article is dedicated to the memory of Professor Rolf Huisgen.

Received: 2 April 2020, Published online: 20 October 2020

Reprinted (adapted) with permission[†] from

Bursch, M.; Kunze, L.; Vibhute, A. M.; Sureshan, K. M.; Jones, P. G.; Hansen, A.; Grimme, S.; Werz, D. B. *Chem. Eur. J.* **2021**, *27*, 4627–4639.

– Copyright © 2020, The Authors.

DOI [10.1002/chem.202004525](https://doi.org/10.1002/chem.202004525)

Own manuscript contribution

- Conception of the study and choice of methods
- Performing DFT/SQM association energy, NBO, DID and ESP calculations
- Interpretation of the results
- Writing the manuscript

^aMulliken Center for Theoretical Chemistry, Institut für Physikalische und Theoretische Chemie, Rheinische Friedrich-Wilhelms-Universität Bonn, Beringstraße 4, 53115 Bonn, Germany

^bInstitut für Organische Chemie, Technische Universität Braunschweig, Hagenring 30, 38106 Braunschweig, Germany

^cSchool of Chemistry, IISER Thiruvananthapuram, Kerala-695551, India

^dInstitut für Anorganische und Analytische Chemie, Technische Universität Braunschweig, Hagenring 30, 38106 Braunschweig, Germany

[†]Permission requests to reuse material from this chapter that is not covered by the Creative Commons Attribution license should be directed to the authors.

Abstract The non-covalent interaction between azide and oxygen containing moieties is investigated by a computational study based on experimental findings. Targeted synthesis of organic compounds with close intramolecular azide-oxygen contacts yielded six new representatives, for which X-ray structures were determined. Two of those compounds were investigated with respect to their potential conformations in the gas-phase and a possible significantly short azide-oxygen contact. Furthermore, a set of 44 high-quality gas-phase computational model systems with intermolecular azide-pnictogen (N, P, As, Sb), chalcogen (O, S, Se, Te), and -halogen (F, Cl, Br, I) contacts is compiled and investigated by semi-empirical quantum mechanical methods, density functional approximations and wave function theory. A local energy decomposition (LED) analysis is applied to study the nature of the non-covalent interaction. The special role of electrostatic and London dispersion interactions is discussed in detail. London dispersion is identified as a dominant factor of the azide-donor interaction with mean London dispersion energy-interaction energy ratios of 1.3. Electrostatic contributions enhance the azide-donor coordination motif. The association energies range from -1.00 to -5.5 kcal mol $^{-1}$.

13.1. Introduction

Non-covalent interactions play a very important role in biological, physical and chemical sciences^{695–699}. They are crucial for crystal packing, for the self-assembly of large molecules in solution, and for biological pattern recognition, to name just a few examples^{31,700,701}. Besides highly electrostatic interactions (e.g. ion-ion, ion-dipole, dipole-dipole), the most prominent type is hydrogen bonding, but chalcogen-chalcogen^{702–705} and halogen-halogen interactions^{706–708} or combinations thereof have also received significant attention during the last few decades. Furthermore, moieties which only consist of π systems often strongly interact with each other by so-called π - π stacking interactions^{709,710} and even between purely sp^3 hybridized hydrocarbon moieties one encounters weak attractive forces that

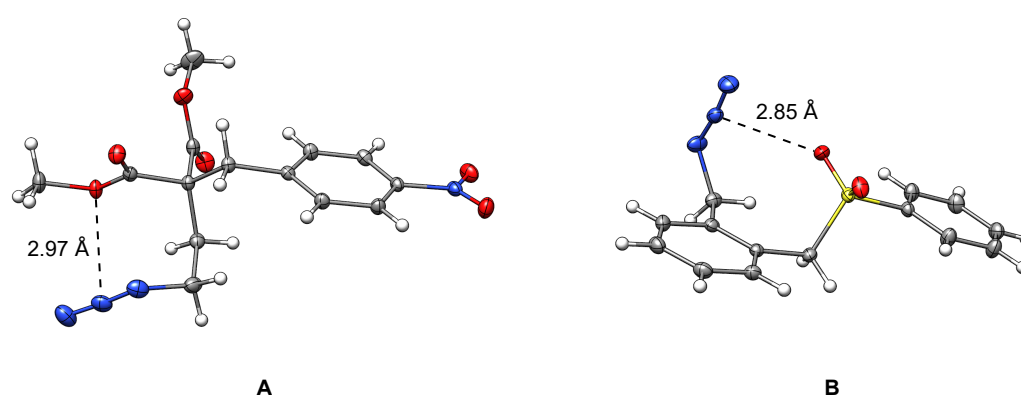


Figure 13.1.: Two representative examples of compounds with close intramolecular oxygen-azide contacts in the solid. Nitrogen is depicted in blue, oxygen in red, sulfur in yellow, carbon in grey. Given are the interatomic distances between the N2 of the azide and the closest oxygen atom. Thermal ellipsoids are shown at 50 % probability.

are mainly based on London dispersion⁷¹¹. All these interactions have been successfully employed in crystal engineering and supramolecular assembly of compounds^{712–721}, and to facilitate catalysis^{722–728}. During our solid-state studies of some compounds containing flexible azide moieties and oxygen atoms, we noticed that mono- and divalent oxygen functionalities often display a close intramolecular contact with the central nitrogen atom (N2) of the azide moiety. In many of these cases, numerous other conformations would have been possible, but nonetheless, the molecular conformation with the closest contact between N2 and O seems to be preferred. Two representative examples of molecules that show close azide-oxygen contacts in the solid state are depicted in figure 13.1.^a In 2017, a close intermolecular contact between azide moieties and the oxygen of cucurbit[6]uril was discovered by Keinan and co-workers, but not investigated in detail⁷²⁹. To investigate whether these interactions lead to a significant energy gain we compiled a larger set of structures involving intermolecular contacts (Figure 13.2). Structures deposited in the Cambridge Crystallographic Data Centre (CCDC)²⁰² were evaluated with respect to pnictogen-, chalcogen- and halogen- (henceforth denoted as PCH) -azide contacts. These contacts include e.g. divalent oxygen moieties as in ethers or esters or monovalent oxygen as found in

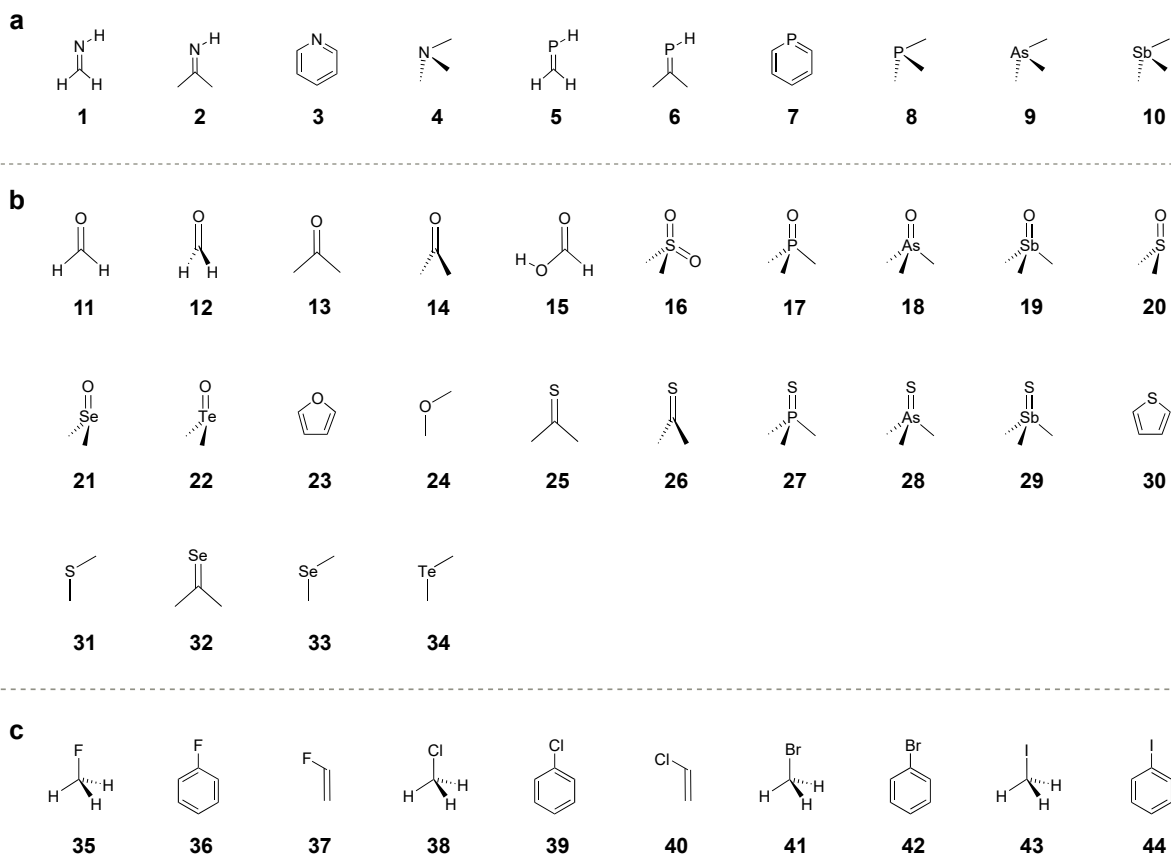


Figure 13.2.: Overview of the investigated interacting model compounds and their orientations. a) Pnictogens; b) chalcogens; c) halogens.

^aDeposition Numbers CCDC 1994147-1994152 contain the supplementary crystallographic data for this paper. These data are provided free of charge by the joint Cambridge Crystallographic Data Centre and Fachinformationszentrum Karlsruhe Access Structures service www.ccdc.cam.ac.uk/structures.

13. Quantification of Non-covalent Interactions in Azide-Pnictogen, -Chalcogen, and -Halogen Contacts

carbonyls, phosphine oxides and sulfoxides. Figure 13.3 depicts the data obtained for azide interacting moieties. It is observed that many of these contacts are much shorter than the sum of the van der Waals radii⁵⁵⁵ (3.07 Å for nitrogen···oxygen, blue dashed line). For the $N3-N2\cdots X$ angle (for a definition, see figure 13.4) there is a strong accumulation of data points between 85° and 130° . Some of these might have to be interpreted with care, since not every structure was individually evaluated. Furthermore, in some cases, the close contacts may have other causes than attractive oxygen-azide interactions. However, the strength and the nature of these interactions have not yet been investigated. In this article, we close this gap using quantum chemical computations that indicate preferred arrangements and respective interaction energies of pnictogens, chalcogens, and halogens interacting with azides.

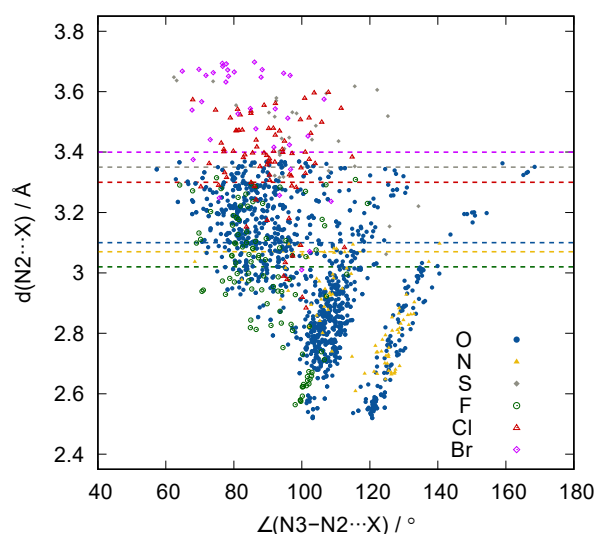


Figure 13.3.: Plot for azide-oxygen, -nitrogen, -sulfur, -fluorine, -chlorine and -bromine contacts of all the structures deposited in the CCDC: $N3-N2\cdots X$ angle (in $^\circ$) vs. $N2\cdots X$ distance (in Å). The dotted lines show the corresponding sum of the van der Waals radii.

13.2. Results and Discussion

Computational details

All quantum-mechanical calculations were performed with the ORCA 4.2.1^{208,286,287} (DFT, MP2, DLPNO-CCSD(T), DID⁷³⁰), MOLPRO2015.1^{731,732} (W2-F12, W1-F12), TURBOMOLE 7.3.1^{206,285} (ESP), MOPAC2016²⁰⁵ (PMx), and xtb 6.2.1⁷³³ (conformational search, GFNn-xTB, driver for MOPAC calculations) program packages. All adduct and monomer structures were optimized using spin-component scaled second-order Møller-Plesset Perturbation Theory (SCS-MP2)^{111,734} applying the large def2-QZVPP²⁴⁰ basis set, for the larger conformer geometries the def2-TZVPP basis set was employed. Local energy decomposition (LED)^{735,736} analyses in the DLPNO-CCSD(T)/def2-QZVPP framework were conducted with *VeryTightPNO* settings^{83,84,293}. Automated conformer search was conducted with the CREST⁶⁴ program applying the iMTD-GC²³¹ algorithm with the GFN2-xTB⁵⁴ tight binding semi-empirical method. Energetic pre-sorting of the conformer rotamer ensemble was performed with the

ENSO^{61,313} script at the PBEh-3c⁶⁹ level of theory (free energies obtained by inclusion of thermostatical and zero-point vibrational energy corrections)⁵¹⁰. Final conformational free energies were calculated at the DLPNO-CCSD(T)/CBS//SCS-MP2/def2-TZVPP level with *VeryTightPNO* settings. The basis set extrapolation method used for DLPNO-CCSD(T) association energies is a two-point extrapolation scheme, applied to single point energies calculated with the def2-TZVPP and def2-QZVPP basis sets. α_{34} and β_{34} parameters for extrapolating the SCF energy and the correlation energy, being 7.88 and 2.97, respectively as suggested by Neese and Valeev²⁹³. W2/W1-F12 calculations were conducted according to the protocol suggested in the respective original publications⁷³⁷. The D3(BJ)-ATM^{59,121,122,124,125} (as part of PBEh-3c and B97-3c¹²⁹) or D4^{115,116} London dispersion corrections were applied for all tested DFAs if not stated else.

Computational Investigations

The intermolecular interactions between organic azide and pnictogen-, chalcogen- and halogen-containing moieties in 44 exemplary model systems (10 pnictogen, 24 chalcogen, 10 halogen, figure 13.2) were investigated with respect to structural parameters and interaction energies. A schematic representation of the investigated orientations is depicted in figure 13.4.

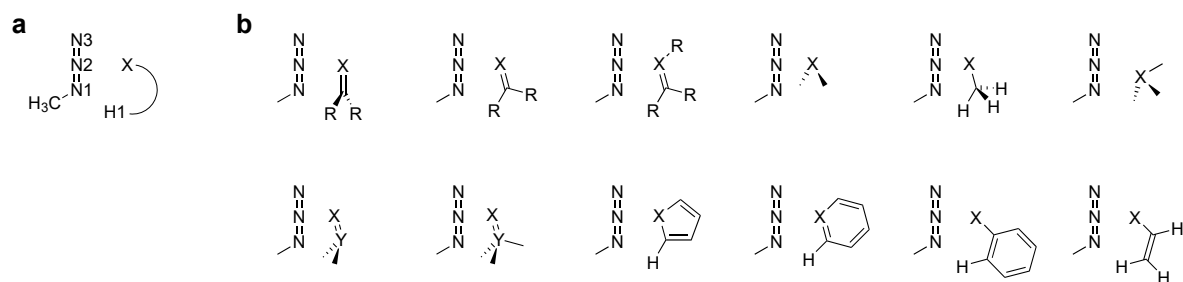


Figure 13.4.: a) Numbering of relevant atom positions; b) Schematic orientations of the interacting methylazide compound pairs. X represents the position of the directly interacting, and Y of the indirectly interacting chalcogen, pnictogen or halogen atoms. R = H, Me.

Structural Properties

For all 44 azide-adducts, the structural features of gas-phase local minimum structures (SCS-MP2/def2-QZVPP) were analyzed (Table 13.1). The model systems, that were chosen to resemble observed solid-state interaction motifs, mostly show distances close to or only slightly below the sum of the van-der-Waals radii of the central nitrogen atom (N2) (approx. 3.07 Å for O···N) and the interacting moiety. In the solid-state structures a large number of very short oxygen nitrogen distances is observed. Nevertheless, the slight shortening compared to the sum of van-der-Waals radii hints at a relevant attractive interaction between the central nitrogen (N2) and the chalcogenide moiety. The predominant orientation of the PCH moiety at N3-N2···X angles of around 80-90° underlines the role of the central nitrogen as interacting atom. For some cases involving a possible interaction with heavier elements like Sb or I, distortions of the N3-N2···X angles result from slight shift of the X-atom away from the azide moiety,

13. Quantification of Non-covalent Interactions in Azide-Pnictogen, -Chalcogen, and -Halogen Contacts

Table 13.1.: Structural parameters of azide adducts **1-44** optimized at the SCS-MP2/def2-QZVPP level of theory.

#	X-N2 / Å	X-N2-N3 / °	X-N1-C / °	$\varphi(\text{N1}\cdots\text{H-X}) / ^\circ$
1	3.125	90.6	173.1	120.7
2	3.170	82.8	179.2	157.4
3	3.052	89.3	174.3	119.4
4	3.071	87.3	175.1	114.6
5	3.501	98.7	161.1	120.3
6	3.562	89.6	168.9	162.8
7	3.498	97.6	162.4	123.2
8	3.546	100.5	159.7	125.8
9	3.581	102.4	157.2	125.2
10	3.706	110.2	147.7	122.2
11	3.068	89.8	174.0	117.3
12	3.104	86.4	175.0	72.8
13	3.118	81.6	179.2	154.8
14	3.033	86.9	176.1	104.8
15	3.082	87.8	175.6	176.0
16	3.045	84.7	178.8	142.1
17	3.008	84.3	179.6	135.0
18	2.973	84.1	178.6	132.9
19	2.923	87.2	179.1	124.5
20	3.038	81.7	178.0	146.6
21	2.981	81.0	176.6	149.5
22	2.963	80.9	176.1	150.6
23	2.961	88.5	174.6	115.8
24	2.878	86.9	172.6	118.2
25	3.594	81.1	177.1	167.6
26	3.451	80.4	177.5	114.2
27	3.531	82.7	177.6	142.6
28	3.523	82.7	177.9	139.7
29	3.456	85.6	175.5	129.3
30	3.337	98.4	161.4	113.0
31	3.309	95.2	165.4	126.8
32	3.669	81.8	176.3	169.1
33	3.382	98.5	161.2	125.7
34	3.474	101.8	157.1	124.0
35	3.020	87.6	175.7	126.1
36	3.119	80.7	177.8	150.5
37	3.169	79.5	177.3	149.1
38	3.439	88.9	171.7	139.0
39	3.443	80.5	178.2	160.5
40	3.471	79.8	178.5	157.2
41	3.559	89.2	170.4	141.9
42	3.538	81.2	176.9	162.5
43	3.724	90.6	168.2	144.2
44	3.678	82.7	174.5	164.5

this may result from the increased size and/or the electronic properties of the corresponding moieties. The slight bending of the azide-moiety ($\theta(\text{N1-N2-N3})_{\text{mean}} = 174.1^\circ$) is almost unaffected by the interacting partner. The C-N1-N2-X dihedral angle indicates the planarity of the coordination pattern. All

investigated systems display an in-plane orientation with the azide moiety.

Association and Interaction Energies

The gas-phase association energies for the azide-donor pairs **1-44** with respect to the relaxed dissociated monomer geometries (interaction energies are calculated with respect to the unrelaxed fragments) were calculated at W2-F12, W1-F12⁷³⁷, and DLPNO-CCSD(T)/*VeryTightPNO*^{83,84,293} level extrapolated to the complete basis set (CBS) limit (Figure 13.5). Deformation energies upon coordination are mainly small on average representing only <3 % of the association energies, with a maximum value of -9.3 % phosphabenzene **7**. For complexes including heavier elements, for which the W2-F12 or W1-F12 approaches are not applicable DLPNO-CCSD(T)/CBS association energies were calculated. This alternative approach proved satisfactorily accurate to reproduce the highly accurate association energies calculated at the W2-F12/W1-F12 level with very small statistical deviations (mean absolute deviation (MAD) = 0.14 kcal mol⁻¹) in agreement with recent benchmark studies^{34,738}. The calculated associa-

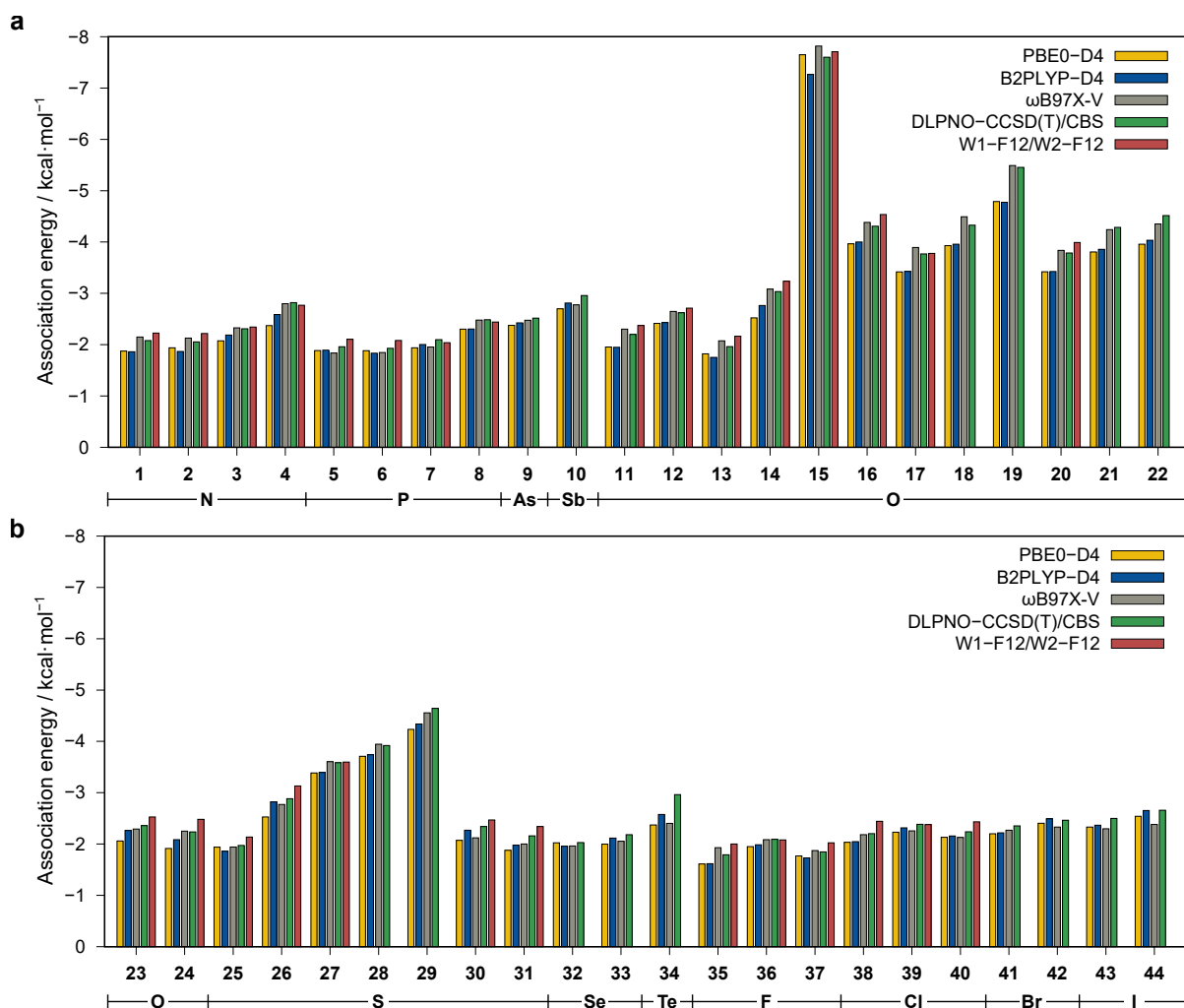


Figure 13.5.: Gas phase association energies of pairs **1-44**. All DFT results obtained with def2-QZVPP basis set.

13. Quantification of Non-covalent Interactions in Azide-Pnictogen, -Chalcogen, and -Halogen Contacts

tion energies range from -1.00 to -8.00 kcal mol $^{-1}$ and several trends are observed. First, chalcogenide compounds seem to yield larger association energies compared to pnictogens and halogens. This is specifically the case for chalcogen atoms involved in highly polar bonds, as in pnictogen-chalcogenides. In systems **17**, **18** and **19**, for example, the increasing electronegativity difference between the oxygen atom and the central pnictogen descending group 15 is well reflected by the increasing association energies, indicating the important role of electrostatic interactions. For less polar bound atoms, this trend is not as pronounced and, in some cases, even reversed e.g. for furan (**23**) and thiophene (**30**). Nevertheless, comparable electronegativity trends are observed for the pnictogens, although to a smaller extent (e.g. aldimine (**1**) compared to phosphalkene **5**). When heavier 4th and 5th row elements are involved, the association energies become systematically larger even though the electronegativity difference decreases or is even reversed. This indicates that, besides electrostatic interactions dispersion interactions can play a dominant role in determining the association energies. Further, secondary pnictogen-pnictogen or pnictogen-chalcogen interactions correlating with electronegativity can influence the observed trends. Overall, the decomposition of the interaction energies indicates that a balance of electrostatic interactions and London dispersion determines the strength of the PCH-azide interaction. Sophisticated WFT-based methods are routinely applicable only to quite small systems (W2/W1-F12: < 30 atoms; DLPNO-CCSD(T) with tight threshold settings and large basis < 150 atoms) because of high computational cost. Systems of more realistic size often include hundreds or thousands of atoms. Therefore, we assessed the reproduction of the association energy by common density functional approximations (DFAs) (applicable for < 500 atoms) and tight binding based semi-empirical quantum mechanical (SQM) methods of the GFNn-xTB method family⁵⁷ (applicable for < 5000 atoms) (Table 13.2). It was found that the range-separated hybrid functional ω B97X-V²⁵⁸ (MD = 0.13, MAD = 0.15 kcal mol $^{-1}$) best reproduces the coupled cluster (CC) based association energies. Further, all other tested D4 corrected hybrid functionals perform reasonably well. Application of more costly double-hybrid methods does not improve the results. Generally, a slight underestimation of the association energy with respect to the CC reference values is observed. Efficient small basis set composite DFT methods such as B97-3c, and specifically PBEh-3c, yield comparably good results to the methods applying a large quadruple- ζ basis set. The SQM methods show a worse performance but both GFN1-⁵³ and GFN2-xTB⁵⁴ yield at least reasonable association energies. Further, the capability of several DFT and WFT based methods to reproduce the unrelaxed dissociation curve (W2-F12//SCS-MP2/def2-QZVPP level) of the azide-donor adduct was assessed (Figure 13.6). Almost all tested methods yield a satisfactory reproduction of the minimum distance, with a consistently very slight overestimation of the X...N₂ distance. The depth and shape of the dissociation potential is generally produced well with deviations below 0.5 kcal mol $^{-1}$. Nevertheless, the error has to be seen in the context of the generally small interaction and association energies. Overall, the range-separated hybrid functional ω B97X-V reproduces the reference dissociation curves best. Surprisingly, the low-cost small basis set composite method PBEh-3c outperforms most of the other methods with respect to the potential depth and the position of the equilibrium distance, even though the interaction energy at increased distances is underestimated.

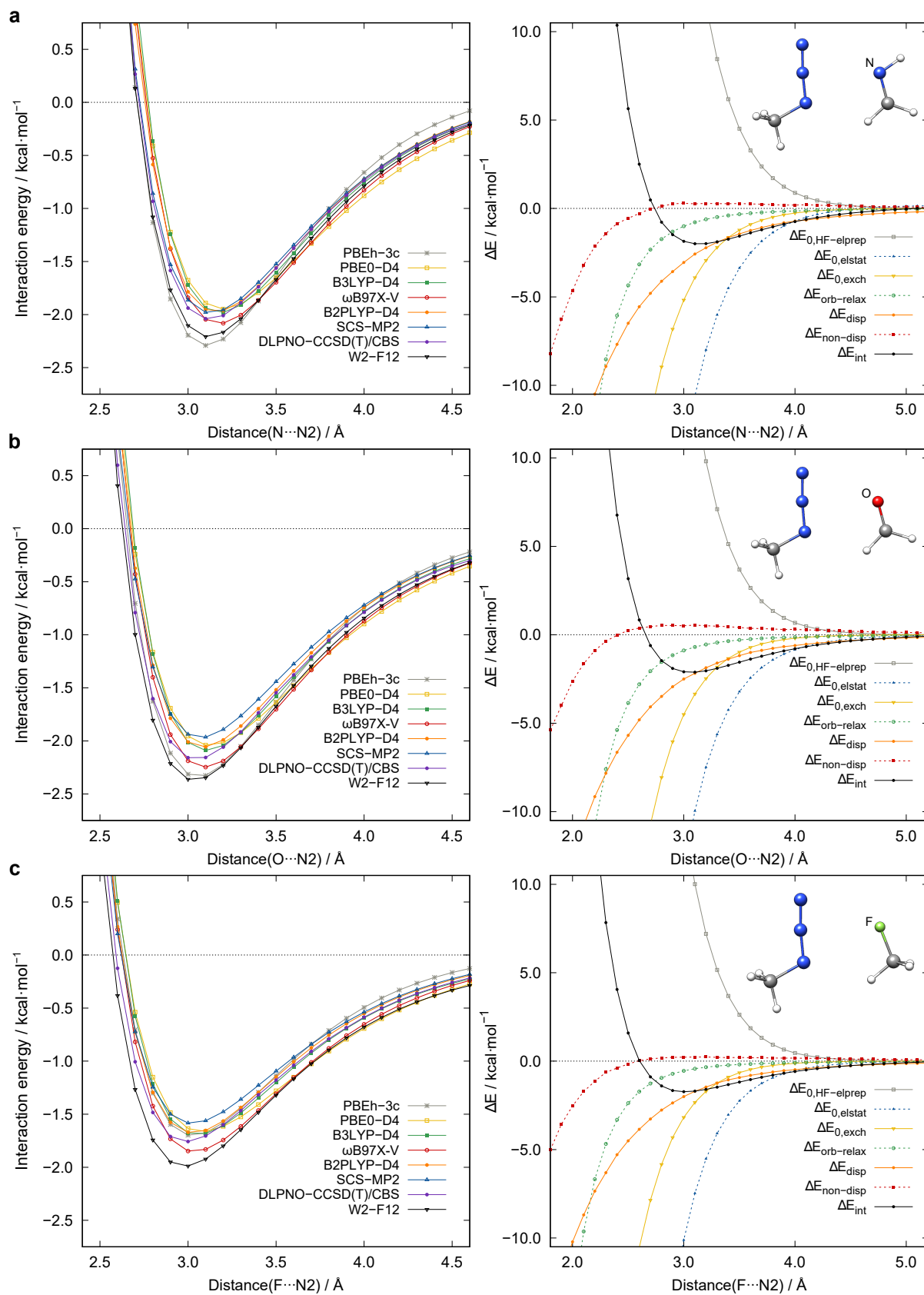


Figure 13.6.: Interaction energy scans and local energy decomposition analyses (DLPNO-CCSD(T)) for a) aldimine (**1**), b) formaldehyde (**11**), and c) fluoromethane (**35**). All results obtained with def2-QZVPP basis set except for the composite methods.

13. Quantification of Non-covalent Interactions in Azide-Pnictogen, -Chalcogen, and -Halogen Contacts

Table 13.2.: Statistical measures (MD = mean deviation; MAD = mean absolute deviation; SD = standard deviation; AMAX = maximum absolute deviation) for all tested DFAs, SQM methods and force fields. If no W2-F12/W1-F12 reference values are available, DLPNO-CCSD(T) values are used as reference. The DLPNO-CCSD(T) values are evaluated with reference to W2-F12/W1-F12 values if available. All values in kcal mol⁻¹.

	Method	MD	MAD	SD	AMAX
WFT	SCS-MP2 ¹¹¹	0.14	0.23	0.24	0.70
	DLPNO-CCSD(T) ^{83,84}	0.13	0.14	0.10	0.25
DFT	PBE-D4 ⁶⁵⁵	0.39	0.39	0.30	1.30
	TPSS-D4 ⁶⁰⁶	0.60	0.60	0.29	1.20
	B3LYP-D4 ^{607,608,665}	0.26	0.26	0.15	0.54
	PBE0-D4 ²¹³	0.32	0.32	0.18	0.71
	ω B97X-V ²⁵⁸	0.13	0.15	0.14	0.56
	PWBP95-D4 ²⁶⁰	0.45	0.45	0.15	0.80
	B2PLYP-D4 ¹¹⁰	0.28	0.28	0.16	0.68
Composite	HF-3c ¹²⁷	-0.76	1.06	1.61	5.54
	B97-3c ¹²⁹	0.76	0.76	0.33	1.41
	PBEh-3c ⁶⁹	-0.20	0.29	0.30	0.85
SQM	GFN1-xTB ⁵³	0.90	1.23	1.16	4.59
	GFN2-xTB ⁵⁴	1.08	1.32	1.06	3.28
	PM6-D3H4X ^{51,153}	3.85	3.96	11.24	49.11
	PM7 ⁵²	2.51	3.10	7.42	32.24

Interaction Energy Decomposition Analysis

Generally, various components can be postulated for the interactions with the azide, principally (i) donor-acceptor interactions (orbital relaxation); (ii) electrostatic interactions; (iii) electron correlation, including specifically long-range correlation effects such as London dispersion, and (iv) Pauli exchange repulsion. Energy decomposition schemes can help to quantify these components and thus help to understand the nature of the interactions. Specifically, canonical Energy Decomposition Analysis⁵¹² (EDA), Symmetry Adapted Perturbation Theory⁷³⁹ (SAPT) and the DLPNO-CCSD(T) based Local Energy Decomposition^{735,736} have proved to yield reasonable insights⁷⁴⁰. Therefore, we applied LED to all complex equilibrium geometries and for three representative model systems, aldimine (**1**), formaldehyde (**11**), and fluoromethane (**35**) as a function of the X...N2 distance (Figure 13.6). The LED scheme decomposes the interaction energy into contributions including the electronic preparation energy at Hartree-Fock (HF) level $E_{HF-elprep}$, which represents the repulsive part of the exchange interaction and can be conceptionally referred to as “Pauli repulsion”. Other major components are the attractive exchange energy E_{exch} , electrostatic interactions E_{elstat} and London dispersion interactions E_{disp} , henceforth named dispersion for simplicity. Minor contributions are represented by the perturbative triples correction to the interaction energy $E^{(T)}$ and $E_{non-disp}$, which mainly represents a correction to errors

in the permanent electrostatic interactions originating from HF overestimation of dipole moments. Another decomposition into unrelaxed (“frozen state”) and relaxed (“SCF state”) energy contributions is also possible allowing the quantification of an orbital relaxation energy contribution $E_{orb-relax}$, which may be to some extent comparable to the orbital relaxation term of Morokuma type EDA schemes and includes charge-transfer (CT), polarization and induction effects⁷⁴¹. The frozen state energy contributions are indicated by the “0” suffix. The total decomposition of the interaction energy follows Equation 13.1.

$$E_{tot} = E_{0,HF-elprep} + E_{0,elstat} + E_{0,exch} + E_{orb-relax} + E_{disp} + E_{non-disp} \quad (13.1)$$

The total dispersion energy term E_{disp} is calculated by summing the CCSD dispersion energy part, the weak-pairs contribution and the scaled intermolecular triples correction $E^{(T)}$ following Equation 13.2. The correction factor γ is the ratio of the strong-pair dispersion contribution and the total intermolecular strong-pair contribution.

$$E_{disp} = E_{disp}^{C-SP} + E^{C-WP} + \gamma E^{(T)} \quad (13.2)$$

The third term is an estimate of the perturbative triples contribution to the intermolecular dispersion energy. The remaining part of the triples contribution is incorporated in the $E_{non-disp}$ contribution (for further details of the energy decomposition see appendix A12). For all investigated systems, the LED scheme identifies exchange, London dispersion, and electrostatic interactions as the dominant attractive component of the interaction energy whereas orbital relaxation effects seem to play a minor role. In the following we investigate the role of these three attractive contributions in some detail. On inspecting the molecular electrostatic potentials (ESPs) (Figure 13.7) a clear correlation of the structural features and the electrostatic properties of the interacting atoms can be recognized. The ESPs show the expected electron-poor region at the central nitrogen atom N2 of the azide moiety. Thus, the electrostatic interaction of electron-rich regions of the interacting molecule should be improved with increased electron density difference between N2 and X. This is in line with the observed structural properties of an angular fixation and shortened distances in cases of strong differences in the electrostatic potential regions of the interacting moieties.

Hydrogen Bonding and Orbital Interactions

In some structures, secondary hydrogen bonds (HBs) contribute to the overall interaction energy. To qualitatively estimate this contribution, a Natural Bond Orbital⁷⁴² (NBO) based approach was applied as recommended by Weinhold *et al.*⁷⁴³ at the PBE0-D4/def2-QZVPP level of theory. In this context, a second-order perturbation theory (SOPT) estimate of the stabilization energy ($\Sigma E_{n \rightarrow \sigma^*, HB}^{(2)}$) resulting from charge-transfer (CT) from the lone-pair n at N1 of the azide-moiety into the anti-bonding or-

13. Quantification of Non-covalent Interactions in Azide-Pnictogen, -Chalcogen, and -Halogen Contacts

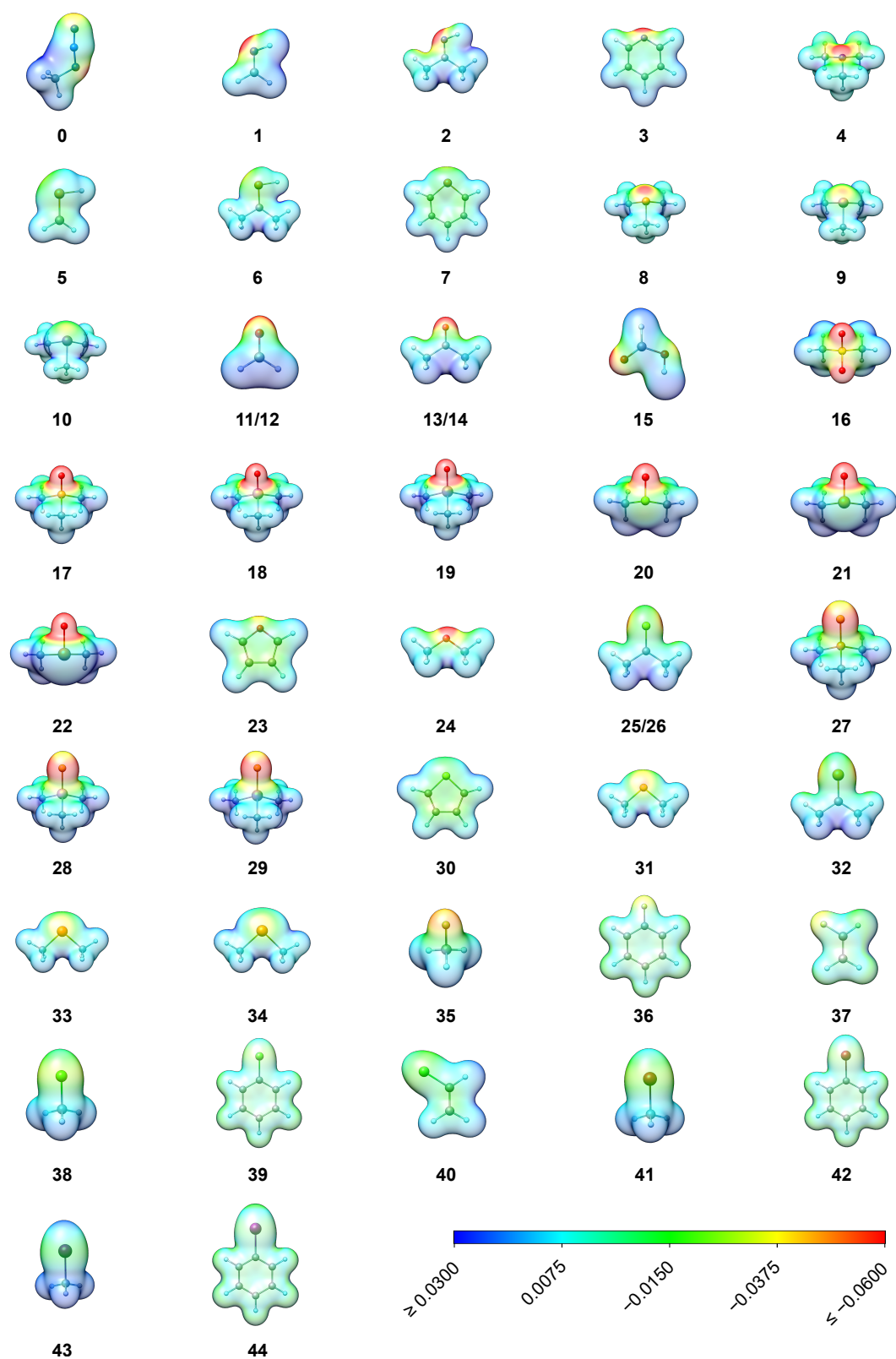


Figure 13.7.: Molecular electrostatic potential (ESP in a.u.) plots at PBE0/def2-SVP//SCS-MP2/def2-QZVPP level with respect to a positive probe charge. Red color indicates attractive, blue repulsive regions.

bital σ_{X-H}^* of the H-bond donor is applied.^b CT is mostly proposed as the dominant attractive energy contribution in hydrogen bonding⁷⁴⁴. Nevertheless, this attractive component has to be offset against the steric repulsion component ($\Sigma E_{\sigma \rightarrow n, HB}^{rep}$) involving the corresponding bonding σ_{X-H} orbital and is estimated from the NBO analysis^{745,746}. The resulting hydrogen bonding strength estimate (E_{HB}^{NBO}) is calculated following equation 13.3.

$$E_{HB}^{NBO} = \Sigma E_{n \rightarrow \sigma^*, HB}^{(2)} + \Sigma E_{\sigma \rightarrow n, HB}^{rep} \quad (13.3)$$

At this point it is to note, that further much smaller attractive components like London dispersion are not included into this estimate, thus for very weak hydrogen bonding contacts, repulsive estimates are expected. This is mostly the case, if the corresponding $N1 \cdots H-X$ angle deviates strongly from the optimum 180° region⁷⁴⁷ which is the case for most presented model systems (cf. figures 13.8, 13.9a, $\varphi(N1 \cdots H-X)_{\text{mean}} = 136^\circ$, table 13.1). The angle dependence of the HB strength estimates for formaldehyde (11) is depicted in figure 13.9b. A clear relation of the CT and steric repulsion estimates with $N1 \cdots H-X$ is observed. Further, the attractive nature of the oxygen \cdots azide contact is verified by the total interaction energy increase with larger φ , even though the hydrogen bonding is enhanced approaching linearity. Except for the strongly H-bound formic acid adduct ($E_{HB}^{NBO} = -6.19 \text{ kcal mol}^{-1}$) the NBO analysis yields mainly slightly repulsive HB estimates for almost all other model systems (Figure 13.8). Overall, this renders an only minor role of hydrogen bonding in the investigated model systems which is in agreement with the observed small angles φ and the comparably large $N1 \cdots H$ distances. Nevertheless, due to other weakly attractive component like London dispersion, the secondarily hydrogen bonded adducts are slightly preferred on the potential energy surface (PES) in the intermolecular case. Thus, to investigate true local minima on the PES, this secondary effect was accepted for the

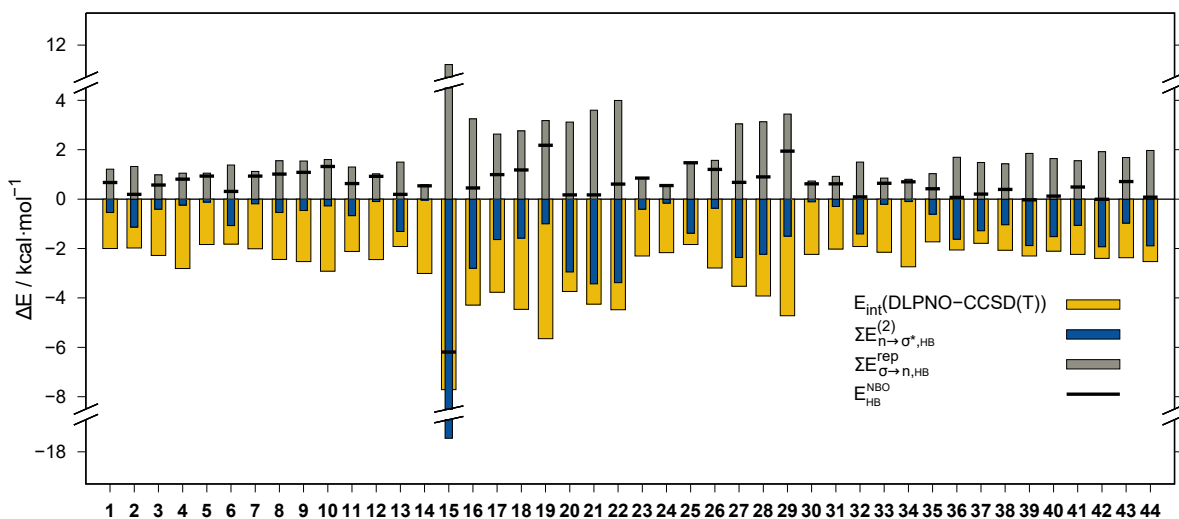


Figure 13.8.: NBO based HB strength estimates for 1-44 with respect to LED interaction energies.

^bTo verify the NBO HB strength estimate we calculated E_{HB}^{NBO} for a purely hydrogen-bonded acetic acid-methylazide adduct taken from the NCI Atlas benchmark by Řezáč³⁶. The CCSD(T)/CBS interaction energy ($-7.87 \text{ kcal mol}^{-1}$) is well reproduced with an NBO estimate of $-8.24 \text{ kcal mol}^{-1}$.

13. Quantification of Non-covalent Interactions in Azide-Pnictogen, -Chalcogen, and -Halogen Contacts

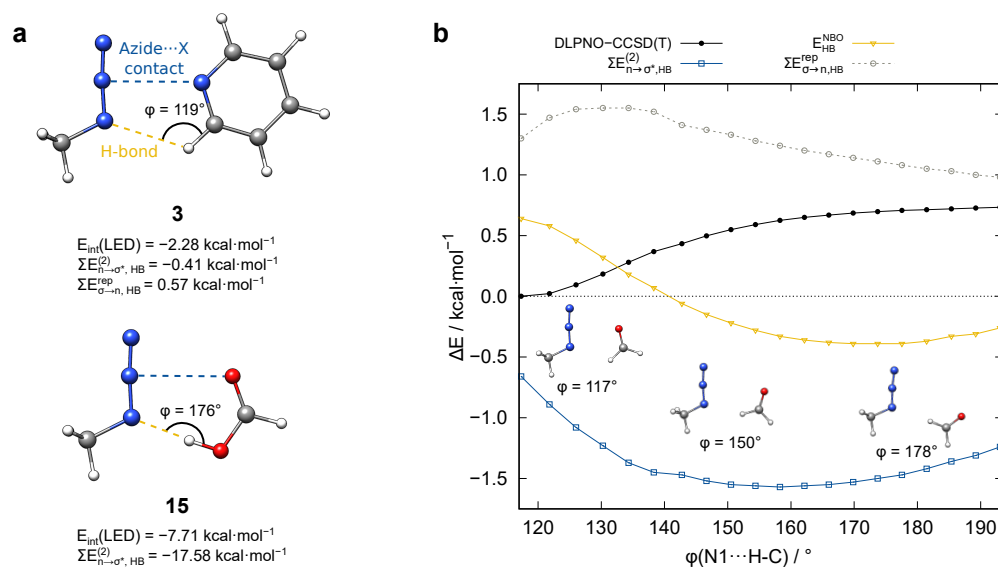


Figure 13.9.: Relative LED interaction energies, CT stabilization energy and steric repulsion energy estimates for hydrogen bonding in **3** and **15**. b) Interaction energy, CT, and steric repulsion estimates as function of angle $\varphi(N1 \cdots H-X)$ for formaldehyde (**11**).

model systems. Deviations from local minimum structures may result in artificially less attractive or even slightly repulsive adduct structures, even though the general nature of the Azide-X interaction is clearly attractive. Therefore, a perfect transfer of the crystal structure motifs into the gas-phase is not possible. Compared to the chalcogen-azide interaction, other interactions such as chalcogen-chalcogen have a significant Lewis-like donor-acceptor bonding character and thus a greater influence of orbital relaxation effects is observed. For the azide-donor interaction this is not generally the case. The LED analysis consistently yields minor orbital relaxation contributions for all 44 systems (Figure 13.11). This is attributable to the nature of the involved frontier molecular orbitals (Figure 13.10). The LUMO of the azide moiety is delocalized over the whole azide function and the orbital contribution at the N2 atom competes with the occupied HOMO-1 that represents the lone-pair (LP) at N1, which is generally involved in the secondary hydrogen bonding. Thus, the overall donor-acceptor interaction cannot benefit from $X \rightarrow N2$ donation. This picture may change upon orientation change of some interaction partners

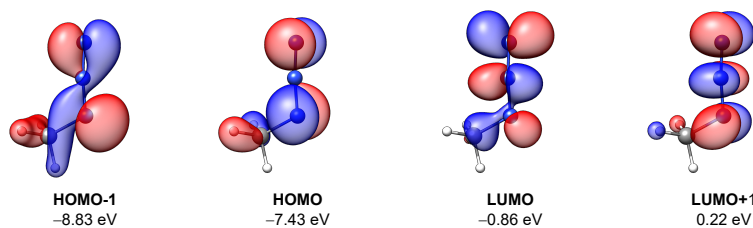


Figure 13.10.: Selected Kohn-Sham molecular orbitals at PBE0/def2-QZVPP//SCS-MP2/def2-QZVPP level of theory for MeN₃. Isosurface value = $0.05 \text{ e}^{-1/2} \text{ bohr}^{-3/2}$.

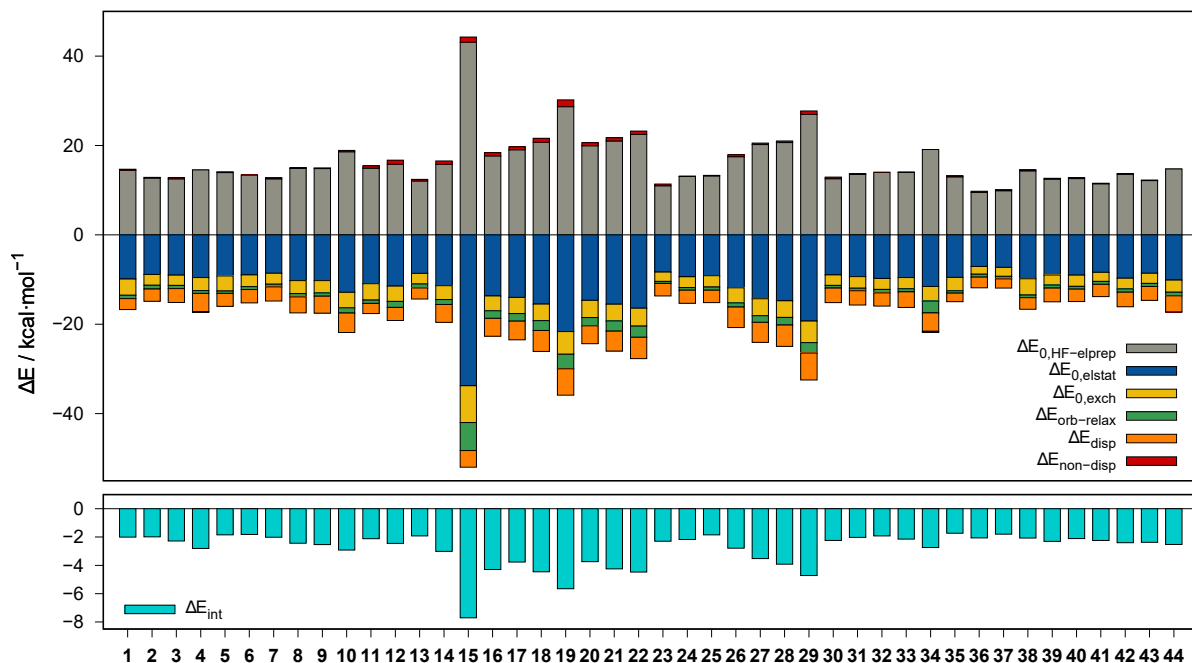


Figure 13.11.: LED contributions and interaction energies for **1-44** at the DLPNO-CCSD(T)/def2-QZVPP level.

with double bond moieties. For the latter, if the orientation changes from an in-plane to an orthogonal structure, the azide can become the electron donor moiety and a small $n \rightarrow \pi^*$ contribution is observed (cf. systems **12**, **14** and **26**). Comparable behavior is observed for systems, that allow for $n \rightarrow \sigma^*$ (X-C/H) donation like the phosphalkene **5**. Here a small CT contribution of $-0.38 \text{ kcal mol}^{-1}$ for the $n \rightarrow \sigma^*$ (P-H) observed. These secondary interactions (pnictogen-pnictogen and pnictogen-chalcogen, see the online Supporting Information of the original publication) explain some comparably large interaction energies observed for systems such as trimethylantimony **10** which involves an $n \rightarrow \sigma^*$ (Sb-C) CT contribution of $-0.72 \text{ kcal mol}^{-1}$ or trimethylantimonyoxide **19** with a contribution of $-1.58 \text{ kcal mol}^{-1}$. These observations are qualitatively in line with larger orbital relaxation terms in the LED analyses for the corresponding systems. Considering these contributions, the corresponding systems end up in a comparable interaction energy range of systems lacking such secondary interactions.

London Dispersion Interaction

Another important attractive component of the interaction energy is London dispersion. The extent of its influence as estimated from LED analysis is shown in figures 13.11 and 13.13. Prior studies indicated, that the DFT-D4 dispersion correction for a somewhat repulsive density functional approximation like B3LYP (with almost no indirect, intrinsic reproduction of London dispersion effects) correlates well with the LED dispersion energy and may be applied for a low-cost estimate of the dispersion interaction energy³³. To verify this estimate, we analyzed the correlation of the B3LYP-D4 correction and the LED dispersion interaction energy for all 44 systems (Figure 13.12). On average 80 % of the LED dispersion energy is covered by the D4 correction to B3LYP, only for **15** is this value underestimated at 63 %.

13. Quantification of Non-covalent Interactions in Azide-Pnictogen, -Chalcogen, and -Halogen Contacts

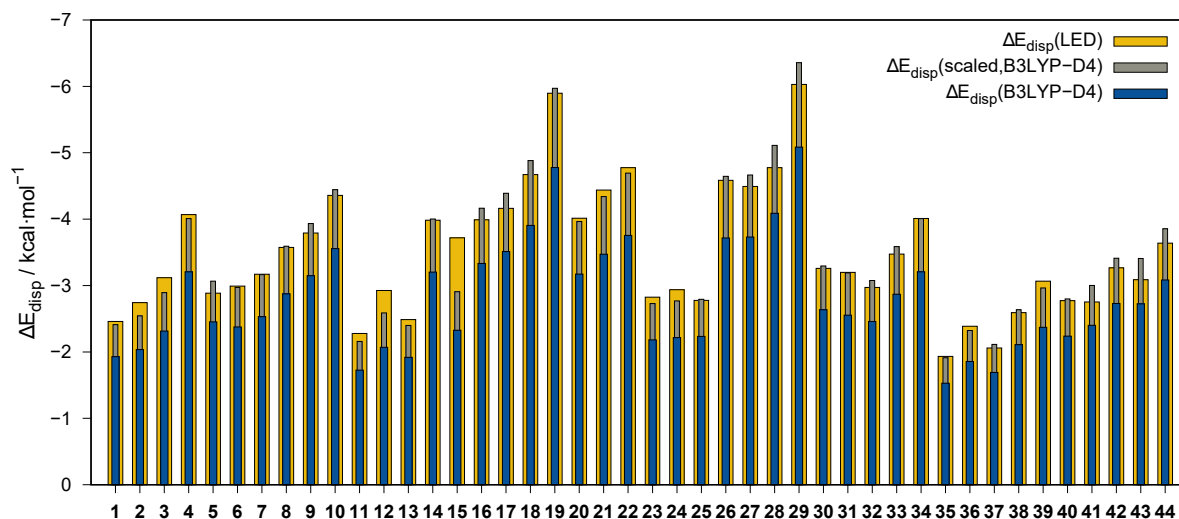


Figure 13.12.: Comparison of the LED London dispersion contribution and the D4 correction to B3LYP to the interaction energy. Scaling factor applied for $\Delta E_{disp}(\text{scaled, B3LYP-D4})$ is 1.25.

A scaling of the B3LYP-D4 correction by a factor of 1.25 yields a 100 % reproduction on average for the investigated systems. Nevertheless, this estimate should be used with caution, as the quality may vary for more exotic systems. The $\Delta E_{disp}/\Delta E_{tot}$ ratio can be further utilized to identify whether the interaction is dominated by London dispersion. A value > 1 indicates an interaction dominated by London dispersion (cf. 1.92 for the methane dimer⁷³⁵). For all systems except **15** (formic acid) this ratio is close to or above 1.00 with a maximum of 1.65 for **26** and a mean value of 1.30 (for the individual data see the online Supporting Information of the original publication). Furthermore, the $\text{N}_2\cdots\text{X}$ distance dependence of the LED dispersion energy and the D4 dispersion correction for four representative DFAs (PBE, PBE0, BLYP^{659,665,748}, B3LYP) was investigated (Figure 13.13) exemplarily for the phosphalkene **5** and acetone **13**. Both repulsive DFA (BLYP, B3LYP) D4 corrections correlate very well with the LED dispersion energy at the dissociative regions. Specifically, at the equilibrium distance the corrections match the LED estimate well. For less repulsive functionals such as PBE and PBE0 the D4 corrections are much smaller. As B3LYP reproduces the association and interaction energies much better than BLYP, the former is recommended for an estimate of the dispersion interaction energy.

Conformational Studies

To estimate the transferability of the observed structural motif preference from the solid to gas-phase, exemplary conformational studies were conducted starting from the molecular solid-state structures of **A** and **B** (cf. figure 13.1). For both structures a conformer ensemble was generated fully automatically applying the CREST⁶⁴ program at the GFN2-xTB level. The obtained conformers were re-ranked according to Gibbs free energy at the DLPNO-CCSD(T)/CBS//SCS-MP2/def2-TZVPP level and analyzed for the presence of an azide-donor contact (Figure 13.14). While for both compounds according to the Gibbs free energy more favorable gas-phase conformers were found, only for **A** the low free energy conformer region is dominated by structures with short azide-donor contacts. Here, the lowest con-

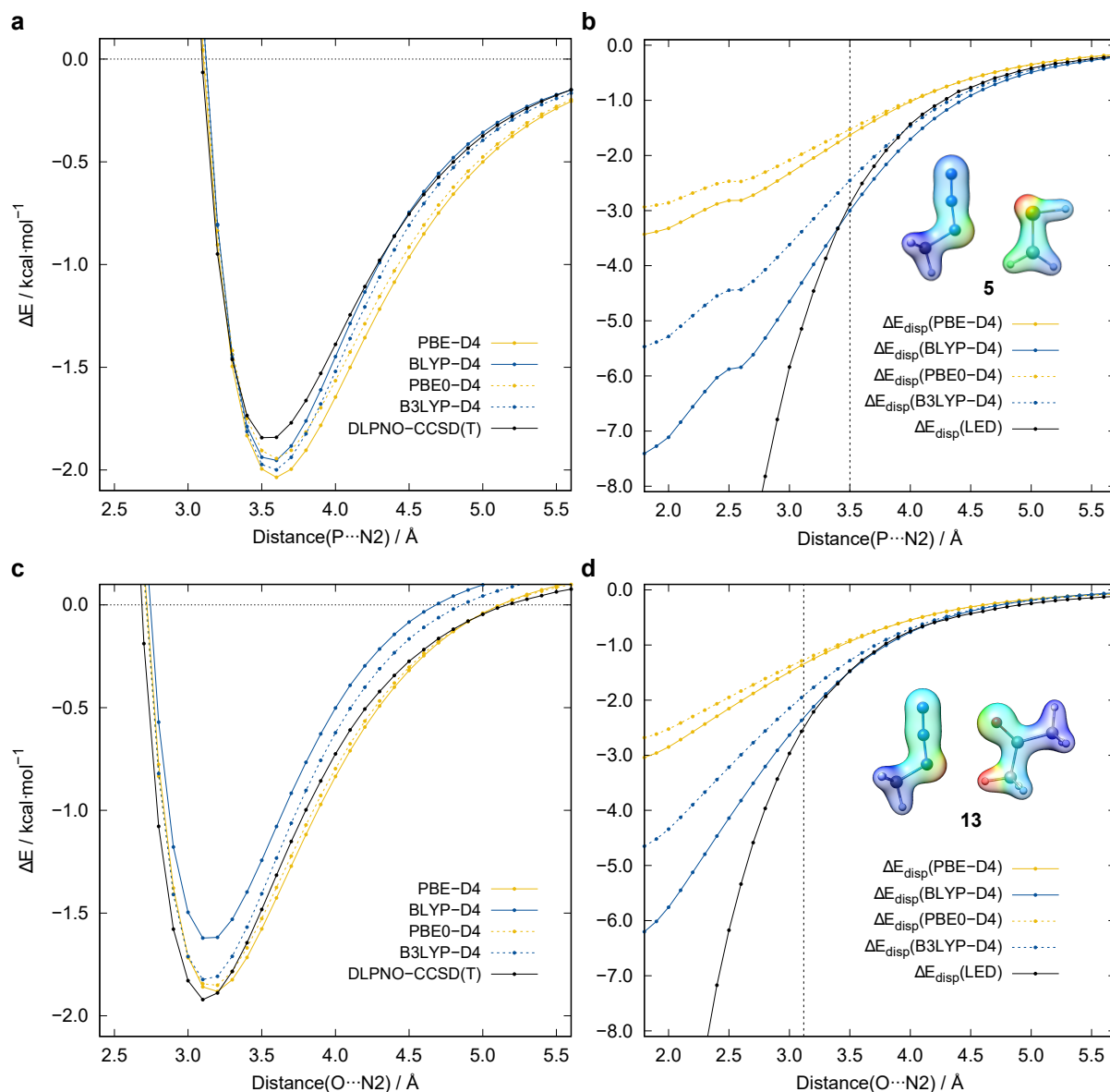


Figure 13.13.: a) Interaction energy and b) dispersion interaction estimates as functions of the P \cdots N2 distance with DID plot for **5**. c) Interaction energy and d) dispersion interaction estimates as functions of the O \cdots N2 distance with DID plot for **13**. Isosurface value = 0.1 e bohr $^{-3}$, blue color indicates low, red color high London dispersion interactions. Vertical dashed lines indicate the respective X \cdots N2 distance.

former shows proximity of the donor moiety to the azide, but as the distance is long, it was classified as non-motif structure. For **B**, the lowest conformers do not show pronounced azide-donor contacts. Here, the first conformer with this motif is approx. 1.3 kcal mol $^{-1}$ higher in free energy than the lowest. Thus, we conclude that the structural features only partly originate from azide-donor interactions as present in the gas-phase, indicating a possible role of solid-state effects such as crystal packing. Crystal effects may be large enough to favor an azide-donor arrangement, even though the attractive interaction may not be large enough to fixate this structural motif in the gas-phase or solution. Furthermore, struc-

13. Quantification of Non-covalent Interactions in Azide-Pnictogen, -Chalcogen, and -Halogen Contacts

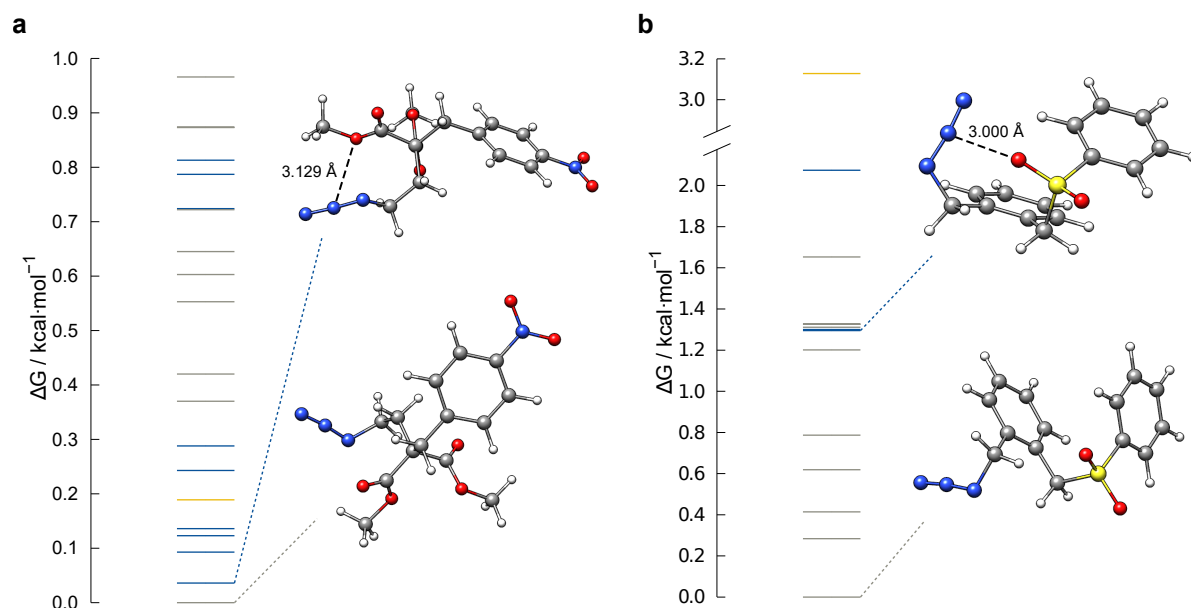


Figure 13.14.: Relative gas phase conformational free energies for a) **A** and b) **B**. The position of the optimized molecular X-ray structure is highlighted in yellow. All conformers containing an azide-oxygen contact are highlighted in blue, all without in grey. All free energies calculated at the DLPNO-CCSD(T)/CBS//SCS-MP2/def2-TZVPP level for $T = 25^\circ\text{C}$.

tural strain and steric repulsion effects are influenced by the bridging moiety between azide and donor. LED analysis on a simplified intermolecular model of **A** (Figure 13.15) optimized with a constrain on the $\text{O}\cdots\text{N}_2$ distance and essential dihedral angles reveals an interaction energy of $-1.79 \text{ kcal mol}^{-1}$, which is in the same scale as comparable model systems (e.g. **24**).

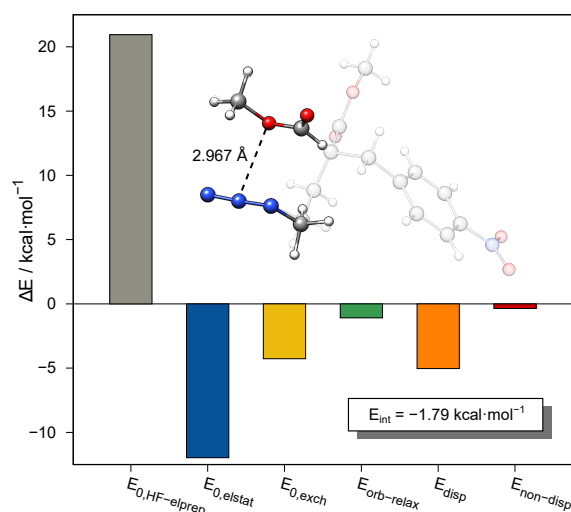


Figure 13.15.: LED analysis of an intermolecular model system of **A** at the DLPNO-CCSD(T)/def2-QZVPP//SCS-MP2/def2-QZVPP level. The X-ray structure is depicted transparently.

13.3. Conclusion and Outlook

The structural motif of an azide moiety in close contact with an electron-rich donor moiety is observed in surprisingly many solid-state structures. To understand the interaction between the azide and the partner molecule or moiety, we created 44 intermolecular model systems to investigate computationally the nature of the interaction in the gas-phase. Further, several new organic compounds were synthesized with the aim of systematically creating the structural motif that was found empirically in the CCDC. Overall, the calculated (W2-F12/W1-F12/DLPNO-CCSD(T)/CBS) association energies for side-on azide-X complexes vary between -1.00 and -5.50 kcal mol⁻¹ (formic acid **15** excluded). The LED interaction energy decomposition analysis identifies electrostatic and London dispersion interactions as the dominating attractive contribution to the interaction energy. If the electrostatic contribution is large enough to overcome less favorable steric motifs and secondary hydrogen bonding is not dominant, the X...N₂ interaction motif is preserved. In this motif, little or no Lewis like donor-acceptor bonding is observed, which is reflected by the comparably small orbital relaxation contributions to the interaction energies. This flexibility of the interaction components further explains the large variety of structure patterns found in many solid-state structures. Comparison of D4 London dispersion corrections to the LED results indicates good comparability of both energy contributions for the investigated systems, in accordance with previous studies. Conformational studies on the newly synthesized compounds indicate that other intermolecular crystal (packing) effects may play an important role in stabilizing this weak azide interaction. Overall, considering the complexity of further decomposing single contributions to the interaction energy to specific parts of the molecular systems, the unbiased azide-X interaction is estimated to 1.5 to 3.0 kcal mol⁻¹. We are convinced that these stabilizing interactions are of importance not only for the arrangement of azide moieties in supramolecular assemblies and crystal engineering (e.g. click chemistry in the solid state)^{749–753}, but are also the basis for conformational bias in azido-functionalized nucleic acids, peptides, proteins and carbohydrates. Future investigations will reveal whether azido-based interactions have a similar potential to facilitate catalysis, as has been extensively and successfully explored for halogen and chalcogen bonding.

Acknowledgements

The German Science Foundation (DFG) is gratefully acknowledged for financial support through a Gottfried Wilhelm Leibniz prize to S.G. and the SPP 1807 “Control of London dispersion interactions in molecular chemistry”. We thank Dr. Alexander Kreft (TU Braunschweig) for helpful assistance. Open access funding was enabled by Projekt DEAL.

Part V.

Final Summary and Conclusion

In this thesis, recently presented efficient composite DFT and semi-empirical electronic structure methods are evaluated and applied for the investigation of problems in inorganic chemistry. Special attention was paid to the geometry optimization of large transition metal and lanthanoid complexes with semi-empirical methods. Even though such compounds are of high interest in various chemical research areas, the number of physical methods that can be used to treat organometallic and other inorganic systems is small. This is mainly due to the electronic complexity of molecules involving inorganic elements. Therefore, it is particularly difficult to find feasible approximations that allow the development of efficient yet sufficiently accurate electronic structure methods. A current approach to solve this problem are the extended tight binding (GFNN-xTB) and force-field (GFN-FF) methods developed by Grimme and co-workers, whose conception theoretically allows the fully quantum mechanical treatment of a wide range of inorganic systems, although the final performance in this area was previously completely unclear. Therefore, comprehensive assessment of these promising methods is indispensable to enable further studies and open up new research fields for computational chemists. Such an evaluation inevitably requires suitable test scenarios covering a wide range of chemical systems. Thus, the first part of this thesis deals with the geometry optimization of large lanthanoid and transition metal complexes.

For lanthanoid complexes, it was demonstrated that GFN1-xTB is able to efficiently optimize diverse lanthanoid complexes with up to several hundreds of atoms at reasonable accuracy (Chapter 3). The optimized structures were directly compared to crystallographically determined structures of high quality (disorder-free, R-factor < 0.05). GFN1-xTB proves to be a robust choice, yielding good results on par with the computationally much more demanding HF-3c method, and clearly outperforming the Sparkle extension of the prominent PM6 method (Sparkle/PM6) in terms of accuracy and speed. This is particularly noteworthy since Sparkle/PM6 was specifically designed for the purpose of treating lanthanoid complexes. This study further underlines the applicability of neglecting f orbitals by absorbing their effect implicitly in the parametrization for geometry optimization of lanthanoid complexes.

GFN1- and GFN2-xTB were further tested for transition metal complexes, which exhibit challenging electronic structures and pronounced structural diversity (Chapter 4). As for the lanthanoids, no suitable benchmark set for a comprehensive assessment was available from the literature. Therefore, a benchmark set of high quality hybrid DFT (TPSSH-D3/def2-TZVPP) gas-phase geometries for 145 realistic 3-5d transition metal complexes was generated (TMG145). Based on this new benchmark set, the performance of the GFNN-xTB methods was assessed and further compared to the prominent competitors PM6-D3H4 and PM7. For the transition metal complexes, the superiority of the GFNN-xTB over the PMx methods was found to be even more striking than for the lanthanoids, in both quality and robustness of the geometry optimization. The GFNN-xTB methods had very high geometry optimization success rates of approx. 90% compared to 50–60% for the PMx methods. This means, that for 90% of the complexes, a reasonably good geometry was obtained after optimization with GFNN-xTB. In the field of supramolecular organometallic complexes, suitable physical methods that combine efficiency and accuracy were not previously available. The GFNN-xTB methods were hence applied for geometry optimization of very large organometallic systems with up to 2800 atoms. Beside the robust and accurate geometry optimization, reasonable description of the thermochemistry is important for ap-

V. Final Summary and Conclusion

plications in terms of efficient reaction path elucidation. Thus, GFN1- and GFN2-xTB were also tested for the calculation of reaction energies and barrier heights of organometallic reactions. Even though it was not specifically designed for this purpose, the GFNn-xTB methods consistently outperform the PMx methods in any aspect. This also holds for conformational energies, for whose calculation the corresponding methods were also assessed in the course of this thesis (Chapter 5).

In this context also a new benchmark set was generated, providing a hitherto unmatched number of accurate double-hybrid DFT (PWPB95-D4/def2-QZVP) reference conformational energies for 969 unique conformers of 40 structurally flexible transition metal complexes (TMCONF40). This study showed that the GFNn-xTB methods can be applied reliably for the generation and energetic presorting of transition metal complex conformers, which was almost impossible before for the given size of the investigated systems at this level of accuracy. It was further demonstrated that a combination of composite DFT-3c (single point energy) and GFNn-xTB (geometry optimization) methods can yield good results at still significantly reduced computational effort compared to a full DFT treatment. Based on these studies, two statements can be made. First, the GFNn-xTB methods are reliably applicable for the geometry optimization of lanthanoid and transition metal complexes. And second, they are unrivaled in this context regarding SQM methods, also outperforming the PMx methods for thermochemistry. Thus, all necessary prerequisites are fulfilled to be able to efficiently investigate reaction mechanisms.

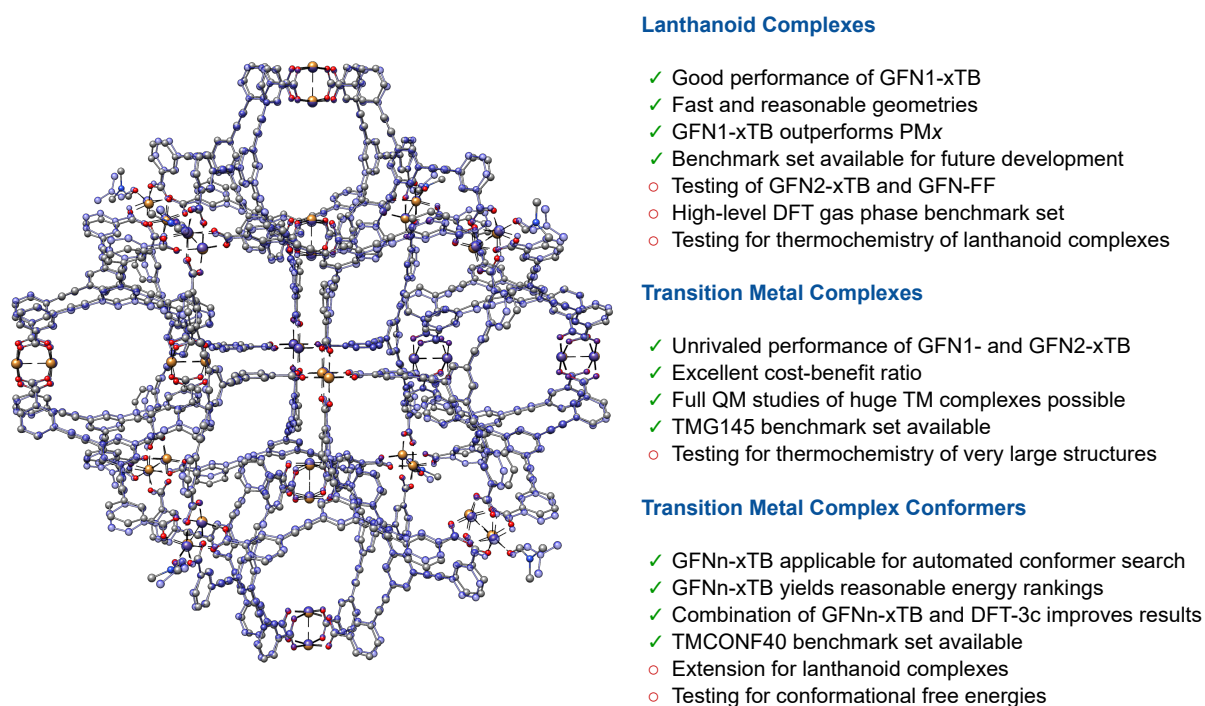


Figure 13.16.: Summarized findings and achievements of part II and future tasks. The discussion of the exemplarily depicted metal organic polyhedron can be found in chapter 4.

Therefore, a combination of GFNn-xTB methods and PBEh-3c was used for the elucidation of complex reaction mechanisms in the field of frustrated Lewis pair chemistry. GFNn-xTB based reaction path

simulations reliably yielded very good transition state geometries close to DFT-3c quality at very small computational effort. This multi-level work flow reduces the computational effort to obtain a transition state from several days to minutes or hours. Further, the investigation of much larger systems becomes possible. In these particular studies, FLP catalyzed hydrogenations of amides are investigated. It was found that halide ions can be used as active Lewis base to hydrogenate amides in combination with the Lewis acid BR_3 ($R = 2,6-F_2-C_6H_3$) which represents a novel type of metal-free hydrogenation activation (Chapter 6). Another metal-free variant applying phosphane oxide–electrophilic phosphonium cation (EPC) Lewis pairs was also investigated in detail. Here, in particular the formation of the respective phosphanes after dihydrogen activation was studied and it was found that the transition state of the dihydrogen activation is energetically lowered by favorable intermolecular non-covalent interactions between the Lewis pair moieties (Chapter 7). Both of these hydrogenation activation variants were further combined in a third study to enable the hydrogenation of secondary amides (Chapter 8). In this case, the interplay of phosphane oxide EPC catalyzed imidoyl chloride formation and halide autoinduced catalytic hydrogenation, was examined in detail. In all three studies the thermochemical properties of the corresponding reaction mechanisms were computed at dispersion corrected (double-)hybrid DFT level of theory (PW6B95-D3/D4/def2-QZVP or PWPB95-D3/def2-QZVPP). Based on the insights from these studies further highly desirable metal-free hydrogenation reactions can be developed. A very impor-

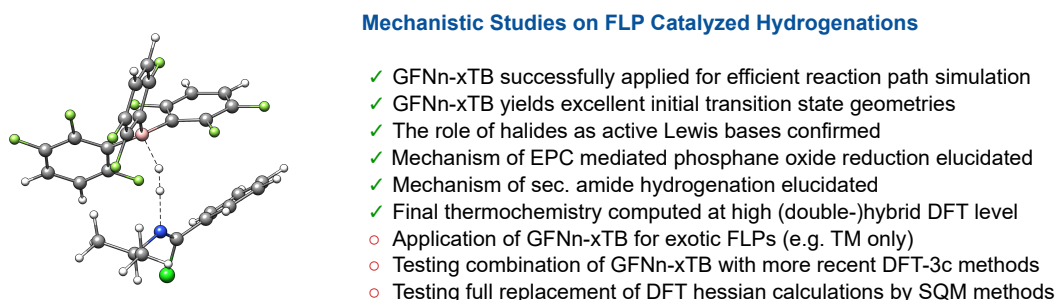


Figure 13.17.: Summarized findings and achievements of part III and future tasks. The discussion of the exemplarily depicted transition state can be found in chapter 8.

tant aspect of modern computational chemistry methods is the reasonable description of non-covalent interactions such as London dispersion. Even though such interactions received much and early attention in organic chemistry, they have long been ignored in inorganic main group chemistry. Therefore, this thesis includes various studies on the influence of London dispersion interactions on structural features, thermochemistry and indirectly spectroscopic properties of novel inorganic molecules. It was shown that for the inorganic Lewis-pair $[I_3Si-BI_3]^-$ the stabilization of the Si–B bond amounts up to 61% (B3LYP-D3/def2-QZVP) of the dissociation free energy (Chapter 9). This Lewis pair is particularly interesting as it contains a key intermediate of halosilicon chemistry, the trichlorosilanide anion.

London dispersion interactions were also identified as decisive factor causing counterintuitive interligand angles in diaryltetraylenes of the type $E\{C_6H_3-2,6-(C_6H_2-2,4,6-iPr_3)_2\}_2$ (Chapter 10; E = Ge, Sn, or Pb). Here, it was also shown that the application of a sophisticated London dispersion corrections to DFT, such as the D3 or D4 models, is indispensable to obtain correct structures that are in line with

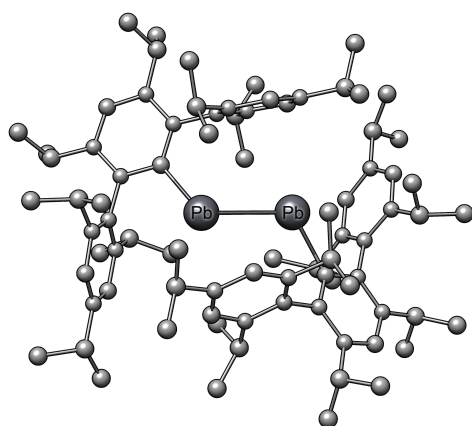
V. Final Summary and Conclusion

experimentally observed structural features.

This is also the case for diplumbynes, heavy alkyne analogues, that are significantly stabilized over their monomeric fragments by attractive London dispersion (Chapter 11). Consideration of London dispersion interactions results in a qualitative change of sign of the dissociation free energy with London dispersion stabilization between 30 and 51 kcal mol⁻¹ (B3LYP-D3/def2-TZVPP). Further, these systems show interesting behavior in solution regarding the UV/VIS absorption spectra. The spectroscopic properties were expected to be in line with different structural features of the Pb–Pb bonding region observed in the crystal structure but were found to be similar for all structurally different diplumbynes in solution. Based on GFN2-xTB molecular dynamics simulations, averaged UV/VIS spectra were calculated explaining the similarity by an unexpected structural flexibility of the C–Pb–Pb–C moiety. This is in line with a donor-acceptor augmented Pb–Pb single bond with only small multiple bond character. Both studies underline that a new perception of steric congestion considering attractive London dispersion interactions in inorganic compounds is necessary. With London dispersion interactions being crucial for correct structure predictions, dispersion corrected composite methods can efficiently provide good molecular structures for the calculation of other spectroscopic properties.

An analytic, indicative and frequently used method in inorganic main group chemistry is hetero nuclear resonance spectroscopy. In particular ²⁹Si NMR can be applied to gain valuable insights into the chemical environment of the respective silicon atom. Nevertheless, comprehensive studies on the computation of ²⁹Si NMR chemical shifts were rare and do not systematically cover the whole structural diversity of silicon compounds. Therefore the performance of prominent DFT methods for the calculation of ²⁹Si NMR chemical shifts was assessed in this thesis (Chapter 12). This was done based on a newly compiled benchmark set termed SiS146, covering a manifold of silicon compounds. The comprehensive assessment revealed that prominent GGA functionals like B97-D or BP86 represent a reliable choice for calculating ²⁹Si NMR chemical shifts on PBEh-3c geometries. If heavy atoms are located in the vicinity of the silicon atom, explicit relativistic treatments have to be applied to obtain reliable results. Beside the highly desirable guidance for computational chemists provided by this study, also possible multi-level approaches applying SQM and FF based geometry optimization and DFT chemical shift calculation were discussed in detail. It was shown that using SQM or FF geometries introduces significant errors in the NMR chemical shift calculation. Nevertheless, empirical linear scaling corrections can be used successfully to reduce this error significantly.

As London dispersion already proved to be crucial in many aspects for the elements of group 14, it was further demonstrated to represent a major component of non-covalent interactions in azide-pnictogen, -chalcogen, and -halogen contacts with no typical donor-acceptor type bonding situation (Chapter 13). Sophisticated DLPNO-CCSD(T) based local energy decomposition analysis revealed London dispersion as dominant interaction energy component on par with electrostatic interactions. Therefore, a new understanding for utilizing London dispersion in stabilizing unexpected coordination patterns can be derived from this study for intermolecular interactions with azides. Overall, this thesis yields valuable insights into fundamental questions of computational inorganic chemistry. It was shown that modern semi-empirical quantum chemical methods can be reliably applied to a variety of inorganic systems including lanthanoids, transition metals, and inorganic main group elements. This fundamental achieve-



Inorganic Main Group Chemistry

- ✓ Decisive role of London dispersion for stabilization of inorganic main group compounds demonstrated for
 - inorganic Lewis pair
 - tetrylenes
 - diplumbynes
- ✓ GFN2-xTB used to study bonding flexibility in diplumbynes
- ✓ Comprehensive study on the calculation of ^{29}Si NMR chemical shifts using dispersion corrected DFT
 - SiS146 benchmark set available
- ✓ Evaluation of SQM and FF structures for NMR predictions
- ✓ In depth local coupled cluster and DFT study on non-covalent interactions in azide-pnictogen, -chalcogen, and -halogen contacts
- Investigation of dialuminenes and other inorganic E-E bonds
- Comprehensive benchmark studies for ^{119}Sn and ^{207}Pb NMR
- Detailed exploration of bonding-flexibility property relationships in inorganic compounds with GFNn-xTB

Figure 13.18.: Summarized findings and achievements of part IV and future tasks. The discussion of the exemplarily depicted diplumbyne can be found in chapter 11.

ment opens up completely new fields of computational chemical research applying the GFNn-xTB and GFN-FF methods to novel inorganic molecules with previously unattainable system sizes. Further, combinations of efficient composite DFT and SQM/FF methods were demonstrated to significantly decrease the computational demand of a wide range of computational work flows, such as reaction path simulation or conformational sampling. Such work flows can yield the same or even better results compared to a full *ab initio* approach. Moreover, the perception of London dispersion interactions as a crucial factor for structural and thermostatistical properties of inorganic molecular compounds is sharpened. Concluding, the results presented in this thesis will be pioneering for future studies in numerous areas of computational inorganic chemistry and will possibly enable easier virtual design of new catalysts or functional inorganic materials and molecules in the future, thus replacing, to a certain extent, elaborate and costly synthetic approaches. In this context, new standard protocols for the computation of kinetic, thermochemical and spectroscopic properties of inorganic compounds, e.g. in catalysis or functional materials research, can be derived. These protocols apply efficient combinations of SQM, FF (GFNn-xTB, GFN-FF) and composite DFT methods (PBEh-3c, B97-3c, $r^2\text{SCAN-3c}$) to replace computationally demanding simulations and will set new scales in efficient inorganic computational chemistry.

And even though the GFNn-xTB and FF methods represent a huge step forward in the efficient simulation of inorganic compounds, numerous challenges remain. These include very basic problems, like the profound description of highly negatively charged or complicated open-shell systems that may also exhibit pronounced multi-reference character. Further, some elements such as the actinoids are still not treatable by SQM and FF methods. The simulation of solvation effects remains challenging as well and typically applied continuum solvation models can prove insufficient for various systems. Moreover, the number of reliable reference data for future method development in the field of inorganic chemistry is still small and should be extended in the future. Nevertheless, the GFNn-xTB and FF methods bear a vast potential for future studies. Specifically, the detailed exploration of the relationship of molec-

V. Final Summary and Conclusion

ular flexibility and properties in inorganic compounds is enabled by these methods. Such studies will fundamentally influence the perception of rigidity in inorganic chemistry and will allow for a deeper understanding of various experimental findings. These are only few possible examples of future developments and applications of new SQM and FF methods in inorganic chemistry while countless more are thinkable. In general, the predictive powers of these methods need to be further explored in close collaboration with experimental chemists in the future.

Part VI.

Appendix

A1. Abbreviations

AES	Anisotropic electrostatics
AIMD	<i>ab initio</i> molecular dynamics
AMAX	Absolute maximum deviation
AO	Atomic orbital
ATM	Axilrod-Teller-Muto
AXC	Anisotropic exchange
biPSi	κ - <i>P,P</i> , <i>Si</i> -Si(Me){(CH ₂) ₃ PPh ₂ } ₂
BJ	Becke-Johnson
BMIM	1-Butyl-3-methylimidazolium
BO	Bond order
Boc	<i>tert</i> -Butyloxycarbonyl
BODIPY	4,4-difluoro-4-bora-3 <i>a</i> ,4 <i>a</i> -diazas-indazene
BSIE	Basis set incompleteness error
BSSE	Basis set superposition error
CAMM	Cumulative atomic multipole moments
CBS	Complete basis set
CC	Coupled cluster
CCDC	Cambridge Crystallographic Data Centre
CCE	Clustered conformer ensemble
CE	Conformer ensemble
CI	Configuration interaction
CN	Coordination number
COSMO	Conductor-like screening model
COSMO-RS	Conductor-like screening model for real solvents
CPCM	Conductor-like polarizable continuum solvation model
CPU	Central processing unit
CREST	Conformer-rotamer ensemble sampling tool
CSD	Cambridge Structural Database
CT	Charge transfer
DFA	Density functional approximation
DFG	Deutsche Forschungsgemeinschaft
DFT	Density functional theory
DFTB	Density functional tight binding
DIBAL	Diisobutylaluminiumhydride
DID	Dispersion interaction density
DLPNO	Domain based local pair natural orbital
ECP	Effective core potential

EDA	Energy decomposition analysis
EDX	Energy-dispersive X-ray
EEQ	Electronegativity equilibrium
EHT	Extended Hückel theory
EN	Electronegativity
EPC	Electrophilic phosphonium cation
ESP	Electrostatic potential
FCI	Fonds der Chemischen Industrie
FF	Force field
FLP	Frustrated Lewis pair
FOD	Fractional occupation density
FT-IR	Fourier-transform infrared
GB	Generalized Born
gCP	Geometrical counterpoise
GGA	Generalized gradient approximation
GIAO	Gauge-including atomic orbital
GSM	Growing string method
GTO	Gaussian type orbital
HALA	heavy atom on the light atom
HB	Hydrogen bond
HF	Hartree-Fock
HOMO	Highest occupied molecular orbital
Hyp	Tris(trimethylsilyl)silyl
Idipp	1,3-bis(2,6-diisopropylphenyl)imidazolin-2-ylidene
IES	Isotropic electrostatics
IXC	Isotropic exchange
KS-DFT	Kohn-Sham density functional theory
LCAO	Linear-combination of atomic orbitals
LED	Local energy decomposition
LFMM	Ligand field molecular mechanics
LMO	Localized molecular orbital
LP	Lone-pair
LSDA	Local spin density approximation
LUMO	Lowest unoccupied molecular orbital
MAD	Mean absolute deviation
MBioF	Metal-biomolecule framework
MD	Molecular dynamics
Mes	Mesityl
MNDO	Modified neglect of diatomic overlap
MO	Molecular orbital
MOF	Metal organic framework
MOM	Metal organic macrocycle
MOP	Metal organic polyhedron
MP	Møller-Plesset
MRMSD	Mean root-mean-square deviation

A1. Abbreviations

MTD	Metadynamics
Nacnac	β -diketiminat
naphth	Naphthalene
NBI	Natural binding index
NBO	Natural Bond Orbital
NDDO	Neglect of diatomic differential overlap
NIR	Near infrared
NLMO	Natural localized molecular orbital
NMR	Nuclear magnetic resonance
NPA	Natural population analysis
PCH	pnictogen-, chalcogen- and halogen
PCS	Perchlorinated oligosilane
PES	Potential energy surface
ppm	parts per million
QM	Quantum mechanical
RI	Resolution-of-identity
RMSD	Root-mean-square deviation
RPA	Random phase approximation
SAPT	Symmetry adapted perturbation theory
SARC	Segmented all-electron relativistically contracted
SC	Structural correctness
SCF	Self-consistent field
SD	Standard deviation
SE	Schrödinger equation
SFR	Spin-free relativistic
SI_{dipp}	1,3-bis(2,6-diisopropylphenyl)imidazolidin-2-ylidene
SIE	Self-interaction error
SO	Spin-orbit
SOPT	Second-order perturbation theory
SPE	Single point energy
SQM	Semi-empirical quantum mechanical
SR	Scalar-relativistic
SRB	Short-ranged basis set
STO	Slater type orbital
TBDPS	<i>tert</i> -Butyldiphenylsilyl
TM	Transition metal
TMS	Tetramethylsilane
TS	Transition state
UEG	Uniform electron gas
UV	Ultraviolet
VIS	Visible
WBI	Wiberg binding index
WFT	Wave function theory
WT	Wall time
ZORA	Zeroth order regular approximation

A2. Supporting Information to Chapter 3

Appendix A2 contains:

- General remarks
- Computational details
- Specification of statistical measures

General Remarks

All raw data and atomic Cartesian coordinates used or generated in this study can be obtained free of charge from the Supplementary Material of the original publication:

Bursch, M.; Hansen, A.; Grimme, S. “Fast and Reasonable Geometry Optimization of Lanthanoid Complexes with an Extended Tight Binding Quantum Chemical Method”, *Inorg. Chem.* **2017**, *56*, 12485–12491.

Computational Details

For the PBE0 calculations high spin systems were assumed applying multiplicities of $M = 2S + 1 = 5$ for **Pm-1-3**, $M = 6$ for **Sm-5**, $M = 9$ for **Ho-5** and $M = 3$ for **Pr-5** with S being the total electron spin of the system. In all GFN1-xTB calculations, employing the xtb 4.8²¹⁶ stand alone program, the lowest spin electron configuration is chosen by default. For geometry optimizations with HF-3c¹²⁷, low-spin electron configurations were used as provided by default from the define program as implemented in TURBOMOLE 7.0.2^{206,207}. Sparkle/PM6¹⁹⁹ calculations were also conducted applying low-spin electron configurations. In some cases the initial coordinates obtained from the CIF file caused problems upon conversion into the .mop format. In these cases the coordinates were reordered and converted. The corresponding coordinates are labeled with '.xrd.mop'. The conformer search was conducted with a development version of a conformer search algorithm including normal-mode-following developed in our lab, that is published separately⁶¹. All geometry optimizations were conducted at an Intel® Xeon® E5-2660 v4 @ 2.00 GHz, 256 GB RAM, 1.8 TB Scratch SATA HDD machine.

Statistical Measures

For property p (bond length, CN_{mean}) with n observations:

$$\delta p = p_{\text{calc}} - p_{\text{ref}} \quad (\text{A2.1})$$

A2. Supporting Information to Chapter 3

Mean deviation (MD):

$$MD = \frac{1}{n} \sum_i^n \delta p \quad (\text{A2.2})$$

Mean absolute deviation (MAD):

$$MAD = \frac{1}{n} \sum_i^n |\delta p| \quad (\text{A2.3})$$

Standard deviation (SD):

$$SD = \sqrt{\frac{\sum_i^n |\delta p - MD|^2}{n - 1}} \quad (\text{A2.4})$$

Mean root-mean-square deviation (MRMSD):

$$MRMSD = \frac{1}{n} \sum_i^n RMSD \quad (\text{A2.5})$$

A3. Supporting Information to Chapter 4

Appendix A3 contains:

- General remarks
- Specification of statistical measures

General Remarks

All raw data can be obtained free of charge from the Supplementary Material of the original publication:

Bursch, M.; Neugebauer, H.; Grimme, S. “Structure Optimisation of Large Transition-Metal Complexes with Extended Tight-Binding Methods”, *Angew. Chem. Int. Ed.* **2019**, *131*, 11195–11204.

Atomic Cartesian coordinates used or generated in this study can be obtained online from:

<https://www.chemie.uni-bonn.de/pctc/mulliken-center/software/tmg145>.

Statistical Measures

For property p (bond length, bond angle) with n observations:

$$\delta p = p_{calc} - p_{ref} \quad (\text{A3.1})$$

Mean deviation (MD):

$$MD = \frac{1}{n} \sum_i^n \delta p \quad (\text{A3.2})$$

Mean absolute deviation (MAD):

$$MAD = \frac{1}{n} \sum_i^n |\delta p| \quad (\text{A3.3})$$

A3. Supporting Information to Chapter 4

Standard deviation (SD):

$$SD = \sqrt{\frac{\sum_i^n |\delta p - MD|^2}{n - 1}} \quad (\text{A3.4})$$

Mean root-mean-square deviation (MRMSD):

Here n is the number of molecules and m is the number of atoms of each Molecule.

$$MRMSD = \frac{1}{n} \sum_i^n \sqrt{\frac{\sum_i^m |\delta p|^2}{m}} \quad (\text{A3.5})$$

A4. Supporting Information to Chapter 5

Appendix A4 contains:

- General remarks
- Specification of statistical measures

General Remarks

All raw data and atomic Cartesian coordinates used or generated in this study can be obtained free of charge from the Supplementary Material of the original publication:

Bursch, M.; Hansen, A.; Pracht, P.; Kohn, J. T.; Grimme, S. "Theoretical Study on Conformational Energies of Transition Metal Complexes", *Phys. Chem. Chem. Phys.* **2021**, *23*, 287–299.

The systems evaluated in this study were generally chosen to cover most transition metals as well as various ligand types and coordination motifs and elements involved in the ligand sphere. The structures of the TMCONF5 subset were chosen to represent the X-ray structure conformation, energetically low lying conformers at the B97-3c and GFN2-xTB levels, an energetically high lying conformer at the B97-3c level and a structure in between the high and low lying conformers at the GFN2-xTB level. By this selection process, a sufficiently large conformational energy range was covered for the TMCONF5 subset. The varying number of evaluated conformers for the TMCONF40 set results from subsequent removal of enantiomers and identical structures originating from the B97-3c reoptimization.

In some cases (**SIGSUX**, **MOGWIP**, **EGOZUV**, **BOBXAS**) GFN1-xTB consistently produced unreasonably high deviations depending on the underlying optimization method. This issue was observed mainly for early transition metals, and can be addressed to an erroneous charge estimate. The corresponding compounds were considered as unreasonable outliers and were excluded from the evaluation. In the case of UFF, **UWUBEV** and **NOXPAP** were excluded accordingly.

As all geometry inputs were initially generated by the CREST program in conjunction with the GFN2-xTB method, in some cases chemical transformations differing from the X-ray input structure are observed (**FEGGII**, **DUGVEH**, **DEFVIT**, **CAFKOJ**, **GOZYAX**). Nevertheless, the resulting structures were reoptimized with B97-3c to obtain the reference geometries and thus, were still used to evaluate energy differences of their conformers.

Based on qualitative fractional occupation density (FOD) analysis, some structures of the original benchmark set of Minenkov *et al.* were discarded. The respective FOD plots are depicted in Figure A4.1.

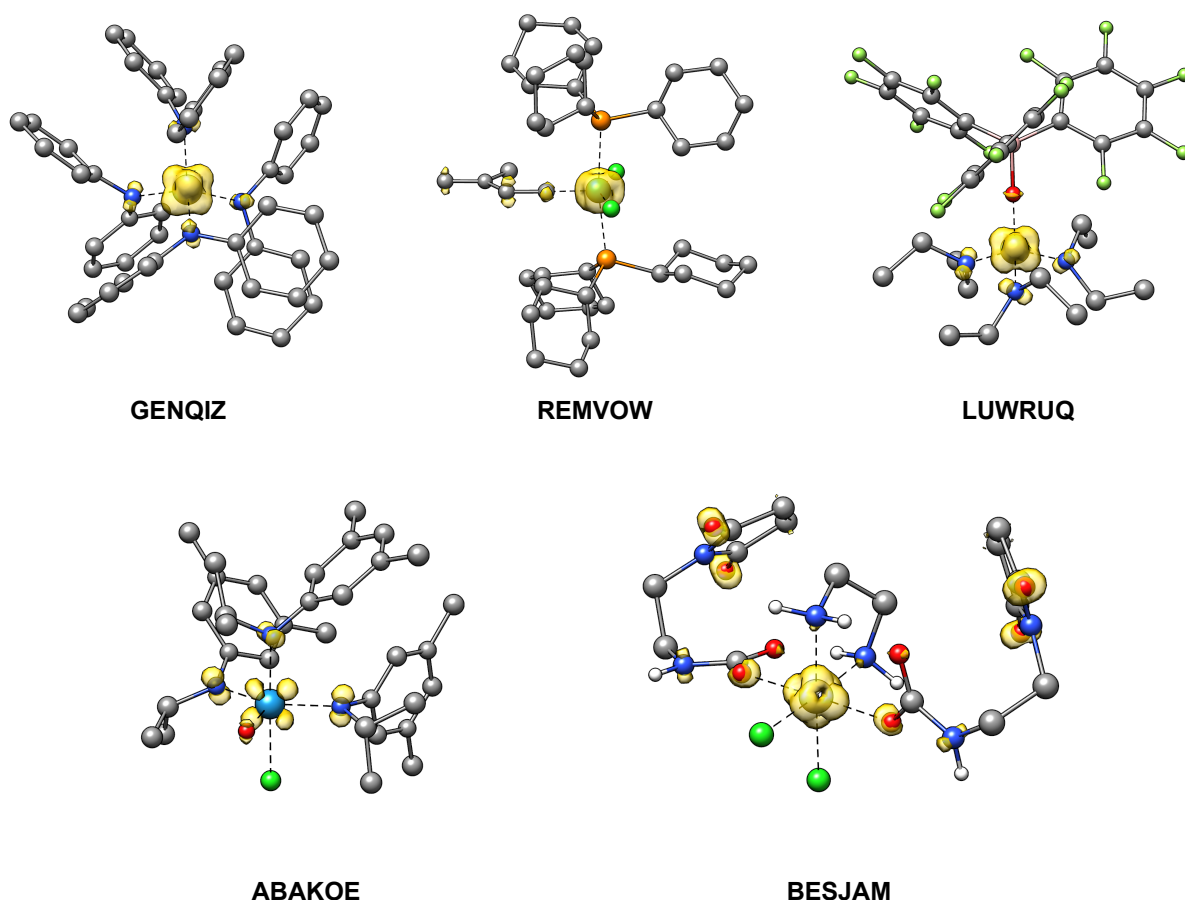


Figure A4.1.: Qualitative FOD analysis of discarded structures. The isosurface value is set to $\sigma = 0.005$ e·bohr⁻³.

Statistical Measures

Mean deviation (MD):

$$MD = \frac{1}{n} \sum_i^n (E_{x_i} - E_{r_i}) \quad (\text{A4.1})$$

Mean absolute deviation (MAD):

$$MAD = \frac{1}{n} \sum_i^n (|E_{x_i} - E_{r_i}|) \quad (\text{A4.2})$$

Pearson correlation coefficient (r_p):

$$r_p = \frac{\sum_{i=1}^n (E_{x_i} - \bar{E}_x)(E_{r_i} - \bar{E}_r)}{\sqrt{\sum_{i=1}^n (E_{x_i} - \bar{E}_x)^2 \sum_{i=1}^n (E_{r_i} - \bar{E}_r)^2}} \quad (\text{A4.3})$$

Spearman correlation coefficient (r_s):

$$r_s = \frac{\sum_{i=1}^n (R_{x_i} - \bar{R}_x)(R_{r_i} - \bar{R}_r)}{\sqrt{\sum_{i=1}^n (R_{x_i} - \bar{R}_x)^2 \sum_{i=1}^n (R_{r_i} - \bar{R}_r)^2}} \quad (\text{A4.4})$$

With E_i being the relative energy of the i^{th} of n conformers, and \bar{E} the average relative conformer energy over all n conformers for the tested method x and the reference r . For the Spearman correlation coefficient ρ_s the same notation is applied for conformer rankings R instead of their relative conformer energies.

A5. Supporting Information to Chapter 6

Appendix A5 contains:

- General remarks
- Computational details
- pK_A value prediction
- Tabulated energy contributions

General Remarks

All experimental details and atomic Cartesian coordinates used or generated in this study can be obtained free of charge from the Supplementary Material of the original publication:

Sitte, N. A.; Bursch, M.; Grimme, S.; Paradies, J. “Frustrated Lewis Pair Catalyzed Hydrogenation of Amides: Halides as Active Lewis Base in the Metal-Free Hydrogen Activation”, *J. Am. Chem. Soc.* **2019**, *141*, 159–162.

Computational Details

All quantum chemical calculations were performed with the TURBOMOLE 7.0.2^{206,207} or TURBOMOLE 7.2³⁷⁴ program package. Geometries were optimized using dispersion corrected composite method PBEh-3c⁶⁹ applying the COSMO³⁷³ solvation model for chloroform ($\epsilon = 4.71$). The numerical quadrature grid m4 was employed for the integration of the exchange-correlation contributions and default convergence criteria for energies and gradients were applied as implemented in TURBOMOLE. All structures were preoptimized applying the fast and robust GFN1-xTB⁵³ tight binding quantum chemical method as implemented in the xtb 5.8 program⁴¹⁸. Minimum structures were verified as minima on the potential energy hyper surface by the absence of imaginary frequencies in the harmonic frequency calculation. All calculations were performed applying the resolution-of-identity (RI) approximation for Coulomb integrals²⁴³ with matching default auxiliary basis sets²⁴⁴. The D3 dispersion correction scheme⁵⁹ applying Becke-Johnson (BJ) damping¹²¹ and including Axilrod-Teller-Muto (ATM)^{124,125} type three-body dispersion to the total dispersion energy was generally applied. For a review on this topic see ref. 31. Ro-vibrational corrections to obtain free energies were obtained from a modified rigid rotor harmonic oscillator statistical treatment⁵¹⁰ ($T = 50.0^\circ\text{C}$, 1 atm pressure) which is based on harmonic frequencies calculated at the geometry optimization level (PBEh-3c(COSMO(CHCl₃))) applying a scaling factor of 0.95. To avoid errors in the harmonic approximation, frequencies with wave numbers

below 100 cm^{-1} were treated partially as rigid rotors. Solvation effects were further considered by the COSMO-RS^{371,372,609} model, used as implemented in COSMOtherm (Version C3.0, release 16.01)³⁷⁵ with the 2016 parametrization for chloroform (parameter file: BP_TZVP_C30_1601.ctd; default G_{solv} option). The calculated solvation corrections were further corrected for the volume work of 1 bar to 1 M ideal gas. The default BP86^{658,659}/def-TZVP^{244,754} level of theory was used for single point calculations on the optimized geometries. Final gas phase single point energies were calculated at the PW6B95³⁷⁰ level of theory with the large polarized quadruple- ζ Gaussian AO basis set def2-QZVP (applying the default effective core potential for iodine)^{241,242} and an m5 grid. Reaction path optimization was performed with the Woelfling program⁷⁵⁵ as implemented in TURBOMOLE 7.0.2 or applying the growing string method (GSM) implementation of Zimmermann and co-workers^{756,757}. Transition states were optimized at the PBEh-3c(COSMO(CHCl₃)) level and further verified by the existence of only one imaginary frequency with $i\omega > 30\text{ cm}^{-1}$.

Final Gibbs free energies were calculated as sum of the gas phase single point energy E , the dispersion correction E_{D3} , the ro-vibrational correction G_{RRHO} , and the solvation correction $\delta G_{\text{solv,corr}}$ (Eq. A5.1).

$$G_{\text{tot}} = E + E_{D3} + G_{RRHO} + \delta G_{\text{solv,corr}} \quad (\text{A5.1})$$

pK_A Value Prediction

pK_a values were calculated at BP86/def-TZVP//BP86-D3(BJ)-ATM/def-TZVP level of theory using COSMOtherm (Version C3.0, release 17.01)⁷⁵⁸ with the 2017 parametrization for acetonitrile (parameter file: BP_TZVP_C30_1701.ctd; ACETONITRILE-ACID option LFER parameters) for $T = 50^\circ\text{C}$.

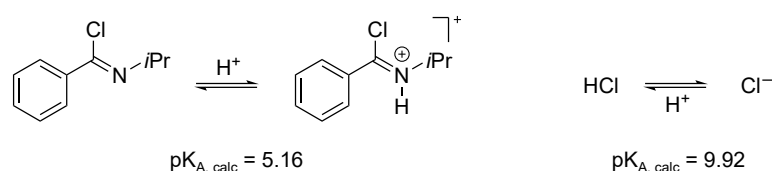


Figure A5.1.: Predicted pK_A values for selected compounds in acetonitrile.

Tabulated (Free-)Energy ContributionsTable A5.1.: Absolute (free-)energy contributions to G_{tot} and the largest imaginary frequency (ImF in cm^{-1}) for all structures involved in the proposed reaction mechanism without additive. All energy values in kcal mol^{-1} . A = Me_4N^+ ; R = 2,6-F₂-C₆H₃.

Structure	ImF	E_{PW6B95}	E_{D3}	G_{RRHO}	δG_{solv}	$\delta G_{\text{solv, corr}}$	G_{tot}
BR ₃	0	-826697.980	-16.441	106.692	-13.007	-10.902	-826618.632
AHBR ₃	0	-961811.279	-23.983	208.348	-30.214	-28.109	-961655.023
H ₂	0	-737.904	-0.018	-2.353	1.215	3.320	-736.955
ACl	0	-423768.400	-4.802	77.998	-30.322	-28.217	-423723.421
TS _{Cl}	-104.9	-1251203.975	-25.732	208.932	-35.010	-32.905	-1251053.680
HCl	0	-289399.938	-0.086	-8.250	-1.387	0.718	-289407.556
ABr	0	-1750800.574	-4.905	76.931	-33.872	-31.767	-1750760.315
TS _{Br}	-83.1	-2578236.867	-26.178	208.217	-35.621	-33.516	-2578088.344
HBr	0	-1616428.244	-0.112	-9.518	-1.807	0.298	-1616437.577
AI	0	-321683.454	-5.172	76.310	-34.703	-32.598	-321644.914
TS _I	-74.5	-1149118.951	-27.132	209.169	-34.854	-32.749	-1148969.664
HI	0	-187307.805	-0.156	-10.621	-3.230	-1.125	-187319.708

A6. Supporting Information to Chapter 7

Appendix A6 contains:

- General remarks
- Computational details
- Details on **1a/5a**, **1j/5j** and **TSj**
- Tabulated energy contributions

General Remarks

All experimental details and atomic Cartesian coordinates used or generated in this study can be obtained free of charge from the Supplementary Material of the original publication:

Stepen, A. J.; Bursch, M.; Grimme, S.; Stephan, D. W.; Paradies, J. "Electrophilic Phosphonium Cation-Mediated Phosphane Oxide Reduction Using Oxalyl Chloride and Hydrogen", *Angew. Chem. Int. Ed.* **2018**, *57*, 15253–15256.

Computational Details

All quantum chemical calculations were performed with the TURBOMOLE 7.0.2^{206,207} or TURBOMOLE 7.2³⁷⁴ program package unless stated otherwise. Geometries were optimized using dispersion corrected composite method PBEh-3c⁶⁹ applying the COSMO³⁷³ solvation model for chloroform ($\epsilon = 4.71$). The numerical quadrature grid m4 was employed for the integration of the exchange-correlation contributions and default convergence criteria for energies and gradients were applied as implemented in TURBOMOLE. All structures were preoptimized applying GFN1-xTB⁵³ in combination with the GBSA solvation model for CHCl_3 as implemented in the xtb 5.8.1 program⁷⁵⁹. Minimum structures were verified as minima on the potential energy hyper surface by the absence of imaginary frequencies in the harmonic frequency calculation. To identify the lowest energy conformers for the systems including cyclohexyl substituents the confscript program applying the MF-MD-GC algorithm⁶¹ for fully automated conformer ensemble generation was applied. The obtained GFN1-xTB conformers were further optimized and validated at PBEh-3c(COSMO(CHCl_3)) level of theory. All calculations were performed applying the resolution-of-identity (RI) approximation for Coulomb integrals²⁴³ with matching default auxiliary basis sets²⁴⁴. The D3 dispersion correction scheme⁵⁹ applying Becke-Johnson (BJ) damping¹²¹ and including Axilrod-Teller-Muto (ATM)^{124,125} type three-body dispersion to the total dispersion energy was generally applied. For a review on this topic see ref. 31. Ro-vibrational corrections

A6. Supporting Information to Chapter 7

to obtain free energies were obtained from a modified rigid rotor harmonic oscillator statistical treatment⁵¹⁰ (T = 130.0°C, 1 atm pressure) which is based on harmonic frequencies calculated at the geometry optimization level (PBEh-3c(COSMO(CHCl₃))) applying a scaling factor of 0.95. To avoid errors in the harmonic approximation, frequencies with wave numbers below 100 cm⁻¹ were treated partially as rigid rotors. Solvation effects were further considered by the COSMO-RS^{371,372,609} model, used as implemented in COSMOtherm (Version C3.0, release 16.01)³⁷⁵ with the 2016 parametrization for chloroform (parameter file: BP_TZVP_C30_1601.ctd; default G_{solv} option). The calculated solvation corrections were further corrected for the volume work of 1 bar to 1 M ideal gas. The default BP86^{658,659}/def-TZVP^{244,754} level of theory was used for single point calculations on the optimized geometries. Final gas phase single point energies were calculated with the ORCA 4.0.0^{208,209,286} program package at the PWPB95²⁶⁰ level of theory with the large polarized quadruple- ζ Gaussian AO basis set def2-QZVPP and the *GRID5* option as implemented in ORCA. For the PWPB95 calculations, the RIJK approximation was applied with matching auxiliary basis sets (*def2/JK*²⁴⁴, *def2-QZVPP/C*²⁹²). Reaction path optimization was performed with the Woelfling program⁷⁵⁵ as implemented in TURBOMOLE 7.0.2 or applying the growing string method (GSM) implementation of Zimmermann and co-workers^{756,757}. Transition states were optimized at the PBEh-3c(COSMO(CHCl₃)) level and further verified by the existence of only one imaginary frequency with $i\omega > 30$ cm⁻¹.

Final Gibbs free energies were calculated as sum of the gas phase single point energy E , the dispersion correction E_{D3} , the ro-vibrational correction G_{RRHO} , and the solvation correction $\delta G_{solv,corr}$ (Eq. A6.1).

$$G_{tot} = E + E_{D3} + G_{RRHO} + \delta G_{solv,corr} \quad (\text{A6.1})$$

Details on 1a/5a, 1j/5j and TSj

The transition state **TSj** (Figure 7.4b) has an asymmetric, non-linear O–H–H–P unit (angles / °: O–H–H = 177.9, P–H–H = 151.1; distances / Å: O–H = 1.341, P–H = 1.936) with a significantly elongated H–H bond distance of 0.914 Å. These distances are consistently longer compared to those observed in **TSa** (R = Ph). Further the P–O distance in the encounter complex **1j/5j** (Figure A6.1b) is significantly longer than in the phenyl derivate. Both structural differences indicate an increased sterical crowding in the cyclohexyl derivatives finally leading to an increased reaction barrier compared to **TSa**.

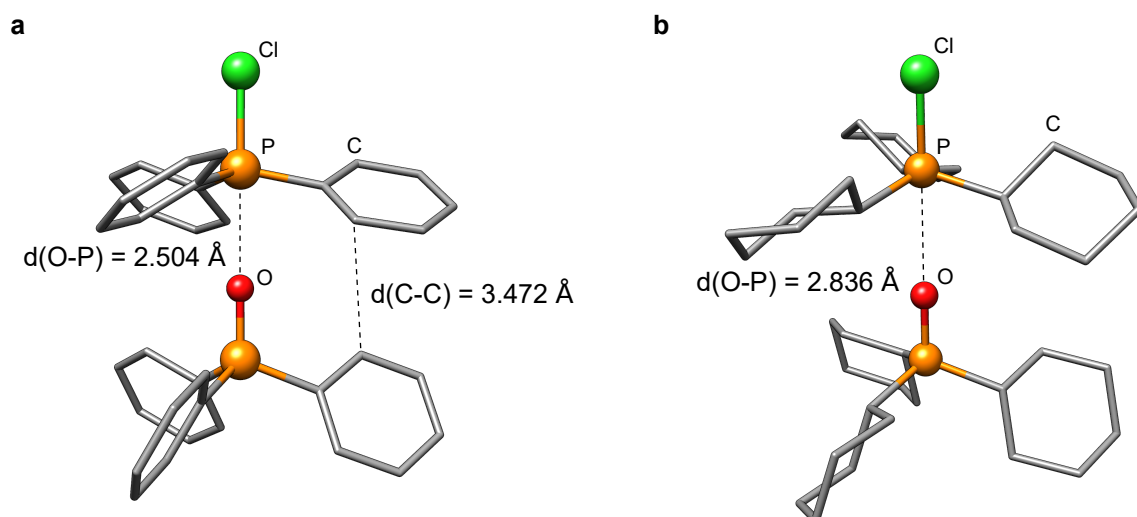


Figure A6.1.: Molecular structures of the encounter complexes a) **1a/5a** (R = Ph) and b) **1j/5j** (R = Cy) at the PBEh-3c(COSMO(CHCl₃)) level of theory. Hydrogen atoms are omitted for clarity.

Tabulated (Free-)Energy Contributions

Table A6.1.: Absolute (free-)energy contributions to G_{tot} and the largest imaginary frequency (ImF in cm^{-1}) for all structures involved in the proposed reaction mechanisms. All energy values in kcal mol^{-1} . If no symmetry is given, the C_1 point group was applied.

Structure	ImF	E_{PWPB95}	E_{D3}	G_{RRHO}	δG_{solv}	$\delta G_{\text{solv, corr}}$	G_{tot}
1a	0	-697466.865	-14.303	131.462	-14.835	-12.032	-697361.738
1a-H	0	-697705.025	-14.575	138.016	-41.697	-38.894	-697620.478
1a/5a	0	-1636394.214	-37.815	281.257	-45.429	-42.625	-1636193.397
2a	0	-650229.669	-13.687	129.365	-11.122	-8.318	-650122.309
2a-H	0	-650471.487	-13.881	136.071	-40.721	-37.917	-650387.214
5a-Cl	0	-1227849.222	-17.783	127.250	-14.476	-11.673	-1227751.428
5a	0	-938911.885	-15.593	129.442	-40.642	-37.838	-938835.874
6a	0	-939400.679	-15.663	133.968	-16.252	-13.449	-939295.822
TSa	-577.3	-1637104.634	-35.690	289.276	-45.935	-43.131	-1636894.179
1j	0	-704270.442	-17.231	256.285	-14.330	-11.527	-704042.916
1j-H	0	-704511.835	-17.472	263.272	-43.163	-40.359	-704306.394
1j/5j	0	-1650008.110	-42.463	533.464	-44.285	-41.482	-1649558.591
2j	0	-657028.807	-16.391	254.415	-10.423	-7.620	-656798.402
2j-H	0	-657280.629	-16.739	261.426	-42.466	-39.663	-657075.604
5j-Cl	0	-1234657.259	-20.574	253.574	-13.460	-10.657	-1234434.916
5j	0	-945720.859	-18.578	254.976	-41.945	-39.141	-945523.602
6j	0	-946214.458	-18.530	259.783	-17.744	-14.941	-945988.146
TSj	-399.8	-1650716.721	-41.659	541.621	-45.199	-42.396	-1650259.155
$\text{Cl}^- (\text{O}_h)$	0	-288835.416	0.000	-13.361	-68.313	-65.509	-288914.286
$(\text{COCl})_2 (\text{C}_{2h})$	0	-719820.492	-1.760	-14.514	-1.294	1.509	-719835.258
$\text{CO} (\text{C}_{6v})$	0	-71108.919	-0.088	-13.915	2.701	5.504	-71117.418
$\text{CO}_2 (\text{D}_{6h})$	0	-118348.068	-0.194	-11.136	2.024	4.828	-118354.570
$\text{H}_2 (\text{D}_{6h})$	0	-734.279	-0.011	-4.497	3.647	6.451	-732.337
$\text{HCl} (\text{C}_{6v})$	0	-289174.998	-0.064	-11.921	1.274	4.077	-289182.906

A7. Supporting Information to Chapter 8

Appendix A7 contains:

- General remarks
- Computational details
- Tabulated energy contributions

General Remarks

All experimental details and atomic Cartesian coordinates used or generated in this study can be obtained free of charge from the Supplementary Material of the original publication:

Köring, L.; Sitte, N. A.; Bursch, M.; Grimme, S.; Paradies, J. "Hydrogenation of Secondary Amides Using Phosphane Oxide and Frustrated Lewis Pair Catalysis", *Chem. Eur. J.* **2021**, *27*, 14179–14183.

Computational Details

All visualizations of molecular structures were created with UCSF Chimera 1.10.2⁷⁶⁰. Quantum chemical calculations were performed with the TURBOMOLE 7.3.1^{206,285} and xtb 6.2.2⁷⁶¹ program packages unless stated otherwise. Geometries were preoptimized with the GFN2-xTB⁵⁴ extended tight binding method with applied GBSA⁵⁷ implicit solvation model for CHCl₃. Final geometry optimizations were conducted with PBEh-3c⁶⁹ applying the COSMO³⁷³ solvation model for chloroform ($\epsilon = 4.71$). The numerical quadrature grid m4 was employed for the integration of the exchange-correlation contributions and default convergence criteria for energies and gradients were applied as implemented in TURBOMOLE. Minimum structures were verified as minima on the potential energy hyper surface by the absence of imaginary frequencies ($i\omega > 35 \text{ cm}^{-1}$) in the harmonic vibrational frequency calculation. If present imaginary frequencies below this threshold were inverted and included in the thermostistical correction. All geometry optimizations and single point calculations were performed applying either the resolution-of-identity (RI) approximation for Coulomb integrals²⁴³ (RIJ, optimizations) or for Coulomb and exchange integrals (RIJK, single point calculations) with matching default auxiliary basis sets²⁴⁴. The D3⁵⁹ (incorporated in the PBEh-3c composite method) and D4^{115,116} London dispersion correction schemes with Becke-Johnson (BJ) damping¹²¹ and including Axilrod-Teller-Muto (ATM)^{124,125} type three-body contributions to the total London dispersion energy were applied. For a review on this topic see ref. 31. Ro-vibrational corrections to obtain free energies were obtained from a modified rigid rotor harmonic oscillator statistical treatment⁵¹⁰ ($T = 70.0^\circ\text{C}$, 1 atm pressure) based on harmonic frequencies calculated at the geometry optimization level (PBEh-3c(COSMO(CHCl₃)))

applying a scaling factor of 0.95. To avoid errors in the harmonic approximation, frequencies with wave numbers below 100 cm^{-1} were treated partially as rigid rotors. Gas phase single point energies were calculated at PW6B95-D4/def2-QZVP level applying the m5 numerical quadrature grid. Solvation effects were further considered by the COSMO-RS^{371,372,609} model, used as implemented in COSMOtherm (Version C3.0, release 16.01)³⁷⁵ with the 2016 parametrization for chloroform (parameter file: BP_TZVP_C30_1601.ctd; default G_{solv} option). Calculated solvation corrections were further corrected for the volume work of 1 bar to 1 M ideal gas. In this framework the default BP86^{658,659}/def-TZVP^{244,754} level of theory was used for single point calculations on the optimized geometries. Reaction path optimization was performed with the growing string method (GSM) implementation of Zimmermann and co-workers^{756,757} applying GFN2-xTB. Transition states were finally optimized at the PBEh-3c(COSMO(CHCl₃)) level and further verified by the existence of only one imaginary frequency with $i\omega > 30 \text{ cm}^{-1}$.

Final Gibbs free energies were calculated as sum of the gas phase single point energy E , the dispersion correction E_{D4} , the ro-vibrational correction G_{RRHO} , and the solvation correction $\delta G_{\text{solv,corr}}$ (Eq. A7.1).

$$G_{\text{tot}} = E + E_{D4} + G_{RRHO} + \delta G_{\text{solv,corr}} \quad (\text{A7.1})$$

Tabulated (Free-)Energy Contributions

Table A7.1.: Absolute (free-)energy contributions to G_{tot} and the largest imaginary frequency (ImF in cm^{-1}) for all structures involved in the proposed reaction mechanisms. All energy values in kcal mol^{-1} . If no symmetry is given, the C_1 point group was applied.

Structure	ImF	E_{PW6B95}	E_{D4}	G_{RRHO}	$\delta G_{\text{solv, corr}}$	G_{tot}
1b	0	-326166.531	-13.925	104.242	-8.962	-326085.176
1e	0	-276740.036	-10.543	71.553	-8.301	-276687.327
2b	0	-567512.816	-14.605	94.614	-5.775	-567438.582
2e (C_s)	0	-518086.548	-11.155	61.882	-4.839	-518040.660
[2b-H] ⁺	0	-567746.516	-14.310	102.918	-42.853	-567700.761
[2e-H] ⁺	0	-518317.043	-10.915	70.507	-44.235	-518301.686
[2b-4e]	0	-1581302.985	-48.702	199.639	-16.694	-1581168.741
[2e-4e]	0	-1531877.551	-45.304	166.913	-15.876	-1531771.818
3a	0	-698554.474	-28.466	140.067	-16.169	-698459.042
EPC	0	-940151.469	-28.920	138.226	-41.440	-940083.603
4e	0	-1013789.090	-27.989	88.073	-10.136	-1013739.142
[Cl-4e] ⁻	0	-1302893.263	-32.007	87.340	-47.235	-1302885.165
[H-4e] ⁻	0	-1014223.171	-29.196	93.061	-44.795	-1014204.101
[5b-H] ⁺	0	-279865.265	-13.872	125.665	-46.155	-279799.627
[5e-H] ⁺ (C_s)	0	-230435.498	-9.979	93.216	-49.068	-230401.329
[6b-H] ⁺	0	-279107.434	-12.592	110.532	-43.287	-279052.780
[6e-H] ⁺ (C_s)	0	-229678.036	-9.214	77.975	-44.774	-229654.049
Cl^- (O_h)	0	-289060.125	0.000	-11.098	-72.325	-289143.547
H_2 (D_{6h})	0	-737.904	-0.037	-2.536	3.601	-736.876
HCl (C_{6v})	0	-289399.938	-0.123	-9.154	1.055	-289408.160
INT1b	0	-1266327.228	-50.799	259.257	-45.775	-1266164.545
INT2b	0	-1555463.600	-55.733	259.247	-34.972	-1555295.058
INT3b	0	-1266297.006	-50.846	259.410	-59.007	-1266147.450
INT4b	0	-976902.141	-48.570	253.566	-43.523	-976740.668
INT5b	0	-278330.139	-11.272	94.960	-41.701	-278288.152
INT6b	0	-568274.376	-15.498	109.062	-7.437	-568188.248
INT6e	0	-518848.387	-11.888	75.309	-6.972	-518791.939
INT7b	0	-279625.345	-13.756	115.747	-5.679	-279529.034
INT7e	0	-230199.377	-10.331	83.276	-4.811	-230131.244
TS1b	-63.0	-1555448.026	-53.105	257.489	-41.648	-1555285.290
TS2b	-544.5	-1266300.401	-50.243	256.227	-52.005	-1266146.423
TS3b	-201.5	-976896.186	-46.637	251.678	-42.812	-976733.957
TS4b	-276.7	-1582029.455	-51.596	209.196	-17.293	-1581889.148
TS4e	-192.5	-1532606.062	-46.883	176.187	-16.305	-1532493.063
TS5b	-512.3	-1582034.505	-54.210	213.057	-18.311	-1581893.969
TS5e	-471.0	-1532609.838	-49.972	180.247	-18.386	-1532497.949
TS6	-96.2	-1303598.072	-30.651	94.513	-63.018	-1303597.228
TS7b	-281.0	-1293403.448	-50.744	220.095	-18.081	-1293252.178
TS7e	-263.5	-1243976.274	-46.361	187.405	-18.094	-1243853.324

A8. Supporting Information to Chapter 9

Appendix A8 contains:

- General remarks
- Computational details
- Tabulated energy contributions and model reactions
- Foster-Boys LMO analysis
- Energy decomposition analysis
- Dispersion analysis

General Remarks

All experimental details and atomic Cartesian coordinates used or generated in this study can be obtained free of charge from the Supplementary Material of the original publication:

Teichmann, J.; Bursch, M.; Köstler, B.; Bolte, M.; Lerner, H.-W.; Grimme, S.; Wagner, M. “Trapping Experiments on a Trichlorosilanide Anion: a Key Intermediate of Halogenosilane Chemistry”, *Inorg. Chem.* **2017**, *56*, 8683–8688.

Computational Details

All visualizations of molecular structures were created with UCSF Chimera 1.10.2⁷⁶⁰. Quantum chemical calculations were performed with the TURBOMOLE 7.0.2^{206,207} program package unless stated otherwise. Gas phase geometries were optimized with the hybrid functional PBE0. The large polarized quadruple- ζ Gaussian AO basis set def2-QZVP²⁴⁰ using a Stuttgart-Dresden ECP²⁴¹ for iodine and the D3^{31,59} London dispersion correction with Becke-Johnson (BJ)¹²¹ damping were generally applied if not stated else. The RI approximation²⁴³ for Coulomb integrals with matching default auxiliary basis sets was used to accelerate all energy calculations. The numerical quadrature grid m4 (m5 for single point energies) was employed for the integration of the exchange-correlation contributions as implemented in TURBOMOLE. TURBOMOLE default convergence criteria for energies and gradients were used. The optimized structures were verified as minima on the potential energy hyper surface by the absence of imaginary frequencies in the harmonic frequency calculation. Single point calculations^a were conducted with the double hybrid exchange correlation functional B2PLYP¹¹⁰ and the hybrid functional

^aFurther data calculated with the PW6B95 functional can be obtained from the Supporting Information of the original publication. These values are not discussed and are therefore omitted for the sake of brevity.

A8. Supporting Information to Chapter 9

B3LYP^{607,608,665}. Ro-vibrational corrections to the free energies were obtained from a modified rigid rotor harmonic oscillator statistical treatment⁵¹⁰ at a temperature of 298.15 K and 1 atm pressure based on analytic harmonic frequencies calculated at geometry optimization level of theory. Frequencies with wave numbers below 100 cm^{-1} were treated partially as rigid rotors to avoid errors in the harmonic approximation. Solvation effects were considered by the means of the COSMO-RS^{371,372,609} model as implemented in COSMOtherm (Version C3.0, release 16.01)³⁷⁵ with the 2014 parametrization for dichloromethane (parameter file: BP_TZVP_C30_1401.ctd; G_{solv} =reference option). Single point calculations in this context were conducted at the default BP86^{658,659}/def-TZVP^{244,754} level of theory on optimized geometries. All solvation corrections were calculated for dichloromethane at a temperature of 298.15 K. Foster-Boys⁵¹¹ localized molecular orbitals (LMO) and Wiberg bond indices (WBI) were calculated based on single point calculations excluding g-functions from the basis set (PBE0/def2-QZVP(-g)). For the energy decomposition analysis, the augmented def2-QZVPD⁷⁶² basis set was applied. Final Gibbs free energies were calculated as sum of the gas phase single point energy E , the dispersion correction E_{D3} , the ro-vibrational correction G_{RRHO} , and the solvation correction δG_{solv} (Eq. A8.1).

$$G_{\text{tot}} = E + E_{D3} + G_{RRHO} + \delta G_{\text{solv}} \quad (\text{A8.1})$$

Relative Gibbs free energies are calculated according to Equation A8.2.

$$\Delta G_{\text{tot}} = \sum G_{\text{tot},\text{products}} - \sum G_{\text{tot},\text{reactants}} \quad (\text{A8.2})$$

Tabulated (Free-)Energy Contributions and Model Reactions

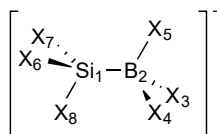


Figure A8.1.: Schematic atom numbering.

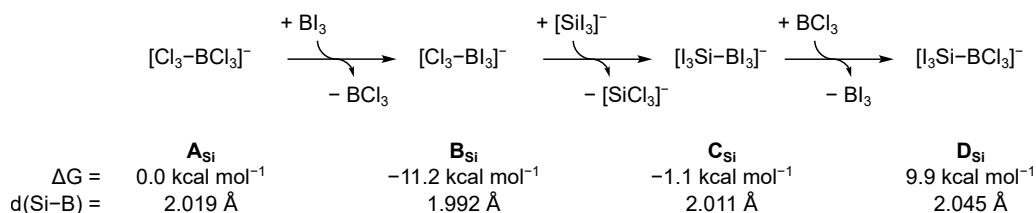


Figure A8.2.: Calculated relative Gibbs free energies (B2PLYP-D3(BJ)/def2-QZVP+COSMO-RS(CH₂Cl₂)/PBE0-D3(BJ)/def2-QZVP) and Si–B bond lengths (PBE0-D3/def2-QZVP) of model compounds **A_{Si}** to **D_{Si}**. All energies in kcal mol⁻¹ are given relative to the corresponding starting compound **A_{Si}** in context of the given model reaction.

Table A8.1.: Absolute (free-)energy contributions to G_{tot} for the adducts **A_{Si}** to **D_{Si}** and its fragments. All energy values in kcal mol⁻¹. The def2-QZVP basis set was generally applied.

Structure	$E_{\text{PBE0-D3(BJ)}}$	E_{B2PLYP}	$E_{\text{D3, B2PLYP}}$	E_{B3LYP}	$E_{\text{D3, B3LYP}}$	G_{RRHO}	δG_{solv}	$G_{\text{tot, B2PLYP}}$	$G_{\text{tot, B3LYP}}$
BCl ₃	-881764.770	-881744.306	-2.790	-881962.272	-5.548	-13.504	-0.025	-881760.624	-881981.351
BI ₃	-576102.461	-575589.780	-5.675	-576081.495	-9.720	-18.652	-5.950	-575620.057	-576115.815
[SiCl ₃] ⁻	-1047839.045	-1047817.086	-3.922	-1048079.298	-7.426	-17.057	-47.169	-1047885.235	-1048150.954
[SiI ₃] ⁻	-742202.683	-741688.166	-7.149	-742223.263	-12.026	-21.151	-46.414	-741762.880	-742302.849
A_{Si}	-1929651.435	-1929599.237	-11.063	-1930075.997	-21.258	-15.824	-42.888	-1929669.011	-1930155.965
B_{Si}	-1624005.705	-1623458.842	-16.307	-1624207.320	-29.314	-19.673	-44.784	-1623539.606	-1624301.084
C_{Si}	-1318357.060	-1317313.814	-21.873	-1318335.552	-37.745	-23.326	-48.189	-1317407.202	-1318444.816
D_{Si}	-1624002.925	-1623455.515	-15.592	-1624205.732	-28.185	-19.787	-45.894	-1623536.787	-1624299.597

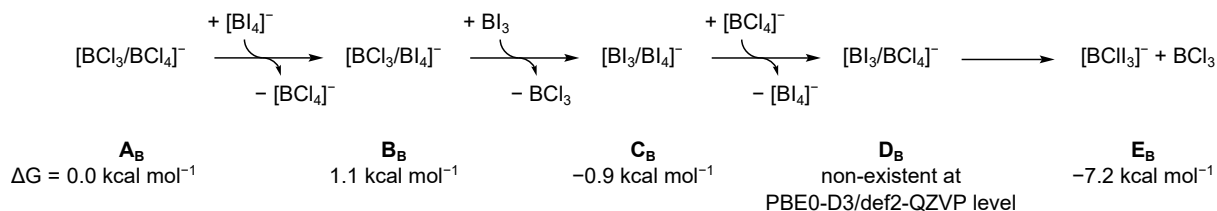


Figure A8.3.: Calculated relative Gibbs free energies (B2PLYP-D3(BJ)/def2-QZVP+COSMO-RS(CH₂Cl₂)/PBE0-D3(BJ)/def2-QZVP) of model compounds **A_B** to **E_B**. All energies in kcal mol⁻¹ are given relative to the corresponding starting compound **A_B** in context of the given model reaction.

Table A8.2.: Absolute (free-)energy contributions to G_{tot} for halide and borate exchange reactions. All energy values in kcal mol^{-1} . The def2-QZVP basis set was generally applied.

Structure	$E_{\text{PBE0-D3(BJ)}}$	$E_{\text{B2PLYP-D3(BJ)}}$	G_{RRHO}	δG_{solv}	G_{tot}
BCl_2I	-779876.819	-779696.012	-15.300	-2.037	-779713.349
BClI_2	-677989.365	-677645.448	-17.024	-3.993	-677666.466
$[\text{SiCl}_2\text{I}]^-$	-945960.549	-945779.502	-18.571	-46.415	-945844.488
$[\text{SiClI}_2]^-$	-844081.656	-843737.481	-19.936	-46.224	-843803.641
$[\text{BCl}_4]^-$	-1170553.867	-1170527.069	-14.588	-48.164	-1170589.820
$[\text{BI}_4]^-$	-763019.482	-762340.727	-20.702	-48.852	-762410.281
A_B	-2052328.081	-2052277.802	-14.535	-42.772	-2052335.108
B_B	-1644791.114	-1644088.006	-20.613	-45.896	-1644154.516
C_B	-1339135.996	-1337942.905	-24.113	-48.891	-1338015.908
E_B	-1746673.938	-1746133.628	-19.635	-48.474	-1746201.737

Foster-Boys LMO Analysis

Table A8.3.: Foster-Boys localized molecular orbital (LMO) analysis of the Si-B bond at the PBE0-D3(BJ)/def2-QZVP(-g) level of theory.

Atom	A_{Si} ($[\text{Cl}_3\text{Si}-\text{BCl}_3]^-$)		B_{Si} ($[\text{Cl}_3\text{Si}-\text{BI}_3]^-$)		C_{Si} ($[\text{I}_3\text{Si}-\text{BI}_3]^-$)		D_{Si} ($[\text{I}_3\text{Si}-\text{BCl}_3]^-$)	
	Si	B	Si	B	Si	B	Si	B
Bondtype	σ		σ		σ		σ	
Occupation	2.00		2.00		2.00		2.00	
Energy (ϵ)	-0.2931		-0.3167		-0.3872		-0.3057	
Centers	1.66		1.76		1.49		1.44	
WBI	0.76		0.79		0.69		0.63	
Localization	0.63	0.45	0.56	0.50	0.75	0.34	0.76	0.34
%s	62.18	44.59	58.52	44.33	75.00	40.23	66.79	46.68
%p	36.09	55.03	38.75	55.56	23.80	61.31	32.18	54.99
%d	1.73	0.41	2.65	0.18	1.10	-1.42	1.03	-1.66

Energy Decomposition Analysis

Table A8.4.: EDA energy contributions for $[\text{I}_3\text{SiBI}_3]^-$ in kcal mol^{-1} . The Si-B distance is given in Å.

PBE0-D3(BJ)/def2-QZVPD							
d(Si-B)	E_{ES}	E_{X}	E_{XR}	E_{OR}	E_{CI}	E_{D3}	$E_{\text{int.}}$
1.4	-285.408	-274.889	1026.630	-343.039	-47.269	-10.098	65.927
1.6	-224.065	-202.558	713.947	-273.880	-38.912	-9.573	-35.041
1.8	-164.075	-146.923	491.232	-213.041	-31.797	-8.975	-73.579
2.0	-115.607	-104.908	334.504	-162.535	-25.773	-8.313	-82.632
2.011	-113.362	-102.975	327.553	-160.113	-25.476	-8.276	-82.650
2.2	-79.714	-73.806	225.682	-122.459	-20.702	-7.638	-78.636
2.4	-54.360	-51.247	151.104	-91.715	-16.465	-7.062	-69.744
2.6	-36.928	-35.192	100.559	-68.679	-12.951	-6.787	-59.977
2.8	-25.127	-23.960	66.617	-51.674	-10.059	-6.231	-50.433
3.0	-17.198	-16.215	43.980	-39.209	-7.698	-5.508	-41.849
3.2	-11.881	-10.938	28.957	-30.083	-5.789	-4.791	-34.525
3.4	-8.308	-7.375	19.022	-23.382	-4.263	-4.119	-28.424
3.6	-5.894	-4.983	12.467	-18.434	-3.059	-3.507	-23.410
3.8	-4.251	-3.383	8.148	-14.755	-2.126	-2.962	-19.328
4.0	-3.121	-2.313	5.308	-12.000	-1.417	-2.485	-16.028
4.2	-2.337	-1.595	3.444	-9.919	-0.895	-2.074	-13.375
4.4	-1.785	-1.110	2.224	-8.337	-0.522	-1.725	-11.254
4.6	-1.391	-0.780	1.428	-7.124	-0.266	-1.432	-9.566
4.8	-1.107	-0.552	0.910	-6.188	-0.102	-1.188	-8.227
B3LYP-D3(BJ)/def2-QZVPD							
d(Si-B)	E_{ES}	E_{X}	E_{XR}	E_{OR}	E_{CI}	E_{D3}	$E_{\text{int.}}$
1.4	-287.620	-254.649	1011.380	-344.823	-31.468	-20.984	71.836
1.6	-225.460	-187.353	703.667	-275.581	-25.189	-19.482	-29.398
1.8	-165.341	-135.712	484.719	-214.191	-20.027	-17.813	-68.365
2.0	-116.884	-96.770	330.658	-163.073	-15.833	-16.028	-77.930
2.011	-114.639	-94.979	323.823	-160.622	-15.631	-15.930	-77.978
2.2	-80.947	-67.947	223.613	-122.541	-12.452	-14.267	-74.540
2.4	-55.467	-47.008	150.144	-91.553	-9.742	-12.801	-66.427
2.6	-37.859	-32.060	100.236	-68.454	-7.578	-12.079	-57.794
2.8	-25.869	-21.558	66.618	-51.501	-5.857	-10.825	-48.991
3.0	-17.765	-14.287	44.117	-39.139	-4.493	-9.293	-40.860
3.2	-12.302	-9.319	29.126	-30.123	-3.417	-7.843	-33.878
3.4	-8.615	-5.968	19.174	-23.516	-2.574	-6.544	-28.043
3.6	-6.116	-3.736	12.584	-18.638	-1.919	-5.411	-23.236
3.8	-4.412	-2.269	8.229	-15.009	-1.413	-4.442	-19.316
4.0	-3.240	-1.320	5.359	-12.288	-1.028	-3.627	-16.144
4.2	-2.427	-0.717	3.473	-10.232	-0.739	-2.952	-13.594
4.4	-1.856	-0.342	2.237	-8.670	-0.526	-2.400	-11.557
4.6	-1.450	-0.117	1.432	-7.479	-0.370	-1.952	-9.937
4.8	-1.157	0.013	0.909	-6.569	-0.260	-1.591	-8.655

Dispersion Analysis

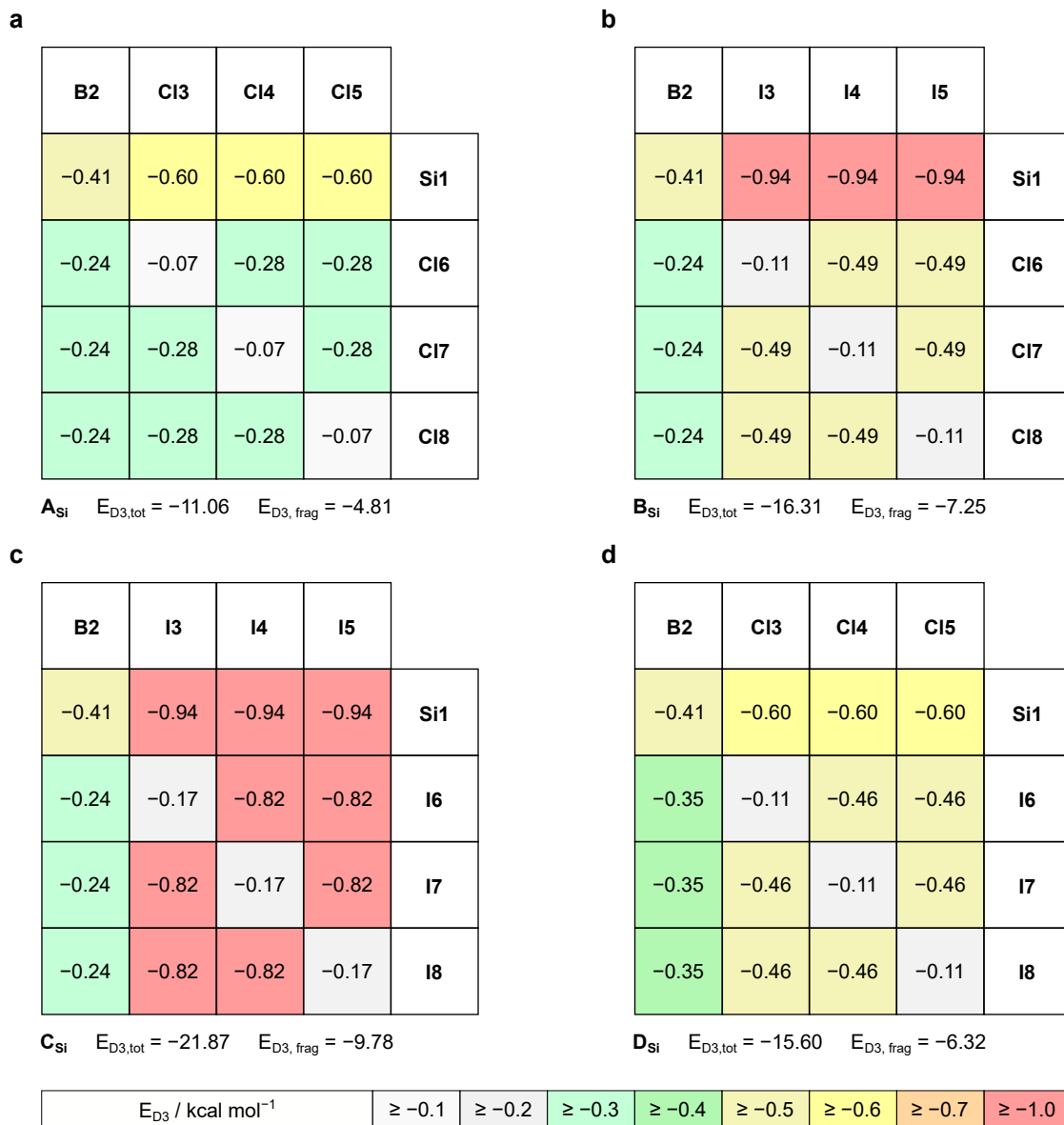


Figure A8.4.: Pair wise D3 interaction contributions at B2PLYP-D3(BJ)//PBE0-D3/def2-QZVP level of theory to the total dispersion term of the minimum structures a) **A_{Si}**, b) **B_{Si}**, c) **C_{Si}**, and d) **D_{Si}** are displayed in a cross-matrix of the two fragments $[R_3Si]^-$ and BX_3 . A red color indicates a large pair wise dispersion energy contribution a grey color a low contribution. $E_{D3,frag}$ represents the sum of all cross-matrix entries while $E_{D3,tot}$ corresponds to the total dispersion energy.

A9. Supporting Information to Chapter 10

Appendix A9 contains:

- General remarks
- Computational details
- Details on structure comparisons
- Tabulated data

General Remarks

All experimental details, atomic Cartesian coordinates used or generated in this study, and further supplementary data can be obtained free of charge from the Supplementary Material of the original publication:

McCrea-Hendrick, M. L.; Bursch, M.; Gullett, K. L.; Maurer, L. R.; Fettinger, J. C.; Grimme, S.; Power, P. P. “Counterintuitive Interligand Angles in the Diaryls $E\{C_6H_3-2,6-(C_6H_2-2,4,6-iPr_3)_2\}_2$ (E = Ge, Sn, or Pb) and Related Species: The Role of London Dispersion Forces”, *Organometallics* **2018**, *37*, 2075–2085.

Computational Details

All quantum chemical calculations except $^{207}Pb\{^1H\}$ NMR gas phase chemical shift predictions and sHF-3c^{127,128} calculations were performed with the TURBOMOLE 7.2 program package^{206,374}. Molecular structures were optimized applying the hybrid DFT functional PBE0²¹³ in combination with the polarized triple- ζ Gaussian AO basis set def2-TZVP²⁴⁰ with no symmetry constraints starting from the crystal structure cutout. Default ECPs^{241,242} were applied for Sn and Pb as implemented in TURBOMOLE. Convergence criteria were set to 10^{-6} E_h for energies and 10^{-4} E_h for the maximum norm of the Cartesian gradient. The numerical quadrature grid m4 grid was employed for the integration of the exchange-correlation as implemented in TURBOMOLE. The resolution-of-identity (RI) approximation²⁴³ for Coulomb integrals with matching default auxiliary basis sets²⁴⁴ was generally applied. The D3 dispersion correction scheme⁵⁹ applying Becke-Johnson (BJ) damping^{121,122} and including Axilrod-Teller-Muto (ATM)^{124,125} type three-body dispersion to the total dispersion energy was applied if not stated else. For a review on this topic see ref. 31. Final single point Energies were calculated with the large quadruple- ζ basis set def2-QZVP at the PBE0/def2-QZVP//PBE0-D3(BJ)-ATM/def2-TZVP level of theory. $^{207}Pb\{^1H\}$ NMR gas phase chemical shifts were calculated at SO-ZORA-PBE0/ZORA/TZ2P//PBE0-D3(BJ - ATM /def2-TZVP^{210,211,559,561,562} applying gauge-including atomic orbitals (GIAO)^{561,563,564} as implemented in the ADF2016⁵⁶⁵ program package. The zeroth-order regular

approximation (ZORA) optimized all electron triple- ζ Slater-type basis set ZORA/TZ2P⁵⁶⁰ was used as implemented in ADF2016. The *SpinOrbit* option was applied as well as a *NumericalQuality verygood* criterion as implemented in ADF2016. No symmetry constraints were applied. PbMe₄ was used as reference system. Crystal structures were fully optimized using a scaled minimal basis set Hartree-Fock with semi-classical correction potentials (sHF-3c) as implemented in the CRYSTAL17^{567,568} program package. Default integral, SCF convergence, and geometry convergence thresholds are used, the space group from the X-ray structure is maintained during the optimization procedure. The Brillouin zone is sampled with a Gamma-centered grid of 2×1×2 k-points. The gas phase structures are treated in identical settings without periodic boundary conditions. All molecular graphics and crystallographic plots were created with UCSF Chimera⁷⁶⁰ or Mercury^{763,764}.

Structure Comparisons

The provided crystal structure molecular cutouts were optimized applying density functional theory at PBE0-D3(BJ)-ATM/def2-TZVP and PBE0/def2-TZVP level of theory. In the second case any dispersion corrections were switched off explicitly. Both calculated structures were compared with respect to the X-ray molecular structure. The numbering of the atoms refers to their position in the Cartesian coordinates input file.

Tabulated Data

Table A9.1.: Structural deviations of the geometry optimized at the PBE0-D3(BJ)-ATM/def2-TZVP level of theory from the crystallographically determined molecular structure. Angles in °, bond lengths in Å. The RMSD in Å represents the heavy atom (all except H) best fit of the calculated and the experimental structure.

Structure	PBE0-D3(BJ)-ATM/def2-TZVP						
Ge(Ar ^{Me6}) ₂	E-C2	E-C50	C2-E-C50	E-C2-C3	E-C2-C7	E-C50-C51	E-C50-C55
	-0.009	-0.009	0.4	-1.1	0.7	-1.1	0.7
	E-C2-C5	C3-C8-C11	C7-C17-C20	E-C50-C53	C51-C79-C82	C55-C56-C59	RMSD
Sn(Ar ^{Me6}) ₂	-0.1	4.3	3.0	-0.1	4.3	3.0	0.575
	E-C2	E-C50	C2-E-C50	E-C2-C3	E-C2-C7	E-C50-C51	E-C50-C55
	0.012	0.012	1.1	-1.7	0.8	-1.7	0.8
Pb(Ar ^{Me6}) ₂	E-C2-C5	C3-C8-C11	C7-C17-C20	E-C50-C53	C51-C79-C82	C55-C56-C59	RMSD
	-2.5	3.0	4.1	-2.5	3.0	4.1	0.625
	E-C2	E-C51	C2-E-C51	E-C2-C3	E-C2-C7	E-C51-C52	E-C51-C52
Ge(Ar ^{iPr4}) ₂	0.013	0.013	2.8	-2.7	2.3	-2.7	2.3
	E-C2-C5	C3-C8-C11	C7-C17-C20	E-C51-C54	C52-C80-C83	C56-C57-C60	RMSD
	-5.1	3.6	5.5	-5.1	3.6	5.5	0.75
Sn(Ar ^{iPr4}) ₂	E-C2	E-C69	C2-E-C69	E-C2-C3	E-C2-C10	E-C69-C70	E-C69-C77
	0.007	0.000	-1.3	-0.2	0.7	-2.9	3.7
	E-C2-C6	C3-C11-C15	C10-C40-C44	E-C69-C73	C70-C78-C82	C77-C107-C111	RMSD
Pb(Ar ^{iPr4}) ₂	0.3	1.7	-5.2	9.6	-1.9	-1.9	0.350
	E-C2	E-C69	C2-E-C69	E-C2-C3	E-C2-C10	E-C69-C70	E-C69-C77
	0.020	0.020	2.4	-0.2	-0.1	-0.2	-0.1
Ge(Ar ^{iPr6}) ₂	E-C2-C6	C3-C11-C15	C10-C40-C44	E-C69-C73	C70-C78-C82	C77-C107-C111	RMSD
	-1.4	0.1	-4.6	-1.4	0.1	-4.6	0.307
	E-C2	E-C69	C2-E-C69	E-C2-C3	E-C2-C10	E-C69-C70	E-C69-C77
Sn(Ar ^{iPr6}) ₂	-0.004	0.011	-0.8	0.5	0.8	-3.7	0.6
	E-C2-C6	C3-C11-C15	C10-C40-C44	E-C69-C73	C70-C78-C82	C77-C107-C111	RMSD
	0.7	0.1	0.6	-1.4	-0.3	3.4	0.146
Pb(Ar ^{iPr6}) ₂	E-C2	E-C87	C2-E-C87	E-C2-C3	E-C2-C10	E-C87-C88	E-C87-C95
	0.009	0.005	-1.6	-1.3	0.5	0.8	-1.5
	E-C2-C6	C3-C11-C15	C10-C49-C53	C10-C49-C53	C10-C49-C53	C95-C134-C138	RMSD
Sn(Ar ^{iPr6}) ₂	0.9	-0.4	0.1	1.2	1.1	-1.2	0.197
	E-C2	E-C87	C2-E-C87	E-C2-C3	E-C2-C10	E-C87-C88	E-C87-C95
	-0.016	-0.021	-0.1	3.7	-4.8	-4.6	2.9
Pb(Ar ^{iPr6}) ₂	E-C2-C6	C3-C49-C53	C10-C11-C15	E-C87-C91	C88-C124-C128	C95-C96-C100	RMSD
	5.9	2.8	-2.7	3.3	-3.0	2.4	0.470
	E-C2	E-C87	C2-E-C87	E-C2-C3	E-C2-C10	E-C71-C72	E-C71-C79
Pb(Ar ^{iPr6}) ₂	-0.006	-0.001	-0.6	0.0	0.0	-3.1	2.6
	E-C2-C6	C3-C11-C15	C10-C43-C47	E-C71-C75	C72-C80-C84	C79-C118-C122	RMSD
	-1.8	-2.7	4.7	4.2	-0.9	0.4	0.307

A9. Supporting Information to Chapter 10

Table A9.2.: Structural deviations of the geometry optimized at the PBE0/def2-TZVP level of theory from the crystallographically determined molecular structure. Angles in °, bond lengths in Å. The RMSD in Å represents the heavy atom (all except H) best fit of the calculated and the experimental structure.

Structure	PBE0/def2-TZVP						
Ge(Ar ^{Me6}) ₂	E-C2	E-C50	C2-E-C50	E-C2-C3	E-C2-C7	E-C50-C51	E-C50-C55
	0.000	0.000	2.2	-2.7	2.5	-2.6	2.4
	E-C2-C5	C3-C8-C11	C7-C17-C20	E-C50-C53	C51-C79-C82	C55-C56-C59	RMSD
Sn(Ar ^{Me6}) ₂	-0.8	2.5	4.5	-0.8	2.5	4.6	0.683
	E-C2	E-C50	C2-E-C50	E-C2-C3	E-C2-C7	E-C50-C51	E-C50-C55
	0.025	0.025	2.2	-2.9	2.4	-2.9	2.4
Pb(Ar ^{Me6}) ₂	E-C2-C5	C3-C8-C11	C7-C17-C20	E-C50-C53	C51-C79-C82	C55-C56-C59	RMSD
	-2.4	1.6	5.4	-2.4	1.6	5.4	0.698
	E-C2	E-C51	C2-E-C51	E-C2-C3	E-C2-C7	E-C51-C52	E-C51-C52
Ge(Ar ^{iPr4}) ₂	0.031	0.031	2.8	-6.2	3.6	-3.2	3.6
	E-C2-C5	C3-C8-C11	C7-C17-C20	E-C51-C54	C52-C80-C83	C56-C57-C60	RMSD
	-3.7	3.3	6.0	-3.7	3.3	6.0	0.786
Sn(Ar ^{iPr4}) ₂	E-C2	E-C69	C2-E-C69	E-C2-C3	E-C2-C10	E-C69-C70	E-C69-C77
	0.024	0.010	0	-4.6	7.3	-6.0	6.1
	E-C2-C6	C3-C11-C15	C10-C40-C44	E-C69-C73	C70-C78-C82	C77-C107-C111	RMSD
Pb(Ar ^{iPr4}) ₂	-1.7	3.9	-7.0	15.0	0.2	-0.4	0.487
	E-C2	E-C69	C2-E-C69	E-C2-C3	E-C2-C10	E-C69-C70	E-C69-C77
	0.032	0.032	4.0	1.7	-1.5	1.7	-1.5
Ge(Ar ^{iPr6}) ₂	E-C2-C6	C3-C11-C15	C10-C40-C44	E-C69-C73	C70-C78-C82	C77-C107-C111	RMSD
	-1.5	0.7	-5.1	-1.5	0.7	-5.1	0.337
	E-C2	E-C69	C2-E-C69	E-C2-C3	E-C2-C10	E-C69-C70	E-C69-C77
Sn(Ar ^{iPr6}) ₂	0.025	0.035	1.6	1.9	-0.4	-2.5	-0.2
	E-C2-C6	C3-C11-C15	C10-C40-C44	E-C69-C73	C70-C78-C82	C77-C107-C111	RMSD
	-0.7	0.5	0.7	-1.6	-0.2	3.2	0.198
Pb(Ar ^{iPr6}) ₂	E-C2	E-C87	C2-E-C87	E-C2-C3	E-C2-C10	E-C87-C88	E-C87-C95
	0.018	0.015	0.2	-0.3	-0.2	0.1	-0.5
	E-C2-C6	C3-C11-C15	C10-C49-C53	C10-C49-C53	C10-C49-C53	C95-C134-C138	RMSD
Sn(Ar ^{iPr6}) ₂	0.1	0.5	-1.5	0.4	-0.5	-0.3	0.234
	E-C2	E-C87	C2-E-C87	E-C2-C3	E-C2-C10	E-C87-C88	E-C87-C95
	-0.001	0.017	6.0	1.2	-2.4	-1.2	0.9
Pb(Ar ^{iPr6}) ₂	E-C2-C6	C3-C49-C53	C10-C11-C15	E-C87-C91	C88-C124-C128	C95-C96-C100	RMSD
	3.3	1.9	-4.5	1.3	0.2	5.4	0.689
	E-C2	E-C87	C2-E-C87	E-C2-C3	E-C2-C10	E-C71-C72	E-C71-C79
Ge(Ar ^{iPr6}) ₂	0.033	0.015	9.3	-1.4	1.3	-1.5	0.8
	E-C2-C6	C3-C11-C15	C10-C43-C47	E-C71-C75	C72-C80-C84	C79-C118-C122	RMSD
	1.4	-0.3	4.8	2.2	-4.2	1.4	0.828

A10. Supporting Information to Chapter 11

Appendix A10 contains:

- General remarks
- Computational details
- Molecular dynamics averaged UV/VIS spectra of all generated structures
- Tabulated data

General Remarks

All experimental details and atomic Cartesian coordinates used or generated in this study can be obtained free of charge from the Supplementary Material of the original publication:

Queen, J. D.; Bursch, M.; Seibert, J.; Maurer, L. R.; Ellis, B. D.; Fettingner, J. C.; Grimme, S.; Power, P. P. "Isolation and Computational Studies of a Series of Terphenyl Substituted Diplumbynes with Ligand Dependent Lead–Lead Multiple-Bonding Character", *J. Am. Chem. Soc.* **2019**, *141*, 14370–14383.

Computational Details

All visualizations of structures, MOs and NBOs were created with UCSF Chimera 1.10.2⁷⁶⁰. Quantum mechanical calculations were performed with the TURBOMOLE 7.0.2^{206,207}, ORCA 4.1^{208,286,603} and xtb 6.1.0⁶⁰⁴ program packages unless otherwise stated. Geometries were preoptimized with the GFN2-xTB⁵⁴ extended tight binding method and finally optimized using the TPSS⁶⁰⁶ meta-GGA functional in combination with the triple- ζ def2-TZVP²⁴⁰ basis set. The numerical quadrature grid m4 grid was employed for the integration of the exchange-correlation contributions and default convergence criteria for energies and gradients were applied as implemented in TURBOMOLE. The default Stuttgart-Dresden effective core potential ECP-46^{241,242} was applied for all Pb atoms. Structures were verified as minima on the potential energy hyper surface by the absence of imaginary frequencies ($i\omega > 30 \text{ cm}^{-1}$) in the harmonic frequency calculation. Imaginary frequencies below this threshold were inverted and included in the thermostistical correction calculation. All geometry optimizations and single point energy calculations were performed applying the resolution-of-identity (RI) approximation for Coulomb integrals²⁴³ with matching default auxiliary basis sets²⁴⁴. The D3⁵⁹ and D4^{115,116} dispersion correction schemes applying Becke-Johnson (BJ) damping^{121,122} and including Axilrod-Teller-Muto (ATM)^{124,125} type three-body dispersion to the total dispersion energy was applied (D3(BJ)-ATM generally applied for geometry optimizations). For a review on this topic see ref. 31. Ro-vibrational

corrections were obtained from a modified rigid rotor harmonic oscillator statistical treatment⁵¹⁰ ($T = 25.0^\circ\text{C}$, 1 atm pressure) based on harmonic frequencies calculated at the geometry optimization level (TPSS-D3(BJ)-ATM/def2-TZVP). To avoid errors in the harmonic approximation, frequencies with wave numbers below 100 cm^{-1} were treated partially as rigid rotors. NBO analyses were carried out with the NBO6⁶⁰⁵ program package implementation in ORCA 4.1 at the geometry optimization level of theory. Final gas phase single point energies were calculated with the PBE0²¹³ and B3LYP^{607,608,665} hybrid functionals with the polarized quadruple- ζ Gaussian AO basis set def2-TZVPP and the m5 grid. Solvation effects were further considered by the COSMO-RS^{371,372,609} model, used as implemented in COSMOtherm (Version C3.0, release 16.01)³⁷⁵ with the 2016 parametrization for toluene (parameter file: BP_TZVP_C30_1601.ctd; default G_{solv} option). Calculated solvation corrections were further corrected for the volume work of 1 bar to 1 M ideal gas. The default BP86^{658,659}/def-TZVP^{244,754} level of theory was used for single point calculations on the optimized geometries.

Final Gibbs free energies were calculated as sum of the gas phase single point energy E , the dispersion correction E_{disp} , the ro-vibrational correction G_{RRHO} , and the solvation correction $\delta G_{\text{solv,corr}}$ (Eq. A10.1).

$$G_{\text{tot}} = E + E_{\text{disp}} + G_{\text{RRHO}} + \delta G_{\text{solv,corr}} \quad (\text{A10.1})$$

UV/VIS spectra were calculated applying simplified Tamm-Dancoff approximated^{611,612} time-dependent density functional theory (sTD-DFT) (ORCA 4.1). For the sTD-DFT calculations the BHLYP⁹⁵ hybrid functional was applied with the def2-TZVP basis set. The RIJCOSX⁶⁵⁰ approximation (*GridX6*) was applied to accelerate the sTD-DFT calculations. All UV/VIS spectra were calculated applying the conductor-like polarizable continuum solvation model⁶⁴³ (CPCM) for *n*-hexane. To obtain averaged UV/VIS spectra molecular dynamics (MD) simulations at GFN2-xTB(GBSA(toluene)) level were carried out starting from the corresponding DFT structures. The simulations were carried out for 1000 ps with preceding equilibration for 100 ps. A time step of 1 fs was used and the SHAKE^{765,766} algorithm was applied, constraining all hydrogen containing bonds. From the resulting trajectory 200 snapshots were taken equidistantly and used as structural input for sTDA-xTB calculations. A standard threshold of 7 eV was applied for the sTDA part. The MD averaged absorption spectrum results from a mean over all individual spectra of the snapshots.

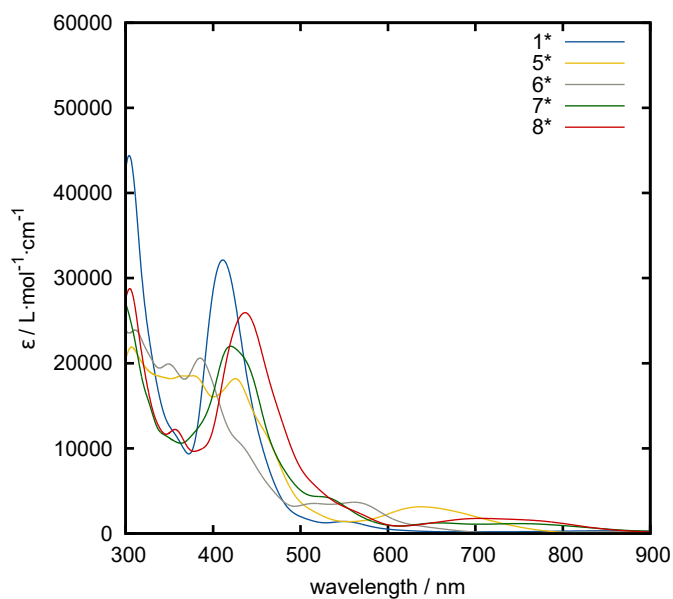


Figure A10.1.: Molecular dynamics averaged UV/VIS spectra of all generated structures at sTD-BHLYP(CPCM(*n*-hexane)) level.

Tabulated Data

Table A10.1.: Structure scan data for the model system Ph-Pb-Pb-Ph.

$\theta(\text{C-Pb-Pb-C})$ / °	$\varphi(\text{C-Pb-Pb})$ / °	E_{TPSS} / kcal mol ⁻¹	$d(\text{Pb-Pb})$ / Å	$\Sigma E^{(2)}$ / kcal mol ⁻¹	NPA/NLMO BO	$E_{\text{exc}}(\text{H} \rightarrow \text{L}+1)$ / eV
100	100	-849.207	3.086	0.00	1.04	1.92
100	105	-849.205	3.072	1.23	1.07	1.87
100	110	-849.203	3.046	2.14	1.10	1.82
100	115	-849.201	3.011	3.66	1.15	1.77
100	120	-849.198	2.972	5.99	1.21	1.72
100	125	-849.196	2.938	9.09	1.26	1.69
100	130	-849.193	2.912	12.52	1.32	1.75
100	90	-849.210	3.062	0.00	1.02	1.99
100	95	-849.205	3.072	1.23	1.07	1.87
110	100	-849.206	3.100	0.00	1.04	2.02
110	105	-849.204	3.077	1.25	1.07	1.97
110	110	-849.202	3.043	2.41	1.11	1.92
110	115	-849.200	2.997	4.54	1.17	1.87
110	120	-849.198	2.949	7.92	1.24	1.83
110	125	-849.196	2.910	12.28	1.30	1.79
110	130	-849.193	2.883	16.73	1.36	1.75
110	90	-849.210	3.070	0.00	1.03	2.10
110	95	-849.204	3.077	1.25	1.07	1.97
120	100	-849.205	3.114	0.00	1.03	2.09
120	105	-849.204	3.090	1.14	1.06	2.06

Table A10.1.: Continued.

$\theta(\text{C-Pb-Pb-C})$ / °	$\varphi(\text{C-Pb-Pb})$ / °	E_{TPSS} / kcal mol ⁻¹	$d(\text{Pb-Pb})$ / Å	$\Sigma E^{(2)}$ / kcal mol ⁻¹	NPA/NLMO BO	$E_{\text{exc}}(\text{H} \rightarrow \text{L}+1)$ / eV
120	110	-849.201	3.044	2.59	1.11	2.01
120	115	-849.199	2.984	5.60	1.18	1.97
120	120	-849.197	2.923	10.73	1.27	1.95
120	125	-849.195	2.881	16.79	1.35	1.92
120	130	-849.193	2.856	22.17	1.41	1.88
120	90	-849.209	3.081	0.00	1.03	2.21
120	95	-849.204	3.090	1.14	1.06	2.06
130	100	-849.205	3.126	0.00	1.02	2.18
130	105	-849.203	3.107	0.00	1.05	2.13
130	110	-849.200	3.052	2.59	1.10	2.09
130	115	-849.198	2.968	7.16	1.20	2.07
130	120	-849.196	2.893	15.22	1.32	2.07
130	125	-849.195	2.852	23.01	1.40	2.06
130	130	-849.193	2.831	28.90	1.46	2.02
130	90	-849.208	3.097	0.00	1.02	2.30
130	95	-849.203	3.107	0.00	1.05	2.13
140	100	-849.204	3.141	0.00	1.02	2.25
140	105	-849.202	3.128	0.00	1.03	2.19
140	110	-849.199	3.074	2.23	1.09	2.15
140	115	-849.196	2.944	9.89	1.24	2.15
140	120	-849.195	2.859	22.44	1.38	2.22
140	125	-849.195	2.825	31.26	1.46	2.21
140	130	-849.193	2.808	36.72	1.50	2.16
140	90	-849.207	3.116	0.00	1.02	2.36
140	95	-849.202	3.128	0.00	1.03	2.19
150	100	-849.204	3.158	0.00	1.01	2.31
150	105	-849.201	3.152	0.00	1.02	2.24
150	110	-849.197	3.115	1.38	1.06	2.19
150	115	-849.194	2.895	17.13	1.31	2.31
150	120	-849.194	2.824	33.31	1.45	2.37
150	125	-849.194	2.800	41.05	1.51	2.36
150	130	-849.193	2.790	44.99	1.55	2.31
150	90	-849.206	3.137	0.00	1.01	2.41
150	95	-849.201	3.152	0.00	1.02	2.24
160	100	-849.203	3.172	0.00	1.00	2.35
160	105	-849.200	3.176	0.00	1.01	2.28
160	110	-849.195	3.168	0.00	1.03	1.92
160	115	-849.193	2.829	34.79	1.43	2.50
160	120	-849.193	2.795	46.41	1.51	2.53
160	125	-849.193	2.781	51.01	1.55	2.52
160	130	-849.193	2.776	52.67	1.58	2.46
160	90	-849.205	3.158	0.00	1.00	2.43
160	95	-849.200	3.176	0.00	1.01	2.28
170	100	-849.203	3.183	0.00	1.00	2.37

Table A10.1.: Continued.

$\theta(\text{C-Pb-Pb-C})$ / °	$\varphi(\text{C-Pb-Pb})$ / °	E_{TPSS} / kcal mol ⁻¹	$d(\text{Pb-Pb})$ / Å	$\Sigma E^{(2)}$ / kcal mol ⁻¹	NPA/NLMO BO	$E_{\text{exc}}(\text{H} \rightarrow \text{L}+1)$ / eV
170	105	-849.199	3.194	0.00	1.00	2.30
170	110	-849.194	3.210	0.00	1.00	2.21
170	115	-849.191	2.789	53.97	1.52	2.21
170	120	-849.193	2.775	58.01	1.56	2.68
170	125	-849.193	2.769	58.90	1.59	2.68
170	130	-849.193	2.767	58.33	1.60	2.62
170	90	-849.204	3.175	0.00	1.00	2.44
170	95	-849.199	3.194	0.00	1.00	2.30
180	100	-849.203	3.186	0.00	1.00	2.38
180	105	-849.199	3.202	0.00	1.00	2.30
180	110	-849.188	2.783	63.17	1.52	2.68
180	115	-849.191	2.774	63.58	1.55	2.73
180	120	-849.192	2.768	63.20	1.58	2.76
180	125	-849.193	2.765	62.12	1.60	2.79
180	130	-849.193	2.765	60.47	1.61	2.76
180	90	-849.203	3.185	0.00	1.00	2.43
180	95	-849.199	3.202	0.00	1.00	2.30
90	90	-849.211	3.057	0.00	1.03	1.88
90	100	-849.207	3.081	0.00	1.05	1.82
90	105	-849.206	3.071	1.12	1.07	1.78
90	110	-849.203	3.051	1.83	1.10	1.74
90	115	-849.201	3.025	2.94	1.13	1.74
90	120	-849.198	2.994	4.56	1.18	1.75
90	125	-849.195	2.966	6.69	1.23	1.78
90	130	-849.192	2.942	9.23	1.27	1.83
90	95	-849.206	3.071	1.12	1.07	1.78

A10. Supporting Information to Chapter 11

Table A10.2.: Absolute contributions to G_{tot} . All calculations were conducted applying the C_1 point group. "frag" denotes the PbR fragment in the doublet ground state. E_{TPSS} in a.u., all other values in kcal mol⁻¹.

Struc.	E_{TPSS}	E_{PBE0}	$E_{D3}(PBE0)$	$E_{D4}(PBE0)$	E_{B3LYP}	$E_{D3}(B3LYP)$	$E_{D4}(B3LYP)$	G_{RRHO}	δG_{solv}
1	-3190.237	-1999307.18	-179.39	-179.66	-2000226.32	-320.25	-307.07	864.84	-32.93
1frag	-1595.083	-999645.99	-75.51	-76.43	-1000111.43	-138.44	-134.09	421.47	-19.09
5	-3662.300	-2295071.51	-216.18	-216.17	-2296138.08	-384.29	-368.14	1063.90	-37.32
5frag	-1831.117	-1147531.36	-93.84	-94.78	-1148070.76	-170.41	-164.82	520.80	-21.47
6	-3662.183	-2294980.66	-228.36	-228.35	-2296034.13	-406.80	-389.96	1069.93	-34.73
6frag	-1831.053	-1147484.63	-98.11	-99.12	-1148017.44	-178.92	-173.24	524.62	-20.71
7	-2718.170	-1703530.90	-148.39	-149.16	-1704297.96	-266.86	-256.46	668.23	-28.58
7frag	-1359.049	-851755.65	-62.57	-63.64	-852144.14	-115.18	-111.97	323.55	-15.84
8	-3535.759	-2216157.95	-169.41	-169.85	-2217108.91	-304.11	-291.41	781.29	-30.26
8frag	-1767.843	-1108069.11	-72.62	-73.52	-1108549.81	-133.14	-128.79	380.06	-17.57
1*	-3190.236	-1999306.20	-177.07	-177.47	-2000223.50	-318.10	-305.03	864.95	-32.89
5*	-3662.289	-2295064.73	-216.54	-216.76	-2296129.81	-385.02	-369.01	1066.59	-37.16
6*	-3662.161	-2294971.43	-223.97	-223.56	-2296026.91	-399.88	-382.73	1069.44	-35.63
7*	-2718.165	-1703524.79	-147.64	-148.66	-1704288.79	-266.99	-256.67	667.44	-28.17
8*	-3535.753	-2216151.70	-168.09	-168.79	-2217099.83	-303.50	-290.92	781.89	-29.67

$$\Delta E_{disp} = E_{disp,complex} - (E_{disp,fragment1} + E_{disp,fragment2}) \quad (\text{A10.2})$$

Table A10.3.: ΔE_{disp} and absolute dispersion corrections for the full complex and its unrelaxed fragments in kcal mol⁻¹.

		PBE0		B3LYP	
		D3(BJ)-ATM	D4	D3(BJ)-ATM	D4
1	$E_{disp,complex}$	-179.39	-179.66	-320.25	-307.07
	$E_{disp,fragment 1}$	-74.22	-74.86	-136.00	-131.34
	$E_{disp,fragment 2}$	-74.22	-74.87	-136.01	-131.35
	ΔE_{disp}	-30.94	-29.93	-48.24	-44.39
5	$E_{disp,complex}$	-216.18	-216.17	-384.29	-368.14
	$E_{disp,fragment 1}$	-93.77	-94.43	-170.25	-164.17
	$E_{disp,fragment 2}$	-93.61	-94.29	-169.94	-163.91
	ΔE_{disp}	-28.79	-27.45	-44.10	-40.07
6	$E_{disp,complex}$	-228.36	-228.35	-406.80	-389.96
	$E_{disp,fragment 1}$	-97.19	-98.11	-177.19	-171.42
	$E_{disp,fragment 2}$	-98.07	-98.56	-178.64	-172.10
	ΔE_{disp}	-33.10	-31.69	-50.97	-46.44
7	$E_{disp,complex}$	-148.39	-149.16	-266.86	-256.46
	$E_{disp,fragment 1}$	-61.73	-62.49	-113.44	-109.86
	$E_{disp,fragment 2}$	-61.73	-62.50	-113.44	-109.86
	ΔE_{disp}	-24.94	-24.17	-39.97	-36.74
8	$E_{disp,complex}$	-169.41	-169.85	-304.11	-291.41
	$E_{disp,fragment 1}$	-72.18	-72.76	-132.02	-127.26
	$E_{disp,fragment 2}$	-72.19	-72.78	-132.05	-127.28
	ΔE_{disp}	-25.04	-24.31	-40.04	-36.87
1*	$E_{disp,complex}$	-177.07	-177.07	-318.10	-305.03
	$E_{disp,fragment 1}$	-75.13	-75.86	-138.03	-133.29
	$E_{disp,fragment 2}$	-75.17	-75.89	-138.09	-133.33
	ΔE_{disp}	-26.76	-25.32	-41.99	-38.41
5*	$E_{disp,complex}$	-216.54	-216.76	-385.02	-369.01
	$E_{disp,fragment 1}$	-93.87	-94.56	-170.25	-164.24
	$E_{disp,fragment 2}$	-93.58	-94.42	-169.98	-164.22
	ΔE_{disp}	-29.09	-27.78	-44.79	-40.54
6*	$E_{disp,complex}$	-223.97	-223.56	-399.88	-382.73
	$E_{disp,fragment 1}$	-97.64	-98.12	-178.02	-171.51
	$E_{disp,fragment 2}$	-97.64	-98.12	-178.03	-171.51
	ΔE_{disp}	-28.69	-27.32	-43.83	-39.72
7*	$E_{disp,complex}$	-147.64	-148.66	-266.99	-256.67
	$E_{disp,fragment 1}$	-63.25	-64.24	-116.57	-113.09
	$E_{disp,fragment 2}$	-63.24	-64.23	-116.55	-113.07
	ΔE_{disp}	-21.15	-20.19	-33.87	-30.52
8*	$E_{disp,complex}$	-168.09	-168.79	-303.50	-290.92
	$E_{disp,fragment 1}$	-73.41	-74.22	-134.76	-130.11
	$E_{disp,fragment 2}$	-73.38	-74.19	-134.70	-130.05
	ΔE_{disp}	-21.29	-20.38	-34.05	-30.76

A11. Supporting Information to Chapter 12

Appendix A11 contains:

- General remarks
- Applied dielectric constants and refractive indices
- Overview of program specific calculation settings
- Specification of statistical measures
- Composition of the *SiS146* benchmark set

General Remarks and Technical Specifications

All raw data and atomic Cartesian coordinates used or generated in this study can be obtained free of charge from the Supplementary Material of the original publication:

Bursch, M.; Gasevic, T.; Stückrath, J. B.; Grimme, S. “Comprehensive Benchmark Study on the Calculation of ^{29}Si NMR Chemical Shifts”, *Inorg. Chem.* **2021**, *60*, 272–285.

Chemical shifts were calculated according to equation A11.1 with $\sigma(^{29}\text{Si}_{\text{TMS}})$ being the ^{29}Si NMR shielding constant for TMS calculated on the structure reoptimized in the respective solvent.

$$\delta(^{29}\text{Si}) = \sigma(^{29}\text{Si}_{\text{TMS}}) - \sigma(^{29}\text{Si}) \quad (\text{A11.1})$$

Table A11.1.: Dielectric constants ϵ and refractive indices n of the used solvents.

Solvent	ϵ	n
Acetonitrile	37.50	1.3442
Benzene	2.28	1.5011
Bromobenzene	5.40	1.5597
Chlorobenzene	5.62	1.5241
Chloroform	4.81	1.4459
Cyclohexane	2.02	1.4266
Dichloromethane	8.93	1.4242
Tetrahydrofuran	7.58	1.4070
Toluene	2.38	1.4961

Table A11.2.: Overview of program specific calculation settings.

Program	Task	Grid	RI	Auxbasis	Solvation	Miscellaneous
ORCA	Geo.-Opt.	Grid4	RIJ	def2/J	CPCM	
ORCA	Frequencies	Grid4	RIJ	def2/J	CPCM	NumFreq
ORCA	NMR (ECP)	Grid5, NoFinalGrid, GridX6, NoFinalGridX	RIJCOSX	def2/J ^a	CPCM	NOSOSCF
ORCA	NMR (ZORA)	Grid7, NoFinalGrid, InatAcc 10, GridX6, NoFinalGridX	RIJCOSX	SARC/J	CPCM	NOSOSCF
ADF	NMR	NumericalQuality good	default	default	COSMO, surf Esurf, solv Rad=1.3, div ndiv=5	nosym

^adef2-TZVP/C applied for the correlation part in double-hybrid calculations.

Statistical Measures

The following statistical measures have been used for the evaluation of the chemical shift data of the benchmark studies with n data points. δ_x denotes the calculated and δ_r the reference, i.e. the experimental value.

Mean deviation (MD):

$$MD = \frac{1}{n} \sum_i^n (\delta_{x_i} - \delta_{r_i}) \quad (\text{A11.2})$$

Mean absolute deviation (MAD):

$$MAD = \frac{1}{n} \sum_i^n (|\delta_{x_i} - \delta_{r_i}|) \quad (\text{A11.3})$$

Determination coefficient (R^2):

$$R^2 = 1 - \frac{\sum_i^n (\delta_{x_i} - \delta_{r_i})^2}{\sum_i^n (\delta_{x_i} - \bar{\delta}_x)^2} \quad (\text{A11.4})$$

Benchmark Set Composition

Table A11.3.: All compound structures (with numbers #C) with the considered ^{29}Si nuclei (with numbers #N) of the *SiS146* benchmark set as well as their respective solvent in the NMR measurement, experimental ^{29}Si NMR chemical shifts δ_{exp} and references (THF = tetrahydrofuran, DCM = dichloromethane). Compounds 1 – 55 belong to the *SiS-L*, 56 – 100 to the *SiS-H* subset *SiS-H*.

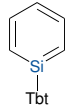
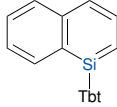
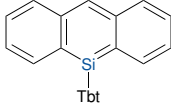
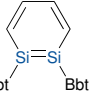
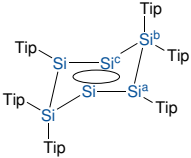
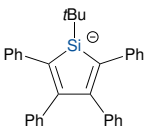
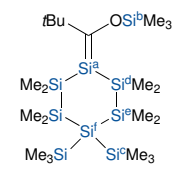
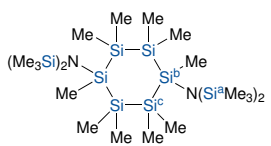
#C	Compound	Solvent	#N	Nucleus	δ_{exp} / ppm	Ref.
1	 Tbt = 2,4,6-[CH(SiMe ₃) ₂] ₃ -C ₆ H ₂	cyclohexane	1	Si	92.5	767
2	 Tbt = 2,4,6-[CH(SiMe ₃) ₂] ₃ -C ₆ H ₂	benzene	2	Si	91.7	768
3	 Tbt = 2,4,6-[CH(SiMe ₃) ₂] ₃ -C ₆ H ₂	benzene	3	Si	87.2	769
4	 Bbt = 2,6-[CH(SiMe ₃) ₂] ₂ -4-[C(SiMe ₃) ₃]-C ₆ H ₂	benzene	4	Si	57.1	770
5	 Tip = 2,4,6- <i>i</i> -Pr ₃ -C ₆ H ₂	benzene	5 6 7	Si ^a Si ^b Si ^c	124.6 -84.8 -89.3	771
6 ¹		THF	8	Si	26.12	772
7		benzene	9 10 11 12 13 14	Si ^a Si ^b Si ^c Si ^d Si ^e Si ^f	37.00 13.16 -8.79 -35.61 ² -37.51 ² -132.43	773
8		benzene	15 16 17	Si ^a Si ^b Si ^c	2.37 -15.38 -37.05	774

Table A11.3.: Continued.

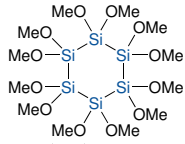
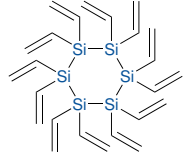
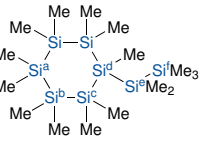
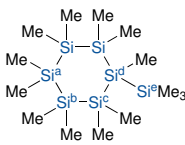
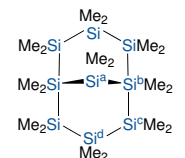
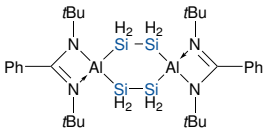
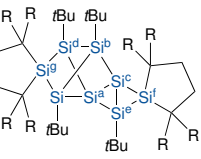
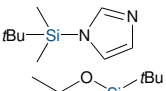
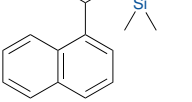
#C	Compound	Solvent	#N	Nucleus	δ_{exp} / ppm	Ref.
9		benzene	18	Si	-9.18	774
10		benzene	19	Si	-36	774
11 ¹		benzene	20	Si ^a	-42.36	775
			21	Si ^b	-40.51	
			22	Si ^c	-37.48	
			23	Si ^d	-72.73	
			24	Si ^e	-37.64	
			25	Si ^f	-14.88	
12 ¹		benzene	26	Si ^a	-42.11	775
			27	Si ^b	-40.63	
			28	Si ^c	-38.75	
			29	Si ^d	-82.06	
			30	Si ^e	-9.36	
13 ¹		benzene	31	Si ^a	-35.37	775
			32	Si ^b	-78.75	
			33	Si ^c	-36.84	
			34	Si ^d	-43.76	
14		benzene	35	Si	-128.9	776
15		benzene	36	Si ^a	-191.9	777
			37	Si ^b	-66.3	
			38	Si ^c	-20	
			39	Si ^d	-12	
			40	Si ^e	7.5	
			41	Si ^f	42.2	
			42	Si ^g	64.7	
16		chloroform	43	Si	17.08	778
17		chloroform	44	Si	18.42	778

Table A11.3.: Continued.

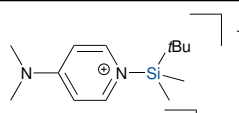
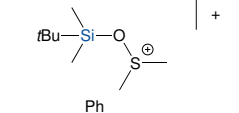
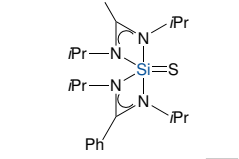
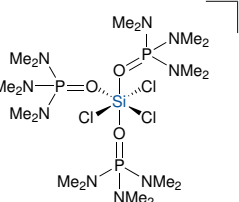
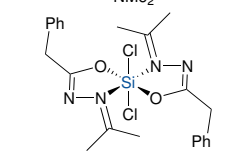
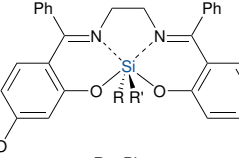
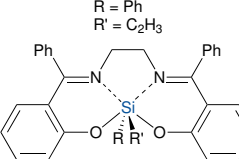
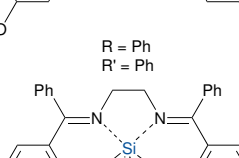
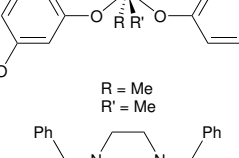
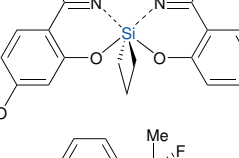
#C	Compound	Solvent	#N	Nucleus	δ_{exp} / ppm	Ref.
18		chloroform	45	Si	33.25	778
19		chloroform	46	Si	45.96	778
20		benzene	47	Si	-70.7	779
21		toluene	48	Si	-205.8	780
22		chloroform	49	Si	-163.7	780
23	 R = Ph R' = C ₂ H ₃	chloroform	50	Si	-178.1	781
24	 R = Ph R' = Ph	chloroform	51	Si	-177.6	781
25	 R = Me R' = Me	chloroform	52	Si	-165.3	781
26		chloroform	53	Si	-153.7	781
27 ¹		chloroform	54	Si	-40.82	782

Table A11.3.: Continued.

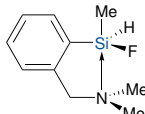
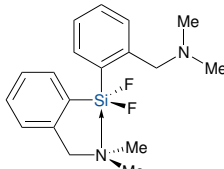
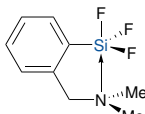
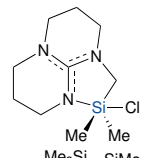
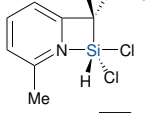
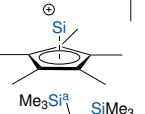
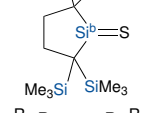

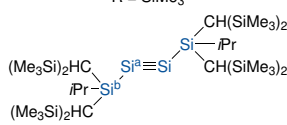
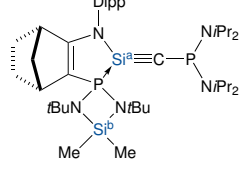
#C	Compound	Solvent	#N	Nucleus	δ_{exp} / ppm	Ref.
28 ¹		chloroform	55	Si	-36.13	782
29 ¹		chloroform	56	Si	-52.95	782
30 ¹		chloroform	57	Si	-102.27	782
31		benzene	58	Si	-49.1	780
32		benzene	59	Si	-64.82	780
33		DCM	60	Si	-400.3	783
34		benzene	61 62	Si ^a Si ^b	1 216.8	784
35		benzene	63 64	Si ^a Si ^b	157 197	785
	R = SiMe ₃					
36		benzene	65 66	Si ^a Si ^b	89.9 20.7	786
37		THF	67 68	Si ^a Si ^b	-89.5 11.5	787
	Dipp = 2,6- <i>i</i> Pr ₂ -C ₆ H ₄					

Table A11.3.: Continued.

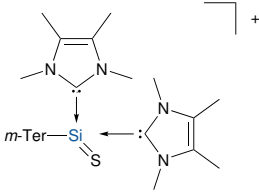
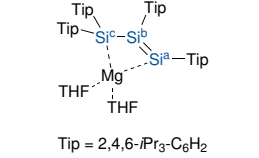
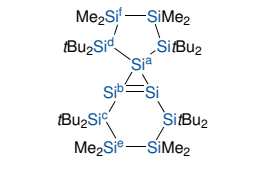
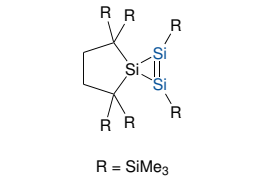
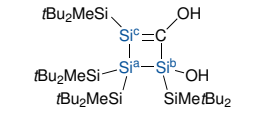
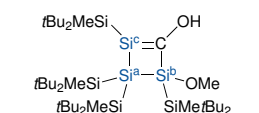
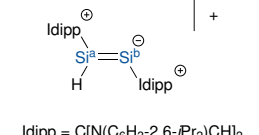
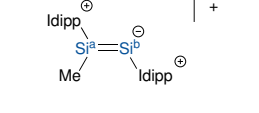
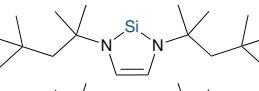
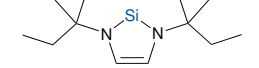
#C	Compound	Solvent	#N	Nucleus	δ_{exp} / ppm	Ref.
38	 $m\text{-Ter} = \text{C}_6\text{H}_3\text{-2,6-(C}_6\text{H}_2\text{-2,4,6-Me}_3\text{)}_2$	acetonitrile	69	Si	-36	788
39	 $\text{Tip} = 2,4,6\text{-iPr}_3\text{-C}_6\text{H}_2$	benzene	70 71 72	Si ^a Si ^b Si ^c	143.9 134.5 -44.4	789
40		benzene	73 74 75 76 77 78	Si ^a Si ^b Si ^c Si ^d Si ^e Si ^f	-85.4 147.1 15 -11.9 -31.5 -41.1	790
41	 $\text{R} = \text{SiMe}_3$	benzene	79	Si	142.9	791
42		benzene	80 81 82	Si ^a Si ^b Si ^c	-97.4 12.7 84.3	792
43		benzene	83 84 85	Si ^a Si ^b Si ^c	-95.3 21.4 90.2	792
44	 $\text{Idipp} = \text{C}[\text{N}(\text{C}_6\text{H}_3\text{-2,6-}i\text{Pr}_2\text{)}\text{CH}_2]_2$	THF	86 87	Si ^a Si ^b	69.4 125.4	793
45	 $\text{Idipp} = \text{C}[\text{N}(\text{C}_6\text{H}_3\text{-2,6-}i\text{Pr}_2\text{)}\text{CH}_2]_2$	THF	88 89	Si ^a Si ^b	102.8 115.2	793
46		benzene	90	Si	81.6	794
47		benzene	91	Si	78.2	794

Table A11.3.: Continued.

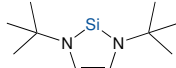
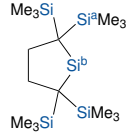
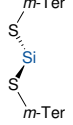
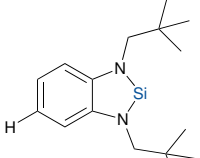
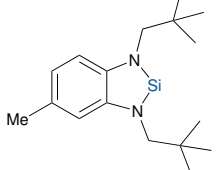
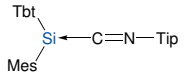
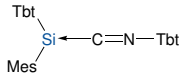
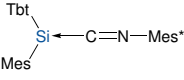
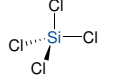
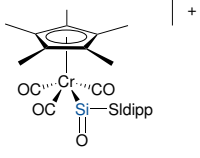
#C	Compound	Solvent	#N	Nucleus	δ_{exp} / ppm	Ref.
48 ¹		benzene	92	Si	78.3	795
49		benzene	93 94	Si ^a Si ^b	-2.8 567.4	796
50		benzene	95	Si	285.5	797
<i>m-Ter</i> = C ₆ H ₃ -2,6-(C ₆ H ₂ -2,4,6-Me ₃) ₂						
51		benzene	96	Si	96.92	798
52		benzene	97	Si	97.72	798
53 ¹		benzene	98	Si	-53.6	799
Tbt = 2,4,6-[CH(SiMe ₃) ₂] ₃ -C ₆ H ₂ Mes = 2,4,6-Me ₃ -C ₆ H ₂ Tip = 2,4,6- <i>i</i> -Pr ₃ -C ₆ H ₂						
54 ¹		benzene	99	Si	-57.4	799
Tbt = 2,4,6-[CH(SiMe ₃) ₂] ₃ -C ₆ H ₂ Mes = 2,4,6-Me ₃ -C ₆ H ₂						
55 ¹		benzene	100	Si	-48.6	799
Tbt = 2,4,6-[CH(SiMe ₃) ₂] ₃ -C ₆ H ₂ Mes = 2,4,6-Me ₃ -C ₆ H ₂ Mes* = 2,4,6- <i>t</i> Bu ₃ -C ₆ H ₂						
56		chloroform	101	Si	-18.5	778
57		chlorobenzene	102	Si	169.6	800
Sldipp = C[N(C ₆ H ₃ -2,6- <i>i</i> Pr ₂)CH ₂] ₂						

Table A11.3.: Continued.

#C	Compound	Solvent	#N	Nucleus	δ_{exp} / ppm	Ref.
58	<p>Sldipp = C[N(C₆H₃-2,6-<i>i</i>Pr₂)CH₂]₂</p>	chlorobenzene	103	Si	828.6	800
59	<p>R = Si<i>t</i>Bu₂Me</p>	THF	104	Si	-15.8	801
60	<p>R = SiMe₃</p>	benzene	105	Si	236.6	802
61	<p>Bbt = 2,6-[CH(SiMe₃)₂]-4-[C(SiMe₃)₃]-C₆H₂</p>	THF	106	Si	-16.46	803
62		benzene	107	Si	-80.8	779
63		benzene	108	Si	227.7	784
64	<p><i>m</i>-Ter = C₆H₃-2,6-(C₆H₂-2,4,6-Me₃)₂</p>	acetonitrile	109	Si	-41.5	788
65		DCM	110	Si	-173.6	804
66		benzene	111	Si	-90.8	805

Table A11.3.: Continued.

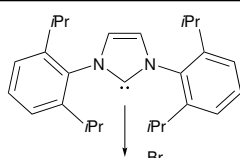
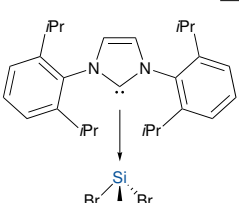
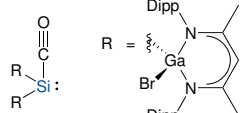
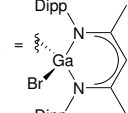
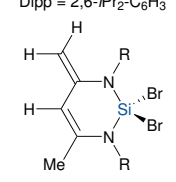
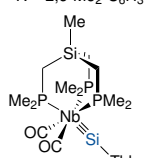
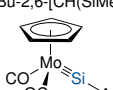
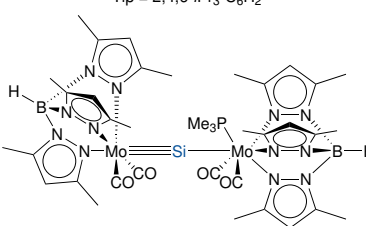
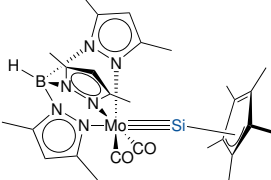
#C	Compound	Solvent	#N	Nucleus	δ_{exp} / ppm	Ref.
67		benzene	112	Si	10.9	805
68		DCM	113	Si	-63.9	805
69	 R = 	benzene	114	Si	-256.5	806
70	 Dipp = 2,6- <i>i</i> Pr ₂ -C ₆ H ₃ R = 2,6-Me ₂ -C ₆ H ₃	benzene	115	Si	-55.1	807
71	 Tbb = 4- <i>t</i> Bu-2,6-[CH(SiMe ₃) ₂] ₂ -C ₆ H ₂	benzene	116	Si	267.8	808
72	 Ar = 2,6-Tip ₂ -C ₆ H ₃ Tip = 2,4,6- <i>i</i> Pr ₃ -C ₆ H ₂	benzene	117	Si	320.1	809
73		THF	118	Si	438.9	810
74		THF	119	Si	-272.4	811

Table A11.3.: Continued.

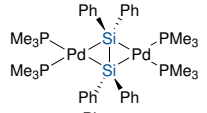
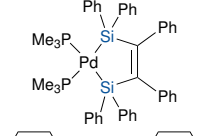
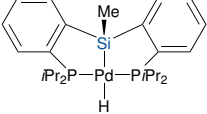
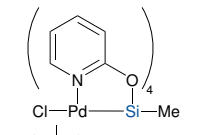
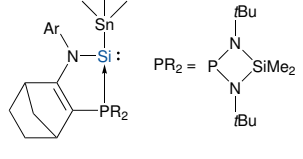
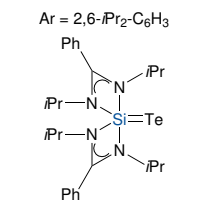
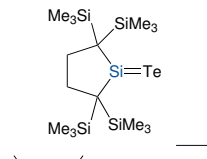
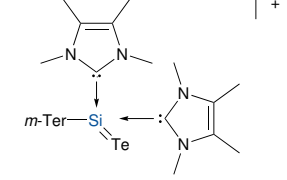
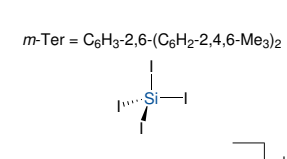
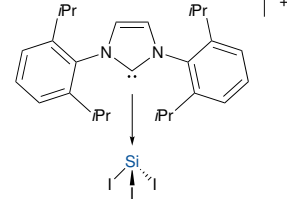
#C	Compound	Solvent	#N	Nucleus	δ_{exp} / ppm	Ref.
75		benzene	120	Si	-35.3	812
76		benzene	121	Si	34.5	812
77		benzene	122	Si	60.82	813
78		chloroform	123	Si	-116.9	814
79		THF	124	Si	-26	815
80		benzene	125	Si	-116.5	779
81		benzene	126	Si	229.5	784
82		acetonitrile	127	Si	-72.2	788
83		benzene	128	Si	-346.6	816
84		chloroform	129	Si	-225.8	816

Table A11.3.: Continued.

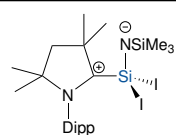
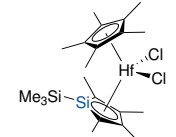
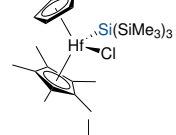
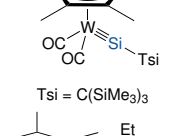
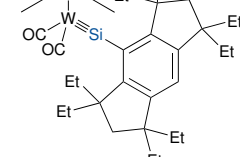
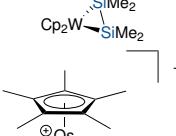
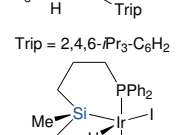
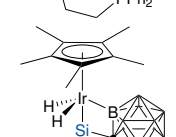
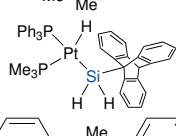
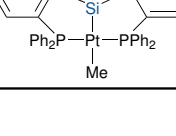

#C	Compound	Solvent	#N	Nucleus	δ_{exp} / ppm	Ref.
85	 Dipp = 2,6- <i>i</i> -Pr ₂ -C ₆ H ₃	benzene	130	Si	-180.7	817
86		benzene	131	Si	49.9	818
87		benzene	132	Si	-77.9	819
88	 Tsi = C(SiMe ₃) ₃	benzene	133	Si	339.1	820
89		toluene	134	Si	302.2	821
90		toluene	135	Si	-48.1	822
91	 Trip = 2,4,6- <i>i</i> -Pr ₃ -C ₆ H ₂	bromobenzene	136	Si	321	823
92		chloroform	137	Si	25.4	824
93		chloroform	138	Si	-31.9	825
94		THF	139	Si	-43.9	826
95		benzene	140	Si	60.5	827

Table A11.3.: Continued.

#C	Compound	Solvent	#N	Nucleus	δ_{exp} / ppm	Ref.
96		benzene	141	Si	55	828
97		benzene	142	Si	394.6	829
98		DCM	143	Si	22.8	830
99		benzene	144	Si	53.4	831
100		benzene	145 146	Si ^a Si ^b	152.5 116.8	832

R = 2,4,6-*i*Pr₃-C₆H₂

¹ The input structure for the geometry optimization was not taken from a crystallographic measurement, but created manually and preoptimized with GFN2-xTB.

² Experimental values of chemically equivalent nuclei have been averaged.

A12. Supporting Information to Chapter 13

Appendix A12 contains:

- General remarks
- Computational details
- Details on LED analysis
- LED analysis of constrained X-ray structure fragments
- Specification of statistical measures

General Remarks

All raw data, experimental details, and atomic Cartesian coordinates used or generated in this study can be obtained free of charge from the Supplementary Material of the original publication:

Bursch, M.; Kunze, L.; Vibhute, A. M.; Hansen, A.; Sureshan, K. M.; Jones, P. G.; Grimme, S.; Werz, D. B. "Quantification of Non-covalent Interactions in Azide-Pnictogen, -Chalcogen, and -Halogen Contacts", *Chem. Eur. J.* **2021**, *27*, 4627–4639.

Atomic Cartesian coordinates can furthermore be obtained online from:

<https://www.chemie.uni-bonn.de/pctc/mulliken-center/software/AZIDE>.

Computational Details

All visualizations of calculated structures, molecular electrostatic potentials or dispersion interaction densities (DID) were created with UCSF Chimera 1.10.2⁷⁶⁰. Møller-Plesset Perturbation Theory (SCS-MP2) applying the large def2-QZVPP basis set and tight convergence criteria for energies and gradients as implemented in ORCA was used for geometry optimization of dimer and monomer structures. Opposite-spin and same-spin scaling parameters were chosen to $c_{OS} = 1.1$ and $c_{SS} = 2/3$, an improvement for gas phase structure optimization³⁵. For SCS-MP2 the frozen core approximation was applied with default settings. *VeryTightPNO* settings were applied for the Local energy decomposition (LED) analyses in the DLPNO-CCSD(T) framework. Default ECP-28²⁴¹ Stuttgart-Dresden effective core potentials (ECPs) were used for all elements with atomic numbers larger than Kr ($Z = 36$) in order to take into account scalar relativistic effects. The resolution-of-identity approximation^{243,833} for Coulomb and Exchange integrals (RIJK) was generally used with matching auxiliary basis sets^{244,245,292} to speed up the SCS-MP2 calculations, while the RI approximation for Coulomb integrals (RIJ) was applied to DFT

calculations. Ro-vibrational were calculated with a modified rigid rotor harmonic oscillator statistical treatment⁵¹⁰ for $T = 25.0^\circ\text{C}$ and 1 atm pressure based on harmonic frequency calculations at the geometry optimization level. Frequencies with wave numbers below 100 cm^{-1} were treated partially as rigid rotors to avoid errors in the harmonic approximation. Final conformational free energies were calculated at the DLPNO-CCSD(T)/CBS//SCS-MP2/def2-TZVPP level with *VeryTightPNO* settings for the lowest re-ranked conformers in a 2 kcal mol^{-1} range.

Gas-phase Gibbs free energies were obtained by summing the gas phase single point energy E , the dispersion correction $E_{disp,D4}$, and the ro-vibrational correction G_{RRHO} (Eq. A12.1).

$$G_{tot} = E + E_{disp,D4} + G_{RRHO} \quad (\text{A12.1})$$

Local Energy Decomposition

Local Energy Decomposition analysis within the DLPNO-CCSD(T) framework is applied using the following partitioning of contributions (contributions in brackets are added):

$$E_{int} = E_{HF-elprep} + E_{elstat} + E_{exch} + E_{C,elprep} + E_{CT,XY}^{C-SP} + E_{CT,YX}^{C-SP} + E_{disp}^{C-SP} + E^{C-WP} + E^{(T)} \quad (\text{A12.2})$$

$$= E_{0,HF-elprep} + E_{0,elstat} + E_{0,exch} + \left(E_{HF-elprep}^{orb-relax} + E_{elstat}^{orb-relax} + E_{exch}^{orb-relax} \right) + \left(E_{C,elprep} + E_{CT,XY}^{C-SP} + E_{CT,YX}^{C-SP} + E_{non-disp}^{(T)} \right) + \left(E_{disp}^{C-SP} + E^{C-WP} + E_{disp}^{(T)} \right) \quad (\text{A12.2a})$$

$$= E_{0,HF-elprep} + E_{0,elstat} + E_{0,exch} + E_{orb-relax} + E_{non-disp} + E_{disp} \quad (\text{A12.2b})$$

Equation A12.2 shows the standard LED partitioning, in Eq. A12.2a all HF contributions ($E_{HF-elprep}$, E_{elstat} , E_{exch}) are split into frozen contributions, denoted by a "0", and orbital relaxation contributions, according to ref. 741. Furthermore, the $E^{(T)}$ triples correction is partitioned into dispersive and non-dispersive triples corrections, according to ref. 740. Equation A12.2b represents the partitioning applied in this work.

LED Analysis of Constrained X-ray Structure Fragments

Table A12.1.: LED analysis on intermolecular model systems for X-ray structures **A** and **B** at DLPNO-CCSD(T)/def2-QZVPP//SCS-MP2/def2-QZVPP level, the descriptor (X,Y) indicates if the fragments (PCH and azide moiety) were saturated with hydrogen or methyl substituents. **B(Me-rep.)** is a methane dimer obtained by constrained optimization of hydrogen-saturated methyl groups from system **B(Me,Me)** and gives an estimate of the methyl group repulsion, all values in kcal mol⁻¹.

	A(H,Me)	B(Me,Me)	B(Me-rep.)	B(Me,Me)-B(Me-rep.)	B(H,Me)
$E_{0,HF-elprep}$	20.941	28.754	12.040	16.714	20.999
$E_{0,elstat}$	-11.969	-16.398	-5.901	-10.497	-13.008
$E_{0,exch}$	-4.269	-5.053	-2.550	-2.503	-3.610
$E_{orb-relax}$	-1.092	-1.897	-0.391	-1.507	-1.312
E_{disp}	-5.036	-5.467	-1.929	-3.538	-4.239
$E_{non-disp}$	-0.363	-0.286	-0.292	0.006	-0.016
E_{int}	-1.787	-0.347	0.977	-1.325	-1.186

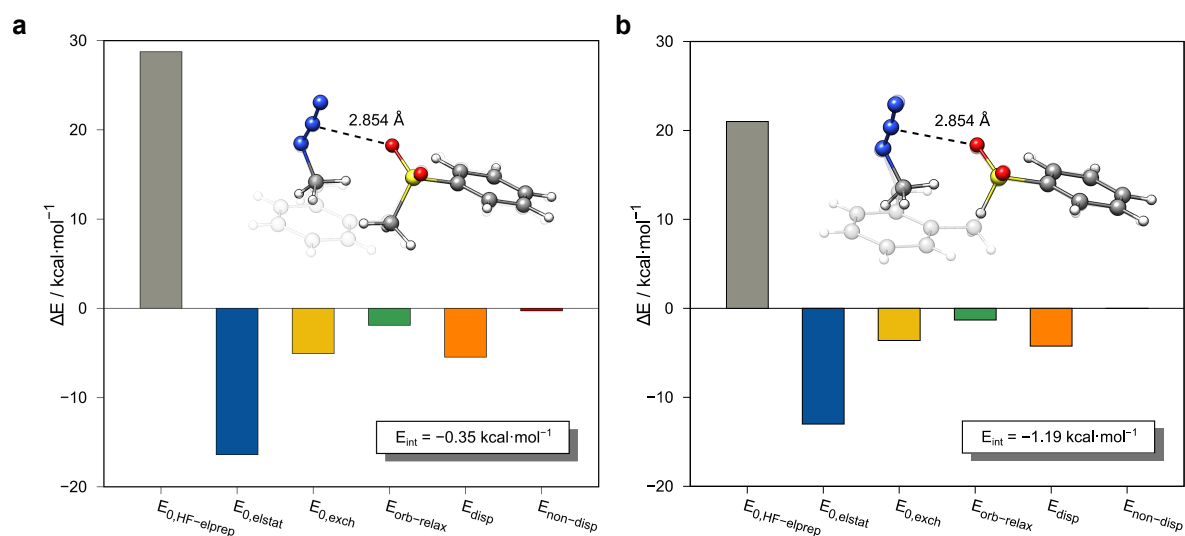


Figure A12.1.: LED analysis on intermolecular model systems a) **B(Me,Me)** and b) **B(H,Me)** at the DLPNO-CCSD(T)/def2-QZVPP//SCS-MP2/def2-QZVPP level. The corresponding X-ray structures are depicted transparently.

Statistical Measures

Statistical measure for a set x_1, \dots, x_n of data points with references r_1, \dots, r_n are :

- Mean deviation (MD):

$$MD = \frac{1}{n} \sum_i^n (x_i - r_i) \quad (\text{A12.3})$$

- Mean absolute deviation (MAD):

$$MAD = \frac{1}{n} \sum_i^n (|x_i - r_i|) \quad (\text{A12.4})$$

- Standard deviation (SD):

$$SD = \sqrt{\frac{1}{n-1} \sum_{i=1}^n ((x_i - r_i) - MD)^2} \quad (\text{A12.5})$$

- Absolute maximum deviation (AMAX):

$$AMAX = \max\{|x_i - r_i|\} \quad (\text{A12.6})$$

Bibliography

- [1] Cavalleri, M. *Int. J. Quantum Chem.* **2013**, *113*, 1–1.
- [2] Thiel, W. *Angew. Chem. Int. Ed.* **2011**, *50*, 9216–9217.
- [3] Poree, C.; Schoenebeck, F. *Acc. Chem. Res.* **2017**, *50*, 605–608.
- [4] Grimme, S.; Schreiner, P. R. *Angew. Chem. Int. Ed.* **2018**, *57*, 4170–4176.
- [5] McArdle, S.; Endo, S.; Aspuru-Guzik, A.; Benjamin, S. C.; Yuan, X. *Rev. Mod. Phys.* **2020**, *92*, 015003.
- [6] Krylov, A.; Windus, T. L.; Barnes, T.; Marin-Rimoldi, E.; Nash, J. A.; Pritchard, B.; Smith, D. G.; Altarawy, D.; Saxe, P.; Clementi, C.; Crawford, T. D.; Harrison, R. J.; Jha, S.; Pande, V. S.; Head-Gordon, T. *J. Chem. Phys.* **2018**, *149*, 180901.
- [7] Breslow, R.; Tirrell, M. V.; Barton, J. K.; Barteau, M. A.; Bertozzi, C. R.; Brown, R. A.; Gast, A. P. et al. *Beyond the Molecular Frontier, Challenges for Chemistry and Chemical Engineering*; National Academies Press: Washington (DC), **2003**.
- [8] *Challenges and Advances in Computational Chemistry and Physics*; Springer, **2006–2021**, Vol. 1–28.
- [9] Young, D. *Computational Chemistry: A Practical Guide for Applying Techniques to Real World Problems*; John Wiley & Sons, Inc.: New York (NY), **2001**.
- [10] Linder, M. *Comput. Struct. Biotechnol. J.* **2012**, *2*, e201209009.
- [11] Lin, X.; Li, X.; Lin, X. *Molecules* **2020**, *25*, 1375.
- [12] Houk, K. N.; Liu, F. *Acc. Chem. Res.* **2017**, *50*, 539–543.
- [13] *Handbook of Computational Chemistry* (Eds. Leszczynski, J.; Kaczmarek-Kedziera, A.; Puzyn, T.; Papadopoulos, M.; Reis, H. K.; Shukla, M. K.); Springer, **2017**.
- [14] Ahn, S.; Hong, M.; Sundararajan, M.; Ess, D. H.; Baik, M. H. *Chem. Rev.* **2019**, *119*, 6509–6560.
- [15] Durand, D. J.; Fey, N. *Chem.* **2019**, *119*, 6561–6594.
- [16] Freeze, J. G.; Kelly, H. R.; Batista, V. S. *Chem. Rev.* **2019**, *119*, 6595–6612.
- [17] Nørskov, J. K.; Bligaard, T.; Rossmeisl, J.; Christensen, C. H. *Nat. Chem.* **2009**, *1*, 37–46.
- [18] Shi, H.; Zhou, T. *Front. Chem. Sci. Eng.* **2021**, *15*, 49–59.
- [19] Varghese, J. J. *Curr. Opin. Chem. Eng.* **2019**, *26*, 20–27.
- [20] Greeley, J. *Annu. Rev. Chem. Biomol. Eng.* **2016**, *7*, 605–635.

Bibliography

- [21] Chen, B. W.; Xu, L.; Mavrikakis, M. *Chem. Rev.* **2021**,
- [22] Sliwoski, G.; Kothiwale, S.; Meiler, J.; Lowe, E. W. *Pharmacol. Rev.* **2014**, *66*, 334–395.
- [23] Vaissier Welborn, V.; Head-Gordon, T. *Chem. Rev.* **2019**, *119*, 6613–6630.
- [24] Hafner, J.; Wolverton, C.; Ceder, G. *MRS Bulletin* **2006**, *31*, 659–665.
- [25] Rogl, P.; Podloucky, R.; Wolf, W. *J. Phase Equilibria Diffus.* **2014**, *35*, 221–222.
- [26] Rankin, D. W. H.; Mitzel, N.; Morrison, C. *Structural Methods in Molecular Inorganic Chemistry*; Wiley, **2013**.
- [27] Schlegel, H. B. *Wiley Interdiscip. Rev. Comput. Mol. Sci.* **2011**, *1*, 790–809.
- [28] Jensen, F. *Introduction to Computational Chemistry*; Wiley, **2007**, Vol. 2.
- [29] Szabo, A.; Ostlund, N. S. *Modern Quantum Chemistry*; Dover Publications, **1996**.
- [30] Elschenbroich, C. *Organometallics*; Springer Vieweg, **2008**.
- [31] Grimme, S.; Hansen, A.; Brandenburg, J. G.; Bannwarth, C. *Chem. Rev.* **2016**, *116*, 5105–5154.
- [32] Liptrot, D. J.; Power, P. P. *Nat. Rev. Chem.* **2017**, *1*, 1–12.
- [33] Bursch, M.; Caldeweyher, E.; Hansen, A.; Neugebauer, H.; Ehlert, S.; Grimme, S. *Acc. Chem. Res.* **2019**, *52*, 258–266.
- [34] Goerigk, L.; Hansen, A.; Bauer, C.; Ehrlich, S.; Najibi, A.; Grimme, S. *Phys. Chem. Chem. Phys.* **2017**, *19*, 32184–32215.
- [35] Risthaus, T.; Steinmetz, M.; Grimme, S. *J. Comput. Chem.* **2014**, *35*, 1509–1516.
- [36] Řezáč, J. *J. Chem. Theory Comput.* **2020**, *16*, 2355–2368.
- [37] Salomon-Ferrer, R.; Case, D. A.; Walker, R. C. *Wiley Interdiscip. Rev. Comput. Mol. Sci.* **2013**, *3*, 198–210.
- [38] Brooks, B. R. et al. *J. Comput. Chem.* **2009**, *30*, 1545–1614.
- [39] Jorgensen, W. L.; Tirado-Rives, J. *J. Am. Chem. Soc.* **1988**, *110*, 1657–1666.
- [40] Rappe, A. K.; Casewit, C. J.; Colwell, K. S.; Goddard, W. A.; Skiff, W. M. *J. Am. Chem. Soc.* **1992**, *114*, 10024–10035.
- [41] Shi, S.; Yan, L.; Yang, Y.; Fisher-Shaulsky, J.; Thacher, T. *J. Comput. Chem.* **2003**, *24*, 1059–1076.
- [42] Allured, V. S.; Kelly, C. M.; Landis, C. R. *J. Am. Chem. Soc.* **1991**, *113*, 1–12.
- [43] Addicoat, M. A.; Vankova, N.; Akter, I. F.; Heine, T. *J. Chem. Theory Comput.* **2014**, *10*, 880–891.
- [44] Comba, P.; Daubinet, A.; Martin, B.; Pietzsch, H.-J.; Stephan, H. *J. Organomet. Chem.* **2006**, *691*, 2495–2502.
- [45] Christensen, A. S.; Kubař, T.; Cui, Q.; Elstner, M. *Chem. Rev.* **2016**, *116*, 5301–5337.
- [46] Thiel, W. *Wiley Interdiscip. Rev. Comput. Mol. Sci.* **2014**, *4*, 145–157.

- [47] Bredow, T.; Jug, K. *MSINDO*, in *Encyclopedia of Computational Chemistry* (Eds. Ragué Schleyer, P.; Allinger, N. L.; Clark, T.; Gasteiger, J.; Kollman, P. A.; Schaefer, H. F.; Schreiner, P. R.; Thiel, W.; Jorgensen, W. L.; Glen, R. C.); Wiley, **2004**.
- [48] Bredow, T.; Geudtner, G.; Jug, K. *J. Comput. Chem.* **2001**, *22*, 861–887.
- [49] Husch, T.; Vaucher, A. C.; Reiher, M. *Int. J. Quantum Chem.* **2018**, *118*, e25799.
- [50] Stewart, J. J. P. *J. Comput. Chem.* **1989**, *10*, 209–220.
- [51] Stewart, J. J. P. *J. Mol. Model.* **2007**, *13*, 1173.
- [52] Stewart, J. J. P. *J. Mol. Model.* **2013**, *19*, 1–32.
- [53] Grimme, S.; Bannwarth, C.; Shushkov, P. *J. Chem. Theory Comput.* **2017**, *13*, 1989–2009.
- [54] Bannwarth, C.; Ehlert, S.; Grimme, S. *J. Chem. Theory Comput.* **2019**, *15*, 1652–1671.
- [55] Pracht, P.; Caldeweyher, E.; Ehlert, E.; Grimme, S. *A Robust Non-Self-Consistent Tight-Binding Quantum Chemistry Method for Large Molecules*, **2019**, ChemRxiv, DOI: 10.26434/chemrxiv.8326202.v1.
- [56] Spicher, S.; Grimme, S. *Angew. Chem. Int. Ed.* **2020**, *59*, 15665–15673.
- [57] Bannwarth, C.; Caldeweyher, E.; Ehlert, S.; Hansen, A.; Pracht, P.; Seibert, J.; Spicher, S.; Grimme, S. *Wiley Interdiscip. Rev. Comput. Mol. Sci.* **2020**, e01493.
- [58] Grimme, S. *J. Comput. Chem.* **2016**, *27*, 1787–1799.
- [59] Grimme, S.; Antony, J.; Ehrlich, S.; Krieg, H. *J. Chem. Phys.* **2010**, *132*.
- [60] Caldeweyher, E.; Brandenburg, J. G. *J. Phys. Condens. Matter* **2018**, *30*, 213001.
- [61] Grimme, S.; Bannwarth, C.; Dohm, S.; Hansen, A.; Pisarek, J.; Pracht, P.; Seibert, J.; Neese, F. *Angew. Chem. Int. Ed.* **2017**, *56*, 14763–14769.
- [62] Seibert, J.; Bannwarth, C.; Grimme, S. *J. Am. Chem. Soc.* **2017**, *139*, 11682–11685.
- [63] Bannwarth, C. N. *Development and Application of Efficient Methods for the Computation of Electronic Spectra of Large Systems*, Dissertation, Universität Bonn, **2018**.
- [64] Pracht, P.; Bohle, F.; Grimme, S. *Phys. Chem. Chem. Phys.* **2020**, *22*, 7169–7192.
- [65] Stephan, D. W. *Org. Biomol. Chem.* **2008**, *6*, 1535–1539.
- [66] Stephan, D. W. *J. Chem. Soc., Dalton Trans.* **2009**, 3129–3136.
- [67] Stephan, D. W.; Erker, G. *Angew. Chem. Int. Ed.* **2015**, *54*, 6400–6441.
- [68] Stephan, D. W.; Erker, G. *Angew. Chem. Int. Ed.* **2010**, *49*, 46–76.
- [69] Grimme, S.; Brandenburg, J. G.; Bannwarth, C.; Hansen, A. *J. Chem. Phys.* **2015**, *143*, 054107.
- [70] Schrödinger, E. *Ann. Phys.* **1926**, *384*, 361–376.
- [71] Helgaker, T.; Jørgensen, P.; Olsen, J. *Molecular Electronic-Structure Theory*; J. Wiley: New York, **2000**.

Bibliography

- [72] Born, M.; Oppenheimer, R. *Ann. Phys.* **1927**, *389*, 457–484.
- [73] Slater, J. C. *Phys. Rev.* **1929**, *34*, 1293–1322.
- [74] Hartree, D. R. *Math. Proc. Camb. Philos. Soc.* **1928**, *24*, 89–110.
- [75] Fock, V. Z. *Phys.* **1930**, *61*, 126–148.
- [76] Pauli, W. Z. *Phys.* **1925**, *31*, 765–783.
- [77] Roothaan, C. C. *Rev. Mod. Phys.* **1951**, *23*, 69–89.
- [78] Hall, G. G. *Proc. R. Soc. Lond.* **1951**, *205*, 541–552.
- [79] Bartlett, R. J. *Annu. Rev. Phys. Chem.* **1981**, *32*, 359–401.
- [80] Bartlett, R. J.; Musiał, M. *Rev. Mod. Phys.* **2007**, *79*, 291–352.
- [81] Bartlett, R. J. *How and Why Coupled-Cluster Theory Became the Pre-eminent Method in ab initio Quantum Chemistry*, in *Theory and Applications of Computational Chemistry: The First Fifty Years*; Elsevier, **2005**.
- [82] Guo, Y.; Riplinger, C.; Becker, U.; Liakos, D. G.; Minenkov, Y.; Cavallo, L.; Neese, F. *J. Chem. Phys.* **2018**, *148*, 011101.
- [83] Riplinger, C.; Sandhoefer, B.; Hansen, A.; Neese, F. *J. Chem. Phys.* **2013**, *139*, 134101.
- [84] Riplinger, C.; Pinski, P.; Becker, U.; Valeev, E. F.; Neese, F. *J. Chem. Phys.* **2016**, *144*, 024109.
- [85] Møller, C.; Plesset, M. S. *Phys. Rev.* **1934**, *46*, 618–622.
- [86] Thomas, L. H. *Math. Proc. Camb. Philos. Soc.* **2008**, *23*, 542–548.
- [87] Fermi, E. Z. *Phys.* **1928**, *48*, 73–79.
- [88] Hohenberg, P.; Kohn, W. *Phys. Rev.* **1964**, *136*, B864.
- [89] Parr, R. G.; Yang, W. *Density-Functional Theory of Atoms and Molecules*; Oxford University Press, **1989**.
- [90] Koch, W.; Holthausen, M. C. *A Chemists Guide to Density Functional Theory*; Wiley, **2001**.
- [91] Kohn, W.; Sham, L. J. *Phys. Rev.* **1965**, *140*, A1133.
- [92] Ziegler, T. *Chem. Rev.* **1991**, *91*, 651–667.
- [93] Perdew, J. P.; Schmidt, K. *AIP Conf. Proc.* **2001**, *577*, 1–20.
- [94] Becke, A. D. *J. Chem. Phys.* **2014**, *140*, 18–301.
- [95] Becke, A. D. *J. Chem. Phys.* **1993**, *98*, 1372–1377.
- [96] Peverati, R.; Truhlar, D. G. *J. Chem. Theory Comput.* **2012**, *8*, 2310–2319.
- [97] Dirac, P. A. *Math. Proc. Camb. Philos. Soc.* **1930**, *26*, 376–385.
- [98] Slater, J. C. *Phys. Rev.* **1951**, *81*, 385–390.

- [99] Sousa, S. F.; Fernandes, P. A.; Ramos, M. J. *J. Phys. Chem. A* **2007**, *111*, 10439–10452.
- [100] Brémond, É.; Savarese, M.; Pérez-Jiménez, Á. J.; Sancho-García, J. C.; Adamo, C. *J. Phys. Chem. Lett.* **2015**, *6*, 3540–3545.
- [101] Brémond, É.; Savarese, M.; Su, N. Q.; Pérez-Jiménez, Á. J.; Xu, X.; Sancho-García, J. C.; Adamo, C. *J. Chem. Theory Comput.* **2016**, *12*, 459–465.
- [102] Yu, H. S.; Li, S. L.; Truhlar, D. G. *J. Chem. Phys.* **2016**, *145*, 130901.
- [103] Brémond, É.; Pérez-Jiménez, Á. J.; Sancho-García, J. C.; Adamo, C. *J. Chem. Phys.* **2019**, *150*, 201102.
- [104] Leininger, T.; Stoll, H.; Werner, H. J.; Savin, A. *Chem. Phys. Lett.* **1997**, *275*, 151–160.
- [105] Iikura, H.; Tsuneda, T.; Yanai, T.; Hirao, K. *J. Chem. Phys.* **2001**, *115*, 3540–3544.
- [106] Chai, J.-D.; Head-Gordon, M. *J. Chem. Phys.* **2008**, *128*, 084106.
- [107] Chai, J.-D.; Head-Gordon, M. *Phys. Chem. Chem. Phys.* **2008**, *10*, 6615–6620.
- [108] Eshuis, H.; Bates, J. E.; Furche, F. *Theor. Chem. Acc.* **2012**, *131*, 1–18.
- [109] Zhao, Y.; Lynch, B. J.; Truhlar, D. G. *J. Phys. Chem. A* **2004**, *108*, 4786–4791.
- [110] Grimme, S. *J. Chem. Phys.* **2006**, *124*, 034108.
- [111] Grimme, S. *J. Chem. Phys.* **2003**, *118*, 9095–9102.
- [112] Dohm, S.; Hansen, A.; Steinmetz, M.; Grimme, S.; Chęcinski, M. P. *J. Chem. Theory Comput.* **2018**, *14*, 2596–2608.
- [113] Eisenschitz, R.; London, F. *Z. Phys.* **1930**, *60*, 491–527.
- [114] London, F. *Z. Phys.* **1930**, *63*, 245–279.
- [115] Caldeweyher, E.; Bannwarth, C.; Grimme, S. *J. Chem. Phys.* **2017**, *147*, 034112.
- [116] Caldeweyher, E.; Ehlert, S.; Hansen, A.; Neugebauer, H.; Spicher, S.; Bannwarth, C.; Grimme, S. *J. Chem. Phys.* **2019**, *150*, 154122.
- [117] Grimme, S. *J. Comput. Chem.* **2004**, *25*, 1463–1473.
- [118] Pyykkö, P.; Atsumi, M. *Chem. Eur. J.* **2009**, *15*, 186–197.
- [119] Casimir, H. B.; Polder, D. *Phys. Rev.* **1948**, *73*, 360–372.
- [120] Starkschall, G.; Gordon, R. G. *J. Chem. Phys.* **1972**, *56*, 2807–2813.
- [121] Grimme, S.; Ehrlich, S.; Goerigk, L. *J. Comput. Chem.* **2011**, *32*, 1456–1465.
- [122] Becke, A. D.; Johnson, E. R. *J. Chem. Phys.* **2005**, *123*, 154101.
- [123] Johnson, E. R.; Becke, A. D. *J. Chem. Phys.* **2005**, *123*, 024101.
- [124] Axilrod, B. M.; Teller, E. *J. Chem. Phys.* **1943**, *11*, 299–300.

Bibliography

- [125] Muto, Y. *Proc. Phys. Math. Soc. Jpn.* **1943**, *17*, 629–631.
- [126] Ghasemi, S. A.; Hofstetter, A.; Saha, S.; Goedecker, S. *Phys. Rev. B* **2015**, *92*, 045131.
- [127] Sure, R.; Grimme, S. *J. Comput. Chem.* **2013**, *34*, 1672–1685.
- [128] Cutini, M.; Civalleri, B.; Corno, M.; Orlando, R.; Brandenburg, J. G.; Maschio, L.; Ugliengo, P. *J. Chem. Theory Comput.* **2016**, *12*, 3340–3352.
- [129] Brandenburg, J. G.; Bannwarth, C.; Hansen, A.; Grimme, S. *J. Chem. Phys.* **2018**, *148*, 064104.
- [130] Grimme, S.; Hansen, A.; Ehlert, S.; Mewes, J.-M. *J. Chem. Phys.* **2021**, *154*, 064103.
- [131] Kruse, H.; Grimme, S. *J. Chem. Phys.* **2012**, *136*, 154101.
- [132] Brandenburg, J. G.; Alessio, M.; Civalleri, B.; Peintinger, M. F.; Bredow, T.; Grimme, S. *J. Phys. Chem. A* **2013**, *117*, 9282–9292.
- [133] Elstner, M.; Seifert, G. *Philos. Trans. R. Soc. A* **2014**, *372*, 20120483.
- [134] Porezag, D.; Frauenheim, T.; Köhler, T.; Seifert, G.; Kaschner, R. *Phys. Rev. B* **1995**, *51*, 12947–12957.
- [135] Aradi, B.; Hourahine, B.; Frauenheim, T. *J. Phys. Chem. A* **2007**, *111*, 5678–5684.
- [136] Seifert, G.; Porezag, D.; Frauenheim, T. *Int. J. Quantum Chem.* **1996**, *58*, 185–192.
- [137] Elstner, M.; Porezag, D.; Jungnickel, G.; Elsner, J.; Haugk, M.; Frauenheim, T.; Suhai, S.; Seifert, G. *Phys. Rev. B* **1998**, *58*, 7260–7268.
- [138] Gaus, M.; Cui, Q.; Elstner, M. *J. Chem. Theory Comput.* **2011**, *7*, 931–948.
- [139] Hourahine, B. et al. *J. Chem. Phys.* **2020**, *152*, 124101.
- [140] Mulliken, R. S. *J. Chem. Phys.* **1955**, *23*, 1833–1840.
- [141] Hubbard, J. *Proc. R. Soc. Lond.* **1963**, *276*, 238–257.
- [142] Mermin, N. D. *Phys. Rev.* **1965**, *137*, A1441.
- [143] Hülsen, M.; Weigand, A.; Dolg, M. *Theor. Chem. Acc.* **2009**, *122*, 23–29.
- [144] Koester, A. M.; Leboeuf, M.; Salahub, D. R. In *Molecular Electrostatic Potentials: Concepts and Applications* (Eds. Murray, J. S., Sen, K.); Elsevier, **1996**, Vol. 3, pp. 105–142.
- [145] *CRC Handbook of Chemistry and Physics* (Ed. Haynes, W. M.); CRC Press, **2016**, 97th Ed.
- [146] Dewar, M. J.; Zoebisch, E. G.; Healy, E. F.; Stewart, J. J. *J. Am. Chem. Soc.* **1985**, *107*, 3902–3909.
- [147] Kolb, M.; Thiel, W. *J. Comput. Chem.* **1993**, *14*, 775–789.
- [148] Weber, W.; Thiel, W. *Theor. Chem. Acc.* **2000**, *103*, 495–506.
- [149] Dral, P. O.; Wu, X.; Spörkel, L.; Koslowski, A.; Weber, W.; Steiger, R.; Scholten, M.; Thiel, W. *J. Chem. Theory Comput.* **2016**, *12*, 1082–1096.

- [150] Rocha, G. B.; Freire, R. O.; Simas, A. M.; Stewart, J. J. P. *J. Comput. Chem.* **2006**, *27*, 1101–1111.
- [151] Bosque, R.; Maseras, F. *J. Comput. Chem.* **2000**, *21*, 562–571.
- [152] Řezáč, J.; Hobza, P. *J. Chem. Theory Comput.* **2012**, *8*, 141–151.
- [153] S. Brahmkshatriya, P.; Dobeš, P.; Fanfrlík, J.; Řezáč, J.; Paruch, K.; Bronowska, A.; Lepšík, M.; Hobza, P. *Curr. Comput.-Aid. Drug.* **2013**, *9*, 118–129.
- [154] Spiegelman, F.; Tarrat, N.; Cuny, J.; Dontot, L.; Posenitskiy, E.; Martí, C.; Simon, A.; Rapacioli, M. *Adv. Phys. X* **2020**, *5*, 1710252.
- [155] Ho, C. L.; Wong, W. Y. *Coord. Chem. Rev.* **2011**, *255*, 2469–2502.
- [156] Warra, A. A. *J. Chem. Pharm. Res.* **2011**, *3*, 951–958.
- [157] Beaumier, E. P.; Pearce, A. J.; See, X. Y.; Tonks, I. A. *Nat. Rev. Chem.* **2019**, *3*, 15–34.
- [158] Kletzin, A.; Adams, M. W. *FEMS Microbiol. Rev.* **2006**, *18*, 5–63.
- [159] Williams, R. J. P. *Eur. J. Biochem.* **1985**, *150*, 231–248.
- [160] Vardhan, H.; Verpoort, F. *Adv. Synth. Catal.* **2015**, *357*, 1351–1368.
- [161] Liang, K.; Ricco, R.; Doherty, C. M.; Styles, M. J.; Bell, S.; Kirby, N.; Mudie, S.; Haylock, D.; Hill, A. J.; Doonan, C. J.; Falcaro, P. *Nat. Commun.* **2015**, *6*, 7240.
- [162] Gandeepan, P.; Müller, T.; Zell, D.; Cera, G.; Warratz, S.; Ackermann, L. *Chem. Rev.* **2019**, *119*, 2192–2452.
- [163] Vogiatzis, K. D.; Polynski, M. V.; Kirkland, J. K.; Townsend, J.; Hashemi, A.; Liu, C.; Pidko, E. A. *Chem. Rev.* **2019**, *119*, 2453–2523.
- [164] Selvaganapathy, M.; Raman, N. *J. Chem. Biol. Ther.* **2016**, *01*, 1–17.
- [165] Malinowski, J.; Zych, D.; Jacewicz, D.; Gawdzik, B.; Drzeżdżon, J. *Int. J. Mol. Sci.* **2020**, *21*, 5443.
- [166] Cotruvo, J. A. *ACS Central Sci.* **2019**, *5*, 1496–1506.
- [167] Featherston, E. R.; Cotruvo, J. A. *Biochim. Biophys. Acta Mol. Cell. Res.* **2021**, *1868*, 118864.
- [168] De Sá, G. F.; Malta, O. L.; De Mello Donegá, C.; Simas, A. M.; Longo, R. L.; Santa-Cruz, P. A.; Da Silva, E. F. *Coord. Chem. Rev.* **2000**, *196*, 165–195.
- [169] Selvin, P. R. *Annu. Rev. Biophys. Biomol. Struct.* **2002**, *31*, 275–302.
- [170] Edelmann, F. T.; Farnaby, J. H.; Jaroschik, F.; Wilson, B. *Coord. Chem. Rev.* **2019**, *398*, 113005.
- [171] Levason, W. *Coord. Chem. Rev.* **2017**, *340*, 1.
- [172] Bünzli, J. C. G. *J. Coord. Chem.* **2014**, *67*, 3706–3733.
- [173] Armelao, L.; Quici, S.; Barigelletti, F.; Accorsi, G.; Bottaro, G.; Cavazzini, M.; Tondello, E. *Coord. Chem. Rev.* **2010**, *254*, 487–505.
- [174] Mader, H. S.; Kele, P.; Saleh, S. M.; Wolfbeis, O. S. *Curr. Opin. Chem. Biol.* **2010**, *14*, 582–596.

Bibliography

- [175] Rocha, J.; Carlos, L. D.; Paz, F. A. A.; Ananias, D.; Perruchas, S.; Sanchez, C.; Férey, G.; Zhu, G.; Zhou, X.; Calvez, G. *Chem. Soc. Rev.* **2011**, *40*, 926–940.
- [176] Cui, Y.; Yue, Y.; Qian, G.; Chen, B. *Chem. Rev.* **2012**, *112*, 1126–1162.
- [177] Almeida Paz, F. A.; Klinowski, J.; Vilela, S. M. F.; Tomé, J. P. C.; Cavaleiro, J. A. S.; Rocha, J.; Nolte, R. J. M.; Sun, X. Z.; Das, M. C.; Gill, R.; Thomas, K. M.; Chen, B. L. *Chem. Soc. Rev.* **2012**, *41*, 1088–1110.
- [178] Trinadhachari, G. N.; Kamat, A. G.; Prabahar, K. J.; Handa, V. K.; Srinu, K. N. V. S.; Babu, K. R.; Sanasi, P. D. *Org. Process Res. Dev.* **2013**, *17*, 406–412.
- [179] de Andrade, A. V.; da Costa, N. B.; Simas, A. M.; de Sá, G. F. *Chem. Phys. Lett.* **1994**, *227*, 349–353.
- [180] de Andrade, A. V.; da Costa, N. B.; Simas, A. M.; de Sá, G. F. *J. Alloys Compd.* **1995**, *225*, 55–59.
- [181] Rocha, G. B.; Freire, R. O.; Da Costa, N. B.; De Sá, G. F.; Simas, A. M. *Inorg. Chem.* **2004**, *43*, 2346–2354.
- [182] Winget, P.; Horn, A. H. C.; Selçuki, C.; Martin, B.; Clark, T. *J. Mol. Model.* **2003**, *9*, 408–414.
- [183] Freire, R. O.; Rocha, G. B.; Simas, A. M. *Inorg. Chem.* **2005**, *44*, 3299–3310.
- [184] Freire, R. O.; da Costa, N. B.; Rocha, G. B.; Simas, A. M. *J. Organomet. Chem.* **2005**, *690*, 4099–4102.
- [185] Freire, R. O.; Rocha, G. B.; Simas, A. M. *Chem. Phys. Lett.* **2005**, *411*, 61–65.
- [186] da Costa, N. B.; Freire, R. O.; Rocha, G. B.; Simas, A. M. *Polyhedron* **2005**, *24*, 3046–3051.
- [187] da Costa, N. B.; Freire, R. O.; Rocha, G. B.; Simas, A. M. *Inorg. Chem. Commun.* **2005**, *8*, 831–835.
- [188] Freire, R. O.; Da Costa, N. B.; Rocha, G. B.; Simas, A. M. *J. Chem. Theory Comput.* **2006**, *2*, 64–74.
- [189] Bastos, C. C.; Freire, R. O.; Rocha, G. B.; Simas, A. M. *J. Photochem. Photobiol. A* **2006**, *177*, 225–237.
- [190] Freire, R. O.; do Monte, E. V.; Rocha, G. B.; Simas, A. M. *J. Organomet. Chem.* **2006**, *691*, 2584–2588.
- [191] Freire, R. O.; Da Costa, N. B.; Rocha, G. B.; Simas, A. M. *J. Phys. Chem. A* **2006**, *110*, 5897–5900.
- [192] Freire, R. O.; Rocha, G. B.; Simas, A. M. *Chem. Phys. Lett.* **2006**, *425*, 138–141.
- [193] Freire, R. O.; Rocha, G. B.; Simas, A. M. *Chem. Phys. Lett.* **2007**, *441*, 354–357.
- [194] Da Costa, N. B.; Freire, R. O.; Simas, A. M.; Rocha, G. B. *J. Phys. Chem. A* **2007**, *111*, 5015–5018.
- [195] Simas, A.M.; Freire, R.O.; Rocha, G.B. *Cerium (III) Complexes Modeling with Sparkle/PM3*, in *ICCS 2007, Lecture Notes in Computer Science* (Eds. Shi, Y.; van Albada, G.D.; Dongarra, J.; Sloot, P. M. A.); Springer, **2007**, Vol. 4488, pp. 312–318.
- [196] Freire, R. O.; Da Costa, N. B.; Rocha, G. B.; Simas, A. M. *J. Chem. Theory Comput.* **2007**, *3*, 1588–1596.
- [197] Simas, A. M.; Freire, R. O.; Rocha, G. B. *J. Organomet. Chem.* **2008**, *693*, 1952–1956.
- [198] Freire, R. O.; Rocha, G. B.; Simas, A. M. *J. Braz. Chem. Soc.* **2009**, *20*, 1638–1645.
- [199] Freire, R. O.; Simas, A. M. *J. Chem. Theory Comput.* **2010**, *6*, 2019–2023.

- [200] Dutra, J. D. L.; Filho, M. A. M.; Rocha, G. B.; Freire, R. O.; Simas, A. M.; Stewart, J. J. P. *J. Chem. Theory Comput.* **2013**, *9*, 3333–3341.
- [201] Filho, M. A. M.; Dutra, J. D. L.; Rocha, G. B.; Freire, R. O.; Simas, A. M. *RSC Adv.* **2013**, *3*, 16747.
- [202] Groom, C. R.; Bruno, I. J.; Lightfoot, M. P.; Ward, S. C. *Acta Cryst. B* **2016**, *72*, 171–179.
- [203] Ásgeirsson, V.; Bauer, C. A.; Grimme, S. *Chem. Sci.* **2017**, *6*, 344–352.
- [204] Grimme, S. *Angew. Chem. Int. Ed.* **2013**, *52*, 6306–6312.
- [205] MOPAC2016, Stewart Computational Chemistry, **2016**; available from <http://OpenMOPAC.net>.
- [206] Furche, F.; Ahlrichs, R.; Hättig, C.; Klopper, W.; Sierka, M.; Weigend, F. *Wiley Interdiscip. Rev. Comput. Mol. Sci.* **2014**, *4*, 91–100.
- [207] TURBOMOLE V7.0.2 **2015**, a development of University of Karlsruhe and Forschungszentrum Karlsruhe GmbH, 1989-2007, TURBOMOLE GmbH, since 2007; available from <http://www.turbomole.com>.
- [208] Neese, F. *Wiley Interdiscip. Rev. Comput. Mol. Sci.* **2012**, *2*, 73–78.
- [209] ORCA – an ab initio, density functional and semiempirical program package, V. 4.0.0, F. Neese, MPI für Chemische Energiekonversion, Mülheim a. d. Ruhr (Germany), **2017**.
- [210] van Lenthe, E.; Baerends, E. J.; Snijders, J. G. *J. Chem. Phys.* **1993**, *99*, 4597–4610.
- [211] van Lenthe, E.; Baerends, E. J.; Snijders, J. G. *J. Chem. Phys.* **1994**, *101*, 9783–9792.
- [212] Van Wüllen, C. *J. Chem. Phys.* **1998**, *109*, 392–399.
- [213] Adamo, C.; Barone, V. *J. Chem. Phys.* **1999**, *110*, 6158–6170.
- [214] Pantazis, D. A.; Neese, F. *J. Chem. Theory Comput.* **2009**, *5*, 2229–2238.
- [215] Aravena, D.; Neese, F.; Pantazis, D. A. *J. Chem. Theory Comput.* **2016**, *12*, 1148–1156.
- [216] *Semiempirical Extended Tight-Binding Program Package xtb*, Version 4.8.0., **2017**, <https://github.com/grimme-lab/xtb>.
- [217] Imaz, I.; Rubio-Martínez, M.; An, J.; Solé-Font, I.; Rosi, N. L.; MasPOCH, D. *Chem. Commun.* **2011**, *47*, 7287.
- [218] Ma, S.; Zhou, H. C. *Chem. Commun.* **2010**, *46*, 44–53.
- [219] Sudik, A. C.; Millward, A. R.; Ockwig, N. W.; Côté, A. P.; Kim, J.; Yaghi, O. M. *J. Am. Chem. Soc.* **2005**, *127*, 7110–7118.
- [220] Talin, A. A.; Centrone, A.; Ford, A. C.; Foster, M. E.; Stavila, V.; Haney, P.; Kinney, R. A.; Szalai, V.; El Gabaly, F.; Yoon, H. P.; Léonard, F.; Allendorf, M. D. *Science* **2014**, *343*, 66–69.
- [221] Zhang, W.; Xiong, R. G. *Chem. Rev.* **2012**, *112*, 1163–1195.
- [222] Wang, J.; He, C.; Wu, P.; Wang, J.; Duan, C. *J. Am. Chem. Soc.* **2011**, *133*, 12402–12405.
- [223] Therrien, B. *Top. Curr. Chem.* **2012**, *319*, 35–55.

Bibliography

- [224] Wu, M.-X.; Yang, Y.-W. *Adv. Mater.* **2017**, *29*, 1606134.
- [225] Prakash, M. J.; Lah, M. S. *Chem. Commun.* **2009**, *129*, 3326–3341.
- [226] Furukawa, H.; Cordova, K. E.; O’Keeffe, M.; Yaghi, O. M. *Science* **2013**, *341*, 1230444.
- [227] Furukawa, H.; Kim, J.; Ockwig, N. W.; O’Keeffe, M.; Yaghi, O. M. *J. Am. Chem. Soc.* **2008**, *130*, 11650–11661.
- [228] Bursch, M.; Hansen, A.; Grimme, S. *Inorg. Chem.* **2017**, *56*, 12485–12491.
- [229] Pracht, P.; Bauer, C. A.; Grimme, S. *J. Comput. Chem.* **2017**, *38*, 2618–2631.
- [230] Pracht, P.; Wilcken, R.; Udvarhelyi, A.; Rodde, S.; Grimme, S. *J. Comput. Aided Mol. Des.* **2018**, *32*, 1139–1149.
- [231] Grimme, S. *J. Chem. Theory Comput.* **2019**, *15*, 2847–2862.
- [232] Nurttilla, S. S.; Brenner, W.; Mosquera, J.; van Vliet, K. M.; Nitschke, J. R.; Reek, J. N. *Chem. Eur. J.* **2019**, *25*, 609–620.
- [233] Berndt, J.-P.; Radchenko, Y.; Becker, J.; Logemann, C.; Bhandari, D. R.; Hrdina, R.; Schreiner, P. R. *Chem. Sci.* **2019**, *10*, 3324–3329.
- [234] Hahn, R.; Bohle, F.; Fang, W.; Walther, A.; Grimme, S.; Esser, B. *J. Am. Chem. Soc.* **2018**, *140*, 17932–17944.
- [235] Abdullin, D.; Fleck, N.; Klein, C.; Brehm, P.; Spicher, S.; Lützen, A.; Grimme, S.; Schiemann, O. *Chem. Eur. J.* **2019**, *25*, 2586–2596.
- [236] Abdullin, D.; Matsuoka, H.; Yulikov, M.; Fleck, N.; Klein, C.; Spicher, S.; Hagelueken, G.; Grimme, S.; Lützen, A.; Schiemann, O. *Chem. Eur. J.* **2019**, *25*, 8820–8828.
- [237] *Semiempirical Extended Tight-Binding Program Package xtb*, Version 6.0.0., **2019**, <https://github.com/grimme-lab/xtb>.
- [238] Staroverov, V. N.; Scuseria, G. E.; Tao, J.; Perdew, J. P. *J. Chem. Phys.* **2003**, *119*, 12129–12137.
- [239] Staroverov, V. N.; Scuseria, G. E.; Tao, J.; Perdew, J. P. *J. Chem. Phys.* **2004**, *121*, 11507.
- [240] Weigend, F.; Ahlrichs, R. *Phys. Chem. Chem. Phys.* **2005**, *7*, 3297.
- [241] Andrae, D.; Häußermann, U.; Dolg, M.; Stoll, H.; Preuß, H. *Theor. Chim. Acta* **1990**, *77*, 123–141.
- [242] Peterson, K. A.; Figgen, D.; Goll, E.; Stoll, H.; Dolg, M. *J. Chem. Phys.* **2003**, *119*, 11113–11123.
- [243] Vahtras, O.; Almlöf, J.; Feyereisen, M. W. *Chem. Phys. Lett.* **1993**, *213*, 514–518.
- [244] Eichkorn, K.; Weigend, F.; Treutler, O.; Ahlrichs, R. *Theor. Chem. Acc.* **1997**, *97*, 119–124.
- [245] Weigend, F. *Phys. Chem. Chem. Phys.* **2006**, *8*, 1057–1065.
- [246] And, M. B.; Kabrede, H. *J. Chem. Theory Comput.* **2006**,
- [247] Waller, M. P.; Braun, H.; Hojdis, N.; Bühl, M. *J. Chem. Theory Comput.* **2007**, *3*, 2234–2242.
- [248] Bühl, M.; Reimann, C.; Pantazis, D. A.; Bredow, T.; Neese, F. *J. Chem. Theory Comput.* **2008**, *4*, 1449–1459.

- [249] Weymuth, T.; Couzijn, E. P. A.; Chen, P.; Reiher, M. *J. Chem. Theory Comput.* **2014**, *10*, 3092–3103.
- [250] Iron, M. A.; Janes, T. *J. Phys. Chem. A* **2019**, *123*, 3761–3781.
- [251] Jian, Z.; Kehr, G.; Daniliuc, C. G.; Wibbeling, B.; Wiegand, T.; Siedow, M.; Eckert, H.; Bursch, M.; Grimme, S.; Erker, G. *J. Am. Chem. Soc.* **2017**, *139*, 6474–6483.
- [252] Clark Still, W.; Tempczyk, A.; Hawley, R. C.; Hendrickson, T. *J. Am. Chem. Soc.* **1990**, *112*, 6127–6129.
- [253] Hönicke, I. M.; Senkovska, I.; Bon, V.; Baburin, I. A.; Bönisch, N.; Raschke, S.; Evans, J. D.; Kaskel, S. *Angew. Chem. Int. Ed.* **2018**, *57*, 13780–13783.
- [254] Byrne, K.; Zubair, M.; Zhu, N.; Zhou, X.-P.; Fox, D. S.; Zhang, H.; Twamley, B.; Lennox, M. J.; Düren, T.; Schmitt, W. *Nat. Commun.* **2017**, *8*, 15268.
- [255] Fujita, D.; Ueda, Y.; Sato, S.; Mizuno, N.; Kumasaka, T.; Fujita, M. *Nature* **2016**, *540*, 563–566.
- [256] Käseborn, M.; Holstein, J. J.; Clever, G. H.; Lützen, A. *Angew. Chem. Int. Ed.* **2018**, *57*, 12171–12175.
- [257] Lin, Y.-S.; Li, G.-D.; Mao, S.-P.; Chai, J.-D. *J. Chem. Theory Comput.* **2013**, *9*, 263–272.
- [258] Mardirossian, N.; Head-Gordon, M. *Phys. Chem. Chem. Phys.* **2014**, *16*, 9904–9924.
- [259] Mardirossian, N.; Head-Gordon, M. *J. Chem. Phys.* **2016**, *144*, 214110.
- [260] Goerigk, L.; Grimme, S. *J. Chem. Theory Comput.* **2011**, *7*, 291–309.
- [261] Kozuch, S.; Gruzman, D.; Martin, J. M. L. *J. Phys. Chem. C* **2010**, 20801–20808.
- [262] Kozuch, S.; Martin, J. M. L. *J. Comput. Chem.* **2013**, *34*, 2327–2344.
- [263] Sperger, T.; Sanhueza, I. A.; Schoenebeck, F. *Acc. Chem. Res.* **2016**, *49*, 1311–1319.
- [264] Qu, Z. W.; Hansen, A.; Grimme, S. *J. Chem. Theory Comput.* **2015**, *11*, 1037–1045.
- [265] Hansen, A.; Bannwarth, C.; Grimme, S.; Petrović, P.; Werlé, C.; Djukic, J.-P. *ChemistryOpen* **2014**, *3*, 177–189.
- [266] Efremenko, I.; Martin, J. M. *AIP Conf. Proc.* **2019**, *2186*, 030005.
- [267] Salomon-Ferrer, R.; Case, D. A.; Walker, R. C. *Wiley Interdiscip. Rev. Comput. Mol. Sci.* **2013**, *3*, 198–210.
- [268] Zhu, X.; Lopes, P. E. M.; MacKerell, A. D. *Wiley Interdiscip. Rev. Comput. Mol. Sci.* **2012**, *2*, 167–185.
- [269] Jorgensen, W. L.; Tirado-Rives, J. *J. Am. Chem. Soc.* **1988**, *110*, 1657–1666.
- [270] Jorgensen, W. L.; Maxwell, D. S.; Tirado-Rives, J. *J. Am. Chem. Soc.* **1996**, *118*, 11225–11236.
- [271] Sobez, J.-G.; Reiher, M. *J. Chem. Inf. Model.* **2020**, *60*, 3884–3900.
- [272] Vitek, A. K.; Jugovic, T. M. E.; Zimmerman, P. M. *ACS Catal.* **2020**, *10*, 7136–7145.
- [273] Hawkins, P. C. D. *J. Chem. Inf. Model.* **2017**, *57*, 1747–1756.
- [274] Hutter, J. *Wiley Interdiscip. Rev. Comput. Mol. Sci.* **2012**, *2*, 604–612.

Bibliography

- [275] Tse, J. S. *Annu. Rev. Phys. Chem.* **2002**, *53*, 249–290.
- [276] Jinnouchi, R.; Miwa, K.; Karsai, F.; Kresse, G.; Asahi, R. *J. Phys. Chem. Lett.* **2020**, *11*, 6946–6955.
- [277] Folmsbee, D.; Hutchison, G. *Int. J. Quantum Chem.* **2021**, *121*, e26381.
- [278] Csonka, G. I.; French, A. D.; Johnson, G. P.; Stortz, C. A. *J. Chem. Theory Comput.* **2009**, *5*, 679–692.
- [279] Kruse, H.; Mladek, A.; Gkionis, K.; Hansen, A.; Grimme, S.; Sponer, J. *J. Chem. Theory Comput.* **2015**, *11*, 4972–4991.
- [280] Řezáč, J.; Bím, D.; Gutten, O.; Rulišek, L. *J. Chem. Theory Comput.* **2018**, *14*, 1254–1266.
- [281] Prasad, V.; Otero-de-la Roza, A.; DiLabio, G. *Sci. Data* **2019**, *6*, 180310.
- [282] Cavasin, A. T.; Hillisch, A.; Uellendahl, F.; Schneckener, S.; Göller, A. H. *J. Chem. Inf. Model.* **2018**, *58*, 1005–1020.
- [283] Sharapa, D. I.; Genaev, A.; Cavallo, L.; Minenkov, Y. *Chem. Phys. Chem.* **2019**, *20*, 92–102.
- [284] Minenkov, Y.; Sharapa, D. I.; Cavallo, L. *J. Chem. Theory Comput.* **2018**, *14*, 3428–3439.
- [285] TURBOMOLE V7.3.1 **2018**, a development of University of Karlsruhe and Forschungszentrum Karlsruhe GmbH, 1989-2007, TURBOMOLE GmbH, since 2007; available from <http://www.turbomole.com>.
- [286] Neese, F. *Wiley Interdiscip. Rev. Comput. Mol. Sci.* **2018**, *8*, e1327.
- [287] ORCA – an ab initio, density functional and semiempirical program package, V. 4.2.1, F. Neese, MPI für Kohlenforschung, Mülheim a. d. Ruhr (Germany), **2019**.
- [288] *Semiempirical Extended Tight-Binding Program Package xtb*, Version 6.3.1., **2020**, <https://github.com/grimme-lab/xtb>.
- [289] Grimme, S.; Hansen, A. *Angew. Chem. Int. Ed.* **2015**, *54*, 12308–12313.
- [290] Bauer, C. A.; Hansen, A.; Grimme, S. *Chem. Eur. J.* **2017**, *23*, 6150–6164.
- [291] Yu, H. S.; He, X.; Li, S. L.; Truhlar, D. G. *Chem. Sci.* **2016**, *7*, 5032–5051.
- [292] Hellweg, A.; Hättig, C.; Höfener, S.; Klopper, W. *Theor. Chem. Acc.* **2007**, *117*, 587–597.
- [293] Pavošević, F.; Peng, C.; Pinski, P.; Riplinger, C.; Neese, F.; Valeev, E. F. *J. Chem. Phys.* **2017**, *146*, 174108.
- [294] Pearson, K. *Philos. Mag.* **1901**, *2*, 559–572.
- [295] Hotelling, H. *J. Educ. Psychol.* **1933**, *24*, 417–441.
- [296] Lloyd, S. *IEEE Trans. Inf. Theorie* **1982**, *28*, 129–137.
- [297] Shao, J.; Tanner, S. W.; Thompson, N.; Cheatham, T. E. *J. Chem. Theory Comput.* **2007**, *3*, 2312–2334.
- [298] Chan, B.; Gill, P. M. W.; Kimura, M. *J. Chem. Theory Comput.* **2019**, *15*, 3610–3622.
- [299] Goerigk, L.; Grimme, S. *Wiley Interdiscip. Rev. Comput. Mol. Sci.* **2014**, *4*, 576–600.

- [300] Petrović, P.; Djukic, J. P.; Hansen, A.; Bannwarth, C.; Grimme, S. *Non-covalent Stabilization in Transition Metal Coordination and Organometallic Complexes*, in *Non-covalent Interactions in the Synthesis and Design of New Compounds*; Wiley, **2016**, pp. 115–143.
- [301] Spicher, S.; Grimme, S. *J. Phys. Chem. Lett.* **2020**, *11*, 6606–6611.
- [302] Bursch, M.; Neugebauer, H.; Grimme, S. *Angew. Chem. Int. Ed.* **2019**, *58*, 11078–11087.
- [303] Minenkov, Y.; Chermak, E.; Cavallo, L. *J. Chem. Theory Comput.* **2016**, *12*, 1542–1560.
- [304] Minenkov, Y.; Chermak, E.; Cavallo, L. *J. Chem. Theory Comput.* **2015**, *11*, 4664–4676.
- [305] Xu, X.; Truhlar, D. G. *J. Chem. Theory Comput.* **2011**, *7*, 2766–2779.
- [306] Mitzel, N. W.; Rankin, D. W. H. *Dalton Trans.* **2003**, 3650.
- [307] Blomeyer, S.; Linnemannstöns, M.; Nissen, J. H.; Paulus, J.; Neumann, B.; Stämmler, H.-G.; Mitzel, N. W. *Angew. Chem. Int. Ed.* **2017**, *56*, 13259–13263.
- [308] Klaeboe, P. *Vib. Spectrosc.* **1995**, *9*, 3–17.
- [309] Schnell, M. *Z. Phys.* **2013**, *227*, 1–21.
- [310] Li, D.; Schwabedissen, J.; Stämmler, H.-G.; Mitzel, N. W.; Willner, H.; Zeng, X. *Phys. Chem. Chem. Phys.* **2016**, *18*, 26245–26253.
- [311] van Vlijmen, H. W.; Schaefer, M.; Karplus, M. *Proteins* **1998**, *33*, 145–158.
- [312] Coutsiaris, E. A.; Seok, C.; Dill, K. A. *J. Comput. Chem.* **2004**, *25*, 1849–1857.
- [313] F. Bohle, ENSO, Mulliken Center for Theoretical Chemistry, Universität Bonn, **2020**.
- [314] Deeth, R. J.; Anastasi, A.; Diedrich, C.; Randell, K. *Coord. Chem. Rev.* **2009**, *253*, 795–816.
- [315] Brown, H. C.; Schlesinger, H. I.; Cardon, S. Z. *J. Am. Chem. Soc.* **1942**, *64*, 325–329.
- [316] Wittig, G.; Benz, E. *Chem. Ber.* **1959**, *92*, 1999–2013.
- [317] Paradies, J. *Synlett* **2013**, *24*, 777–780.
- [318] Wang, L.; Kehr, G.; Daniliuc, C. G.; Brinkkötter, M.; Wiegand, T.; Wübker, A. L.; Eckert, H.; Liu, L.; Brandenburg, J. G.; Grimme, S.; Erker, G. *Chem. Sci.* **2018**, *9*, 4859–4865.
- [319] Stephan, D. W. *J. Am. Chem. Soc.* **2015**, *137*, 10018–10032.
- [320] Stephan, D. W.; Erker, G. *Isr. J. Chem.* **2015**, *55*, 133.
- [321] Stephan, D. W. *Acc. Chem. Res.* **2015**, *48*, 306–316.
- [322] Lam, J.; Szkop, K. M.; Mosaféri, E.; Stephan, D. W. *Chem. Soc. Rev.* **2019**, *48*, 3592–3612.
- [323] Mömming, C. M.; Otten, E.; Kehr, G.; Fröhlich, R.; Grimme, S.; Stephan, D. W.; Erker, G. *Angew. Chem. Int. Ed.* **2009**, *48*, 6643–6646.

Bibliography

- [324] Ye, K. Y.; Bursch, M.; Qu, Z. W.; Daniliuc, C. G.; Grimme, S.; Kehr, G.; Erker, G. *Chem. Commun.* **2017**, *53*, 633–635.
- [325] Otten, E.; Neu, R. C.; Stephan, D. W. *J. Am. Chem. Soc.* **2009**, *131*, 9918–9919.
- [326] Grimme, S.; Kruse, H.; Goerigk, L.; Erker, G. *Angew. Chem. Int. Ed.* **2010**, *49*, 1402–1405.
- [327] Liu, L.; Lukose, B.; Ensing, B. *J. Phys. Chem. C* **2017**, *18*, 10.
- [328] Pérez, P.; Yepes, D.; Jaque, P.; Chamorro, E.; Domingo, L. R.; Rojas, R. S.; Toro-Labbé, A. *Phys. Chem. Chem. Phys.* **2015**, *17*, 10715–10725.
- [329] Jiang, B.; Zhang, Q.; Dang, L. *Org. Chem. Front.* **2018**, *5*, 1905–1915.
- [330] Villegas-Escobar, N.; Toro-Labbé, A.; Becerra, M.; Real-Enriquez, M.; Mora, J. R.; Rincon, L. *J. Mol. Model.* **2017**, *23*, 1–10.
- [331] Frömel, S.; Daniliuc, C. G.; Bannwarth, C.; Grimme, S.; Bussmann, K.; Kehr, G.; Erker, G. *Dalton Trans.* **2016**, *45*, 19230–19233.
- [332] Bannwarth, C.; Hansen, A.; Grimme, S. *Isr. J. Chem.* **2015**, *55*, 235–242.
- [333] Zhang, J.; Shao, Y.; Li, Y.; Liu, Y.; Ke, Z. *Chin. Chem. Lett.* **2018**, *29*, 1226–1232.
- [334] Heshmat, M.; Ensing, B. *J. Phys. Chem. A* **2020**, *124*, 6399–6410.
- [335] Dohm, S.; Bursch, M.; Hansen, A.; Grimme, S. *J. Chem. Theory Comput.* **2020**, *16*, 2002–2012.
- [336] Smith, A. M.; Whyman, R. *Chem. Rev.* **2014**, *114*, 5477–5510.
- [337] Schneider, H. J.; Adkins, H.; McElvain, S. M. *J. Am. Chem. Soc.* **1952**, *74*, 4287–4290.
- [338] Adkins, H.; Wojcik, B. *J. Am. Chem. Soc.* **1934**, *56*, 247.
- [339] Stein, M.; Breit, B. *Angew. Chem. Int. Ed.* **2013**, *52*, 2231–2234.
- [340] Núñez Magro, A. A.; Eastham, G. R.; Cole-Hamilton, D. J. *Chem. Commun.* **2007**, 3154–3156.
- [341] Coetzee, J.; Dodds, D. L.; Klankermayer, J.; Brosinski, S.; Leitner, W.; Slawin, A. M.; Cole-Hamilton, D. J. *Chem. Eur. J.* **2013**, *19*, 11039–11050.
- [342] Zhou, S.; Junge, K.; Addis, D.; Das, S.; Beller, M. *Angew. Chem. Int. Ed.* **2009**, *48*, 9507–9510.
- [343] Hanada, S.; Tsutsumi, E.; Motoyama, Y.; Nagashima, H. *J. Am. Chem. Soc.* **2009**, *131*, 15032–15040.
- [344] Kuwano, R.; Takahashi, M.; Ito, Y. *Tetrahedron Lett.* **1998**, *39*, 1017–1020.
- [345] Kovalenko, O. O.; Volkov, A.; Adolfsson, H. *Org. Lett.* **2015**, *17*, 446–449.
- [346] Das, S.; Addis, D.; Zhou, S.; Junge, K.; Beller, M. *J. Am. Chem. Soc.* **2010**, *132*, 4971.
- [347] Chardon, A.; Mohy El Dine, T.; Legay, R.; De Paolis, M.; Rouden, J.; Blanchet, J. *Chem. Eur. J.* **2017**, *23*, 2005–2009.
- [348] Chadwick, R. C.; Kardelis, V.; Lim, P.; Adronov, A. *J. Org. Chem.* **2014**, *79*, 7728–7733.

- [349] Huang, P. Q.; Lang, Q. W.; Wang, Y. R. *J. Org. Chem.* **2016**, *81*, 4235–4243.
- [350] Augurusa, A.; Mehta, M.; Perez, M.; Zhu, J.; Stephan, D. W. *Chem. Commun.* **2016**, *52*, 12195–12198.
- [351] Barbe, G.; Charette, A. B. *J. Am. Chem. Soc.* **2008**, *130*, 18–19.
- [352] Pelletier, G.; Bechara, W. S.; Charette, A. B. *J. Am. Chem. Soc.* **2010**, *132*, 12817–12819.
- [353] Welch, G. C.; San Juan, R. R.; Masuda, J. D.; Stephan, D. W. *Science* **2006**, *314*, 1124–1126.
- [354] Ullrich, M.; Lough, A. J.; Stephan, D. W. *J. Am. Chem. Soc.* **2009**, *131*, 52–53.
- [355] Welch, G. C.; Stephan, D. W. *J. Am. Chem. Soc.* **2007**, *129*, 1880–1881.
- [356] Tussing, S.; Greb, L.; Tamke, S.; Schirmer, B.; Muhle-Goll, C.; Luy, B.; Paradies, J. *Chem. Eur. J.* **2015**, *21*, 8056–8059.
- [357] Nicasio, J. A.; Steinberg, S.; Inés, B.; Alcarazo, M. *Chem. Eur. J.* **2013**, *19*, 11016–11020.
- [358] Tussing, S.; Kaupmees, K.; Paradies, J. *Chem. Eur. J.* **2016**, *22*, 7422–7426.
- [359] Greb, L.; Daniliuc, C. G.; Bergander, K.; Paradies, J. *Angew. Chem. Int. Ed.* **2013**, *52*, 5876–5879.
- [360] Zelli, R.; Zeinyeh, W.; Haudecoeur, R.; Alliot, J.; Boucherle, B.; Callebaut, I.; Décout, J. L. *Org. Lett.* **2017**, *19*, 6360–6363.
- [361] Lebel, H. *Thioamides*, in *Science of Synthesis* (Ed. Charette, A. B.); Wiley, **2005**, Vol. 22, pp. 141–180.
- [362] Salmon, R.; Efremov, I. V. *Oxalyl Chloride*, in *Encyclopedia of Reagents for Organic Synthesis*; Wiley, **2008**.
- [363] Greb, L.; Tussing, S.; Schirmer, B.; Oña-Burgos, P.; Kaupmees, K.; Lökov, M.; Leito, I.; Grimme, S.; Paradies, J. *Chem. Sci.* **2013**, *4*, 2788–2796.
- [364] Greb, L.; Oña-Burgos, P.; Schirmer, B.; Grimme, S.; Stephan, D. W.; Paradies, J. *Angew. Chem. Int. Ed.* **2012**, *51*, 10164–10168.
- [365] Mahdi, T.; Stephan, D. W. *J. Am. Chem. Soc.* **2014**, *136*, 15809–15812.
- [366] Scott, D. J.; Fuchter, M. J.; Ashley, A. E. *J. Am. Chem. Soc.* **2014**, *136*, 15813–15816.
- [367] Kütt, A.; Selberg, S.; Kaljurand, I.; Tshepelevitsh, S.; Heering, A.; Darnell, A.; Kaupmees, K.; Piirsalu, M.; Leito, I. *Tetrahedron Lett.* **2018**, *59*, 3738–3748.
- [368] Braun, J. V. *Ber. Dtsch. Chem. Ges.* **1904**, *37*, 3210–3213.
- [369] Bieron, J. F.; Dinan, F. J. *Rearrangement and Elimination of the Amido Group*, in *The Chemistry of Amides* (Ed. Zabicky, J.); Wiley, **1970**, pp. 245–288.
- [370] Zhao, Y.; Truhlar, D. G. *J. Phys. Chem. A* **2005**, *109*, 5656–5667.
- [371] Klamt, A. *J. Phys. Chem.* **1995**, *99*, 2224–2235.
- [372] Eckert, F.; Klamt, A. *AIChE Journal* **2002**, *48*, 369–385.
- [373] Klamt, A.; Schüürmann, G. *J. Chem. Soc., Perkin Trans. 2* **1993**, *0*, 799–805.

Bibliography

- [374] TURBOMOLE V7.2 **2017**, a development of University of Karlsruhe and Forschungszentrum Karlsruhe GmbH, 1989-2007, TURBOMOLE GmbH, since 2007; available from <http://www.turbomole.com>.
- [375] F. Eckert and A. Klamt, COSMOtherm, Version C3.0, Release 16.01; COSMOlogic GmbH & Co. KG, Leverkusen, Germany, **2016**.
- [376] Eggersdorfer, M.; Laudert, D.; Létinois, U.; McClymont, T.; Medlock, J.; Netscher, T.; Bonrath, W. *Angew. Chem. Int. Ed.* **2012**, *51*, 12960–12990.
- [377] Horner, L.; Balzer, W. D. *Tetrahedron Lett.* **1965**, *6*, 1157–1162.
- [378] Bauld, N. L.; Farr, F. J. *Am. Chem. Soc.* **1969**, *91*, 2788.
- [379] Tang, R.; Mislow, K. *J. Am. Chem. Soc.* **1969**, *91*, 5644–5645.
- [380] Naumann, K.; Zon, G.; Mislow, K. *J. Am. Chem. Soc.* **1969**, *91*, 7012–7023.
- [381] Marsi, K. L. *J. Org. Chem.* **1974**, *39*, 265–267.
- [382] Coumbe, T.; Lawrence, N. J.; Muhammad, F. *Tetrahedron Lett.* **1994**, *35*, 625–628.
- [383] Wu, H. C.; Yu, J. Q.; Spencer, J. B. *Org. Lett.* **2004**, *6*, 4675–4678.
- [384] Berthod, M.; Favre-Réguillon, A.; Mohamad, J.; Mignani, G.; Docherty, G.; Lemaire, M. *Synlett* **2007**, *2007*, 1545–1548.
- [385] Petit, C.; Favre-Reguillon, A.; Albela, B.; Bonneviot, L.; Mignani, G.; Lemaire, M. *Organometallics* **2009**, *28*, 6379–6382.
- [386] O'Brien, C. J.; Tellez, J. L.; Nixon, Z. S.; Kang, L. J.; Carter, A. L.; Kunkel, S. R.; Przeworski, K. C.; Chass, G. A. *Angew. Chem. Int. Ed.* **2009**, *48*, 6836–6839.
- [387] Li, P.; Wischert, R.; Métivier, P. *Angew. Chem. Int. Ed.* **2017**, *56*, 15989–15992.
- [388] Rajendran, K. V.; Gilheany, D. G. *Chem. Commun.* **2012**, *48*, 817–819.
- [389] Rajendran, K. V.; Gilheany, D. G. *Chem. Commun.* **2012**, *48*, 10040–10042.
- [390] Babad, H.; Zeiler, A. G. *Chem. Rev.* **1973**, *73*, 75–91.
- [391] Horner, L.; Hoffmann, H.; Beck, P. *Chem. Ber.* **1958**, *91*, 1583–1588.
- [392] Yano, T.; Hoshino, M.; Kuroboshi, M.; Tanaka, H. *Synlett* **2010**, *2010*, 801–803.
- [393] Yano, T.; Kuroboshi, M.; Tanaka, H. *Tetrahedron Lett.* **2010**, *51*, 698–701.
- [394] Tishkov, A.; Massonne, K.; Mirk, D.; Henkelmann, J.; Maase, M.; Wettling, T. *Method for Synthesizing Cyclohexyl-substituted Phosphines*; BASF SE, Ludwigshafen, US 2010/0137643 A1, **2010**.
- [395] Caputo, C. B.; Hounjet, L. J.; Dobrovetsky, R.; Stephan, D. W. *Science* **2013**, *341*, 1374–1377.
- [396] Hounjet, L. J.; Caputo, C. B.; Stephan, D. W. *Dalton Trans.* **2013**, *42*, 2629–2635.
- [397] Pérez, M.; Caputo, C. B.; Dobrovetsky, R.; Stephan, D. W. *Proc. Natl. Acad. Sci. U. S. A.* **2014**, *111*, 10917–10921.

- [398] Holthausen, M. H.; Mehta, M.; Stephan, D. W. *Angew. Chem. Int. Ed.* **2014**, *53*, 6538–6541.
- [399] Weicker, S. A.; Stephan, D. W. *Bull. Chem. Soc. Jpn.* **2015**, *88*, 1003–1016.
- [400] Holthausen, M. H.; Hiranandani, R. R.; Stephan, D. W. *Chem. Sci.* **2015**, *6*, 2016–2021.
- [401] vom Stein, T.; Pérez, M.; Dobrovetsky, R.; Winkelhaus, D.; Caputo, C. B.; Stephan, D. W. *Angew. Chem. Int. Ed.* **2015**, *54*, 10178–10182.
- [402] Blackwell, J. M.; Sonmor, E. R.; Scoccitti, T.; Piers, W. E. *Org. Lett.* **2000**, *2*, 3921–3923.
- [403] Rubin, M.; Schwier, T.; Gevorgyan, V. *J. Org. Chem.* **2002**, *67*, 1936–1940.
- [404] Hermeke, J.; Mewald, M.; Oestreich, M. *J. Am. Chem. Soc.* **2013**, *135*, 17537–17546.
- [405] Simonneau, A.; Oestreich, M. *Angew. Chem. Int. Ed.* **2013**, *52*, 11905–11907.
- [406] Greb, L.; Tamke, S.; Paradies, J. *Chem. Commun.* **2014**, *50*, 2318–2320.
- [407] Oestreich, M.; Hermeke, J.; Mohr, J. *Chem. Soc. Rev.* **2015**, *44*, 2202–2220.
- [408] Holthausen, M. H.; Bayne, J. M.; Mallov, I.; Dobrovetsky, R.; Stephan, D. W. *J. Am. Chem. Soc.* **2015**, *137*, 7298–7301.
- [409] Pérez, M.; Qu, Z.-W.; Caputo, C. B.; Podgorny, V.; Hounjet, L. J.; Hansen, A.; Dobrovetsky, R.; Grimme, S.; Stephan, D. W. *Chem. Eur. J.* **2015**, *21*, 6491–6500.
- [410] Mehta, M.; Holthausen, M. H.; Mallov, I.; Pérez, M.; Qu, Z.-W.; Grimme, S.; Stephan, D. W. *Angew. Chem. Int. Ed.* **2015**, *54*, 8250–8254.
- [411] Mehta, M.; Garcia De La Arada, I.; Perez, M.; Porwal, D.; Oestreich, M.; Stephan, D. W. *Organometallics* **2016**, *35*, 1030–1035.
- [412] Fasano, V.; LaFortune, J. H.; Bayne, J. M.; Ingleson, M. J.; Stephan, D. W. *Chem. Commun.* **2018**, *54*, 662–665.
- [413] Godfrey, S. M.; McAuliffe, C. A.; Pritchard, R. G.; Sheffield, J. M. *Chem. Commun.* **1996**, 2521–2522.
- [414] Bricklebank, N.; Godfrey, S. M.; McAuliffe, C. A.; Deplano, P.; Mercuri, M. L.; Sheffield, J. M. *J. Chem. Soc., Dalton Trans.* **1998**, 2379–2382.
- [415] Godfrey, S. M.; McAuliffe, C. A.; Mushtaq, I.; Pritchard, R. G.; Sheffield, J. M. *J. Chem. Soc., Dalton Trans.* **1998**, 3815–3818.
- [416] Godfrey, S. M.; McAuliffe, C. A.; Pritchard, R. G.; Sheffield, J. M. *Chem. Commun.* **1998**, 921–922.
- [417] Naumann, D.; Butler, H.; Gnann, R. *Z. Anorg. Allg. Chem.* **1992**, *618*, 74–76.
- [418] *Semiempirical Extended Tight-Binding Program Package xtb*, Version 5.8.0., **2018**, <https://github.com/grimme-lab/xtb>.
- [419] Sabatini, M. T.; Boulton, L. T.; Sheppard, T. D. *Sci. Adv.* **2017**, *3*, e1701028.
- [420] Zheng, K.; Hong, R. *Nat. Prod. Rep.* **2019**, *36*, 1546–1575.

Bibliography

- [421] Lin, H.; Thayer, D. A.; Wong, C.-H.; Walsh, C. T. *Chem. Biol.* **2004**, *11*, 1635–1642.
- [422] Larock, R. C. *Comprehensive Organic Transformations: A Guide to Functional Group Preparations*; Wiley, **1999**.
- [423] Cabrero-Antonino, J. R.; Adam, R.; Papa, V.; Beller, M. *Nat. Commun.* **2020**, *11*, 3893.
- [424] Cabrero-Antonino, J. R.; Alberico, E.; Junge, K.; Junge, H.; Beller, M. *Chem. Sci.* **2016**, *7*, 3432–3442.
- [425] Garg, J. A.; Chakraborty, S.; Ben-David, Y.; Milstein, D. *Chem. Commun.* **2016**, *52*, 5285–5288.
- [426] Yuan, M.-L.; Xie, J.-H.; Zhou, Q.-L. *ChemCatChem* **2016**, *8*, 3036–3040.
- [427] Papa, V.; Cabrero-Antonino, J. R.; Spannenberg, A.; Junge, K.; Beller, M. *Catal. Sci. Technol.* **2020**, *10*, 6116–6128.
- [428] Igarashi, M.; Fuchikami, T. *Tetrahedron Lett.* **2001**, *42*, 1945–1947.
- [429] Matsubara, K.; Iura, T.; Maki, T.; Nagashima, H. *J. Org. Chem.* **2002**, *67*, 4985–4988.
- [430] Hanada, S.; Ishida, T.; Motoyama, Y.; Nagashima, H. *J. Org. Chem.* **2007**, *72*, 7551–7559.
- [431] Cheng, C.; Brookhart, M. *J. Am. Chem. Soc.* **2012**, *134*, 11304–11307.
- [432] Reeves, J. T.; Tan, Z.; Marsini, M. A.; Han, Z. S.; Xu, Y.; Reeves, D. C.; Lee, H.; Lu, B. Z.; Senanayake, C. H. *Adv. Synth. Catal.* **2013**, *355*, 47–52.
- [433] Simmons, B. J.; Hoffmann, M.; Hwang, J.; Jackl, M. K.; Garg, N. K. *Org. Lett.* **2017**, *19*, 1910–1913.
- [434] Li, Y.; Molina de La Torre, J. A.; Grabow, K.; Bentrup, U.; Junge, K.; Zhou, S.; Brückner, A.; Beller, M. *Angew. Chem. Int. Ed.* **2013**, *52*, 11577–11580.
- [435] Blondiaux, E.; Cantat, T. *Chem. Commun.* **2014**, *50*, 9349–9352.
- [436] Fu, M.-C.; Shang, R.; Cheng, W.-M.; Fu, Y. *Angew. Chem. Int. Ed.* **2015**, *54*, 9042–9046.
- [437] Mukherjee, D.; Shirase, S.; Mashima, K.; Okuda, J. *Angew. Chem. Int. Ed.* **2016**, *55*, 13326–13329.
- [438] Sitte, N. A.; Bursch, M.; Grimme, S.; Paradies, J. *J. Am. Chem. Soc.* **2019**, *141*, 159–162.
- [439] Braun, J. V.; Pinkernelle, W. *Ber. dtsh. Chem. Ges. A/B* **1934**, *67*, 1218–1220.
- [440] Vaughan, W. R.; Carlson, R. D. *J. Am. Chem. Soc.* **1962**, *84*, 769–774.
- [441] Denton, R. M.; An, J.; Adeniran, B. *Chem. Commun.* **2010**, *46*, 3025–3027.
- [442] Stepen, A. J.; Bursch, M.; Grimme, S.; Stephan, D. W.; Paradies, J. *Angew. Chem. Int. Ed.* **2018**, *57*, 15253–15256.
- [443] Garcia, J.; Urpí, F.; Vilarrasa, J. *Tetrahedron Lett.* **1984**, *25*, 4841–4844.
- [444] Fairfull-Smith, K. E.; Jenkins, I. D.; Loughlin, W. A. *Org. Biomol. Chem.* **2004**, *2*, 1979–1986.
- [445] Mayer, U.; Gutmann, V.; Gerger, W. *Chem. Monthly* **1975**, *106*, 1235–1257.

- [446] Gutmann, V. *Coord. Chem. Rev.* **1976**, *18*, 225–255.
- [447] Beckett, M. A.; Strickland, G. C.; Holland, J. R.; Sukumar Varma, K. *Polymer* **1996**, *37*, 4629–4631.
- [448] Beckett, M. A.; Brassington, D. S.; Coles, S. J.; Hursthouse, M. B. *Inorg. Chem. Commun.* **2000**, *3*, 530–533.
- [449] Morgan, M. M.; Marwitz, A. J. V.; Piers, W. E.; Parvez, M. *Organometallics* **2013**, *32*, 317–322.
- [450] Sumerin, V.; Schulz, F.; Atsumi, M.; Wang, C.; Nieger, M.; Leskelä, M.; Repo, T.; Pyykkö, P.; Rieger, B. *J. Am. Chem. Soc.* **2008**, *130*, 14117–14119.
- [451] Stephan, D. W. *Org. Biomol. Chem.* **2012**, *10*, 5740–5746.
- [452] Hatnean, J. A.; Thomson, J. W.; Chase, P. A.; Stephan, D. W. *Chem. Commun.* **2013**, *50*, 301–303.
- [453] Weetman, C.; Inoue, S. *ChemCatChem* **2018**, *10*, 4213–4228.
- [454] Leitao, E. M.; Jurca, T.; Manners, I. *Nat. Chem.* **2013**, *5*, 817–829.
- [455] Hanusch, F.; Groll, L.; Inoue, S. *Chem. Sci.* **2021**, *12*, 2001–2015.
- [456] Franz, A. K.; Wilson, S. O. *J. Med. Chem.* **2013**, *56*, 388–405.
- [457] Aldridge, S.; Jones, C. *Chem. Soc. Rev.* **2016**, *45*, 763–764.
- [458] Bertrand, G. *Chem. Rev.* **2010**, *110*, 3851.
- [459] Gilliard, R. J.; Chiu, C. W. **2020**, *39*, 4123–4126.
- [460] Manners, I. *Angew. Chem. Int. Ed.* **1996**, *35*, 1602–1621.
- [461] Power, P. P. **2010**, *463*, 171–177.
- [462] Weetman, C. *Chem. Eur. J.* **2021**, *27*, 1941–1954.
- [463] Pyykkö, P. *Chem. Rev.* **1988**, *88*, 563–594.
- [464] Lee, V. Y. *Organosilicon Compounds*; Academic Press, **2017**.
- [465] Auner, N. *Verfahren zur Herstellung Silicium aus Halogensilanen*, DE Patent WO2006125425 A1, **2006**.
- [466] Hammad, A.; Amanatides, E.; Mataras, D.; Rapakoulias, D. *Thin Solid Films* **2004**, *451-452*, 255–258.
- [467] Chung, K. H.; Sturm, J. C.; Sanchez, E.; Singh, K. K.; Kuppurao, S. *Semicond. Sci. Technol.* **2007**, *22*, 158–160.
- [468] Kaczmarczyk, A.; Urry, G. *J. Am. Chem. Soc.* **1960**, *82*, 751–752.
- [469] Kaczmarczyk, A.; Millard, M.; Urry, G. *J. Inorg. Nucl. Chem.* **1961**, *17*, 186–188.
- [470] Nuss, J.; Urry, G. *J. Inorg. Nucl. Chem.* **1964**, *26*, 435–444.
- [471] Kaczmarczyk, A.; Millard, M.; Nuss, J.; Urry, G. *J. Inorg. Nucl. Chem.* **1964**, *26*, 421–425.
- [472] Urry, G. *Acc. Chem. Res.* **1970**, *3*, 306–312.
- [473] Fleming, D. K. *Acta Cryst. B* **1972**, *B28*, 1233–1236.

Bibliography

- [474] Meyer-Wegner, F.; Nadj, A.; Bolte, M.; Auner, N.; Wagner, M.; Holthausen, M. C.; Lerner, H.-W. *Chem. Eur. J.* **2011**, *17*, 4715–9.
- [475] Tillmann, J.; Meyer-Wegner, F.; Nadj, A.; Becker-Baldus, J.; Sinke, T.; Bolte, M.; Holthausen, M. C.; Wagner, M.; Lerner, H.-W. *Inorg. Chem.* **2012**, *51*, 8599–8606.
- [476] Schweizer, J. I.; Scheibel, M. G.; Diefenbach, M.; Neumeyer, F.; Würtele, C.; Kulminskaya, N.; Linser, R.; Auner, N.; Schneider, S.; Holthausen, M. C. *Angew. Chem. Int. Ed.* **2016**, *55*, 1782–1786.
- [477] Schweizer, J. I.; Meyer, L.; Nadj, A.; Diefenbach, M.; Holthausen, M. C. *Chem. Eur. J.* **2016**, *22*, 14328–14335.
- [478] Moxter, M.; Tillmann, J.; Füser, M.; Bolte, M.; Lerner, H.-W.; Wagner, M. *Chem. Eur. J.* **2016**, *22*, 16028–16031.
- [479] Orlandi, M.; Tosi, F.; Bonsignore, M.; Benaglia, M. *Org. Lett.* **2015**, *17*, 3941–3943.
- [480] Orlandi, M.; Benaglia, M.; Tosi, F.; Annunziata, R.; Cozzi, F. *J. Org. Chem.* **2016**, *81*, 3037–3041.
- [481] Zon, G.; DeBruin, E. K.; Naumann, K.; Mislow, K. *J. Am. Chem. Soc.* **1969**, *91*, 7023–7027.
- [482] Tsui, F.-P.; Vogel, T. M.; Zon, G. *J. Org. Chem.* **1975**, *40*, 761–766.
- [483] Krenske, E. H. *J. Org. Chem.* **2012**, *77*, 3969–3977.
- [484] Krenske, E. H. *J. Org. Chem.* **2012**, *77*, 1–4.
- [485] Tillmann, J.; Meyer, L.; Schweizer, J. I.; Bolte, M.; Lerner, H.-W.; Wagner, M.; Holthausen, M. C. *Chem. Eur. J.* **2014**, *20*, 9234–9239.
- [486] Choi, S. B.; Kim, B. K.; Boudjouk, P.; Grier, D. G. *J. Am. Chem. Soc.* **2001**, *123*, 8117–8118.
- [487] Dai, X.; Choi, S. B.; Braun, C. W.; Vaidya, P.; Kilina, S.; Ugrinov, A.; Schulz, D. L.; Boudjouk, P. *Inorg. Chem.* **2011**, *50*, 4047–4053.
- [488] Pokhodnya, K.; Olson, C.; Dai, X.; Schulz, D. L.; Boudjouk, P.; Sergeeva, A. P.; Boldyrev, A. I. *J. Chem. Phys.* **2011**, *134*.
- [489] Tillmann, J.; Moxter, M.; Bolte, M.; Lerner, H.-W.; Wagner, M. *Inorg. Chem.* **2015**, *54*, 9611–9618.
- [490] Tillmann, J.; Wender, J. H.; Bahr, U.; Bolte, M.; Lerner, H.-W.; Holthausen, M. C.; Wagner, M. *Angew. Chem. Int. Ed.* **2015**, *54*, 5429–5433.
- [491] Benkeser, R. A.; Hickner, R. A. *J. Am. Chem. Soc.* **1958**, *80*, 5298–5300.
- [492] Benkeser, R. A.; Smith, W. E. *J. Am. Chem. Soc.* **1968**, *90*, 5307–5309.
- [493] Benkeser, R. A. *J. Am. Chem. Soc.* **1969**, *489*, 3666–3667.
- [494] Benkeser, R. A. *Acc. Chem. Res.* **1971**, *4*, 94–100.
- [495] Cho, Y. S.; Kang, S.-H.; Han, J. S.; Yoo, B. R.; Jung, I. N. *J. Am. Chem. Soc.* **2001**, *123*, 5584–5585.
- [496] Kang, S. H.; Han, J. S.; Yoo, B. R.; Lee, M. E.; Jung, I. N. *Organometallics* **2003**, *22*, 529–534.

- [497] Jung, D. E.; Kang, S. H.; Han, J. S.; Lim, W. C.; Park, Y. W.; Yoo, B. R. *J. Organomet. Chem.* **2007**, *692*, 3901–3906.
- [498] Hong, S. H.; Hyun, S. I.; Jung, I. N.; Han, W.-S.; Kim, M.-H.; Yun, H.; Nam, S.-W.; Kang, S. O. *Organometallics* **2010**, *29*, 687–691.
- [499] Kolesnikov, S. P.; Maksimov, S. N.; Smolenskii, E. A. *Russ. Chem. Bull., Int. Ed.* **2001**, *50*, 740–742.
- [500] Appel, R. *Angew. Chem.* **1975**, *87*, 863–874.
- [501] Corey, E.; Fuchs, P. *Tetrahedron Lett.* **1972**, *13*, 3769–3772.
- [502] Vollhardt, K. P. C.; Schore, N. E. *Organische Chemie*; Wiley, **2005**.
- [503] Tillmann, J. C. *Chlorid-Induzierter Aufbau Perchlorierter Oligosilane Ausgehend Von Si₂Cl₆ oder HSiCl₃*, Dissertation, Universität Frankfurt, **2015**.
- [504] Sheikh, S. U. *J. Therm. Anal. Calorim.* **1980**, *18*, 299–306.
- [505] Nöth, H.; Wrackmeyer, B. *Nuclear Magnetic Resonance Spectroscopy of Boron Compounds* (Eds. Diehl, P.; Fluck, E.; Kosfeld, R.); Springer, **1978**.
- [506] Jansen, M.; Friede, B. *Acta Cryst. C* **1996**, *52*, 1333–1334.
- [507] Hübner, A.; Bolte, M.; Lerner, H.-W.; Wagner, M. *Angew. Chem. Int. Ed.* **2014**, *53*, 10408–10411.
- [508] Braunschweig, H.; Radacki, K.; Uttinger, K. *Inorg. Chem.* **2007**, *46*, 8796–8800.
- [509] Berger, M.; Auner, N.; Bolte, M. *Acta Cryst. C* **2014**, *70*, 1088–1091.
- [510] Grimme, S. *Chem. Eur. J.* **2012**, *18*, 9955–9964.
- [511] Foster, J. M.; Boys, S. F. *Rev. Mod. Phys.* **1960**, *32*, 300–302.
- [512] von Hopffgarten, M.; Frenking, G. *Wiley Interdiscip. Rev. Comput. Mol. Sci.* **2012**, *2*, 43–62.
- [513] Hitchcock, P. B.; Lappert, M. F.; Miles, S. J.; Thorne, A. J. *J. Chem. Soc., Chem. Commun.* **1984**, *347*, 480–482.
- [514] Goldberg, D. E.; Hitchcock, P. B.; Lappert, M. F.; Thomas, K. M.; Thorne, A. J.; Fjeldberg, T.; Haaland, A.; Schilling, B. E. *J. Chem. Soc., Dalton Trans.* **1986**, *11*, 2387–2394.
- [515] Goldberg, D. E.; Harris, D. H.; Lappert, M. F.; Thomas, K. M. *J. Chem. Soc., Chem. Commun.* **1976**, *0*, 261–262.
- [516] Fjeldberg, T.; Haaland, A.; Schilling, B. E.; Lappert, M. F.; Thorne, A. J. *J. Chem. Soc., Dalton Trans.* **1986**, 1551–1556.
- [517] Fjeldberg, T.; Haaland, A.; Lappert, M. F.; Schilling, B. E.; Seip, R.; Thorne, A. J. *J. Chem. Soc., Chem. Commun.* **1982**, 1407–1408.
- [518] Davidson, P. J.; Harris, D. H.; Lappert, M. F. *J. Chem. Soc., Dalton Trans.* **1976**, *3*, 2268–2274.
- [519] Lee, V. Y.; Sekiguchi, A. *Organometallic Compounds of Low-Coordinate Si, Ge, Sn and Pb: From Phantom Species to Stable Compounds*; Wiley, **2010**.

Bibliography

- [520] Mizuhata, Y.; Sasamori, T.; Tokitoh, N. *Chem. Rev.* **2009**, *109*, 3479–3511.
- [521] Lappert, M. F. *Main Group Metal Chemistry* **1994**, *17*, 183–208.
- [522] Weidenbruch, M.; Schlaefke, J.; Schäfer, A.; Peters, K.; von Schnering, H. G.; Marsmann, H. *Angew. Chem. Int. Ed.* **1994**, *33*, 1846–1848.
- [523] Spikes, G. H.; Peng, Y.; Fettinger, J. C.; Power, P. P. *Z. Anorg. Allg. Chem.* **2006**, *632*, 1005–1010.
- [524] Simons, R. S.; Pu, L.; Olmstead, M. M.; Power, P. P. *Organometallics* **1997**, *16*, 1920–1925.
- [525] Klinkhammer, K. W.; Schwarz, W. *Angew. Chem. Int. Ed.* **1995**, *34*, 1334–1336.
- [526] Protchenko, A. V.; Bates, J. I.; Saleh, L. M.; Blake, M. P.; Schwarz, A. D.; Kolychev, E. L.; Thompson, A. L.; Jones, C.; Mountford, P.; Aldridge, S. *J. Am. Chem. Soc.* **2016**, *138*, 4555–4564.
- [527] Rekker, B. D.; Brown, T. M.; Fettinger, J. C.; Tuononen, H. M.; Power, P. P. *J. Am. Chem. Soc.* **2012**, *134*, 6504–6507.
- [528] Rekker, B. D.; Brown, T. M.; Fettinger, J. C.; Lips, F.; Tuononen, H. M.; Herber, R. H.; Power, P. P. *J. Am. Chem. Soc.* **2013**, *135*, 10134–10148.
- [529] Hadlington, T. J.; Abdalla, J. A.; Tirfoin, R.; Aldridge, S.; Jones, C. *Chem. Commun.* **2016**, *52*, 1717–1720.
- [530] Lappert, M. F.; Slade, M. J.; Atwood, J. L.; Zaworotko, M. J. *J. Chem. Soc., Chem. Commun.* **1980**, *62*, 621–622.
- [531] Braunschweig, H.; Hitchcock, P. B.; Lappert, M. F.; Pierssens, L. J.-M. *Angew. Chem. Int. Ed.* **1994**, *33*, 1156–1158.
- [532] Babcock, J. R.; Liable-Sands, L.; Rheingold, A. L.; Sita, L. R. *Organometallics* **1999**, *18*, 4437–4441.
- [533] Hitchcock, P. B.; Hu, J.; Lappert, M. F.; Layh, M.; Severn, J. *Chem. Commun.* **1997**, *621*, 1189–1190.
- [534] Gehrhus, B.; Hitchcock, P. B.; Lappert, M. F. *Angew. Chem. Int. Ed.* **1997**, *36*, 2514–2516.
- [535] Westerhausen, M.; Greul, J.; Hausen, H. D.; Schwarz, W. *Z. Anorg. Allg. Chem.* **1996**, *622*, 1295–1305.
- [536] Harris, D. H.; Lappert, M. F. *J. Chem. Soc., Chem. Commun.* **1974**, 895–896.
- [537] Schaeffer, C. D.; Zuckerman, J. J. *J. Am. Chem. Soc.* **1974**, *96*, 7160–7162.
- [538] Stanciu, C.; Richards, A. F.; Fettinger, J. C.; Brynda, M.; Power, P. P. *J. Organomet. Chem.* **2006**, *691*, 2540–2545.
- [539] Nembenna, S.; Singh, S.; Jana, A.; Roesky, H. W.; Yang, Y.; Ye, H.; Ott, H.; Stalke, D. *Inorg. Chem.* **2009**, *48*, 2273–2276.
- [540] Dickie, D. A.; Macintosh, I. S.; Ino, D. D.; He, Q.; Labeodan, O. A.; Jennings, M. C.; Schatte, G.; Walsby, C. J.; Clyburne, J. A. *Can. J. Chem.* **2008**, *86*, 20–31.
- [541] Cetinkaya, B.; Gümürkü, I.; Lappert, M. F.; Atwood, J. L.; Shakir, R. *J. Am. Chem. Soc.* **1980**, *102*, 2088–2089.
- [542] Boyle, T. J.; Tribby, L. J.; Ottley, L. A. M.; Han, S. M. *Eur. J. Inorg. Chem.* **2009**, *2009*, 5550–5560.

- [543] Boyle, T. J.; Doan, T. Q.; Steele, L. A. M.; Apblett, C.; Hoppe, S. M.; Hawthorne, K.; Kalinich, R. M.; Sigmund, W. M. *Dalton Trans.* **2012**, *41*, 9349–9364.
- [544] Protchenko, A. V.; Birjkumar, K. H.; Dange, D.; Schwarz, A. D.; Vidovic, D.; Jones, C.; Kaltsoyannis, N.; Mountford, P.; Aldridge, S. *J. Am. Chem. Soc.* **2012**, *134*, 6500–6503.
- [545] Chorley, R. W.; Hitchcock, P. B.; Lappert, M. F. *J. Chem. Soc., Dalton Trans.* **1992**, 1451–1452.
- [546] Wang, S.; McCrea-Hendrick, M. L.; Weinstein, C. M.; Caputo, C. A.; Hoppe, E.; Fettingner, J. C.; Olmstead, M. M.; Power, P. P. *J. Am. Chem. Soc.* **2017**, *139*, 6586–6595.
- [547] Wang, S.; McCrea-Hendrick, M. L.; Weinstein, C. M.; Caputo, C. A.; Hoppe, E.; Fettingner, J. C.; Olmstead, M. M.; Power, P. P. *J. Am. Chem. Soc.* **2017**, *139*, 6596–6604.
- [548] Schiemenz, B.; Power, P. P. *Organometallics* **1996**, *15*, 958–964.
- [549] SAINT (Version 7.68 s), Bruker AXS Inc., Madison, Wisconsin, USA, **2009**.
- [550] Sheldrick, G. M. SADABS, University of Göttingen, Germany, **2012**.
- [551] Blessing, R. H. *Acta Cryst. A* **1995**, *51*, 33–38.
- [552] SHELXTL 6.1, Bruker AXS Inc., Madison, Wisconsin, USA., **2000**.
- [553] Sheldrick, G. M. *Acta Cryst. A* **2008**, *64*, 112–122.
- [554] Spek, A. L. *Acta Cryst. C* **2015**, *71*, 9–18.
- [555] Bondi, A. *J. Phys. Chem.* **1966**, *70*, 3006–3007.
- [556] Rowland, R. S.; Taylor, R. *J. Phys. Chem.* **1996**, *100*, 7384–7391.
- [557] Wegner, G. L.; Berger, R. J.; Schier, A.; Schmidbaur, H. *Organometallics* **2001**, *20*, 418–423.
- [558] Wilfling, P.; Schittelkopf, K.; Flock, M.; Herber, R. H.; Power, P. P.; Fischer, R. C. *Organometallics* **2015**, *34*, 2222–2232.
- [559] van Lenthe, E.; Snijders, J. G.; Baerends, E. J. *J. Chem. Phys.* **1996**, *105*, 6505–6516.
- [560] van Lenthe, E.; Baerends, E. J. *J. Comput. Chem.* **2003**, *24*, 1142–1156.
- [561] Schreckenbach, G.; Ziegler, T. *J. Phys. Chem.* **1995**, *99*, 606–611.
- [562] Krykunov, M.; Ziegler, T.; van Lenthe, E. *Int. J. Quantum Chem.* **2009**, *109*, 1676–1683.
- [563] Ditchfield, R. *Mol. Phys.* **1974**, *27*, 789–807.
- [564] Wolinski, K.; Hinton, J. F.; Pulay, P. *J. Am. Chem. Soc.* **1990**, *112*, 8251–8260.
- [565] Baerends, E. J. et al. ADF2016, SCM, Theoretical Chemistry, Vrije Universiteit, Amsterdam, The Netherlands, <https://www.scm.com>.
- [566] Pearson, R. G. *J. Am. Chem. Soc.* **1988**, *110*, 2092–2097.

Bibliography

- [567] Dovesi, R.; Erba, A.; Orlando, R.; Zicovich-Wilson, C. M.; Civalieri, B.; Maschio, L.; Rérat, M.; Casassa, S.; Baima, J.; Salustro, S.; Kirtman, B. *Wiley Interdiscip. Rev. Comput. Mol. Sci.* **2018**, *8*.
- [568] Erba, A.; Baima, J.; Bush, I.; Orlando, R.; Dovesi, R. *J. Chem. Theory Comput.* **2017**, *13*, 5019–5027.
- [569] Moellmann, J.; Grimme, S. *Phys. Chem. Chem. Phys.* **2010**, *12*, 8500–8504.
- [570] Pu, L.; Twamley, B.; Power, P. P. *J. Am. Chem. Soc.* **2000**, *122*, 3524–3525.
- [571] Phillips, A. D.; Wright, R. J.; Olmstead, M. M.; Power, P. P. *J. Am. Chem. Soc.* **2002**, *124*, 5930–5931.
- [572] Stender, M.; Phillips, A. D.; Wright, R. J.; Power, P. P. *Angew. Chem. Int. Ed.* **2002**, *41*, 1785–1787.
- [573] Sekiguchi, A.; Kinjo, R.; Ichinohe, M. *Science* **2004**, *305*, 1755–1757.
- [574] Wiberg, N.; Niedermayer, W.; Fischer, G.; Nöth, H.; Suter, M. *Eur. J. Inorg. Chem.* **2002**, *2002*, 1066–1070.
- [575] Wiberg, N.; Vasisht, S. K.; Fischer, G.; Mayer, P. *Z. Anorg. Allg. Chem.* **2004**, *630*, 1823–1828.
- [576] Peng, Y.; Fischer, R. C.; Merrill, W. A.; Fischer, J.; Pu, L.; Ellis, B. D.; Fettinger, J. C.; Herber, R. H.; Power, P. P. *Chem. Sci.* **2010**, *1*, 461–468.
- [577] Pu, L.; Phillips, A. D.; Richards, A. F.; Stender, M.; Simons, R. S.; Olmstead, M. M.; Power, P. P. *J. Am. Chem. Soc.* **2003**, *125*, 11626–11636.
- [578] Hadlington, T. J.; Jones, C. *Chem. Commun.* **2014**, *50*, 2321–2323.
- [579] Li, J.; Schenk, C.; Goedecke, C.; Frenking, G.; Jones, C. *J. Am. Chem. Soc.* **2011**, *133*, 18622–18625.
- [580] Hadlington, T. J.; Hermann, M.; Li, J.; Frenking, G.; Jones, C. *Angew. Chem. Int. Ed.* **2013**, *52*, 10199–10203.
- [581] Sugiyama, Y.; Sasamori, T.; Hosoi, Y.; Furukawa, Y.; Takagi, N.; Nagase, S.; Tokitoh, N. *J. Am. Chem. Soc.* **2006**, *128*, 1023–1031.
- [582] Sasamori, T.; Hironaka, K.; Sugiyama, Y.; Takagi, N.; Nagase, S.; Hosoi, Y.; Furukawa, Y.; Tokitoh, N. *J. Am. Chem. Soc.* **2008**, *130*, 13856–13857.
- [583] Murata, Y.; Ichinohe, M.; Sekiguchi, A. *J. Am. Chem. Soc.* **2010**, *132*, 16768–16770.
- [584] Ishida, S.; Sugawara, R.; Misawa, Y.; Iwamoto, T. *Angew. Chem. Int. Ed.* **2013**, *52*, 12869–12873.
- [585] Pyykkö, P. *J. Phys. Chem. A* **2015**, *119*, 2326–2337.
- [586] Kutzelnigg, W. *Angew. Chem. Int. Ed.* **1984**, *23*, 272–295.
- [587] Chen, Y.; Hartmann, M.; Diedenhofen, M.; Frenking, G. *Angew. Chem. Int. Ed.* **2001**, *40*, 2051–2055.
- [588] Takagi, N.; Nagase, S. *Organometallics* **2007**, *26*, 3627–3629.
- [589] Takagi, N.; Nagase, S. *Organometallics* **2007**, *26*, 469–471.
- [590] Jung, Y.; Brynda, M.; Power, P. P.; Head-Gordon, M. *J. Am. Chem. Soc.* **2006**, *128*, 7185–7192.
- [591] Liptrot, D. J.; Power, P. P. *Nat. Rev. Chem.* **2017**, *1*, 1–12.

- [592] Seidu, I.; Seth, M.; Ziegler, T. *Inorg. Chem.* **2013**, *52*, 8378–8388.
- [593] Pangborn, A. B.; Giardello, M. A.; Grubbs, R. H.; Rosen, R. K.; Timmers, F. J. *Organometallics* **1996**, *15*, 1518–1520.
- [594] Fulmer, G. R.; Miller, A. J.; Sherden, N. H.; Gottlieb, H. E.; Nudelman, A.; Stoltz, B. M.; Bercaw, J. E.; Goldberg, K. I. *Organometallics* **2010**, *29*, 2176–2179.
- [595] Bukhryakov, K. V.; Schrock, R. R.; Hoveyda, A. H.; Müller, P.; Becker, J. *Org. Lett.* **2017**, *19*, 2607–2609.
- [596] Rivard, E.; Fischer, R. C.; Wolf, R.; Peng, Y.; Merrill, W. A.; Schley, N. D.; Zhu, Z.; Pu, L.; Fettingner, J. C.; Teat, S. J.; Nowik, I.; Herber, R. H.; Takagi, N.; Nagase, S.; Power, P. P. *J. Am. Chem. Soc.* **2007**, *129*, 16197–16208.
- [597] Hino, S.; Olmstead, M.; Phillips, A. D.; Wright, R. J.; Power, P. P. *Inorg. Chem.* **2004**, *43*, 7346–7352.
- [598] Hicks, J.; Juckel, M.; Paparo, A.; Dange, D.; Jones, C. *Organometallics* **2018**, *37*, 4810–4813.
- [599] Sheldrick, G. M. SADABS, University of Göttingen, Germany, **1996**.
- [600] Sheldrick, G. M. TWINABS, University of Göttingen, Germany, **2012**.
- [601] Sheldrick, G. M. *Acta Cryst. A* **2015**, *71*, 3–8.
- [602] Sheldrick, G. M. *Acta Cryst. C* **2015**, *71*, 3–8.
- [603] ORCA – an ab initio, density functional and semiempirical program package, V. 4.1.0, F. Neese, MPI für Kohlenforschung, Mülheim a. d. Ruhr (Germany), **2018**.
- [604] *Semiempirical Extended Tight-Binding Program Package xtb*, Version 6.1.0., **2019**, <https://github.com/grimme-lab/xtb>.
- [605] Glendening, E. D.; Badenhoop, J. K.; Reed, A. E.; Carpenter, J. E.; Bohmann, J. A.; Morales, C. M.; Landis, C. R.; Weinhold, F. NBO6, Theoretical Chemistry Institute, University of Wisconsin, **2013**.
- [606] Tao, J.; Perdew, J. P.; Staroverov, V. N.; Scuseria, G. E. *Phys. Rev. Lett.* **2003**, *91*, 146401.
- [607] Becke, A. D. *J. Chem. Phys.* **1993**, *98*, 5648–5652.
- [608] Stephens, P. J.; Devlin, F. J.; Chabalowski, C. F.; Frisch, M. J. *J. Phys. Chem.* **1994**, *98*, 11623–11627.
- [609] Klamt, A.; Jonas, V.; Bürger, T.; Lohrenz, J. C. *J. Phys. Chem. A* **1998**, *102*, 5074–5085.
- [610] Grimme, S.; Bannwarth, C. *J. Chem. Phys.* **2016**, *145*, 54103.
- [611] Grimme, S. *J. Chem. Phys.* **2013**, *138*, 244104.
- [612] Bannwarth, C.; Grimme, S. *Comput. Theor. Chem.* **2014**, *1040-1041*, 45–53.
- [613] Pu, L.; Twamley, B.; Power, P. P. *Organometallics* **2000**, *19*, 2874–2881.
- [614] Weiß, S.; Auer, M.; Eichele, K.; Schubert, H.; Wesemann, L. *Organometallics* **2019**, *38*, 417–423.
- [615] Schneider, J.; Sindlinger, C. P.; Eichele, K.; Schubert, H.; Wesemann, L. *J. Am. Chem. Soc.* **2017**, *139*, 6542–6545.

Bibliography

- [616] Preut, H.; Huber, F. *Z. Anorg. Allg. Chem.* **1976**, *419*, 92–96.
- [617] Klinkhammer, K. *Polyhedron* **2002**, *21*, 587–598.
- [618] *Calculation of NMR and EPR Parameters* (Eds. Kaupp, M.; Bühl, M.; Malkin, V. G.); Wiley, **2004**.
- [619] Tossell, J. A.; Lazzeretti, P. *J. Chem. Phys.* **1986**, *84*, 369–374.
- [620] Cheeseman, J. R.; Trucks, G. W.; Keith, T. A.; Frisch, M. J. *J. Chem. Phys.* **1996**, *104*, 5497–5509.
- [621] Casanovas, J.; Illas, F.; Pacchioni, G. *Chem. Phys. Lett.* **2000**, *326*, 523–529.
- [622] van Wüllen, C. *Phys. Chem. Chem. Phys.* **2000**, *2*, 2137–2144.
- [623] Stoychev, G. L.; Auer, A. A.; Izsak, R.; Neese, F. *J. Chem. Theory Comput.* **2018**, *14*, 619–637.
- [624] Zhao, Y.; Truhlar, D. G. *J. Phys. Chem. A* **2008**, *112*, 6794–6799.
- [625] Gregor, T.; Mauri, F.; Car, R. *J. Chem. Phys.* **1999**, *111*, 1815–1822.
- [626] Heine, T.; Goursot, A.; Seifert, G.; Weber, J. *J. Phys. Chem. A* **2001**, *105*, 620–626.
- [627] Corminbœuf, C.; Heine, T.; Weber, J. *Chem. Phys. Lett.* **2002**, *357*, 1–7.
- [628] Alam, T. M.; Henry, M. *Phys. Chem. Chem. Phys.* **2000**, *2*, 23–28.
- [629] Auer, D.; Kaupp, M.; Strohmann, C. *Organometallics* **2004**, *23*, 3647–3655.
- [630] van der Boon, L. J. P.; Hendriks, J. H.; Roolvink, D.; O’Kennedy, S. J.; Lutz, M.; Slootweg, J. C.; Ehlers, A. W.; Lammertsma, K. *Eur. J. Inorg. Chem.* **2019**, *2019*, 3318–3328.
- [631] Arz, M. I.; Geiß, D.; Straßmann, M.; Schnakenburg, G.; Filippou, A. C. *Chem. Sci.* **2015**, *6*, 6515–6524.
- [632] Poblador-Bahamonde, A. I.; Poteau, R.; Raynaud, C.; Eisenstein, O. *Dalton Trans.* **2011**, *40*, 11321–11326.
- [633] Autschbach, J.; Sutter, K.; Truflandier, L. A.; Brendler, E.; Wagler, J. *Chem. Eur. J.* **2012**, *18*, 12803–12813.
- [634] Truflandier, L. A.; Brendler, E.; Wagler, J.; Autschbach, J. *Angew. Chem. Int. Ed.* **2011**, *50*, 255–259.
- [635] Karni, M.; Apeloig, Y.; Takagi, N.; Nagase, S. *Organometallics* **2005**, *24*, 6319–6330.
- [636] Du, V. A.; Stipicic, G. N.; Schubert, U. *Eur. J. Inorg. Chem.* **2011**, *2011*, 3365–3373.
- [637] Boese, A. D.; Handy, N. C. *J. Chem. Phys.* **2001**, *114*, 5497–5503.
- [638] Zhang, C.; Patschinski, P.; Stephenson, D. S.; Panisch, R.; Wender, J. H.; Holthausen, M. C.; Zipse, H. *Phys. Chem. Chem. Phys.* **2014**, *16*, 16642–16650.
- [639] Fedorov, S.; Rusakov, Y. Y.; Krivdin, L. *Russ. J. Org. Chem.* **2017**, *53*, 643–651.
- [640] te Velde, G.; Bickelhaupt, F. M.; Baerends, E. J.; Fonseca Guerra, C.; van Gisbergen, S. J. A.; Snijders, J. G.; Ziegler, T. *J. Comput. Chem.* **2001**, *22*, 931–967.
- [641] ADF 2019.3, SCM, Theoretical Chemistry, Vrije Universiteit, Amsterdam, The Netherlands, <http://www.scm.com>.

- [642] *Semiempirical Extended Tight-Binding Program Package xtb*, Version 6.3.3., 2020, <https://github.com/grimme-lab/xtb>.
- [643] Barone, V.; Cossi, M. *J. Phys. Chem. A* **1998**, *102*, 1995–2001.
- [644] Jensen, F. *J. Chem. Theory Comput.* **2015**, *11*, 132–138.
- [645] Tatewaki, H.; Huzinaga, S. *J. Comput. Chem.* **1980**, *1*, 205–228.
- [646] Jensen, F. *J. Chem. Phys.* **2001**, *115*, 9113–9125.
- [647] Dunning, T. H. *J. Chem. Phys.* **1989**, *90*, 1007–1023.
- [648] Peterson, K. A. *J. Chem. Phys.* **2003**, *119*, 11099–11112.
- [649] Peterson, K. A.; Figgen, D.; Goll, E.; Stoll, H.; Dolg, M. *J. Chem. Phys.* **2003**, *119*, 11113–11123.
- [650] Neese, F.; Wennmohs, F.; Hansen, A.; Becker, U. *Chem. Phys.* **2009**, *356*, 98–109.
- [651] Wolff, S. K.; Ziegler, T.; van Lenthe, E.; Baerends, E. J. *J. Chem. Phys.* **1999**, *110*, 7689–7698.
- [652] Pantazis, D. A.; Chen, X. Y.; Landis, C. R.; Neese, F. *J. Chem. Theory Comput.* **2008**, *4*, 908–919.
- [653] Pantazis, D. A.; Neese, F. *Theor. Chem. Acc.* **2012**, *131*, 1–7.
- [654] Pye, C. C.; Ziegler, T. *Theor. Chem. Acc.* **1999**, *101*, 396–408.
- [655] Perdew, J. P.; Burke, K.; Ernzerhof, M. *Phys. Rev. Lett.* **1996**, *77*, 3865–3868.
- [656] Zhang, Y.; Yang, W. *Phys. Rev. Lett.* **1998**, *80*, 890.
- [657] Handy, N. C.; Cohen, A. J. *Mol. Phys.* **2001**, *99*, 403–412.
- [658] Perdew, J. P. *Phys. Rev. B* **1986**, *33*, 8822–8824.
- [659] Becke, A. D. *Phys. Rev. A* **1988**, *38*, 3098–3100.
- [660] Perdew, J. P.; Ruzsinszky, A.; Csonka, G. I.; Constantin, L. A.; Sun, J. *Phys. Rev. Lett.* **2009**, *103*, 026403.
- [661] Perdew, J. P.; Ruzsinszky, A.; Csonka, G. I.; Constantin, L. A.; Sun, J. *Phys. Rev. Lett.* **2011**, *106*, 179902.
- [662] Zhao, Y.; Truhlar, D. G. *J. Chem. Phys.* **2006**, *125*, 194101.
- [663] Keal, T. W.; Tozer, D. J. *J. Chem. Phys.* **2003**, *119*, 3015–3024.
- [664] Sun, J.; Ruzsinszky, A.; Perdew, J. P. *Phys. Rev. Lett.* **2015**, *115*, 036402.
- [665] Lee, C.; Yang, W.; Parr, R. G. *Phys. Rev. B* **1988**, *37*, 785–789.
- [666] Yanai, T.; Tew, D. P.; Handy, N. C. *Chem. Phys. Lett.* **2004**, *393*, 51–57.
- [667] Boese, A. D.; Martin, J. M. *J. Chem. Phys.* **2004**, *121*, 3405–3416.
- [668] Zhao, Y.; Truhlar, D. G. *Theor. Chem. Acc.* **2008**, *120*, 215–241.
- [669] Kozuch, S.; Martin, J. M. L. *Phys. Chem. Chem. Phys.* **2011**, *13*, 20104.

Bibliography

- [670] Santra, G.; Sylvetsky, N.; Martin, J. M. *J. Phys. Chem. A* **2019**, *24*, 5129–5143.
- [671] Kozuch, S.; Gruzman, D.; Martin, J. M. *J. Phys. Chem. C* **2010**, *114*, 20801–20808.
- [672] Karton, A.; Tarnopolsky, A.; Lamère, J. F.; Schatz, G. C.; Martin, J. M. *J. Phys. Chem. A* **2008**, *112*, 12868–12886.
- [673] Schwabe, T.; Grimme, S. *Phys. Chem. Chem. Phys.* **2006**, *8*, 4398–4401.
- [674] Tomasi, J.; Persico, M. *Chem. Rev.* **1994**, *94*, 2027–2094.
- [675] Perdew, J. P.; Ruzsinszky, A.; Tao, J.; Staroverov, V. N.; Scuseria, G. E.; Csonka, G. I. *J. Chem. Phys.* **2005**, *123*, 062201.
- [676] Allen, M. J.; Keal, T. W.; Tozer, D. J. *Chem. Phys. Lett.* **2003**, *380*, 70–77.
- [677] Arz, M. I.; Strassmann, M.; Geiss, D.; Schnakenburg, G.; Filippou, A. C. *J. Am. Chem. Soc.* **2016**, *138*, 4589–4600.
- [678] Kira, M.; Ishida, S.; Iwamoto, T.; Kabuto, C. *J. Am. Chem. Soc.* **1999**, *121*, 9722–9723.
- [679] Latypov, S. K.; Polyancev, F. M.; Yakhvarov, D. G.; Sinyashin, O. G. *Phys. Chem. Chem. Phys.* **2015**, *17*, 6976–6987.
- [680] Rablen, P. R.; Pearlman, S. A.; Finkbiner, J. *J. Phys. Chem. A* **1999**, *103*, 7357–7363.
- [681] Jain, R.; Bally, T.; Rablen, P. R. *J. Org. Chem.* **2009**, *74*, 4017–4023.
- [682] Aliev, A. E.; Courtier-Murias, D.; Zhou, S. *J. Mol. Struct: THEOCHEM* **2009**, *893*, 1–5.
- [683] Konstantinov, I. A.; Broadbelt, L. J. *J. Phys. Chem. A* **2011**, *115*, 12364–12372.
- [684] Iron, M. A. *J. Chem. Theory Comput.* **2017**, *13*, 5798–5819.
- [685] Rusakov, Y. Y.; Rusakova, I. L.; Krivdin, L. B. *Int. J. Quantum Chem.* **2016**, *116*, 1404–1412.
- [686] Vícha, J.; Novotný, J.; Straka, M.; Repisky, M.; Ruud, K.; Komorovsky, S.; Marek, R. *Phys. Chem. Chem. Phys.* **2015**, *17*, 24944–24955.
- [687] Vaara, J.; Mannunen, P.; Lantto, P. *Perturbational and ECP Calculation of Relativistic Effects in NMR Shielding and Spin-Spin Coupling*, in *Calculation of NMR and EPR Parameters* (Eds. Kaupp, M.; Bühl, M.; Malkin, V. G.); Wiley, **2004**, pp. 209–226.
- [688] Autschbach, J. *Calculating NMR Chemical Shifts and J-Couplings for Heavy Element Compounds*, in *Encyclopedia of Analytical Chemistry: Applications, Theory and Instrumentation* (Ed. Meyers, R. A.); Wiley, **2006**, pp. 1–14.
- [689] Vícha, J.; Novotný, J.; Komorovsky, S.; Straka, M.; Kaupp, M.; Marek, R. *Chem. Rev.* **2020**, *120*, 7065–7103.
- [690] Hrobárik, P.; Hrobáriková, V.; Greif, A. H.; Kaupp, M. *Angew. Chem. Int. Ed.* **2012**, *51*, 10884–10888.
- [691] Saue, T. *ChemPhysChem* **2011**, *12*, 3077–3094.

- [692] Filippou, A. C.; Baars, B.; Chernov, O.; Lebedev, Y. N.; Schnakenburg, G. *Angew. Chem. Int. Ed.* **2014**, *53*, 565–570.
- [693] Sola, E.; Garcia-Camprubí, A.; Andrés, J. L.; Martín, M.; Plou, P. *J. Am. Chem. Soc.* **2010**, *132*, 9111–9121.
- [694] Stoychev, G. L.; Auer, A. A.; Neese, F. *J. Chem. Theory Comput.* **2018**, *14*, 4756–4771.
- [695] Mahadevi, A. S.; Sastry, G. N. *Chem. Rev.* **2013**, *113*, 2100–2138.
- [696] Biedermann, F.; Schneider, H. J. *Chem. Rev.* **2016**, *116*, 5216–5300.
- [697] Schneider, H. J. *Angew. Chem. Int. Ed.* **2009**, *48*, 3924–3977.
- [698] Varadwaj, P. R.; Varadwaj, A.; Marques, H. M.; Yamashita, K. *Sci. Rep.* **2019**, *9*, 1–29.
- [699] Otero de la Roza, A.; DiLabio, G. A. *Non-Covalent Interactions in Quantum Chemistry and Physics: Theory and Applications*; Elsevier, **2017**.
- [700] Lehn, J.-M. *Supramolecular Chemistry: Concepts and Perspectives*; Wiley, **1995**.
- [701] Steed, J. W.; Atwood, J. L. *Supramolecular Chemistry*; Wiley, **2000**.
- [702] Gleiter, R.; Haberhauer, G.; Werz, D. B.; Rominger, F.; Bleiholder, C. *Chem. Rev.* **2018**, *118*, 2010–2041.
- [703] Wonner, P.; Dreger, A.; Vogel, L.; Engelage, E.; Huber, S. M. *Angew. Chem. Int. Ed.* **2019**, *58*, 16923–16927.
- [704] Bleiholder, C.; Werz, D. B.; Köppel, H.; Gleiter, R. *J. Am. Chem. Soc.* **2006**, *128*, 2666–2674.
- [705] Bleiholder, C.; Gleiter, R.; Werz, D. B.; Köppel, H. *Inorg. Chem.* **2007**, *46*, 2249–2260.
- [706] Gilday, L. C.; Robinson, S. W.; Barendt, T. A.; Langton, M. J.; Mullaney, B. R.; Beer, P. D. *Chem. Rev.* **2015**, *115*, 7118–7195.
- [707] Bulfield, D.; Huber, S. M. *Chem. Eur. J.* **2016**, *22*, 14434–14450.
- [708] Cavallo, G.; Metrangolo, P.; Milani, R.; Pilati, T.; Priimagi, A.; Resnati, G.; Terraneo, G. *Chem. Rev.* **2016**, *116*, 2478–2601.
- [709] Hunter, C. A.; Sanders, J. K. *J. Am. Chem. Soc.* **1990**, *112*, 5525–5534.
- [710] Riley, K. E.; Hobza, P. *Acc. Chem. Res.* **2013**, *46*, 927–936.
- [711] Wagner, J. P.; Schreiner, P. R. *Angew. Chem. Int. Ed.* **2015**, *54*, 12274–12296.
- [712] Saha, S.; Desiraju, G. R. *Chem. Eur. J.* **2017**, *23*, 4936–4943.
- [713] Wang, H.; Bisoyi, H. K.; Urbas, A. M.; Bunning, T. J.; Li, Q. *Chem. Eur. J.* **2019**, *25*, 1369–1378.
- [714] Scilabra, P.; Terraneo, G.; Resnati, G. *Acc. Chem. Res.* **2019**, *52*, 1313–1324.
- [715] Werz, D. B.; Gleiter, R.; Rominger, F. *J. Org. Chem.* **2002**, *67*, 4290–4297.
- [716] Werz, D. B.; Gleiter, R.; Rominger, F. *Organometallics* **2003**, *22*, 843–849.
- [717] Werz, D. B.; Gleiter, R.; Rominger, F. *J. Org. Chem.* **2004**, *69*, 2945–2952.

Bibliography

- [718] Dumele, O.; Schreib, B.; Warzok, U.; Trapp, N.; Schalley, C. A.; Diederich, F. *Angew. Chem. Int. Ed.* **2017**, *56*, 1152–1157.
- [719] Lee, L. M.; Tsemperouli, M.; Poblador-Bahamonde, A. I.; Benz, S.; Sakai, N.; Sugihara, K.; Matile, S. *J. Am. Chem. Soc.* **2019**, *141*, 810–814.
- [720] DeCicco, R. C.; Luo, L.; Goroff, N. S. *Acc. Chem. Res.* **2019**, *52*, 2080–2089.
- [721] Vanderkooy, A.; Gupta, A. K.; Földes, T.; Lindblad, S.; Orthaber, A.; Pápai, I.; Erdélyi, M. *Angew. Chem. Int. Ed.* **2019**, *58*, 9012–9016.
- [722] Benz, S.; Poblador-Bahamonde, A. I.; Low-Ders, N.; Matile, S. *Angew. Chem. Int. Ed.* **2018**, *57*, 5408–5412.
- [723] Breugst, M.; von der Heiden, D. *Chem. Eur. J.* **2018**, *24*, 9187–9199.
- [724] Chan, Y. C.; Yeung, Y. Y. *Org. Lett.* **2019**, *21*, 5665–5669.
- [725] Jungbauer, S. H.; Huber, S. M. *J. Am. Chem. Soc.* **2015**, *137*, 12110–12120.
- [726] Yatham, V. R.; Harnying, W.; Kootz, D.; Neudörfl, J. M.; Schlörer, N. E.; Berkessel, A. *J. Am. Chem. Soc.* **2016**, *138*, 2670–2677.
- [727] Wonner, P.; Vogel, L.; Düser, M.; Gomes, L.; Kniep, F.; Mallick, B.; Werz, D. B.; Huber, S. M. *Angew. Chem. Int. Ed.* **2017**, *56*, 12009–12012.
- [728] Saito, M.; Kobayashi, Y.; Tsuzuki, S.; Takemoto, Y. *Angew. Chem. Int. Ed.* **2017**, *56*, 7653–7657.
- [729] Reany, O.; Li, A.; Yefet, M.; Gilson, M. K.; Keinan, E. *J. Am. Chem. Soc.* **2017**, *139*, 8138–8145.
- [730] Wuttke, A.; Mata, R. A. *J. Comput. Chem.* **2017**, *38*, 15–23.
- [731] Werner, H. J.; Knowles, P. J.; Knizia, G.; Manby, F. R.; Schütz, M. *Wiley Interdiscip. Rev. Comput. Mol. Sci.* **2012**, *2*, 242–253.
- [732] MOLPRO, version 2015.1, a package of ab initio programs, see <http://www.molpro.net>.
- [733] *Semiempirical Extended Tight-Binding Program Package xtb*, Version 6.2.1., **2019**, <https://github.com/grimme-lab/xtb>.
- [734] Grimme, S.; Hujo, W.; Kirchner, B. *Phys. Chem. Chem. Phys.* **2012**, *14*, 4875–4883.
- [735] Schneider, W. B.; Bistoni, G.; Sparta, M.; Saitow, M.; Riplinger, C.; Auer, A. A.; Neese, F. *J. Chem. Theory Comput.* **2016**, *12*, 4778–4792.
- [736] Bistoni, G. *Wiley Interdiscip. Rev. Comput. Mol. Sci.* **2020**, *10*, e1442.
- [737] Karton, A.; Martin, J. M. *J. Chem. Phys.* **2012**, *136*, 124114.
- [738] Liakos, D. G.; Guo, Y.; Neese, F. *J. Phys. Chem. A* **2020**, *124*, 90–100.
- [739] Jeziors, B.; Robert, I.; Szalewicz, K. *Chem. Rev.* **1994**, *94*, 1887–1930.
- [740] Lu, Q.; Neese, F.; Bistoni, G. *Phys. Chem. Chem. Phys.* **2019**, *21*, 11569–11577.

- [741] Altun, A.; Neese, F.; Bistoni, G. *J. Chem. Theory Comput.* **2019**, *15*, 215–228.
- [742] Carpenter, J. E.; Weinhold, F. *J. Am. Chem. Soc.* **1988**, *110*, 368–372.
- [743] Weinhold, F.; Glendening, E. D. *J. Phys. Chem. A* **2017**, *2017*, 121.
- [744] Nemes, C. T.; Laconsay, C. J.; Galbraith, J. M. *Phys. Chem. Chem. Phys.* **2018**, *20*, 20963–20969.
- [745] Szatyłowicz, H.; Sadlej-Sosnowska, N. *J. Chem. Inf. Model* **2010**, *50*, 2151–2161.
- [746] Szatyłowicz, H.; Jezierska, A.; Sadlej-Sosnowska, N. *Struct. Chem.* **2016**, *27*, 367–376.
- [747] Nepal, B.; Scheiner, S. *Chem. Phys. Lett.* **2015**, *630*, 6–11.
- [748] Miehllich, B.; Savin, A.; Stoll, H.; Preuss, H. *Chem. Phys. Lett.* **1989**, *157*, 200–206.
- [749] Athiyarath, V.; Sureshan, K. M. *Angew. Chem. Int. Ed.* **2019**, *58*, 612–617.
- [750] Mohanrao, R.; Sureshan, K. M. *Angew. Chem. Int. Ed.* **2018**, *57*, 12435–12439.
- [751] Hema, K.; Sureshan, K. M. *Angew. Chem. Int. Ed.* **2019**, *58*, 2754–2759.
- [752] Hema, K.; Gonnade, R. G.; Sureshan, K. M. *Angew. Chem. Int. Ed.* **2020**, *59*, 2897–2903.
- [753] Hema, K.; Sureshan, K. M. *Acc. Chem. Res.* **2019**, *52*, 3149–3163.
- [754] Schäfer, A.; Horn, H.; Ahlrichs, R. *J. Chem. Phys.* **1992**, *97*, 2571–2577.
- [755] Plessow, P. *J. Chem. Theory Comput.* **2013**, *9*, 1305–1310.
- [756] Zimmerman, P. M. *J. Chem. Phys.* **2013**, *138*, 184102.
- [757] Zimmerman, P. M. *J. Chem. Theory Comput.* **2013**, *9*, 3043–3050.
- [758] F. Eckert and A. Klamt, COSMOtherm, Version C3.0, Release 17.01; COSMOlogic GmbH & Co. KG, Leverkusen, Germany, **2017**.
- [759] *Semiempirical Extended Tight-Binding Program Package xtb*, Version 5.8.1., **2018**, <https://github.com/grimme-lab/xtb>.
- [760] Pettersen, E. F.; Goddard, T. D.; Huang, C. C.; Couch, G. S.; Greenblatt, D. M.; Meng, E. C.; Ferrin, T. E. *J. Comput. Chem.* **2004**, *25*, 1605–1612.
- [761] *Semiempirical Extended Tight-Binding Program Package xtb*, Version 6.2.2., **2019**, <https://github.com/grimme-lab/xtb>.
- [762] Rappoport, D.; Furche, F. *J. Chem. Phys.* **2010**, *133*, 134105.
- [763] Macrae, C. F.; Edgington, P. R.; McCabe, P.; Pidcock, E.; Shields, G. P.; Taylor, R.; Towler, M.; Van De Streek, J. *J. Appl. Crystallogr.* **2006**, *39*, 453–457.
- [764] Macrae, C. F.; Bruno, I. J.; Chisholm, J. A.; Edgington, P. R.; McCabe, P.; Pidcock, E.; Rodriguez-Monge, L.; Taylor, R.; van de Streek, J.; Wood, P. A. *J. Appl. Crystallogr.* **2008**, *41*, 466–470.
- [765] Ryckaert, J.-P.; Ciccotti, G.; Berendsen, H. J. *J. Comput. Phys.* **1977**, *23*, 327–341.

Bibliography

- [766] van Gunsteren, W.; Berendsen, H. J. *Mol. Phys.* **1977**, *34*, 1311–1327.
- [767] Wakita, K.; Tokitoh, N.; Okazaki, R.; Nagase, S. *Angew. Chem. Int. Ed.* **2000**, *39*, 634–636.
- [768] Takeda, N.; Shinohara, A.; Tokitoh, N. *Organometallics* **2002**, *21*, 4024–4026.
- [769] Takeda, N.; Shinohara, A.; Tokitoh, N. *Organometallics* **2002**, *21*, 256–258.
- [770] Han, J. S.; Sasamori, T.; Mizuhata, Y.; Tokitoh, N. *Dalton Trans.* **2010**, *39*, 9238.
- [771] Abersfelder, K.; White, A. J. P.; Rzepa, H. S.; Scheschkewitz, D. *Science* **2010**, *327*, 564–566.
- [772] Hong, J. H.; Boudjouk, P. *J. Am. Chem. Soc.* **1993**, *115*, 5883–5884.
- [773] Stueger, H.; Hasken, B.; Haas, M.; Rausch, M.; Fischer, R.; Torvisco, A. *Organometallics* **2014**, *33*, 231–239.
- [774] Omatsu, Y.; Mizuhata, Y.; Tokitoh, N. *Z. Anorg. Allg. Chem.* **2018**, *644*, 930–934.
- [775] Hengge, E.; Jenkner, P. K. *Z. Anorg. Allg. Chem.* **1991**, *606*, 97–104.
- [776] Li, J.; Zhong, M.; Keil, H.; Zhu, H.; Herbst-Irmer, R.; Stalke, D.; De, S.; Koley, D.; Roesky, H. W. *Chem. Commun.* **2019**, *55*, 2360–2363.
- [777] Akasaka, N.; Ishida, S.; Iwamoto, T. *Inorganics* **2018**, *6*, 107.
- [778] Zhang, C.; Patschinski, P.; Stephenson, D. S.; Panisch, R.; Wender, J. H.; Holthausen, M. C.; Zipse, H. *Phys. Chem. Chem. Phys.* **2014**, *16*, 16642–16650.
- [779] Junold, K.; Baus, J. A.; Burschka, C.; Auerhammer, D.; Tacke, R. *Chem. Eur. J.* **2012**, *18*, 16288–16291.
- [780] Du, V. A.; Stipicic, G. N.; Schubert, U. *Eur. J. Inorg. Chem.* **2011**, *2011*, 3365–3373.
- [781] Wagler, J.; Böhme, U.; Brendler, E.; Blaurock, S.; Roewer, G. *Z. Anorg. Allg. Chem.* **2005**, *631*, 2907–2913.
- [782] Helmer, B. J.; West, R.; Corriu, R.; Poirier, M.; Royo, G.; De Saxce, A. *J. Organomet. Chem.* **1983**, *251*, 295–298.
- [783] Jutzi, P. *Science* **2004**, *305*, 849–851.
- [784] Iwamoto, T.; Sato, K.; Ishida, S.; Kabuto, C.; Kira, M. *J. Am. Chem. Soc.* **2006**, *128*, 16914–16920.
- [785] Ishida, S.; Iwamoto, T.; Kabuto, C.; Kira, M. *Nature* **2003**, *421*, 725–727.
- [786] Sekiguchi, A. *Science* **2004**, *305*, 1755–1757.
- [787] Gau, D.; Kato, T.; Saffon-Merceron, N.; De Cózar, A.; Cossío, F. P.; Baceiredo, A. *Angew. Chem. Int. Ed.* **2010**, *49*, 6585–6588.
- [788] Sarkar, D.; Wendel, D.; Ahmad, S. U.; Szilvási, T.; Pöthig, A.; Inoue, S. *Dalton Trans.* **2017**, *46*, 16014–16018.
- [789] Abersfelder, K.; Güclü, D.; Scheschkewitz, D. *Angew. Chem. Int. Ed.* **2006**, *45*, 1643–1645.
- [790] Tsurusaki, A.; Kamiyama, J.; Kyushin, S. *J. Am. Chem. Soc.* **2014**, *136*, 12896–12898.
- [791] Uchiyama, K.; Nagendran, S.; Ishida, S.; Iwamoto, T.; Kira, M. *J. Am. Chem. Soc.* **2007**, *129*, 10638–10639.

- [792] Cowley, M. J.; Ohmori, Y.; Huch, V.; Ichinohe, M.; Sekiguchi, A.; Scheschkewitz, D. *Angew. Chem. Int. Ed.* **2013**, *52*, 13247–13250.
- [793] Arz, M. I.; Straßmann, M.; Geiß, D.; Schnakenburg, G.; Filippou, A. C. *J. Am. Chem. Soc.* **2016**, *138*, 4589–4600.
- [794] Mitra, A.; Brodovitch, J.-C.; Krempner, C.; Percival, P. W.; Vyas, P.; West, R. *Angew. Chem. Int. Ed.* **2010**, *49*, 2893–2895.
- [795] Denk, M.; Lennon, R.; Hayashi, R.; West, R.; Belyakov, A. V.; Verne, H. P.; Haaland, A.; Wagner, M.; Metzler, N. *J. Am. Chem. Soc.* **1994**, *116*, 2691–2692.
- [796] Kira, M.; Ishida, S.; Iwamoto, T.; Kabuto, C. *J. Am. Chem. Soc.* **1999**, *121*, 9722–9723.
- [797] Rekken, B. D.; Brown, T. M.; Fettingner, J. C.; Tuononen, H. M.; Power, P. P. *J. Am. Chem. Soc.* **2012**, *134*, 6504–6507.
- [798] Gehrhus, B.; Lappert, M. F.; Heinicke, J.; Boese, R.; Bläser, D. *J. Chem. Soc., Chem. Commun.* **1995**, 1931–1932.
- [799] Takeda, N.; Suzuki, H.; Tokitoh, N.; Okazaki, R.; Nagase, S. *J. Am. Chem. Soc.* **1997**, *119*, 1456–1457.
- [800] Filippou, A. C.; Baars, B.; Chernov, O.; Lebedev, Y. N.; Schnakenburg, G. *Angew. Chem. Int. Ed.* **2014**, *53*, 565–570.
- [801] Takanashi, K.; Lee, V. Y.; Ichinohe, M.; Sekiguchi, A. *Angew. Chem. Int. Ed.* **2006**, *45*, 3269–3272.
- [802] Iwamoto, T.; Masuda, H.; Kabuto, C.; Kira, M. *Organometallics* **2005**, *24*, 197–199.
- [803] Sugahara, T.; Sasamori, T.; Tokitoh, N. *Angew. Chem. Int. Ed.* **2017**, *56*, 9920–9923.
- [804] Junold, K.; Burschka, C.; Bertermann, R.; Tacke, R. *Dalton Trans.* **2010**, *39*, 9401.
- [805] Filippou, A. C.; Chernov, O.; Schnakenburg, G. *Angew. Chem. Int. Ed.* **2009**, *48*, 5687–5690.
- [806] Ganesamoorthy, C.; Schoening, J.; Wölper, C.; Song, L.; Schreiner, P. R.; Schulz, S. *Nat. Chem.* **2020**, *12*, 608–614.
- [807] Xiong, Y.; Yao, S.; Driess, M. *Dalton Trans.* **2009**, 421–423.
- [808] Filippou, A. C.; Hoffmann, D.; Schnakenburg, G. *Chem. Sci.* **2017**, *8*, 6290–6299.
- [809] Filippou, A. C.; Chernov, O.; Stumpf, K. W.; Schnakenburg, G. *Angew. Chem. Int. Ed.* **2010**, *49*, 3296–3300.
- [810] Ghana, P.; Arz, M. I.; Chakraborty, U.; Schnakenburg, G.; Filippou, A. C. *J. Am. Chem. Soc.* **2018**, *140*, 7187–7198.
- [811] Ghana, P.; Arz, M. I.; Schnakenburg, G.; Straßmann, M.; Filippou, A. C. *Organometallics* **2018**, *37*, 772–780.
- [812] Tanabe, M.; Jiang, J.; Yamazawa, H.; Osakada, K.; Ohmura, T.; Suginome, M. *Organometallics* **2011**, *30*, 3981–3991.
- [813] Suh, H.-W.; Balcells, D.; Edwards, A. J.; Guard, L. M.; Hazari, N.; Mader, E. A.; Mercado, B. Q.; Repisky, M. *Inorg. Chem.* **2015**, *54*, 11411–11422.

Bibliography

- [814] Ehrlich, L.; Gericke, R.; Brendler, E.; Wagler, J. *Inorganics* **2018**, *6*, 119.
- [815] Rodriguez, R.; Contie, Y.; Gau, D.; Saffon-Merceron, N.; Miqueu, K.; Sotiropoulos, J.-M.; Baceiredo, A.; Kato, T. *Angew. Chem. Int. Ed.* **2013**, *52*, 8437–8440.
- [816] Filippou, A. C.; Lebedev, Y. N.; Chernov, O.; Straßmann, M.; Schnakenburg, G. *Angew. Chem. Int. Ed.* **2013**, *52*, 6974–6978.
- [817] Li, Y.; Chan, Y.-C.; Li, Y.; Purushothaman, I.; De, S.; Parameswaran, P.; So, C.-W. *Inorg. Chem.* **2016**, *55*, 9091–9098.
- [818] Dysard, J. M.; Tilley, T. D. *J. Am. Chem. Soc.* **1998**, *120*, 8245–8246.
- [819] Woo, H. G.; Heyn, R. H.; Tilley, T. D. *J. Am. Chem. Soc.* **1992**, *114*, 5698–5707.
- [820] Fukuda, T.; Yoshimoto, T.; Hashimoto, H.; Tobita, H. *Organometallics* **2016**, *35*, 921–924.
- [821] Yoshimoto, T.; Hashimoto, H.; Hayakawa, N.; Matsuo, T.; Tobita, H. *Organometallics* **2016**, *35*, 3444–3447.
- [822] Berry, D. H.; Chey, J. H.; Zipin, H. S.; Carroll, P. J. *J. Am. Chem. Soc.* **1990**, *112*, 452–453.
- [823] Hayes, P. G.; Xu, Z.; Beddie, C.; Keith, J. M.; Hall, M. B.; Tilley, T. D. *J. Am. Chem. Soc.* **2013**, *135*, 11780–11783.
- [824] Sola, E.; García-Camprubí, A.; Andrés, J. L.; Martín, M.; Plou, P. *J. Am. Chem. Soc.* **2010**, *132*, 9111–9121.
- [825] Lee, Y.-J.; Lee, J.-D.; Kim, S.-J.; Ko, J.; Suh, I.-H.; Cheong, M.; Kang, S. O. *Organometallics* **2004**, *23*, 135–143.
- [826] Nakata, N.; Kato, N.; Sekizawa, N.; Ishii, A. *Inorganics* **2017**, *5*, 72.
- [827] Mitton, S. J.; McDonald, R.; Turculet, L. *Organometallics* **2009**, *28*, 5122–5136.
- [828] Baus, J. A.; Mück, F. M.; Bertermann, R.; Tacke, R. *Eur. J. Inorg. Chem.* **2016**, *2016*, 4867–4871.
- [829] Watanabe, C.; Inagawa, Y.; Iwamoto, T.; Kira, M. *Dalton Trans.* **2010**, *39*, 9414.
- [830] Sangtrirutnugul, P.; Tilley, T. D. *Organometallics* **2008**, *27*, 2223–2230.
- [831] Theil, M.; Jutzi, P.; Neumann, B.; Stammler, A.; Stammler, H.-G. *Organometallics* **2000**, *19*, 2937–2940.
- [832] Nguyen, T.-I.; Scheschkewitz, D. *J. Am. Chem. Soc.* **2005**, *127*, 10174–10175.
- [833] Kendall, R. A.; Früchtl, H. A. *Theor. Chem. Acc.* **1997**, *97*, 158–163.

Acknowledgment

Finally, I would like to thank many people without whom this work would not have been possible.

In particular, I would like to thank my PhD supervisor Prof. Dr. Stefan Grimme, who gave me great freedom from the very beginning to participate in many exciting projects and for the constant scientific and financial support. He warmly welcomed me into his research group at a point where my scientific future was more than uncertain.

Further, I would like to thank Prof. Dr. Thomas Bredow for taking over the second review of my thesis and the fruitful feedback as my mentor in the Bonn International Graduate School of Chemistry (BIGS Chemistry) program.

I thank my colleagues, first of all Dr. Christoph Bannwarth as a long-time office colleague and role model, Dr. Rebecca Sure, Dr. Gerit Brandenburg, Fabian Bohle, Sebastian Dohm, Sebastian Spicher, Hagen Neugebauer, Jeroen Koopman, Dr. Jakob Seibert, Dr. Eike Caldeweyher, Philipp Pracht, Julius Stüeckrath, Thomas Gasevic, Sebastian Ehlert, Dr. Jan Mewes, Leonard Maurer, and Jana Pisarek for the pleasant years, fruitful cooperation and the one or other heated discussion.

I further thank Dr. Christoph Bannwarth, Jeroen Koopman, Sebastian Spicher, and Dr. Jakob Seibert for proof reading parts of this thesis.

Furthermore, I would like to thank the numerous international collaborators for all the exciting projects and the pleasant cooperation during the last years. Here I would like to thank Prof. Dr. Gerhard Erker, Prof. Dr. Jan Paradies, Prof. Dr. Matthias Wagner, Prof. Dr. Philipp P. Power, Prof. Dr. Daniel B. Werz, Prof. Dr. John M. Lupton, Prof. Dr. Jack R. Norton, Prof. Dr. Malcolm E. Kenney and Prof. Dr. Lutz Ackermann in particular.

I am also grateful for the opportunity to work with and the pleasant conversations with Prof. Dr. Sergey A. Katsyuba during his stays in Bonn as well as for the steady technical and administrative support by Jens Mekelburger, Dr. Werner Reckien and Claudia Kronz.

Moreover, I would like to thank Dr. Andreas Hansen in particular for his constant friendly and academic support.

And last but not least, I thank from the bottom of my heart my family and my girlfriend, who have supported me unconditionally all these years.